DOE/NV/25946--247

Nevada Test Site–Directed Research and Development

FY 2006 Report

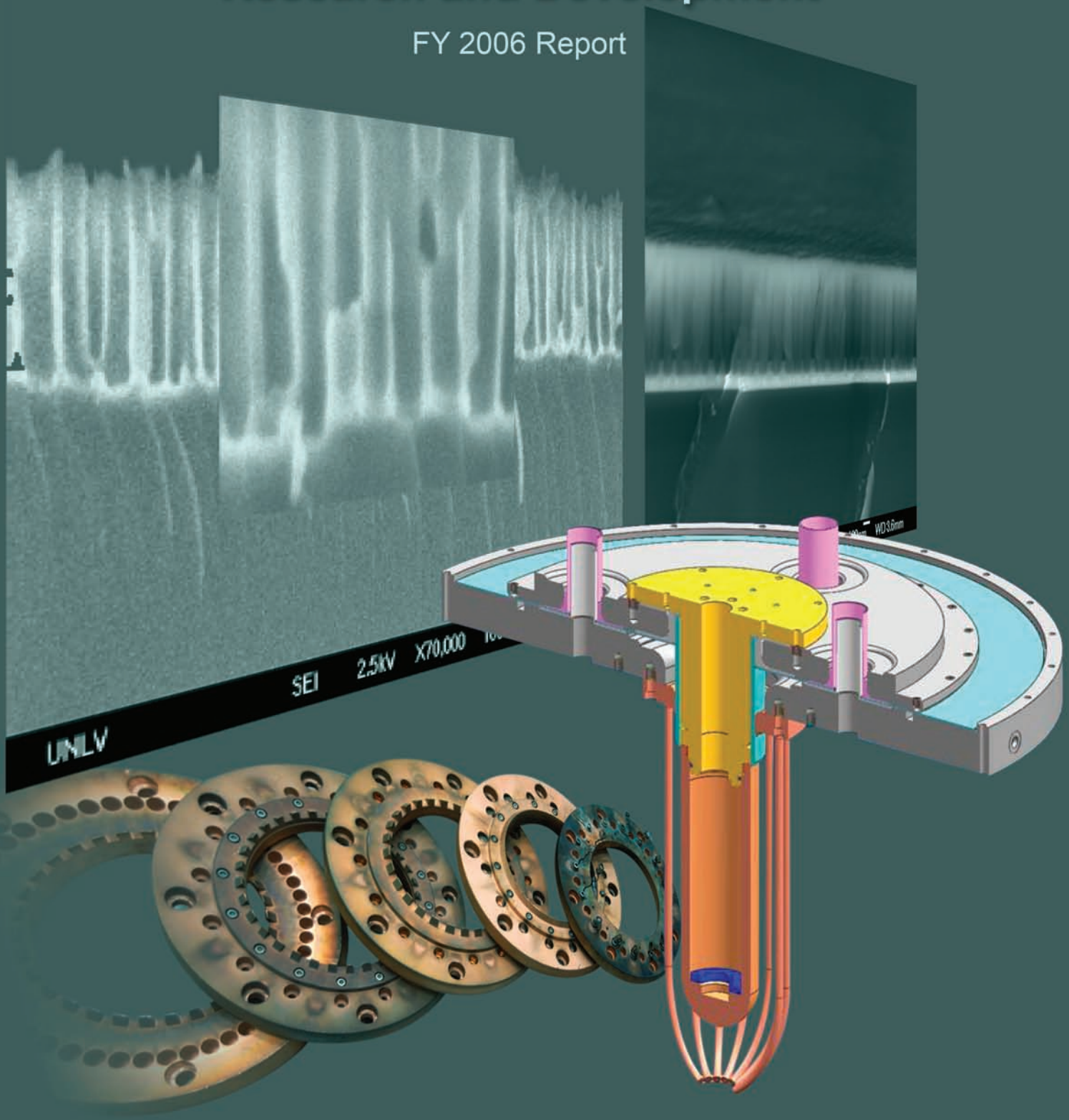

Site Directed R&D SDRD

This work was supported by the U.S. Department of Energy, National Nuclear Security Administration, Nevada Site Office, under Contract No. DE-AC52-06NA25946.

Report Date: August 2007

Disclaimer

Availability Statement

Available for sale to the public from—

U.S. Department of Commerce
National Technical Information Service
5285 Port Royal Road
Springfield, VA, 22161-0002
Telephone: 800.553.6847
Fax: 703.605.6900
E-mail: orders@ntis.gov
Online Ordering: http://www.ntis.gov/ordering.htm

Available electronically at http://www.osti.gov/bridge

Available for a processing fee to U.S. Department of Energy and its contractors, in paper, from—

U.S. Department of Energy
Office of Scientific and Technical Information
P.O. Box 62
Oak Ridge, TN 37831-0062
Telephone: 865.576.8401
Fax: 865.576.5728
E-mail: reports@adonis.osti.gov

DOE/NV/25946--247

Nevada Test Site–Directed Research and Development

FY 2006 Report

This work was supported by the U.S. Department of Energy, National Nuclear Security Administration Nevada Site Office, under Contract No. DE-AC52-06NA25946.

Report Date: **August 2007**

Detectors and Sensors

Electronics

Photonics

this page intentionally left blank

SDRD FY 2006

The Nevada Test Site–Directed Research and Development (SDRD) program completed its fifth successful year of research and development activities in FY 2006. Forty new projects were selected for funding this year, and ten FY 2005 projects were brought to conclusion. The total funds expended by the SDRD program were $6 million, for an average per-project cost of $120 thousand. Beginning in May, 2006 programmatic burden rates were applied to SDRD project costs. An external audit conducted in September 2006 verified that appropriate accounting practices were applied to the SDRD program. Highlights for the year included: the filing of 27 invention disclosures for intellectual property generated by FY 2006 projects; programmatic adoption of four FY 2005 SDRD-developed technologies; participation in the tri-Lab Laboratory Directed Research and Development (LDRD) and SDRD program review that was broadly attended by NTS, NNSA, LDRD, and U.S. Department of Homeland Security representatives; peer reviews of all FY 2006 projects; and the successful completion of 50 R&D projects, as presented in this report.

In response to a company-wide call, authors throughout the NTS complex submitted 132 proposals for FY 2006 SDRD projects. The SDRD program has seen a dramatic increase in the yearly total of submitted proposals—from 69 in FY 2002 to 132 this year—even as the size of the program has remained fairly constant. The quantity and quality of these submissions helped ensure a strongly competitive program and provided a diverse set of innovative ideas, making project selection both challenging and rewarding. Proposals were evaluated for technical merit, including such factors as innovation, probability of success, potential benefit, and mission applicability. Authors and reviewers benefited from the use of a shortfalls list entitled the "NTS Technology Needs Assessment" that was compiled from NTS, National Weapons Laboratory, and NNSA sources. This tool proved to be of considerable value in aligning the SDRD program with mission priorities, and it is expected that the NTS Technology Needs Assessment will continue to be updated and expanded in future years. The 50 projects selected for FY 2006 showcase a wealth of creative approaches to innovative technical research with high potential payoff. These endeavors benefited from an impressive cross section of resources and capabilities, and addressed development needs in a variety of technologies, with potential applications to a broad selection of programmatic activities.

Several metrics have been selected and tracked as indicators of the overall effectiveness of the SDRD program at developing innovative solutions to NTS mission technology requirements. A compilation of these metrics appears in Figure 1. Since the introduction of the SDRD program, more than 90% of the inventions disclosed to the contractor's Intellectual Property office have been generated in the pursuit of SDRD projects. The number of invention disclosures filed (blue bars in Figure 1) has increased steadily and significantly each year to an all-time high of 27 in FY 2006—a clear indicator of both the increase in the innovative quality of selected projects and a cultural sea change in the value attached to intellectual property. The red bars in Figure 1 represent a histogram of the number of projects from a particular fiscal year in which developed technologies were subsequently picked up by programs. In some cases, demonstrated feasibility was sufficient to encourage further

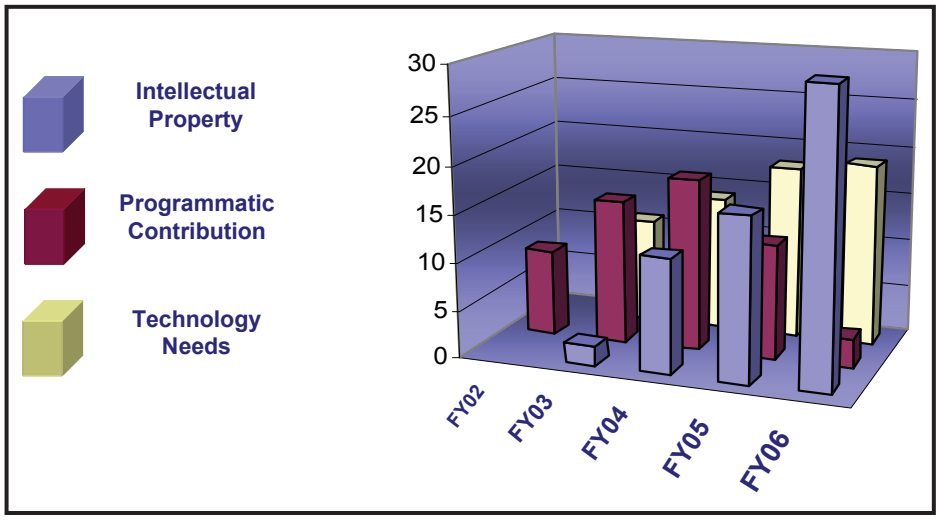

research. In other cases, technology innovation has been directly incorporated into new or existing instrumentation or software. It often requires some period of time for SDRD success stories to be communicated to programmatic decision makers, and for funding decisions to be made to implement these technologies. This lag time is evident in the lower number of implemented FY 2006 technologies and by the fact that the data show increases in numbers for all years each time the metric is revised. The third metric shown in Figure 1 indicates how well the SDRD program is strategically aligned with the NTS mission. Each year the NTS Technology Needs Assessment is updated with the most current technology development requirements, as foretold by NNSA strategic plans and management, NTS contractor managers and technical staff, and National Weapons Laboratory management and staff. In the annual process of revising this document, which identifies anticipated technology needs currently under development as well as the gaps that still need addressing, the number of prior year gaps since addressed by SDRD-funded projects are tabulated. These addressed needs are represented by the yellow bars in Figure 1.

This final program report covers SDRD project activities that occurred from October 2005 through September 2006. The numerous achievements it describes are a tribute to the skill and enthusiasm Principal Investigators brought to their individual projects. While many of the R&D efforts drew to successful and natural conclusions, some spawned follow-on work that may lead to further research. The desired result of all SDRD activities is to develop and/or refine technologies that are implemented by programs. Some of the following project reports clearly identify R&D efforts with those kinds of results. Others, best characterized as feasibility studies, resulted in negative findings—the entirely valid conclusion, often reached in the pursuit of "high-risk" research—that a particular technology is currently impractical. Both types of results help move NSTec toward a more vital technology base by identifying technologies that can be directly related to our programmatic mission.

In conclusion, FY 2006 saw continued evolution of a strong, innovative R&D program that benefited from increased competitiveness and a maturation of the planning and management techniques vital to aligning SDRD with anticipated needs for future NTS mission requirements.

I would like to extend a very special thank you to the editing team of Katharine Streeton, Heidi Utz, and Michele Vochosky, for compiling, editing, and publishing this report; to Project Controls Engineer Pat Herrin, for her valuable contributions to tracking progress and costs on the array of FY 2006 projects; to Kim Liu-Bacon and her team for compiling the financial data necessary to fulfill congressionally mandated reporting requirements; and to NTS technical site representatives Howard Bender, Chris Hagen, Steve Iversen, Warnick Kernan, and Bill Nishimura, for helping implement and manage a very productive year of R&D at the NTS!

Wil Lewis, SDRD Program Manager

this page intentionally left blank

Los Alamos Operations (LAO)
P.O. Box 809
Los Alamos, New Mexico 87544

Livermore Operations (LO)
P.O. Box 2710
Livermore, California 94551-2710

Nevada Test Site (NTS)
P.O. Box 98521
Las Vegas, Nevada 89193-8521

North Las Vegas (NLV)
P.O. Box 98521
North Las Vegas, Nevada 89193-8521

Remote Sensing Laboratory – Andrews Air Force Base (RSL–A)
P.O. Box 380
Suitland, Maryland 20752-0108
(Andrews Air Force Base)

Remote Sensing Laboratory – Nellis Air Force Base (RSL–N)
P.O. Box 98521
Las Vegas, Nevada 89193-8521
(Nellis Air Force Base)

Special Technologies Laboratory (STL)
5520-B Ekwill Street
Santa Barbara, California 93111

this page intentionally left blank

A

AC	alternating current
AChE	acetylcholinesterase
ADC	adaptive down conversion or analog-to-digital converter
AFRL	Air Force Research Laboratory
AlInGaP	aluminium indium gallium phosphide
AMS	accelerator mass spectrometry
AR	anti-reflective (coating)

B

BGO	$Bi_4Ge_3O_{12}$, bismuth germanate
BiMOSFET	bipolar metal-oxide semiconductor field effect transistor
BNL	Brookhaven National Laboratory
BuChE	butyrylcholinesterase

C

CAD	computer-aided design
CCD	charge-coupled device
ChE	cholinesterase
CNT	carbon nanotube
COTS	commercial off-the-shelf

D

DAQ_	data acquisition (system)
DARHT	dual-axis radiographic hydrodynamic test facility
DC	direct current
D-D	deuterium-deuterium
D-T	deuterium-tritium
DEM	digital elevation model
DHS	U.S. Department of Homeland Security
DMC	detector modeling capability
DMD	digital mirror device
DNDO	Domestic Nuclear Detection Office (U.S. Department of Homeland Security)
DoD	U.S. Department of Defense
DOE	U.S. Department of Energy
DPF	dense plasma focus

DPFA	dense plasma focus accelerator
DQE	detective quantum efficiency
DSLR	digital single-lens reflex
DTRA	U.S. Defense Threat Reduction Agency

E

EASLM	electrically addressed spatial light modulator
EDFA	erbium-doped fiber amplifier
EIMS	electron impact mass spectrometry
EMI	electromagnetic interference
EMP	electromagnetic pulse
EO	electro-optic
EOS	equation of state
ESF	edge-spread function
ET	equivalent time

F

FFT	fast Fourier transform
FORTE	Fast Onboard Recording of Transient Experiment (data)
FORTRAN	IBM Mathematical Formula Translating System [computer programming language]
FOV	field of view
FQY	fluorescence quantum yielf
FTIR	Fourier transform infrared spectroscopy
FWHM	full-width at half-maximum

G

GC	gross counts
GDMS	glow discharge mass spectrometry
GLV	grating light valve
GPS	Global Positioning System
GSM	Global System for Mobile Communication (System)

H

H	horizontal
HBT	Hilbert transform–based technique

I

ICF	inertial-confinement fusion
IDL	Interactive Data Language [software package]
IEEE	Institute of Electrical and Electronics Engineers
InGaN	indium gallium nitride
IP	image plate (phosphor systems)
IR	infrared
ITO	indium-tin-oxide

L

LA	laser ablation
LA-ICPMS	laser ablation–inductively coupled plasma mass spectrometry
LA-MC-ICPMS	laser ablation multicollector inductively coupled plasma mass spectrometry
LANL	Los Alamos National Laboratory
LAO	Los Alamos Operations (NSTec)
LBNL	Lawrence Berkeley National Laboratory
LC	liquid crystal
LCP	left-circular polarization
LCSLM	liquid crystal spatial light modulator
LED	light-emitting diode
LiF	lithium fluoride
LIFI/S	laser-induced fluorescence imaging spectroscopy
LIMS	laser ionization mass spectrometry
LLD	lower lever discriminator
LLNL	Lawrence Livermore National Laboratory
LO	Livermore Operations (NSTec)
LOS	line of sight
LPADC	low-power, analog-to-digital converter
LPL	Long Pulse Lab (LO)
LSO	lutetium oxyorthosilicate

M

MACS	Multiple Application Computer Systems
MCA	multichannel analyzer
MCNP	Monte Carlo N-Particle [transport code]
MCNP MCTAL	MCNP tally result [file format]
MCNPX	Monte Carlo N-Particle Extended version [transport code]
MCP	microchannel plate
MCPI	microchannel plate intensifier

MEMS	microelectromechanical systems
MFP	microfiber plate(s)
MHD	magnetohydrodynamic
MIXS	multi-imaging x-ray streak (camera)
MNRC	McClellan Nuclear Radiation Center
MOSFET	metal-oxide semiconductor field-effect transistor
MPS	Multiple Platform Systems
MS	mass spectrometry or mass spectrometer
MSE	multiscale entropy (extraction)
MSP	microsphere plate(s)
MTF	modulation transfer function
M-Z	Mach-Zehnder

N

NaI	sodium iodide
NASA	National Aeronautics and Space Administration
ND	neutral density (filter)
Nd:YAG	neodymium:yttrium-aluminum-garnet [laser]
NFG	novel fiber geometry
NIF	National Ignition Facility
NiO	nickel oxide
NIST	National Institute of Standards and Technology
NLV	North Las Vegas Operations (NSTec)
NNSA	U.S. Department of Energy, National Nuclear Security Administration
NREL	U.S. Department of Energy, National Renewable Energy Laboratory
NSLS	National Synchrotron Light Source
NSTec	National Security Technologies, LLC
NTS	Nevada Test Site
NVT	Nyquist Violation Technology

O

OP	organophosphates
OPH	organophosphorus hydrolase

P

PCB	printed circuit board
PCMCIA	Personal Computer Memory Card International Association
PDV	photonic Doppler velocimetry
PEM	photoelectromagnetic

PFD	proximity-focused diode
PFP	polyfluoro-alt-phenylene
PHA	pulse-height analysis
PIMS	Penning ionization mass spectrometry
PIPS	passivated implanted planar silicon
PMT	photomultiplier tube
POx	paraoxon
PPXS	parallel pulse-height x-ray spectrometer
PSF	point spread function

Q

QCC	Quadratic Compression Conversion
QE	quantum efficiency

R

R&D	research & development
RC	resistor-capacitor
RCP	right-circular polarization
RF	radio frequency
RIID	radioisotope identification device
RIMS	resonance ionization mass spectrometry
RITS	radiographic integrated test stand
RSL	Remote Sensing Laboratory (NSTec)
RSL–A	Remote Sensing Laboratory – Andrews Air Force Base
RSL–N	Remote Sensing Laboratory – Nellis Air Force Base

S

SDD	silicon drift detector
SEM	scanning electron miscroscopy
SLM	spatial light modulator
SNL	Sandia National Laboratories
SNM	special nuclear material
SNR	signal-to-noise ratio
SPL	Short Pulse Lab (LO)
SPRT	sequential probability ratio test
SRIM	stopping and range of ions in matter [code]
SSB	single sideband
SSMS	spark source mass spectrometry
STL	Special Technologies Laboratory (NSTec)

T

2-D	two-dimensional
3-D	three-dimensional
TCP/IP	Transmission Control Protocol/Internet Protocol
TIMS	thermal ionization mass spectrometry
TSF	Teflon-scintillator-filled
T-T	tritium-tritium

U

UCLA	University of California, Los Angeles
UCSB	University of California, Santa Barbara
UNLV	University of Nevada, Las Vegas
UNR	University of Nevada, Reno
URA	uniformly redundant array
USAF	U.S. Air Force
USB	universal serial bus [interface]
USRP	Universal Software Radio Peripheral
UV	ultraviolet
UV Vis	ultraviolet-visible spectroscopy or spectrophotometry

V

V	vertical
VDC	volts of direct current
VISAR	velocity interferometer system for any reflector
VUV	vacuum ultraviolet [ring]

X

XML	extensible mark-up language
XPS	x-ray photoelectron spectrometry
XRD	x-ray diode

Z

ZnO	zinc oxide

Accelerators and Pulsed Power

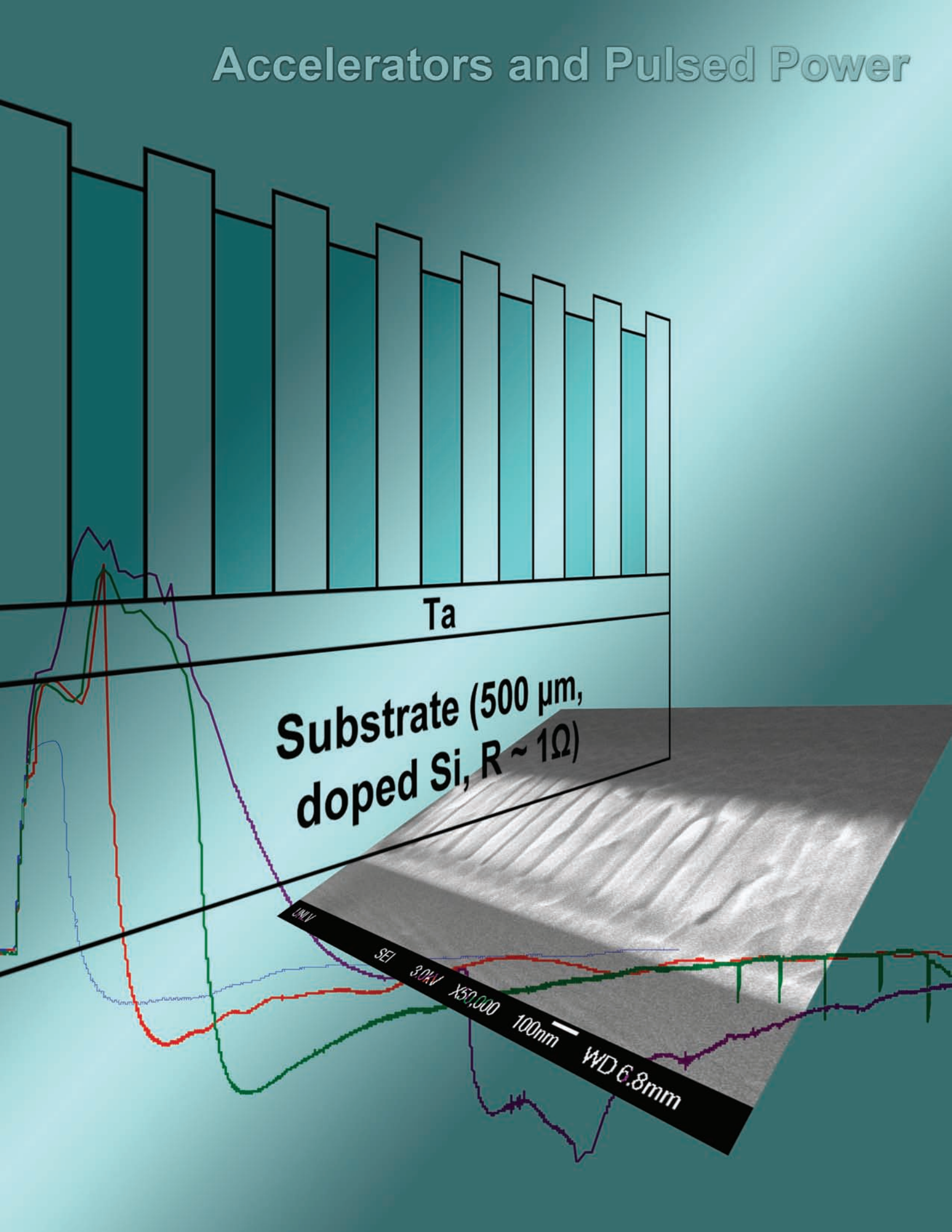

Resonance Shadowgraphy

Gene Capelle,[1] *Roderick Tiangco*
Special Technologies Laboratory

Our team developed an experimental setup consisting of a plume generator, a tunable laser illumination system, and a CCD–based detection system. This setup successfully yielded a resonance shadowgraph image. This report describes the experimental setup and presents shadowgraph results and suggestions for apparatus improvement.

Background

In equipment such as Sandia's Z and RITS machines, an intense, focused e-beam is driven into high-Z targets to produce x-rays for radiographic imaging. However, with this type of machine or diode, plasmas form on both the anode and cathode. Such plasmas in turn affect the produced x-ray dose and its effective source size (a larger source size results in lower resolution x-ray images). To mitigate this effect, we sought to better understand plasma formation, time evolution, and behavior.

Typical plasma measurement techniques using lasers (such as shadowgraphy and/or photography) are generally limited to densities $>10^{16}/cm^3$. Densities earlier in the e-beam pulse, when the plasma has already begun to interact with the e-beam, are $\leq 10^{15}/cm^3$, and hence, a challenge to directly measure. We proposed to make a shadowgraphy image of a plume using a laser wavelength tuned to an atomic or ionic resonance absorption line of one of the species in the plasma cloud. Normal shadowgraphy depends primarily on the scattering of light out of the laser beam to produce a shadow image (shadowgraph). However, when the laser is tuned to resonance, a resonant absorption term will remove additional light from the beam, thus increasing the effective opacity of the target plasma and allowing "thinner" (lower concentration) areas of the plume to be visualized (i.e., sensitivity will increase, and it should therefore be possible to track the time-space evolution of the plasma from earlier times in its evolution).

Project

This project sought to assemble the equipment and demonstrate resonance shadowgraphy in the laboratory. The experiment setup (Figure 1) consisted of the plume to be studied, the probe laser, and the detector. The plume system consisted of a vacuum chamber with multiple quartz windows. The chamber was typically operated at a pressure of 10^{-4} torr or less and contained a flat aluminum target (Figure 2). A small, pulsed neodymium:yttrium-aluminum-garnet (Nd:YAG) laser, focused through the top chamber window onto the aluminum target, produced a plasma above the target when pulsed

[1] capellga@nv.doe.gov, 805-681-2252

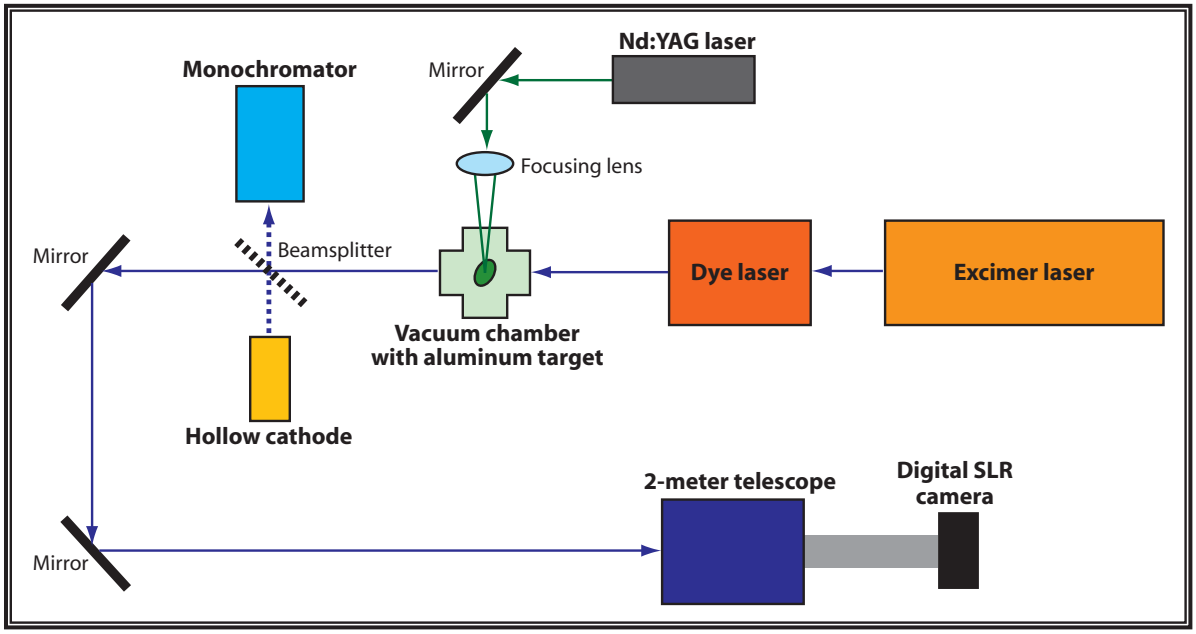

Figure 1. Experiment setup

(Figure 3). The target holder was designed to be movable from outside the vacuum system, to access "fresh" areas when an area became too deeply pitted. Output of the Nd:YAG laser, at both 532 nm and 1064 nm, was ~10 ns in pulse width, with ~180 mJ per pulse. To aid alignment, two "goalposts" were set up in front of and behind the plume (Figures 2–3). The distances between the parallel sides of the small and large goalposts were 5 mm and 7 mm.

The shadowgraphy laser illumination system is a 308-nm, excimer-pumped, tunable dye laser. This laser was tuned to the aluminum resonance at 394.4 nm; output was approximately 24 ns and up to 10 mJ per pulse. Line width was <0.1 nm. The roughly triangular dye laser output was expanded (reverse Galilean telescope) to be larger than the plume area (~15 × 15 mm). For wavelength measurement, a small portion of the dye laser beam was sent to a monochromator equipped with a photomultiplier detector. An aluminum hollow cathode resonance lamp was also directed into the monochromator for precise wavelength calibration to the aluminum resonance; the dye laser was then tuned to this wavelength. After exiting the plume chamber, the laser beam was optically folded with two mirrors, allowing the detector to be placed at a standoff of ~25 ft. This simulated the standoff that would be necessary at the Z machine or RITS to enable operation outside the radiation shield wall.

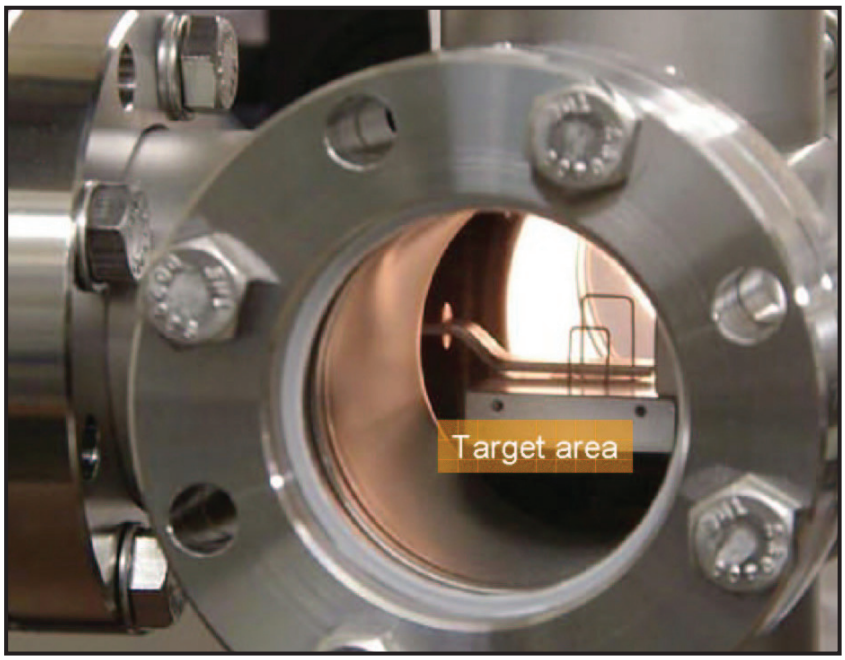

Figure 2. Plume generation area with movable aluminum target

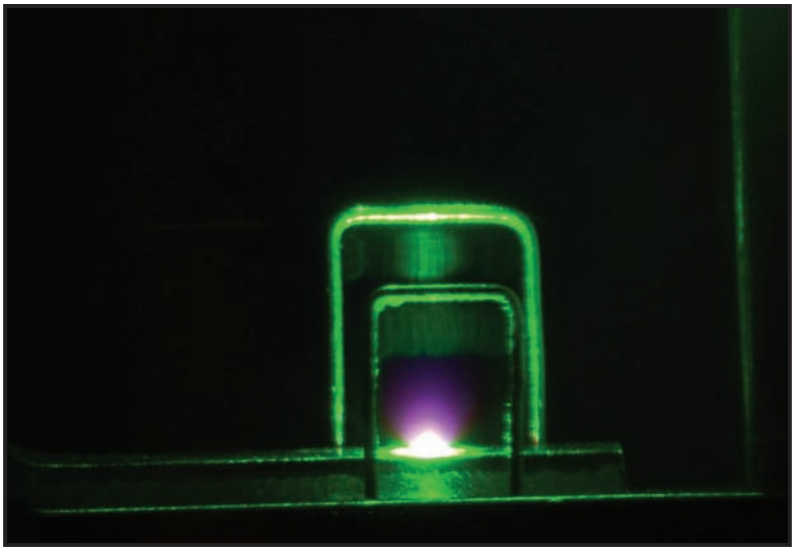

Figure 3. Photo through telescope of plume created by Nd:YAG laser focused on aluminum target

The detection system started with an 8-in. diameter, 2000-mm focal length Cassegrain telescope. To decrease unwanted light, the input aperture was masked to a 2" × 2" opening to collect light only from the area in which the dye laser entered the telescope. Additionally, one or more optical filters were placed in this input opening to eliminate unwanted background light. A custom extension tube was mounted to the back of the telescope, to allow such close focusing. To this we mounted a Nikon D50 digital single-lens reflex (DSLR) camera to be used as the detector. To increase sensitivity below 400 nm, we modified the camera by removing the UV/IR filter that is normally mounted in front of the 6-megapixel CCD chip. Removal of this filter also tended to give some of the images a reddish tint.

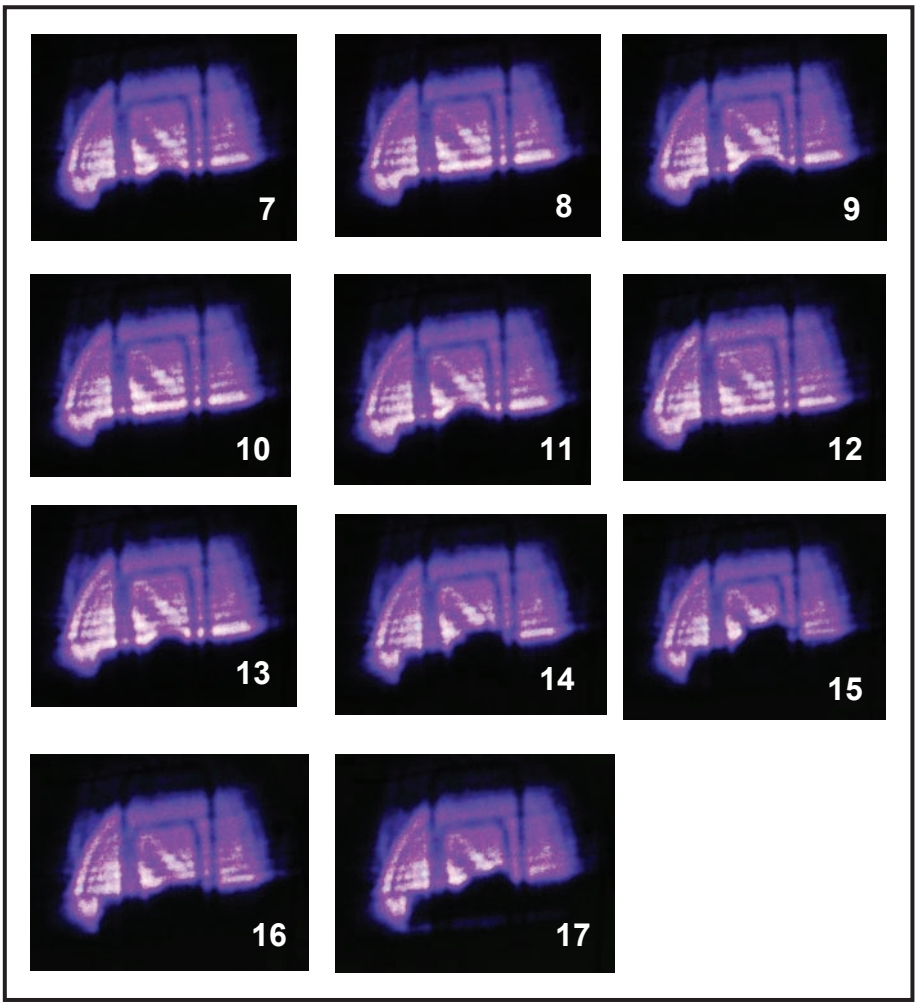

Figure 4. Series of resonance shadowgraph images on screen at 6 ft

A digital delay generator controlled the timing of both the yttrium-aluminum-garnet (YAG) laser (for plasma cloud production) and excimer laser (for dye laser beam timing through the plasma). Exact beam times through the sample area were monitored with silicon photodetectors and an oscilloscope.

Results

After some experimentation, our team could reliably produce resonance shadowgraph images of an aluminum cloud that we generated in a vacuum system. The detectable plasma clouds that the small Nd:YAG laser could generate were relatively small, on the order of a few millimeters high. The first resonance shadowgraph images we recorded were produced by imaging the target area with a 12-in. focal-length lens onto a screen ~6 ft from the plume. The enlarged image was photographed in a darkened room using the DSLR along with the regular lens, plus a BG3 filter that blocked 532 nm and other extraneous light. This setup was used to optimize experimental parameters, specifically the necessary filtering and the time delay between the Nd:YAG pulse that produces the plume and the dye laser pulse that interrogates it. Optimal delay was found to be in the range of 200–400 ns. Figure 4 shows the resonance shadowgraph images. First, we set up conditions for imaging (photo 7). Then the YAG laser was blocked (no plasma, no shadow [photo 8]) and unblocked (shadow [photo 9]). The dye laser timing was then increased to 1 μsec later (no shadow [photo 10]), then returned to 270 ns (shadow [photo 11]). Next, the dye laser was tuned to 390 nm (4.4 nm off resonance, no shadow [photo 12]), then returned to resonance (photo 13). Plume shadows varied in shape, as the aluminum sample position was changed from shot to shot (photos 14–17).

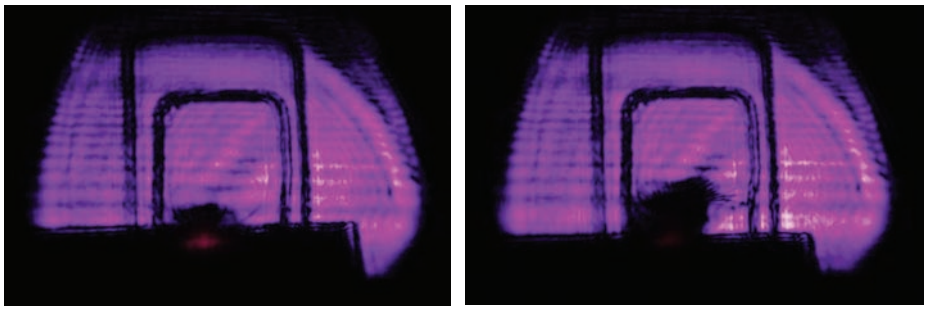

Figure 5. Photos through telescope at 26 ft; red spot at base of plume is plasma light leakthrough from point of laser impact on aluminum target. Target position was moved between shots.

Next, the DSLR detector was set up on the telescope, located 26 ft from the plume. The system was centered and focused on the target "goalposts," and shadowgraph images were successfully recorded (Figure 5). Reasonable images were obtained using either the BG3 filter or the 394-nm, 10-nm-wide

band-pass filter. For situations in which more plasma light exists, the narrow 394-nm filter would be the filter of choice. To avoid overexposure, dye laser energy was reduced to ≤100 μJ/pulse, and a Wratten OD2 neutral-density filter was placed in front of the first filter. Because of this, the shadowgraphy images could be recorded with the room lights on, even though the DSLR shutter-open time was nearly 1 sec. Additionally, the bright plasma light flash generated by the Nd:YAG–aluminum target interaction was barely visible.

Conclusion

Resonance shadowgraphy images were successfully generated using the experimental setup. When the laser was tuned off-resonance (resulting in conditions for normal [nonresonant] shadowgraphy), all traces of a plume shadow disappeared. Thus, resonance shadowgraphy is much more sensitive than normal shadowgraphy. Also, surprisingly little tunable laser energy was required to generate the images. Therefore, should we encounter a situation with much brighter plasma light backgrounds, we could increase laser pulse energy by an order of magnitude and compensate by adding an additional factor of 10 attenuation at the telescope input, thereby reducing plasma light by that additional factor.

Our results show that this resonance shadowgraphy technique would be very useful at places such as Z and RITS, since it would expand their plasma diagnostic capabilities to considerably lower concentrations and earlier times in the life of the plasma. There is, however, more work that should be done on this system to make it a reliable, fieldable system. First, increased magnification would be advantageous, since we used only a small part of the total 6 megapixels of resolution that the detector offers. Second, the probe laser beam should be cleaned up to make it more homogeneous, if possible. The dye laser head we used always had poor beam quality, which manifested in our results as intensity variations across the image; this, in turn, affected the quality of the shadow image. Some of these intensity variations may also have been the result of interference effects from windows or other optical elements. Third, the probe laser should be placed at a 25–30 ft standoff from the plume in order to mirror experimental conditions at places like RITS. Fourth, fielding this setup would be much easier if the laser system could be made more compact.

Acknowledgment

Thanks to Mark Johnston of SNL, for helpful discussions regarding RITS, the Z machine, and this project.

Neutron Monochromator

Brent Davis[1]
North Las Vegas Operations

Gamma rays present formidable difficulties when making measurements of the neutron emission characteristics of a radiation source. Time of flight techniques allow the neutron flux to be distinguished from gamma-ray interactions, but large distances from the radiation source decrease temporal resolution. Neutron scattering that occurs between the source and the sensor obscures temporal behavior measurements of neutron emission. An effective neutron monochromator would allow a particular neutron energy to be measured at very close distances from the radiation source without interference from gamma rays or scattered neutrons. Properly designed, such a monochromator could radically improve measurements of the temporal characteristics of neutron emission.

Background

In the classical sense, a monochromator is an optical device that transmits selected wavelengths of light from a wider range of input wavelengths. The neutron monochromator developed in this project does not select a specific wavelength from a spectrum. Instead, it allows neutrons of a specific energy (such as those produced from deuterium-deuterium [D-D], deuterium-tritium [D-T], or tritium-tritium [T-T] reactions) to be measured without significant interference from gamma/x-rays that originate at the same location in time and space. The emphasis has been to design neutron monochromators that can measure neutron intensities of two common energies, 14.0 and 2.45 MeV. Where possible, the device's temporal response was considered so that temporal measurements would detect detail (fine structure) associated with neutron production.

Project

The ability to measure specific energetic neutrons, without gamma radiation interference (typically produced simultaneously with neutron emission), depends on:

1) neutron velocity,
2) neutron interaction with a dielectric medium to produce light (scintillations), and
3) velocity of that light within the dielectric medium.

[1] davisba@nv.doe.gov, 702-295-2563

Furthermore, the dielectric medium must serve as an optical transmission conduit, exhibiting both low attenuation and dispersion factors.

The developed neutron monochromator uses a phenomenon referred to as "scintillation bunching." This term describes a mechanism by which the intensity of a wavefront of light produced by scintillations increases as it propagates along an optical conduit. Bunching occurs if the light's wavefront and the energetic neutron-scintillating interactions with the optical conduit occur at the same spatial and temporal positions throughout the length of the monochromator.

As a function of time, t, the physical location of any neutron propagating parallel to the monochromator's axis is:

$$X_n(t) = tv_n, \quad \textbf{(1)}$$

where

$v_n = c[1-(E_0/E)^2]^{1/2}$,

c = velocity of light in a vacuum,

E_0 = neutron rest mass energy, and

E = neutron kinetic energy.

The position of the light produced from neutron-scintillator interactions along the dielectric medium is defined by:

$$X_l(t) = tv_l, \quad \textbf{(2)}$$

where

$v_l = c/N$, and

N = scintillating conduit's refractive index.

X_l is also a function of the monochromator's geometry. In this case, the geometry is a spiral on the surface of the conical section with a constantly changing pitch. The minor diameter of the conical section is 24 in.; the major diameter is 48 in. The refractive index of the scintillating conduit is 1.47. Figure 1 shows the general figuration of the device designed for 14-MeV neutrons. Figure 2 depicts a set of scintillating fibers used for the prototype neutron monochromator.

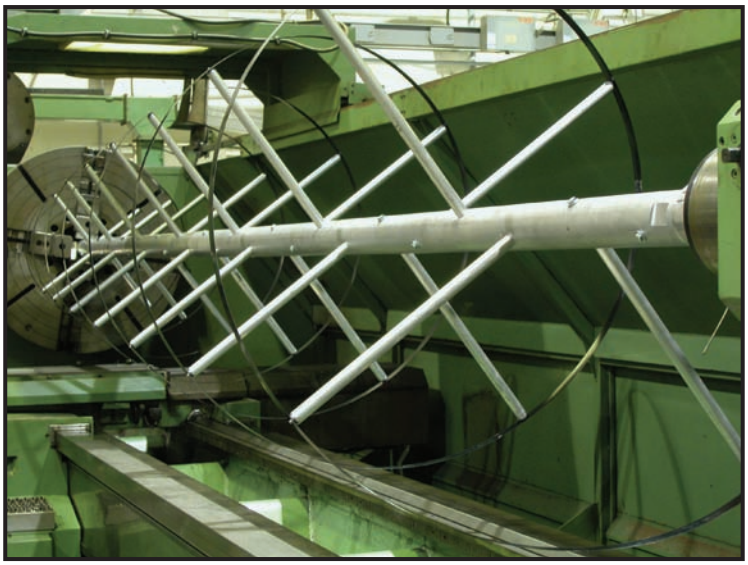

Figure 1. Neutron monochromator subassembly

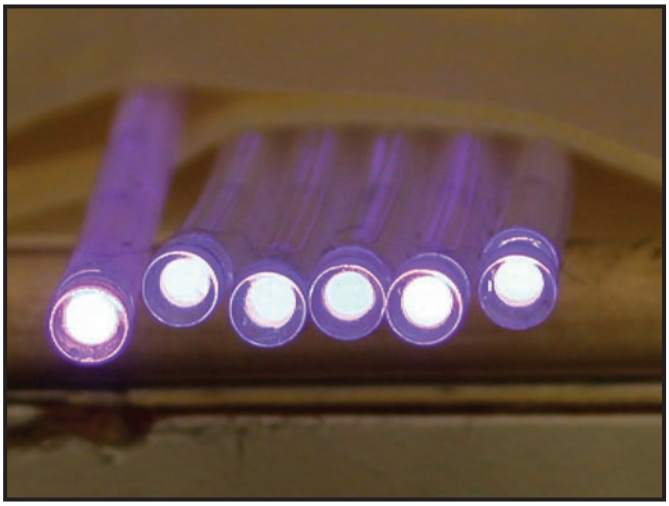

Figure 2. Teflon tubing, scintillator-filled conduit showing Plexiglas windows

The length of the spiral is described by the function, $F_s(\phi)$, where ϕ is angular position of the spiraling dielectric medium relative to the monochromator's axis. Consequently,

$$t = F_s(\phi) /(v_/) = F_s(\phi)\ N/c$$
$$t = X_n/v_n = X_n/(\ c[1-(E_0/E)^2]^{1/2}) \quad \textbf{(3)}$$
$$F_s(\phi)\ N/c = X_n/(\ c[1-(E_0/E)^2]^{1/2}),$$

or

$$F_s(\phi) = X_n/(N([1-(E_0/E)^2]^{1/2})). \quad \textbf{(4)}$$

The Dense Plasma Focus (DPF) neutron generator at the Las Vegas facility yields a radiation output (a mixture of neutrons and gamma/x-rays) with ~100-ns duration (full-width at half-maximum [FWHM]). Consequently, the time of flight of light through the monochromator's spiraled, dielectric medium was designed to be approximately that same value. This would allow the monochromator's output signal from neutrons to occur ~100 ns following the very first neutron-scintillator interaction. The 100-ns requirement defines the total length of the scintillating conduit in its spiraling path.

Scintillation bunching does not effectively occur with any of the photon-scintillator interactions. Although the light intensity from these interactions are very large compared to that from the neutrons, the light production occurs with a duration equivalent to the difference between the spiral arc length and the monochromator axis length, divided by the speed of light. In contrast, the individual scintillations from neutron interactions are additive and are continuously bunched into a narrow packet during the entire time of the neutrons' parallel flight along the monochromator's axis. The neutron signal through scintillating bunching is expected to be of large amplitude and short duration, while the photo-induced signals should have comparatively low amplitudes spread out over ~100-ns duration. In effect, the monochromator's geometric configuration allows the signal from neutron-scintillator interactions to be both intensified and separated from photon-scintillator interactions—if the neutrons and photons share a common spatial and temporal origin.

The Monochromator's Spiral Path

Determining the exact path of the monochromator's spiral is complicated by a constantly changing pitch and a diverging neutron flux. To define the final path, we made several compromises that were expected to only slightly impact the monochromator's ability to measure neutrons at short distances from the emission source, and without major interference from the associated gamma/x-ray emissions. The required path length of the dielectric conduit was calculated then compared with computer models. Thus, iterations to the mathematical equation allowed an acceptable configuration to be established.

The Scintillating Medium

Two approaches were taken to establish an acceptable scintillating medium for the monochromator. First, we purchased a 5-mm (0.197-in.)-diameter scintillating fiber (BCF-10) from Bicron. The supplier expressed concern that its bending radii might be too large for our application but advised us that a 1.5-ft-radius would be acceptable. Some of the material received on 3-ft-diameter spools was broken into two pieces, presumably caused by the spool's bending radius. In addition, its optical transmission capabilities suffered from multiple, circular fractures that penetrated deeply and perpendicularly toward the cylindrical axis (Figure 3).

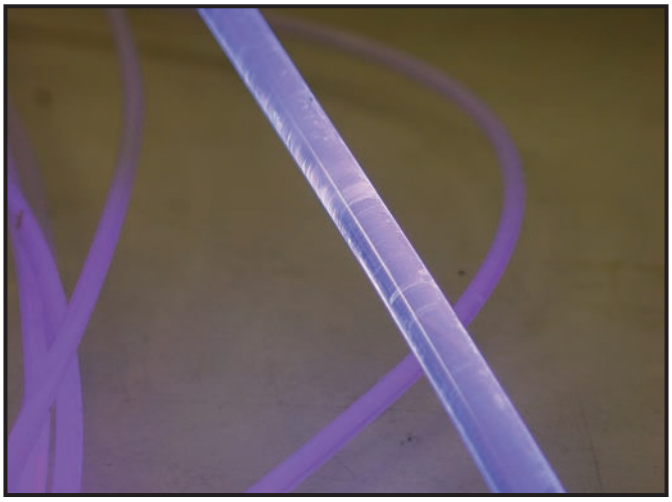

Figure 3. BCF-10 (5-mm-diameter) fiber showing diametric material fractures (light, circular rings)

The number of these fractures increased with time, either from handling or from stress caused by the spiral path of the monochromator. The instability of optical transmission created by the fiber's changing physical condition deterred serious consideration of this material for the prototype monochromators.

As a second option, scintillating conduit was produced on-site by filling 0.059-in. (inner) diameter Teflon tubing (0.016-in.-thick wall) with Bicron's liquid scintillator, BC-517P. This liquid was selected because of its optical transmission capabilities, refractive index, viscosity, and low flash point. The small Teflon tubing was chosen to minimize internal dispersion of the expected scintillating light, and because its refractive index (3.35) assured that the filled tubing would act as an optical fiber. However, tiny air bubbles from the scintillator gradually formed on the inside walls of the tubing after the filling process (Figure 4). These bubbles caused severe attenuation to light transmission along the special conduit, and we spent much time eliminating them.

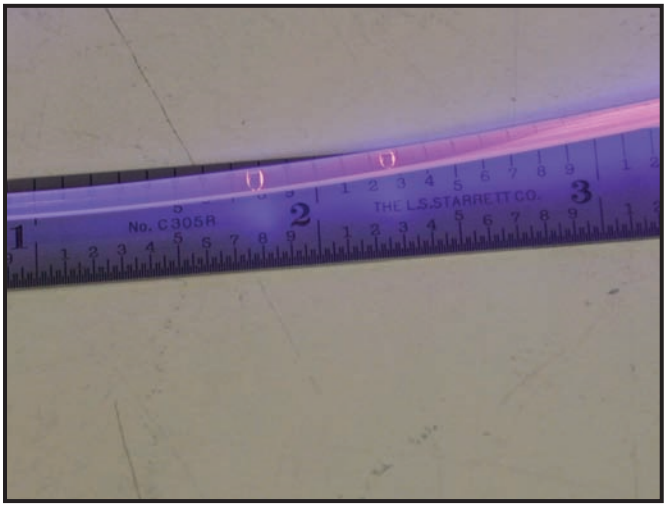

Figure 4. TSF "fiber" with air bubbles

Medium Transmission

Optical measurements determined that a 10-ft-long section of Teflon-scintillator-filled (TSF) conduit exhibited about a 23% optical transmission (for ~400-nm light), as shown in Figure 5.

That the light output from the solid BCF-10 scintillating fiber was greater than that from the TSF fiber is attributed to its larger size (0.197-in. versus 0.059-in. diameter).

To address the TSF fibers' large attenuation, these fibers were cut into ~10-ft lengths and assembled to the monochromator's spiral in groups of ten. The final configuration contained 70 of these special scintillating conduits. At the end of each set of ten fibers was a light sensor to measure light output. Signal output from each of the seven sensors was recorded during the monochromator tests, then mathematically combined via computer programming.

Measurements

A series of measurements was made using a prototype DPF neutron generator as the radiation source. Since the generator's working gas mixture was deuterium, only the 2.45-MeV neutron monochromator was evaluated.

Preliminary signal data evaluations indicated that the monochromator was working properly. However, a more detailed study and follow-up experiments demonstrated that signals from radiation directly onto the sensors' photomultiplier tube had overwhelmed any monochromator output. Consequently, the sensors were heavily shielded with lead.

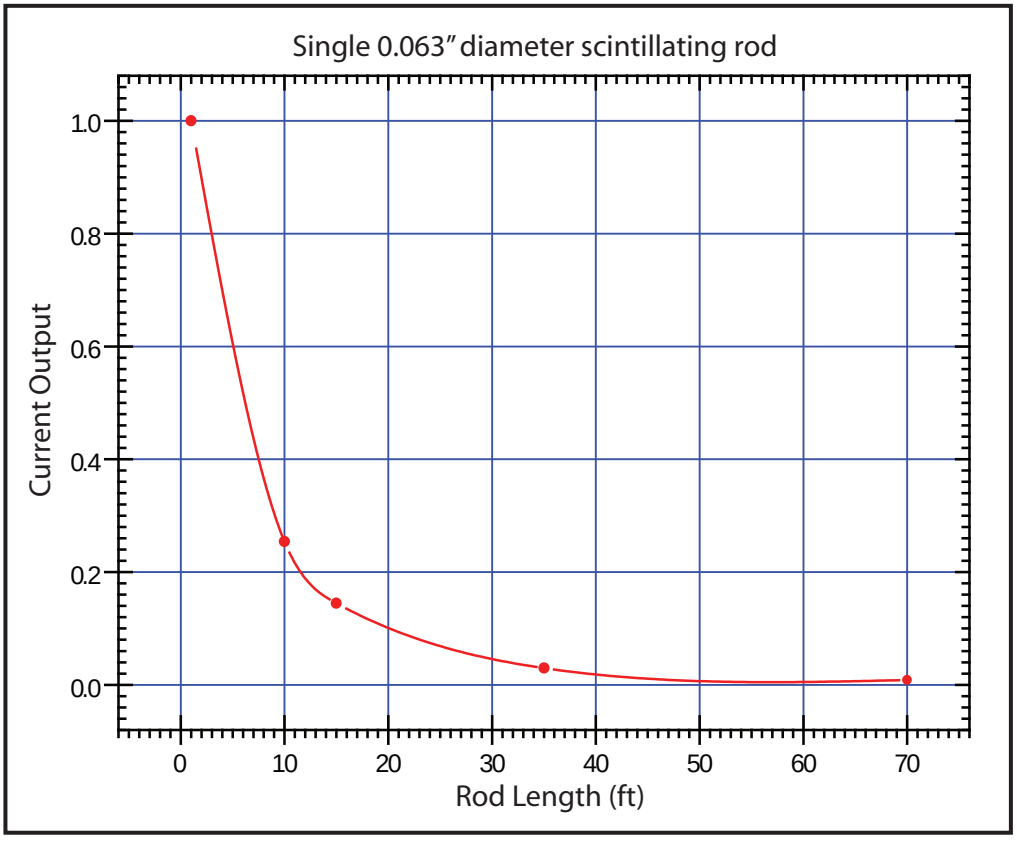

Figure 5. Optical transmission qualities of the TSF "fiber" to ~400-nm light

Figure 6 shows a composite of signals that measure DPF output behavior. All signal amplitudes have been normalized to the first trace. Traces 1 (black) and 2 (green) represent the signals from the generator's standard, unshielded monitor. There are two gamma bursts measured by the detector monitor, separated by ~145 ns. Neutron output is recorded at ~460 ns following the initial gamma output (a time of flight phenomenon). The signal output (traces 3 [blue] and 4 [red]) are from the monochromator's detector 8, which has been decoupled from its scintillation fiber. These recordings show the same two gamma bursts produced by the generator's monitor. Signals produced by neutrons (if the scintillator fiber had been in place) would be significantly masked by the second gamma burst because the prototype monochromator would produce a signal from the neutron at ~100 ns following the initiation of the first gamma burst.

We used 2-in.-thick lead bricks to shield several of the monochromator detectors, followed by several additional measurements. Figure 7 shows one of the series of measurements made following proper radiation shielding of the monochromator's detectors. All signals have been "aligned" in

time, based on their major peak. This display demonstrates the signal amplitude differences between monochromator sensors. Within reason, each sensor should have yielded a similar signal amplitude. Their failure to do so was caused by small gas bubbles that developed randomly (over time) within liquid scintillation "fibers." The degree of optical attenuation within the liquid scintillator depended on bubble quantity and location.

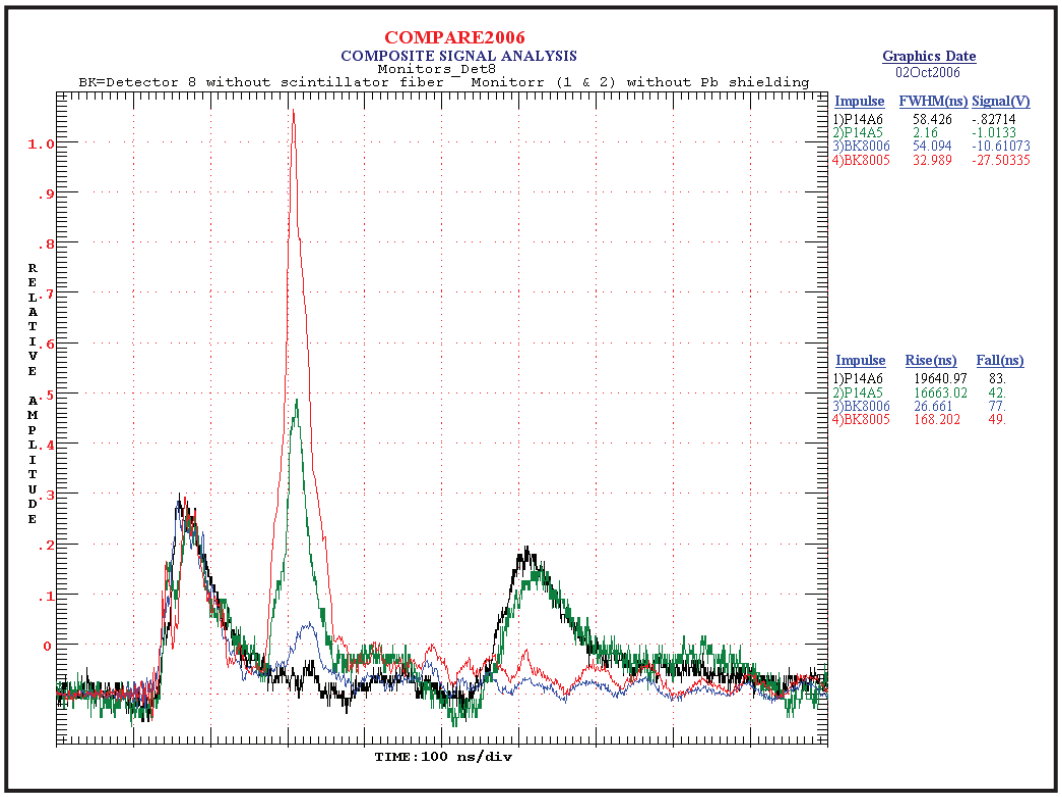

Figure 6. Behavior of DPF gamma and neutron emission

The display also shows an unusual (unexpected) temporal behavior from the radiation source. Without definitive timing information between the standard radiation source detector monitors and the monochromator signals, it was impossible to determine much more than the fact that the detectors functioned. Evidently, prior to the monochromator experiments, accurate timing was not considered important in DPF measurements.

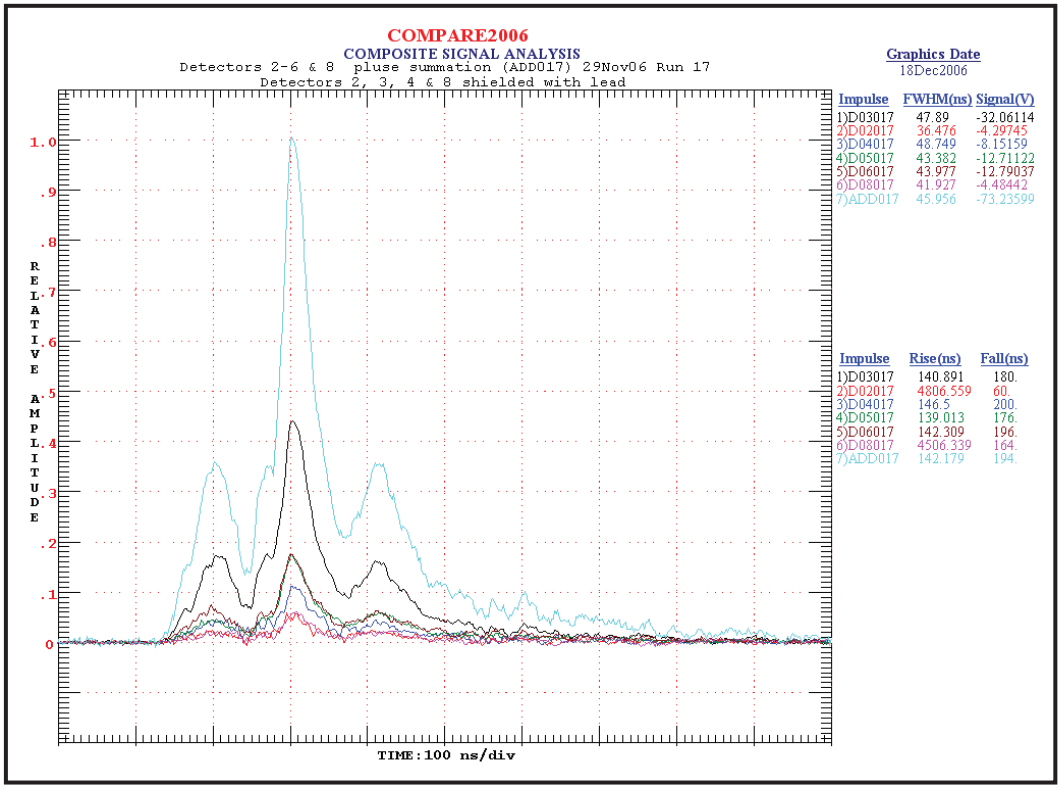

Figure 7. Monochromator signal output from sensors 2–6 and 8

We also discovered that the main DPF system data associated with its temporal characteristics was unreliable. The monitoring detectors were typically operating outside of their linear signal capabilities, which caused unacceptable distortion to the system's true output characteristics.

In an attempt to avoid these monitoring issues, we established a new detector for the radiation source by placing a lead-shielded detector (containing a small unshielded fluor) at roughly the same location as monochromator detector 3. Figure 8 shows the signal comparison between the new monitor and monochromator 3. Except for signal amplitude, there appears to be little difference between the two signals. Since both detectors (except for their scintillators) are shielded from DPF prompt gamma rays, the data imply that the first signals from these two detectors are induced by neutrons. However, the two secondary "bumps" following the main signal remain unexplained. There still seems to be no evidence to support reliable conclusions about the monochromator's true performance.

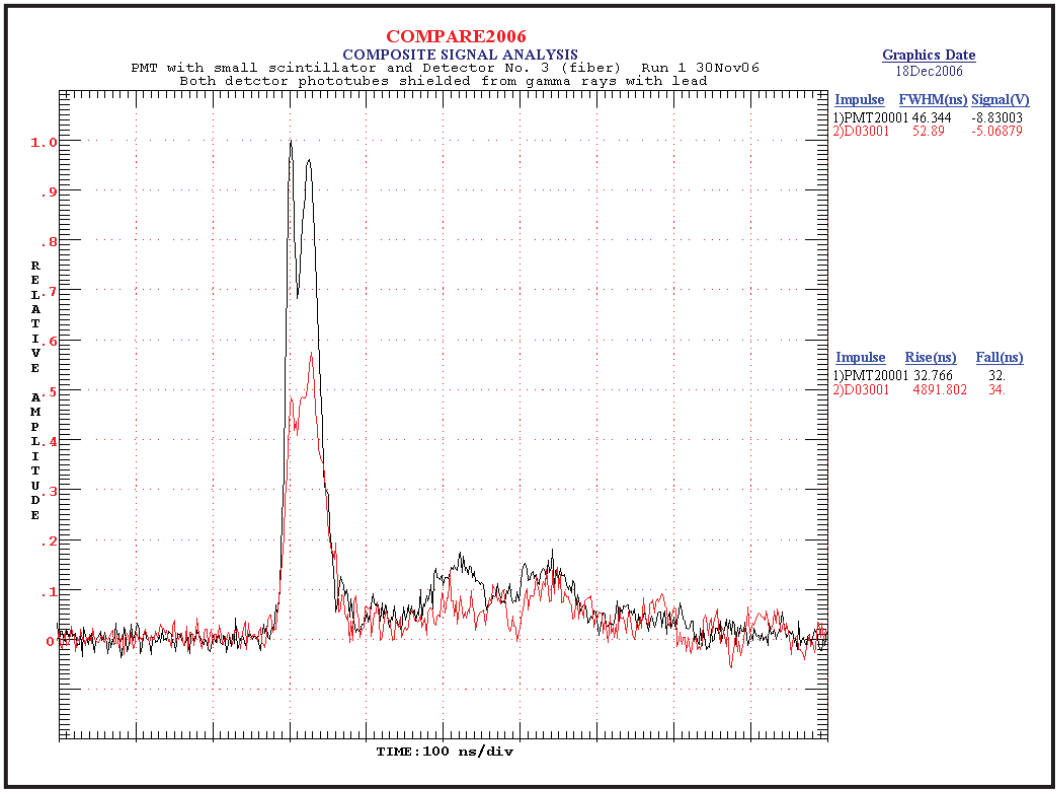

Figure 8. Signal comparison of new monitor and monochromator 3

Conclusion

During this project, both a 14-MeV and a 2.45-MeV prototype neutron monochromator were designed, but only the latter was tested. The monochromator's radiation sensitivity was compromised by scintillating "fiber" degradations. The solid fiber's optical transmission changed with time, caused by small fractures that slowly developed within the material. Tiny gas bubbles gradually developed in the liquid scintillator, which was contained within small Teflon tubing. These changes altered the fibers' optical characteristics as a function of time. Consequently, neither fiber is considered a good choice for a working monochromator.

The best scintillating fiber would be solid (to reduce optical dispersion and prevent fractures) and diametrically small. There is supporting evidence that the fractures introduced within the solid "fiber" were highly dependent on its large (5-mm) diameter. Bicron BCF-12 solid, 2.4-mm-diameter fiber is recommended to replace existing monochromator fiber. Although the BCF-12 has a slightly larger decay time, its optical transmission is about 23% better than that of BC-517P. The refractive index of

the BCF-12 is 1.6 (cladding is 1.49), compared to the BC-517P value of 1.47 (fluorinated ethylene propylene Teflon is 1.37). This difference may require a slight redesign of the existing monochrometers' spiral paths.

Inadequate information regarding the true temporal characteristics of the DPF radiation output made it impossible to determine with confidence that the monochromator was functioning correctly. The DPF system's data acquisition techniques and instrumentation should be improved to allow timing and temporal behavior information to be reliably and accurately recorded. More design work also must be done to incorporate adequate gamma-ray shielding for the monochromator's sensors.

this page intentionally left blank

Parallel Pulse-height X-ray Spectrometer

Fletcher J. Goldin,[1] *Stephen Mitchell*
Livermore Operations

The ultimate goal of this project was to advance the development of an x-ray spectrometer for use with flash x-ray generators typical of those used in radiography of hydrodynamic experiments. This was attempted by introducing the x-ray flux onto an array of scintillating elements using one of two configurations: parallel to the array axis (end-on) or orthogonal to the array axis (side-on); the light output of the elements, measured by imaging the array face, would then provide x-ray spectral information. For the end-on geometry, if no more than a single x-ray photon entered a given element, its output would be proportional to the x-ray energy; for the side-on geometry, x-ray energy would be deduced by the extent of penetration into the array. At least in the first instance, this was essentially pulse-height analysis (PHA), but done in parallel (as required for an impulsive input) rather than in sequence. Thus, the device was dubbed the parallel pulse-height x-ray spectrometer (PPXS). Due to the extremely low signal levels and significant noise, this end-on configuration gave discouraging results. However, the side-on concept showed promise as the heart of a flash x-ray spectrometer.

Background

A wide range of U.S. DOE hydrodynamic and other experiments depend on flash x-ray radiography. Spectral information about the x-ray source can aid source development, application, and data interpretation, but the short duration (10s of ns) of the x-ray burst precludes conventional PHA. Consequently, current spectral measurements rely on differential absorption of x-ray photons by filtration of various materials and thicknesses. But a fundamental problem—the very weak dependence of the total cross section with photon energy (in this regime)—means that small inaccuracies in raw data are magnified in the unfolded spectra. These considerations motivated this project. The most important application of the PPXS would be in the ~0.3–3 MeV range (cross sections in this regime are essentially flat vs. energy, rendering differential absorption least effective), but for practical reasons, these tests occurred in the ~50–400 keV range.

Project

Two geometries (end-on and side-on) were investigated numerically and experimentally. For the end-on concept, x-rays entered an array of scintillating elements from one end. The elements were separated by reflecting walls for optical isolation and light-piping, and the back side was imaged.

[1] goldinfj@nv.doe.gov, 925-960-2686

If the number of elements accepting more than one photon is statistically insignificant (e.g., <1%), then a histogram of the brightness levels of the array output would correspond to the spectrum of the input x-rays. This was done by lens- and butt-coupling an intensified camera to the array, as depicted in Figure 1(a) and (b). An alternate approach used the side-on geometry shown in Figure 1(c), where depth of penetration (possibly behind a step wedge filter) provided the spectral information.

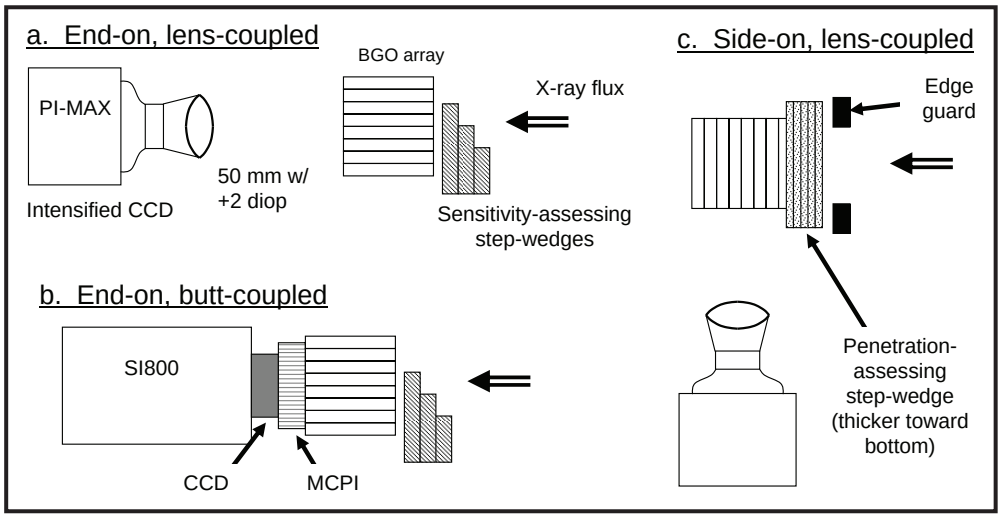

Figure 1. Three configurations used: end-on incident x-ray flux with lens- (a) and butt- (b) coupling of BGO to microchannel plate; with flux entering side (c)

A scintillator that could be used for this scheme would need (1) a combination of stopping power and thickness (element length) sufficient to absorb nearly all the energy of the most energetic photons, (2) stopping power and element width to mitigate against cross talk, and (3) enough elements that a histogram of those illuminated would give statistically meaningful spectral information. The high stopping power implies an inorganic material that would require individual cutting, polishing, and coating of four sides; for the thousands of elements needed, costs would be >$100K. Fortunately, it was possible to obtain an existing array from LLNL not designed for this project, but with specifications near ours. The array was a 76 × 76 square array of bismuth germanate ($Bi_4Ge_3O_{12}$, commonly BGO) elements, each 40 mm long and separated by an aluminized Mylar wall, with a net pitch, including walls, of 50 mm/76. This met requirements (1) and (3), since modeling indicates only ~1% of the energy of a 400-keV photon will exit the back side of 40-mm slab of BGO, and up to ~600 elements could be illuminated in a single shot with only a tolerable ~1% intercepting multiple photons (Goldin, 1996). Much more problematic was requirement (2), as discussed below.

While this project's goal was to find a path for spectral measurements in the 0.3–3 MeV energy range, practical issues with the x-ray source and the BGO array dictated experimentation in the <500-keV regime. This was done using a Scandiflash 450 x-ray pulse generator. This source uses a 20-stage, 18-J, 450-kV (maximum erected voltage) Marx bank to drive a vacuum-diode x-ray head, and produces ~25 mR of x-radiation at 30 cm in a 20-ns pulse. The spectrum is approximately bremsstrahlung, mixed with line radiation, modified by absorption by the tungsten anode and aluminum vacuum window. The generator, a qualified operator, and a safe and efficient facility (Site 300) were graciously contributed by LLNL B-Division.

End-on Geometry

Energy deposition in the scintillation array was modeled using the Monte Carlo N-Particle eXtended (MCNPX) Version 2.5D particle transport code (provided by LANL). BGO material density was taken as 7.13 g/cm^3, and the walls were taken as 100 mm, 90% mylar/10% Al. More than 150 problems were performed, each with 10^7 particle histories for minimal statistical variances. These calculations primarily investigated cell-to-cell cross talk (due to radiation, not optical, transport). A sampling of the results is summarized graphically in Figure 2(b) (note the logarithmic ordinate) and numerically in Table 1. As expected, the cross talk increases with both energy and proximity to the cell wall of photon input. At, say, 100 keV (the expected peak for a 450 keV endpoint source), for central incidence, only a tolerable 3% of the energy is deposited in the adjacent cell(s), but this rises to a significant 9% for incidence 75% of the way from the center to the wall. Though difficult to define a tolerable cutoff, the situation at 400 keV (which represents only a very small fraction of

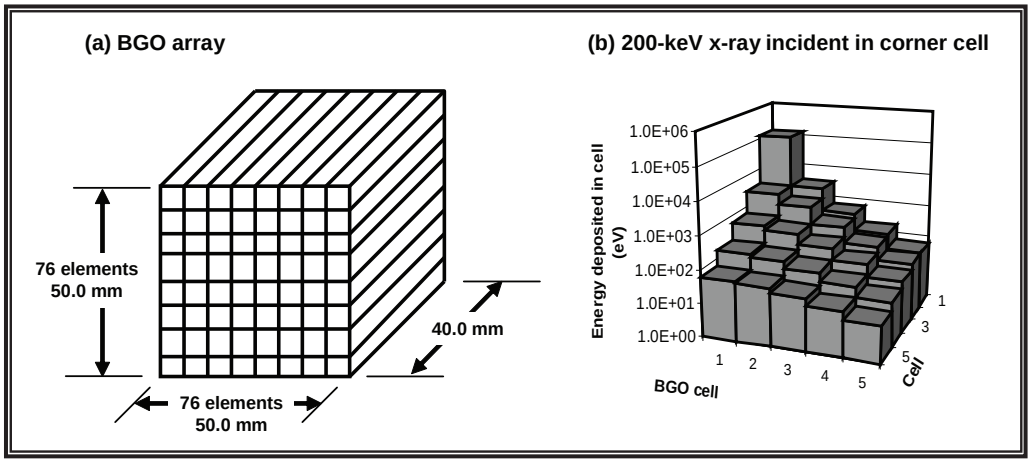

Figure 2. (a) MCNPX model of BGO array with light-piping walls; (b) energy deposited in nearby cells for a single 200-keV photon entering the center of the cell at (1,1). Note the logarithmic ordinate.

Table 1. MCNPX-calculated values for fraction of energy deposited in entrance/nearest neighbor/ next-nearest neighbor cells, given single photon entering cell at center, edge, and three intermediate points, all for four typical energies

Position	Eγ (keV): 50	Eγ (keV): 100	Eγ (keV): 200	Eγ (keV): 400
Center	0.994/0.001/0.000	0.749/0.030/0.005	0.794/0.022/0.004	0.705/0.016/0.005
¼ to edge	0.994/0.002/0.000	0.746/0.041/0.006	0.792/0.029/0.005	0.704/0.020/0.005
½ to edge	0.992/0.005/0.000	0.733/0.058/0.007	0.784/0.039/0.006	0.700/0.026/0.006
¾ to edge	0.986/0.011/0.000	0.706/0.087/0.009	0.768/0.057/0.007	0.689/0.035/0.007
At edge	0.554/0.441/0.000	0.410/0.360/0.012	0.432/0.379/0.009	0.379/0.338/0.008

x-rays) is probably acceptable. This implies that to avoid the error of counting two adjacent illuminated cells as having received two x-ray photons, in practice the flux might need to be so low that one could safely assume any such pair was receiving energy from a single photon.

End-on x-ray input was first tested using a Princeton Instruments PI-MAX 1k:GEN3, $1k^2$, 16-bit intensified camera. A Nikkor 50mm f:1.2 lens, together with a +2 diopter close-up lens, allowed a magnification of 0.2, so that most of the 13-mm-square CCD array was used to image the BGO. The camera-lens combination was tested at this magnification with visible (450 nm, near BGO output peak) pulsed input, and was found, at maximum gain, to have an absolute sensitivity of 500 counts/(pJ/cm^2). Given the optical coupling efficiency of ~3×10^{-3} and BGO output of ~10^4 visible photons/MeV absorbed, the net result is that 3–4 visible photons would be expected per CCD element for the light produced by a single 100-keV photon, which appeared to correspond to being just barely detectable (with a signal-to-noise ratio of ~1). After dark-field, flat-field, and resolution data were taken, the system was set up with the BGO array and flash x-ray source. The maximum source-to-BGO distance allowed by the facility was 4.5 m, which was used to minimize the x-ray flux as well as the angle between the outer (high aspect-ratio) BGO elements and the x-ray beam axis. Calculations implied that at this distance, some attenuation would still be needed to limit the photons intercepted by the BGO to a few hundred; this was done with 9 mm of Al (which, of course, modestly hardened the spectrum).

We addressed two primary questions: whether single-photon events could be measured, and if radiation transport–induced cross talk would be consistent with modeling. (Note: the latter would be qualitative, as the model was for various single energies and the experiment used a broad, largely unknown spectrum.) Since even in the absence of interference, either electromagnetic interference or hard radiation, from the x-ray generator single-photon events would be at the edge of detectability, this lower limit was investigated with step wedges to see at what attenuation the signal merged with the noise.

Unfortunately, the noise was far greater than anticipated. Various tests indicated this was principally from scattered x-rays, and so shielding was built up around both the generator head and BGO/camera combination. Figure 3(a) shows some of this, but a factor of 3 reduction was the best achieved. As is obvious from the step wedge image of Figure 3(b), this was completely inadequate. Also seen in Figure 3(a) is a tungsten roll bar used to measure the edge spread as a check on the MCNPX cross-talk calculations, but again noise (or low signal-to-noise ratio) precluded any useful measurement.

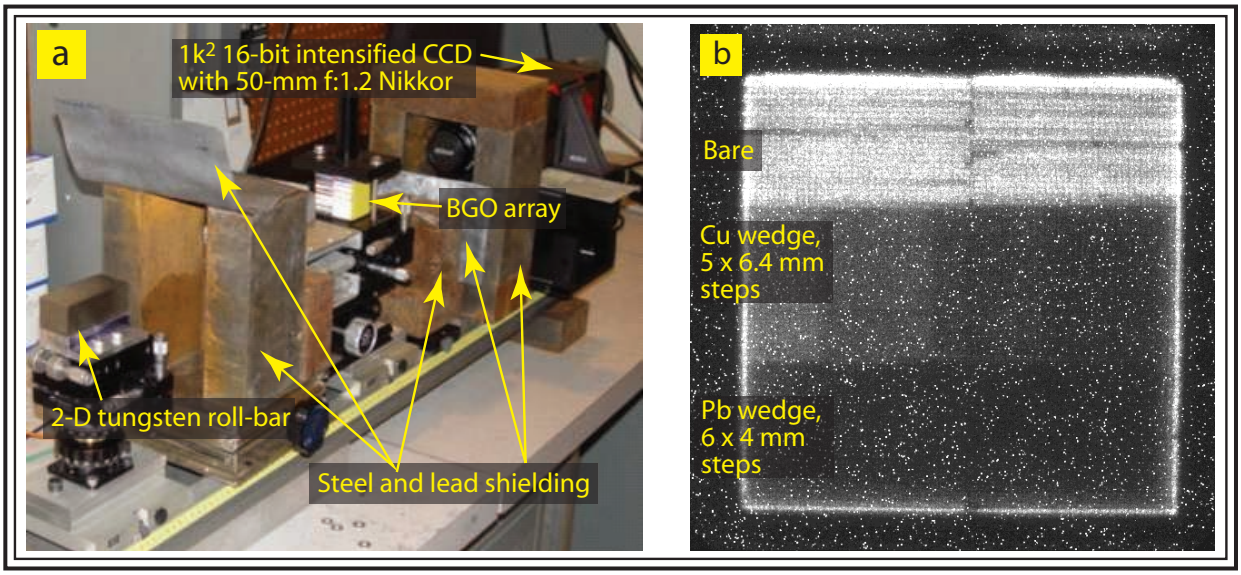

Figure 3. (a) End-on configuration with roll bar target showing shielding; (b) image of no wedge (top), 5-step Cu (middle), and 6-step Pb (bottom) step-wedge targets

These problems led to a new configuration in which the BGO array was in direct contact with the imaging system. While this could make little difference to the absolute noise, the signal was greatly enhanced. (Optical coupling was increased by a factor or ~200 at the cost of optical responsivity reduction for this MCP/CCD combination of ~0.5.) No off-the-shelf system that allowed this was available, so a housing was built that gave a soft-contact butt-coupling of the BGO, an independent MCP, and an SI-800 4k², 16-bit CCD camera. Noise was still too high for step wedge tests, as depicted in Figure 4(a), to show detectability of single photons, but the edge-spread function could now be seen. The image of Figure 4(b) was taken with a 1.5-mm Ta knife edge at a 4.4° angle across the array face. This angle corresponds to walking off by one BGO element vertically over a transit of 13.

The line-out shown in Figure 4(c) along one row of elements [depicted in red in Figure 4(b)] shows a nearly full rise in intensity in about this many elements, which demonstrated that the edge spread must be much less than a cell width, consistent with the MCNPX modeling.

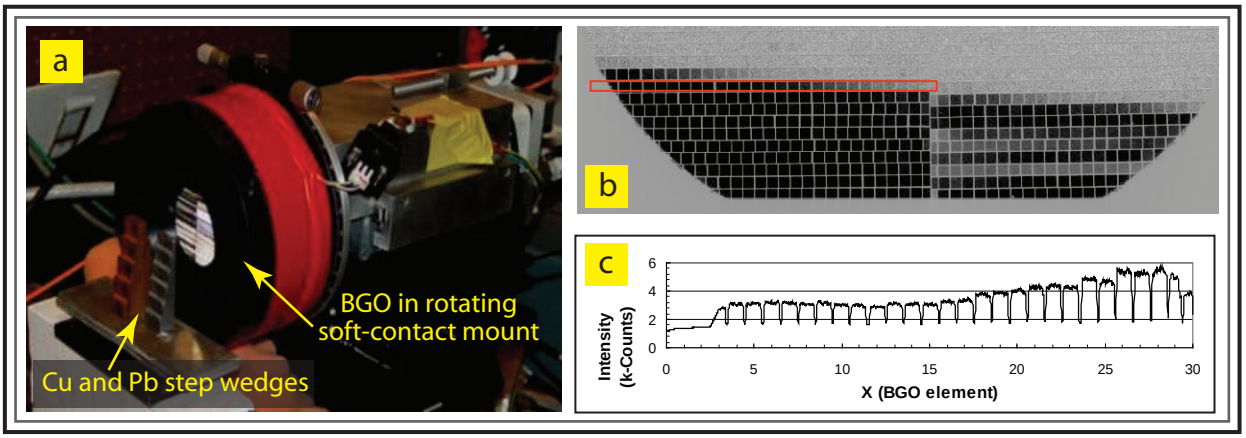

Figure 4. Butt-coupled setup with step-wedges (a) and image with slanted Ta knife edge (b) and line-out (c) (red rectangle in 4b) showing min/max transition over ~12 cells

Side-on Geometry

Approximately eight to nine months into the project, when the probability of overcoming the difficulties encountered in detecting single-photon events with available equipment and time was depressingly low, we turned to performing initial numerical calculations and tests of an alternate scheme. The BGO was turned 90° relative to the source for side-on x-ray incidence [Figure 1(c)]. Imaging what would now be the array side would then measure the distribution of x-ray penetration depth, a function of the energy spectrum. As detecting single-photon events is now not required, the source-to-scintillator distance was decreased to 2.0 m, for a factor of five increase in flux.

Further, a step wedge could exploit the two dimensions of the array to give penetration information behind attenuators of various thicknesses in a single shot. Nine-step wedges of Al and Cu were constructed so as to give 10 attenuation thicknesses (including bare), so that each step filtered approximately seven BGO rows. Energy deposition in each BGO element behind each wedge step, for 12 energies in the range of interest, was calculated with MCNPX, and the results for the Cu case for three representative energies are summarized in Figure 5. Figure 5(a) shows the total integrated energy absorbed behind each step—equivalent to the information gained from the normal use of a step wedge in front of a conventional detecting element, such as film or a scintillation sheet imaged from behind. Figure 5(b) shows the vastly enhanced data set of spatially resolved energy deposition behind the 10 steps this configuration gave.

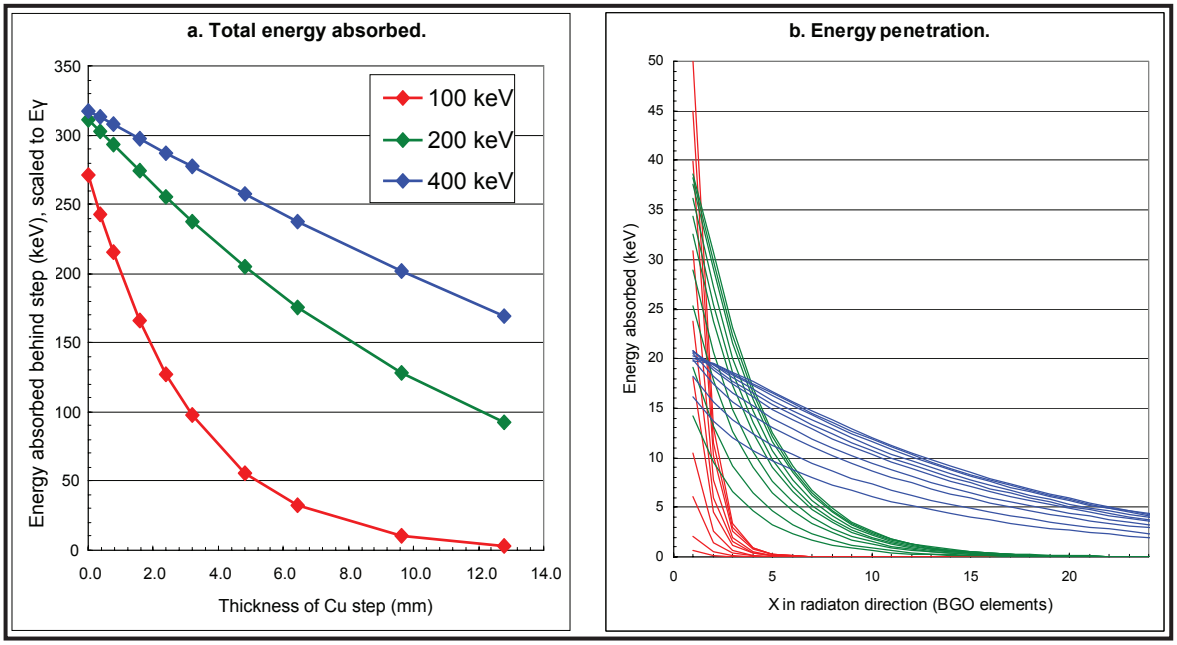

Figure 5. MCNPX calculation of energy deposited behind the 10 steps of Cu step wedge of Figure 6—total (a), and in successive cells (b), for three energies

The three images shown in Figure 6 were produced in three shots: (a) at a reduced 250 kV for a softer spectrum, (b) at the usual (maximum) 450 kV charging voltage, and (c) to 450 kV with a 0.05-mm sheet of lead in front for a harder spectrum. X-rays entered from above, and in all cases the Cu wedge was in place with thinner steps to the right. Energy absorption can be readily seen to increase with thinner steps, but also, penetration depth can be seen to increase as the spectrum hardens.

These observations are verified in the line-outs of the intensity profiles behind three representative steps (bare, 2.4 mm, and 12.8 mm) shown in Figure 7(a). (The spikes are an artifact of the flat-field image, used to correct for cell-to-cell variation, which was acquired by uniformly illuminating the side of the BGO array away from the camera and had artificially low counts at the cell walls.) In Figure 7(b), the same data are plotted, but with all the line-outs behind the same wedge scaled to the same peak height. It can then be seen that, with no step material, the spatial decay length increases markedly with increasing spectral hardness, only slightly behind step 4, and effectively not at all by step 9. It is this "difference of differences" that would allow a more accurate unfolding of an x-ray spectrum from the side-on data than would be possible from the simple integrated absorption of a conventional system.

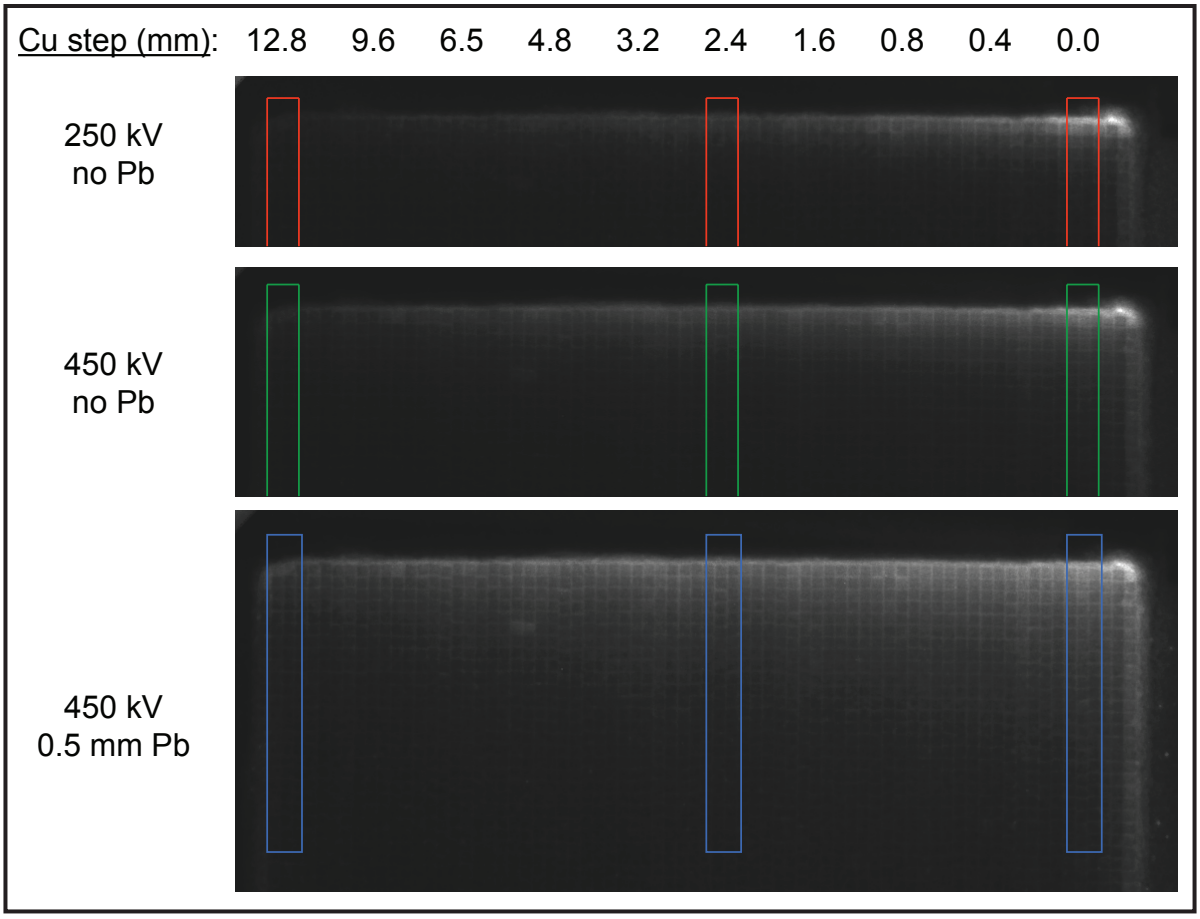

Figure 6. BGO array behind 10-step Cu wedge with x-ray flux entering from *top*

Conclusion

Calculations for, and tests of, two different geometries—end-on and side-on x-ray input—were carried out. For the end-on calculations, two classes of problems were discovered and not overcome: excessive noise and element cross talk. Further work might sufficiently mitigate the noise with optical transport of the image to a lead pig containing the camera (although this would presumably decrease the already intrinsically very low signal). Approaches to the cross-talk issue might include either larger elements, possibly with shielding between (with concomitant loss in number); many more smaller elements so that the footprint of an individual photon event might be imaged (presumably at much increased cost); or a flux low enough that the occurrence of x-rays incident in adjacent cells would be statistically insignificant (which would degrade overall statistics). This project, however, is not a cause for optimism.

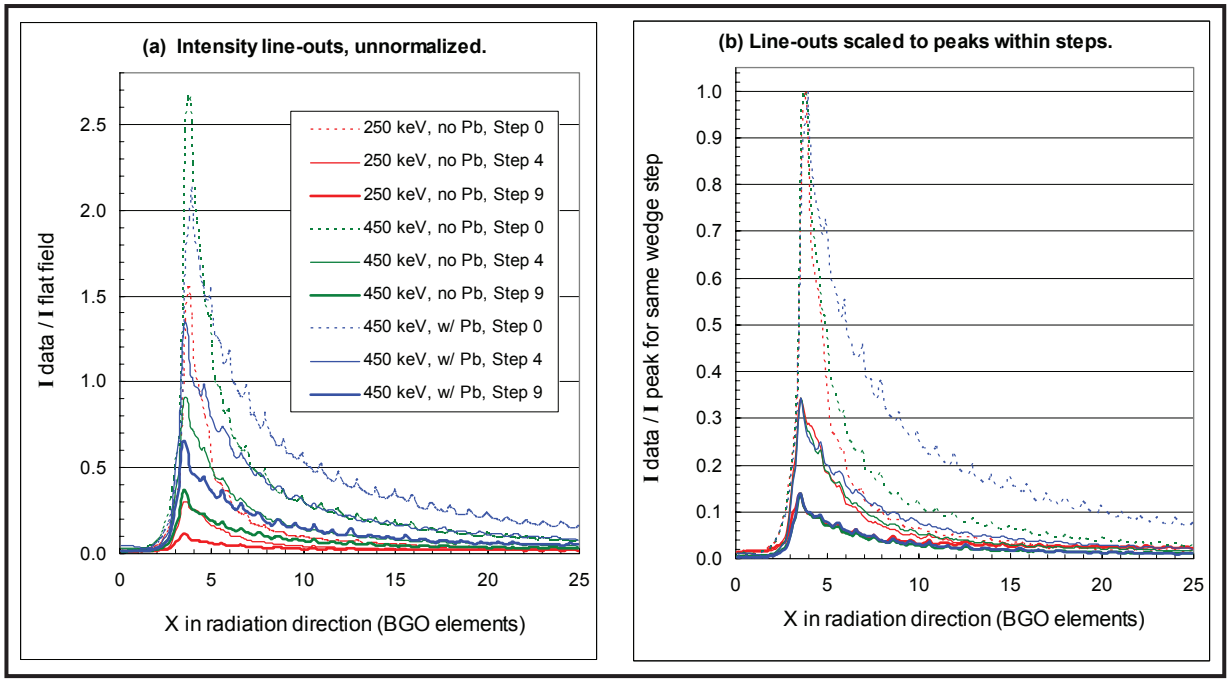

Figure 7. Line-outs of intensity behind three representative steps of the Cu step-wedge of Figure 6 (a) raw and (b) peak-normalized the line-outs of a given step

The side-on geometry was much more promising. The data from three different input spectra clearly indicated their differences and were in accordance with modeling predictions. However, it would appear that to actually unfold a spectrum would require a fairly sophisticated reduction algorithm, probably involving a calculated (modeled) prediction with a best-guess spectrum (based on bremsstrahlung/line radiation given the target material and voltage), comparing that with the data, adjusting as appropriate, and iterating until converging on a good match. A start on this might be possible with the calculations and data generated in this work, only a sample of which is shown here.

Acknowledgments

The investigators appreciate the enthusiastic assistance of Charles Cook III, James Lister, and Gary Mease of LLNL in operating the pulsed x-ray generator, and Jerald Cradick and Charles Diamond of NSTec LO for assembling and operating the imaging systems and making other technical contributions. We also thank Daniel Lowe of the University of Nevada, Las Vegas, Radiological Computational Center, for running our MCNPX codes on their clusters.

Reference

Goldin, F. J., E. J. McCrea, R. E. Stewart, "Bismuth germanate (BGO) array for spectroscopy of gamma pulse," in *SPIE Conference Proceedings: Gamma-Ray and Cosmic-Ray Detectors, Techniques, and Missions*, Denver, Colorado, August 5, 1996, B. D. Ramsey, T. A. Parnell (eds.) **2806** (October 1996) 536–544.

A Tagged Photon Source for Energy-dependent Radiography

Tim Ashenfelter, Peter Heimberg (former employee), Michael J. Hornish,[1] Eric Moore
Remote Sensing Laboratory – Andrews

Michael Mendez, Ken Moy
Special Technologies Laboratory

This report represents the second phase of a two-year project involving the study of a "tagged" photon system that utilizes nearly monoenergetic electron beams emanating from a heated, polarized, pyroelectric crystal. FY 2005 achievements included initial beam characterization studies with existing capabilities at STL, Monte Carlo simulations of forward bremsstrahlung photon production, and development of a photoelectric injection system utilizing UV light-emitting diodes. This second phase has involved establishing an experimental electron beam facility at RSL–Andrews (RSL–A) to conduct more extensive beam characterization studies and to perform measurements of deflected electrons in coincidence with their corresponding bremsstrahlung photons. Although the ultimate goal of "tagging" photons has yet to be realized, a large vacuum chamber and the equipment necessary for conducting further pyroelectric beam studies have been assembled, thereby providing a facility that will enhance future experimental investigations and enable beam study for a far wider range of applications.

Background

Over the past 15 to 20 years, significant progress has been made in studying and understanding electron beam production through the use of pyroelectric crystals. This phenomenon involves utilizing the large electric fields generated by moderately heating such a crystal in the presence of a dilute gas, resulting in the production of a self-focused electron beam (from one end of the crystal). Indeed, the first known observation of x-rays resulting from such electron beams incident on metallic targets occurred in 1992 (Brownridge). Further studies have ascertained more information about these beams' nearly monoenergetic nature, as well as their energy of up to 170 keV (Brownridge, 2001). Recently, these crystals have been used to drive fusion reactions by accelerating deuterium ions (Naranjo, 2005).

[1] hornismj@nv.doe.gov, 301-817-3347

Under the SDRD program, a group of researchers at STL has conducted detailed studies on the behavior of these crystals (Quam, 2004) and has exploited this phenomenon to generate terahertz radiation (Quam, 2005). Finally, as part of the FY 2006 SDRD program, the same STL group has studied the possibility of employing this technology as a neutron source.

The principle behind the present concept was to impinge the electron beam on a thin aluminum target. The passage of electrons through the foil will cause them to radiate bremsstrahlung photons a small percentage of the time. For those electrons that do emit photons, this process reduces the corresponding electron energy from its initial value, E_{beam}, to a smaller value, $E_{electron}$. On the downstream side of the foil, the emergent electrons will then be exposed to a magnetic field that has been introduced with a dipole magnet, thereby deflecting electrons with a curvature directly proportional to their velocity. Placing a solid-state, charged particle detector at an appropriate position relative to the path of the deflected electrons of interest will enable electron measurement; only those that have radiated a photon of a given energy will be incident on the detector and register a signal.

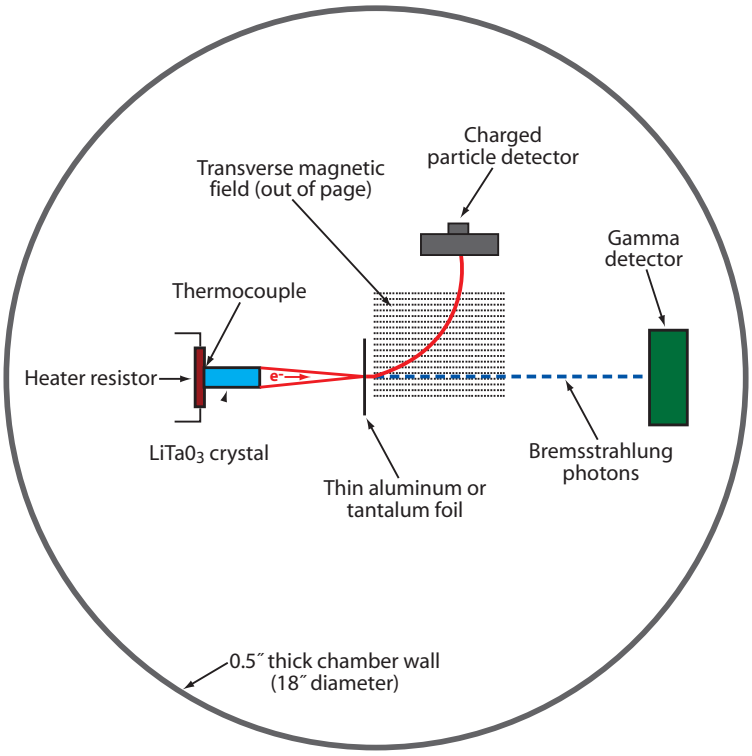

Figure 1. Diagram (not to scale) of the "tagger" apparatus to be used inside a large vacuum chamber. The red, curved line shows the path of an electron (incident on the silicon detector) that has radiated a bremsstrahlung photon (measured by an appropriate gamma/x-ray detector). Thus, the photon can be "tagged."

Meanwhile, the bremsstrahlung photons possess energies, represented by E_{photon}, that are determined by the difference between the initial beam energy and the electron energy following photon emission ($E_{photon} = E_{beam} - E_{electron}$). These photons proceed undeflected by the magnetic field; it is a straightforward process to measure them with an appropriate detector (e.g., a CsI crystal) in coincidence with their associated, reduced-energy electrons. Hence, one can individually "tag" a given photon with its electron, allowing one to choose which photon energies to utilize. This process can be achieved by moving the detector to different locations to measure electrons of differing energies. Thus, one can easily imagine using this "tunable" photon source for low-dose radiography purposes by placing an object to be imaged between the magnet and the photon detector. Figure 1 details the proposed setup of such a "tagged" photon system.

To lay the foundation for future explorations of this potential "tagger" capability, it is necessary to conduct additional pyroelectric beam studies to better characterize the electron beams. These studies should include further exploration of the spread in the electron beam energy, which is generally thought to be no greater than ~10%. Furthermore, increasing the beam energy would be an important step in broadening this method's potential scope. Finally, achieving some stability in terms of beam energy and the amount of beam current produced would be imperative for establishing reproducibility in the electron beam. To build on the progress made during FY 2005, we hoped to further characterize electron beam properties and attempt to optimize the parameters to make progress in measuring electron-photon coincidence events.

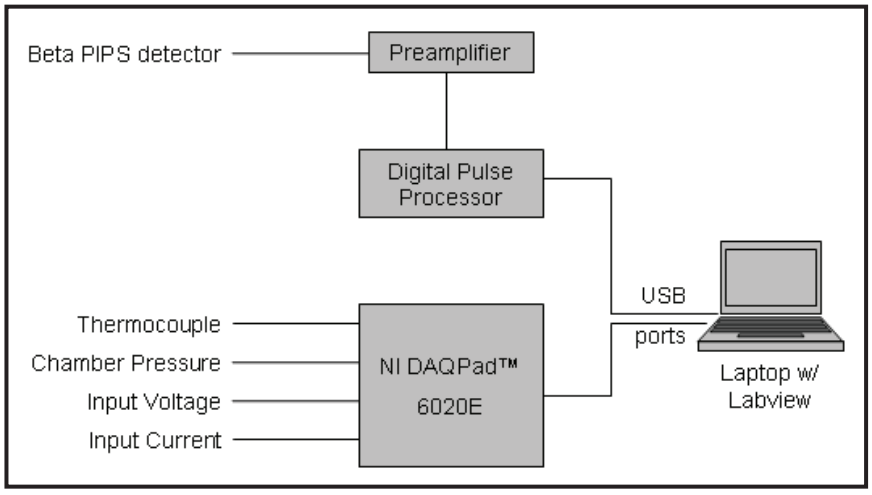

Figure 2. The electronics and DAQ system for the initial "tagger" experiment

Project

Existing STL facilities have proven valuable in performing initial electron beam studies. However, in order to set up an apparatus with which to conduct further beam characterization studies and take electron-photon coincidence measurements, we needed to obtain a larger vacuum chamber that could more easily accommodate the necessary components (Figure 1). Thus, with the help of our STL collaborators, we designed, ordered, and fabricated a large, spherical (18-in. diam) vacuum chamber with multiple ports. To ensure that the system was functional and could be operated safely and securely, we initially assembled and tested the finished chamber setup and its corresponding, oil-free, turbomolecular vacuum pump at STL. In addition, we procured a LabVIEW-based data acquisition system (DAQ).

The lithium tantalate ($LiTaO_3$) crystal, vacuum chamber, vacuum pump, and all associated electronics were shipped to RSL–A. Electrical work was performed in the laboratory area to provide a dedicated power outlet for all of the "tagger's" needs. Passivated implanted planar silicon (PIPS) detectors with two different thicknesses were acquired for use in measuring electron beam properties and for making electron-photon coincidence measurements. System setup is rather straightforward, as shown by the simplified schematic (without photon detector) in Figure 2.

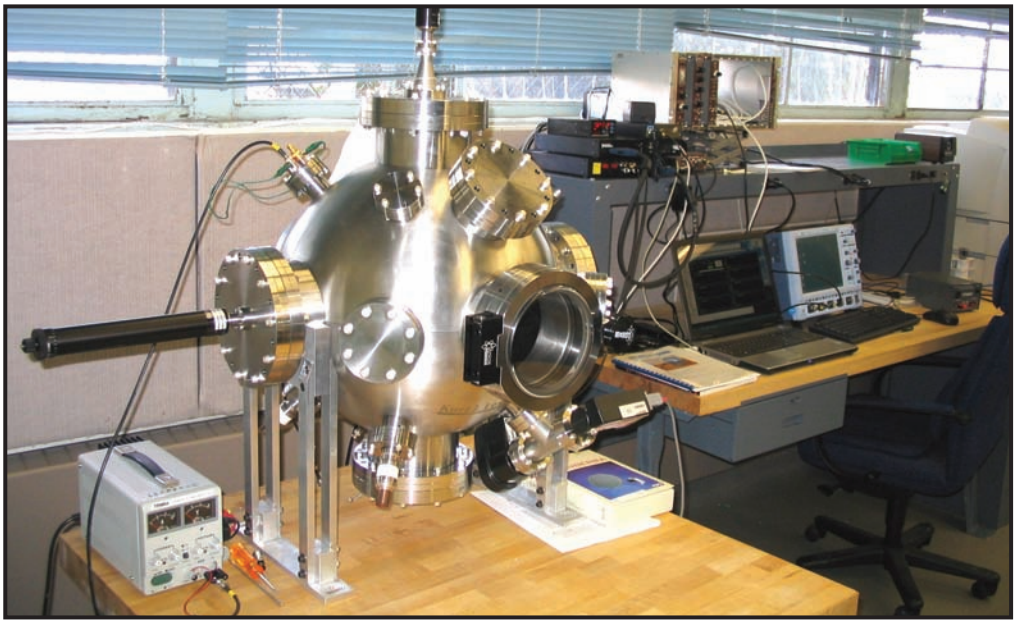

Figure 3. Laboratory set-up, including the large, 18-in.-diameter vacuum chamber and corresponding electronics, DAQ, and laptop used to conduct experimental measurements

All equipment successfully arrived and was assembled. On receipt, the acquisition electronics were configured to measure crystal temperature with a thermocouple, and to record the signal from the beta PIPS detectors through a preamplifier and digital pulse processor. The laboratory setup appears in Figure 3, and the vacuum chamber and crystal are presented in Figure 4.

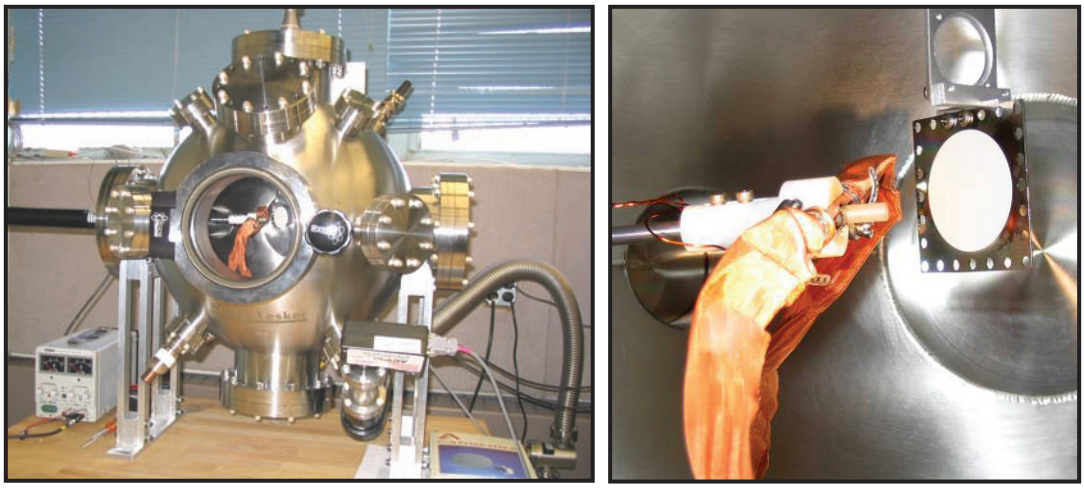

Figure 4. The $LiTaO_3$ crystal shown inside the chamber at left is shown in detail in the right-hand image, along with a zinc sulphide (ZnS) phosphor used to visually verify the presence of an electron beam while in operation

We have tested the vacuum system, and stable vacuum pressures have been achieved. Meanwhile, preliminary crystal-heating tests have also been performed. The crystal was heated to a suitable temperature for electron beam production by passing an electrical current from a DC power supply through the attached heater resistor. However, a visible beam was not successfully generated, and scheduling limitations prevented further studies.

Conclusion

The pyroelectric electron beam apparatus described above has been assembled at RSL–A, and tests of the vacuum system have been performed to verify system integrity and functionality. Preliminary attempts to heat the crystal unfortunately failed to produce an accelerated electron beam, and limited efforts to correct the problem were unsuccessful.

References

Brownridge, J. D., "Pyroelectric X-ray generator," *Nature* **358** (23 July 1992) 287–288.

Brownridge, J. D., S. M. Shafroth, D. W. Trott, B. R. Stoner, W. M. Hooke, "Observation of multiple nearly monoenergetic electron production by heated pyroelectric crystals in ambient gas," *Appl. Phys. Lett.* **78**, 8 (February 2001) 1158.

Naranjo, B., J. K. Gimzewski, S. Putterman, "Observation of nuclear fusion driven by a pyroelectric crystal," *Nature* **434** (28 April 2005) 1115–1117.

Quam, W., M. Mendez, K. Moy, S. Sawyer, S. Weeks, "Lithium Niobate Terahertz Generator," *Nevada Test Site–Directed Research, Development, and Demonstration*, FY 2004, Bechtel Nevada, Las Vegas, Nevada, 2005, 31–34.

Quam, W., S. Weeks, "Heat-stimulated Lithium Niobate X-ray Source," *Nevada Test Site–Directed Research, Development, and Demonstration*, FY 2003, Bechtel Nevada, Las Vegas, Nevada, 2004, 51–54.

Portable X-ray Spot-size Diagnostic

Stephen S. Lutz,[1] *Roderick Tiangco*
Special Technologies Laboratory

Our team assembled and fielded a portable spot-size measurement for bremsstrahlung sources. We tested detector and resolution for sources with endpoint energies from 0.25 to 8 MeV. Dynamic range comparisons were made with an image plate phosphor detection system over this same energy range.

Background

Radiography is an important tool for probing metallic density profiles in dynamic experiments. Both NNSA subcritical and hydrotest programs employ radiography extensively. Source brightness is a critical figure of merit for understanding any radiographic system. To determine brightness, one must know the source strength, typically expressed as the number of rads at a meter (dosimetry) and spatial extent (spot size). Historically, spot size is measured with an imaging detector, generally a phosphor or x-ray film. Our team proposed developing a portable system to standardize spot-size measurement and provide a measurement in situations in which a local detection system is unavailable. Further, there are some sites in which removal of the phosphors may be difficult and time-consuming. For example, at DARHT there are issues with contamination at the working point, necessitating bagging of phosphors on the point, and swiping upon removal. At the NTS Cygnus facility, the phosphors must be removed and brought "uphole" for reading.

Project

This project comprised two parts. First, we surveyed and ranked commercially available, large-area, bremsstrahlung radiation-imaging technology. Technology was ranked in terms of cost, performance, and portability, and a selection was made. We then purchased a detector. Part two involved testing, fielding, and characterizing the selected detection system at several NNSA facilities.

Product Survey

Early on, we decided to use a large-area, solid-state silicon (Si) detector for the imager. Competing technologies included image plate (IP) phosphor systems, wet film, and camera/radiation-to-light converter (scintillator) systems. IP phosphor system performance makes it the current standard for radiation imaging, especially at low to modest energy (0.1–1 MeV). The medical industry now uses IP phosphors almost exclusively for standard radiography tasks. This technology, however, entails

[1] lutzss@nv.doe.gov, 805-681-2244

a relatively large and delicate reader system. A typical phosphor scanner, about the size of a modest copy machine, usually requires a factory technician for setup. Field efforts such as the Nuclear Emergency Search Team utilize this technology. However, the field deployment device is generally large, involving steamer trunk–sized packaging.

The team ruled out wet film, based on its complexity of development and waste stream. Scintillator arrays, coupled to a large, scientific-grade CCD camera offer the best detection at higher energy. Thus, it is the detector of choice at both the DARHT and Cygnus facilities. However, complexity, weight, and cost are negatives for this relatively straightforward application.

Large-area (>40 mm^2) Si detectors have been available for more than 10 years. The basic detector configuration employs an optical sensor, generally based on amorphous Si, close-coupled to a phosphor. In this scheme, most of the bremsstrahlung energy is deposited during interaction with the phosphor, which in turn produces light that is detected by the Si panel. Early models suffered from longevity and reliability issues. They were susceptible to radiation damage, expressed as dropped pixels, dropped columns, and enhanced fixed-pattern noise.

We contacted three detector vendors about their products: Varian, Rad-icon, and Envision. A recent innovation in detector architecture, developed for use with higher energy-penetrating radiation, places the associated electronic circuitry outside the detector plane. This enables the control, amplification, and analog-to-digital electronics to be encased in lead shielding. Both Varian and Rad-icon offered such a configuration. However, at the time of purchase, Varian was withdrawing their product because of an unknown performance problem. Hence, we elected to procure the Rad-icon system.

Figure 1. Detector with laptop computer in travel case

The Rad-icon detector consists of a 2048 × 2000 pixel array. It produces 12-bit data (4096 count maximum) and is coupled to a user-friendly universal serial bus (USB) interface. It comes with custom software that allows one to configure the device to trigger remotely, syncing it with an external pulsed radiation source. This capability was essential for our application.

The laptop-sized detector can be packed in an airline carry-on bag, along with a readout computer (Figure 1). Its active area is seen as a black recess, on the order of 100 mm^2.

Detector Characterization

The detector was tested with four different pulsed radiation sources:

- Platts flash – 250-keV endpoint, tungsten anode
- 705 Febetron – 2-MeV electron source, Ta target, 25-mm Al filtration
- Cygnus rod-pinch diode – 2.2-MeV endpoint, tungsten anode
- Radiographic integrated test stand (RITS) – 8-MeV SNL diode development test stand

We first tested the detector with the Platts flash source. Early on, we noticed that the detector was susceptible to triggering on the electromagnetic pulse (EMP) associated with the firing of the Platts Marx bank. This observation was particularly troublesome because the Platts flash is a relatively quiet source. This was an issue because the detector requires a 125-ms pretrigger to reset the thermal noise buildup immediately before signal integration. When the Marx bank triggered, the device would retrigger, effectively causing the radiation to come in the middle of the reset cycle. We overcame this problem with the Platts source by overdriving the trigger then attenuating the signal at the detector trigger input. When fielding the device in relatively noisy environments, such as RITS and the Febetron, we used a Faraday cage, complete with 60-cycle line filters, a fiber-optic control line for the trigger, and USB data transfer. With these provisions, the detector triggered reliably and provided consistent image data.

Detector and beam source characterizations were generally accomplished by using a rolled-edge target in two different radiographic geometries. To characterize detector resolution, an edge was placed close to the detector. This geometry is analogous to launching an image of a step function into the detector. Blurring of the step, as measured by the edge-spread function (ESF), is presumably due to a combination of radiation-induced scatter in the detector, optical scatter in the associated phosphor, and the electrical response of the detector. Source-spot measurement is accomplished by placing the rolled edge near the source, effectively magnifying the penumbral source distribution for detection.

We generated a metric for measuring the blur circle, based on the ESF, by using an algorithm that relates the 50% point of the fast Fourier transform power spectrum with that of a uniformly filled circle. This "LANL spot-size metric" is quoted in Table 1.

Table 1. Detector performance comparisons with different radiation sources

Detector	Detector Blur (mm)	Dynamic Range	Source
Rad-icon sensor	0.31	1153	Platts (250 KeV)
Phosphor - 7000 series Fuji	0.4	702	Platts (250 KeV)
Phosphor - 5000 series Fuji	0.38	262	Platts (250 KeV)
Rad-icon sensor	0.49	102	Febetron (2 MeV)
Phosphor - 5000 series Fuji	0.54	55	Febetron (2 MeV)
Rad-icon sensor	0.91	7.2	Cygnus (2 MeV)
Phosphor - SNL 3000 series	0.65	18	Cygnus (2 MeV)
Rad-icon sensor	12.9[1]	99	RITS (8 MeV)
Phosphor - SNL series 3000	12.9[1]	200	RITS (8 MeV)
[1] Beams spot size, not detector blur			

Relative dynamic range data were obtained by dividing the 1σ value of the noise distribution, measured in the region attenuated by the edge, into the mean value of the unattenuated region. A similar calculation was made for an IP phosphor system. These dynamic range numbers do not define the detector's absolute range and must only be used to compare solid-state detector performance with that of the IP phosphor in the specific experiment. The color-coded measurement pairing appears in Table 1.

The solid-state sensor exhibits significant fixed-pattern noise, with variations in noise and sensitivity across the image plane. This noise was removed by acquiring dark fields characterizing baseline noise variations, and flat fields characterizing sensitivity variations. All the data presented in this report have been corrected for this fixed-pattern noise.

A sample of the solid-state sensor data, exposed using a 250-keV endpoint Platts source, appears in Figure 2. In this energy range, the solid-state detector outperformed the scanner systems, as shown in the dynamic range numbers in Table 1. The Rad-icon sensor's relative performance decreases with increasing source energy. However, the solid-state sensor always performed adequately enough to provide accurate and reliable spot-size data.

Figure 3 shows an image of a rolled edge taken at the RITS accelerator. This edge was configured to allow source spot-size measurement, as seen by the gradual, well-resolved, graded range of intensity values in the rolled-edge transition region.

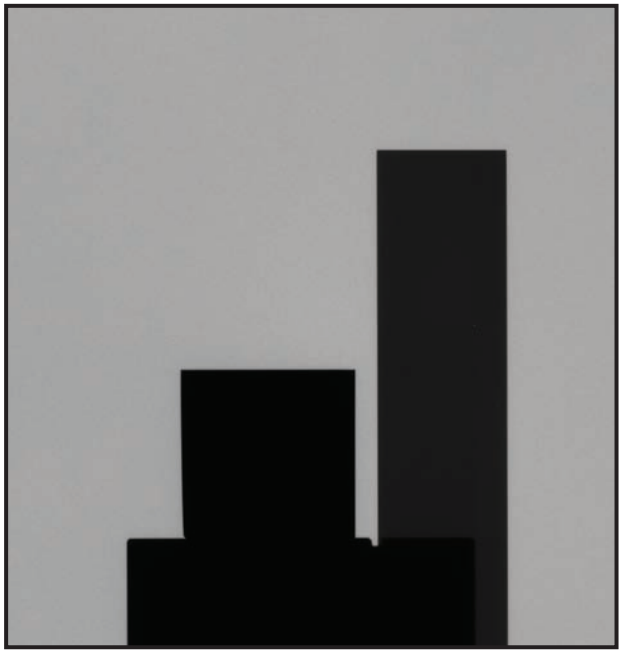

Figure 2. Platts flash radiograph: 250-keV endpoint spectra showing rolled edge close-coupled to detector for detector resolution measurement

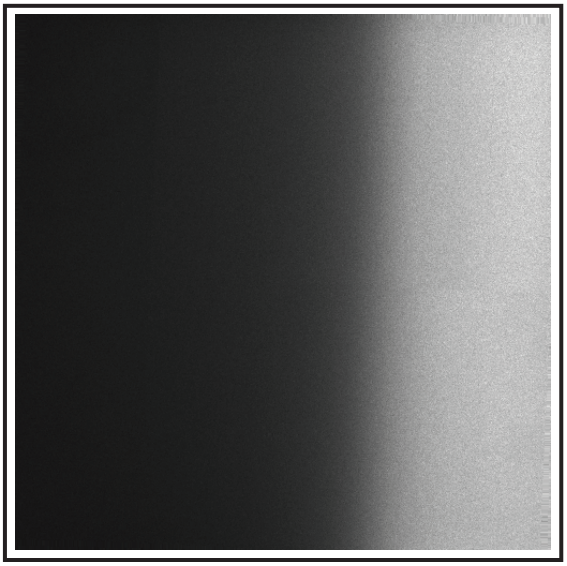

Figure 3. ESF image taken at RITS accelerator

Conclusion

This detector is applicable as a portable spot-size detector over a wide range of beam energies and operated reliably in adverse EMP environments. The device showed no signs of degradation over the course of this study. It has already been programmatically applied in the activation of Cygnus, in preparation for the Thermos subcritical series.

Acknowledgments

The authors would like to thank Sal Portillo, of SNL, and John Smith, of LANL, for their assistance in obtaining data at the RITS and Cygnus facilities, respectively.

Anode Preionizing Systems

E. Chris Hagen, B. T. Meehan[1]
North Las Vegas

Several SDRD projects have had as their goal the optimization of specific operational parameters of the dense plasma focus (DPF) fusion neutron source. This project similarly concentrated on one phase of the physical sequence that leads to fusion. We explored the science of the initial "breakdown and inverse pinch" step of the plasma generation sequence and attempted to optimize it. Uniform initiation of plasma ionization is extremely important to the DPF's ability to efficiently produce neutrons and photons, and investigating methods of improving plasma annulus uniformity was the purpose of this project. Several theoretical approaches were prototyped and tested. We concluded that, of the means available to us to change during this experiment, changing the shape of the cathode ring was most likely to affect the initial shape and uniformity of the plasma shockwave.

Background

DPF devices generate Z-pinch plasmas, compressing and heating them to temperature and pressure regimes sufficient to initiate nuclear fusion. The more symmetrically the gas is assembled before compression, the more efficient the fusion burn will be. In a DPF, the process occurs in phases: plasma initiation at the base of the anode, plasma transport from the base to the top of the anode ("run-down"), plasma compression ("pinch"), and the disassembly of the hot, dense plasma. A detailed description of the phases follows.

The DPF works by first ionizing a rarified working gas and then pushing through a large amount of current from a capacitor bank. The anode rises from 0 kV to many 10s of kV; in our case, 35 kV. The source tube (Figure 1) is filled with a rarified atmosphere of a gas, typically deuterium at a few torr. As the voltage on the anode rises, the resultant electric field between the triangular prisms on the inner circumference rises, and field emission electrons are emitted. A Pyrex cylinder prevents the electrons from reaching the anode. When the voltage of the anode exceeds the breakdown voltage of the gas in the source tube, an arc discharge occurs. This discharge has very low impedance, and plasma current begins to flow. If the cloud of field emission electrons is uniform, and if the physical geometry of the tube is sufficiently good, the discharge will be fairly uniform around the base, forming an annular sheet at the base of the anode. The current passing through the plasma sheet at the base of

[1] meehanbt@nv.doe.gov, 702-295-0490

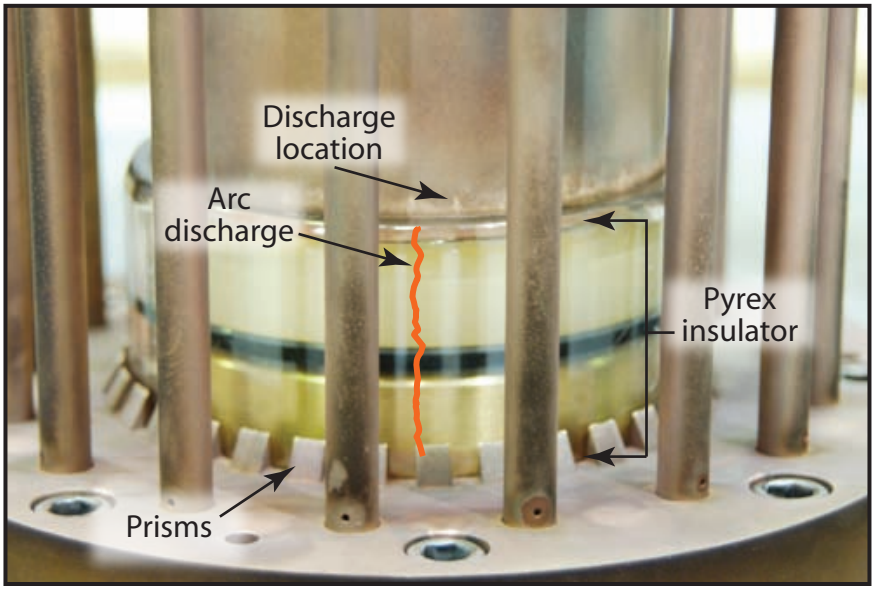

Figure 1. Breech region of the tube, showing field-emission prisms, cylindrical Pyrex insulator surrounding the anode, and the cage of cathode bars. This particular assembly was fired numerous times; thus, the residual effects of high current have become visible. Features to be noted are the shiny points of the prisms and the arc marks directly above the corners of the prisms. These marks are asymmetrical in depth and length, indicating unevenness of process initiation.

the anode generates a magnetic field that forces the plasma annulus toward the top of the anode, trapping the gas above it in a magnetic piston. The piston then rapidly accelerates toward the top of the anode, where the entrained gas is Z-pinched.

The process is very sensitive to any disturbance in the plasma, particularly those early in the formation of the plasma annulus. The most sensitive stage is the initial formation of the annulus, during the initial ionization of the rarified working gas. If the ionization is uneven about the anode, the plasma annulus will not accelerate at a uniform rate. At best, this may prevent the Z-pinch from happening on the axis of the anode; at worst, it may prevent the Z-pinch from occurring at all.

We aimed to investigate methods of increasing DPF neutron yield and the efficiency of the conversion of electrical power into neutron yield. Of the practical methods available to us, we chose to optimize the shape of the cathode ring as a means of ensuring a stable and symmetrical initiation of the current sheet. In this project, we tested some of these theoretical improvements on the NSTec DPF.

Project

Several methods to ensure uniform plasma ionization at the anode base were proposed. Prototype components, allowing investigation of several of these hypotheses, were fabricated and tested in the NSTec DPF. Various approaches considered by the DPF team are detailed below.

High-voltage Breakdown in Gas-filled Gaps

The breakdown of a gas insulator under an impulse of high voltage differs from that of a steady DC voltage. Two factors govern the differences between DC (Paschen discharge, shown in Figure 2) and impulse breakdown characteristics of a given gap. The first is a delay characteristic of the time required to form the electron streamers that eventually short out the gap. The second delay is an additive statistical delay in the time between the high-voltage pulse and the gap breakdown. For a given high-voltage gap, two things must take place for the gap to conduct under a high-voltage pulse: an electron must be present, and that electron must be capable of creating an electron streamer from the cathode to the anode. While electrons are naturally present as a result of cosmic radiation and natural background radiation, they rarely appear in the gap at the exact moment that the high-voltage pulse arrives. Consequently, all high-voltage gaps have jitter and delay when driven with a high-voltage pulse, which means they are difficult to engineer for specific purposes.

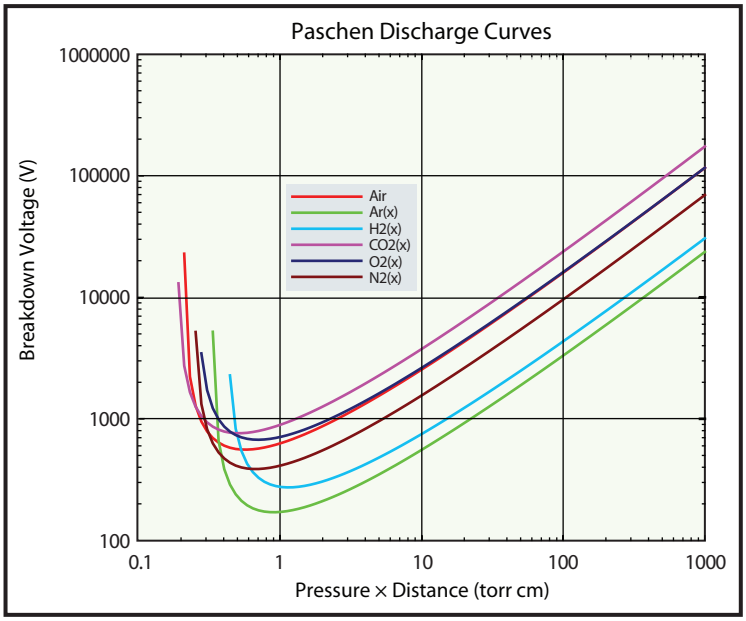

Figure 2. Paschen discharge characteristics of various gasses

Assuming that an electron's presence in the vicinity of the gap is governed by a Poisson distribution, we can model the length of time that we would have to wait for an electron to arrive as the probability of a single event from Poisson statistics,

$$w(t) = re^{-rt}, \quad \textbf{(1)}$$

where r is the rate at which electrons enter the gap, and t is time. The most probable waiting time would be inversely proportional to the electron generation rate. Next, in order for the electron streamer to cause the gap to conduct, the generated electron must become proximal to the cathode. The location of the electron is more of a geometric consideration, but since it depends on a preceding event, the probability is multiplicative. Essentially, generating more electrons in the gap will reduce statistical jitter.

Radioisotopes

The EG&G Kryton high-speed, high-current gas switch contains a small amount of ^{63}Ni. ^{63}Ni is a radioactive element that emits β^- particles. The β^- particles ionize the gas they strike, and this keep-alive ionization results in an extremely fast switch. Thus, a possible simple solution to ensure uniform DPF initiation might be to dope the cathode with a radioisotope. However, this method is potentially unsafe: using radioisotopes strong enough to increase the rate of electron generation in the violent environment within the tube poses a contamination hazard during maintenance. For this reason, the radioisotope-doped electrodes were not explored during this project. When the testing of a DPF with ^{3}H as part of the working gas occurs in future DPF research, there will be some residual β^- radioactivity in the breach region of the anode-cathode assembly, which will allow us to explore this possibility.

Increasing Cathode Electron Field Emission

By increasing the field emission of the electrons during the leading edge of the voltage pulse when it arrives at the DPF, the electron density in the gap near the cathode will increase, thereby helping in the formation of high-voltage streamers from the cathode to the anode and making it easier for the plasma current sheath to form. To test this concept, we altered the construction of the cathode base rings, some of which are shown in Figure 3.

Charge density and electric fields are enhanced in regions of large curvature on conductors. The induced surface charges on the cathode ring concentrate in the vicinity of the inner edge, where the voltage gradient is largest. If we also make the cathode sharp in this area, charges will further concentrate; this, in turn, will enhance the voltage gradient. Charges A and B in Figure 4 repel each other with more force than charges C and D because charges C and D are *constrained* to be in the surface of the conductor, and therefore only repel each other with the component of force parallel to the surface. The more curved the surface, the smaller the component of force parallel to the surface.

Increasing the local electric field increases the local field emission of electrons. The field emission of electrons can be described by Fowler-Nordheim tunneling through the surface barrier of the conductor, where the probability of a conduction band electron tunneling through a potential barrier (work function) near an electric field is:

$$\exp\left(-\frac{4\sqrt{2\,q\,m_e}\,\varphi_B^{\,3/2}}{3\hbar E}\right). \tag{2}$$

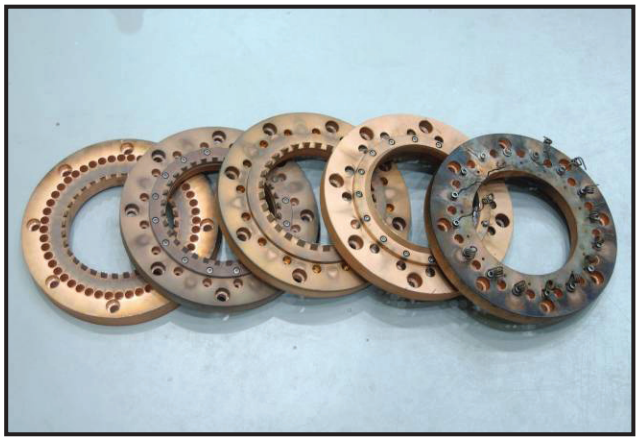

Figure 3. Experimental cathode ring configurations used during this experiment

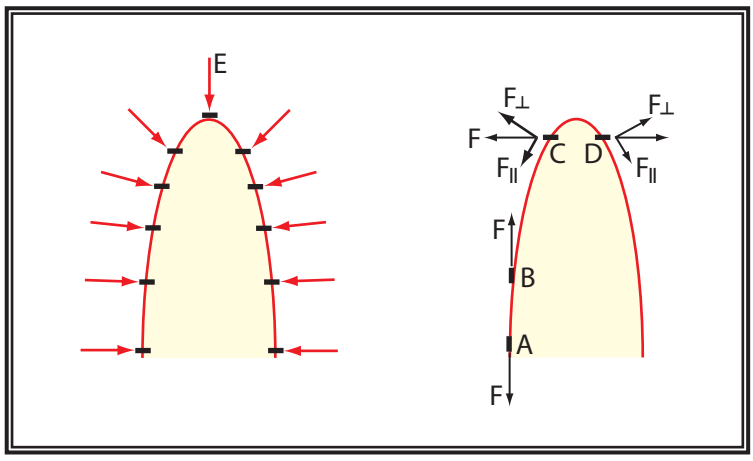

Figure 4. Forces on charges constrained to the surface of a conductor

Equation 2 shows that increasing the electric field at the surface of the conductor increases the probability of electron tunneling, and therefore increases the dark current of the conductor. Several designs for sharp cathode bases were considered, and two were implemented, as described below.

Knife Edge Cathode Base

A tungsten knife edge was constructed because it was possible to construct a far sharper edge out of tungsten than would be practically accomplished with copper, a softer metal. The installed knife edge cathode base is shown in Figure 5.

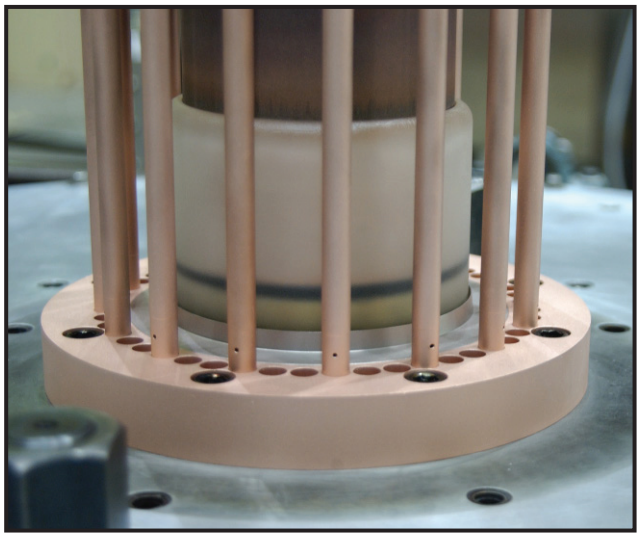

Figure 5. Tungsten knife edge cathode base

The knife edge cathode base was tested at various pressures and gas loadings. The results did not differentiate its performance from the "ring of teeth" design that was used on the majority of the DPF configurations before this experiment.

Sparse Point Array Cathode Base

A sparse "ring of teeth" cathode base under construction at the time of this report was not tested. The reason for the sparse "ring of teeth" design was that the sharp points would have much higher curvature than the tungsten knife edge, and would therefore have much greater corona current.

High-resistance and Inductance Field Points

While the knife edge and sparse point array designs focused on enhancing field emission (dark current) in the cathode base, the high-resistance and inductance design sought to control the current flow in the

glow and arc phase of discharge. The theory is that the high-resistance points will facilitate balanced current flow, which will promote uniform formation of the plasma sheath at the anode base, leading to a symmetric pinch. Inductors were placed at the base of the tube (Figure 6), and some data acquired. Unfortunately the tube region is so violent that, although mechanically stiff, the wires did not survive. Based on electrical tests with plasma discharges, we think that relatively high impedance is preferable.

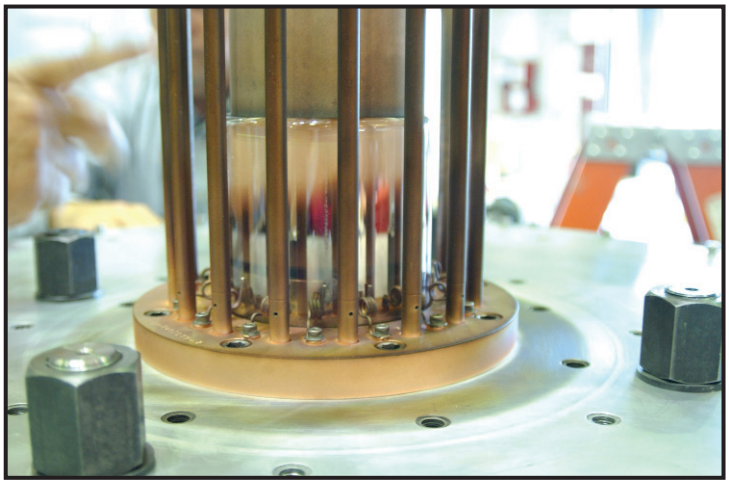

Figure 6. Inductive field point prototypes; shown are the inductors that replaced the prisms on the cathode base during a feasibility test

Exploding Wire

The "exploding wire" experiment proposed by Lyle Jensen was not performed in FY 2006. In this arrangement, the anode and cathode will be connected electrically with extremely fine aluminum or tungsten wires. When a voltage is applied to the DPF, a current will be forced through the wires that far exceeds their current capacity. This will cause the wires to rapidly heat and boil off metal ions from their surface; eventually the wires will be converted completely to plasma. This plasma will form the start of the magnetohydrodynamic shockwave. The benefit is that the shockwave will be uniform, and will form all around the anode at the same time. The drawback is that it can only be done once before the DPF will have to be disassembled and rewired, or the DPF will have to be operated in its ordinary knife-edge-initiated, plasma shock mode.

Conclusion

Without being able to observe the formation of the plasma shockwave, any optimization in current sheet uniformity would be difficult to achieve. Computer models that were run to model the electric field present in the anode-cathode breach did reveal that the design of the cathode ring was sharpened in the wrong place. The models indicated that the largest improvement in electric field strength would come from sharpening the inside edge near the glass insulator so that the points were toward the glass instead of perpendicular to it. Further testing with the deuterium-tritium gas mixture will allow us to further investigate how ionizing radiation could improve the performance of the anode-cathode gap in the DPF.

Acknowledgment

The authors would like to thank Lyle Jensen for many helpful discussions and for the exploding wire idea.

Silver Chalcogenides: Unique Megagauss Field Sensors

Stephen Mitchell[1]
North Las Vegas

Silver chalcogenides (Ag_2Te) have been shown (Husmann, 2002) to have potential for use in magnetic measurement devices. With applied magnetic field, the materials' electrical resistance displays a large linear increase, without saturation into the megagauss regime. This paper reports the progress and results our team made in synthesizing, fabricating, and characterizing thin-film and bulk Ag_2Te–based materials. The thin-film Ag_2Te sensor elements were fabricated in millimeter-sized packaging as field sensors for dynamic magnetic field measurements during high-power or explosively driven pulsed-power experiments. Such experiments are typically accompanied by electrical noise and signal issues commonly associated with B-dots or Rogowski coils.

Background

Pulsed-power machines capable of producing tremendous energy face various diagnostic and characterizing challenges. Such devices, which may produce 10–100 MAs, have traditionally relied on Faraday rotation and Rogowski coil technology for time-varying current measurements. Faraday rotation requires a host of costly optical components, including fibers, polarizers, retarders, lasers, and detectors, as well as setup, alignment, and time-consuming post-processing to unwrap the time-dependent current signal. Rogowski coils face potential problems such as physical distortion due to the tremendous magnetically induced pressures, which is proportional to the magnetic field squared (B^2), as well as electrical breakdown in the intense field region. Other related challenges include, but are not limited to, bandwidth and inductance limitations, and susceptibility issues to electromagnetic interference (EMI).

A unique alternative is to exploit silver chalcogenides materials as magnetic measurement sensors. Silver chalcogenides have been shown to be very sensitive measurement devices capable of yielding highly accurate magnetic measurements (Husmann, 2002). This project sought to use the materials' electrical resistance in a novel application for measuring extremely high magnetic fields to display a large linear increase with applied magnetic field without saturation.

[1] mitchese@nv.doe.gov, 702-794-1694

Project

Sensor Circuit Strategies

The sensor material Ag_2Te is magnetoresistive. We took advantage of this intrinsic feature by developing a method of measuring the change of resistance, as a function of the applied external magnetic field. The method of transporting such a measurement from the experiment to data-recording instruments was of particular interest.

Two promising strategies were investigated: by utilizing the sensor element in a resistor-capacitor (RC) timer circuit, such as the familiar 555 IC family variety, the output data would be represented as either a pulse length or frequency-modulated optical output. Such an optical signal would then be converted back to an electrical signal, recorded, and finally postprocessed to unravel the corresponding time-dependent magnetic field. With this method, the signal would be in essence a "phaselike" measurement and thereby would not suffer from amplitude, absolute measurement, or calibration-related issues concerning diagnostic interfaces. The other alternative was to use the sensor element as a terminator in a microwave transmission line. In this case, the change in reflected microwave radiation would represent a quantitative measurement of the magnetic field.

In any event, both methodologies seemed equally promising. But the capital equipment requirements of the microwave technique, as well as experimental constraints and challenges imposed by possible explosive-driven pulsed-power devices, made us focus on the timer circuitry.

Sensor Element Fabrication

Four forms of Ag_2Te for sensor elements were explored: 1) melting into quartz capillaries, 2) using native crystals, 3) using thin films outside the capillaries, and 4) using thin films on glass slides.

The native crystals were determined to possess too large of a cross section, giving rise to too low (~1 Ω) electrical resistances. Resistance this low is not only out of the normal operating range of typical RC timing circuits, but would also represent too much of a load, causing potential overheating of the element.

To give reasonable resistances, we made several attempts to melt the Ag_2Te into very thin (~300-μm inside diameter) capillaries. However, it was determined that surface tension kept the Ag_2Te from coalescing into a fine wire. Thin films of Ag_2Te deposited on the capillary gave large resistances, but the very thin and narrow conduction path was prone to physical damage.

We therefore worked primarily with thin films on glass substrates. The resistance of a native crystal ~1 mm × 1 mm × 3 mm was on the order of an Ω. This meant that we needed to develop thin films with thicknesses of ~1 μm to reach the minimum 100-Ω resistance values required by RC timing circuits.

Thin Film Preparation

The Polaron E5200 sputter coater (Figure 1) was to deposit a layer of pure silver on our substrates. A convenient thickness was determined to be 100–600 nm. Sputter depth profile for the 3000 sec was performed on the Ag-deposited substrates. Thus, the sputter rate was determined to be about 0.6 nm/sec to yield an Ag layer of about 300 nm thick to start. Thickness and composition characterization measurements were performed at the Desert Research Institute's (DRI's) X-ray Photoelectron Spectrometry (XPS) Sputter Depth Profiling facility.

Figure 1. Polaron E5200 sputter coater

The silver layer was subsequently converted into telluride by heating the silver film in an evacuated glass or quartz tube with elemental tellurium. Heating occurred in two stages: 1) at 200°C, to form the telluride, and 2) at 300°C, to create well-formed crystallites. The silver migrated on the substrate and did not form a film when the material was exposed to a much higher temperature. We found by heating the Te in vacuum, a mirror film formed on the tube before introducing the silver. Presumably,

this increased the surface area and vaporization/reaction rate. Previous researchers used a hydrogen stream to mobilize the tellurium. However, this method was rejected due to safety risk and toxicity issues related to the potential presence of H_2Te.

Once the Ag_2Te film was formed, Ag pads were deposited on each side of the substrate, thereby making electrical connection with commercially available metal particle–loaded paint, and we covered the sensor area with cellulose acetate–based lacquer (automotive window heater repair paint and nailpolish, respectively). This made a robust sensor element for the evaluation of circuit and transport properties.

Sensor Element Characterization

The Ag_2Te was chemically characterized at DRI's XPS machine. The anticipated result was that of the expected 2:1 stoichiometric quantities (Figure 2). The main line is Ag 3d, and the smaller line is Si 2p, presumed to be that of the substrate constituent.

The Ag_2Te layer was further characterized for its magnetoresistance by introduction into a superconducting solenoid, which has a magnetic range of ±9 T (Figure 3).

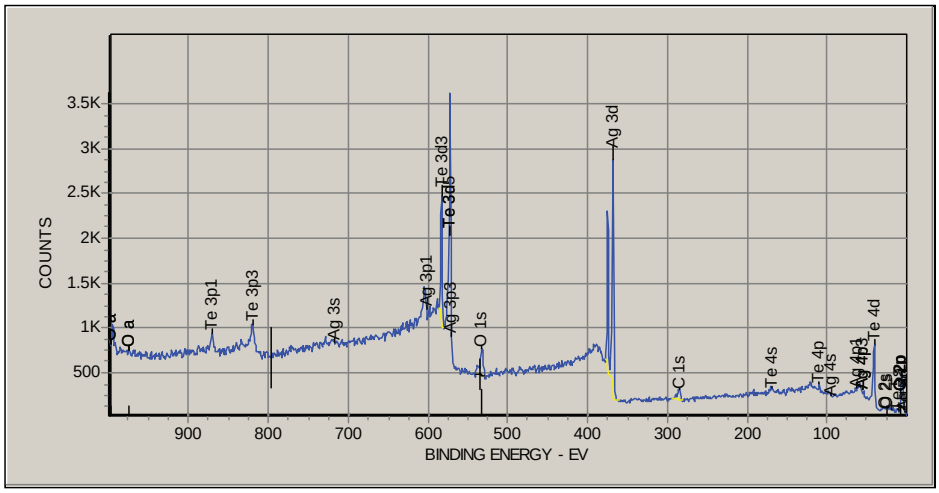

XPS Line	Adj'ed Be	FWHM	Area	Scans	Norm Area	Atom %
C 1s	284.596	4.031	600.544	1.000	299.804	28.288
Ag 3d	368.361	8.106	10233.919	1.000	297.892	28.107
Te 3d3	583.023	2.097	3265.566	1.000	159.003	15.003
O 1s	532.493	3.939	1513.587	1.000	303.144	28.603

Figure 2. Composition analysis of Ag_2Te material

Figure 3. Physical Property Measurement System (PPMS)

We found that we could get a film with approximately 6% resistance change per Tesla (Figure 4). Resistivity was measured to be $\Delta\rho/\rho_o \approx 0.11(\Delta B/T)$, while a change in the electrical resistance, $\Delta R(B)/\Delta B$, was $\approx 5\Omega/T$.

This change in the electrical resistance with respect to changing magnetic field was expected to lead to an equivalent change in frequency in the timer circuit.

Sensor Circuit Issues

We focused our attention on surface-mount timer circuits. The smaller footprint of surface-mount components allows smaller sensors (higher spatial resolution) and minimizes inductive loops (more robust behavior in time-varying magnetic fields). With just an external capacitor and the sensor element (Figure 5), our final surface-mount device, the MIC1557, yields a square wave at several megahertz. Also required is the electrooptic modulator (Figure 6) to transport the results to the data-logging setup. During the experiment, this setup is powered by a small hearing aid–sized battery cell.

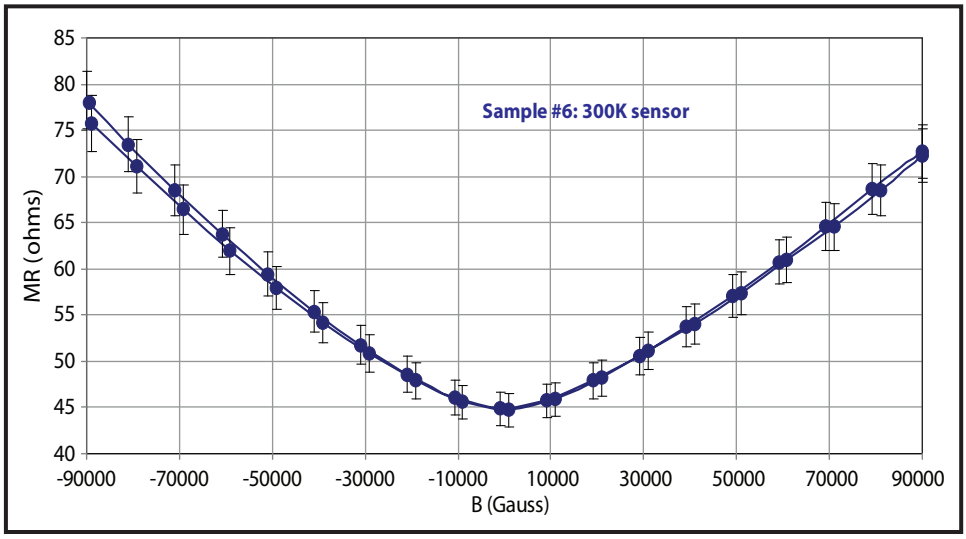

Figure 4. Sensors' magnetoresistive response to applied magnetic field

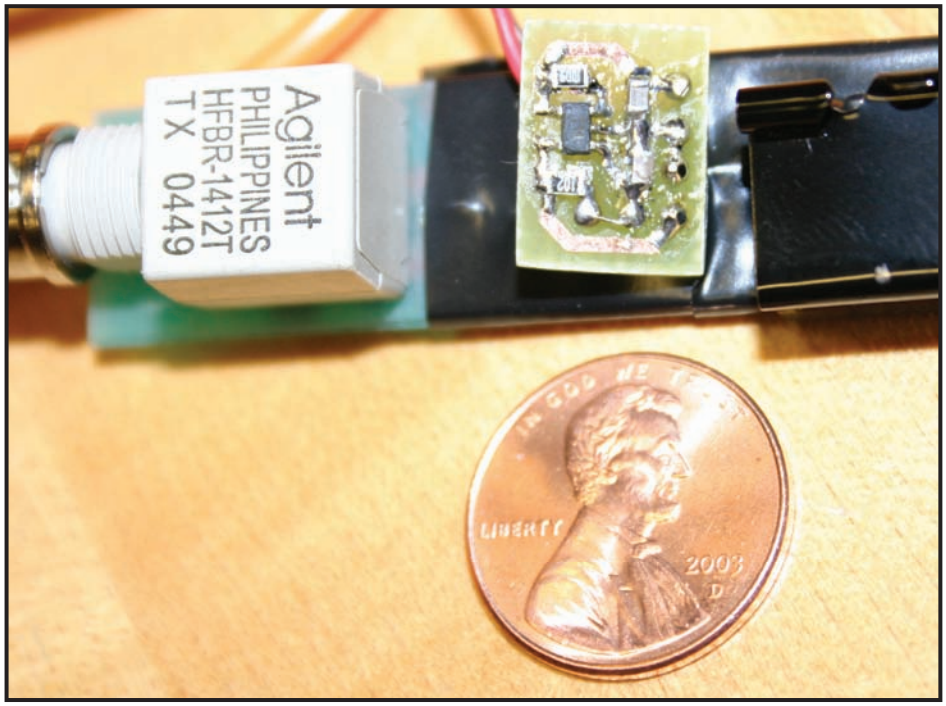

Figure 5. Surface-mounted timer circuit with Ag_2Te sensor element

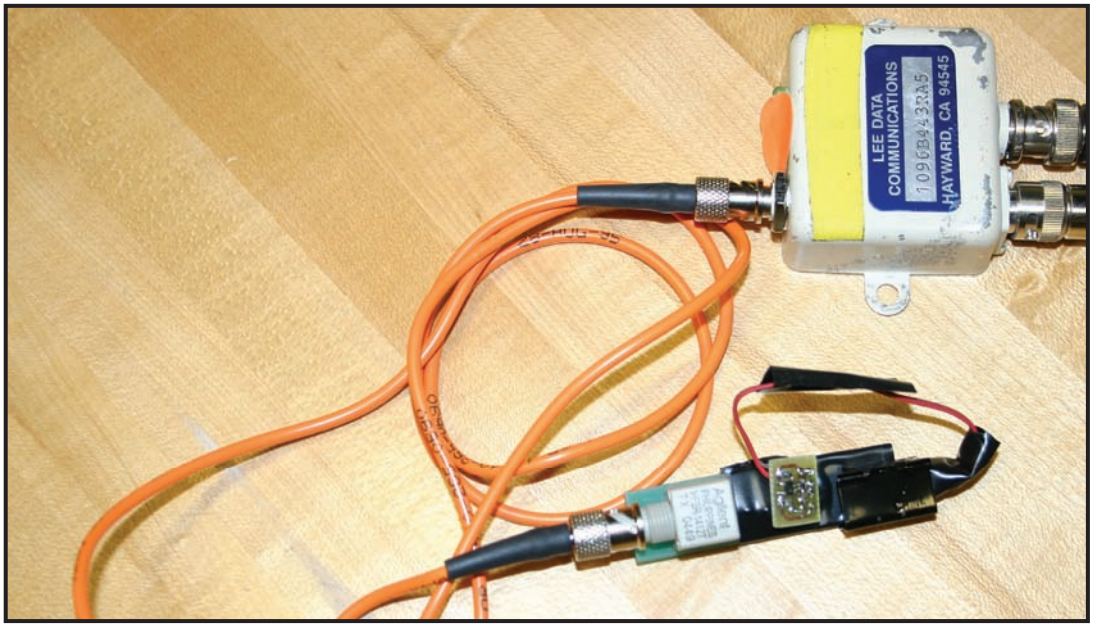

Figure 6. E-O and O-E transmitter and receiver with circuit

The final circuit produced an anticipated frequency response, dependent on a large, external, applied magnetic field, with a time resolution of microseconds (Figure 7).

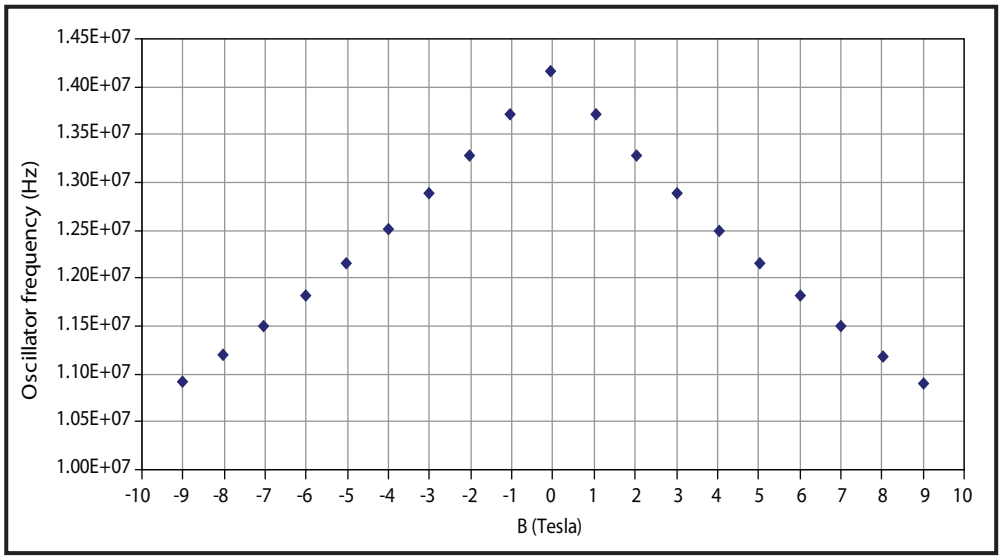

Figure 7. Frequency response to applied magnetic field

Conclusion

We have successfully developed a magnetoresistive element via thin-film sputter deposition and demonstrated its response in an external high-magnetic field. We further explored cost-effective methods to transport a representation of the changing electrical resistance measurements, which are often made in a hostile environment, immune to EMI-susceptibility related issues.

Toward the end of this research, our processes, procedures, and facilities improved greatly, thus producing sensors with reproducible results and qualities (Figure 8).

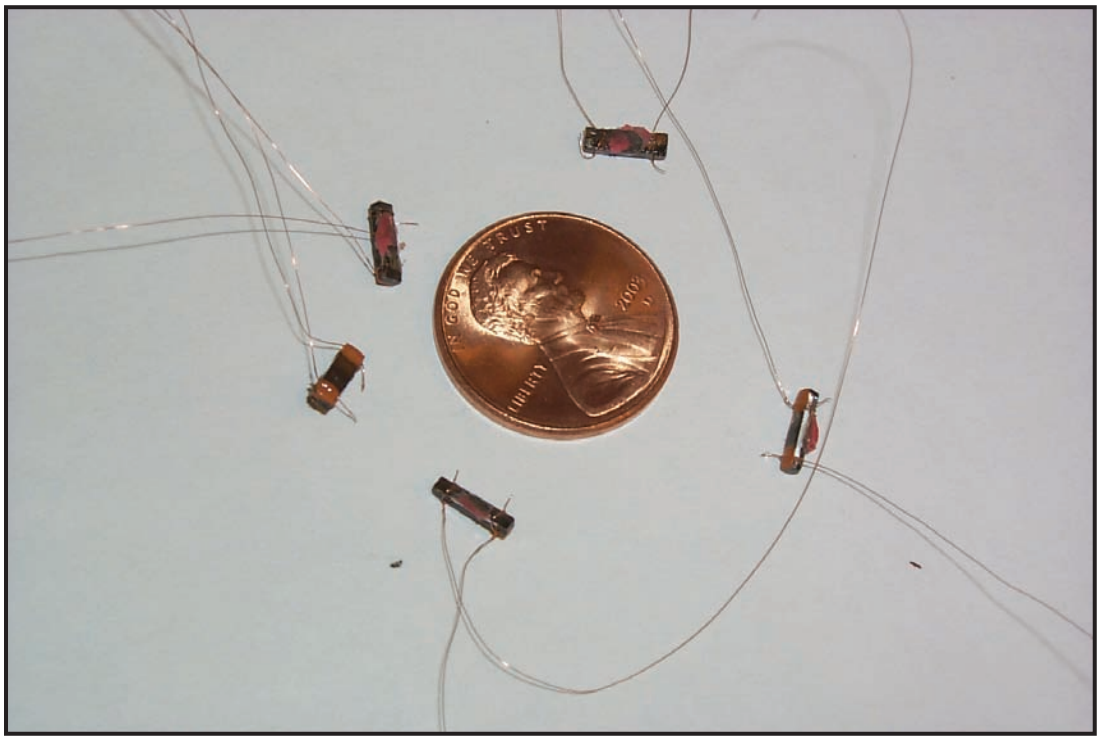

Figure 8. Final configuration of the last five Ag_2Te sensors produced. A "penny" reference is shown for scale.

Existing NSTec and national laboratory pulsed-power machines (Atlas, Cygnus, dense plasma focus, explosive-driven pulsed power, etc.) may benefit greatly by inducting these devices into the existing diagnostics suite. This would be especially true for explosive-driven sources, in which costly diagnostics would be expended. These devices may be an ideal, cost-effective alternative for obtaining essentially the same measurement.

Future Work

The practicality of silver chalcogenide based-sensors has yet to be demonstrated in available pulsed-power devices configured to deliver >10 T dynamic pulse.

As indicated earlier in this report, of the two strategies for measurement transport, exploring the material as an RF Loss probe may also prove to be an effective measuring method. Bulk material as terminations/boundaries in microwave application exhibiting field-dependent impedance changes may be very sensitive to reflection/transmission changes.

Other future work could include continued investigations and evaluations into the stoichiometric range and limits for optimal sensor constituents.

Acknowledgments

We wish to thank DOE/NNSA affiliations and sponsorships, DRI, and other invaluable assistance and support: Andrew Cornelius (Professor of Physics, UNLV), Daniel Antonio, Matthew Jacobsen, Bill O'Donnell, Amo Sanchez, and Ed McCrea (NSTec).

Reference

Husmann, A., J. B. Betts, G. S. Boebinger, A. Migliori, T. F. Rosenbaum, M.-L. Saboungi, "MegaGauss Sensors," *Nature* **417** (2002) 421.

this page intentionally left blank

Pyroelectric Crystal Neutron Source

Wayne Lenhard, Austin Moy, Ken Moy[1]
Special Technologies Laboratory

This project sought to replicate and extend work performed by University of California at Los Angeles (UCLA) researchers, who developed a compact neutron source using the pyroelectric crystal lithium tantalate ($LiTaO_3$) (Naranjo, 2005). A tungsten tip attached to the end of the heated crystal was used to enhance the electric field to generate deuterons from the ambient deuterium gas. With a heating cycle that lasted ~4 mins, the deuterons were accelerated to strike a deuterated target to induce deuterium-deuterium (D-D) fusion reactions that peaked with an output rate of ~800 n/s. D-D fusion occurs with a 50% branching ratio for reactions D(d, ^{3}He)n and D(d, p)t. This project attempted to increase the number of fusion reactions to produce a higher neutron output. Our goal was to accomplish this by replacing the single tip with an array of emitters fabricated by Biswajit Das and A. N. Banerjee, of the Nevada Nanotechnology Center at the University of Nevada, Las Vegas (UNLV), and by enhancing spontaneous crystal polarization by operating at cryogenic temperatures.

Background

Since the "pyroelectric" effect was recorded by ancient Greeks in 314 BC, recent scientific study by Weis and Gaylord (1985) has brought about a clearer understanding of the phenomenon. For crystals with high pyroelectric constants such as $LiTaO_3$, an increase in bulk crystal temperature results in an increase in the relative motion of Li and Ta atoms with respect to the O atoms in the crystal structure. Below the Curie temperature, movement of these atoms causes a change in spontaneous crystal polarization. For a cylindrical crystal fixed at a constant temperature, spontaneous polarization charges induced in the interior volume are compensated by surface charges at the end faces. During the warming stage of a heating/cooling cycle, a temperature increase reduces spontaneous polarization, thereby decreasing the polarization charges in the internal volume (Figure 1). If the ambient environment is not conducive to immediately producing compensating charges to balance the change in polarization charges, then a net static charge is present at the exterior/interior surface of the end faces to produce an external electric field. Through field ionization (quantum mechanical tunneling of electrons enhanced by the external electric field) of the ambient gas atoms, the electrons and ions produced will accelerate toward the crystal faces to neutralize the surface charges at a rate dependent on the gas pressure. At the –z cut face, the external field focuses and accelerates electrons toward and ions away from the crystal; the opposite effect is felt by electrons and ions at the +z face.

[1] moykj@nv.doe.gov, 805-681-2284

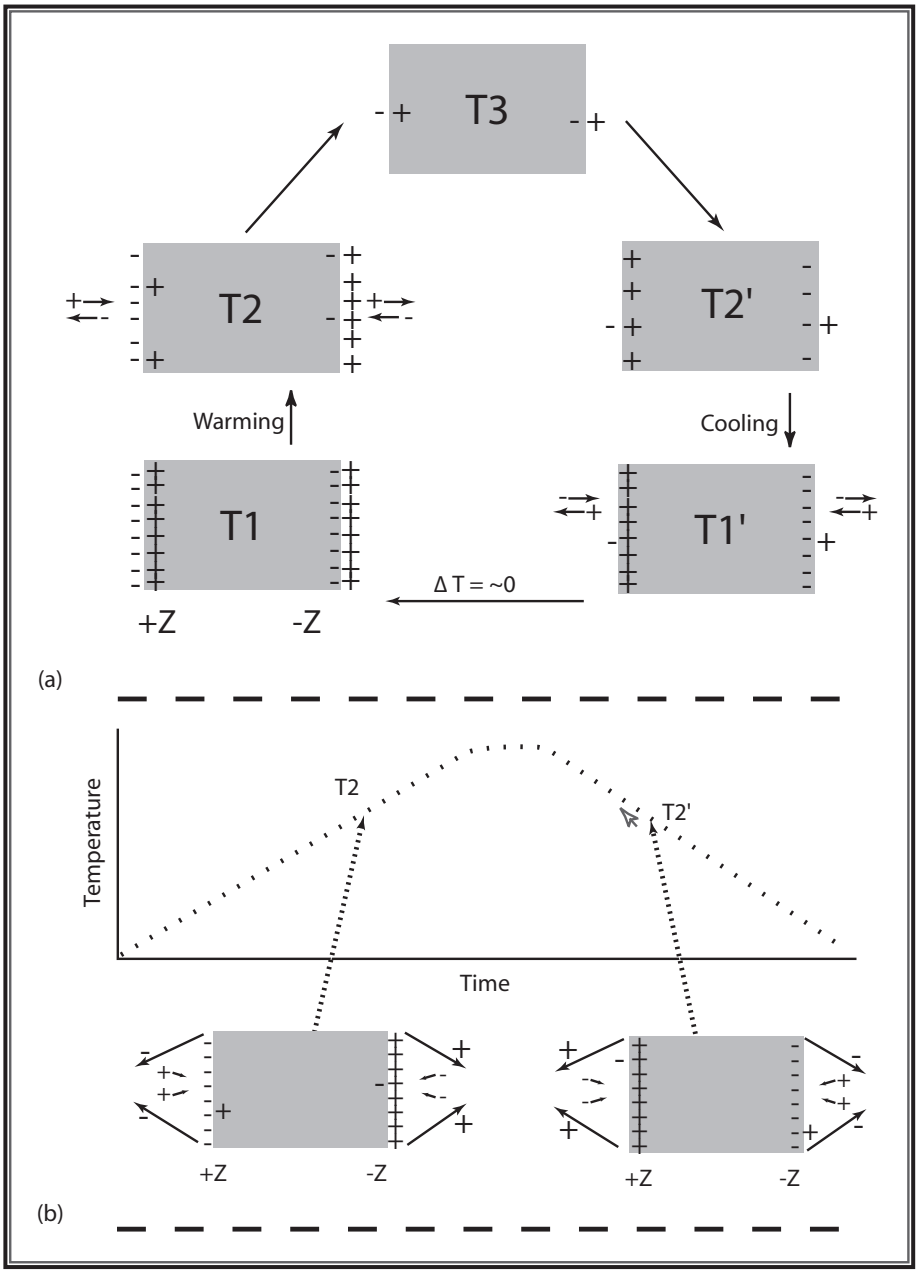

Figure 1. As a cylindrical pyroelectric crystal immersed in a gaseous environment undergoes a heating/cooling cycle, the change in spontaneous polarization $\Delta P_s = -\gamma \Delta T$ can yield up to 10^{-2} C/m^2, resulting in ~150 kV on the crystal faces to field-ionize gas atoms. During the heating stage, the induced potential and resulting electric field accelerates ions toward the +z plane and away from the –z face; contrastingly, electrons are repelled away from the +z plane and attracted to the –z face. The exact opposite effect occurs during the cooling stage.

Over time, this process builds up the surface charges to reduce the electric field, which then decreases electron/ion production. As the warming stage ends, dropping below the threshold for field ionization, compensated charge production is terminated. When the crystal begins to cool, the decreasing temperature raises the spontaneous polarization to increase the polarization charges. As in the heating stage, if compensated charges are not produced in lockstep, a net static charge builds. However, during the cooling stage, the net static charge results in the opposite polarity electric field. Thus, ions are accelerated toward the –z surface and electrons are repelled. Complementarily, the electrons are accelerated toward the +z surface and ions are repelled. When crystal cooling halts, the polarization charge balances to end electron/ion production.

Using deuterium as the residual gas for the heated/cooled $LiTaO_3$, deuterons can be produced by field ionization. With a deuterium-encapsulated material such as TiD_2 or ErD_3 serving as the incident target, the accelerated deuterons interact with the deuterium atoms on one-half of the cycle, initiating the D-D fusion reactions D(*d*, ^{3}He)*n* and D(*d, p*)*t*. With equal 50% branching ratios for both reactions, half of the interactions will yield a source of neutrons.

This project attempted to produce neutrons by replicating the work of the UCLA team, and to then increase neutron production by enhancing the electric field created at the –z face using a nanostructure array instead of a single tungsten tip. Further enhancement in electron/ion production is expected by decreasing the initial temperature of the heating cycle.

Project

Collaboration

State-of-the-art research in nanostructure development by Das and Banerjee has led to the fabrication of TaO_2 pillars interspersed in an ordered matrix of Al_2O_3 with ~70-nm spacing (Das, 2005). These 500-nm-tall pillars were grown on a heavily doped, 500-µm-thick Si substrate (Figure 2). Since TaO_2 was too insulating for our application, Das and Banerjee developed similarly periodic structures with metallic pillars (e.g., Cr, Ta, W, or Ni) suitable for enhancing electron/ion production (Figure 3). An exhaustive search finally led to a research lab that deuterates titanium and erbium to form TiD_2 and ErD_3 for use as targets. Unfortunately, neither source was able to produce the needed materials for testing before fiscal year end.

Laboratory Test System

While attempting to obtain the source and target materials, the laboratory test system was built around a 12-in.-diameter-high vacuum sphere fabricated by the Kurt J. Lesker Company and pumped by a magnetically levitated, water-cooled Ebara turbo pump connected to a Varian dry-scroll pump. A gate valve used to isolate the chamber from the turbo pump shuts after the desired vacuum pressure is reached. The source assembly comprises a 5-mm-diameter × 20-mm-long $LiTaO_3$ pyroelectric crystal epoxied to a 10-Ω, 10-W resistor heater and embedded in a solid copper cylindrical block.

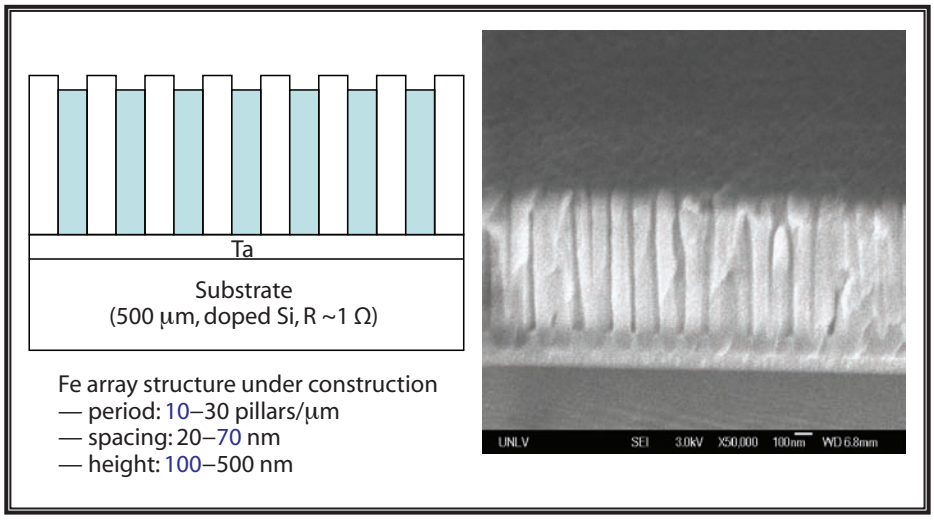

Figure 2. Schematic and electron micrograph of TaO_2 nanostructure

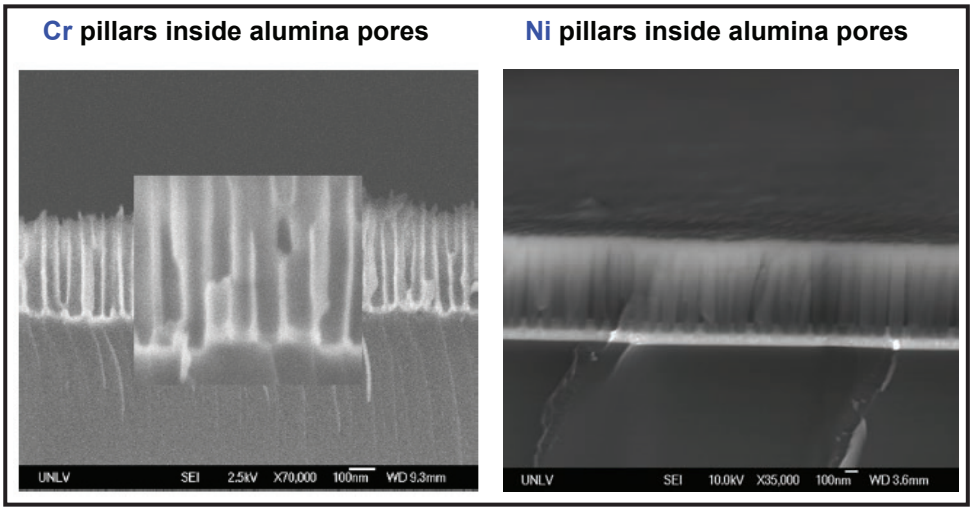

Figure 3. Electron micrograph of nanostructure with Cr and Ni pillars inside Al_2O_3 matrix

A type-K thermocouple is epoxied to the resistor end of the pyroelectric crystal to monitor temperature change. This assembly is mounted on a vacuum feedthrough to permit external positional adjustment. A target ladder similarly mounted onto a vacuum feedthrough to permit selection between target and P22 phosphor (ZnS:Ag) screen is oriented perpendicular to the source assembly (Figure 4). A hinged glass port permits fast turnaround and easy access to the vacuum chamber,

while also providing a visual confirmation of the internal layout. A visible spot glowing on the P22 phosphor confirms electron emission. National Instruments' LabVIEW-based data acquisition system simultaneously monitors the chamber vacuum pressure, emission current, heater current, and crystal temperature. Research grade (99.999% pure) deuterium is used as the ambient gas for deuteron production. A polyvinyltoluene plastic–based scintillator (Rexon RP-408) photomultiplier tube detector (Hamamatsu H2431-50) interfaced to counting electronics (ORTEC 935/572) is employed to measure the neutron output.

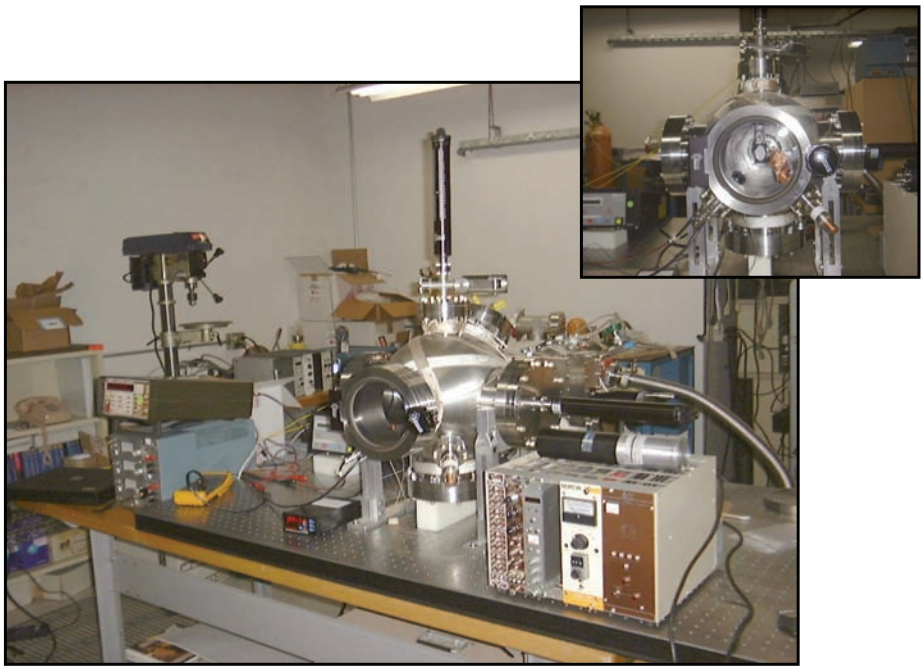

Figure 4. Laboratory setup of experimental apparatus used in the pyroelectric crystal tests. Inset: vacuum chamber with a hinged viewport showing the pyroelectric crystal and P22 phosphor screen for visualizing the electron emission.

Results

Pyroelectric Crystal Tests

After fully developing the laboratory test system, we set out to evaluate and optimize the $LiTaO_3$ crystal performance. We conducted a series of comprehensive measurements to determine the optimum parameters for a heating cycle that could provide maximum electron/ion production. These parameters included heating time, heating rate, and initial crystal temperature prior to the heating

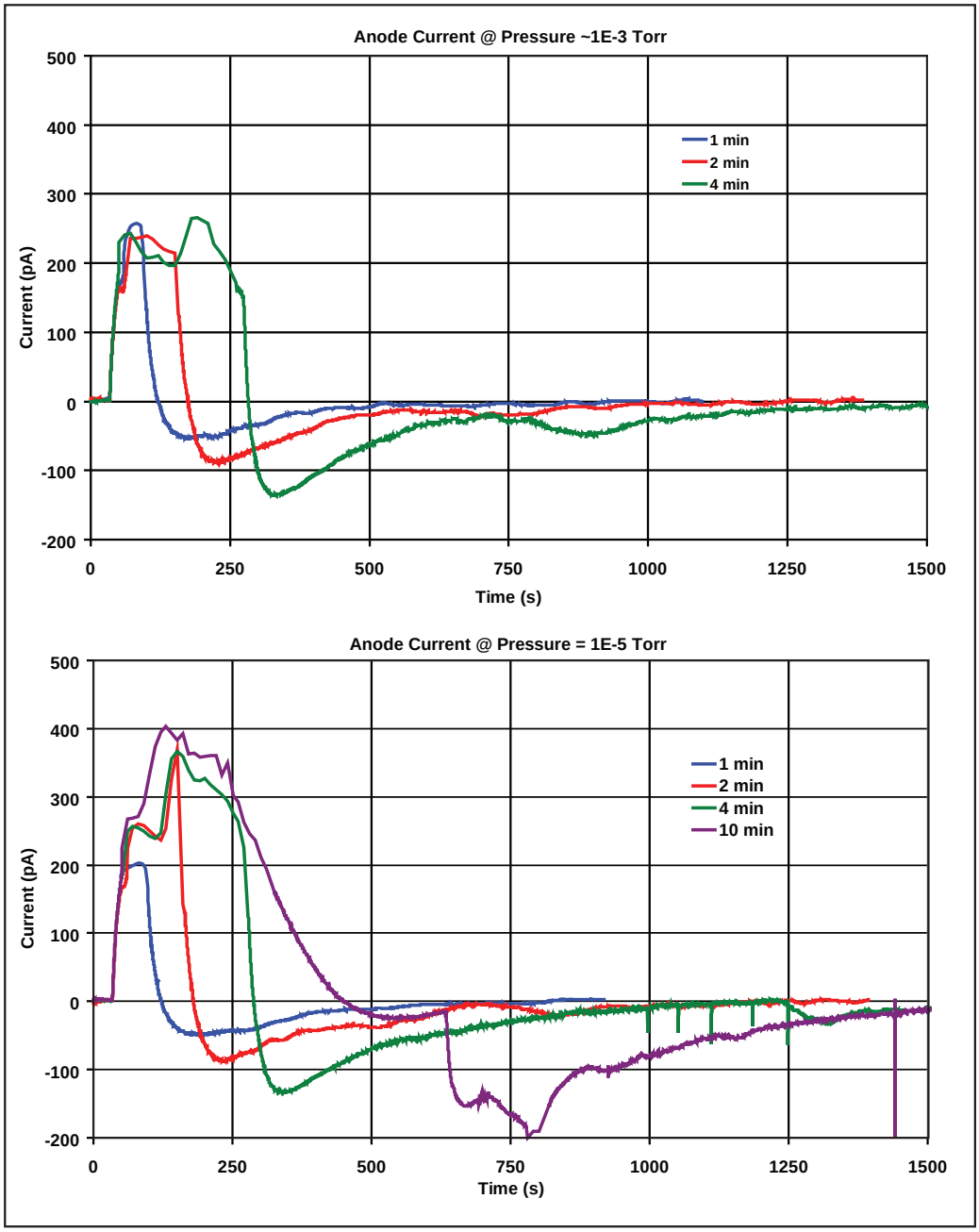

Figure 5. Current emission from $LiTaO_3$ as a function of heating time for two ambient vacuum pressures

cycle. They were then combined in tests with a set of ambient pressures to further maximize total electron/ion production. Principally, the maximum production rate and integrated charge in a heating cycle should yield the highest neutron output. Representative heating cycle test results varying from 1-, 2-, 4-, and 10-min heating durations appear in Figure 5. The small increase in emission between 10^{-3} to 10^{-5} Torr pressure for similar heating times can be attributed to fewer ambient atoms available for compensation charge at the lower pressure.

The total ion production (positive charge, +Q) for these tests appears in Figure 6. As shown, total ion production increased linearly as a function of heating time but became nonlinear after the heating time exceeded ~6 mins. At 10 mins, ion output for the bare $LiTaO_3$ crystal was ~100 nC.

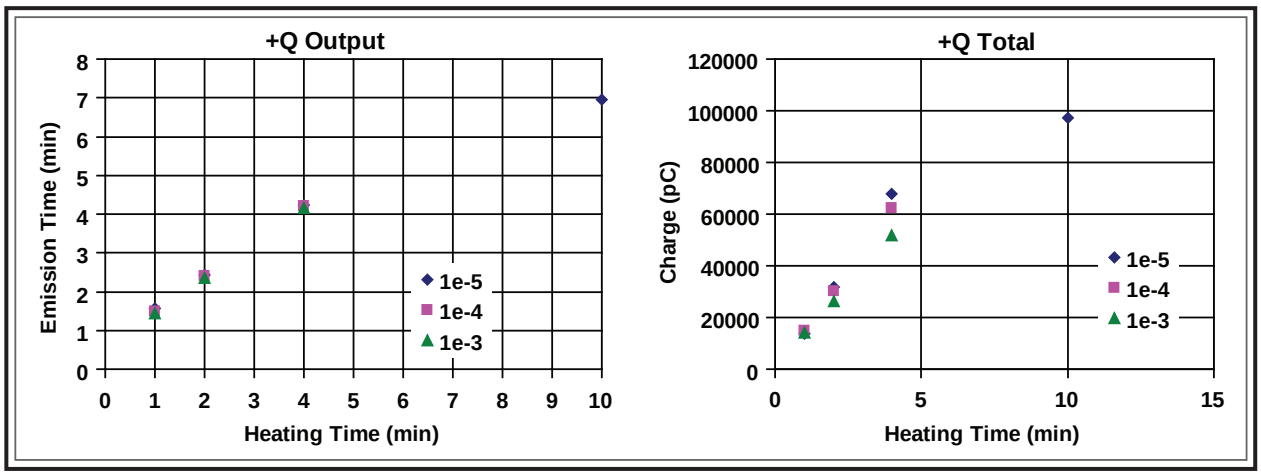

Figure 6. Integrated ion emission from $LiTaO_3$ as a function of heating time for ambient vacuum pressures ranging from 10^{-3} to 10^{-5} Torr

Future Tests

The path forward would be to take the incomplete metallic array structures under development at UNLV and use conductive epoxy to attach them to the $LiTaO_3$ crystal. With these added structures, similar heat-cycle tests could be conducted to determine maximum electron/ion production. Our UNLV collaborators could iterate array structure parameters such as pillar height, periodicity, spacing, and metallic formulation for further optimization. With a TiD_2 or ErD_3 deuterated target and deuterium gas, we would anticipate measurement of a maximum neutron output rate up to 10^4 n/s for a 10-min heating cycle. Additional enhancement in neutron production could be expected if the pyroelectric crystal was initially lowered to cryogenic temperatures to provide a greater temperature increase (ΔT) in a heating cycle.

Conclusion

Our team developed an experimental test station with quick turnaround, fast pump-down, and high-vacuum (to 10^{-7} Torr) operational capabilities for compact neutron production using a pyroelectric crystal. Given the difficulties in locating a source for deuterated targets and in developing metallic periodic nanostructures, our work only yielded ions. The main objective, to produce neutrons, may be undertaken in further work.

If this concept is proven, it may lead to a handheld, robust neutron source based on easily switched-on/off, low-voltage battery power that could be used to heat a small pyroelectric crystal. In addition to providing a check source for field detector operations, it might also provide a very convenient diagnostic tool for active interrogation of shipping containers for the presence of fissile material or special nuclear material (SNM). This neutron-based diagnostic could complement a suite of tools necessary to DOE missions and programs in Stockpile Stewardship, Homeland Security, and other government agencies.

Acknowledgments

The authors wish to thank our collaborators, Biswajit Das, Director of the Nevada Nanotechnology Center at UNLV, and A. N. Banerjee, also of the Nevada Nanotechnology Center at UNLV, for developing the field-emission array structures and for illuminating discussions during the life of the project. We are indebted to Jim Tinsley, for help with neutron measurements; Brent Davis and Pat O'Gara, for providing the neutron detector; Mike Mendez, for supplying the data acquisition equipment; Bill Quam, for providing the $LiTaO_3$/resistor assembly; and Glen Anthony, for superb technical support in developing the test chamber. We also thank Seth Putterman, of UCLA, for initial discussions.

References

Brownridge, J. D., S. M. Shafroth, "Using static charge on pyroelectric crystals to produce self-focusing electron and ion beams and transport through tubes," *J. Electrost.* **63**, 3–4 (2005) 249–259.

Das, B., P. Singaraju, "Novel quantum wire infrared photodetectors," *Infrared Phys. & Technol.* **46** (2005) 209–218.

Fowler, R. H., L. Nordheim, "Electron Emission in Intense Electric Fields," *Proc. R. Soc. London, Ser. A: Containing Papers of a Mathematical and Physical Character* **119**, 781 (May 1, 1928) 173–181.

Geuther, J. A., Y. Danon, "Electron and positive ion acceleration with pyroelectric crystals," *J. Appl. Phys.* **97** (2005) 074109.

Naranjo, B., J. K. Gimzewski, S. Putterman, "Observation of nuclear fusion driven by a pyroelectric crystal," *Nature (London)* **434** (2005) 1115–1117.

Weis, R. S., T. K. Gaylord, "Lithium niobate: Summary of physical properties and crystal structure," *Appl. Phys. A: Materials Science & Processing* **37**, 4 (August 1985) 191–203.

this page intentionally left blank

Nanomaterial-enhanced Compact X-ray Sources

Travis Pond, Ke-Xun "Kevin" Sun,[1] John Yuhas
Livermore Operations

The goal of this research, to produce a nanomaterial-enhanced, compact x-ray source, was pursued in four critical technical areas. First, we successfully demonstrated that gold coating on carbon nanotubes (CNTs) can be applied by a sputtering coating method. This achievement enables low-cost fabrication of a large class of metal nanostructures based on inexpensive CNTs, and the fine-tuning of nanomaterial properties through adjusting the coating composition and nanomaterial structures. Second, we accomplished the design of a compact x-ray source for *in situ* testing of an x-ray streak camera. Third, the streak camera design and camera were improved to allow the camera to perform as a highly sensitive, fast x-ray detector. Fourth, we designed optical and photoelectron experiments and purchased parts.

Background

This project is a continuation of an FY 2005 project, in which we accomplished the conceptual and system design of a nanomaterial-enhanced compact x-ray source (Sun, 2006). The key design concept is the use of nanomaterials to enhance overall x-ray generation efficiency in two steps: from input photons to photoelectrons at photocathode, and from photoelectrons to x-ray photons in anode. When this concept is applied, the ability to use compact equipment may reduce the need to build larger, expensive x-ray machines.

This year, we developed the nanomaterial coating and characterization procedures, the engineering design of the compact x-ray source for *in situ* calibration, and the test system for the new x-ray source.

Project

Gold-coated CNTs

Nanomaterial can enhance photoelectron interaction cross sections by structural factors. However, atom-photon interactions are still the fundamental physical processes relied on to generate photoelectrons and x-ray photons. Photoelectrons generated from gold (Au) using UV light produce robust photocathodes. The Au surface is insensitive to environmental influences in storage, and only requires a lower-grade vacuum to operate. Given the robustness of Au, as well as the recently successful development of the UV comb generator at NSTec, it is desirable to develop Au-based nanostructures that

[1] sunke@nv.doe.gov, 925-960-2514

will enhance the efficiency of photoelectron generation. But, Au-based nanostructures were rarely available—until recently. Commercially produced CNTs can be now purchased at a reasonable cost. Although nanostructured metallic and oxide materials have been generalized to include many other atomic and compound species, the initial CNTs made are still the most cost-effective nanosized materials on the market. Therefore, we decided to use Au-coated CNT. For our work, the CNTs function as the supporting frames of the nanostructure, and Au coating facilitates desired surface properties.

Our search to find Au coating and nanomaterial characterization capabilities led us to two national laboratories: we utilized the Vacuum Processing Lab at LLNL for its Au sputtering coating processes, and the Molecular Foundry at LBNL for scanning electron microscopy (SEM).

Figure 1 shows the Au-coated CNTs. The sputtering coating technique was accomplished at LLNL, and the SEM images were taken at LBNL. Figure 1 shows SEM images of two CNTs coated with Au, ~100 Å (Figure 1A) and ~500 Å (Figure 1B). The magnification rates of the images are 64.37×10^3 and 80.08×10^3, respectively. The diameters in the densest regions of the coated CNTs were measured using CCD image analysis software. The statistical difference between the diameters of the two kinds of coated CNTs is ~200 to 400%, much greater than the ~20% difference in magnification. Therefore, we can safely conclude that the difference in CNT diameters is due to the different coating thicknesses.

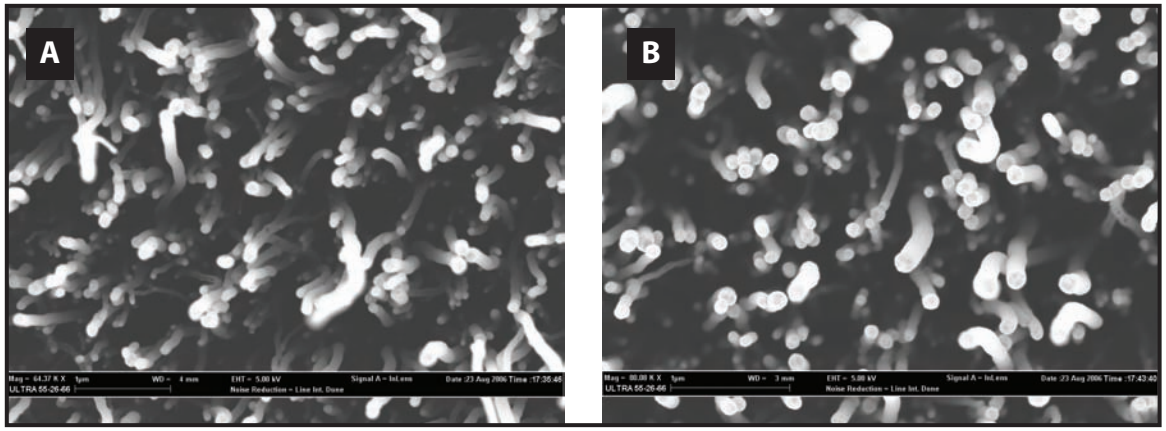

Figure 1. SEM images of Au-coated CNT. (A) Coating thickness 100 Å, at a magnification of 64.37×10^3. (B) Coating thickness 500 Å, at a magnification of 80.08×10^3. The statistical difference between the diameters of two kinds of the coated CNTs is mostly due to the difference in the coating thicknesses.

Another key observation can be made: the Au is coated onto the CNT body in the observable field depth. This is achieved by correctly using sputtering coating methods instead of evaporative coatings. Quite often evaporative coatings are applied only on the tip of the fine structure, whereas the

sputtering coating process results in uniform coating around the whole body of the CNT. The successful demonstration of Au coating on the lengthy CNT bodies is an important milestone in this SDRD nanomaterial research.

Figure 2 depicts the images of Au-coated CNT arrays at reduced magnification in order to show the density of the CNT arrays. The magnification values of images in Figures 2A and B are 30.45×10^3 and 22.29×10^3, respectively. With the aid of a CCD-imaging software, we estimated that the density of Au-coated CNTs is ~1.6 to $2.0 \times 10^7/mm^2$, or 16 to 20 millions of Au-coated CNTs per square millimeter, a very high density of CNTs.

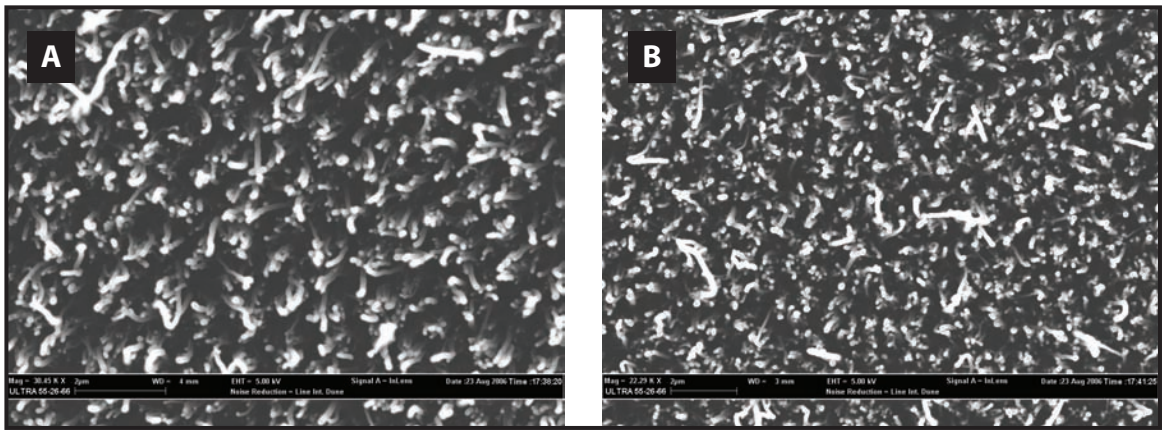

Figure 2. SEM images of dense Au-coated CNT arrays. (A) Coating thickness 100 Å, at a magnification of 30.45×10^3. (B) Coating thickness 500 Å, at a magnification of 22.29×10^3.

When such a densely packed, Au-coated CNT array is illuminated with UV light, the multiple reflections of light migrating within, or diffused through the CNT array, should result in considerably higher interaction cross sections of photoelectrical effects, thus producing times-higher counts of photoelectrons. Since Au has a high reflectivity, ~96%, the light path may cascade many times before it fades away.

In addition to enhancement due to nanomaterials, some surface microstructures will further enhance the light absorption at the photocathode, thus increasing photoelectric efficiency. Figure 3 shows a possible scheme using a cone structure. The apex angle of the cone is designed ~30°, so that the incident light will less likely be reflected back from the cone with rough walls made of nanomaterials.

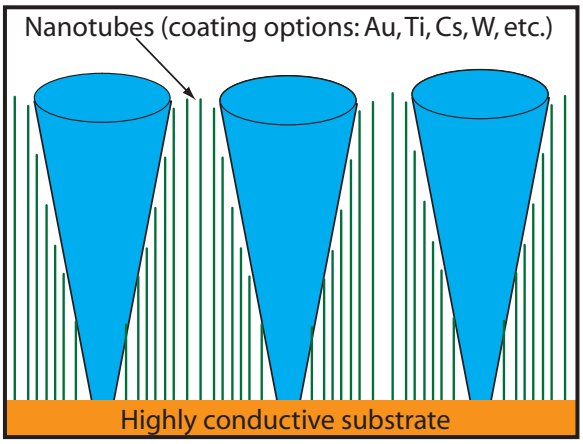

Figure 3. Micropatterned, coated CNT array

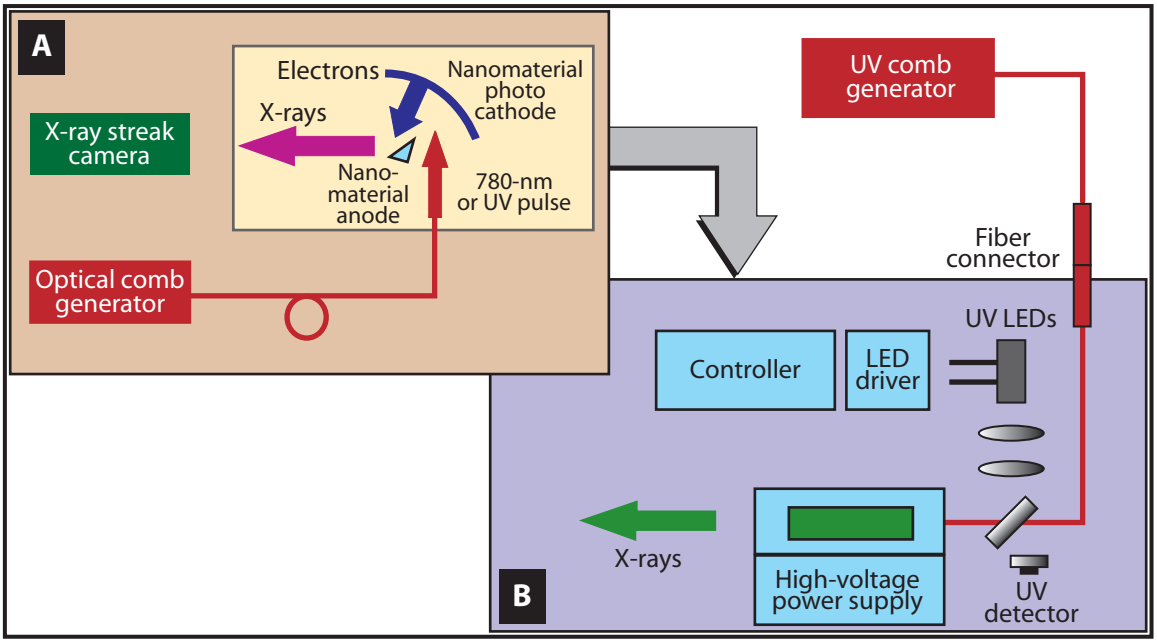

Figure 4. Laboratory design for *in vacuo* experiment of compact x-ray source

Experiment Setup for Photoelectric Effect Measurement and X-ray Generation

We have designed an experiment to measure both the photoelectric effect and x-ray generation from the nanomaterials. Figure 4A shows a previous system design, where x-rays would be generated by the electron collision process at a nanomaterial anode. The electrons would be, in turn, generated from a

nanomaterial photocathode illuminated with optical pulse train for photoelectric process. Figure 4B illustrates the most recent experimental setup design. The test apparatus was designed for use in the vacuum chamber at the south wing of the Manson x-ray source. The apparatus, mounted on a 12" × 12" square optical breadboard, is inversely suspended on the lid of the vacuum chamber. Most electronics and fiber-optic feedthroughs will be directly mounted on the vacuum lid. The light source will use a UV LED emitting at ~255 to 266-nm wavelengths targeted at a Au-coated nanotube photocathode. The UV light will be collected and transformed by a pair of lenses to form a spot size of ~1 cm. The relatively large spot size implies a larger photoelectron emission area, reducing the charge density and, thus, space-charge effects. The second UV input path is through a large-diameter optical fiber from a UV comb generator. The x-ray generator is configured to allow easy replacement of the photocathode and the anode. The electronics components selected permit the circuit to operate under vacuum, as a test of the *in situ* x-ray generator electronics concept. The total power consumption is designed to be ~2 W. Therefore, only moderate cooling methods will be needed.

Compact X-ray Source for In situ Calibration of the X-ray Cameras

After we encountered some difficulty in characterization of the nanomaterials, some effort was expended on the design of compact x-ray sources for calibration of x-ray framing or the x-ray streak cameras. The central goal is to enable *in situ* calibration, namely, delivery of the x-ray to the camera photocathodes for calibration while the cameras are mounted in the experiment.

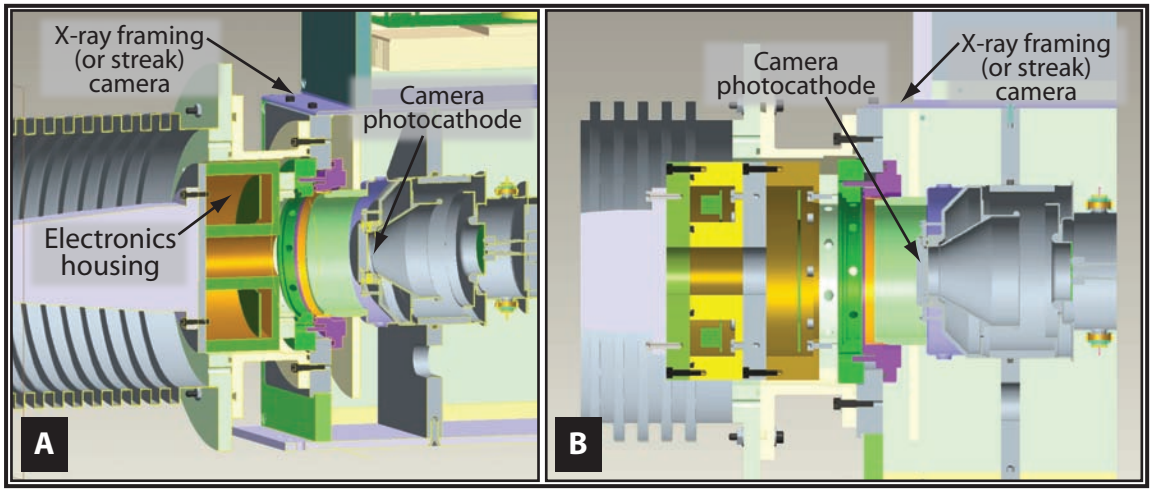

Figure 5. Design of the *in situ* compact x-ray source to be mounted in front of an x-ray framing or x-ray streak camera. Two versions of the design are shown: (A) single-layer electronics housing for complex electronics but simpler optics, and (B) a two-layer housing design for simpler electronics but complex UV optics and x-ray generator.

Figure 5 shows the CAD model of the compact x-ray source housing with either an x-ray framing camera or x-ray streak camera in front. The hole patterns on the original camera front flange are preserved. The configuration on the left in Figure 5 shows a single-layer housing, which has a large enough volume to house a relatively complex electronics assembly. The other configuration shows a two-layer housing design, where the electronics and x-ray generator are separately placed in two segments. In this case, electronics circuits must be simplified to occupy less volume, but more complex UV optics and the x-ray generator can be installed.

Balancing the trade-off, we designed an electronics circuit to fit the two-layer structure. The electronics circuit will be able to safely deliver up to 15 kV of high voltage without overheating. We have also designed the UV optics delivery system consisting of two curved mirrors. The optics will focus the UV light from the output fiber of the UV comb generator, and will also direct UV light at an off-center location on the camera photocathode.

Conclusion

Excellent progress was made in designing and building a nanomaterial-enhanced compact x-ray source. The Au coating that was applied on densely packed CNTs using a sputtering coating technique was highly successful. We designed and purchased components for an experiment. Several practical versions of the compact x-ray sources for *in situ* calibration of x-ray framing and x-ray streak cameras were designed.

Acknowledgments

The sputtering coating process was conducted at Lawrence Livermore National Laboratory. The SEM images were taken at Lawrence Berkeley National Laboratory.

Reference

Sun, K-X., "Nanomaterial-Enhanced X-Ray Sources: Materials Study and Compact X-Ray Comb Generator," *Nevada Test Site–Directed Research, Development, and Demonstration*, FY 2005, Bechtel Nevada/National Security Technologies, LLC, Las Vegas, Nevada, 2006, 41–44.

Large-format Phosphor Imager

James R. Tinsley[1]
Special Technologies Laboratory

This project studied the feasibility of a novel method for manufacturing large pieces of lutetium oxyorthosilicate (LSO) scintillator of sufficient size and thickness to demonstrate the method as a valid replacement for scintillating tile arrays often used in radiation-imaging systems. A process developed at the University of Nevada, Reno (UNR), for sintering ceramic powders into macroscopic pieces with excellent optical qualities was used to make a sample of LSO scintillator suitable for use as a radiation imager. This process can be scaled up to produce significantly larger pieces of LSO than can be cut from single crystals.

Background

There exists a need for large-format (≥15 cm on a side × ≥1 mm thick) radiation imagers that can be read in real time using video cameras. Radiography is a fundamental diagnostic used throughout the NNSA complex. Systems that use penetrating radiations, such as hard x-rays and energetic protons, are becoming increasingly common as radiography is applied to larger and more massive objects. Applications include Proton Radiography, hard x-ray radiography for subcritical experiments, and use on the LANL DARHT facility.

In addition to suitable radiation sources, these new systems require an image plane on which the pattern of ionizing radiation is transformed into light that can be recorded using video cameras. At present, such imagers are made by tiling plates of polished scintillating crystals, principally LSO. Unfortunately, the joints between tiles and defects in the crystals themselves interfere with image quality. The resulting imperfections can be partially cancelled through background subtractions, but will leave artifacts in the experimental images. Scintillating materials with fewer defects do exist, but their scintillation properties make them much less attractive for radiation imaging. Earlier attempts to mitigate these problems have had limited success. Examples include "grouting" the scintillating crystals with index-matching materials and coating the crystals' edges with black paint in an attempt to eliminate total internal reflection. Efforts to maximize the optical quality of the scintillating tiles by selecting the best of numerous different crystals have proven to be very expensive, time-consuming and, in the end, not completely successful.

[1] tinslejr@nv.doe.gov, 805-681-2282

Project

Dr. Olivia Graeve, of the UNR Department of Metallurgical and Materials Engineering, has demonstrated the ability to sinter ceramic powders into macroscopic pieces exhibiting excellent optical qualities. Since LSO is a ceramic that has been doped with cerium to cause it to scintillate, one should in principle be able to use the same technique to make scintillator pieces of arbitrary size.

To achieve such good optical properties, it is necessary to start with a powder consisting of extremely fine, very uniform particles. No suitable powder for LSO or any other phosphor material is available commercially. Therefore, we had to fabricate the material from scratch before we could attempt sintering. Fabrication and sintering of suitable powder were together considered too large a scope to accomplish successfully in a single fiscal year. Consequently, the powder synthesis was completed in FY 2005, and sintering was deferred to FY 2006.

Using a straightforward combustion synthesis, Dr. Graeve's group at UNR was able to manufacture LSO powders with the desired characteristics. The powder synthesis was accomplished early enough in FY 2005 that sufficient time remained to perform several test sinterings, thereby getting a head start on the FY 2006 work. We began FY 2006 by addressing several problems that had been identified with the sintered pieces (Tinsley, 2006). One, the failure to achieve optical transparency, was due to the impurities remaining in the LSO powder, even after detritus from the combustion was eliminated through calcinations. A significant portion of the FY 2006 effort was expended in addressing this issue.

X-ray diffraction measurements showed that, in addition to Lu_2SiO_5 (a.k.a. LSO), two other substances were present as minor constituents: Lu_2O_3 and $Lu_2Si_2O_7$. Photoluminescence measurements showed that the additional substances did not reduce the light output of sintered powder, but they did scatter the light by a significant amount, causing the final piece to be translucent, not transparent. The fact that the elemental composition of the two unwanted components averaged out to that of LSO indicated that the reaction stoichiometry was correct; therefore, no changes in the ratios of starting materials would solve the problem.

The other variable we were able to manipulate was the reaction temperature, which is most easily varied by changing the *synthesis temperature*. (In this case, the synthesis temperature was increased from the nominal value of 773K [500°C].) This is the temperature to which the combustion chamber is raised before the precursor chemicals decompose and combust; the reaction typically takes several minutes after the temperature has been elevated to the desired level. In other words, the combustion chamber applies *external* heat to the reaction.

LSO purity increased with the rising synthesis temperature; the most pure LSO was obtained at 1273K (1000°C). To determine purity, we compared an x-ray diffraction spectrum of the powder with the known spectra of Lu_2SiO_5, Lu_2O_3, and $Lu_2Si_2O_7$ (Figure 1). Since 1273K is the maximum

setting for the combustion chamber, it appeared likely that additional heat must be added *internally* by adding "fuel" to the initial mixture. For this fuel, we used carbonic dihydrazide (CH_6N_4O), since it releases heat upon decomposition but does not disturb the stoichiometry of the reaction.

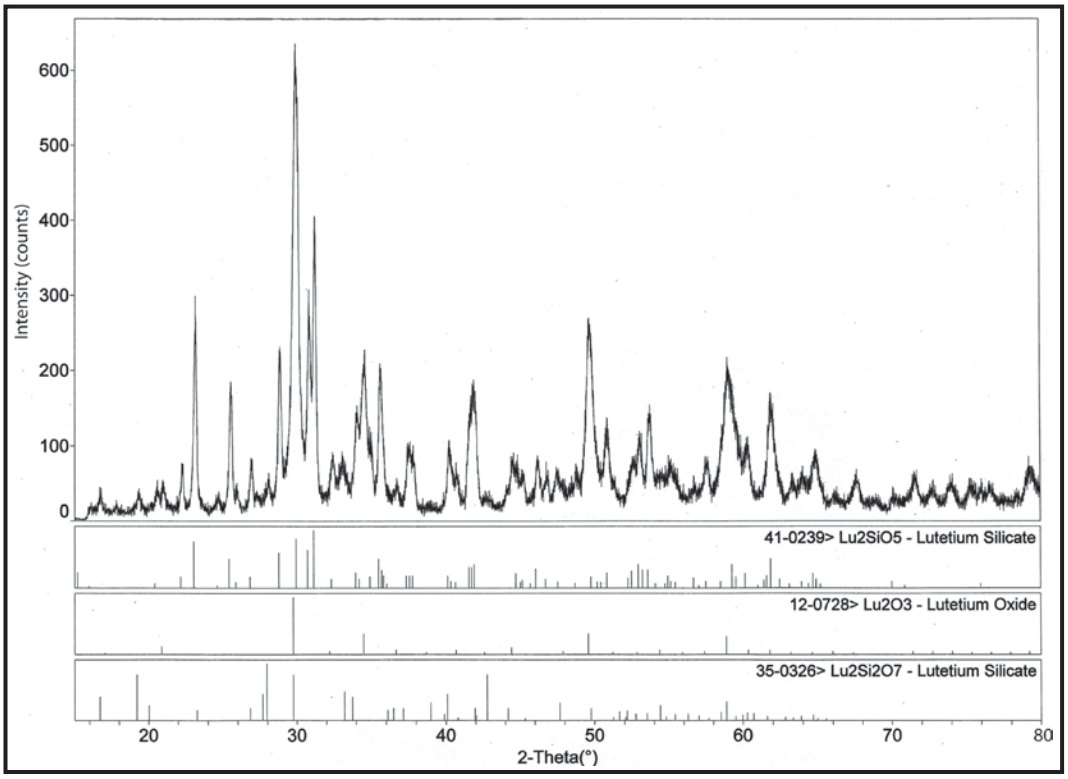

Figure 1. X-ray diffraction measurement of LSO powder. Positions and relative strengths of lines corresponding to individual constituents are also shown.

The next set of experiments involved adding various amounts of fuel to the initial mixture, performing x-ray diffraction measurements on the resulting powder for phase identification (i.e., assessing LSO purity), and performing photoluminescence measurements to monitor the luminescence of the material. The latter were conducted to ensure that no cerium dopant was lost or converted from the desired trivalent form into the tetravalent form, either of which would be detrimental to the material's scintillation properties. (The optimum amount of cerium is 0.05% of the lutetium content, too low to show up in x-ray diffraction measurements.) The optimum ratio of CH_6N_4O to lutetium nitrate was found to be 4:1.

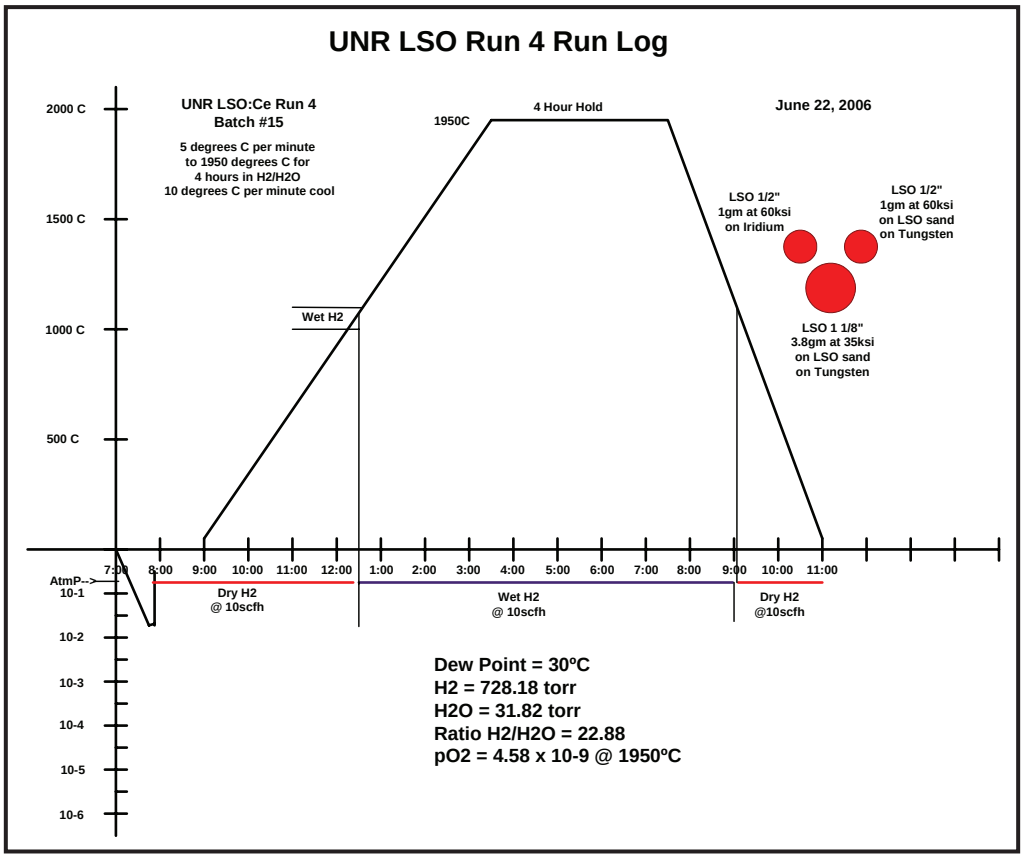

Figure 2. Final sample sintering protocol

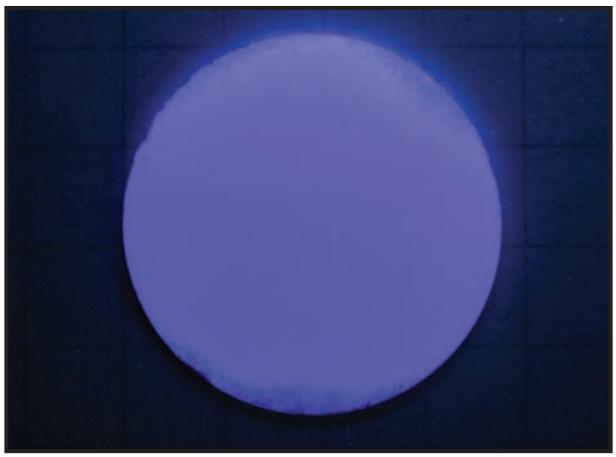

Figure 3. Photo of 25-mm × 1-mm-thick sintered sample illuminated by UV lamp

Unfortunately, during this last round of experiments, UNR's x-ray diffraction equipment broke down, resulting in a few months of lost time before repair. Accordingly, only one 25-mm-diam × 1-mm-thick sample and two 10 mm × 1 mm samples of sintered LSO could be produced in the remaining time available with the "best" powder sample. (A summary of the sintering protocol appears in Figure 2). This sample (Figure 3) was still merely translucent, although its brightness, light spectrum (Figure 4), and scintillation decay time (70 ns) all matched single-crystal LSO.

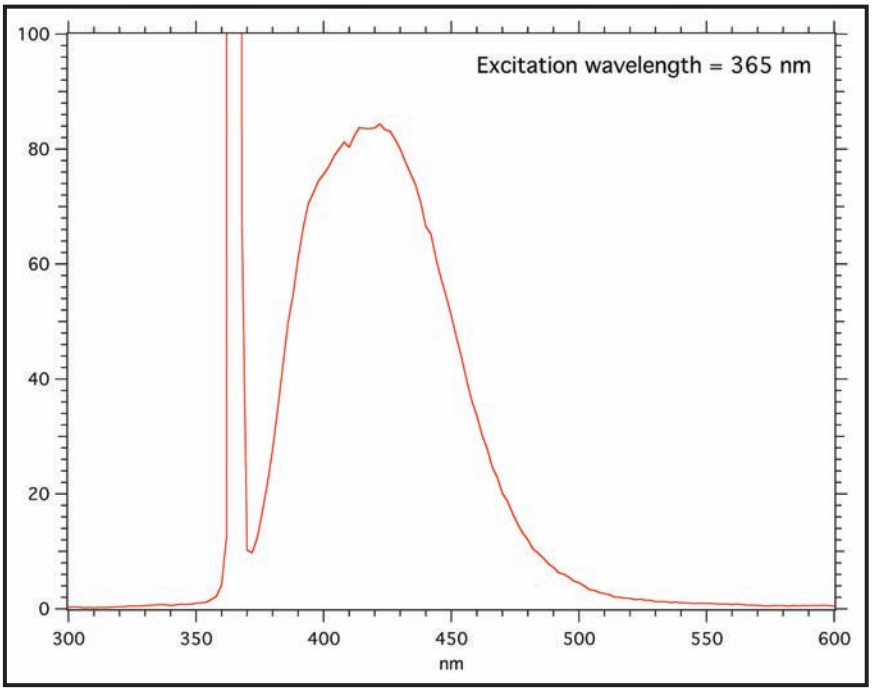

Figure 4. Emission spectrum of sintered sample excited by 365-nm light. Off-scale peak is due to excitation light.

One concise way to express the amount of light scattered by the sample is to measure the linespread function. The surface of a sample that was partially covered with a sharp-edged mask was illuminated with a 366-nm UV lamp; the pattern of the light transmitted through the sample was then recorded. The intensity of the transmitted light along a line perpendicular to the mask edge was plotted, along with the point-by-point derivative of the intensity (Figure 5, with masked portion at left). Since the emission light was all generated very near the surface illuminated by the lamp, the curves describe the light scattering through the entire 1-mm sample thickness. The derivative was fairly well approximated by a Gaussian peak with a full-width at half-maximum (FWHM) of 1.8 mm. This was consistent with a resolution measurement made by replacing the edge mask with a USAF 1951 transmission

resolution test pattern; the smallest element resolved was 0.5 line pairs/mm. When the sintered sample was replaced with a 3-mm-thick piece of single-crystal LSO, the resolution measured using the USAF pattern was ~6 line pairs/mm.

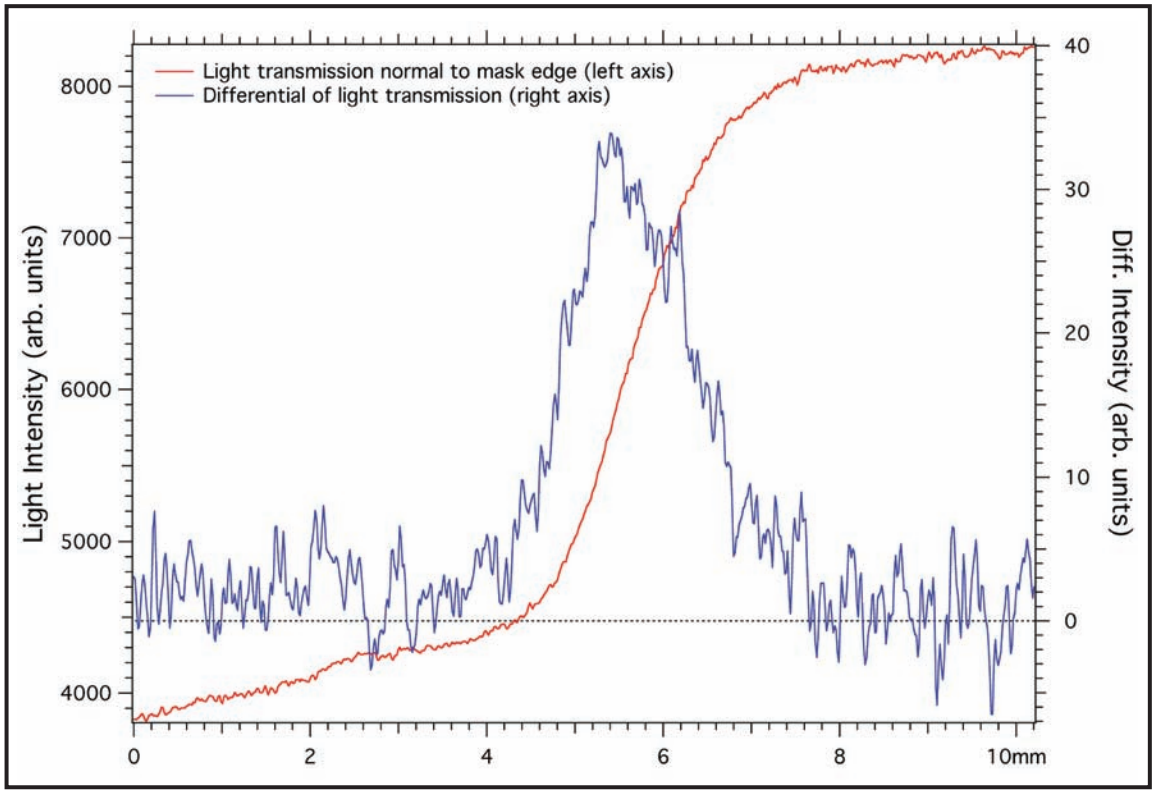

Figure 5. Light transmission profile transverse to edge of mask (red) and its differential (blue). The FWHM of the latter is 1.8 mm.

The sintered sample tolerated the same amount of handling as other optical components, such as being clamped into optical mounts, etc. One of the 10-mm samples was dropped onto a hard surface from as high as ~15 cm without breaking. No controlled mechanical strength tests were performed, but the samples appeared to be similarly rugged as other common ceramic materials, such as glasses and inorganic scintillators.

X-ray diffraction analysis of the sintered material showed that there was some loss of silicon and oxygen during sintering. We hope this loss can be overcome through additional sintering studies in which parameters such as the oven's atmospheric composition and pressure are further varied. In particular, a much higher partial pressure of oxygen is almost certainly called for.

Anticipating achievement of sufficient transparency, the next step would be to produce larger pieces of LSO to put into actual imaging systems. In order to make pieces as large as 15 × 15 cm, two pieces of equipment would need to be obtained. The first is a press capable of applying 35000 psi to the entire surface of the powder prior to sintering. The estimate for a sufficiently powerful press is $50000–$60000. The second is a sintering oven large enough to hold the piece. An estimate of $200000–$210000 has been obtained for one suitable oven, though it may be possible to gain access to a large enough oven, and thus avoid this outlay.

Conclusion

The synthesis of very fine, very uniform LSO powder, and subsequent sintering into macroscopic pieces, was successfully demonstrated. The scintillation properties have been preserved, but the optical characteristics are not yet adequate for imaging purposes. Based on Dr. Graeve's experience with similar ceramics, we are confident that increased transparency can be achieved with several months of additional effort.

A patent disclosure has been filed on the work completed in this project.

Acknowledgments

The author would like to acknowledge the contributions of Brett Pearson and other students in Dr. Graeve's lab at UNR.

Reference

Tinsley, J. R., "Large-Format Phosphor Imager," *Nevada Test Site–Directed Research, Development, and Demonstration*, FY 2005, Bechtel Nevada/National Security Technologies, LLC, Las Vegas, Nevada, 2006, 373–379.

this page intentionally left blank

Atomic Vapor Generator

E. Chris Hagen, Lee H. Ziegler[1]
North Las Vegas

A dense plasma focus (DPF) generator has been used to produce plasmas from four metals—copper, iron, tin, and tungsten. Optical spectra from these plasmas were measured along with the usual diagnostics of neutron yield, x-ray output, rundown time, and consistency of neutron yield. Time-resolved spectra were taken that show the evolution of individual components in these plasmas. This work shows the promise of being able to measure concentrations and density of the components in these plamas if additional work is completed.

Background

DPF generators are simple and reliable sources of pulsed neutrons and pulsed x-rays. The NSTec DPF, located at NLV, operates at 100 kJ, 35 kV, and delivers up to 1.5 MA to the pinch. Its average neutron yield is 7×10^{10} neutrons per pulse, with occasional shots of $>10^{11}$ neutrons per pulse. The DPF is employed to develop pulsed neutron and photon diagnostics, as well as to calibrate these diagnostics in support of programs directed by the national laboratories.

The NSTec DPF has been in operation for several years. In collaboration with Texas A&M University, NSTec staff has helped establish accuracy in measuring neutron yield. Additional collaborations with colleagues at SNL and the University of New Mexico have allowed cross-calibrations based on the associated particle technique using indium. An additional study with our own health physics group has confirmed consensus on our neutron yield measurements.

During operation, the DPF ionizes and compresses the load gas into a small, cylindrically shaped region that is ~1 mm in diameter and 1.5 cm long. This cylinder is formed just off the end of the anode, typically on the radius of the anode. Electrons form a beam and attach to the center of the anode, while the positive ions expand to the cathode and the chamber housing. The electron current vaporizes some of the anode material, which is also ejected to the chamber walls.

This project had two objectives. The first was to see if the neutron yield could be increased by placing deuterated materials in the space where the pinch stagnates. The second objective was to measure the spectra of various metals when they were embedded as a small slug in the center of the anode tip.

[1] zieglelh@nv.doe.gov, 702-295-3092

Project

Optical spectra were obtained using pure copper anodes. These spectra were recorded locally, captured solely with a 60-ft-long fiber. Some of these spectra are shown in the report "Dynamic Plasma Properties via Spectrometry," included in this publication (Ziegler, 2007).

In pursuit of increasing neutron yield, deuterated polyethylene, and later, a piece of tin were introduced into the DPF chamber area. The samples were placed on a glass rod supported from the bottom of the DPF chamber. While the experiment with the deuterated polyethylene worked, we did not see an increase in neutron yield or any change in DPF performance. The polyethylene and a few centimeters of the glass rod were vaporized, but the rest of the glass rod remained intact. The results were the same for the tin when it was placed in the chamber where the pinch reaches maximum compression. A program called Specline noted a possible tin line at 684 nm, and a manual scan showed that there were also five other intense tin lines in this spectrum (Figure 1). All these lines can be attributed to doubly ionized tin.

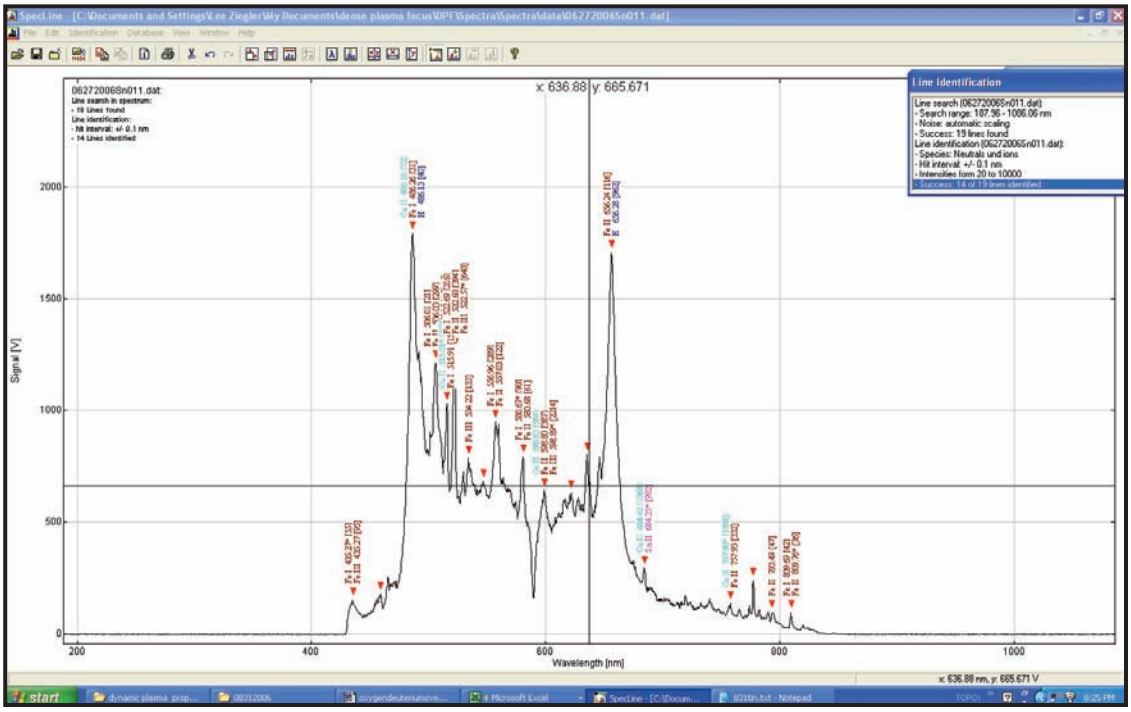

Figure 1. Optical spectrum from pinch with a piece of tin located in the DPF 33 chamber in the area of maximum compression. One tin line, at 684 nm, was identified. Five other lines were visible when the spectrum was analyzed manually.

The six tin lines that were found and their relative intensities are listed in Table 1.

Table 1. Tin lines and their relative intensities

Line position (nm)	Relative intensity
533	730
556	84
645	2052
684	982
719	1157
774	1000

Experiments to increase neutron yield using deuterated polyethlene were discontinued, and we turned to measuring spectra of metals fitted onto the end of the anode. As part of this second phase, we inserted a tungsten plug in the end of the anode and obtained several spectra. The tungsten plug developed an evaporation dip that resembled a tornado cloud. This tornado-shaped hole was at an angle of about 30° to the axis of the anode, but no tungsten lines were seen in these spectra.

By this time, we had begun to notice the similarity of spectra with very different experimental configurations. We had taken a series of spectra from one anode with an iron plug centered in the end of the anode. In an attempt to simplify these spectral measurements, a copper liner was inserted in the tube housing, thus shielding all iron components in the tube assembly from ultraviolet radiation that was suspected of ionizing the outer steel vacuum chamber. This effort was surprisingly unsuccessful. Figure 2 shows a comparison of three spectra measured with different DPF load configurations. The blue spectrum was measured without the copper liner but with the iron plug in the anode. The magenta spectrum was measured with the copper liner inserted next to the outer wall of the tube. The black spectrum was taken with the copper liner still in the tube, but with a pure copper anode.

These spectra were taken remotely. The blue spectrum (without the liner) was triggered in synchronization with the triggering of the DPF and used a 20-μs integration time, while the spectrum measured with the copper liner used an integration time of 100 μs. The black spectrum's integration time was 10 μs.

The final experiment was performed with the pure copper anode and the copper liner inserted in the tube. These spectra were taken with a 10-μs integration time. The timing was adjusted so that the start of each integration time was different with respect to the trigger that initiates the plasma rundown.

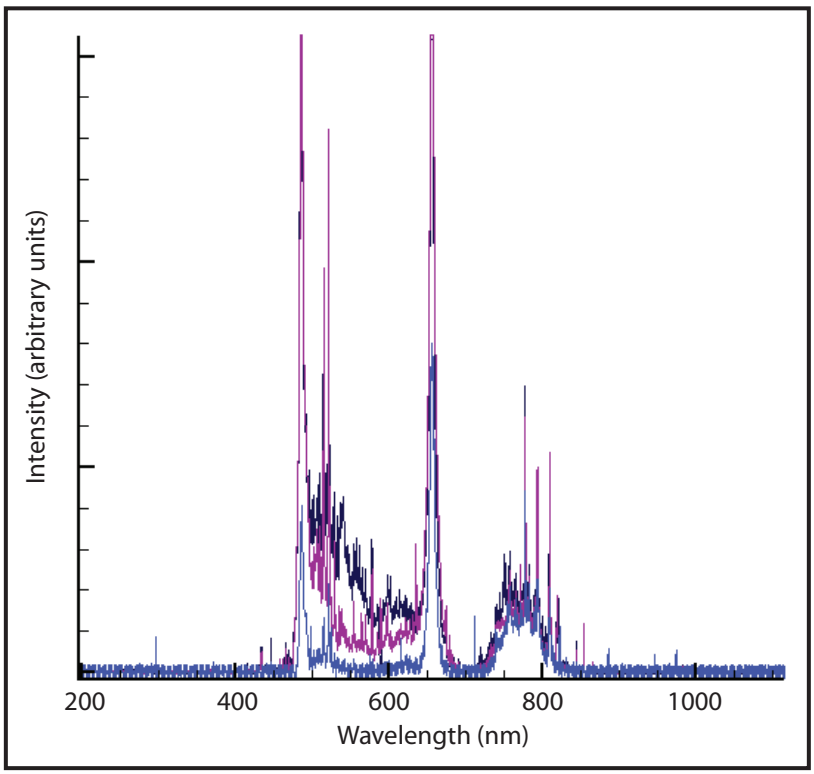

Figure 2. Spectra with (red) and without (blue) a copper liner, and then with a pure (black) copper anode. We intended to eliminate some of the iron lines in these spectra but were unsuccessful.

The pinch with this anode and gas pressure occurred at 4.8 μs after the trigger and the beginning of the plasma rundown. These spectra are shown in Figure 3. It was observed that at 20 μs, the spectra began to decrease in intensity.

Conclusion

We have demonstrated that we can measure spectra of some metals when the metal is held in the region of the pinch. In addition, we have measured spectra of various gases. Our effort thus far indicates that definitive measurements are possible. Papers by several researchers [(Skladnik-Sadowska, January 2006; October 2006), (Sadowski, 2005), (Harital, 2005)] have shown that these spectra are even more interesting when taken in a time-resolved mode. Therefore, by varying the time in relation to the DPF trigger, it should be possible to follow the generation of the ions produced by the electron current vaporizing the center of the anode of the DPF.

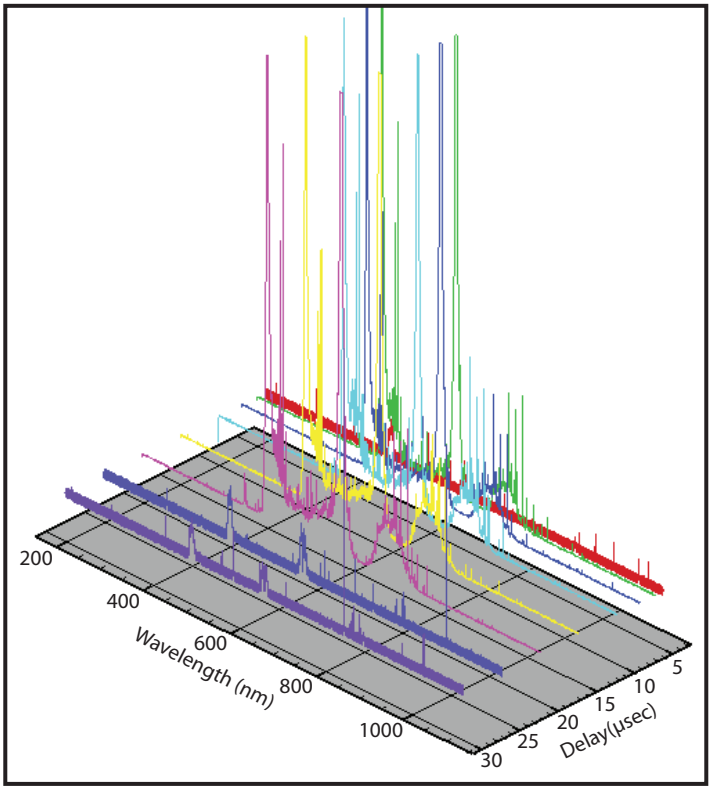

Figure 3. Spectra obtained at 0.2 µs prior to the pinch (red), at the time of the pinch (blue), and at delays of 5, 10, 15, 20, and 25 µs after the pinch.

References

Harilal, S. S., B. O'Shay, M. S. Tillack, M. V. Mathew, "Spectroscopic characterization of laser-induced tin plasma," *J. Appl. Phys.* **98** (July 2005) 013306.

Sadowski, M. J., K. Malinowski, E. Skladnik-Sadowska, M. Scholz, A. Tsarenko, J. Zebrowski, "Time-resolved optical spectroscopy of high-temperature plasmas," *Proc. SPIE* **5948** (2005) 5940806.

Skladnik-Sadowska, E., P. Kubes, K. Malinowski, M. J. Sadowski, M. Scholz, A. V. Tsarenko, "Time-resolved Optical Spectroscopy of Plasma Interaction with CD_2 Fiber in PF-1000 Facility." *AIP Conf. Proc.*, *6th International Conference on Dense Z-Pinches, Oxford, United Kingdom* **808** (January 2006) 203–206.

Skladnik-Sadowska, E., K. Malinowski, M. J. Sadowski, P. Kubes, M. Scholz, M. Paduch, L. Karpinski, A. Marchenko, A. Tsarenko, "Temporal and spatial measurements of plasma electron-density from linear-stark broadening of D_β (486 nm) in PF-1000 experiment," *Czech. J. Phys.* **56**, Suppl. 1 (October 2006) B383–B388(1).

Ziegler, L. H., E. C. Hagen, "Dynamic Plasma Properties via Spectrometry," *Nevada Test Site–Directed Research and Development,* FY 2006, National Security Technologies, LLC, Las Vegas, Nevada, 2007, 89–94.

Dynamic Plasma Properties via Spectrometry

E. Chris Hagen, Lee H. Ziegler[1]
North Las Vegas

Optical spectra from a dense plasma focus (DPF) machine have been measured using simple, commercially available spectrometers. The practical issues of operating sensitive spectrometers in the harsh electromagnetic pulse (EMP) and radiation environment presented by the DPF have been solved. The spectrometers were run locally in a time-integrating mode, and remotely, in a time-resolved mode, using short integration times. Physical characteristics, specifically temperature, density, and pressure, in the pinched plasma region affect the observed spectra. It is now possible for us to acquire spectroscopic data to use in the diagnosis and improvement of DPF machines. Furthermore, the effects of the interaction between the plasma and contaminants seeded into it can also be investigated using these tools.

Background

DPF devices operate through three phases—initiation, rundown of the plasma "snowplow," and the final Z-pinch. In order to optimize the output of these devices, it is necessary to measure the operation parameters as they occur. The first two phases are completed in ~5 μs. The Z-pinch lasts about 100 ns. DPF devices are in use at NSTec for purposes of neutron diagnostics development, neutron calibration, and materials investigation. With active plasma diagnostics, these machines can be made to perform optimally, and basic physics issues such as modes of operation can be resolved.

Emission/absorption data obtained with a spectrometer will allow the reaction rate, temperature, and pressure of individual gas species as a function of time to be inferred. Sadowski and others have used optical spectral measurements to estimate plasma concentration and observe the temporal changes in the plasma during the rundown phase (Sadowski, 2005; Skladnik-Sadowska, 2006). When combined with dynamic volumetric measurements, the density can also be inferred. Given accurate measurements of these properties, the equation of state can be derived.

Additionally, the analysis of plasma impurity composition can be accomplished using optical spectroscopy (Tsarenko, 2001).

[1] zieglelh@nv.doe.gov, 702-295-3092

Project

Initially, two Ocean Optics Composite-Grating series spectrometers were borrowed from NLV associates. Four additional Ocean Optics spectrometers with unique spectral ranges were acquired and used on this project.

Figure 1 shows both lines of normal width and an extremely broadened line that comes from the heated and compressed gas in the pinch region.

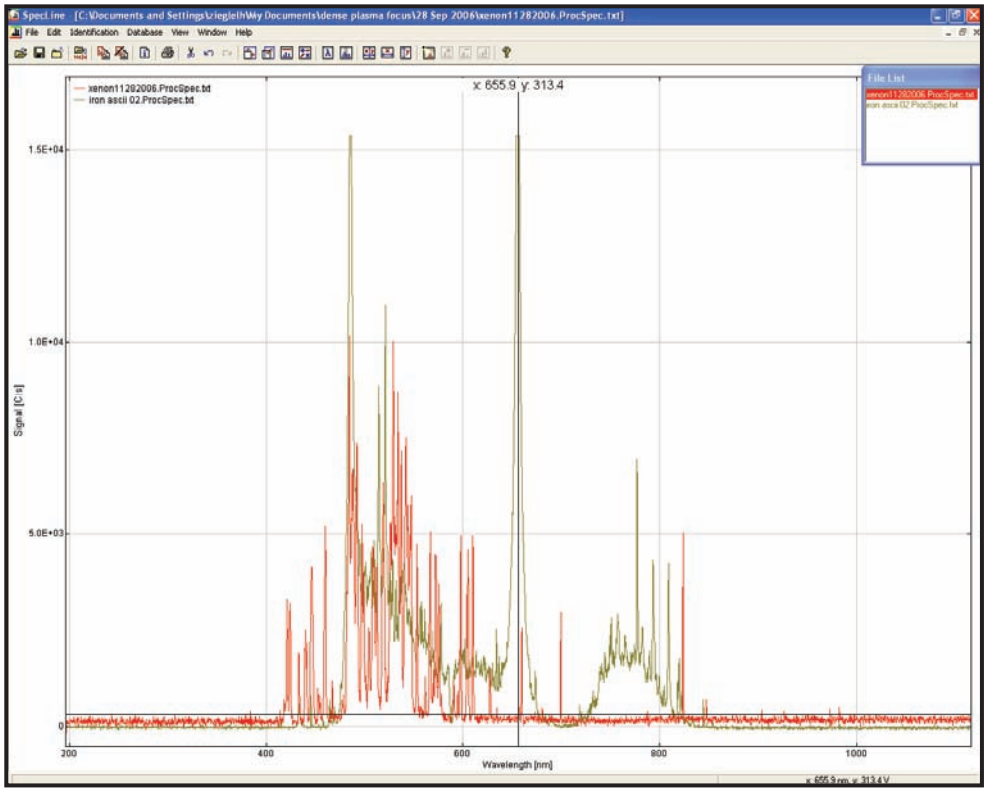

Figure 1. Comparison of a normal spectrum from a xenon flash lamp (red) with a typical spectrum measured on the DPF

Early spectra recorded in this project were taken with the spectrometers triggered manually. Light emitted by the plasma in the DPF generator during rundown and pinch was collected and transmitted to the spectrometers with a standard fiber-optic cable that was aimed in the direction of the pinch. The 60-ft fiber-optic cable was long enough to adequately attenuate the intense spectra to avoid saturating the spectrometers. Figure 2 shows a comparison of oxygen and deuterium spectra. The integration time for these spectra was 100 milliseconds.

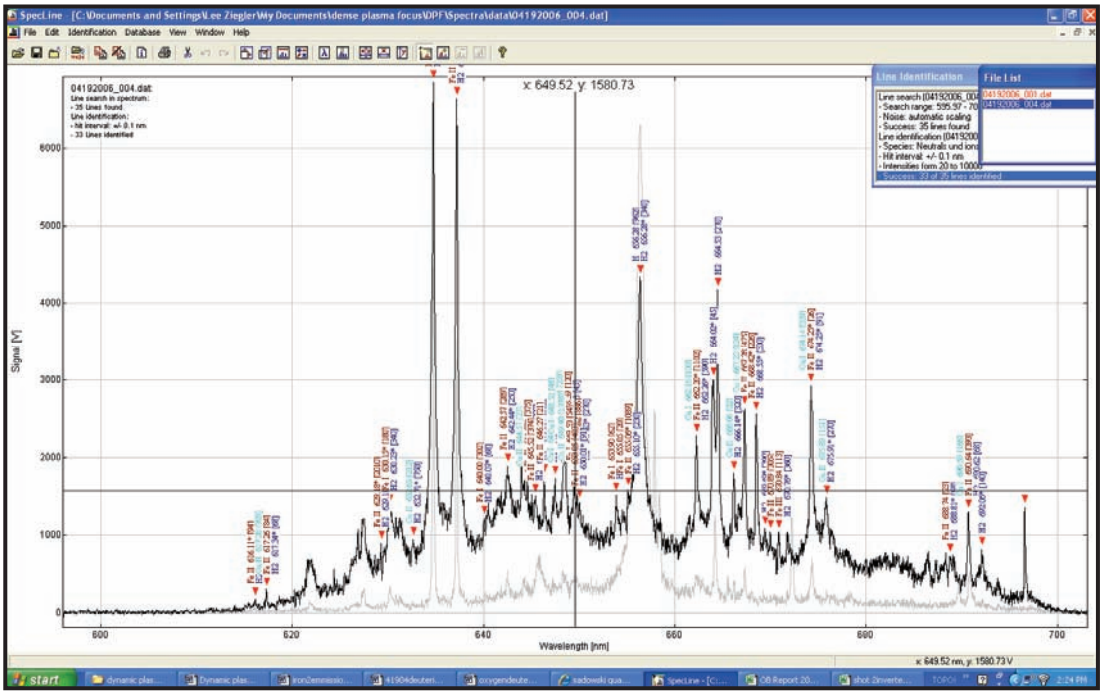

Figure 2. Manually triggered spectra using a fiber-optic cable to transmit the spectra to a spectrometer housed in a diagnostic trailer. The underlying spectra (grey) were acquired while oxygen was ionized. The overlaying spectra were acquired when the DPF chamber was filled with 5 torr deuterium. Comparing the spectra helps in analyzing the data.

Remote operation was accomplished by enclosing the spectrometer and the operating computer in an EMP-proof enclosure that also included an uninterrupted power supply, an optical-to-electrical trigger converter, and a DG-535 pulse generator. A 2-m-long fiber coupled a lens to the spectrometer. An ND-2 filter was used in conjunction with the lens to prevent the spectrometer from saturating. An optical trigger sent to the spectrometer was synchronized with the trigger to the DPF generator. Figure 3 shows the experimental setup.

Figures 4 and 5 show a typical spectrum from one of the experimental configurations investigated during our performance studies on the NLV DPF. This spectrum was obtained from a configuration employing a ceramic insulator between the anode and cathode. This anode had a 0.5-cm-diameter iron slug inserted in the center of the anode end. This series of spectra were taken using a 20-μs integration time synchronized with the start of the rundown phase of the DPF generator.

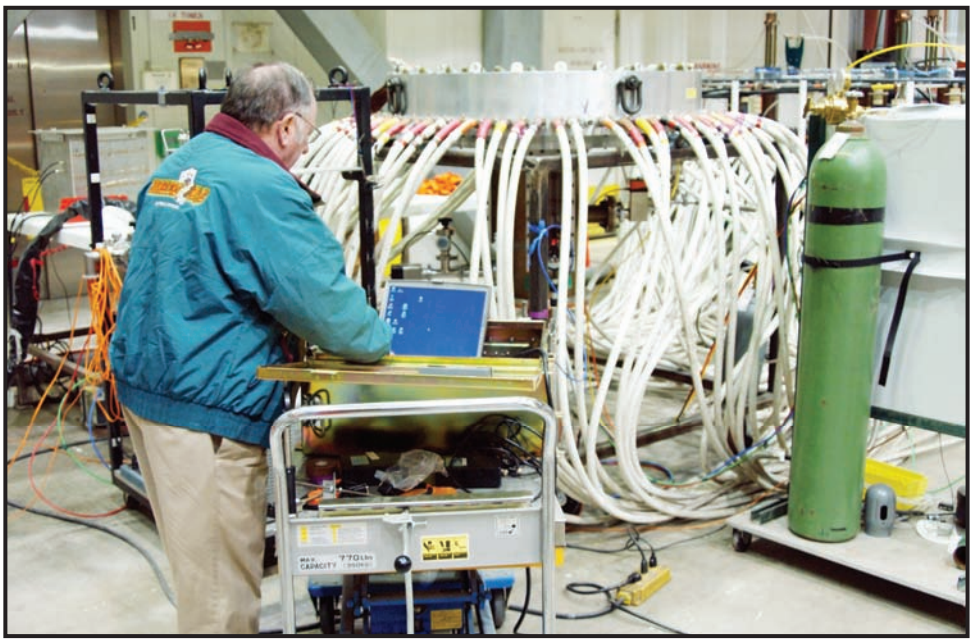

Figure 3. Operating the software for an Ocean Optics spectrometer housed in an EMP-proof housing. The spectrometer, a trigger generator, a laptop computer, and a UPS are contained in the EMP housing.

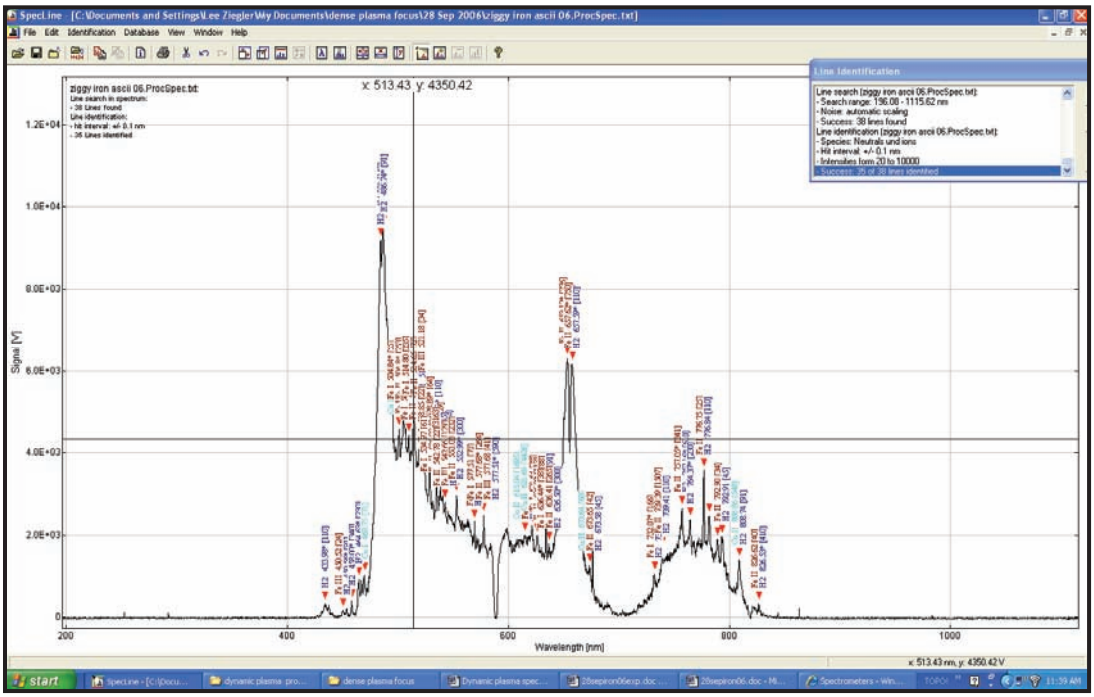

Figure 4. Full spectrum obtained using a 20-µs integration time

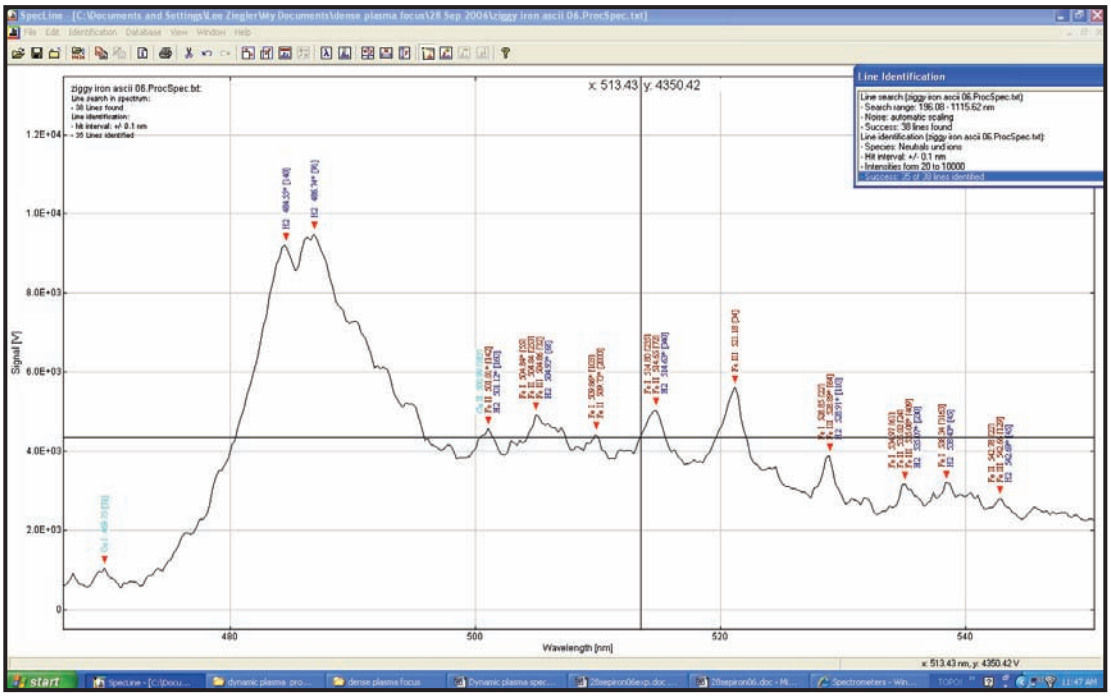

Figure 5. Expanded section of spectrum in Figure 4 showing the structure in the D_β emission line. Quite often, contributions from iron and copper are included in these spectral regions.

Conclusion

Two modes of acquiring optical spectra from a DPF generator—locally and remotely—were developed. The local operating mode allowed multiple spectrometers to be used simultaneously. While the spectrometer can be operated remotely, the integration time is still very long compared with the rundown of the plasma and the duration of the pinch. Sadowski used a spectrometer that could integrate in as short a time as 0.5 μs (Sadowski, 2005; Skladnik-Sadowska, 2006). Using this short integration time, they were able to measure the spectra during the pinch. Analysis of these spectra enable estimation of the density of the plasma during pinch.

Spectra from different gases and mixtures of gases were measured. We hope to be able to continue this work, and eventually develop the capability of measuring the concentrations of the components in the plasma.

References

Sadowski, M. J., K. Malinowski, E. Skladnik-Sadowska, M. Scholz, A. Tsarenko, J. Zebrowski, "Time-resolved optical spectroscopy of high-temperature plasmas," *Proc. SPIE* **5948** (2005) 5940806.

Skladnik-Sadowska, E., P. Kubes, K. Malinowski, M. J. Sadowski, M. Scholz, A. V. Tsarenko, "Time-resolved Optical Spectroscopy of Plasma Interaction with CD_2 Fiber in PF-1000 Facility," *AIP Conf. Proc.*, *6th International Conference on Dense Z-Pinches, Oxford, United Kingdom* **808** (January 2006) 203–206.

Tsarenko, A. V., V. V. Chebotarev, M. J. Sadowski, V. I. Tereshin, "A method of impurity diagnostics in dense plasma systems," *Nukleonika* **46**, 1 (2001) S37–S40.

Computer Sciences

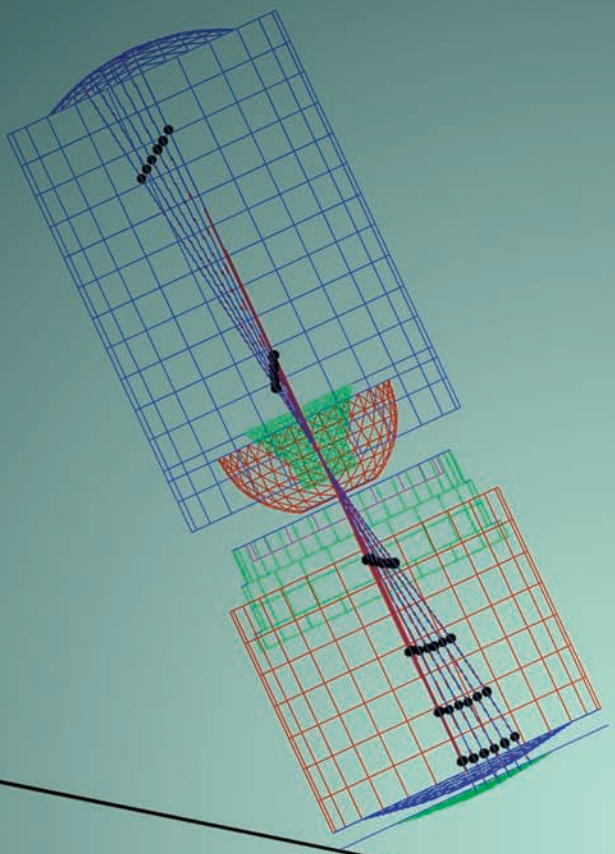

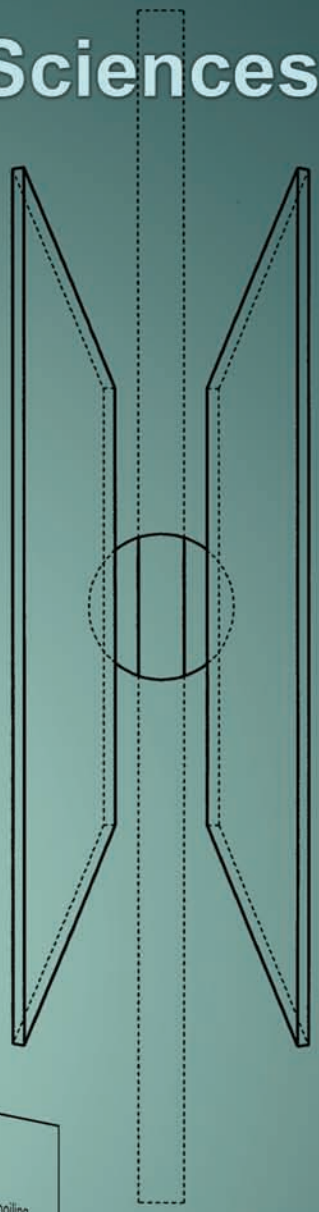

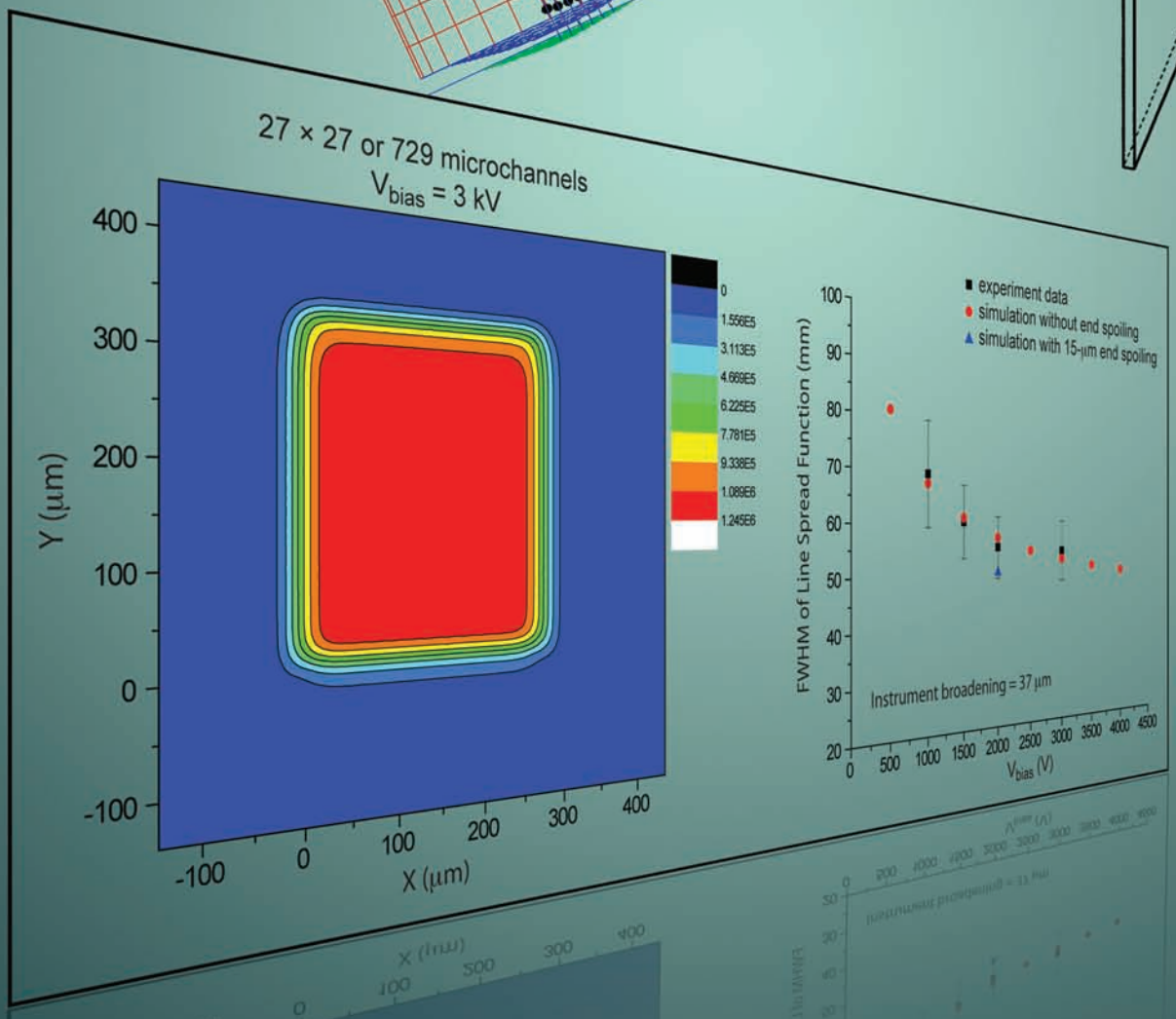

Detector Modeling Capability

Michael Berninger,[1] *Bob Hilko, Alfred Meidinger*
Los Alamos Operations

Stephen S. Lutz
Special Technologies Laboratory

The detector modeling capability (DMC) code was proven useful in calculating a high-fidelity, nonlinear detector response to the x-ray spectrum entering the detector. The DMC code assesses the detective quantum efficiency (DQE), point spread function (PSF), and modulation transfer function (MTF) of a radiographic detector. The code also predicts the outcome of an experiment by converting a synthetic radiograph calculated with the Monte Carlo N-Particle (MCNP) code to a measurable quantity. Programmed to operate with data libraries for a variety of detectors, the DMC is currently implemented for a lutetium oxyorthosilicate (LSO) detector. With the LSO, the DMC code converted the calculated radiograph with light-yield, blurring, radiographic and scintillation photon noise, and a scaling factor that represented the collection efficiency of a camera. DMC code results were validated by comparison with the LSO data from the Armando subcritical experiment. This report describes the features of the DMC and illustrates that its calculations, in good agreement with existing radiographic step-wedge data, offer improved understanding of detector physics.

Background

A detector response is a nonlinear scale function that quantitatively defines how a detector material is excited by an x-ray flux. X-rays are extremely useful for measuring the density distributions in objects because they can penetrate materials, but their short wavelengths make them invisible to most imaging systems. Detectors, such as phosphors, film emulsions, and scintillators are the media through which x-rays can be measured: film emulsions undergo a chemical change in opacity that is measured with a densitometer, and scintillators emit light in response to x-rays. Thus, a detector response is the function of the relative magnitude of the physical changes produced in a detector when exposed to x-rays.

Furthermore, the detector response depends on the wavelength, λ, of the x-ray. For example, when a flux of 200 keV x-rays deposits 1 MeV of energy in the scintillator material LSO, it will yield twice the magnitude of visible light as an equivalent deposition from 700-keV x-rays. In general, detector response is measured with calibrations.

[1] berninmj@nv.doe.gov, 505-663-2032

The detector response can be represented in a number of useful ways, but to the researcher the most important are DQE and the magnitude of the blur. The DQE describes how much emission, such as scintillation light, a detector outputs from the system for a given number of input x-rays. The resolution of the detector response can be quantified with the MTF or PSF.

It is important to accurately calculate the fidelity of the detector system when designing radiographic diagnostics or analyzing radiographic data. To support these efforts, this research developed a detector modeling software tool, the DMC, which calculates the responses of materials with user-defined radiographic inputs and detector geometries.

Project

The DMC is an interactive program driven through a graphical interface (Figure 1). The code calculates a detector response when a user specifies the inputs and outputs of the radiographic system and the detector, including the x-ray spectrum incident on the detector, the detector material and its physical dimensions, and if desired, a camera collection-efficiency factor. Once the system attributes are input, the user chooses which aspect of the detector response to calculate, such as the DQE or MTF. The calculated response function can be displayed and saved as a text or image file (.txt or .tif). Validation of the DMC calculations occurs when they are compared to the detector geometry data stored in the code's libraries.

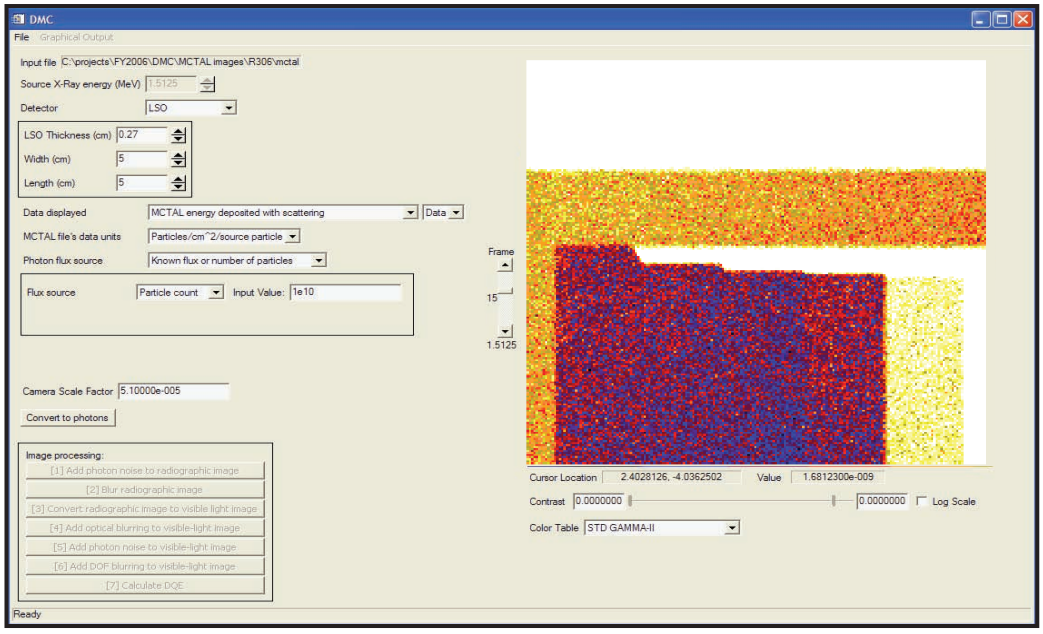

Figure 1. The DMC main user screen with a synthetic radiograph displayed

The physics principle underpinning the DMC code is the detector response function that scales the x-ray flux. The response function is expressed linearly with the equation

$$R(k,r) = E_{dep}(k,h,w,t) * \varepsilon(k) * cam \otimes PSF(k,r) \otimes \frac{dE}{dt}(k,t), \quad \textbf{(1)}$$

where the units of the response are the same as the measurable physical quantity, such as the number of scintillation photons yielded or the optical density per input x-ray photon with wave number $k = 2\pi/\lambda$. Depending on the detector, the response will be a nonlinear measure of either x-ray photon counting or the secondary excitations caused when an x-ray photon deposits energy in the detector. By the time of this report, we were testing the code by defining an LSO scintillator with the dimensions h, w, and t, where h is the detector's height (5 cm), w the width (5 cm), and t the thickness (2.7 mm). LSO responds to the magnitude of the deposited energy; thus, the first term in the equation E_{dep} (units MeV per incident x-ray), the x-ray deposited energy, varies nonlinearly with the wave number k and is dependent upon the size of the detector. This energy will yield an amount of light, $\varepsilon(k)$, nonlinear with k where the units of ε are emission photons/MeV. The factor *cam* is a proportionality constant that accounts for the camera's collection solid angle and magnification, and the efficiency of the light-collection device, in this case a CCD camera. The last parameter involves the PSF characterizing the amount of radiation scattering that occurs within the detector and accounts for optical blur if the camera system has been characterized. The PSF is a function of radius r and the wave number of the incident x-rays. A high-energy x-ray tends to deposit energy at greater distances away from the point of incidence than a low-energy x-ray. Not only does the energy spread laterally, but it is also deposited to finite depths in the detector. The energy deposition throughout the detector's thickness is accounted for by the function *dE/dt* that depends on the wave number of the incident x-ray and the thickness of the detector. Depth-dependent features of the response, such as depth-of-field blur and saturation, are evaluated by *dE/dt*.

The core of the DMC code will be the libraries (Figure 2) prepared for each type of detector with tables of functions that define the terms E_{dep}, $\varepsilon(k)$, *PSF(k,r)*, and *dE/dt(k,t)* (Equation 1) over a domain of k, r, and t. The only DMC library currently installed is for LSO. The *PSF(k,r)* calculated for a piece of LSO t = 1 mm thick (Figure 3a) and three incident x-ray wave numbers (k), shows the highly nonlinear characteristics of the energy deposition with radius and k. The highly nonlinear visible light yielded per MeV of energy deposited (Figure 3b) in LSO (Dorenbos, 1994) is also tabulated within the libraries. The thickness of the detector and the x-ray wave number will be the keys that the DMC uses to reference and interpolate an appropriate response for the given detector definitions.

The data that populates the tables is compiled from the literature, experiments, and calculations. The data for the DMC LSO library was compiled from three sources. The light-yield data was referenced

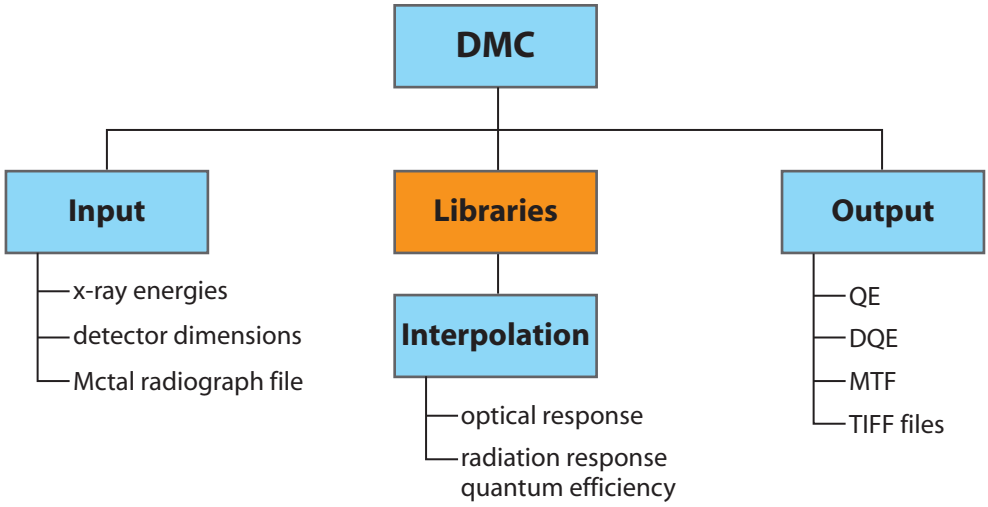

Figure 2. A schematic of the DMC code

in literature, the optical blur was measured at STL, and three quantities were calculated with MCNP, the amount of energy deposited within the LSO for different t and k, the radial dependence of the scattering from the interaction point, and the depth-dependence of the deposited x-rays.

The operation of the DMC code follows two logic paths: a detector response can be constructed and displayed for an input spectrum, or the DMC can process a synthetic radiograph. In each case, the user must define the detector and its dimensions and then select how the detector response will be constructed.

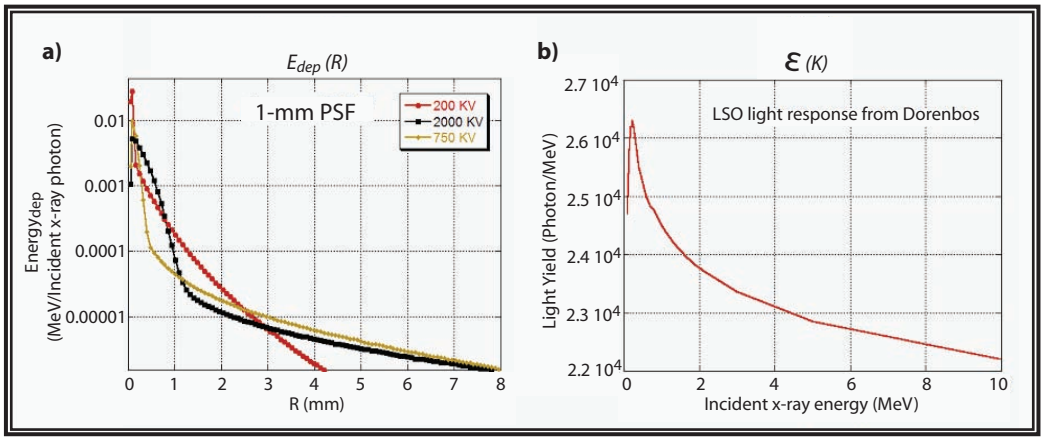

Figure 3. (a) E_{dep} was calculated for a range of incident x-rays and thicknesses of LSO. (b) The plot of ε was found in the literature (Dorenbos, 1994).

Should the user choose to process a response to an input spectrum, the DMC reads a spectrum file (ASCII text) with X,Y pairs that define the x-ray energy and its associated flux quantity. The code will display the contents of the spectrum file (Figure 4). After defining the detector, the user can then calculate the DQE, MTF, or PSF. The calculated response is displayed in a plot, which can be modified and saved as X,Y pairs in a text file.

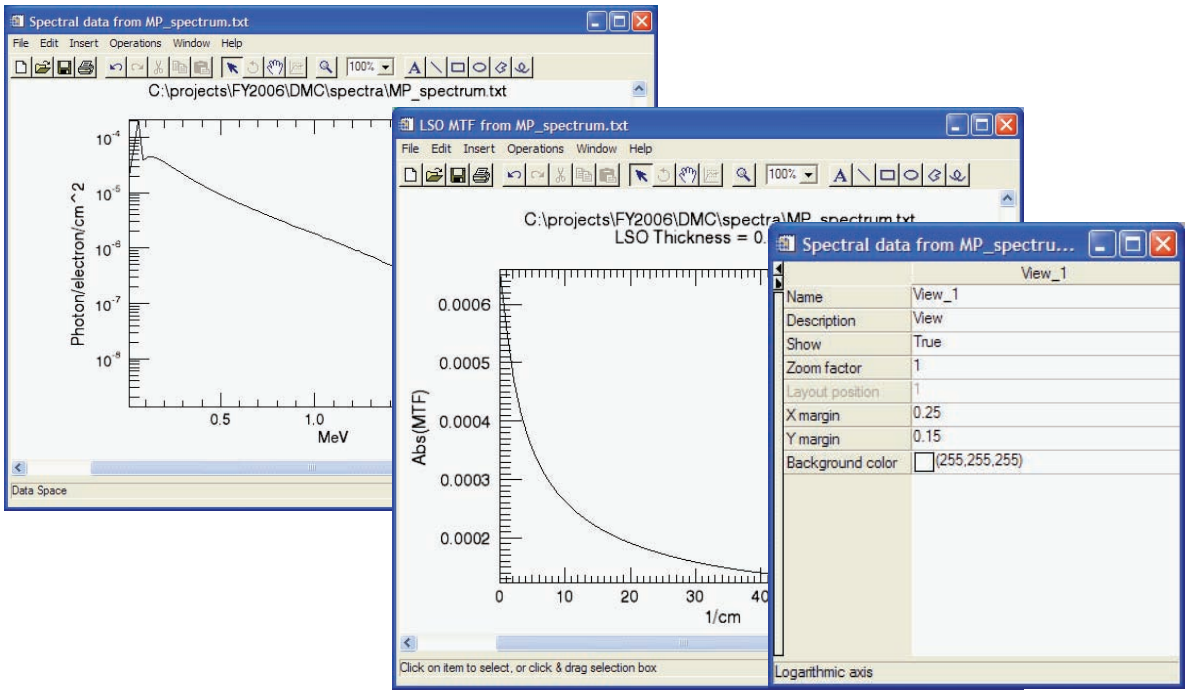

Figure 4. An input spectrum is displayed with a calculated MTF in separate windows, while a pop-up window is used for interactively modifying the graphical displays

For the DMC to process a synthetic radiograph, the user loads an MCNP MCTAL (MCNP tally results)-formatted file that contains the image plane reconstruction of the magnitude of the x-ray transmission through dense objects. This transmission can be segmented with frames defined for small domains of energy (called bins) in the x-ray spectrum incident on the image plane by MCNP and stored in the MCTAL file. Each frame depicts what the radiographic image would be if only that bin of x-ray energy crossed the image plane. A cross section of the frames for a given pixel defines the x-ray spectrum that strikes the pixel. The sum of the frames creates the total radiographic image. There are two versions of the synthetic radiograph within the MCTAL file, each segmented into frames by energy: the transmission with x-ray scattering accounts and the directly transmitted x-rays

(without scattering). The MCTAL file also contains images of the MCNP-calculated statistical error. The DMC extracts all the images and frames of the synthetic radiograph (including the error images) from the MCTAL file. The frames can be viewed individually on the main DMC screen (Figure 1). Many color tables are available to enhance the synthetic radiograph's display.

After defining the detector and its dimensions, the image can be processed in a number of ways. A typical set of processing steps would be to add photon noise, convert the x-rays to visible light (for LSO), blur, then to some scaled quantity like CCD counts with a camera-scaling factor. The DMC processes each frame by calculating the product of the synthesized x-ray fluxes with the calculated detector response $I(k) = R(k)S(k)$, where the spectral quantity S is the number of x-rays with wave number k provided. The final step would be to sum the frames

$$I_{total} = \sum I(k), \qquad I_{total} = \sum_{k} I(k) \tag{2}$$

and output the synthetic image to a tagged-image file (.tif) for further comparison and analysis.

The DMC code's accuracy and precision are validated through comparison with the data from a detector using overlaid LSO lineouts. The comparison (Figure 5) of the DMC–processed image with the step-wedge data from a radiographic experiment showed very good agreement. With confidence in the accuracy of the detector modeling, we can use the DMC to obtain new knowledge of the physics of the detector's operational characteristics. For example, we can obtain a better understanding of the sources of photon noise in a radiographic experiment. Figure 6 shows that at least half of the standard deviation from photon noise in the darker (lower transmission) regions of interest come from the background of the detector itself rather than from the photon noise created by the detector's collection of x-rays.

Conclusion

The DMC methodology for creating a physics-based model of the detector response has demonstrated value for calculating high-fidelity synthetic radiographs and performing quantitative analysis. Designed to operate with libraries containing data for a variety of detectors, the DMC code is used for calculating detector responses to known fluxes of x-rays. By calculating the DQE, PSF, and MTF of a radiographic detector, we can better design the radiographic detectors for an experiment. The DMC code can accurately construct a synthetic radiographic image with the MCNP code. The DMC converts the calculated radiograph with a light-yield, blurring, radiographic and scintillation photon noise, and a scaling factor that represents the collection efficiency of a camera. The good agreement shown between the DMC calculations and existing data has confirmed the DMC's ability to provide an increased comprehension of the detector physics.

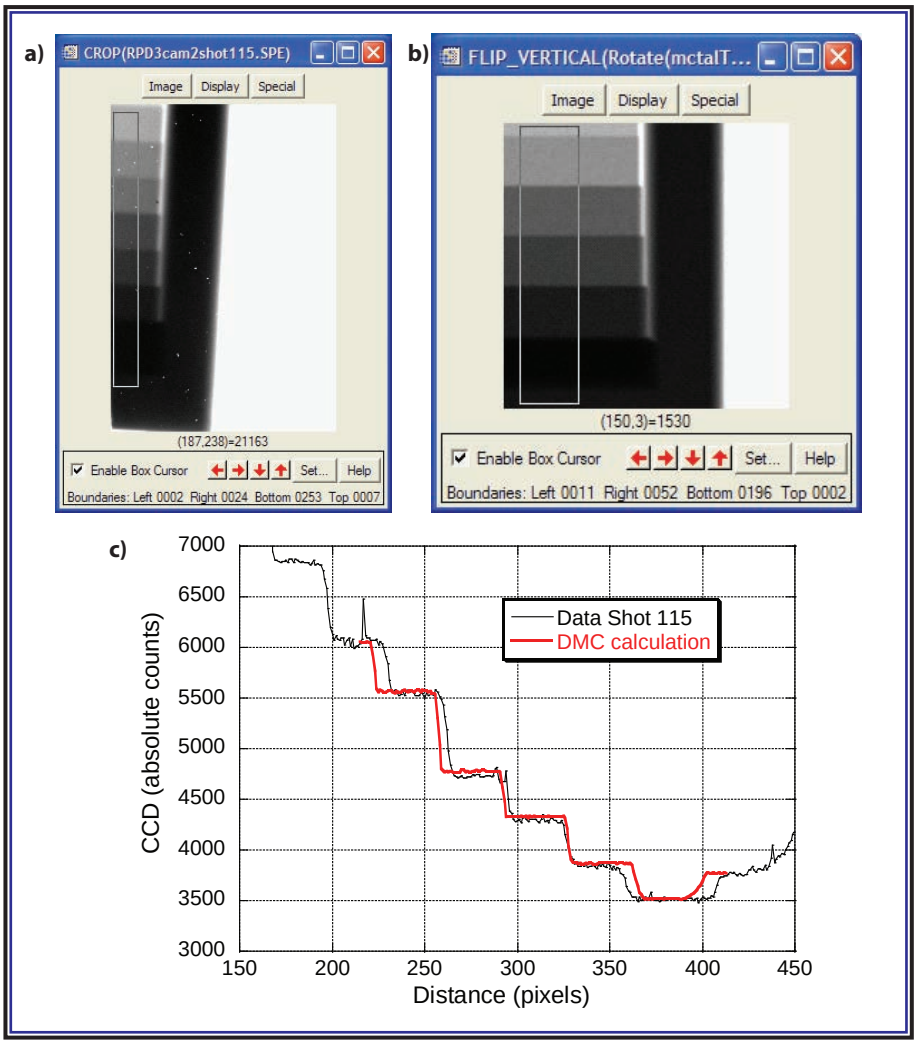

Figure 5. (a) The step-wedge data from the Armando radiographic experiment. (b) A DMC–processed synthetic radiograph of the step-wedge data calculated in MCNP. (c) Regions of interest (white boxes on a, b) collapsed and plotted.

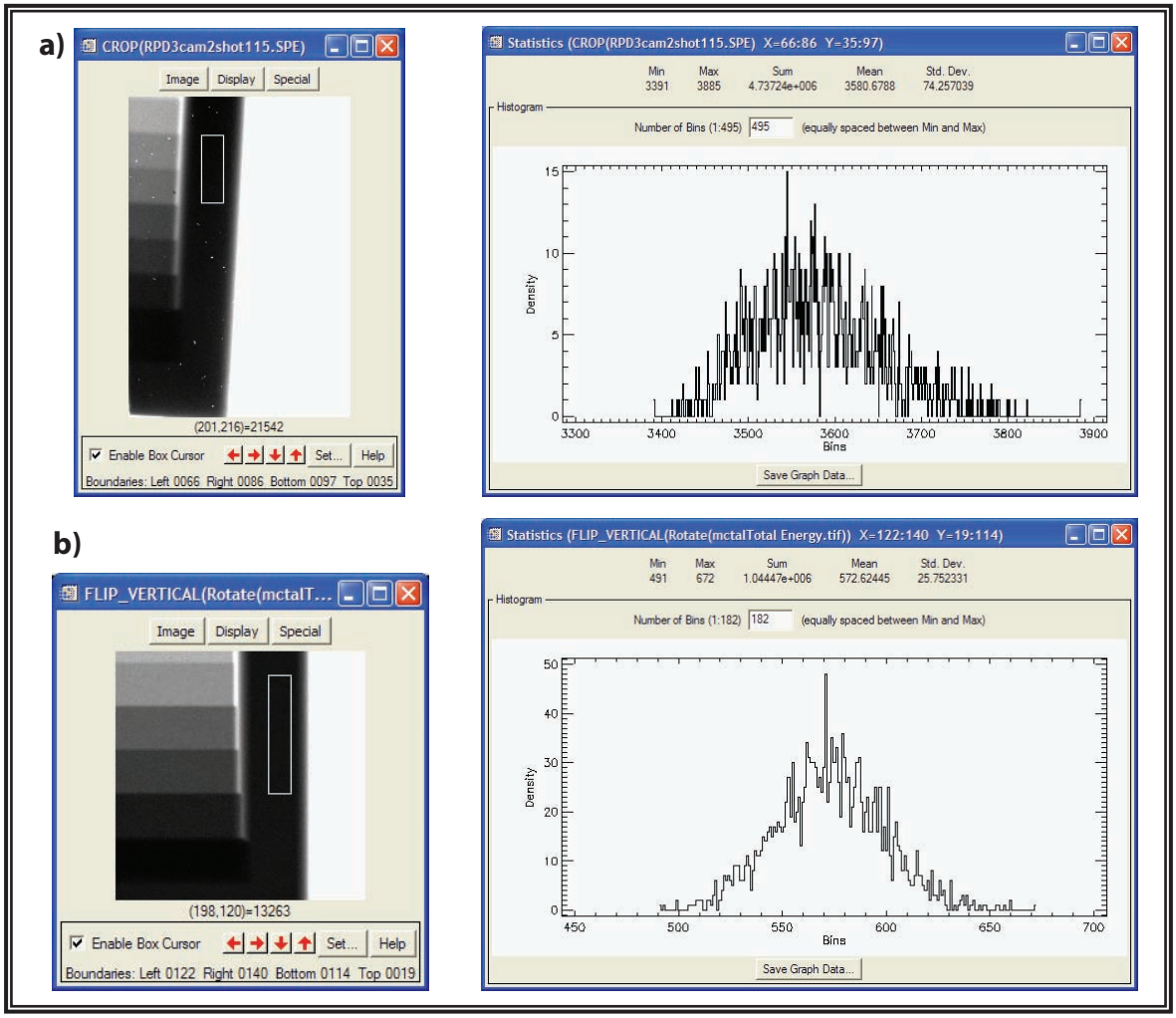

Figure 6. (a) The step-wedge data from the Armando radiographic experiment with the noise distribution in the region of interest. (b) The DMC–processed synthetic radiograph of the step-wedge data with the synthetic photon noise distribution.

Acknowledgments

The team expresses their appreciation to Jim Pendleton and Dawn Lenz, of ITT, and Franklin Bunker.

Reference

Dorenbos, P., J. T. M de Haas, C. W. E. van Eijk, C. L. Melcher, J. S. Schweitzer, "Non-linear response in the scintillation yield of $Lu_2SiO_5:Ce_3+$," *IEEE Trans. on Nucl. Sci.* **41**, 4 (1994) 735–737.

this page intentionally left blank

Fluorescence Calibration

John Di Benedetto, James Herning[1]
Special Technologies Laboratory

This project sought to design and build an optical system that would couple field instruments to a laboratory spectrometer and develop a calibration method that could be shared across the fluorescence remote-sensing community. This project's team designed such an optical system, and radiometric modeling indicated sufficient power for calibration measurements to be made.

Background

Over the last two decades, fluorescence has emerged as a quantitative diagnostic technique for trace detection. This has proven especially true in such medical applications as flow cytometry. Absolute emission yields are required for radiometric calibration, much like those used in thermal imaging. However, the problem is more complex, since excitation and emission wavelengths must be considered, along with polarization effects, non-Lambertian surface emission, and a much larger dynamic range of intensities than normally encountered in reflectance or emissivity measurements.

In the past few years, the development of fluorescence remote sensing as a detection method for the intelligence community has highlighted the need for the generation of intensity-calibrated, laser-induced fluorescence imaging/spectroscopy (LIFI/S) data sets. Past work performed at STL to generate such data sets showed that using conventional sample geometries in commercial instruments gave less than satisfying standard yield values compared with field system geometries. Surface orientation and roughness can affect yield values in ways analogous to the offsets seen in reflectance (e.g., bidirectional reflectance in trees). Intensity-calibrated data sets would enable the cross-calibration of field systems and create data sets that would be exchangeable among various groups throughout the community, so that calibrated spectral libraries could be shared.

This project sought to develop a simple but extremely stable, potentially all-reflective optical illuminator and receiver, with an interface to laboratory and field instruments through fiber-optic bundles and ports for instantaneous field-of-view camera calibration. The resulting system would generate intensity-calibrated data sets by coupling our LIFI/S field instruments to a laboratory spectrometer. This system would allow us to study the effects of sample orientation and coarse roughness.

[1] herninjw@nv.doe.gov, 805-681-2215

Project

The project had three main design goals: 1) to minimize the illuminator/receiver angle with respect to the calibration unit as much as possible, as most remote-sensing measurements are made at nadir with respect to the target of interest; 2) to couple the system to our laboratory spectrometer and field instruments; and 3) to build the calibration system out of inexpensive, commercial off-the-shelf components. Unfortunately, due to design constraints introduced by our optical source (the laboratory spectrometer), meeting all these goals was impossible without a significant loss of throughput with respect to the native output of said optical source.

As a reference instrument, we used a Hitachi F4500 Spectrofluorimeter, which imaged the excitation grating slit onto the sample plane. Thus, it was necessary to incorporate fiber bundles that could pick up a rectangular beam with a 9 mm × 2 mm profile. We chose a bundle design of 91 fibers, each with a 400-µm diameter. The bundle end that would interface with the Hitachi had fibers arrayed in stacked rows in a 9.12 mm × 2.14 mm profile. The end that would interface with the calibration platform was a closely packed circular arrangement with a 5.28-mm diameter. This design aspect proved most troublesome. Our effort to manipulate and capture an extended source of this size (5.28 mm) with a numerical aperture of 0.22 was quite challenging.

To incorporate an excitation receiver and emission transmitter fiber bundles, the Hitachi required modifications to the existing sample stage. In an effort to balance excitation power against bandwidth, we chose a 5-nm band-pass slit width. The fiber-to-spectrometer interface appears in Figure 1.

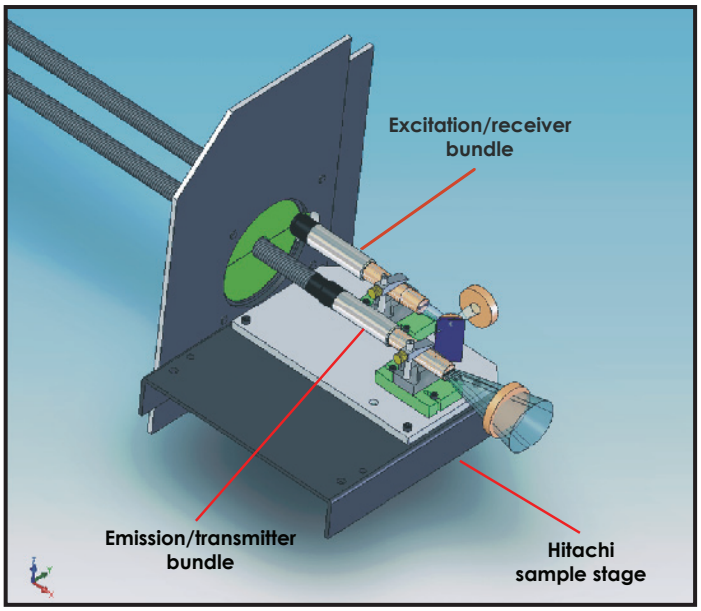

Figure 1. Fiber bundle interface to Hitachi sample stage

While the system was not completely assembled and tested due to supply problems regarding the required fiber-optic assemblies, we have procured all system components and system design has been determined. The basic calibration unit design would consist of the source fiber object collected onto a mirror element, then imaged onto the sample plane with the resultant fluorescent output from the sample collected by the second mirror element and imaged onto the receiver fiber. The second fiber bundle would then project the beam back into the spectrometer on the sample stage (Figure 1). The system would be coupled to our field LIFI/S instruments by having the second mirror element mounted on an arm attached to a rotation stage (Figure 2). The aperture, resulting from mirror rotation, would allow an imaging system to view the illuminated sample stage at a number of calibration distances. Sample output would be measured using the Hitachi. The second mirror element would then be rotated out of the way to allow direct sample viewing by the field instrument under test. The mirrors (3 in. diameter, f = 203.2 mm) represented our effort to maximize collection efficiency while reducing the required minimum standoff of the LIFI/S instruments from the second mirror element plane.

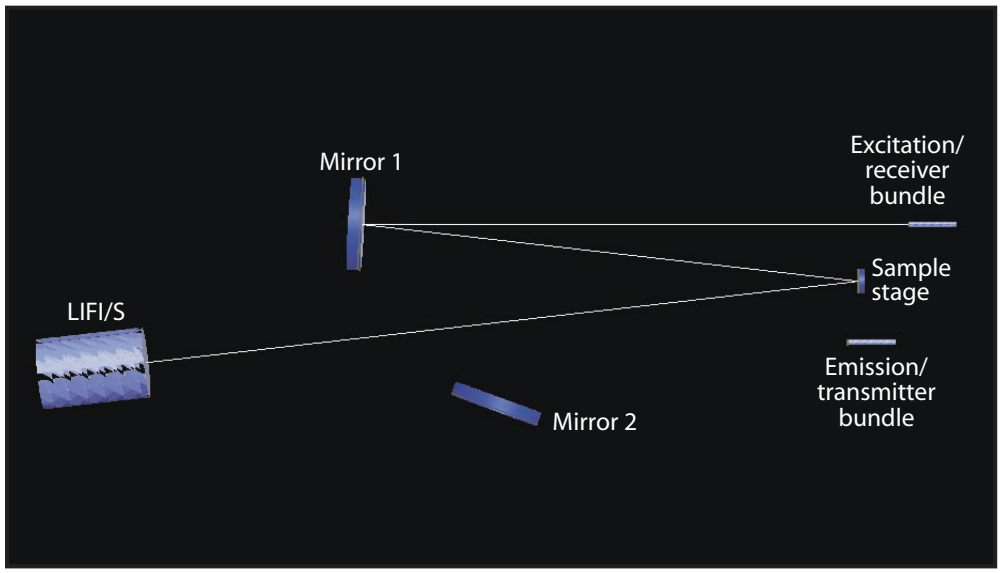

Figure 2. System design showing interface with LIFI/S

This design necessitated either an aperture stop or some form of relay system to constrain the source beam onto the first mirror element (Figure 3). By incorporating a baffle between the two mirror elements and an aperture stop in front of the source beam, we could maximize the power onto the first mirror. However, this yielded a throughput of only 9%.

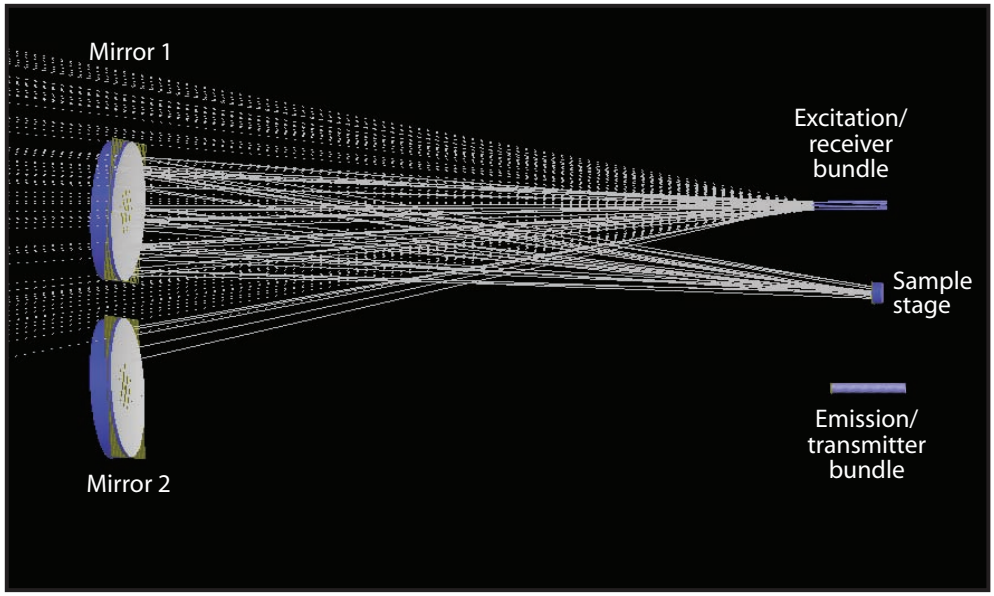

Figure 3. Basic design concept for the calibration unit showing overfill of source collection mirror

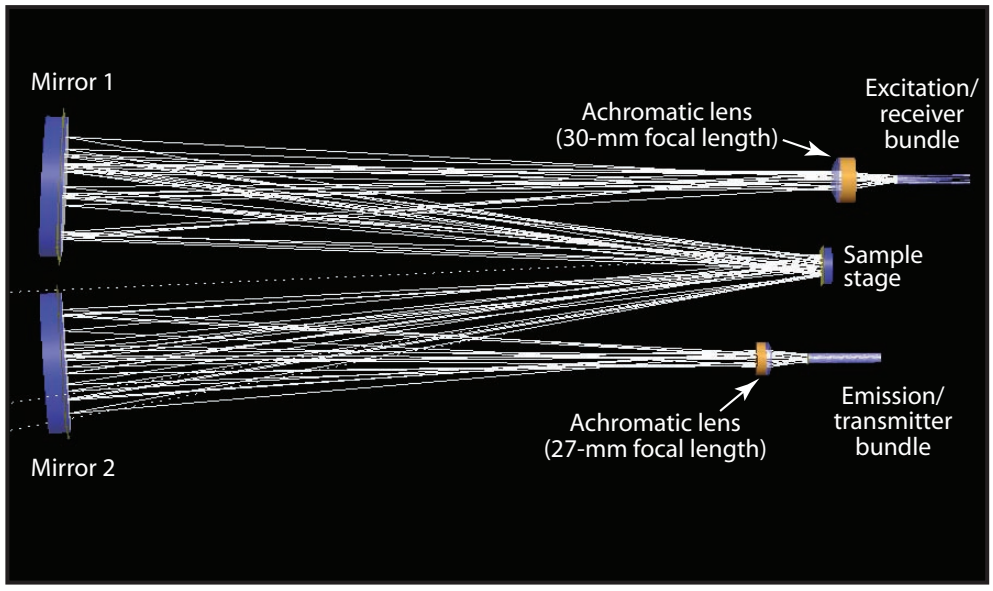

Figure 4. Final system design transfers all of the source power to the sample stage

Such an approach proved untenable, as radiometric modeling gave the maximum possible power reaching the Hitachi emission input port in the single-digit picowatt range. We explored various mirror-based relay assemblies, but geometric constraints combined with the étendue of the source fiber proved this approach was not feasible.

The final design (Figure 4) incorporated achromatic lenses in front of the source fiber and receiver fibers, with focal lengths of 30 mm and 27 mm, respectively. The resultant spot size on the sample stage was 14 mm in diameter, nicely lending itself to the use of 2-cm sample cuvettes (and also an acceptable size for collected field samples). Using the fluorescence standard Rhodamine 101, which has a published quantum efficiency of 1 using 450–465 nm excitation (Flanagan, 1997), radiometric modeling showed sufficient power incident on both the Hitachi and the LIFI/S field instruments for calibration measurements to be made.

We purchased and/or fabricated all of the necessary components for this system. Final testing of the system awaits acquisition of custom fiber bundle and achromats.

Conclusion

Our team designed an inexpensive system for radiometrically calibrating our LIFI/S field instruments. In order to study the effects of sample orientation and coarse roughness of field samples, we will need to acquire an appropriate set of UV-Vis achromats. Once the system has been fully characterized, it will provide for the collection of intensity-calibrated field data from our LIFI/S instruments. This will allow for the completion of a calibration method, which will be shared and hopefully adopted by the fluorescence remote-sensing community.

Reference

Flanagan, J. H., S. E. Romero, B. L. Legendre, R. P. Hammer, S. A. Soper, "Heavy-atom modified near-IR fluorescent dyes for DNA sequencing applications: synthesis and photophysical characterization," *Proc. SPIE* **2980** (1997) 328–337.

this page intentionally left blank

Monte Carlo Simulation of High-speed Gated X-ray Detectors

Craig A. Kruschwitz,[1] *Dane Morgan, Jiaming Morgan (former employee), Ming Wu*
Los Alamos Operations

This research continues work started in FY 2005 to develop a Monte Carlo simulation code for modeling secondary electron emission processes and electron dynamics in a microchannel plate (MCP), a key component of many high-speed, gated x-ray detectors. At that time, our team focused on developing the basic simulation code and DC mode applications. In FY 2006, we further developed the code and concentrated on pulse mode applications. We successfully incorporated space-charge and wall-charging models for modeling gain saturation. We also conducted a series of MCP spatial resolution simulations.

Background

High-speed, gated x-ray detectors based on straight-channel MCPs are a powerful diagnostic tool for two-dimensional, time-resolved imaging and time-resolved x-ray spectroscopy in laser-driven inertial confinement fusion and fast Z-pinch experiments. These detectors consist of a gold photocathode coated on the front of the MCP, a phosphor screen coated on a fiber-optic faceplate, and a film recorder or CCD. High-speed gating is achieved by sending a subnanosecond high-voltage pulse through a microstrip transmission line coated onto the MCP. When the high-voltage pulse is propagated along the strip line, MCP gating occurs wherever voltage is applied.

The electron gain in an MCP is highly nonlinear with the applied voltage; therefore, the MCP's optical gate can be much narrower than the voltage pulse width. Also, impedance mismatches between the microstrip and the high-performance pulsers used to supply the gating voltage affect the voltage waveforms along the MCP. This presents obvious problems when interpreting the data and makes understanding MCP behavior under time-dependent voltages essential. Monte Carlo–based computer simulations of MCP response to a steady-state voltage have been performed in the past (Ito, 1984; Guest, 1971), but these models were not developed for pulsed voltages and did not include several other important effects, such as elastic reflection of electrons from the channel wall and gain saturation due to space-charge and wall-charging effects. We have expanded the MCP simulation code developed in FY 2005 to include these capabilities.

[1] kruschca@nv.doe.gov, 505-663-2023

Project

An MCP is essentially an array of parallel continuous electron multipliers. The individual MCP channels are typically about 10 μm in diameter, and the plates themselves are generally 450–600 μm thick. Typically, the channels are set an angle α to the normal surface of the MCP (Wiza, 1979). Often, an MCP is characterized by the ratio of its thickness to channel diameter (or L/D ratio).

The program we developed (detailed description in Wu, 2006) was written in ITT Visual Information Solutions' Interactive Data Language (IDL) and describes the cascade and dynamics of electrons in a single microchannel. Standard equations give the mean secondary emission yield as a function of incident energy and angle relative to the surface normal. Electron trajectories are calculated using straightforward, nonrelativistic equations of motions.

We have implemented a model for approximating the space-charge effects in the channel at high electron numbers. This model treats the electron cloud as a uniform cylinder of charge and solves for the radial potential resulting from such a charge distribution. The axial component of the electric field is assumed to be unchanged. The space-charge field deflects electrons in the channel, shortening the time between collisions, and therefore decreasing impact energy. When the space-charge field is strong enough, the average impact energy is reduced so that the average secondary yield = 1. This results in saturation.

Wall-charging can also lead to saturation. As the number of secondary electrons freed from the lead glass wall of the microchannel grows, a positive charge builds up on the channel walls. The time scale for the replenishment of this charge is quite long (milliseconds) because of the low conductivity of the lead glass. As implemented in the simulation, wall-charging decreases the axial component of the electric field in the area immediately below the wall-charged area, which reduces electron acceleration, and thus, the resulting secondary yield. This model ignores any radial effects with the justification that the cylindrical geometry leads to a cancellation of the radial component. This assumption is acceptable near the channel center, but perhaps is not acceptable nearer the channel wall.

DC Saturation: Modeling and Measurements

In order to verify the simple saturation model for both DC and pulsed voltages, we compared simulations using the above algorithms to MCP sensitivity data gathered at the LO Short-Pulse Laser Facility. For the DC measurements, an MCP was held at various DC bias voltages and illuminated by a deep ultraviolet femtosecond laser. The short-pulse laser system provides 200-nm laser light with a 150–200-fs pulse width at 150–200-μJ energy per pulse. We estimate that the laser produced about 100–1000 electrons per channel once geometric factors and the photocathode quantum efficiency are accounted for (assumed to be 0.1–1.0%). Because the laser pulse is much shorter than the transit time of electrons cascaded through the MCP channel, the electron bunch was introduced at the

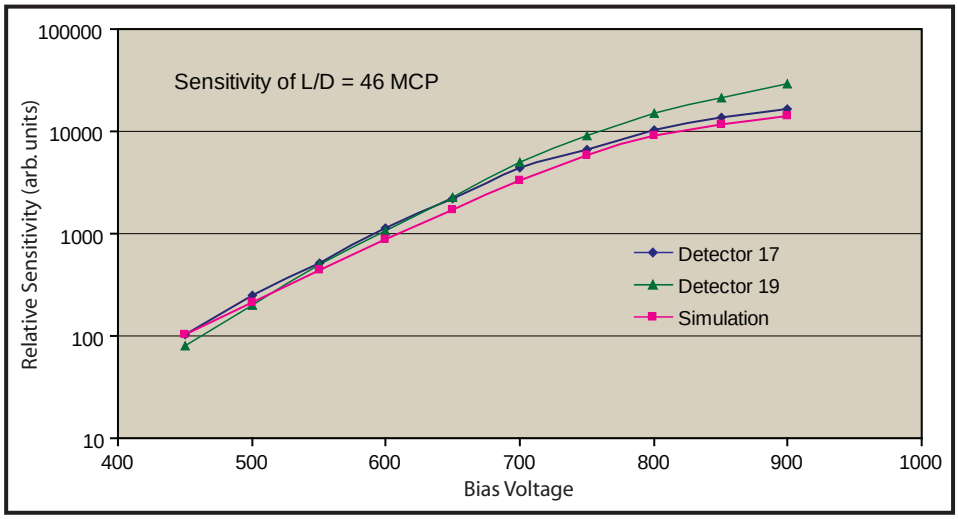

Figure 1. MCP saturation data and simulation in DC mode. The data were obtained at LO's Short-Pulse Laser Facility. The simulations assume a cascade launched by 500 electrons. Saturation onset occurs at ~700 V.

beginning of the simulation. Experimental results and the simulation appear in Figure 1. The results show that the MCP begins to saturate at ~700 V. For the simulations, 500 electrons were assumed to be introduced in the channel by the laser. The simulations match the data very well.

Pulsed Voltage Saturation: Modeling and Measurements

We also investigated MCP saturation in pulsed mode. The gated x-ray detectors are operated in pulsed mode, and in high x-ray flux environments, this issue is of great interest. Sensitivity data for an L/D = 46, 10-μm pore MCP pulsed with a 400-ps square pulse were collected at the LO Short-Pulse Laser Facility. MCP sensitivities were measured as a function of laser power (Figure 2), along with the simulated sensitivities and the measured applied voltage pulse. For the simulations, the number of input electrons was increased until the response showed saturation. In Figure 2, sensitivity curves have been scaled such that linear response regions coincide.

Gate Profile Modeling and Measurements

Another interesting use of the Monte Carlo code is in simulating MCP gate profiles. A gate profile (also called an optical gate profile) is essentially an MCP's time-dependent sensitivity when a voltage pulse is applied. Since the gain increases nonlinearly with the voltage, the gate profile is significantly narrower than the voltage pulse. Because the code we developed can deal quite easily with time-varying voltages, we can simulate the gate profile. Figure 3 shows the result of both measured and simulated gate profiles. The simulations used voltage pulse profiles measured at various distances

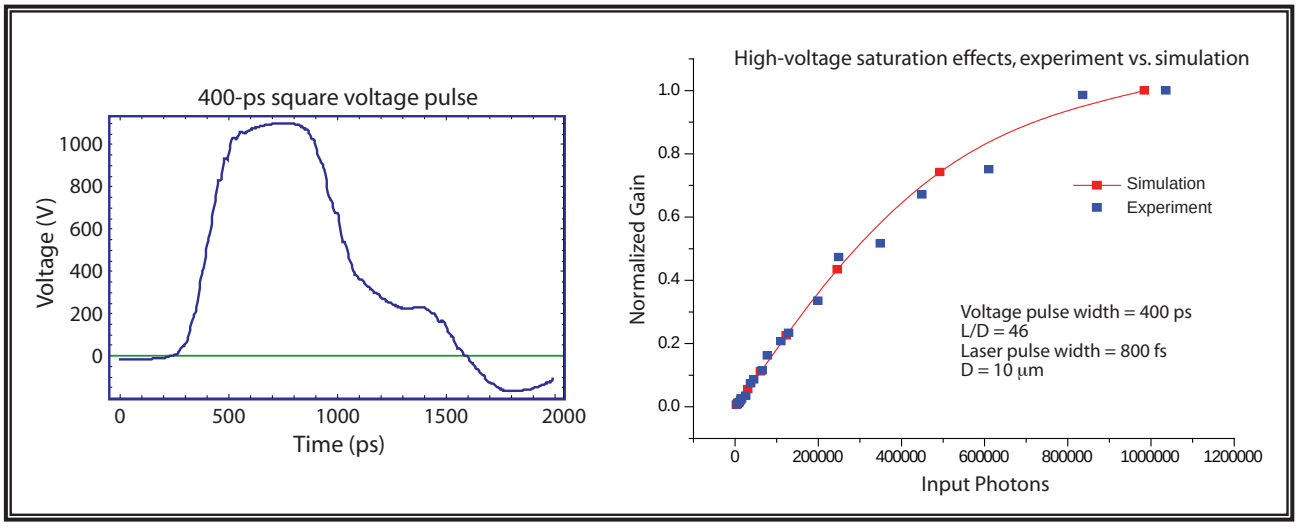

Figure 2. 400-ps square pulse from pulser used in experiments (left); simulated and measured sensitivity as a function of laser intensity (right)

along the length of one of the MCP microstrip coatings using a picoprobe. Agreement between simulated and measured gate profiles is clearly very good. This data was supplied to us by Greg Rochau at SNL.

Spatial Resolution Modeling

The Monte Carlo code gives the energy and direction of the electrons emerging from the channel. We can use this data to calculate electron spreading between the MCP output face and phosphor for a given phosphor bias. Output end-spoiling, the penetration of the microstrip coating down some distance into the MCP pore, is potentially important here, as it acts as a collimator for the output electrons. We approximate this effect by setting E = 0 in the end-spoiled region, which we take to be the last 1–1.5-channel diameter lengths of the channel.

For our resolution calculations, we have generated a set of output electrons from a 729-channel array, resulting in a rectangular image of a 27 × 27 channel area (Figure 4). The line-spread function was calculated by examining the edges of this rectangle. These simulations were conducted for various phosphor bias voltages. Simulated resolutions were then compared with measured resolutions. These measurements were performed using the Manson x-ray source at SNL, with a resolution target consisting of a series of edge patterns. Comparison results appear in Figure 4. Agreement between the simulations and experiment are excellent, particularly the simulations without end-spoiling.

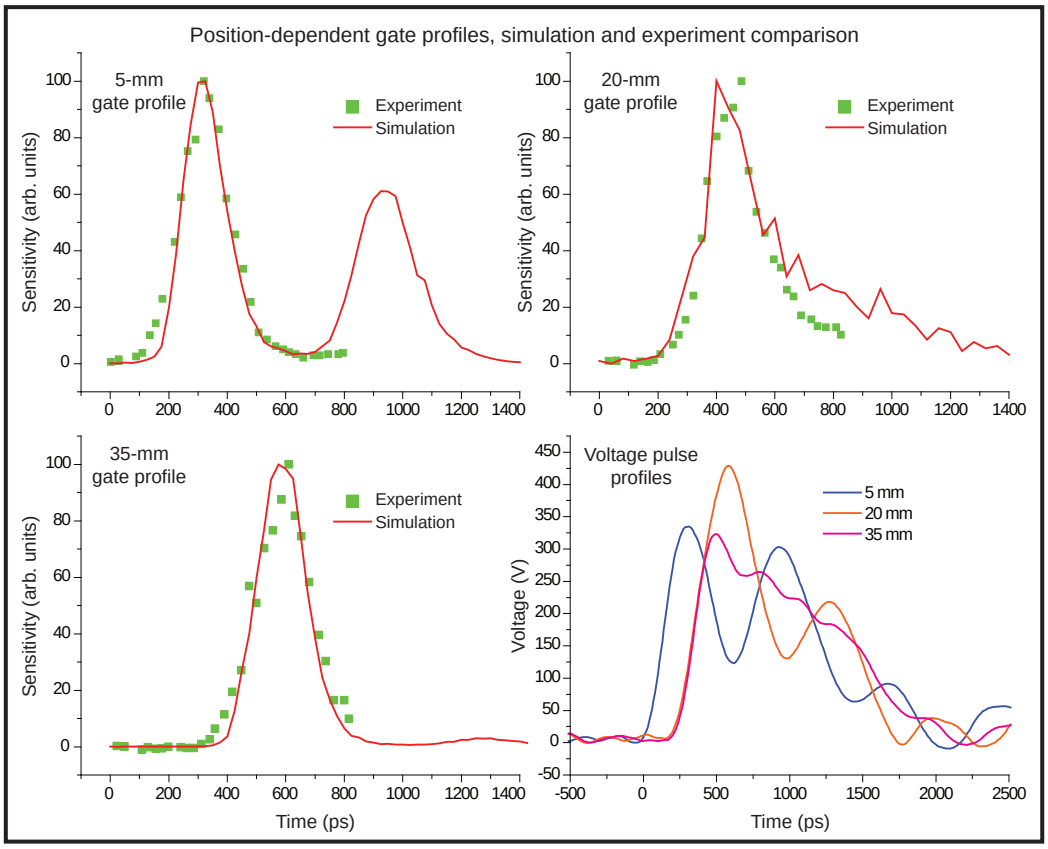

Figure 3. Measured and simulated MCP gate profiles. Also shown are picoprobe voltage pulse profile measurements, used for the simulations.

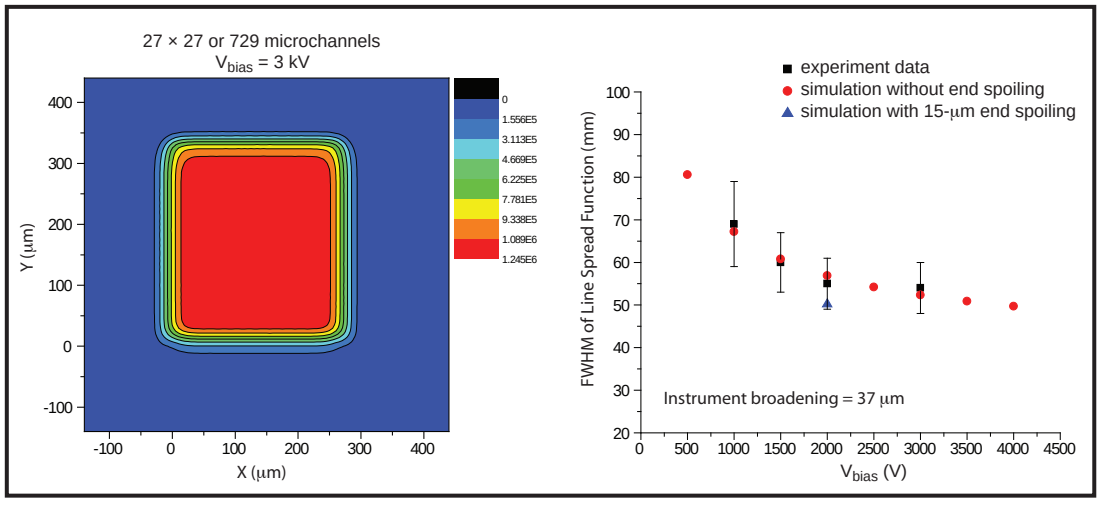

Figure 4. Simulated pattern of electron impacts from 729 microchannels (27 × 27 channel area) on the phosphor for a 3-kV phosphor bias (left); full-width at half-maximum of simulated and measured line-spread functions (right)

Conclusion

We made significant progress in expanding and improving our Monte Carlo simulation software. Simple models to approximate the effects of space-charge and channel wall charging on the MCP sensitivity were added to the existing simulation programs. These effects led to MCP saturation at high electron numbers (Wiza, 1979). Comparisons to MCP saturation data collected at LO for both static and pulsed voltage biases show excellent agreement. We have also used the code to simulate the time-dependent MCP sensitivity to a voltage pulse, called a gate profile. Agreement between simulated and measured gate profiles is excellent. Simulations of interaction between the MCP output electrons and an imaging phosphor have been performed, and the resulting spatial resolution investigated as a function of phosphor bias. Agreement between the simulated and measured spatial resolution is very good.

We consider what we have accomplished to have significantly improved on our work of last year and on similar work performed in the past. This year, we have presented our results at two conferences, the American Physical Society Division of Plasma Physics meeting in Denver, Colorado, in October 2005; and the High Temperature Plasma Diagnostics Conference in Williamsburg, Virginia, in May 2006. Significant interest in this research was evident at both conferences, and scientists at SNL, LLNL, and LANL have shown a special interest in our simulations. In the very near future, the codes promise to find use in programmatic work at SNL and possibly at LLNL.

References

Guest, A. J., "A computer model of channel multiplier plate performance," *Acta Elec.* **14**, 1 (1971) 79.

Ito, M., H. Kume, K. Oba, "Computer analysis of the timing properties in micro-channel plate photomultiplier tubes," *IEEE Trans. Nucl. Sci.* **NS-31**, 1 (February 1984) 408.

Wiza, J. L., "Microchannel plate detectors," *Nucl. Instrum. Methods* **162** (1979) 587.

Wu, M., C. Kruschwitz, D. Morgan, J. Morgan, "Monte Carlo Simulation of High-Speed Gated X-ray Detectors," *Nevada Test Site–Directed Research, Development, and Demonstration,* FY 2005, Bechtel Nevada/National Security Technologies, LLC, Las Vegas, Nevada, 2006, 113–119.

Multiscale Entropy Extraction of Weak Signals

Kevin R. Kyle[1]
Special Technologies Laboratory

This project applied information theory entropy analysis to extract weak signals from high-noise-level backgrounds. Specifically, our team chose multiscale entropy (MSE), a technique that examines the system's information entropy over multiple timescales. MSE analysis was applied to two types of data sets: spectral data of varying signal-to-noise levels, and magnetic field measurements in the presence of varying electrical fields and radiation sources. We hoped to discover a means of identifying the signal's spectral or time-variant components based on its MSE signature. Analysis of Fourier transform infrared spectroscopy (FTIR) interferograms demonstrated the utility of MSE in identifying small signatures from both data-rich and data-poor regions of the complex time-variant signal.

Background

Time-variant data from real-time sensor systems is often represented by weak but real signals superimposed on a background signal. In well-behaved systems, the signal of interest is more intense than the background fluctuations and can be readily discerned. Weaker signals may be obscured by background noise, both random (white) and systematic, and by very large DC backgrounds. This project explored the application of information entropy analysis as a means of discriminating real signals from background.

A method of measuring the complexity of finite-length time series (Shannon, 1948), information entropy analysis finds application as a tool in both physical and physiological systems. Entropy analysis in physical systems is used to reveal differences between noise (white and 1/f noise) and weak signals based on changes in the signal complexity between baseline (noise only) and nonbaseline (noise and signal). Due to the complex nature of the noise signal, weak signals lost in seemingly random, uncorrelated background signals are not readily apparent in the time series of a signal intensity measurement. A variety of entropy analysis methods exist for computing the complexity of a time series sample. Many standard methods, such as Fourier entropy and approximate entropy, gauge the regularity, or predictability, of a series on a single timescale. However, this measurement does not distinguish between regularity and complexity, and may in fact report a system entropy that is reduced relative to background, due to the introduction of a regular or periodic component. A means of describing time localization of the signal components would eliminate this effect.

[1] kylekr@nv.doe.gov, 805-681-2283

MSE is a new method that examines system entropy over multiple time scales (Costa, 2002; "Multiscale entropy analysis of biological signals," 2005; "Multiscale Entropy Analysis [MSE]," 2005). It is a type of wavelet transform, in which the time and frequency of a particular component are represented as the probability of a component occurring in a discrete time domain. Using MSE, completely ordered and completely random signals are shown not to contribute to time series complexity. Real signals on the background are registered as correlated signals across multiple time scales, which contribute to system complexity more than random noise. MSE has been successfully used as a diagnostic tool in distinguishing healthy, congestive, and atrial fibrillation heart subjects (Costa, 2003). Our project focused on applying entropy analysis, emphasizing MSE, to the problem of measuring weak time-fluctuating signals on top of a much larger (potentially orders of magnitude) background signal.

Project

We explored the application of MSE to two disparate problems: 1) identifying known components of a chemical spectrum, such as Raman or infrared, with the intent to use MSE to fingerprint chemicals in low signal-to-noise spectra, based on their MSE signature; 2) using the detection of charge generation and movement from the induced weak magnetic field resulting from said charge movement. The application of such magnetic field measurements would include the detection of active electronic systems (e.g., capacitive charging and discharging) within enclosures, as well as stochastic charged-particle sources, such as radioactive materials.

Our team obtained MSE software online at the program author's Web site (Costa, "MSE.C," 2005). This freeware download included the C MSE source code for UNIX and the source code for subroutine SampleEN (Lake, 2005). The code was compiled using a Digital Mars C++ compiler for Windows. The resulting object code was compatible with Windows using the Command prompt. A graphical version of MSE was programmed using IGOR Pro (WaveMetrics). MSE analysis yielded a plot of component probability over multiple time scales, where 0 is the point-by-point time scale, and n is the time scale summed over n + 1 points.

Test data sets consisted of simple periodic functions and linear combinations of functions. MSE was performed over 20 time scales. The base functions and resulting MSE signatures appear in Figure 1. A constant function does not contribute to the MSE analysis, having no complexity over all time scales. The magnitude of the constant does not affect MSE analysis. A periodic function, such as the sine wave in Figure 1, gives a distinct MSE signature in terms of the probability of a component contributing to the signal over a discrete time scale. The sine wave in linear combination with a large DC offset results in the MSE signature of the sine wave. The sine wave MSE signature is also unaffected by the sine function phase, e.g., MSE(sin(x)) = MSE(cos(x)). These early data illustrated the promise of MSE as a signal analysis tool.

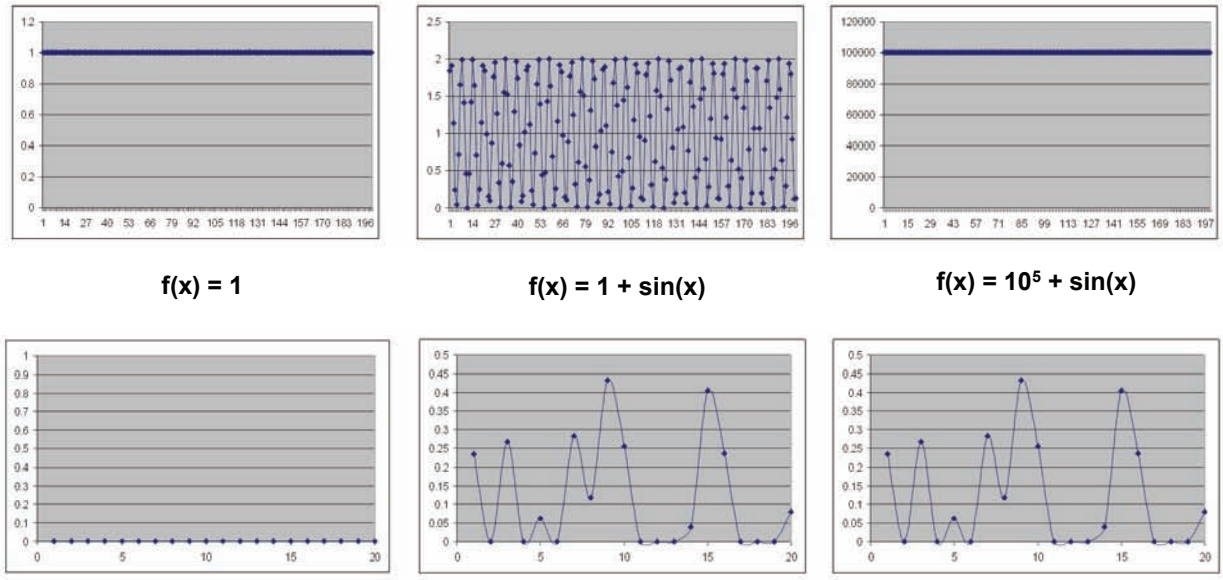

Figure 1. MSE analysis of simple functions (top). MSE signature (bottom) is unaffected by a large DC background.

Spectral data sets consisted of dispersive Raman spectra of varying concentrations: $UO_2(NO_3)_2$ in alkaline $NaNO_3$, and FTIR spectra of varying concentrations of Freon in air. The data were analyzed both as spectra (frequency domain) and interferograms (time domain). Percent of sample component was calculated as a linear combination of the background and the pure sample. We utilized MSE plots of spectra representing noise (0% sample component) and "pure" sample (100% sample component) in the analysis of unknowns. We expected that MSE would be more applicable to the time domain data, where correlations across time scales exist for single spectral components. Unlike the test function, the MSE of Raman spectral data were complex, exhibiting a variant background signature in both magnitude and background features. In the case of an unstable background, MSE plots were equally variant in component probability over the multiple time scales and could not be used to estimate the contribution of target sample to the Raman spectra.

The FTIR spectra of Freon provided test data with a stable background (Figure 2a). Instrumental noise was constant from spectrum to spectrum, while background signals due to water vapor and carbon dioxide varied only in intensity. Freon concentrations were measured as a percentage relative to starting concentration.

MSE analysis of the spectra themselves yielded wide variability of component probabilities (Figure 2b). This would be the result of substituting an energy scale for a time scale when computing the multiple time scales. The IR spectra signals would be expected to show little correlation over multiple energy scales.

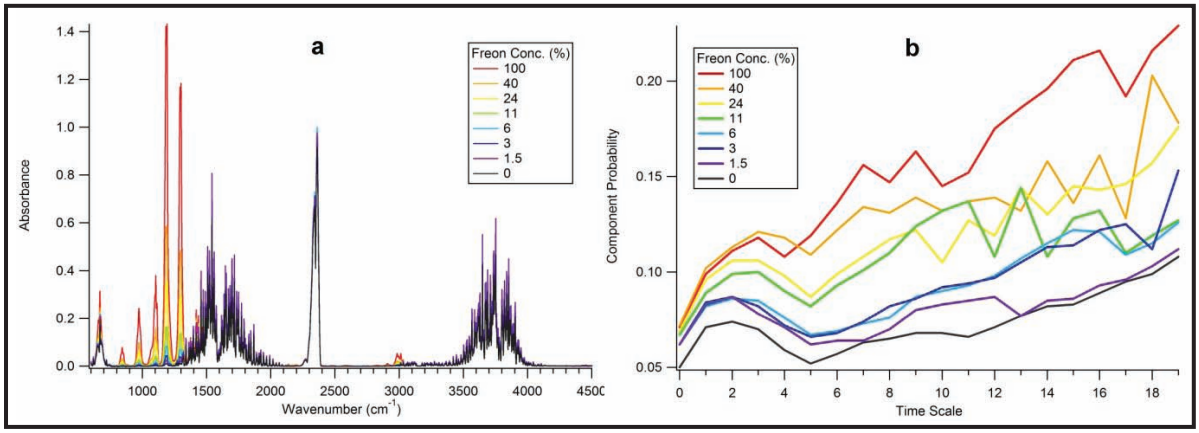

Figure 2. (a) FTIR spectrum of varying concentrations of Freon in air and (b) the corresponding MSE analysis

We also performed MSE analysis on the raw interferograms generated at each Freon concentration. While the independent variable in the interferogram is a displacement distance of a mirror, it is directly proportional to time and will be henceforth referred to as a time scale. Two regions of interest were analyzed (Figure 3a). The region of intense signal comprises primarily Freon data superimposed on spectral background signal and noise. The low-intensity region comprises mainly instrumental noise. The expansion of the data-rich region shown in Figure 3b illustrates the time-dependent nature of the Freon interferograms, wherein the small variations in amplitude due to Freon are added as subtle features to the background signal.

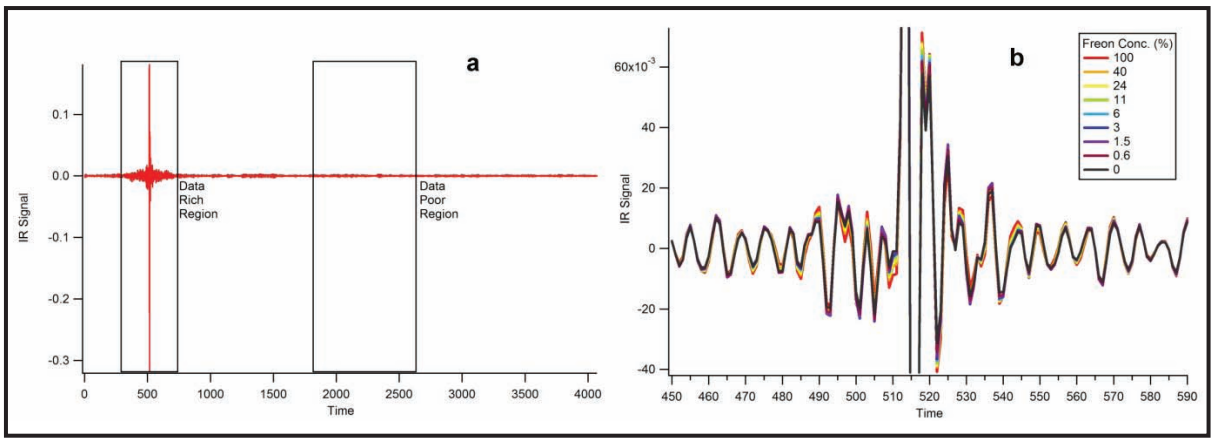

Figure 3. (a) Infrared interferogram of Freon at various concentrations; (b) expanded view, illustrating the time-dependent nature of the Freon signal

The MSE analysis of the data-rich (spectral) region (Figure 4a) of the interferogram reveals the contribution of the Freon component to the time-varying signal. The greatest contribution is to time scales less than six. There is, however, no observed Freon component in time scales between 13 and 16 elements in length. The MSE analysis of the data-poor region reveals very little contribution of Freon over any time scale (Figure 4b). Curve-fitting of a function composed of a linear combination of the 100% and 0% Freon MSE curves yields the plot shown in Figure 5 for the 11% Freon data-rich region. By this fit, the calculated Freon concentration is 10%. Other plots were fit with similarly good correlation to actual Freon concentrations. This analysis method assumes an a priori knowledge of the contribution of background and sample to component probabilities. These data demonstrate the viability of the application of MSE to spectral data sets represented by small, time-variant signals on a more intense background.

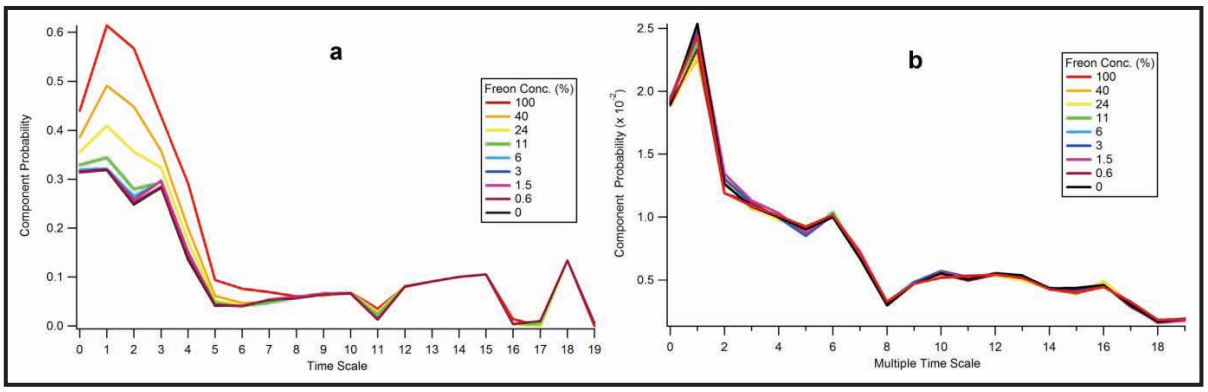

Figure 4. MSE analysis of Freon interferograms in the (a) data-rich and (b) data-poor regions of the interferogram defined in Figure 3

We collected time-variant magnetic field data from several electronic circuit and radiation sources. Our goal was the potential identification and discrimination of each magnetic field source based on its MSE analysis signature. Detection was performed using a GEM Systems GSM-19 Overhauser Magnetometer operated in Base Station mode. We chose this magnetometer for its broad signal dynamic range with very high sensitivity. Due to metallic objects within the Earth's magnetic field, typical signals range from 10,000 to 100,000 nT. In Santa Barbara, California, the Earth's observed magnetic field was 40,000 nT. Because of the magnetometer's high sensitivity (0.01 nT), we anticipated detection of very small signal fluctuations on the high background signal. However, background noise, which comprised ~10% of total signal, obscured any fine detail that might be present and thereby obfuscated any time-variant signatures that might indicate processes within the circuit. As a result, we did not apply MSE analysis to these signals. However, overall changes in the magnetometer readings could still be used to detect energized circuitry (Figure 6a). We observed a difference

of several thousand nT between quiescent and active AC and DC circuit modules from 3 ft away. Magnetic field fluctuations arising from simple AC and DC circuits within metallic enclosures could also be measured (Figure 6b).

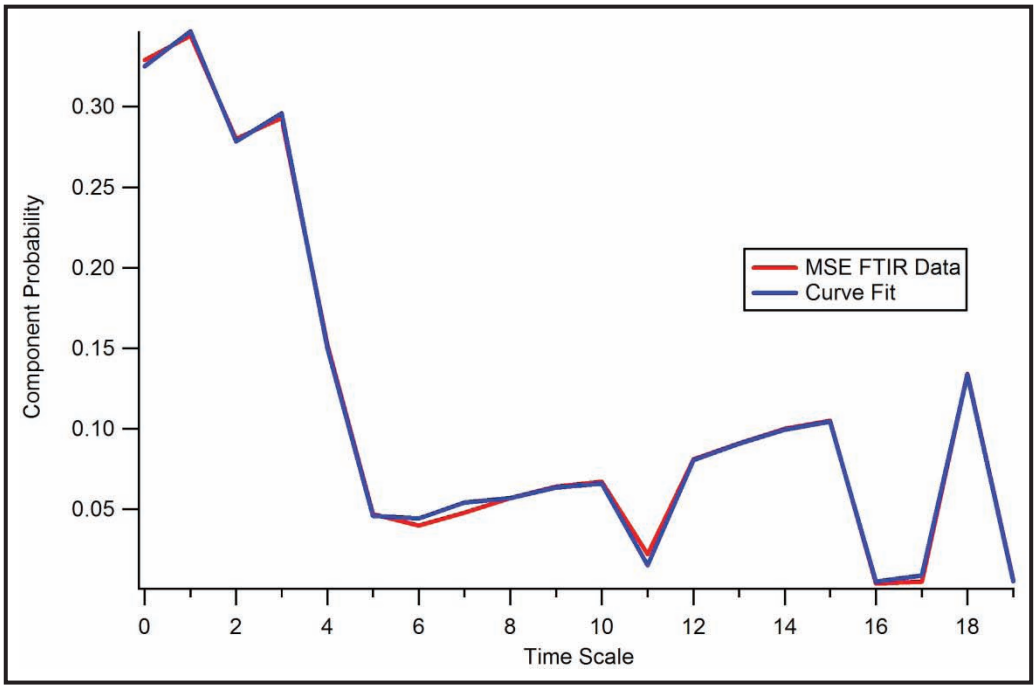

Figure 5. Curve fit of linear combination of 0 and 100% Freon MSE functions to the 11% Freon MSE curve

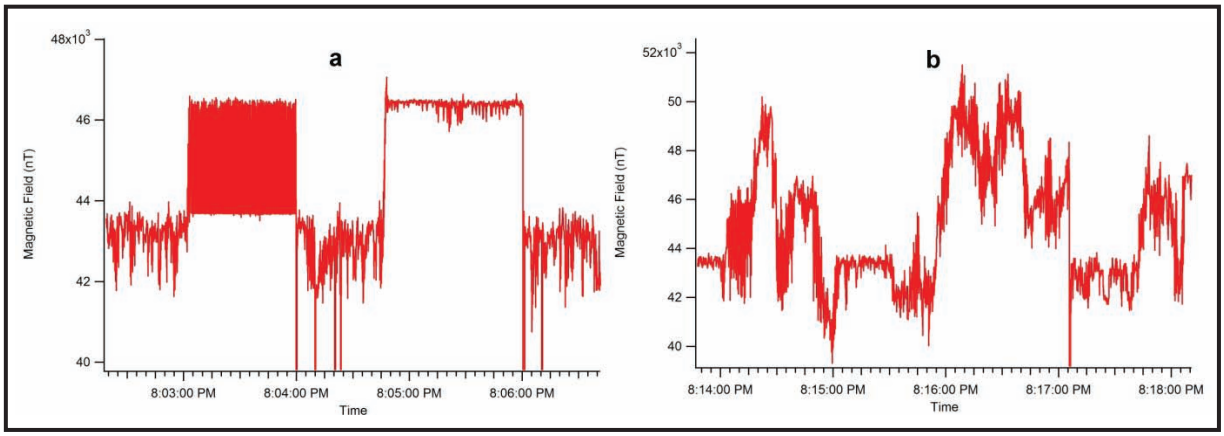

Figure 6. Detection of unshielded (a) and shielded (b) AC and DC circuitry by Overhauser magnetometry

Conclusion

Time-variant spectral systems can be treated as a signal stream, subject to the rules of information theory. As such, the definitions and analytical techniques of information theory are applicable. The application of MSE analysis to a series of spectral data sets yielded signatures for spectral signal, noise, and background. MSE signatures were shown to scale linearly with component concentrations when the MSE curves for full-scale signal and background were known. Follow-on study should detail the effect of multicomponent systems and application to more complex, multidimensional systems, such as video images.

References

Costa, M., "MSE.C," http://www.physionet.org/physiotools/mse/mse.c, accessed October 26, 2005.

Costa, M., A. L. Goldberger, C.-K. Peng, "Multiscale entropy analysis of biological signals," *Phys. Rev. E* **71** (2005) 021906.

Costa, M., A. L. Goldberger, C.-K. Peng, "Multiscale entropy analysis of complex physiological time series," *Phys. Rev. Lett.* **89**, 6 (July 2002) 068102.

Costa, M., A. L. Goldberger, C.-K. Peng, "Multiscale Entropy Analysis (MSE)," http://www.physionet.org/physiotools/mse/tutorial/, (2005), accessed October 26, 2005.

Costa M., J. A. Healey, "Multiscale entropy analysis of complex heart rate dynamics: discrimination of age and heart failure effects," *Computers in Cardiology* **30** (September 2003) 705–708.

Lake, D. K., "Sampen.C," http://www.physionet.org/physiotools/sampen/c/, accessed October 26, 2005.

Shannon, C. E., "A Mathematical Theory of Communication," *Bell System Technical Journal* **27** (July and October 1948) 379–423, 623–656.

this page intentionally left blank

Dense Plasma Focus Computer Modeling

B. T. Meehan,[1] *E. Chris Hagen*
North Las Vegas

If computer models can be shown to approximate the experimental performance of our dense plasma focus (DPF) machine, plasma dynamics models can be used to aid in the design of newer, higher performing plasma focus machines for various customer needs. This will effect a large time savings, rapidly increase our understanding of DPF operation details, and aid in both improving the performance of our DPFs and our ability to tailor their performance to customers' individual requirements. In short, we will be able to generate better sources, faster, at lower cost. Sophisticated plasma physics computer codes exist and can be obtained inexpensively. These codes are powerful and general, and can be adapted to model the plasma dynamics of a DPF. They are not suitable for modeling the dynamics within the Z-pinch itself, but are capable of modeling the plasma initiation, rundown, and compression phases, since they employ the magnetohydrodynamic (MHD) approximation. The plasma modeling codes fit into a larger framework of computer modeling that can be used to predict neutron yield and device performance for various DPF designs that will end up producing smaller and safer experiments. This project tested a specific plasma modeling code, MACH2.

Background

In anode and cathode design research, experimenters will typically have many ideas about how to improve DPF performance factors. These factors could be total neutron yield, neutron and x-ray yield, pulse width, etc. However, given their limited R&D funds, the number of trial anode-cathode arrangements that researchers can engineer and fabricate is very limited by both time and cost. A computer code that could help evaluate the performance of various designs prior to fabrication would increase the probability of a successful trial performance enhancement for the DPF.

Plasma modeling codes are typically MHD codes, meaning that the code operates on some simplifying assumptions about the plasma it is to model. Strictly speaking, this means that the plasma itself is considered to be a conductive fluid. In MACH2, the fluid is then governed by a set of differential equations from both electromagnetic and fluid dynamics theories. MACH2 tracks the state of the fill gas in the DPF by a tabular equation of state routine called SESAME, which is produced and maintained separately by LANL.

[1] meehanbt@nv.doe.gov, 702-295-0490

MACH2 makes the simplifying assumption that the conductive fluid possesses either rectangular or cylindrical symmetry. This greatly accelerates calculations but makes it impossible to model effects in the DPF that are not cylindrically symmetrical. This makes the code ineffective for studying how the cathode bars affect the plasma flow, as well as unbalanced initiation of the plasma shockwave. Because of the above considerations, MACH2 DPF models exhibit many characteristics of live DPF data but cannot hope to model the DPF in microscopic detail, since the MHD assumption is invalid during late phases of the DPF operating sequence.

MACH2 can be used to assist in designing anode-cathode arrangements that may have better performance than traditional Mather or Filippov designs. MACH2 has also been able to give the DPF team insight into some scorching and crimping phenomena observed in existing experimental arrangements, and has shown data for current and rundown time that agree with experimental observations.

Project

Seed Model

MACH2 was originally developed by the Air Force Research Laboratory (AFRL) and may not be distributed without its permission. Permission was obtained from the AFRL for its use. To help develop a simple working model of the DPF, we contracted with NumerEx to provide a seed model and training for one user. NumerEx also provided a modernized version of MACH2 Linux binary that was a great improvement over the AFRL distribution version. The seed model will offer a very good starting point for the DPF team's modeling efforts. MACH2 will serve as a design tool for future DPF designs. Some of the initial modeling successes are detailed below.

Test Calculations

Crimped Anode Base

MACH2 has helped us develop some possible explanations for DPF-related phenomena, such as a crimped copper anode base that was discovered after a series of shots with an anode that had thinner than usual copper walls. Following the shot series, the anode had a slight ring crimped in the walls at its base. Since it was inspected prior to installation, the crimping must have happened during the shot series. A photograph of a thick-walled, noncrimped anode next to the crimped anode appears in Figure 1. The thick-walled anode is on the right; the thin-walled anode is on the left. The crimp is visible between the anodes, just above where the brass baseplate screws into the thin copper jacket.

The pressure must have been electromagnetic in origin, most likely due to magnetic pressure. MACH2 allowed us to visualize the magnetic field during the rundown and pinch phase. The magnetic pressure model is shown in Figure 2, and was taken from a data set that models an anode

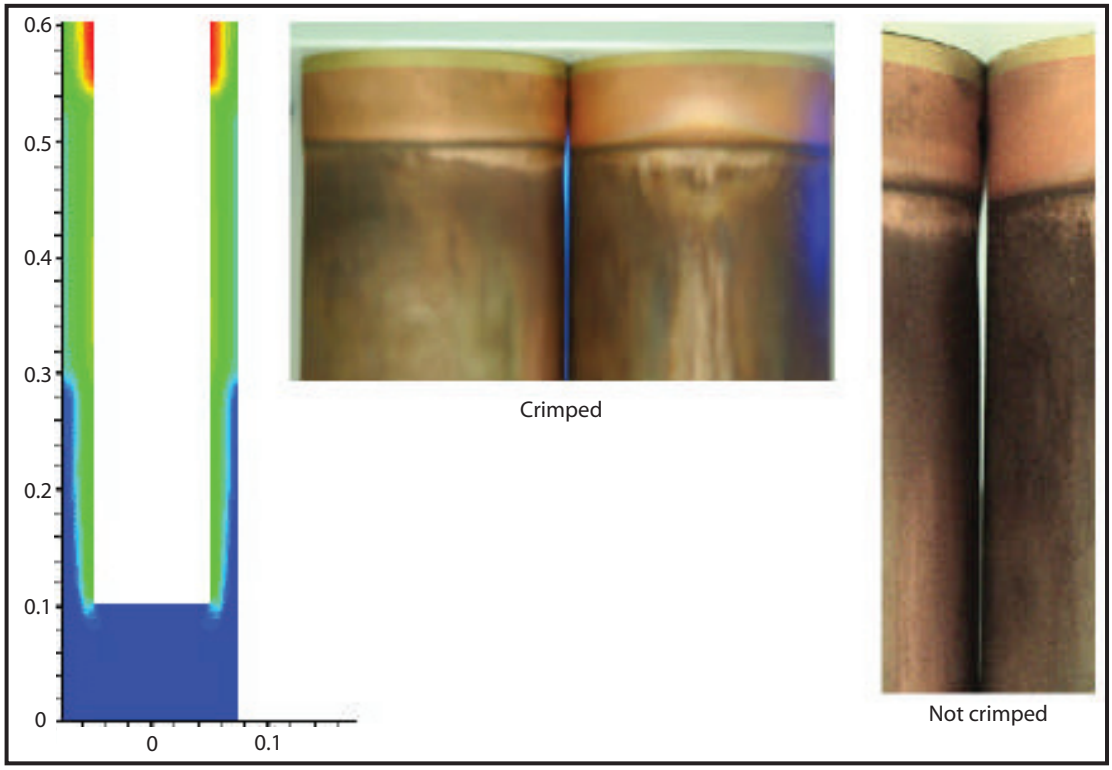

Figure 1. Crimped anode base and magnetic pressure calculation

similar to the crimped anode. The contours in the magnetic pressure model shown in the figure are the squared magnitude of the magnetic field, which is proportional to the magnetic pressure (Holt, 1965).

$$P_{magnetic} = \frac{B^2}{2\mu_0} \quad (1)$$

MACH2 calculates the maximum field to be in the region just below the insulator on the anode, in the vicinity of the experimentally observed crimp.

Dying Sinusoid Current Graphs

MACH2 can track the current and voltage supplied to the plasma focus device it is simulating. As the simulation is currently set up, the pinch does not show up in the current trace, and the current that MACH2 calculates is significantly higher than that measured by our Rogowski and Faraday rotator current detectors. The discrepancies in the current trace are likely due to the simplified nature of the

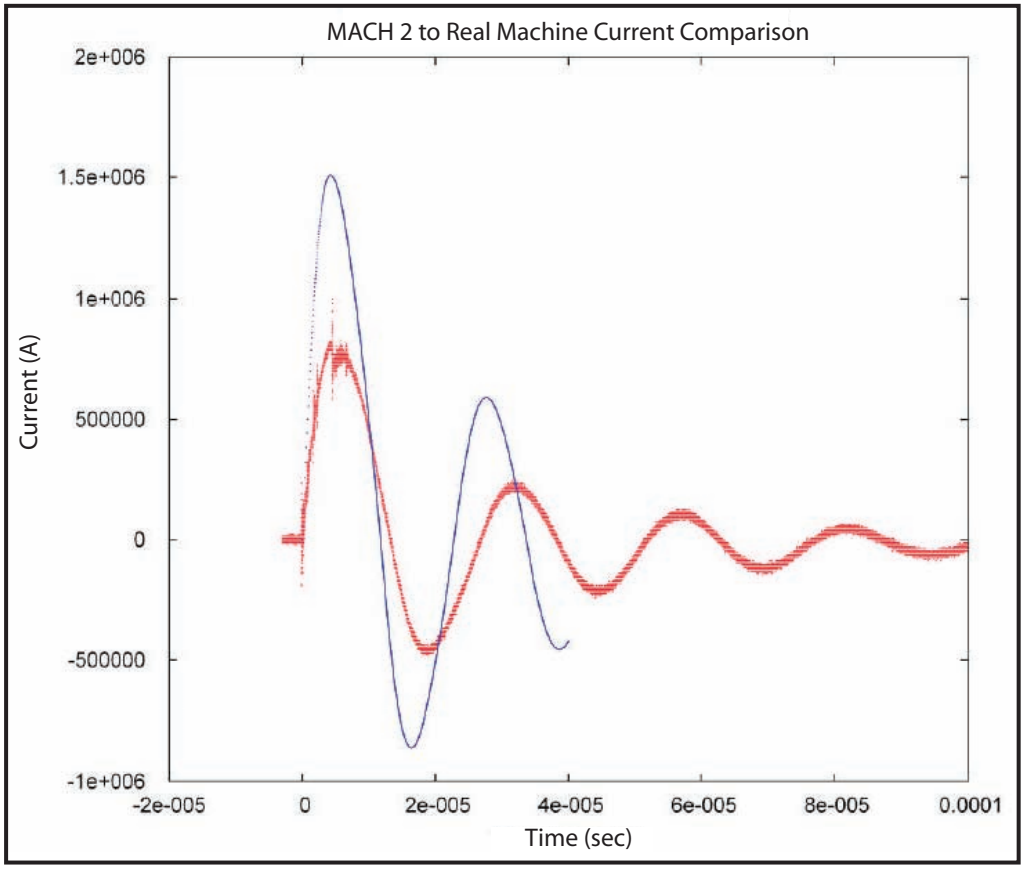

Figure 2. MACH2–calculated current shown with actual DPF current (red)

MACH2 model that the current traces were taken from. The MACH2 model now being used does not take into account the shunt current–damping resistors across the source. Future efforts in refining and improving the DPF model will likely address this, but it is not a simple fix. The MACH2 code offers the ability to specify a series L-R-C driver circuit, and the circuit that drives the DPF is somewhat more complicated. A new FORTRAN routine would have to be written to handle the circuit dynamics of the actual driver circuit.

Hole Burning in Top of Anode

The Z-pinch phenomenon occurs on the axis of the cylindrical DPF anode. This hole burned in the anode was always known to be due to the Z-pinch on the anode axis (Figure 3). The MACH2 model does indeed show the plasma burning the top of the anode, but it shows this burn continuing several hundred nanoseconds after the pinch. Knowing that the hole-burning takes place after the Z-pinch

is completely finished can help the DPF analysis team design experiments that only see the radiation from the pinch, without being polluted by bremsstrahlung from the pinch electrons crashing into the anode.

Also visible in the simulated anode in Figure 3 is the plasma's tendency to attach to sharp surfaces at the bottom of the anode just before the pinch occurs. The plasma attaching to the sharp surfaces causes the shockwave to distort and forces the pinch to occur further below the anode than would occur if the plasma were following a much more rounded anode shape. This also causes the shape of the pinch region to be elongated. It is not currently known if this causes the neutron yield to increase, but this concept will be investigated in future experiments.

Figure 3. Hole burning in anode top

Rundown Time Comparison

As the plasma sheath is magnetically propelled down the anode, this "magnetic piston" pushes more and more gas in front of it. The speed of the gas piston is a function of the magnetic driving force (plasma current and magnetic field) as well as a function of the increasing mass being accelerated. We measured rundown times for a large range of pressures, and from MACH2 have a set of calculated rundown times. The graph in Figure 4 shows the results of the MACH2 calculation compared to observations. There is qualitative similarity, but the rundown time that MACH2 calculates is different from that which is observed. The discrepancy is attributed to the effect of insulator length on rundown time, which would be how the "inverse pinch" phase of the rundown affects plasma shockwave formation during the rundown phase. The discrepancy is being investigated. Figure 4 depicts a data set that showed an unusually good agreement with the MACH2 model.

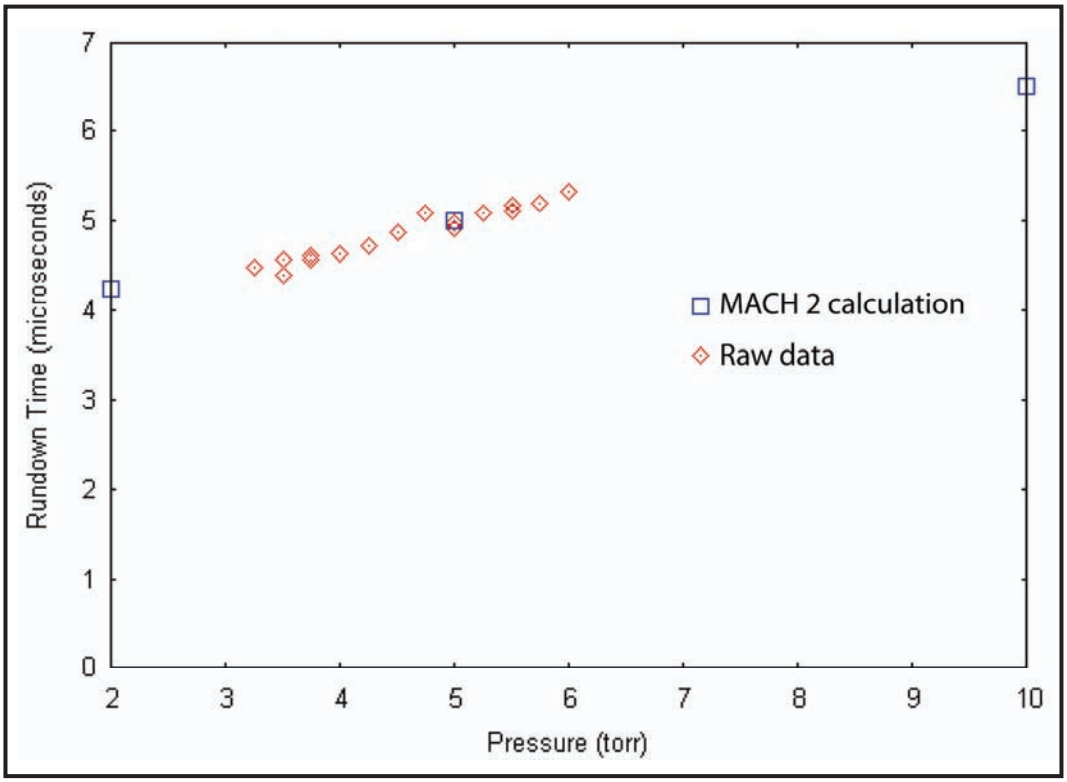

Figure 4. Actual and calculated rundown times

Streak Image Comparison with MACH2

The Novel Fiber Geometry Project, (Berninger, 2007) used a streak camera to record images from a fiber-optic array to image the plasma at the end of the anode at the moments surrounding the Z-pinch. The images are taken perpendicular to the axis of the plasma focus, and look straight through the plasma shock at the moment of the Z-pinch. To help interpret the streak images, the plasma density was integrated through the radial coordinate for several time steps of the MACH2 data to attempt to calculate a similar image to compare to the Novel Fiber Geometry data. In the image in Figure 5, the MACH2 image shows the hot ball of plasma leaving the top of the anode following the pinch. This is compared to the Novel Fiber Geometry image to the right, which shows different dynamics for the hot plasma ball leaving the top of the anode, and illustrates several structures that are not found in the MACH2 data. We hope that analyzing this data will help improve the MACH2 model and increase our understanding of Novel Fiber Geometry project data.

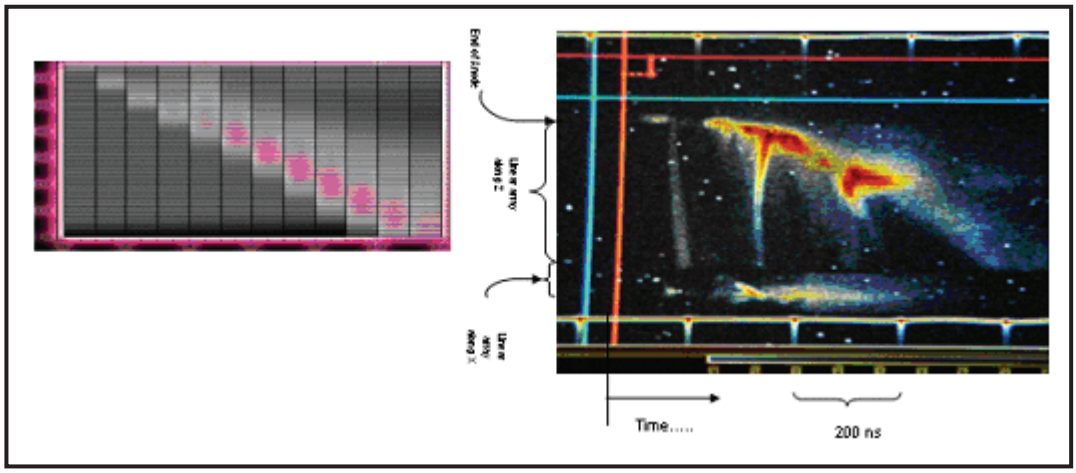

Figure 5. Streak camera images of pinch with MACH2 calculation of same. The anode is the top of the picture, and Time flows to the right

Plasma Sheath Shape During Rundown

The $\vec{j} \times \vec{B}$ force that propels the sheath down the anode is obviously a function of the magnitude of the magnetic field strength, B, and the magnitude and direction of the current density, j. Both these vector components are changing as the sheath accelerates and gathers more gas, and as the anode current changes. We have used a fast framing camera to observe the sheath in flight. The two renderings in Figure 6 show that the shape of the sheath at the end of the rundown phase was well predicted.

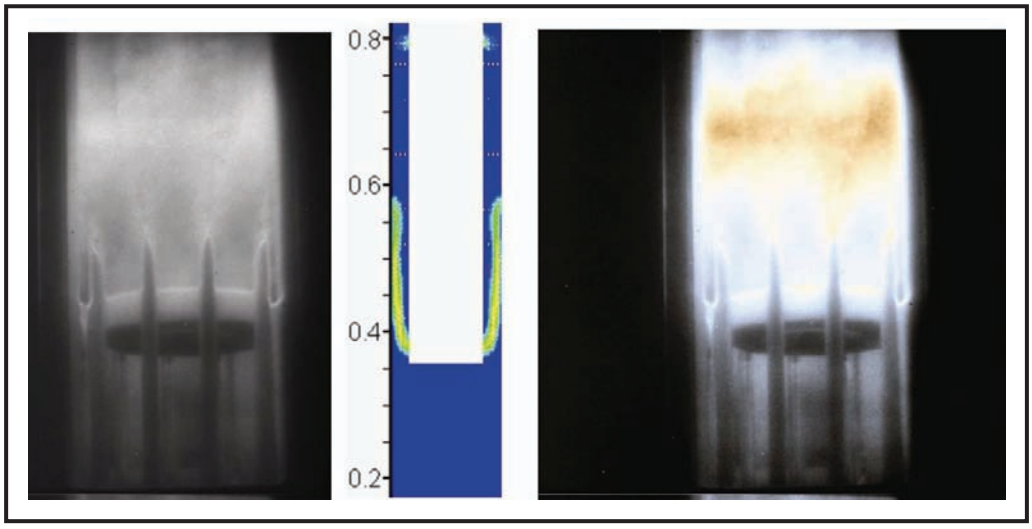

Figure 6. Framing camera data (left), MACH2 model (center), and enhanced version of the framing camera data (right)

Conclusion

Prior to the availability of MACH2, the effects of changes to the DPF had to be inferred from the physical artifacts present on the anode and cathode, as well as interpreted from recorded machine diagnostics. Often, several configurations had to be tested in sequence to prove or disprove a design hypothesis. Already, MACH2 models have helped us explain several observable effects in the DPF.

As can be seen from the above comparisons between experiment and calculation, even at this early stage, good qualitative agreement exists in many cases. In other cases, model refinement is necessary. More evidence must be compiled with shadowgraphs, streak camera, and framing camera data.

Finally, MHD–based, two-dimensional codes, such as MACH2, are inherently limited by the simplifying assumptions used in their programming. We may need to use other programs or call on other organizations to help us generate predictions and models. In the future, it will be necessary to determine when the MHD model's behavior begins to differ significantly from the reality of the behavior that may occur inside the DPF. Knowing when the MHD model begins to break down helps us understand where the computer model can be trusted and where it begins to perform unrealistically. The DPF team will continue to search for methods of achieving a theoretical Z-pinch model and for other areas in which our present MHD codes may be of use.

Acknowledgments

We would like to thank Michael Frese and Sherry Frese, of NumerEx, for many helpful suggestions that led to the smooth and rapid installation of MACH2, and for applying it to our specific application, the DPF. Thanks are also due to the entire DPF team as they assembled the data sets used for the validation work and provided much insight and critical thought to help this project succeed.

References

Berninger, M., "Novel Fiber Array Diagnostic Geometry," *Nevada Test Site–Directed Research, Development, and Demonstration,* FY 2006, National Security Technologies, LLC, Las Vegas, Nevada, 2007, 295–301.

Holt, E. H., R. E. Haskell, *Foundations of Plasma Physics*, New York: Macmillan, 1965, 433.

Streak Tube Performance Limits

J. M. Richter[1]
Livermore Operations

The new transmission-line deflection structures in the streak tubes manufactured at LO will enable sweeps in the subnanosecond range. The higher photoelectron currents needed to maintain image brightness at these speeds may result in space-charge effects such as defocusing and current limiting. Electron trajectory modeling with the Charged Particle Optics boundary element code CPO-3D was conducted to determine the performance limits of the optical streak tube and to explore possible tube improvements. Difficulties in analyzing the modeling output prevented generation of design drawings showing proposed tube changes; however, several pre- and post-processing routines developed in the course of this work will facilitate future modeling efforts.

Background

The optical streak tube manufactured at LO is shown in Figure 1, and an axial view of the accelerator slot, anode aperture, and deflection plates is given in Figure 2. The streak tube is an electrostatic inverting image tube with ~1X magnification. A narrow slot in the accelerator electrode limits the active imaging area to a 1 × 50-mm slit. The long axis of this image contains the time-varying spatial information that is swept across the output screen by voltage ramps applied to the deflection plates. A common-mode deflection bias compresses the slit image in the sweep direction by a factor of two to three, which increases the temporal resolution. A reverse bias between the cathode and accelerator prevents any photoelectron flow until a gate pulse is applied.

The G-1 electrode in Figure 1 is usually shunted to the accelerator. The entire tail end of the tube, from the anode cone to the screen, is typically at ground potential. The deflection plates are isolated from the anode so that separate deflection potentials can be applied via the feedthroughs.

Both optical and x-ray versions of this tube have been designed and manufactured. Although the advent of transmission-line deflection structures (Shellman, 2006) enables sweeps in the subnanosecond range, the higher photoelectron currents needed to maintain image brightness at these speeds may result in space-charge effects such as defocusing and current limiting. A more dramatic effect that has been observed at high currents is spatial pinching of the swept image. This is probably caused by space-charge effects at the deflection plates where the peak current density occurs due to electrons crossing the tube axis. These effects have never been modeled to determine the threshold current levels at which the effects become problematic.

[1] richtejm@nv.doe.gov, 925-960-2511

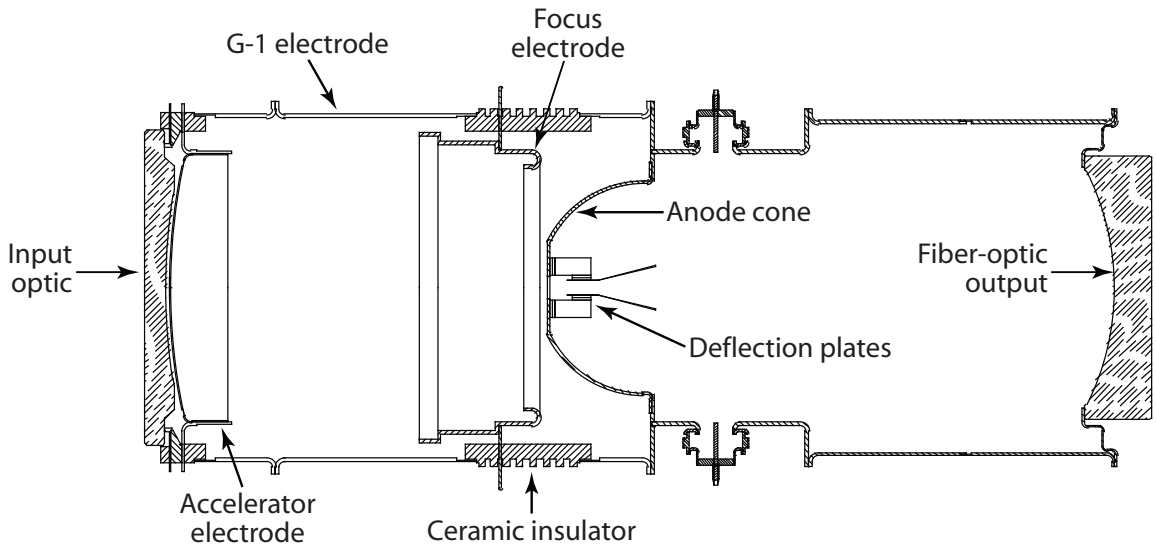

Figure 1. Cross section of the optical streak tube showing the component parts. The photocathode is deposited on the inside surface of the input optic. The phosphor screen is deposited on the inside surface of the output optic.

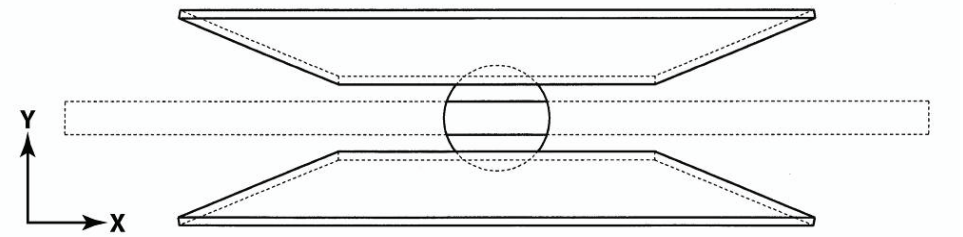

Figure 2. Axial view of the flared deflection plates, anode aperture, and accelerator slot viewed from the screen toward the cathode. The slot dimension is 2 × 50 mm, aperture diameter is 6 mm, and minimum deflection spacing is 4 mm.

Project

Two different electron trajectory codes used in a previous SDRD project (Richter, 2006) were available for this project: the Field Precision finite element codes (Field Precision, 2006) and the CPO

boundary element codes (CPO, 2006). The Field Precision codes support both electric and magnetic fields with space charge. The CPO codes have limited support for magnetic fields but were chosen for this project because they are easier to use.

An existing CPO-3D quarter model of the optical streak tube with symmetry on the two radial axes was used to study electron trajectories with common-mode bias potentials on the deflection plates. A half model with symmetry along the spatial axis (perpendicular to the sweep axis) was generated later for deflection studies. The deflection sensitivity obtained with the half model agreed with measured values from streak tube characterization tests.

At my request, the vendor updated CPO-3D to provide all of the trajectory intercept data needed to fully automate the analysis of focal quality at the output screen. The updated code now identifies the intercept data for each ray at each test plane and electrode in a concise format that is convenient for input to a post-processor.

Interactive Data Language (IDL) (IDL, 2006) preprocessor and postprocessor routines were developed to generate ray launch parameters for CPO-3D, and to read, analyze, and plot the trajectory output data. The IDL program STRAY generates launch parameters for any number of rays launched from any cathode with a circular profile. Any number of launch positions or emission angles may be specified along the transverse X and Y axes.

The IDL program ReadCPO extracts trajectory data from a CPO output file with any number of rays, launch points, and test planes. The program calculates the mean position, energy, travel time, magnification, focal spot size, eccentricity, and focus condition for each ray launch group at each test plane or electrode intercept. Ideally, all of the rays from a given launch point should come to a point focus at the screen. By examining the velocity components of the outermost rays of each launch group at each test plane, it can be determined whether the test plane is before or after best focus, i.e., whether the rays are converging or diverging. These calculated results, together with the original trajectory data, the ray launch positions, and the operating potentials, are saved in an IDL data file and a print file. This program can be readily modified to handle the output generated by the Field Precision trajectory codes.

The IDL data file from ReadCPO can generate multiframe focal spot plots and to perform additional analyses. IDL iTool object graphics are used to generate a gridded array of plots depicting the ray intercepts at the screen for each selected launch point. A reference circle can be displayed with each spot plot to gauge the focal quality. The object graphics can be easily manipulated via a point-and-click interface. New plots can be generated via IDL batch files that can be edited as needed to select the desired data and plot format.

The streak tube screen has a nominal active diameter of 62 mm that accommodates a 44-mm-square output image. Tube symmetry allowed evaluation of the focal properties in this region by examining only one quadrant of the output square. A CPO-3D model of the optical streak tube was generated

with six groups of nine 1-eV electrons emitted from six launch points, ranging from the tube axis to 20 mm off-axis at 4-mm intervals. Emission angles of 0° ±10° and ±20° from the cathode normal in both the spatial and temporal axes were used. Three separate runs with deflection potentials of 0, 600, and 1200 V yielded 18 focal spots at the screen. All three runs used the same operating potentials: 0, 720, 2150, and 20000 V for the photocathode, accelerator, focus, and anode-screen electrodes, respectively, with a retarding common-mode deflection bias of 400 V.

Figure 3 shows the trajectories for six groups of rays with 1200 V deflection on the temporal axis.

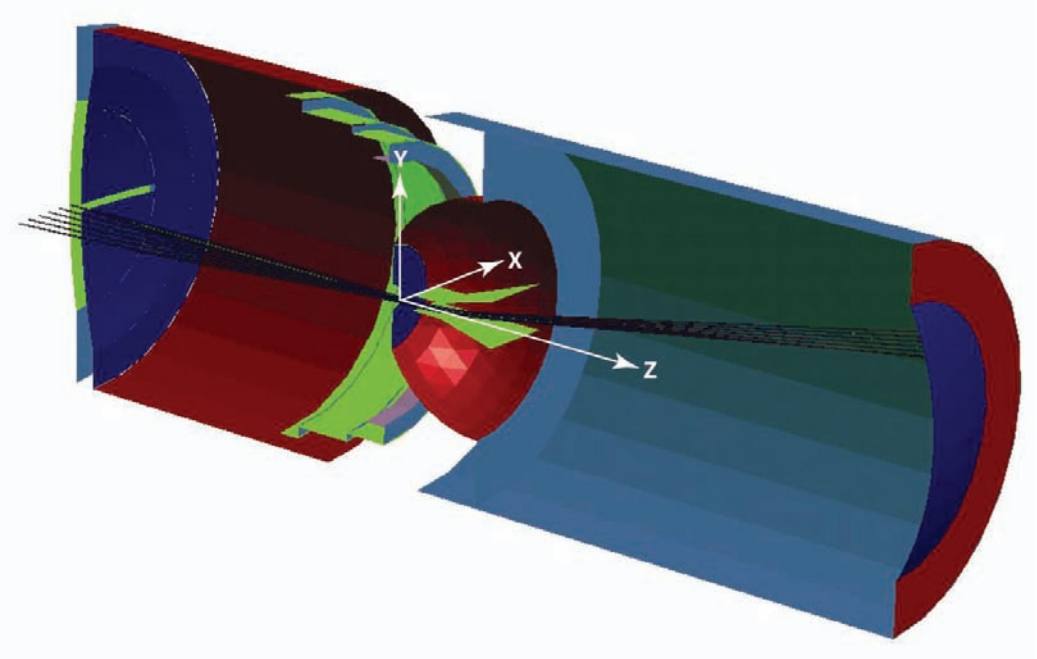

Figure 3. A CPO-3D optical streak tube model showing six sets of rays launched from the cathode (green) at 4-mm intervals ranging from 0 to 20 mm off axis. The slot in the accelerator (blue) is offset from the cathode by 4 mm. The anode aperture (blue) is 6 mm in diameter and the deflection plate spacing is 4 mm. The beams have been deflected upwards by 22.4 mm before reaching the screen (blue).

Figures 4 and 5 show the trajectories in Figure 3 projected onto the temporal and spatial planes, respectively. Figure 5 shows that the rays cross the tube axis in the flat region of the deflection plates. The axial crossover point is very near the center of curvature of the photocathode. The electron travel-time summary from ReadCPO shows that the off-axis rays take progressively longer to reach the screen than the axial rays, with a maximum differential of 0.1 ns. The mean travel times for the

18 ray groups in the deflection study ranged from 6.33 to 6.46 ns. This time difference of 0.13 ns would constitute a 13% distortion on a 1-ns sweep. The longer travel times for off-axis rays could be corrected by decreasing the screen radius of curvature appropriately.

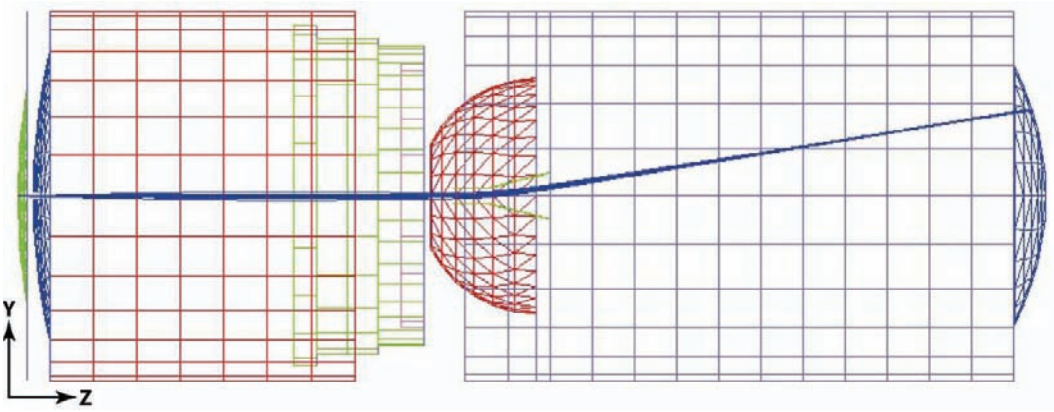

Figure 4. The trajectories in Figure 3 projected onto the Y–Z plane. This view shows 22.4-mm deflection along the temporal Y axis, with the green deflection plates shown in profile. The boundary cells for each electrode are depicted in the same colors as in Figure 3.

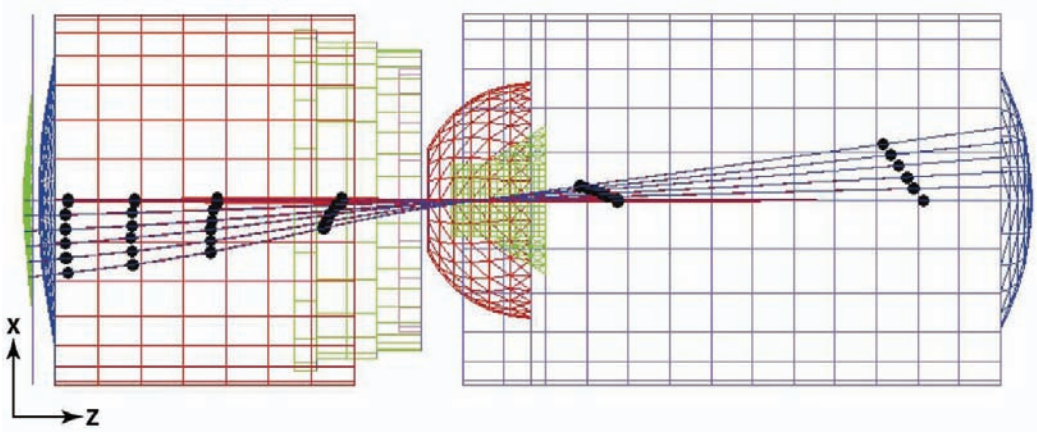

Figure 5. The trajectories in Figure 3 projected onto the X–Z plane. This view shows the six groups of rays along the spatial X axis, with the deflection plates depicted from above. The electron travel times along the ray paths are marked at 1-ns intervals.

Figure 6 shows the screen intercepts obtained from the three deflection runs described earlier for rays that were launched 4, 12, and 20 mm from the tube axis. This provides a snapshot of the focal properties for a swept image via a 3 × 3 array of focal plots. The launch parameters for each focal spot are noted in the plot title. Rays emitted into the spatial X and temporal Y planes are marked with squares and diamonds, respectively. In addition, rays with positive emission angles from the cathode normal are marked with a '+' sign. For most of the spot patterns in Figure 6, the rays with positive emission angles are to the left or below the central ray, which is marked with an asterisk. This indicates that the rays have crossed the best focal position before reaching the screen and are thus diverging at the screen. Based on operating experience with the LO streak tube, the large temporal spread in the top row could be reduced by decreasing the common-mode bias on the deflection plates, which would increase the focal length on the temporal axis. The overall focal results could also be improved by decreasing the screen radius of curvature.

Note that all of the focal spots in Figure 6 fall within the 100-μm reference circles. The best focus with less than 9 μm of spatial and temporal spread occurs for the 4-mm launch with 600-V deflection. The largest spread of 93 μm occurs on the temporal axis at maximum deflection. An analysis of the focal positions shows that the mean spatial magnification ranges from 0.981 with no deflection to 0.967 with 1200-V deflection, which amounts to 1.4% barrel distortion on the spatial axis. The temporal deflection decreases by roughly 0.4% with increasing spatial launch position, but the mean deflection ratio is only 1.97 for a voltage ratio of two, which constitutes a 1.5% deflection nonlinearity with 0.4% barrel distortion on the temporal axis.

Conclusion

The IDL processing tools developed during the course of this project are critical for the analysis of electron trajectories generated by CPO-3D. These IDL codes are readily adaptable for use with the Field Precision trajectory codes. The multiplot format, together with the imaging calculations from ReadCPO, facilitate the evaluation of image quality, resolution, distortion, and electron travel time as a function of electrode shape and operating potentials. These new tools, in conjunction with the CPO and Field Precision trajectory codes, provide a powerful mechanism for analyzing the performance of existing and future tube designs.

A CPO-3D model of the optical streak tube was generated to examine focal properties as a function of deflection over the full active area of the phosphor screen. The results indicated that the tube performance at high sweep speeds could be improved by reducing the radius of curvature of the screen electrode. Further work should be done to examine the space-charge effects that will likely become evident at the higher sweep speeds made possible by the new transmission-line deflection structures.

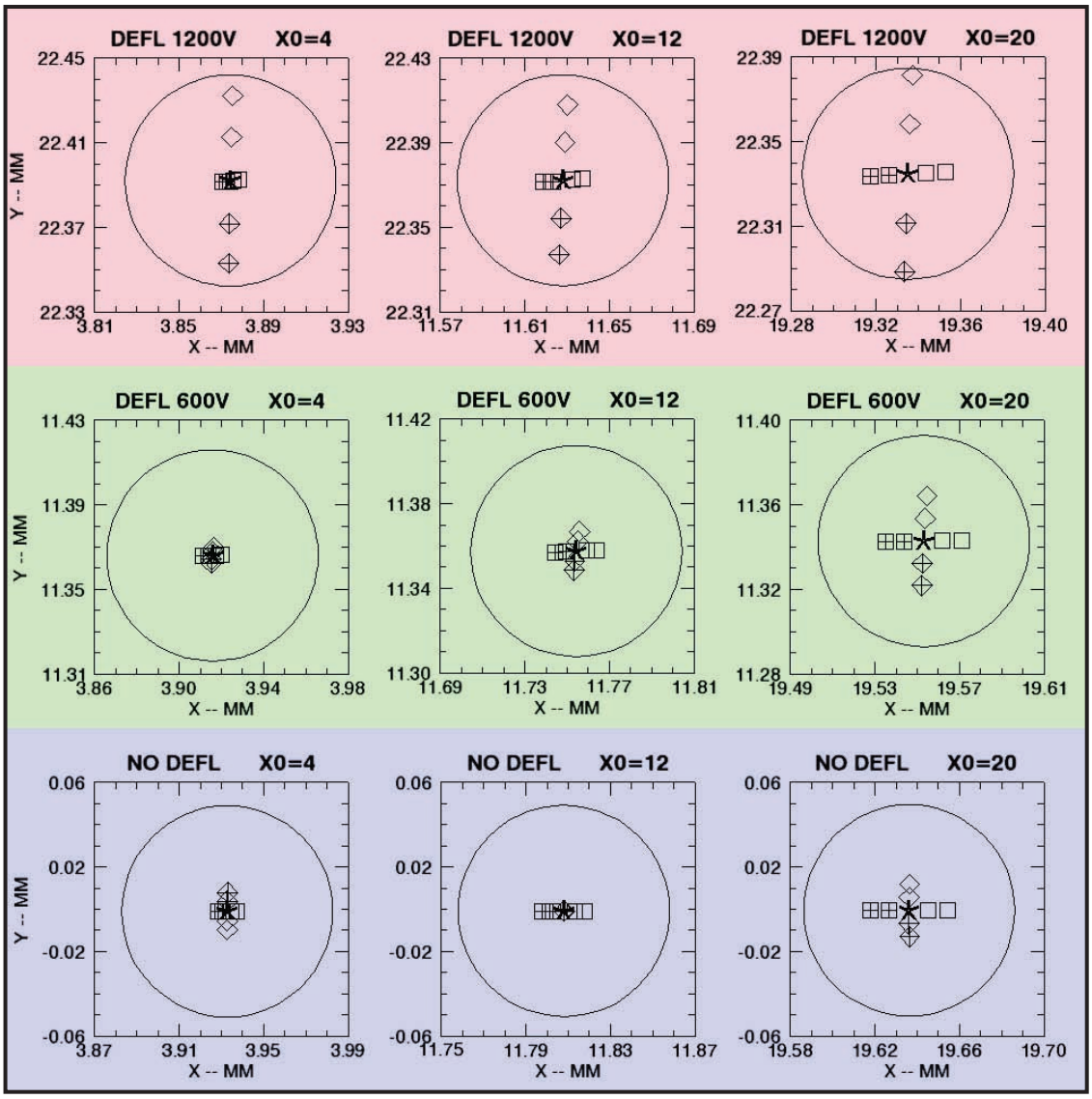

Figure 6. Spot diagrams for three sets of nine rays launched 4, 12, and 20 mm from the tube axis with 1200-, 600-, and 0-V vertical deflection. The launch parameters are shown at the top of each plot. The 100-µm reference circle is centered on the mean landing position of each group. Rays emitted normal to the cathode surface are marked with an asterisk. Rays emitted ±10° or ±20° from the cathode normal in the X and Y directions are marked with squares (X, spatial) and diamonds (Y, temporal), respectively, with a '+' sign for positive emission angles.

References

CPO, Charged Particle Optics, boundary element code, CPO Ltd., http://www.electronoptics.com/, accessed September 28, 2006.

CPO, Charged Particle Optics, boundary element code, http://www.simion.com/cpo/, accessed September 28, 2006.

Field Precision, finite element code, Field Precision LLC, http://www.fieldp.com/index.html, accessed September 28, 2006.

IDL, Interactive Data Language, ITT Visual Information Solutions, http://www.ittvis.com/idl/, accessed September 28, 2006.

Richter, J. M., "Electron Trajectory Codes for Image Tube Design," *Nevada Test Site–Directed Research, Development, and Demonstration*, FY 2005, Bechtel Nevada/National Security Technologies, LLC, Las Vegas, Nevada, 2006, 99–105.

Shellman, R. A., "Optimization of Streak Tube Temporal Resolution," *Nevada Test Site–Directed Research, Development, and Demonstration*, FY 2005, Bechtel Nevada/National Security Technologies, LLC, Las Vegas, Nevada, 2006, 107–112.

Time Frequency Analysis

Sarah Giandoni (former employee), Fred Sanders, Thomas W. Tunnell[1]
Los Alamos Operations

This project developed and applied a Hilbert transform–based technique (HBT) to the time frequency analysis of Mach-Zehnder (M-Z) interferometry data and other oscillatory waveforms in the RF range. For the sample data supplied, HBT failed to show any advantage over techniques now used to unfold M-Z data; investigation of the potential value of applying HBT to other data will be continued with programmatic funding. However, during this SDRD project, two unique analysis routines emerged: adaptive down conversion (ADC) and Nyquist Violation Technology (NVT). ADC reprocesses waveforms to isolate signals of interest, and NVT provides a means to override the Nyquist limitations encountered when characterizing high signal-to-noise narrowband signals. We anticipate that improvements to the ADC tool may address the shortcomings experienced in applying HBT to M-Z data.

Background

In FY 2005, LAO scientists successfully used HBT in processing photon Doppler velocimetry (PDV) data to obtain fine time resolution. That effort was the basis for this SDRD work, which proposed to develop and refine time frequency analysis techniques for a broad spectrum of problems. The HBT approach models data as chirped RF signals through a fast Fourier transform (FFT) technique that advances the phase of the signal by 90°. By comparing this phase-advanced signal, called the Hilbert transform, with the data, one can deduce the phase even when amplitude variations are present in the signal. The frequency may then be computed from the time derivative of the phase. This project sought to apply HBT to M-Z data as well as other RF signals of interest, where amplitude fluctuations can complicate the phase extraction. For underground test M-Z data, fiber darkening from radiation can cause significant amplitude attenuation. Additionally, applying HBT to Faraday rotation, microwave interferometry, and atmospheric RF data, such as the Fast Onboard Recording of Transient Experiment (FORTE) satellite data, were investigated (Jacobson, 2001). In the course of this work, new technical concepts, ADC and NVT, were developed.

[1] tunneltw@nv.doe.gov, 505-663-2012

Project

HBT

Five sample M-Z data sets were supplied by Kirk Miller of STL. These data sets were acquired using α-cans with α values ranging from 100–2000 generations/μs. These multifringe data had fewer than four or five fringes present before the voltage peak. The oscillatory nature in the M-Z data derives from the fact that the phase of the waveform is a direct measure of the voltage output of the α-can. Because the voltage output is exponential, the phase increases slowly at first, but thereafter increases at faster and faster rates through the voltage peak of the α-can.

Applying HBT to the M-Z data proved difficult. The early time portion of these multifringe data contained significant low-frequency content that generated low-frequency distortions in the Hilbert transform. These distortions created baseline problems throughout the data. After many failed attempts to remove the distortions, they were finally reduced considerably by using the time derivative of the signal and the time derivative of its Hilbert transform.

Good agreement between current unfolding techniques and HBT were noted in the region spanning the first fringe through the voltage peak. Problems in agreement for data prior to the first fringe were probably due to residual low baseline distortions. Therefore, a combined analysis approach was used, where data prior to the first fringe peak were unfolded with standard arc cosine routines and data after the first fringe were unfolded with HBT. Although this method helped improve agreement prior to the first fringe, the analyses were not in complete agreement with the STL unfolds.

Sample results are plotted for the 100 generation/μs data in Figure 1. These M-Z data were unfolded to produce phase $\Phi_{HBT}(t)$. The unfolded phase was compared with the arc cosine, Φ_{ARC} (t), supplied by STL. The ratio, Ratio(t) = Φ_{ARC} (t) / $\Phi_{HBT}(t)$, of these two unfolded phases was also computed (Figure 2).

The data in Figure 1 are plotted without any baseline correction. The first fringe occurs at –4.3 ns, with increasing modulation beyond. The peak voltage occurs at 25 ns. At this point the voltage begins to decrease, which results in a phase reversal in the data. This phase reversal appears as a strange peak that is not only well below the other peaks but also below the early time data values.

The ratio of the unfolded phases (Figure 2) shows good agreement between the HBT and traditional approaches beginning with the first fringe out to the voltage peak. However, the portion prior to the first fringe shows some disagreement, which is likely due to slight differences in how the data were baselined.

The α-can sample data did not show much amplitude attenuation, as they were not subject to radiation that could cause fiber darkening. To predict performance under conditions of fiber darkening, a simple model was run to attenuate the amplitude based on the unfolded voltage. Under a test scenario, the unfolded voltage is a measure of the gamma flux. These simulated fiber-darkened data

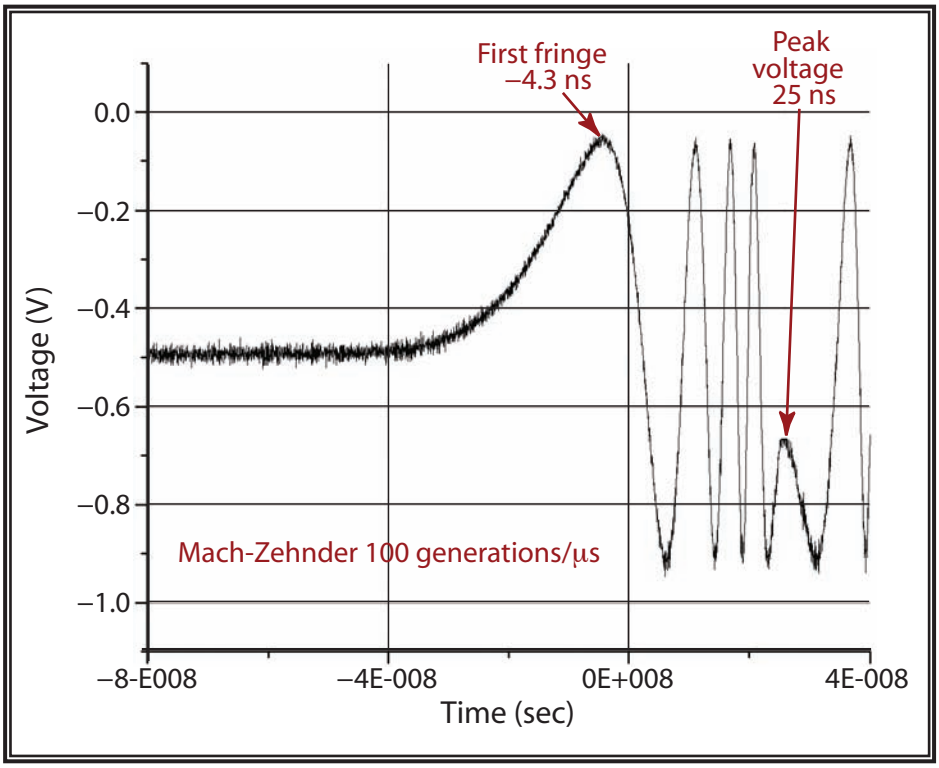

Figure 1. Sample M-Z data

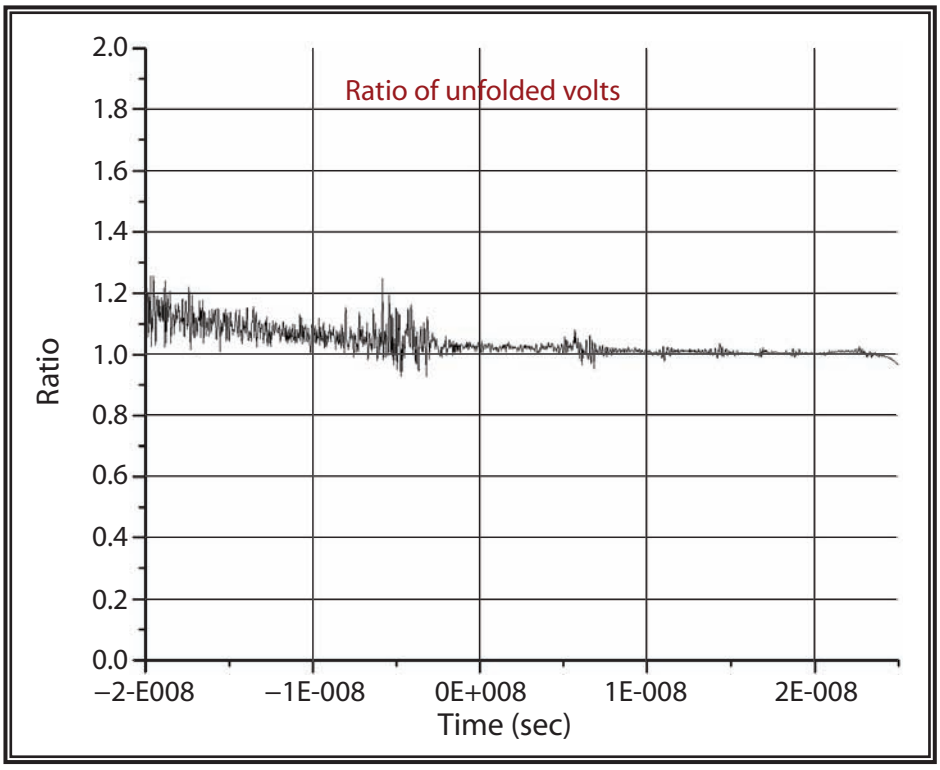

Figure 2. Ratio of unfolded voltages

provided results nearly identical (within 1% or less) to the unattenuated data. The simulated fiber darkening of the 100 generation/μs data are shown in Figure 3. The attenuation is obvious. The HBT was able to process this attenuated data to recover the phase to within 1% or better.

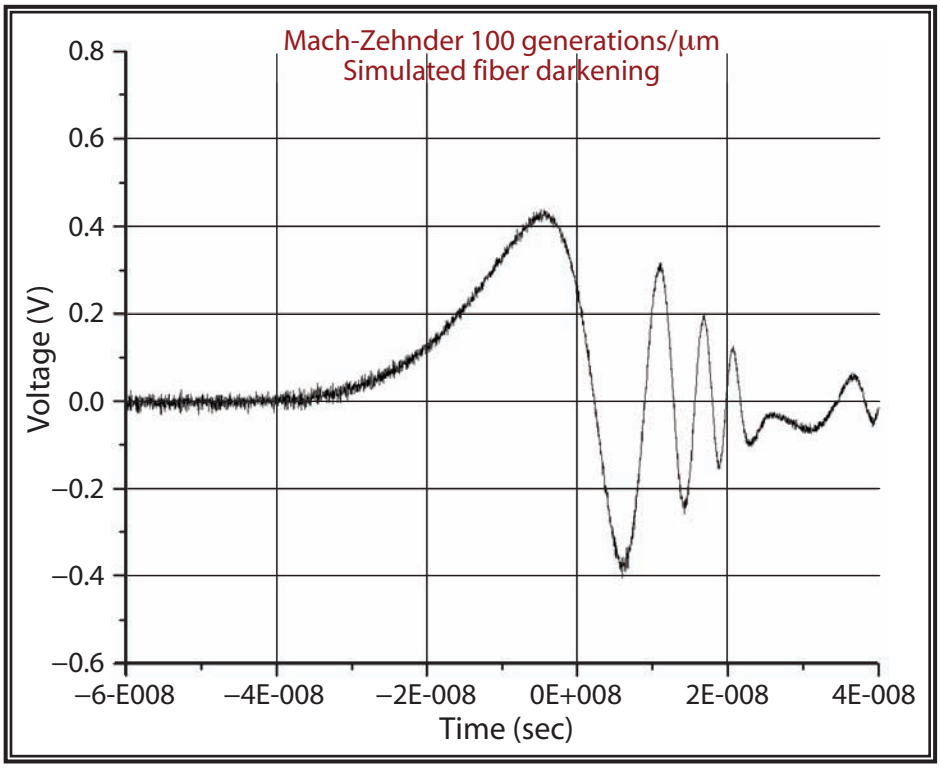

Figure 3. 100 generations/μs data with simulated fiber darkening

An important element in the M-Z data acquisition is the sensitivity of the M-Z. This sensitivity is quantified in terms of the number of voltages per passage of 1 increase of π in phase, or V_π. Our sample data were acquired with V_π of 5.7 V per π radian, implying that HBT can effectively interpret multifringe data. For example, the combined technique performed just as well for the 100 generations/μs data as the 2000 generations/μs data. The difference of the gammas is a factor of 20. We conclude that the HBT techniques would have performed very well if the 100 generations/μs data set had been acquired with a more sensitive M-Z with a V_π of 5.7/20, or 0.285 V per π radian. These data would have contained 80–100 fringes prior to the voltage peak. The first fringe peak would occur at roughly 1% of the voltage peak. In practice, even with fiber darkening, HBT is feasible.

These results led us to conclude that the HBT approach has relevance for low α data acquired with very sensitive M-Zs that produce 80 or more fringes. In addition, HBT can handle amplitude

attenuation that might occur due to fiber darkening. Finally, to address similar difficulties with early time PDV data from Asay foil experiments, modifications are envisioned in the HBT approach that may address the remaining issues for M-Z data. These modifications are discussed in the "ADC" section, below.

Another goal of this project was to evaluate the viability of using HBT to unfold other oscillatory data, such as Faraday rotation and microwave interferometry data. Testing HBT on the Faraday rotation data is now being conducted on a project outside this SDRD. Likewise, the success and promise of the HBT approach to PDV data has encouraged one LANL experimenter to use HBT on microwave interferometry data.

ADC

One approach that was attempted for processing the M-Z data was to digitally mix the data with a narrowband RF signal to move the data to a higher frequency domain. Although this did not work, it introduced the concept of digitally engineering an optimal RF signal for mixing. Because the procedure relied on extracting the frequency trace in the Fourier spectrogram as the engineered signal, and a Fourier spectrogram is not the best tool for understanding M-Z data, the effort also failed. However, exploring such engineered digital signals led to the development of ADC.

ADC reprocesses waveforms to isolate specific signals of interest. Isolation of these signals may be necessary due to the interference of other signals. The ADC process is as follows:

1. Interpolate data with FFT to double-sample frequency.
2. Compute FFT power spectrum.
3. Extract frequency and bandwidth as a function of time.
4. Convert to approximate frequency f(t).
5. Integrate to obtain phase $\Phi(t)$.
6. Compute mixing functions sin ($\Phi(t)$) and cos ($\Phi(t)$).
7. Multiply each mixing function by the data.
8. Low-pass filter the products.
9. Regenerate data using sin ($\Phi(t)$) and cos ($\Phi(t)$) mixing functions.
10. Generate Hilbert transform using sin (P(t)) and cos (P(t)) mixing functions.

After some initial testing, the ADC made an immediate transition to programmatic work, where it was incorporated into the PDV analysis code. An example of ADC applied to PDV data from SNL Asay foil experiments is presented in Figure 4.

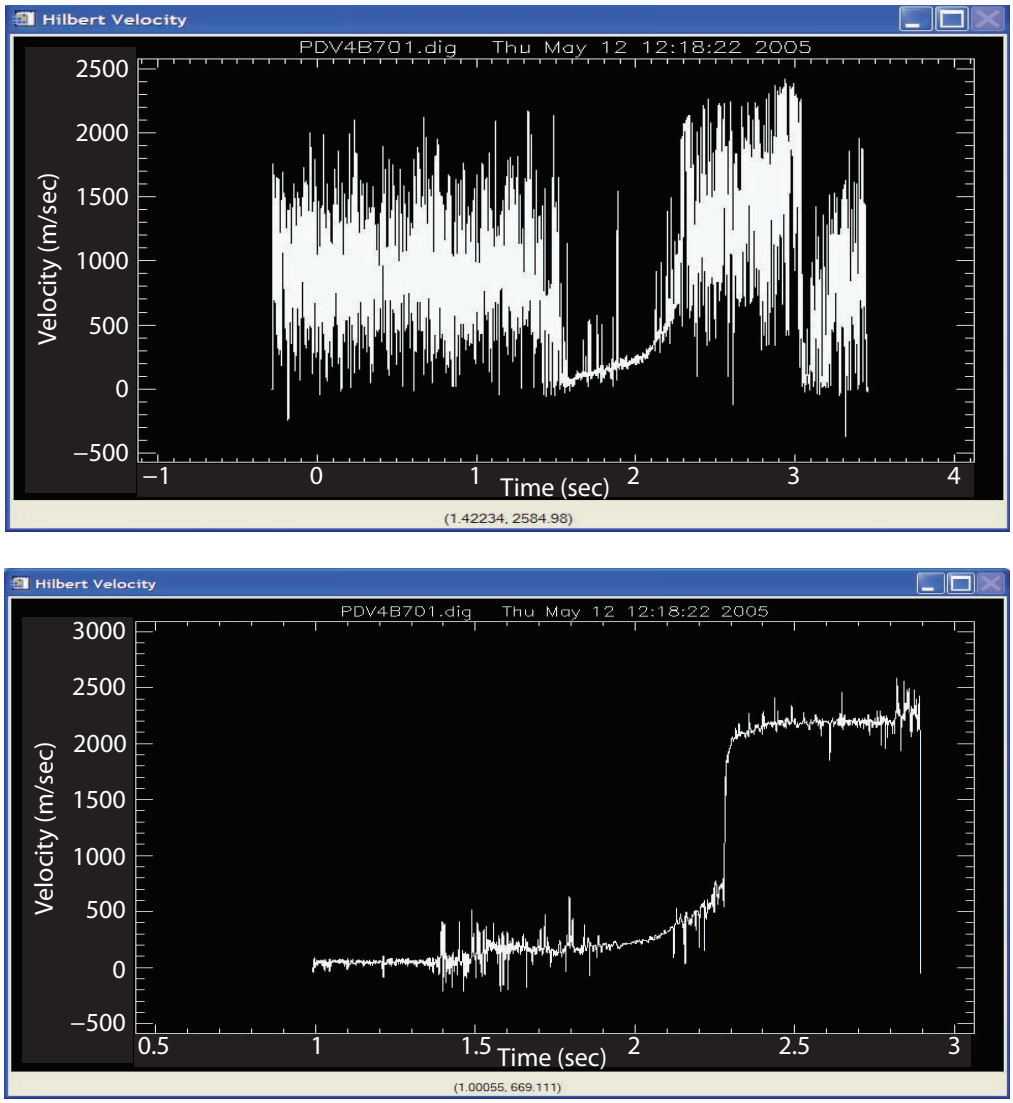

Figure 4. PDV data from SNL processed without (top) and with ADC (bottom)

The top screen in Figure 4 shows the unfolded HBT velocity, which is noisy due to interference of clock noise. Interference after 2.2 μs is so intense that no detailed information can be deduced. The bottom screen in Figure 4 shows HBT processing after ADC preprocessing. The noise spikes are greatly reduced, and an estimate of 2200 m/sec can be seen at the bottom of the screen by placing one's cursor on the plot.

Possible improvements to ADC may warrant us to revisit using HBT on M-Z data. To begin, rather than using an FFT spectrogram to mix the data, one would preprocess the data with an adaptive Gaussian filter that is very similar to the AWARE algorithm developed by LANL for its reaction history analysis (Hodson, 1980). The width of the Gaussian filter depends on the curvature (i.e., second derivative in the data), which is directly related to the instantaneous frequency in an oscillatory waveform. The curvature, then, would be used to determine the approximate frequency and phase $\Phi(t)$ in the ADC approach. A technology abstract describing ADC was prepared and submitted.

NVT

The NVT routine was discovered during an input error while trying to process M-Z data with a Fourier spectrogram. Digital acquisition systems typically have employed analog bandwidths to low-pass filter data well below the Nyquist limit prior to digitization. The rationale for this filtering had always been that, due to Nyquist aliasing, the user would be unable to resolve frequencies above the Nyquist limit. Hardcore digital experts may have a difficult time understanding that this long-assumed "truth" is not completely true. In fact, in a set of very limited applications, this "truth" is *not* true. A high signal-to-noise chirped signal can be reasonably resolved well beyond Nyquist limits, and exactly resolved if acquired with a second digital acquisition system operating at another optimum Nyquist limit. Unfortunately, the broadband noise remains out of control. Transient behaviors may not be detected, however.

The NVT operates by this principle: Two digitizers with sample intervals t_M and t_N can be used in conjunction to resolve frequencies above their individual Nyquist limits. Their combined Nyquist limit is determined by finding positive integers M and N, such that $t_M / M = t_N / N$, where M and N have no common prime numbers. If $t = t_M / M = t_N / N$, then the Nyquist limit for the two digitizers is ½ t.

Standard analysis techniques can be used to unambiguously resolve narrowband frequency information by comparing the apparent frequencies. The values of these apparent frequencies will obey certain relationships depending on how many times Nyquist has been violated. High signal-to-noise ratio is required, as the broadband noise cannot be resolved. A technology abstract was completed and submitted for the NVT.

FORTE

Under this project, NSTec scientists contacted LANL FORTE personnel to discuss possible applications of these methods to their work. After they were familiarized with ADC, a small modeling and analysis task was performed on simulated data. The simulation demonstrated ADC's ability to resolve detail on brief anomalies in simulated atmospheric RF data. A follow-up visit is in order.

Conclusion

This time frequency analysis project applied HBT to unfold M-Z data, and experienced some problems unfolding sample α-can data ranging from 100–2000 generations/μs. After modification, the HBT produced improved results. While performance was good after the first fringe to the voltage peak, problems persisted for the early time M-Z data. A fiber-darkening simulation followed by HBT analysis showed that HBT would still extract phase information, even with amplitude reductions by a factor of 5. Additionally, HBT performance can be expected to improve with the use of more sensitive M-Zs that would produce more fringes in the data sets.

This research also led to the development of the ADC and NVT tools. ADC mixes a digital signal with the data; this isolates the signal of interest to create high signal-to-noise ratios. While the ADC failed to bring benefit to M-Z data, it was quickly transitioned to programmatic use for PDV analysis. With modifications, the ADC may be suitable for use in preprocessing M-Z data to be processed with HBT. The NVT was also briefly discussed. It provides a means of beating Nyquist limitations in characterizing high signal-to-noise narrowband signals.

Finally, FORTE personnel at LANL were contacted to discuss possible applications. ADC's ability to extract detail in brief anomalies was demonstrated and may generate additional interest.

References

Hodson, E. K., D. R. Thayer, C. Franklin, "Adaptive Gaussian Filtering and Local Frequency Estimates using Local Curvature Analysis," Los Alamos National Laboratory Report, LA-UR-80-0481 (February 1980).

Jacobson, A. R., X. M. Shao, "Using geomagnetic birefringence to locate sources of impulsive, terrestrial VHF signals detected by satellites on board," *Radio Science* **36**, 4 (July-August 2001) 671–680.

Prototyping Search Software with Multiple Algorithm Options

Warnick Kernan, Ding Yuan[1]
Remote Sensing Laboratory – Nellis

A search software prototype based on a sequential probability ratio test (SPRT) approach has been implemented in the Mathematica platform. The software uses an algorithm developed over the course of this research that offers multiple options on population distribution, confidence selection, stop handling, alarm calculation, and other sampling controls. Field radiation data were collected and analyzed. The results confirmed that the algorithm is suitable for integration into a radiation detector prototype.

Background

Conventional search (alarm-generating) algorithms employed by field radiation detectors mostly adopt a scheme of fixed sample size, which mitigates potential sampling errors and substantiates the confidence levels of the alarm decisions. But because fixed sample size algorithms often use a fixed response time delay, regardless of sources of different radiation levels, they do not work under changing confidence levels for different missions, and a manual setting is often required to separate threshold sources from background.

Generally, confidence levels are related to sample sizes and will affect the speed and cost of the field operations, and missions with different objectives may require different confidence levels. For instance, for declaring background, an algorithm with higher confidence is preferred for searching a high-level radiation target, and an algorithm with lower confidence is preferred for searching low-level nuclear fuel waste.

The sequential search algorithm we investigated is based on the SPRT method proposed by Wald (1947). The key features of the SPRT method are its dynamic sample size and its two-way controllable confidence levels. Some advantages of SPRT over conventional sampling methods have been evaluated for portal monitor application by Coop (1985), and further confirmed by a simple trial study by Kernan and Yuan (2006). The adaptation of this method for a search algorithm could improve both data accuracy and operation efficiency for field search missions.

SPRT itself does not offer specifics on population estimations, radiation calculation, alarm generation, and stop handling. In particular, most applied SPRT studies had been focused on cases where the null and the alternative distribution were of the same distribution family. In those cases, the probability ratio easily reduces to a simple parametric ratio. In reality, the null and the alternative

[1] yuand@nv.doe.gov, 702-295-8735

distributions can be of different families, and subsequently the computational burden is increased. The objective of the project was to investigate multiple implementation options that would allow comparisons of different distribution families, and put together the optimized bits and pieces into a workable SPRT-based search algorithm.

Project

Sequential Method

Let us consider a field radiation observation sequence $x_1, x_2, \ldots x_k, \ldots$, for example, gamma gross counts (GC) measured over half-second intervals. The data point x_k can be potentially drawn from the background radiation that follows a null distribution $H_0 \sim f_0(x)$, or from a high radiation source (plus background) that follows an alternative distribution $H_1 \sim f_1(x)$. The search algorithm needs to make a choice between the two hypotheses based on the current x_k and previous observations. The SPRT method offers a third decision option where no choice is made and an additional sample is drawn. Essentially, the SPRT method computes the following log-likelihood probability ratio:

$$LLR_k = \log\left(\left(f_1(x_1)\, f_1(x_2)\ldots f_1(x_k)\right) / \left(f_0(x_1)\, f_0(x_2)\ldots f_0(x_k)\right)\right)$$

and makes a choice according to the following rules as established by Wald:

If $LLR_k < A$, then accept H_0;

If $LLR_k > B$, then accept H_1;

If $A \le LLR_k \le B$, then take one additional sample and recompute LLR_k,

where $A = \log(\beta / (1 - \alpha))$ and $B = \log((1 - \beta) / \alpha)$ are decision thresholds, and $\alpha = \Pr ob\,(H_1 \mid H_0)$ and $\beta = \Pr ob\,(H_0 \mid H_1)$ are prespecified, acceptable false positive and false negative rates.

Key Algorithm Features

The SPRT decision procedure does not tell how to determine the distribution functions. In an area with very low radiation background, the detector-measured GCs may be assumed to be primarily caused by the detector's internal white noise, which usually follows a normal distribution. When a high-radiation source is involved, the GCs measured by the detector most likely will follow a Poisson distribution. For these reasons, field GCs may switch distribution types between normal and Poisson. For algorithm study, we considered the following four possible (H_0, H_1) pairs: normal vs. normal, normal vs. Poisson, Poisson vs. normal, and Poisson vs. Poisson. Notice that H_0 and H_1 are from different distribution families; the LLR_k discussed earlier cannot be reduced to simple parametric ratios.

The original Wald's rules weigh the null and alternative hypotheses equally. In a search practice, if we want to declare a "background" sample, we may want to take additional measures to increase the confidence to guarantee that a source would not be undetected due to false negative error. On the other

hand, if we see a high GC value, we want to declare it to be a "source" as soon as possible in order to bring it to the attention of the operator. For these reasons, Wald's original rules were modified in the algorithm below, which became the search rules of this project:

If $LLR_k < A$ and $k \geq N_0$, then accept H_0;

If $LLR_k > B$, and $k \geq N_1$, then accept H_1;

If $A \leq LLR_k \leq B$ and otherwise, then take one additional sample and recompute LLR_k, where N_0 and N_1 (with $N_1 \leq N_0$) are preselected integers for H_1 and H_0, respectively.

Once H_1 is accepted, the software uses the following program for computing the alarm level:

$$AL = Ceiling\left(Log_b\left((\mu_1 - \mu_0) / (\rho\sigma_0)\right)\right),$$

where b is the base of the logarithm, μ_0 and μ_1 are the sample background and source means, σ_0 is the sample standard deviation, and ρ $(0 < \rho)$ is a scale factor. The software defaults are $b = 2$ and $\rho = 1$.

Test Data

Data were collected at RSL in the area in front of the deployment building next to the truck scale and the anechoic chamber. To maintain consistent and repeatable paths as well as walking speed for the experiment, a 50-ft cord was tied to the operator's waist at one end and to a barrel at the other end (the barrel was used as the source holder). Two sources, one ^{252}Cf (0.27 mCi) and one ^{137}Cs (40 μCi), were used for the data collection. The background was measured over the same path before both tests. Data points were collected in half-second intervals and aggregated into 1-sec data points. The distance between data points is roughly one foot. The field data are plotted together with background data in Figure 1.

Selected Results

The default and the SPRT–calculated gamma alarms using ^{137}Cs data with different hypothesis alternatives are plotted in Figure 2.

Considering the data in Figure 2, an observer could quickly conclude that the SPRT algorithms reduced the false gamma alarm rates significantly. This reduction could not be achieved simply by adjusting the alarm cutoff threshold in the default alarm data, as recommended for experienced operators by many commercial detector manufacturers. For instance, moving the cutoff threshold in the default alarm plot (top plot, Figure 2) upward by two levels would still leave too many false alarms (third-level alarms). As for the performances for various hypothesis alternatives, the Normal-Poisson option seems to be working best for the gamma data.

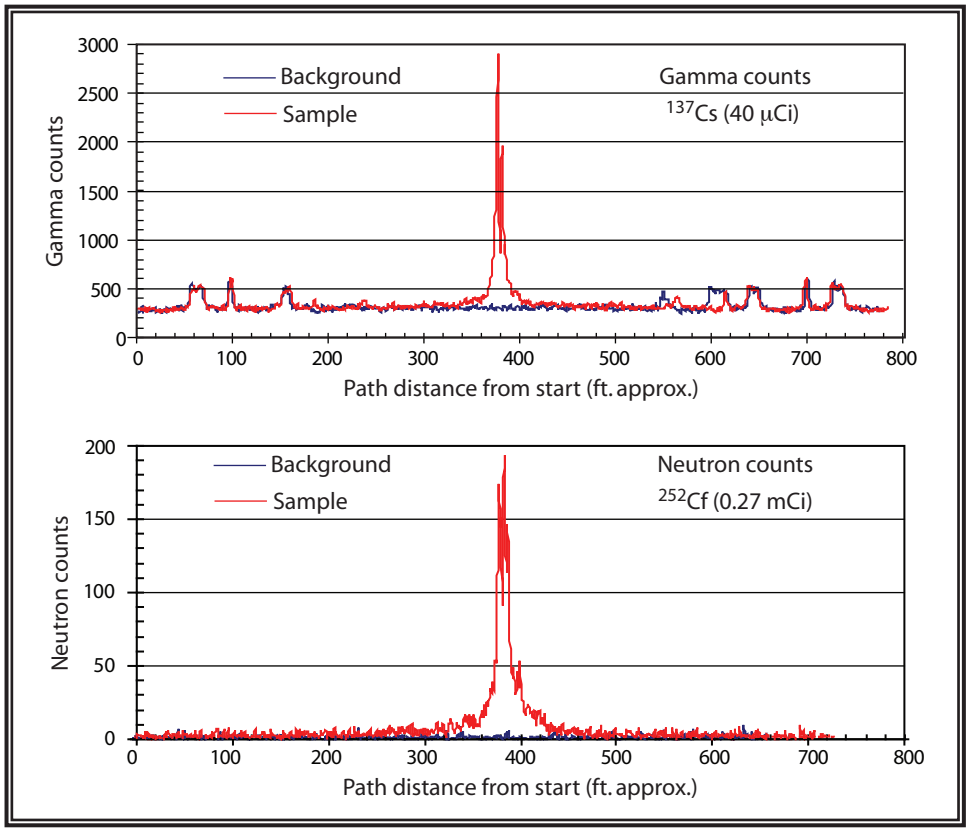

Figure 1. Gamma and neutron data collected for the software evaluation

The default and SPRT–calculated neutron alarms using ^{252}Cf data with different hypothesis alternatives are plotted in Figure 3. It is also clear that the SPRT method reduced the false neutron alarm rates substantially. However, among all possible SPRT alternatives, it is unclear which option performed best. We intend to believe that the Normal-Poisson option remains a better choice for neutron detection.

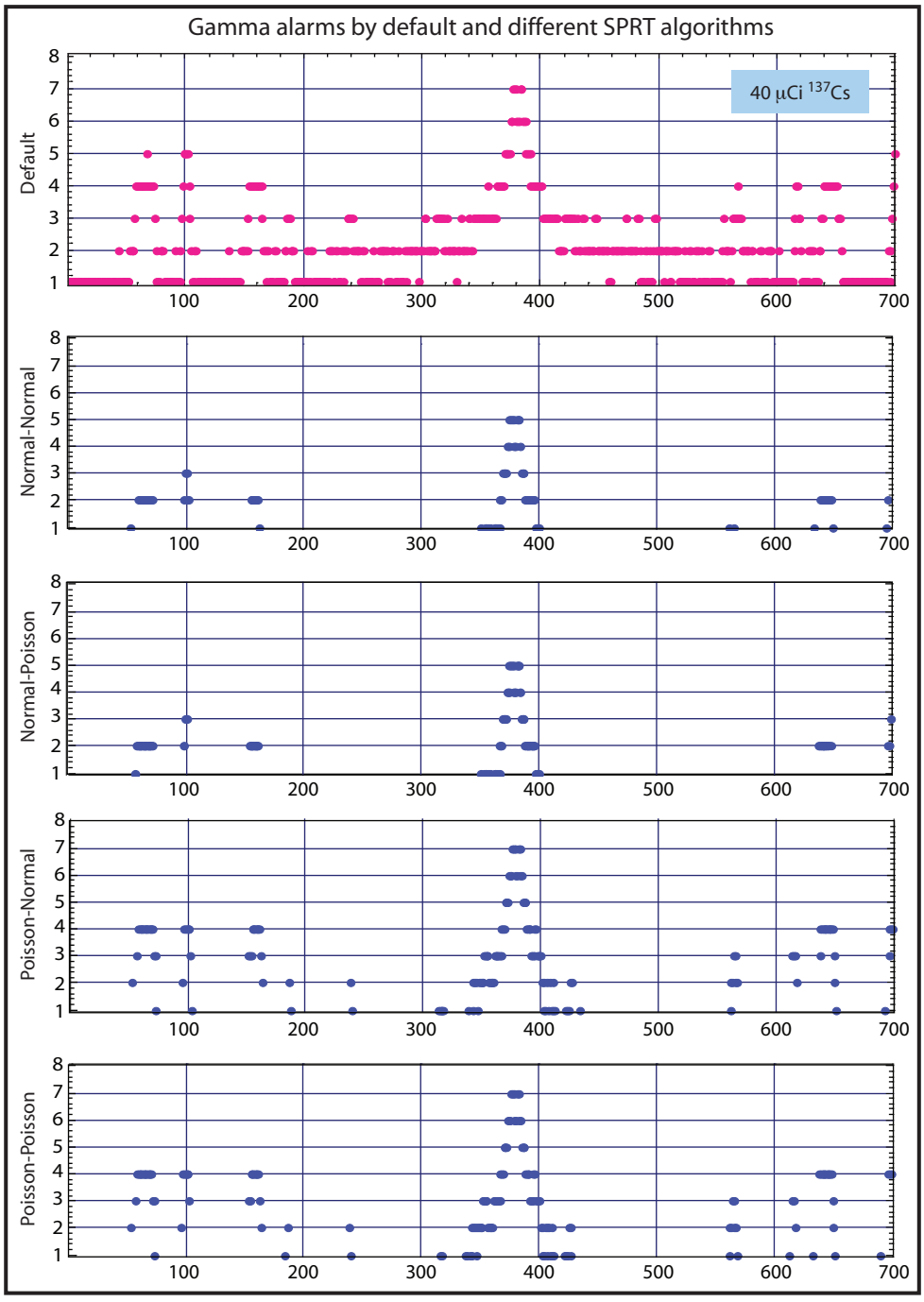

Figure 2. Comparison of gamma alarms of ^{137}Cs for default and various SPRT distribution options. The horizontal axis shows the data-point locations on the sampling path, and the vertical axis shows the alarm level. The raw gamma counts appear in Figure 1.

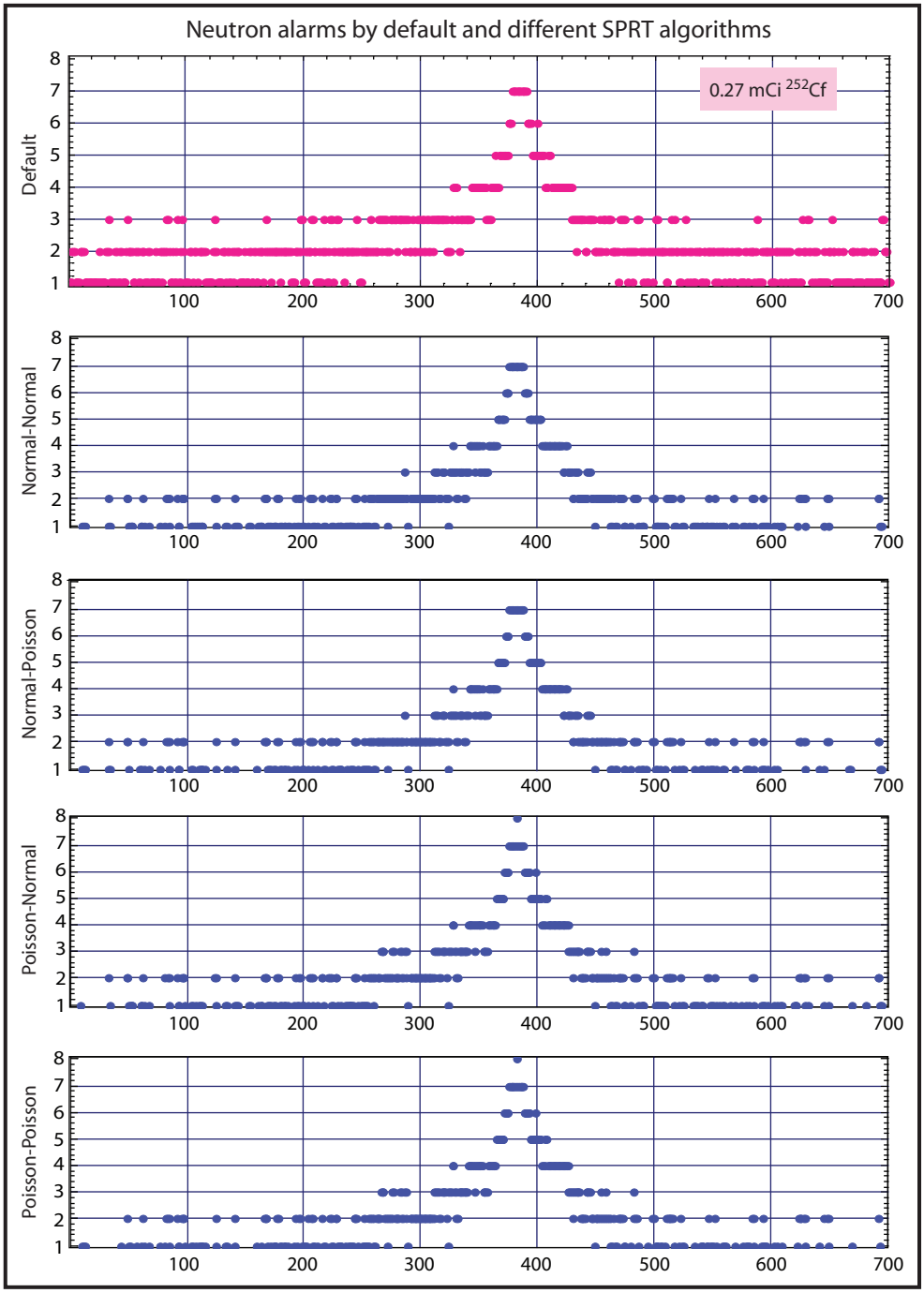

Figure 3. Comparison of neutron alarms of ^{252}Cf for default and various SPRT distribution options. See Figure 1 for related raw neutron count data.

Conclusion

A search software prototype with multiple SPRT algorithmic options was developed and tested using field gamma and neutron data. The results suggest the embedded SPRT algorithm reduces false alarm rates, improves response speed, and offers adjustable confidence levels for missions with different objectives. These advantages would improve the performance of emergency response missions.

The algorithm developed in the project can still be improved. Most importantly, we need to continue testing a new sample mean estimation method, derived by Mukhopadhyay and Ciconetti (2004), and alternative sample queuing schemes for spatial uncertainty reduction.

We recommend that a detector prototype is built on this algorithm and tested in real-time processing.

Acknowledgments

Vince Wolf and Tricia Nix of RSL provided data collection support.

References

Coop, K. L., "Computer Simulation of the Sequential Probability Ratio Test for Nuclear Safeguards," LA-10499-MS, Los Alamos National Laboratory, Los Alamos, New Mexico, 1985.

Kernan, W., D. Yuan, "Sequential Probability Ratio Test for Radiation Detection," *Nevada Test Site–Directed Research, Development, and Demonstration,* FY 2005, Bechtel Nevada/National Security Technologies, LLC, Las Vegas, Nevada, 2006, 67–72.

Mukhopadhyay, N., G. Ciconetti, "Application of sequentially estimating the mean in a normal distribution having equal mean and variance," *Sequential Analysis* **23**, 4 (2004) 625–665.

Wald, A., *Sequential Analysis*, 1947, Reprinted by Dover Publications, Mineola, New York, 2004.

this page intentionally left blank

Detectors and Sensors

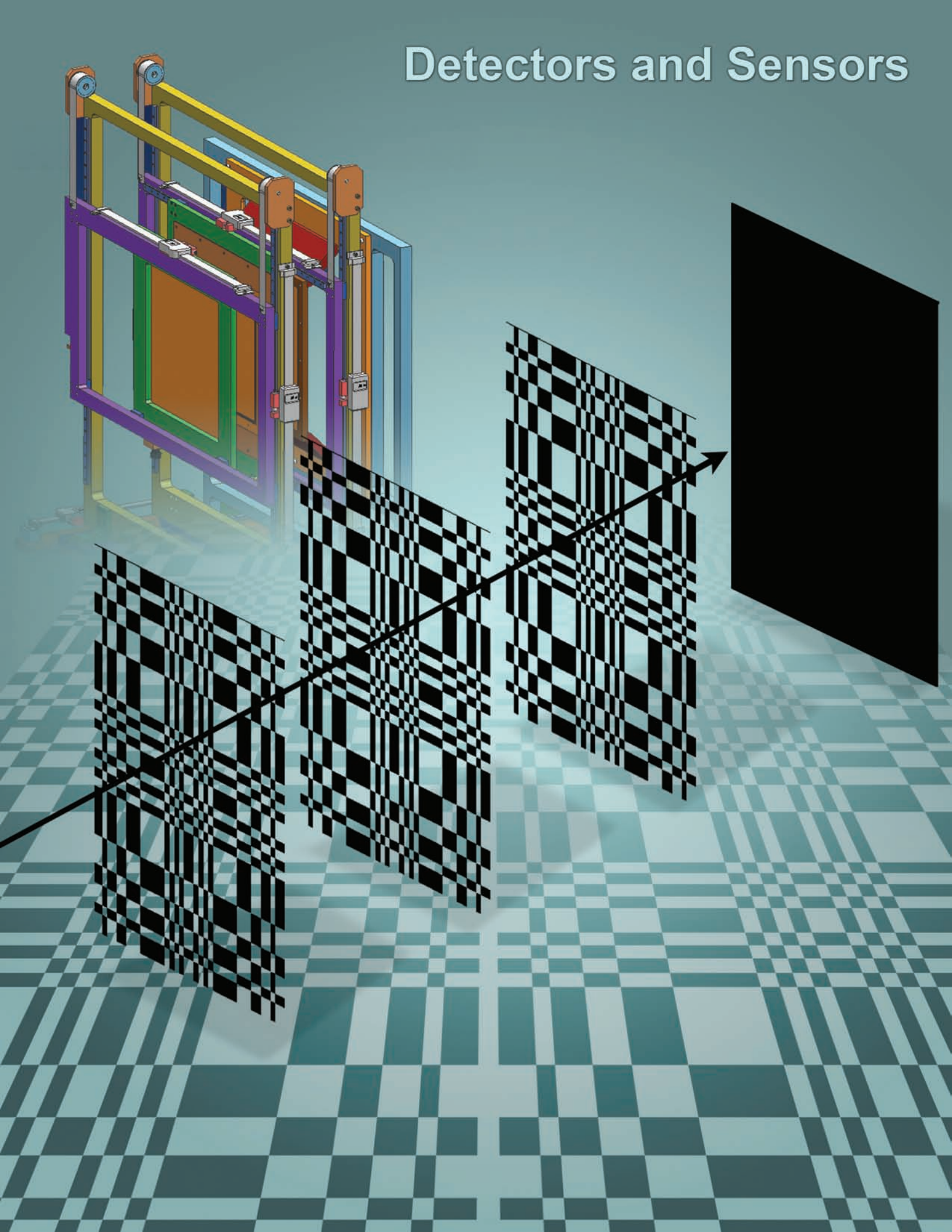

Single-pulse Detection of Infrared Synchrotron Light

Steven Becker[1]
North Las Vegas Operations

Richard Hacking, Robert Malone
Los Alamos Operations

Ken Moy, Gerald Stevens, Dale Turley
Special Technologies Laboratory

A current Laboratory-Directed Research and Development (LDRD #79877) project at SNL is performing dynamic reflectance measurements of shocked materials at near-IR to mid-IR wavelengths (1000–6000 nm). The project will provide emissivity data for standard materials used in pyrometry measurements of dynamically compressed samples (e.g., shock or isentropic compression). Work is underway to bring a small-impact system to BNL, where the National Synchrotron Light Source (NSLS) will be used as a broadband-IR source. Light emitted by the NSLS is composed of 2-ns pulses that repeat at 20-ns intervals. By comparison, the fastest IR detectors operated by SNL/NSTec have a rise time >20 ns, which is insufficient to resolve individual light pulses.

This SDRD proposal sought to develop high-bandwidth diagnostics to measure the IR wavelengths generated at the synchrotron. In addition, we proposed to use these diagnostics to measure the dynamic reflectivity of coatings developed by SNL to enhance the emissivity of materials employed in equation-of-state (EOS) experiments. This project represented the first time that an impact source was operated at a synchrotron. During its course, 12 shock experiments were completed using the impact source and the new IR diagnostic.

[1] beckersa@nv.doe.gov, 702-295-0612

Background

For hydrodynamic modeling codes to be accurate, they require well-characterized thermodynamic EOS parameters, such as temperature. Two values, radiance and emissivity, must be measured or assumed to determine the temperature of a dynamically compressed material. Radiance, emissivity, and temperature are related by Planck's law (DeWitt, 1988)

$$L = \varepsilon \frac{c_1}{\lambda^5 \left(e^{c_2/\lambda T} - 1 \right)}, \quad (1)$$

where L is the spectral radiance, ε is the object's emissivity, and T is its temperature.

Fiber-based optical pyrometers (Figure 1; Bergstresser, 2002) have been used to measure the radiance of accelerated materials, but reflectance ($\approx$ 1-emittance) measurements have not always been compatible with the experiment. Since emissivity can change during testing, the measured radiance from each detector was converted to temperature by bracketing the emissivity with the maximum emissivity of 1 and the static emissivity (Seifter, 2004) measured before the experiment (Figure 2; Bergstresser, 2004). An analysis can contain significant errors (Figure 3; Partouch-Sebban, 2003), especially at longer wavelengths. Previous reflectance measurements have been made employing flash lamps (Stevens, 2005) or lasers as the light source, but this was the first attempt to use the broadband-IR light generated at a synchrotron with an impact source.

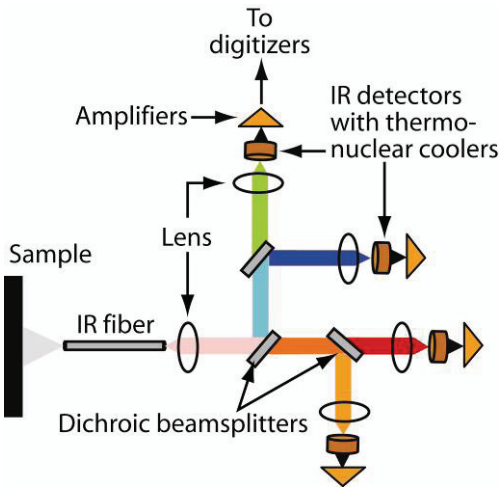

Figure 1. IR optical pyrometer layout

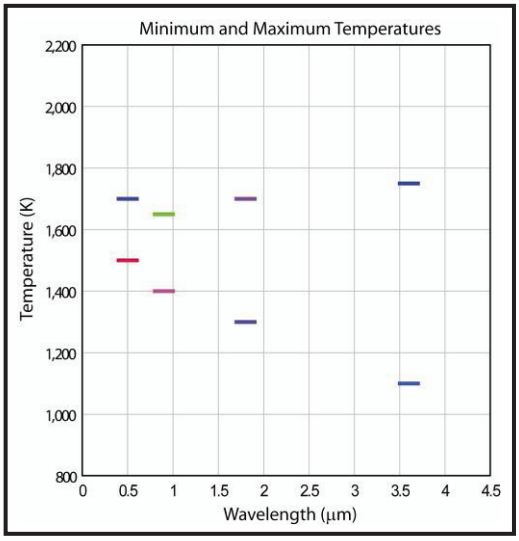

Figure 2. Results from converting radiance to temperature by using a minimum and maximum emissivity

Dynamic temperature measurements can be technically challenging, as stray light (Poulsen, 2000) generated from lithium fluoride (LiF) window edges, glue, air bubbles, and interference from other diagnostics can easily reduce accuracy. Extensive calibrations are also required before every test. A typical experiment generates stray light that can be much brighter than radiance emitted from a metal shocked at low pressures. Figure 2 shows a temperature discrepancy at 0.5 μm, a typical result of stray light contaminating the experiment. Figure 3 illustrates that a large emissivity error can be overcome if the measurement can be made at the shorter wavelengths; however, this area is susceptible to stray light, and the signal-to-noise ratio (SNR) is generally poor at low temperatures. Such measurements could be improved if a thin layer of high-emissivity material were applied to the target (Perez, 1991). This layer should have minimal effect on thermal diffusion while increasing apparent emissivity. Higher emissivity would yield an improved SNR and eliminate the need to characterize the surface of each target material.

Project

Our early focus was on identifying IR detectors with a fast enough response to measure the 2-ns pulses at 2–5 μm. The only large-diameter, commercial detectors available are photoelectromagnetic (PEM) detectors made by Vigo. These 1-GHz-bandwidth instruments are designed for CO_2 laser-pulse detection but have low responsivity (40 mV/W). After preliminary trials at STL, we tested one detector at the NSLS (Figure 4). Test data with the synchrotron in standard mode indicated that if

the noise were reduced on the PEM detectors, sufficient light would exist to build a three- or four-channel spectrometer that could measure dynamic reflectance. Further investigation showed that the noise was deriving from the Vigo power supply design, and Boston Electronics worked with Vigo to reduce it to an acceptable level.

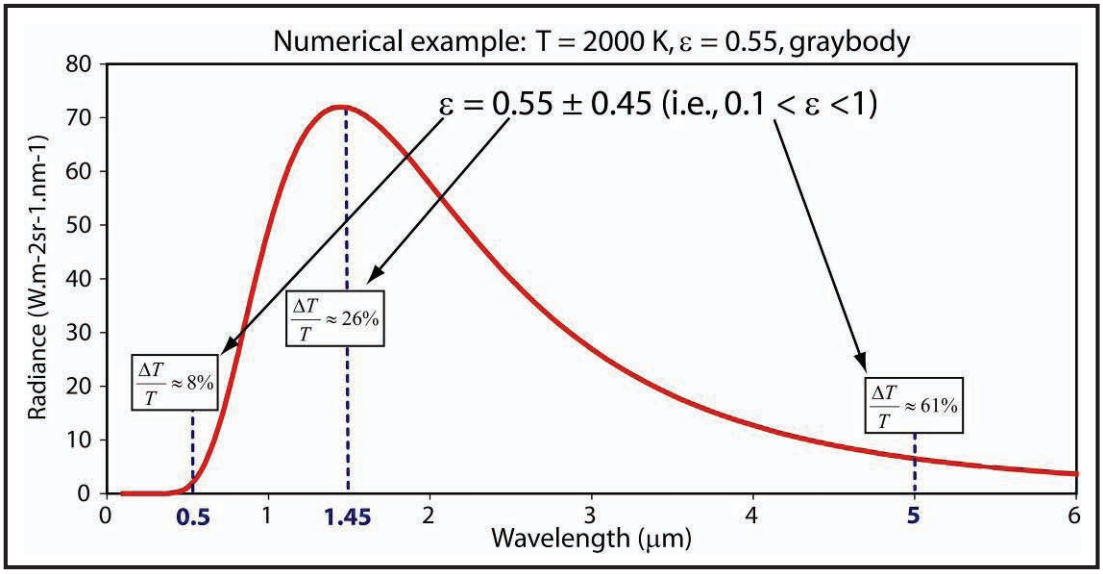

Figure 3. Analysis error on a metal target at various wavelengths

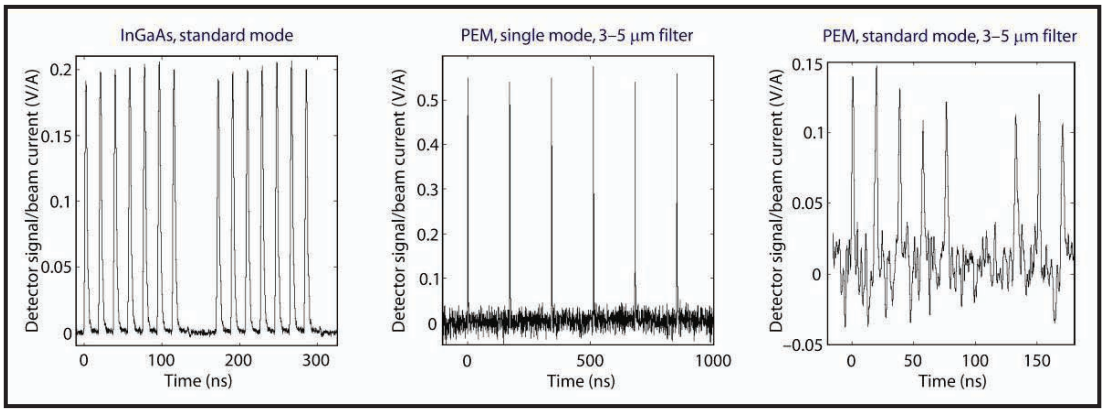

Figure 4. Detector tests at NSLS

After these detector tests, Exxon offered to share its area on beam U1a of the vacuum ultraviolet (VUV) ring at the NSLS. Beam time became available at the end of FY 2006. Detector evaluation was stopped, and an optical design was completed. SNL also decided to accelerate construction of the impact source. The low responsivity of the PEM detectors dictated the use of reflective optical components and eliminated the possible use of IR fiber and refractive optics. After several iterations, the optical design shown in Figure 5 was agreed on and tested at SNL. This design incorporated two parabolic mirrors to reduce the beam size and another parabolic mirror to focus light on the target and to collect light for the IR detectors. The parabolic mirror in the containment chamber was offset so that it could not direct any debris out of the vacuum port window.

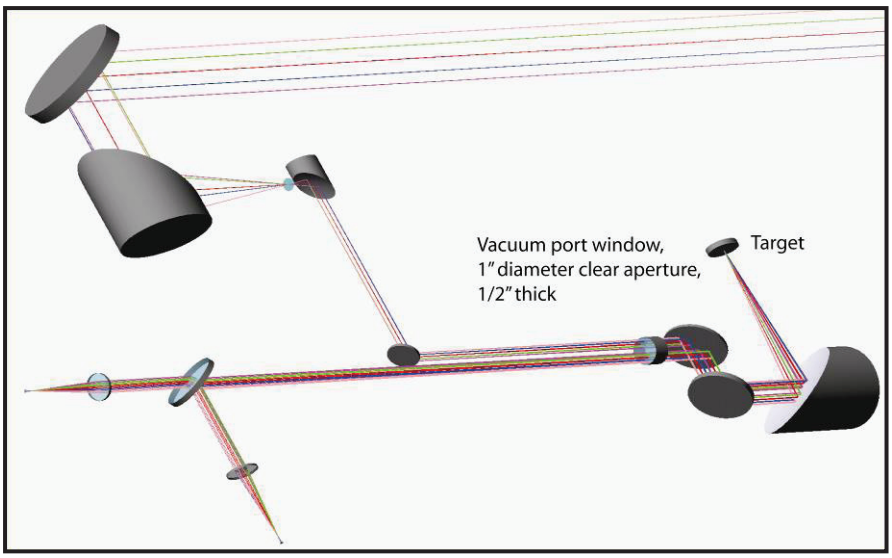

Figure 5. Optical layout to reflect the synchrotron beam off the target and into IR detectors

Figure 6 shows the impact source setup at NSLS. Twelve experiments were completed on the first series: three for velocity and tilt measurements, and nine for reflectance. The samples of interest were glued in the middle of two sapphire windows and then compressed with the impact source. The materials tested were copper, aluminum, a chromium coating, and an SNL proprietary coating. Sample data from a copper experiment appear in Figure 7.

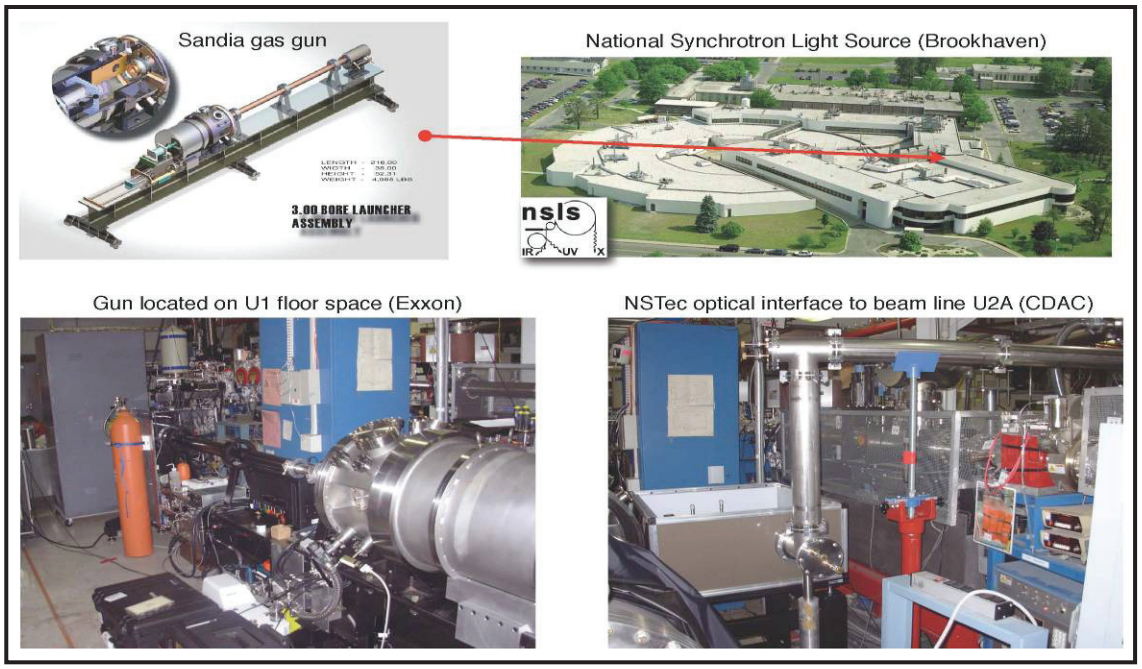

Figure 6. Physical layout of small impact source at NSLS

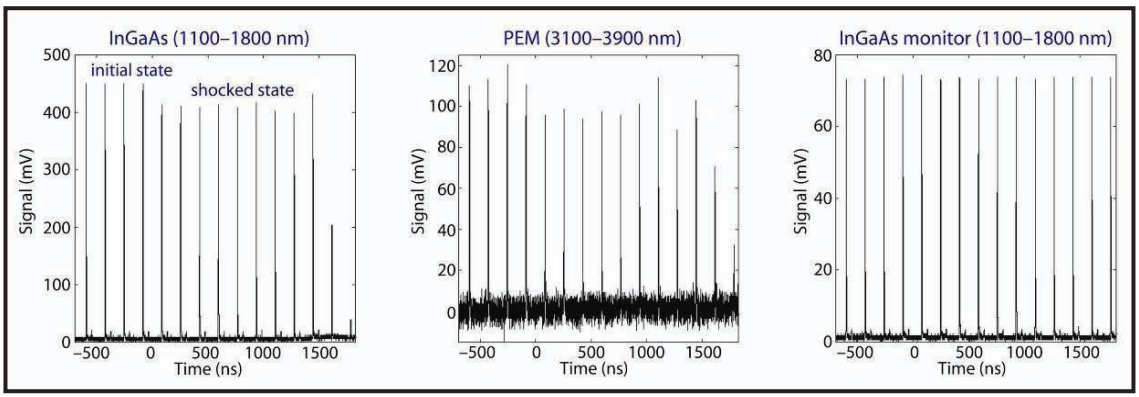

Figure 7. Sample reflectance data (dynamic reflectance of copper shocked to 8 GPa within sapphire windows [NSLS06-19]) at NSLS. Near-IR reflectance (left) shows a minor drop (~10%) at shock breakout. Mid-IR reflectance (center) decreases slightly as well, although detector noise makes the measurement more ambiguous. A monitor signal (right) upstream of the sample shows the consistency of the synchrotron emission (VUV ring, single-bunch mode).

Conclusion

As expected, emissivity increased as the sample was shocked, and the coatings with enhanced emissivity behaved similarly to the Cu and Al samples at pressures of up to 8 GPa. The tests proved successful, but several areas of potential improvement do exist. The team could not get the parabolic mirrors to recollimate the IR beam, so the parabolic mirrors were replaced with spherical mirrors. The beam is not conical, and the optical design must be modified to compensate for the actual beam dimensions. The PEM detectors' SNR must be improved. Electromagnetic interference shielding should help quiet some of the baseline noise, which appears to derive from the synchrotron. Anti-reflective coating of all the windows in the optical path will also help improve signal amplitudes. The search for better detectors will continue. Further experiments are planned to verify that the effects from the epoxy are minimal. A diffuse reflectance measurement will be added, and we will attempt to heat the samples prior to shocking. The team expects to submit a paper for journal publication at the conclusion of these experiments.

References

Bergstresser, T., S. Becker, "Temperature Measurement of Isentropically Accelerated Flyer Plates," in *Shock Compression of Condensed Matter 2001: Proceedings of the Conference of the American Physical Society, Topical Group on Shock Compression of Condensed Matter*, June 24–29, 2001, M. D. Furnish, N. N. Thadhani, Y. Horie (eds.), 2002, 1169–1172.

Bergstresser, T., Sandia National Laboratories, lecture, "Pyrometry Experiments on Saturn," March 25, 2004.

DeWitt, D. P., G. D. Nutter (eds.), *Theory and Practice of Radiation Thermometry,* Wiley-Interscience, New York, 1988.

Partouch-Sebban, D., "High Speed Multi-Wavelength Pyrometry and Emissivity Measurement of Shocked Metals," in *Shock Compression of Condensed Matter 2003*, *Proceedings of the Conference of the American Physical Society, Topical Group on Shock Compression of Condensed Matter*, M. D. Furnish, Y. M. Gupta, J. W. Forbes (eds.), 2003, 1293–1298.

Perez, M., "Residual Temperature Measurements of Shocked Copper and Iron Plates by Infrared Pyrometry," in *Shock Compression of Condensed Matter 1991,* S. C. Schmidt, R. D. Dick, J. W. Forbes, D. G. Tasker (ed.), Amsterdam: Elsevier, 1992, 737–740.

Poulsen, P., D. Baum, P. Fiske, D. Holtkamp, "Temperature Measurement on Shocked Surfaces," Lawrence Livermore National Laboratory, UCRL-JC-139909, August, 2000.

Seifter, A., M. Grover, D. B. Holtkamp, J. R. Payton, P. Rodriquez, D. Turley, A. W. Obst, "Low-Temperature Measurements on Shock Loaded Tin," DOE/NV/11718--996, Bechtel Nevada, Las Vegas, Nevada, September, 2004.

Stevens, G., D. Turley, L. Veeser, "Optical Diagnostics for Phase Changes," *Nevada Test Site–Directed Research, Development, and Demonstration,* FY 2004, Bechtel Nevada, Las Vegas, Nevada, 2005, 281–286.

Quantum Wire Detector

Warnick Kernan[1]
Remote Sensing Laboratory – Nellis

Quantum containment effects have been an area of active investigation in recent years. This collaboration between NSTec and the University of Nevada, Las Vegas (UNLV), intended to use advances in nanoscale fabrication techniques to develop radiation detectors with wires of nanometer diameter and micrometer length. We hoped to discover if charge confinement would lead to improved charge collection and/or reduced susceptibility to radiation damage. These structures may inherently have high spatial resolution. Micrometer thicknesses are comparable to the range of alpha particles from common sources, and the structures are intended for direct alpha and neutron detection via a converter layer.

Background

Two concepts for using nanowire structures as radiation detectors are of interest to this project. The first concept involves directly measuring ionization from charged particles. The second entails measuring scintillation light from a scintillator used to detect the radiation. Note that the diameter range to be attempted for the wires in this work corresponds to structures that function in the mesophysics to the quantum wire region.

There are several reasons for using nanowire structures as radiation detectors: 1) Confinement within the wires may lead to radiation detectors with a high immunity to radiation damage; 2) these devices permit fabrication of fast detectors with high spatial resolution; and 3) fabrication methods may be scaled to make large-area detectors. However, difficulties in extracting the charge generated by the passage of charged particles from the structures constitute a considerable area of technical risk for this project.

Charged Particle Detection

The range of a ~5.5-MeV alpha particle in aluminum is well above 10 μm (Figure 1). Energies of this magnitude are easily available from commercial alpha sources, such as ^{241}Am. Assuming a conversion of deposited energy to the creation of electron-hole pairs of 4.3 eV/e-h in the wire material, ~1×10^5 electron-hole pairs are created for every alpha particle that completely deposits its energy. However, pairs that are created in the "dead" portion (i.e., in the matrix material) are not collected and counted, and thus do not contribute to the possible signal.

[1] kernanwj@nv.doe.gov, 702-295-8600

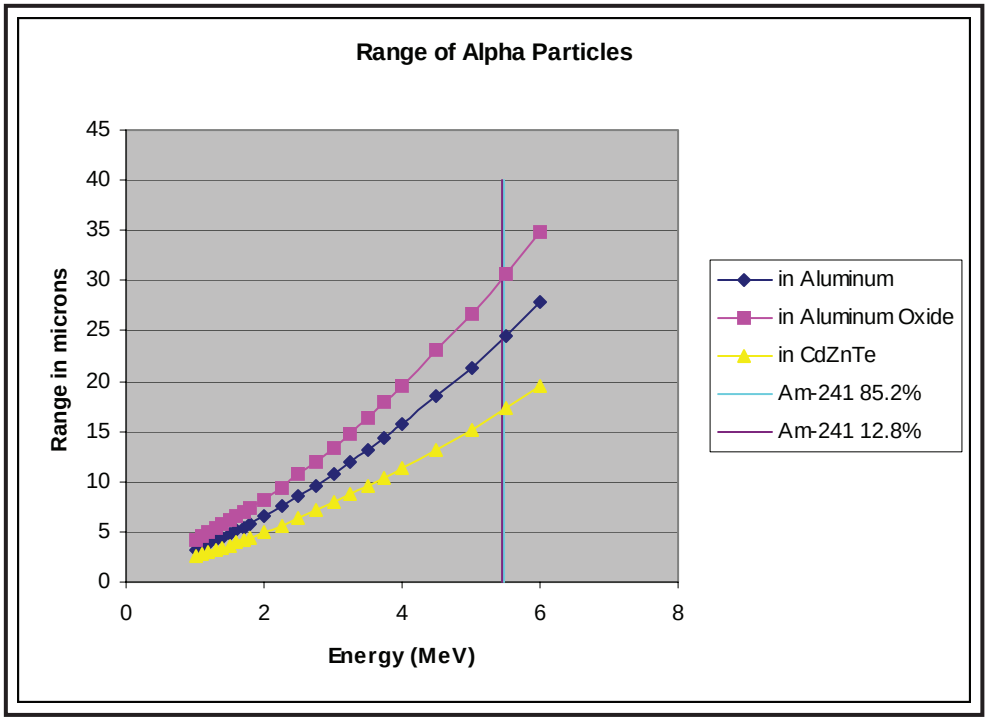

Figure 1. Range of alpha particles (^{4}He) calculations made using the stopping and range of ions in matter (SRIM) code, written by James Ziegler (2007)

An alpha source such as ^{241}Am can be used to determine whether the containment effects intrinsic to the quantum wire structure will permit efficient collection of the electrons and holes created by the passage of an alpha. The wire material should be chosen to allow for long carrier lifetimes and effective manufacturing. Many wires will be ganged together to form a pixel. However, given the wire diameters, very highly resolved pixels can still be formed with multiple wires. Initially a pixel might be 1 mm on a side. (Note that 1 mm represents 50 to 100 times the alpha particle range.) The slenderness of the wire relative to the alpha range will ensure that the charge will be distributed over many wires within a pixel.

The first stage of this work was to build and test these structures with light, and subsequently with alpha particles, to assess if the charge could be efficiently collected. If successful, we could explore the possibility of exploiting these structures' exceptional characteristics (rapid charge collection, high

spatial resolution, and the potential for large-area detectors) for making novel radiation detectors. If the results are encouraging, our interest would turn to attempting to make position-sensitive, fast-response neutron detectors by adding layers of boron or lithium on the surface, using the reactions:

$$^{10}B + n \rightarrow {}^{7}Li + \alpha, \quad \textbf{(1)}$$

where the reaction quotient would be Q = 2.792 MeV (ground state [6%] and 2.310 MeV excited state [94%]). The energy of the α is 1.47 MeV (94%) and 1.77 MeV (6%) (Knoll, 2000).

The other candidate reaction is:

$$^{6}Li + n \rightarrow {}^{3}H + \alpha, \quad \textbf{(2)}$$

where Q = 4.78 MeV. Here, both the triton and the alpha would be available for detection. The triton might actually have better range (Figure 2), which would help for getting out of the converter layer and depositing more uniformly over the active structure. The energies are 2.73 MeV for ^{3}H and 2.05 MeV for the alpha.

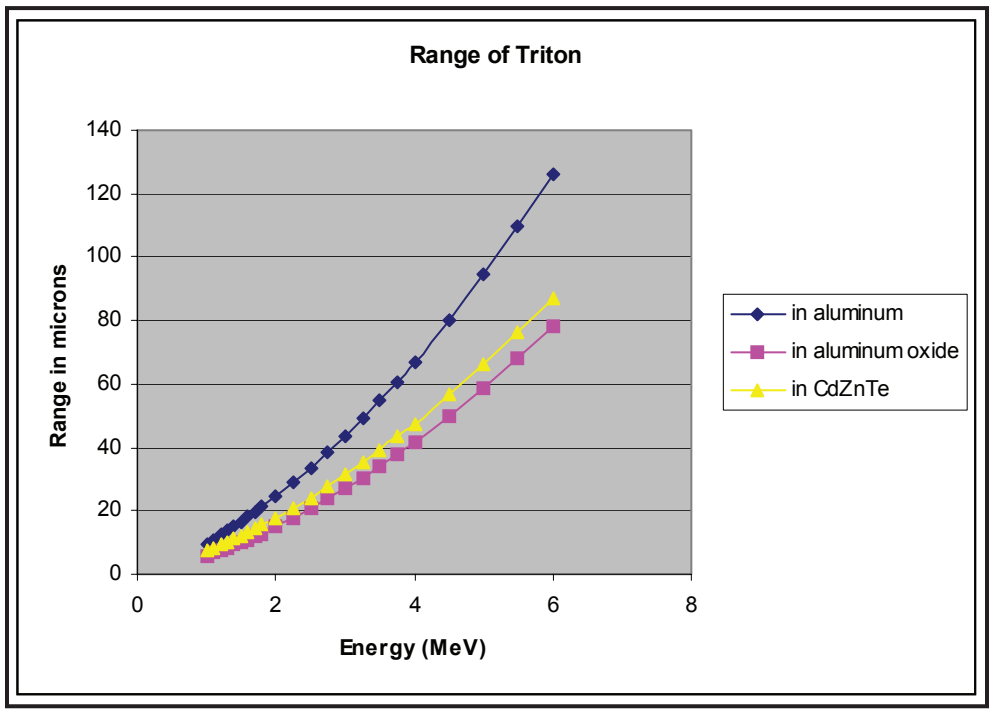

Figure 2. Range of tritons (^{3}H) (calculations made using SRIM)

Scintillator Light Detection

The aforementioned quantum wire structures are also sensitive to light. An additional research area could be to investigate if these thin structures could also be used to detect the light from a radiation interacting in a scintillator. In this case, these structures would be highly compact and allow for a position-sensitive detector.

Project

We fabricated a mask for a prototype with micron-scale wires for use with established lithographic and etching techniques. Structures using a variety of materials may be built both as learning devices and to check predictions. The prototype will be implemented on a glass substrate containing patterned electrodes that will allow evaluation of the detector's spatial sensitivity to eliminate bulk effects arising from the use of silicon (Si) or other substrates. Thick films of semiconductor material will be deposited on the patterned glass substrate, which will then be lithographically patterned and etched

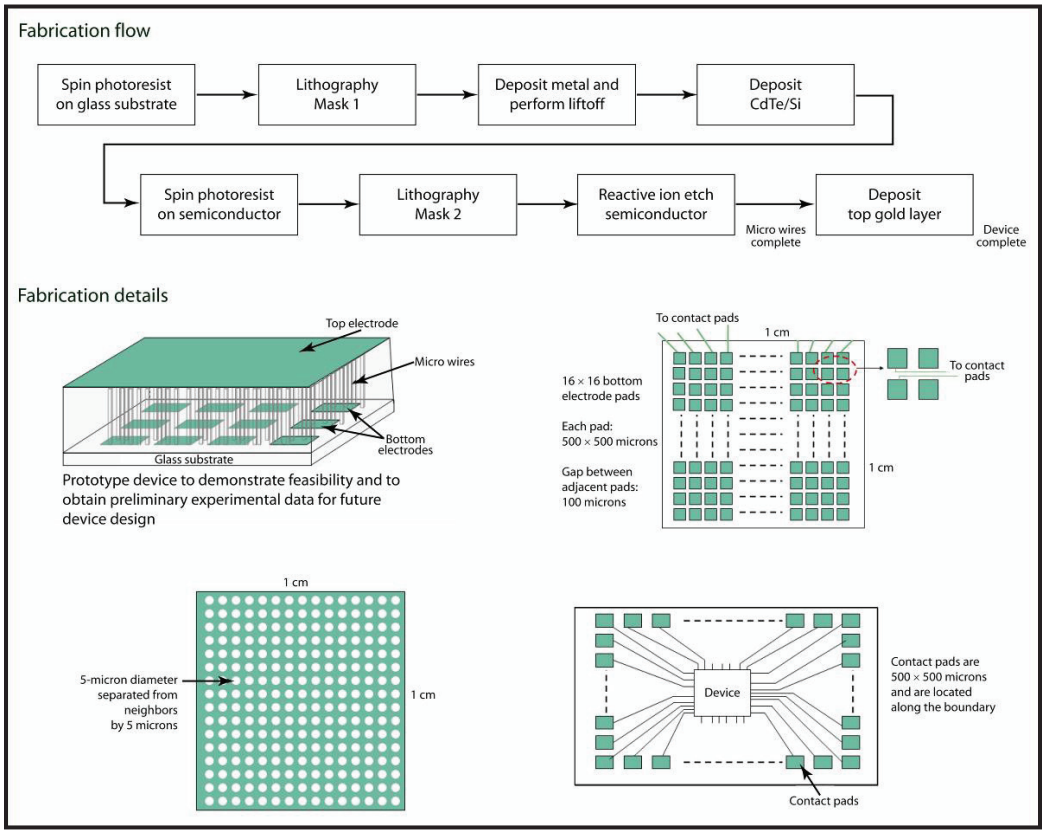

Figure 3. Fabrication flow chart and diagrams of mask and device

to create the semiconductor microwires. The fabrication experience and characterization results will be used as guides for future implementation of the high-performance quantum wire radiation detector. Equipment for device characterization and a photoresist spinner were ordered for the project. The device configuration design was completed, the mask layout finalized, a mask fabrication vendor was identified, and masks were fabricated. The mask will be used to create the metal pattern for the bottom electrodes. The semiconductor material will then be deposited on the defined electrodes.

A fabrication map and other mask fabrication details are shown in Figure 3, while a photograph of the completed mask and a scanning electron microscopy (SEM) image of a cross section appear in Figure 4.

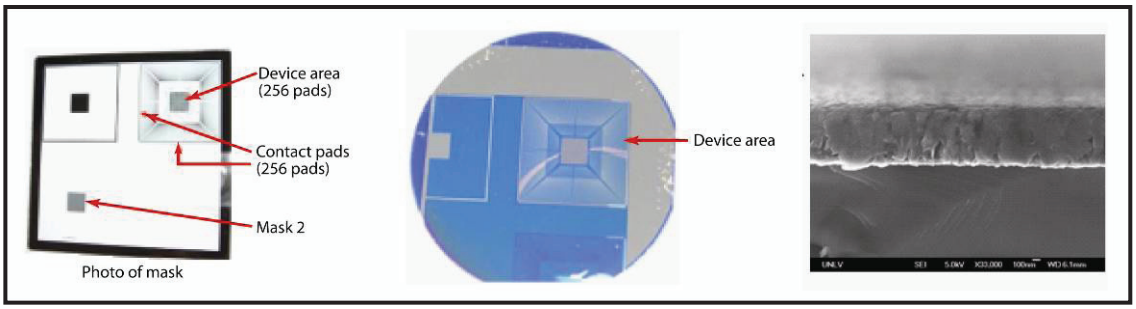

Figure 4. Completed mask and cross-sectional SEM image of potential semiconductor of Si substrate

Conclusion

By the end of this effort, we had manufactured the mask. A structure containing pillars with diameters on the order of a micrometer will be constructed as a proof of concept. The choice of material for the wires is still being decided. The work would then be extended from micrometer- to nanometer-scale wire to investigate detectors based on quantum wires, where the quantum mechanical confinement is expected to enhance collection efficiency. The quantum wires can be implemented using a nonlithographic nanofabrication technique developed at UNLV. Various trade-offs for fabrication are still being considered. Different materials may be used for the nanowires, e.g., cadmium telluride (CdTe) or tantalum oxide (Ta_2O_5). For tantalum oxide, the technique is to deposit a thin layer of, e.g., tantalum (Ta), on the semiconductor surface, followed by the deposition of an aluminum layer. Next, the aluminum film would be anodized to form an alumina template with the substrate as the back contact. A two-step anodization process would improve pore uniformity and periodicity. The Ta layer would then be oxidized by reanodization in citric acid. During this process, the tantalum oxide (Ta_2O_5) would grow inside the pores of the alumina template, forming nanopillars. The porous

alumina layer would then be removed by etching in a phosphoric/chromic acid solution to form freestanding Ta_2O_5 pillars. Reactive ion etching would be used to transfer the pillar structures to the substrate material, thus forming the desired quantum wires.

Acknowledgment

The author would like to thank Biswajit Das of the University of Nevada, Las Vegas, for his substantial contribution to this research.

References

Knoll, G. F., *Radiation Detection and Measurement*, 3rd ed., John Wiley & Sons, New York, 2000, 505–536.

Ziegler, James, "The Stopping and Range of Ions in Matter," http://www.srim.org/, accessed May 10, 2007.

Boron Materials for Neutron Detection

Clare Kimblin,[1] *Harry McHugh*
Special Technologies Laboratory

In collaboration with University of California, Santa Barbara (UCSB), Professor Guillermo Bazan and his researchers, we synthesized and characterized new luminescent, boron-rich conjugated polymer (CP) materials with promising optical and electronic properties. In addition, we evaluated radiation effects on the optical properties of conjugated polymers as thin films and in binary solutions. Scintillation was observed when certain polymers were exposed to a Platts-type pulsed x-ray source; however, no significant scintillation was seen when polymer films were exposed to a neutron source. In addition to investigating optical properties, we designed and fabricated a low-band-gap, polymer-based electronic device on a boron carbide substrate. The device could be used to determine whether neutrons incident on an adjacent boron-carbide film can be detected by measuring current flow (or charge spikes) as a result of neutron conversion by boron and subsequent alpha-induced ionization within the polymer.

Background

Improving current capabilities for identifying proliferant signatures requires innovative methods of detecting special nuclear material (SNM). Our work aimed to advance materials synthesis on the molecular scale by creating and evaluating new boron-rich polymers and semiconducting polymer-based electronic devices whose optical and/or electronic properties may be exploited for use in neutron detection. One goal was to preliminarily explore the optical properties of high-neutron-cross-section, luminescent conjugated polymers as both neutron converters and alpha track indicators. A second goal was to explore the use of semiconducting polymer devices containing ^{10}B for neutron sensing. Indeed, a semiconducting boron/carbon alloy that yields single neutron detection with insignificant gamma sensitivity has been reported (Robertson, 2002). Conjugated-polymer semiconductors are easier to fabricate than traditional semiconductors, and advances in printing electronics may one day permit fabrication of lightweight, flexible/formable, scaleable plastic neutron sensors. Large-area detectors are required to detect the low neutron flux associated with SNM. Portal monitoring is a potential use of a large array, where the goal of shorter integration time requires large cross-sectional areas for detection.

[1] kimblicw@nv.doe.gov, 805-681-2257

Thermal neutrons are converted to energetic particles by high-neutron-cross-section atoms. Examples of naturally occurring high-neutron-cross-section nuclei are ^{3}He (5330 barns), ^{7}Li (942 barns), ^{10}B (3838 barns), ^{113}Cd (19800 barns), and $^{157,155}Gd$ (259000 and 49700 barns) (Friedlander, 1981). While ^{113}Cd and ^{157}Gd are exceptionally high-cross-section nuclei, their neutron capture produces highly energetic gamma rays that pass through thin detector materials without eliciting a detectable response. Conversely, the interaction of boron nuclei with neutrons produces highly energetic alpha particles (Equation 1) with significantly shorter mean-free-paths than high-energy gamma radiation.

$$^{10}B\ (^{1}n, \alpha\ (1.47\ MeV), ^{7}Li\ (0.84\ MeV)) \qquad \sigma_n = 3838\ barns \tag{1}$$

Despite a smaller neutron cross section, a 20-μm thickness of ^{10}B will convert 60% of incident thermal neutrons. Subsequently, the highly charged alpha particle produced will be stopped in ~2 μm of ^{10}B (at 19.8% natural abundance). In a silicon semiconductor, the strongly ionizing alpha particle can generate 10^5 electron-hole pairs. Boron has the further advantage of being a nonmetal that has been successfully incorporated into luminescent conjugated polymers and semiconductors.

Based on these properties, we anticipated that an ideal material for neutron capture and sensing might be a homogeneous, boron-rich, conjugated polymer within which a neutron is converted to an alpha particle, causing an optical and/or electronic signature within the conversion medium. Capture material thickness would then not be compromised by a need for the alpha particle (with shorter range) to exit and cause an observable change in a second sensing layer. High-cross-section, heterogeneous, boron-loaded polymer scintillators are commercially available from Saint-Gobain and have been reported by Z. W. Bell (2003).[2] In both the Saint-Gobain and Bell polymers, however, the fluorophore is a separate constituent blended into the polymer. The use of a homogenous material in which the fluorophore or electronic indicator were itself boron-rich would allow for thinner, single-layer converter/absorber materials with equally high concentrations of boron converter and alpha track indicator, enabling higher sensitivities.

To achieve this goal, we fabricated and investigated the optical properties of boron-rich fluorescent polymers. We also created a polymer semiconducting device on a boron-carbide film. Due to complications in attaching electrodes, and a shortage of high-quality boron-carbide films, we could not test the device in FY 2006.

[2] Z. W. Bell et al. report a heterogeneous blend of carborane, chemically bonded to a silicone rubber, and a scintillator. Material containing up to 18% boron by weight was prepared.

Project

Synthesis of Neutron-sensitive Solutions and Thin Films

Based on the properties described above, we sought fluorescent, conjugated polymers with a boron content of >20% by weight. Since such polymers were not available, we synthesized them. Our first consideration was to significantly increase boron content in conjugated polymers by covalently attaching boron-rich, cagelike structures. Initially, however, a more straightforward method using ion exchange was pursued. By exchanging boron-rich anions for bromide, boron-rich luminescent polymers were fabricated in Guillermo Bazan's laboratory at UCSB. The reaction concept appears in Figure 1.

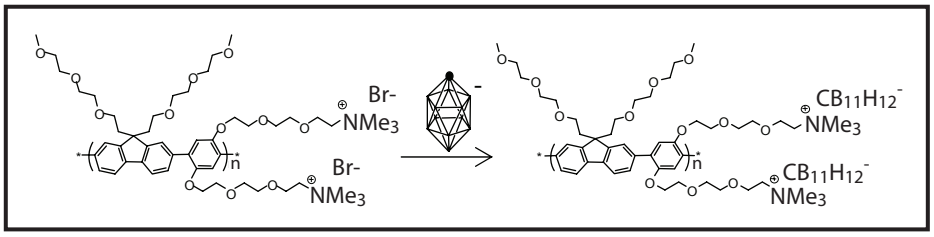

Figure 1. PFP-Br (left). Bromide ion is exchanged with carborane anion to produce PFP-$CB_{11}H_{12}$. A boron atom is indicated by each vertex of the cage structure above, with carbon represented by the black circle at the apex of the cage.

Characterization techniques suggested that more than half the bromide ions were exchanged for a boron-rich anion in PFP-$CB_{11}H_{12}$.

Measurements of Fluorescence and Scintillation Yield

As documented in Table 1, the quantum yields of polyfluoro-alt-phenylene (PFP) polymer compounds in solution resemble those of the parent polymer PFP-Br, and range from 65% to 78%. Stoke's shifts were also similar to those of the parent polymer, PFP-Br (40 nm). Quantum yields of polymer films are considerably lower. Table 1 also includes quantum yields of fluorescent-conjugated polymers containing little or no boron. We also investigated these polymers as neutron indicators because they are potentially suited to functionalization with a boron constituent or for use in a blend (e.g., with boron carbide nanoparticles) or with a boron converter layer. We compared optical properties of solutions and films of PFP-neutral, PFP-Br, 5-(2'ethyl-hexyloxy)-*p*-phenylene vinylene (MEH-PPV) (10-µm-thick film), and a neutral boron-linked polythiophene (PTh-BPh)[3]

[3] Sample provided by Professor F. Jaekle (Rutgers University).

with a 21% quantum yield but impressive 100-nm Stoke's shift (Sundararaman, 2005). As a reference, we used a Saint-Gobain blended polymer (BC-454, natural boron-loaded plastic scintillator, 10 mm diameter, ~3 mm thick).[4]

While it was clear that the polymers were all fluorescent in solution and as solids, it was not known whether the polymers in solution or as thin films would scintillate. To test for scintillation, we used a pulsed (100-ns-wide pulse), Platts-type x-ray source to irradiate binary solutions and pure polymer thin films. Relative scintillation peak heights appear in Table 1, Column 5. PFP-type polymers that were dissolved in aromatic solvents scintillated. Of note, PFP-neutral (1% in toluene) demonstrated 62% scintillation output relative to the BC-454 reference. PTh-BPh (3% in toluene) had the second highest scintillation output.

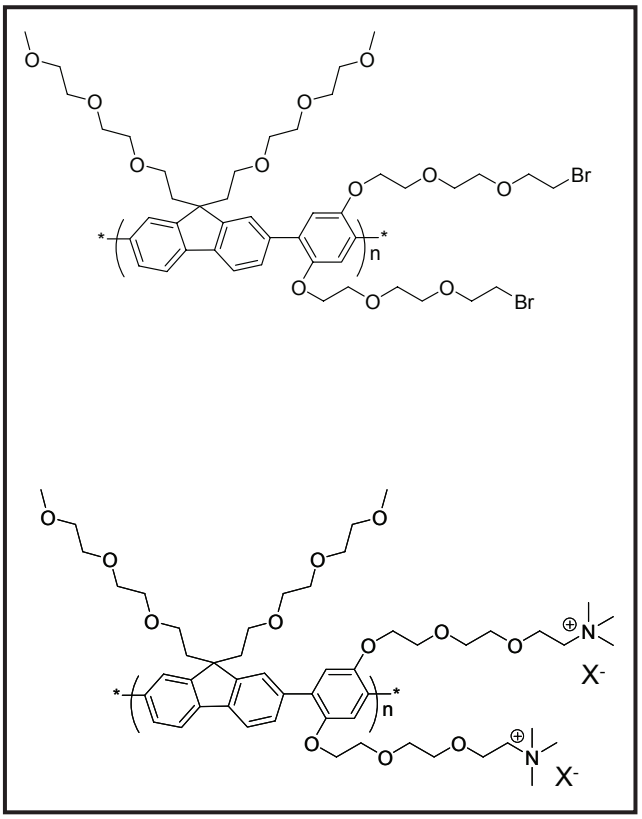

Figure 2. Structures of PFP-neutral (top) and PFP-X (bottom). Refer to Table 1.

[4] BC-454 has a reported scintillation light output of 48% anthracene, and is composed of polyvinyl toluene (>85% by weight), natural boron (5% by weight), and aromatic fluorophores (<5% by weight).

Table 1. Column 2 provides traditional fluorescence quantum yields (FQY) in units of percent anthracene. Column 3 indicates the solvent used for the FQY measurement. Column 4 provides FQY for films in units of peak height relative to BC-454. Column 5 shows the scintillation percentage of solutions and one film, relative to BC-454. Scintillation solution compositions appear in Column 6. Figure 2 shows the structures of PFP-neutral (top) and PFP-X (X = Br^-, $B_{11}H_{14}^-$, $CB_{11}H_{12}^-$) (bottom).

Polymer	FQY in solution (% anthracene)	Solvent used for QY quantification	FQY as film (% anthracene)	Scintillation Output (% BC-454)	% polymer by weight in solvent used for scintillation study
BC-454	48 (% anthracene)	PVT[$]	Unknown	100	<5% fluors in PVT
PFP-neutral	78.2	Chloroform	8.2	62	1% in toluene
PFP-$B_{11}H_{14}$	65	Toluene	5.5, 15.6*	12	1% in toluene
PFP-$CB_{11}H_{12}$	66.9	Acetone	5.4	1.5*	2% in acetone[^]
PFP-Br	69.7	Water	6, 17.7*	1.7*	1% in methanol[^]
PTh-BPh	21	Methylene chloride	Unknown	17	3% in toluene
MEH-PPV	15.6	Toluene	NM (expect ca. 10%)	Negligible	1% in toluene
PFP-neutral film	x	none	(8.2)	1	Thin film
Toluene	x	x	x	0.3	Toluene only

[$]PVT = polyvinyltoluene

[#]PFP and MEH-PPV solution quantum yields (QYs) were measured using a fluorescein standard (10^{-5} M in water, pH = 11, and QY = 92%). For QY measurements, PFP polymer concentrations were adjusted to 0.01 mg/ml with the QY solvent listed.

NM = not measured.

***QY of film increased after 4–5 minutes irradiation**

[^]Unsuitable, aliphatic scintillation solvent. (Suitably solubilizing polar aromatic solvents required. Aromatic solvents should optimize energy transfer from the solvent to the polymer, with minimal quenching.)

Scintillation tests with thin films were less promising. We tested thin film samples (microns thick) on 15 × 15 mm glass slides in airtight film holders. Only PFP-neutral demonstrated scintillation significantly above background (background was measured with a glass slide with no polymer). Possible reasons for low scintillation include quenching via interchain pathways (exacerbated by any impurities), film thickness, and film opacity (films varied in transparency, from fully transparent to cloudy). Polymer dilution in a plastic "solvent," such as polyvinyl toluene, might favor scintillation pathways.

Measurements of Thin Film Neutron Sensitivity

The negligible scintillation from homogeneous thin films did not suggest promising results with a neutron source. To test, we positioned films (some adjacent to an isotopically rich ^{10}B carbide film) in front of a photomultiplier tube (PMT) at a gain of 10^5, and exposed them to a ^{252}Cf source emitting 10^4 neutrons per second. In the initial configuration we observed false positives that we attributed to gamma radiation emitted by the ^{252}Cf source, making it necessary to shield the PMT. Shielding was achieved by placing the ^{252}Cf source in a high-density polyethylene enclosure, with the PMT and sample in a lead cylinder with hevimet doors. The most strongly scintillating, and therefore most promising, film (PFP-neutral) was positioned adjacent to a boron-carbide converter film (0.7–1.1-μm thick, on 70-nm chromium), ~10 cm from the source. No statistically significant neutron response was observed. We tested other films, with similar outcomes. Film thickness, opacity, and possible impurities that quench scintillation are all likely to impede detection. Despite being stronger scintillators in solution, we did not rigorously test solution samples with the neutron source because the low boron content in the dilute samples would not have led to appreciable neutron conversion. We have begun synthesis on a neutral polymer with covalently bound carborane groups (Figure 3). Covalent attachment of carborane directly to the polymer backbone would ensure that two carborane cages would be attached per repeating unit, yielding a polymer that is 20% boron by weight. Additionally, neutral polymers are more soluble in traditional scintillating solvents.

Neutron Detection by Charge Deposition

To determine if a semiconducting polymer device indicates the presence of an alpha ionization track generated by neutron conversion in the adjacent B_4C layer, our team built a simple, semiconducting polymer device on a boron-carbide platform. McHugh has demonstrated that amorphous silicon diodes on boron-carbide substrates detect neutrons by generation of electron-hole pairs in the silicon (2006). We hoped to determine whether or not a more easily fabricated, polymeric semiconductor layer could be used. If successful, layers of a boron-loaded polymer could eventually be used, negating the need for a boron-carbide substrate. The basic concept was simulated by sandwiching a polymer mixture used in solar cells (PCBM [[6,6]-Phenyl-C_{61}-butyric acid methyl ester, electron acceptor] and P3HT [poly(3-hexylthiophene, semiconducting polymer]) between a gold-coated, 17 × 17 mm boron-carbide substrate and aluminum cathodes (Figure 4).

Due to fabrication issues, we were unable to test the ability of the organic semiconducting device to convert alpha energy to a charge detectable under reverse bias. Two devices were fabricated, but the material deposition on the conductive boron carbide/chromium substrate was likely too uneven to hold off bias voltages, and the devices were shorted. Additional boron carbide substrates were not available in FY 2006; hence, additional devices could not be tested.

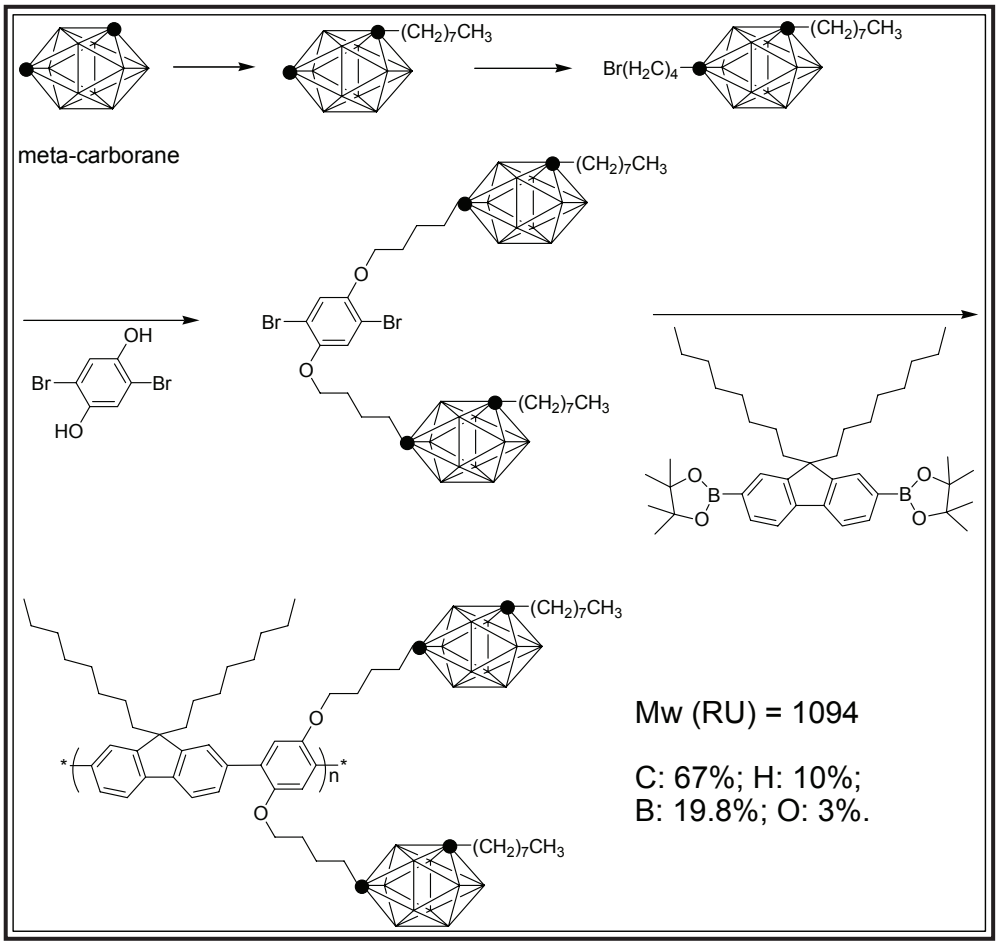

Figure 3. Synthesis of neutral boron-rich (20% B by weight), luminescent conjugated polymer.

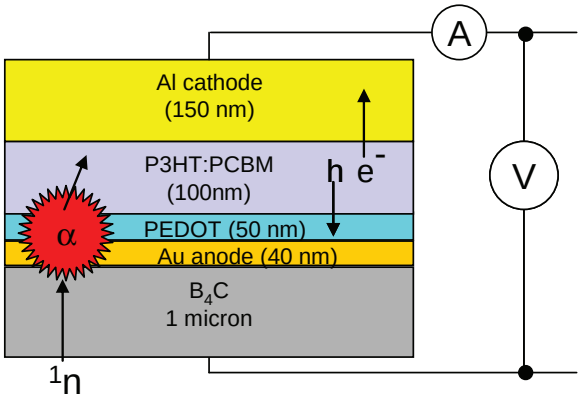

Figure 4. Device with polymeric low-band-gap material (P3HT:PCBM) on a boron-carbide substrate. PEDOT (poly(3,4-ethylene-dioxythiophene)) helps create a smooth surface for P3HT:PCBM deposition and lowers the hole injection barrier.

Conclusion

We have assessed the optical properties of a variety of conjugated polymers. Two new, boron-rich (up to 20% B), ionic, fluorescent-conjugated polymers, PFP-$B_{11}H_{14}$ and PFP-$CB_{11}H_{12}$, have been synthesized and characterized. In solution, their quantum yields were >60%, but significant scintillation was observed only for the neutral polymer with no boron content, PFP-neutral (1% solution in toluene). PFP-$CB_{11}H_{12}$ and other polar polymers we tested were in poor scintillating solvents and should be tested in polar aromatic solvents. Based on the scintillation output of the neutral PFP polymer, a neutral boron-rich conjugated polymer that will have two carboranes covalently attached per repeating unit (giving 20% boron by weight) has been designed, and monomeric precursor synthesized. Of the thin films, only PFP-neutral had reasonable scintillation output, and that was only 1% of BC-454. Fluorescence quantum yields are significantly lower in films than in solvents, and the films' quantum yields may be too low to detect significant scintillation. This points to the utility of a scintillation solvent for energy transfer to the polymer with minimal quenching. We anticipate that dilution of luminescent polymers in a traditional plastic scintillator solvent (e.g., PVT) would improve scintillation output. We observed no statistically significant neutron response with thin films in the presence of a neutron source. Despite greater scintillation strength in solution, we did not rigorously test solution samples with a neutron source because the boron content in the dilute samples would not have led to appreciable neutron conversion. Future work may explore the use of plastic solvents such as polyvinyltoluene, polyboronates, borate sol-gels, or boron nanoparticles.

In addition to investigating optical properties, we designed and fabricated a low-band-gap, polymer-based electronic device. Due to fabrication issues, we could not test a viable device this year. If future funding is obtained, this device could be used to determine whether neutrons incident on an adjacent boron-carbide film can be detected by measuring current flow (or charge spikes) as a result of neutron conversion by boron and subsequent alpha-induced ionization within the polymer. If devices demonstrate promising results, methods to create a boron-rich semiconducting layer could be investigated. Possible methods include use of a conjugated organoboron polymer layer or the addition of boron nanoparticles to a known semiconducting plastic.

Acknowledgments

Polymers were synthesized, and characterized solutions, films, and devices were provided by Guillermo Bazan (professor), Corey Hoven (graduate student), and Fuke Wang (post-doc), of UCSB. The authors would like to thank the following STL employees: John Di Benedetto, Steve Lutz, Kirk Miller, Jim Tinsley, Mike Grover, Glen Anthony, Rod Tiangco, and Wayne Lenhard, for helpful discussions and/or aid in performing tests. Additionally, we thank Paul Puskarich (U.S. Department of Homeland Security scholar and summer intern), who helped to perform neutron tests; Paul Stradins (National Renewable Energy Laboratory), for a donation of $^{10}B_4C$-sputtered

slides; and Frieder Jaekle (professor, Rutgers University), for giving us a sample of PTh-BPh. We also thank Graca Vicente (professor, Louisiana State University) and Bruno Fabre (professor, Université de Rennes), for a sample of a carboranyl pyrrole polymer (results not described in this report).

References

Bell, Z. W., L. Maya, G. M. Brown, F. V. Sloop Jr., "Boron-loaded Silicone Rubber Scintillators," Y/DX-2540, Oak Ridge National Laboratory, Oak Ridge, Tennessee, 2003.

Friedlander, G., J. W. Kennedy, E. S. Macias, J. M. Miller, *Nuclear and Radiochemistry*, 3rd ed., John Wiley & Sons, New York, 1981.

McHugh, H., K. Moy, "Multilayer solid-state neutron detector," *Nevada Test Site–Directed Research, Development, and Demonstration*, FY 2005, Bechtel Nevada/National Security Technologies, LLC, Las Vegas, Nevada, 2006, 143–149.

Robertson, B. W., S. Adenwalla., A. Harken, P. Welsch, J. I. Brand, P. A. Dowben, J. P. Claassen, "A class of boron-rich solid-state neutron detectors," *Appl. Phys. Lett.* **80**, 19 (May 2002) 3644–3646.

Sundararaman, A., M. Victor, R. Varughese, F. Jaekle, "A family of main-chain polymeric Lewis acids: Synthesis and fluorescent sensing properties of boron-modified polythiophenes," *J. Am. Chem. Soc.* **127**, 40 (2005) 13748–13749.

this page intentionally left blank

Reactive Optical Diffractive Materials for Sensing Nerve Agents

Clare Kimblin,[1] *Roderick Tiangco*
Special Technologies Laboratory

This project built on FY 2005 work, in which we reported a new method amenable to the remote sensing of toxic organophosphates (OPs) (Kimblin, 2006). Our method paired an enzyme inhibited by OPs with a reflective hologram encapsulated in a reactive, hydrated hydrogel. The hydrogel is affected by the production of charge within it, and swells due to protonation by an acid generated from enzyme activity. Swelling results in a red shift of light reflected by the embedded hologram. The reflective material's ability to colorimetrically indicate the presence of OPs was demonstrated using the OP enzyme inhibitor paraoxon (POx) and the enzyme butyrylcholinesterase (BuChE). In the absence of POx, a 60-nm visible shift in Bragg-reflected light was observed, but in the presence of POx, the red shift was rapidly quenched. In FY 2006, a lower detection limit (1–5 μM POx, where 2.5 μM POx = 0.68 mg/L solution) was established using BuChE, and a method to induce a color change in the presence of inhibitor was demonstrated. Additionally, an OP-hydrolyzing enzyme, organophosphorous hydrolase (OPH), was used to directly indicate the presence of POx with a color change, though with diminished sensitivity. OPH activity was maintained following its attachment to a neutral hydrogel, with no decrease observed after repeated uses over a four-day period. The role that reflective holographic materials could play in remote detection was shown by employing a simple setup comprising a white-light source, mirror, and telescope. Reactivity studies were performed using flow cells with removable windows, upon which holograms had been fabricated.

Background

Chemical sensors of nerve agents are required for nonproliferation monitoring and interdiction (NNSA), and for protection of civilians and troops (U.S. Department of Homeland Security, U.S. Department of Defense). Discrete methods amenable to the remote detection of OPs would provide safe alternatives to handheld devices. In an effort to create a low-power or unpowered sensor that detects OPs remotely and without an RF signal, we paired either a cholinesterase enzyme inhibited by OPs, (BuChE), or a hydrolytic enzyme that reacts directly with OPs, (OPH), with reflective holographic materials.

Funding for this project began in FY 2005, when we demonstrated that BuChE could be paired with a reflective holographic material to indicate the presence of POx. In FY 2006, detection techniques

[1] kimblicw@nv.doe.gov, 805-681-2257

and limits were improved. Additionally, a second class of hydrolytic enzymes was used for direct OP sensing. We found that, when attached to a hydrogel, OPH stability was improved, and the bound enzyme could be used repeatedly for POx detection.

Material Overview

Reactive Hologram

Changes in pH and other solution reactivity can be monitored by observing shifts in the wavelength of light reflected by holographic gratings embedded in reactive, swellable hydrogel films (Marshall, 2003). The wavelength of light diffracted by the grating, and thus the apparent hologram color, are directly proportional to the fringe spacing, in accordance with Bragg's law:

$$m\lambda_{max} = 2nd \sin \theta, \quad \textbf{(1)}$$

where:

m = diffraction order

λ_{max} = diffracted light wavelength

n = average refractive index

d = spacing between diffracting planes

θ = angle of light incident on, and reflected from, diffracting planes.

To minimize charge repulsion and because of osmotic effects, a hydrogel with charged (anionic or cationic functionalities) absorbs more water into its pores than a neutral hydrogel (Mayes, 2002). Solvent migration into, or out of, the hydrogel results in swelling or shrinking, respectively. This solvent migration also affects the grating spacing. Volume changes within the material lead to an increase or decrease in the spacing, d, between silver fringes and bring about a shift in the Bragg-reflected wavelength.

Light diffracted by the holographic material will be red-shifted due to solvent migration into the hydrogel (hydrogel swelling → increase in d) and blue-shifted due to solvent migration out of the hydrogel (hydrogel shrinkage → decrease in d).

Butyrylcholinesterase (BuChE)

Cholinesterases (ChE), such as acetylcholinesterase (AChE) and butyrylcholinesterase (BuChE), catalyze the hydrolysis of the neurotransmitter acetylcholine (ACh^+) (Equation 2). In doing so, they "turn off" the nerve impulse triggered by ACh^+. One hydrolysis product is acetic acid. Thus, in the presence of excess acetylcholine substrate, the solution pH decreases as the reaction proceeds, at a rate of ~50 μs/turnover (Millard, 1999).

$$ACh^+ + H_20 \xrightarrow{ChE} acetate^- + H^+ + choline^+ \quad \textbf{(2)}$$

The molecular structures of substrates ACh^+ and acetylthiocholine (ATC^+), and the OP ChE inhibitor POx are presented in Figure 1.

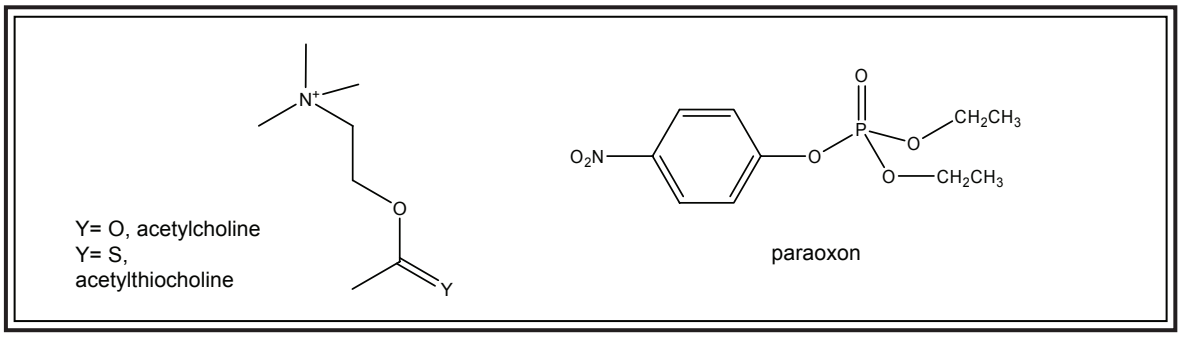

Figure 1. Molecular structures of the choline substrates (left) and the organophosphate ChE-inhibitor POx (right). POx blocks the ChE active site, preventing turnover of ACh and ATC.

Toxic OPs interfere with nerve impulse transmission because they inhibit the active sites of ChEs and prevent the breakdown of acetylcholine to choline and acetic acid (Equation 3) (Rand, 2004).

$$ACh^+ + \text{“OP”} \xrightarrow{ChE} ChE - \text{“OP”} + ACh^+ \quad \textbf{(3)}$$

We paired a pH-sensitive holographic material that responds optically to pH changes with BuChE and excess choline substrate (ACh^+ or ATC^+). In the absence of inhibitor (and added base) ATC^+ turnover results in the production of acetic acid, with a resultant observable color change. Under these conditions, no color change is observed in the presence of inhibitor (POx). The contrast between the control response (no POx) to the experimental (in the presence of POx) would permit identification of inhibitor. We also altered reaction conditions (by addition of base) such that detection would not rely on comparison to a control reaction. This enabled us to demonstrate a sensor using BuChE in which a color change directly indicated the presence of organophosphate inhibitor.

Organophosphorus Hydrolase (OPH)

Rather than being inhibited by OPs, the enzyme OPH hydrolyzes P-I, P-S, and P-O bonds in all presently known neurotoxins, including P-F bonds in sarin and soman, as well as certain OP pesticides (such as POx and parathion). In cleaving P-O, P-F, P-S, or P-CN bonds, two protons and an alcohol are generated (Mulchandani, 2001) (Figure 2).

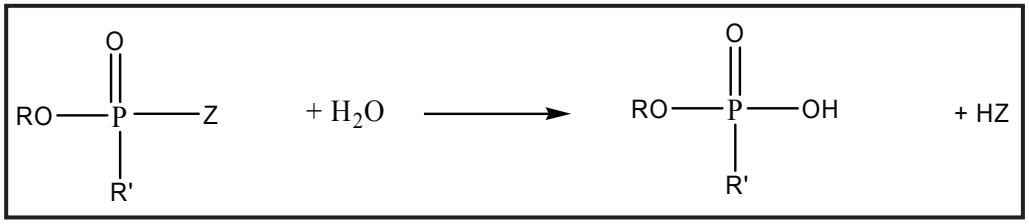

Figure 2. Hydrolysis of phosphorus bonds

We demonstrated the use of a reflective hologram to generate a color change resulting from hydrogel protonation by POx hydrolysis products. Using OPH, we demonstrated that the acid produced directly from OP hydrolysis can be used to protonate a pH-sensitive hologram, thus eliciting a direct colorimetric response in the presence of POx, without the need for another substrate and without inhibition of the enzyme. Because the amount of POx present directly determines the amount of acid produced, detection limits were considerably higher. The system could be used repeatedly following exposure to POx, however, since the method does not rely on enzyme inhibition.

Project

Hologram Fabrication and General Setup

To quantitatively measure diffraction wavelength from the windows of the flow cell, we used an Ocean Optics spectrometer (HR2000CG-UV-NIR) in our setup (Figure 3). We exposed holograms at a 4° angle, such that white light incident on the hologram reflected diffracted light without simultaneously back-reflecting the white-light source. We then fed buffer, enzyme, inhibitor, and ATC (in BuChE tests) into the flow cell by adding the solutions to the cuvette. In the first project phase (FY 2005), all reactions were performed in a cuvette that also contained a hologram on a glass microscope slide. Due to uneven hydrogel application and curing, and/or poor penetration of silver ions into the slightly hydrophobic hydrogel pores, these holograms were frequently nonuniform in their appearance, and only small portions of a slide reflected brightly. In FY 2006, we improved hydrogel uniformity by optimizing monomer solution volume added to the windows and by curing beneath an optical flat. Silver uptake was enhanced by protonating the hydrogel with perchloric acid prior to adding a silver perchlorate/perchloric acid solution.

BuChE Tests

After repeated testing, we determined the conditions for optimal sensitivity. Variables included buffer concentration and pH, enzyme amount, substrate concentration (ATC), POx concentration, and "incubation" time. We performed tests by first flowing buffer through the flow cell until a constant diffraction wavelength was reached. Wavelength shifts were recorded versus time. We conducted the inhibition tests in the same manner but added inhibitor to the enzyme solution 5 minutes before

adding POx. Under these conditions, the maximum diffraction shift reached 30 nm in ~20 minutes. In the presence of 1-µM POx, the shift was quenched. Greater dilution of the generated acid resulted in longer response times (Figure 4).

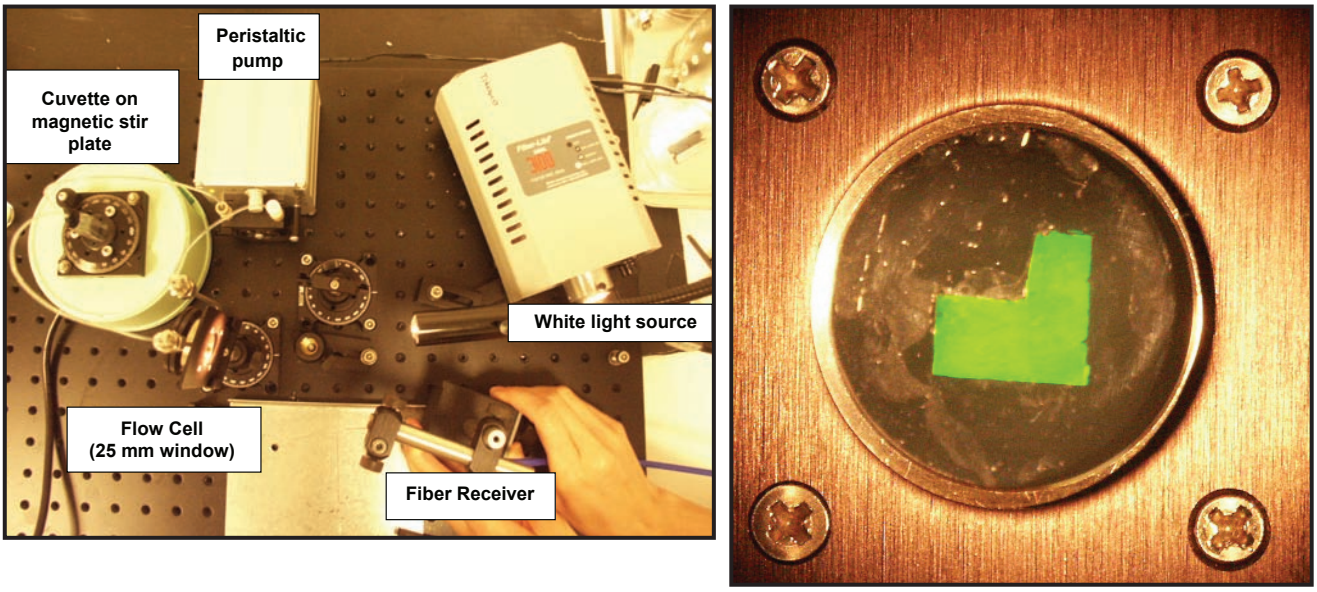

Figure 3. (left) Setup viewed from above workbench; (right) L-shaped hologram (used for most tests) on 25-mm window in flow cell

Addition of Base to Yield Direct Color Change

In an effort to create a system with the sensitivity afforded by BuChE and ATC that demonstrates a color change in the presence of POx, we created a scheme involving base addition. We determined the amount of base required to exactly counteract all of the acid created by the hydrolysis of ATC to acetic acid by BuChE. In the presence of the inhibitor, POx, an un-neutralized base would lead to a blue shift.

Results were very promising. The presence of 4-µM POx (red line) was indicated by a 28-nm blue shift (40 nm when using a new hologram), whereas in the absence of inhibitor (purple and green lines), a blue shift was seen only initially (until sufficient acid was generated to neutralize the base present) (Figure 5).

OPH Tests

A change in diffraction wavelength in the presence of POx was indicated directly by using the hydrolytic enzyme OPH. The presence of 0.47-mM POx was indicated by a 29-nm red shift. Because

the source of acid was the POx itself, detection limits did not compare favorably with those obtained using BuChE and ATC. However, the method could be directly applicable to detection of higher concentrations of organophosphate pesticides since they are toxic to humans at higher levels than organophosphate nerve agents. Furthermore OPH is *not* inhibited by OPs and is stable when attached to a hydrogel; therefore, the system can be used repeatedly.

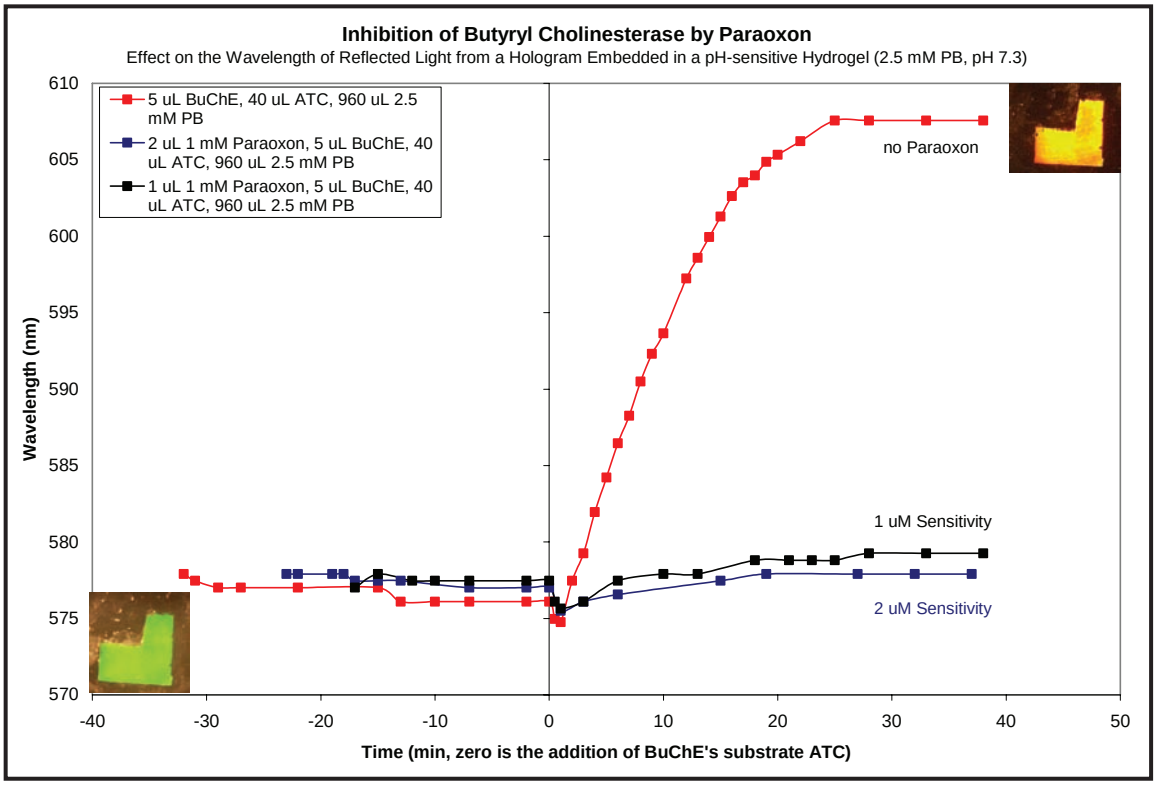

Figure 4. BuChE-inhibition test results demonstrating the difference between inhibited and uninhibited BuChE. The uninhibited run is represented by the red line ($\delta\lambda$ = 30 nm). The black line represents inhibition with 1-µM POx, while purple is 2 µM.

Remote Sensing Demonstration

We demonstrated the remote sensing potential of reactive holograms using the setup shown in Figure 6. White light incident on the hologram was diffracted, and Bragg-reflected light was returned to a telescope, placed 26 m away, using a mirror positioned at the appropriate angle. The observed image appears in Figure 6 (inset).

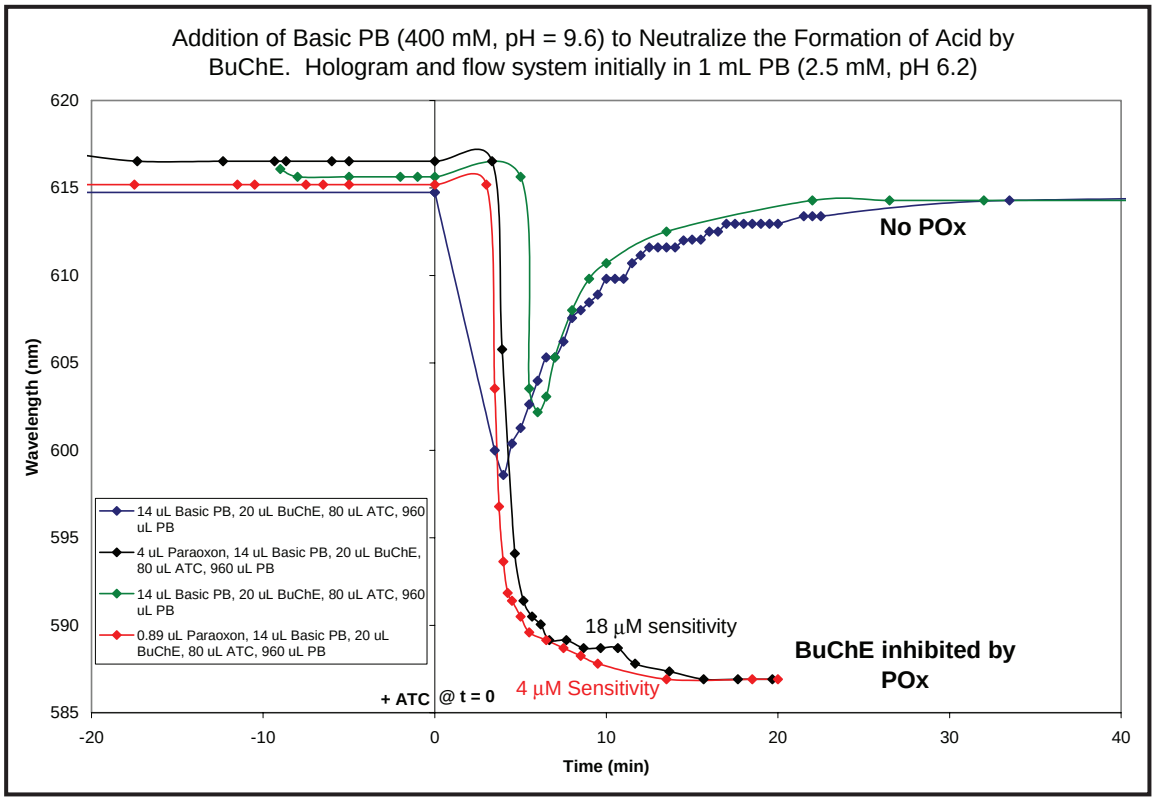

Figure 5. Persistent color change in the presence of POx inhibitor (red and black lines). With no inhibitor (purple and green lines), the original color is retained after an initial shift (prior to complete base neutralization).

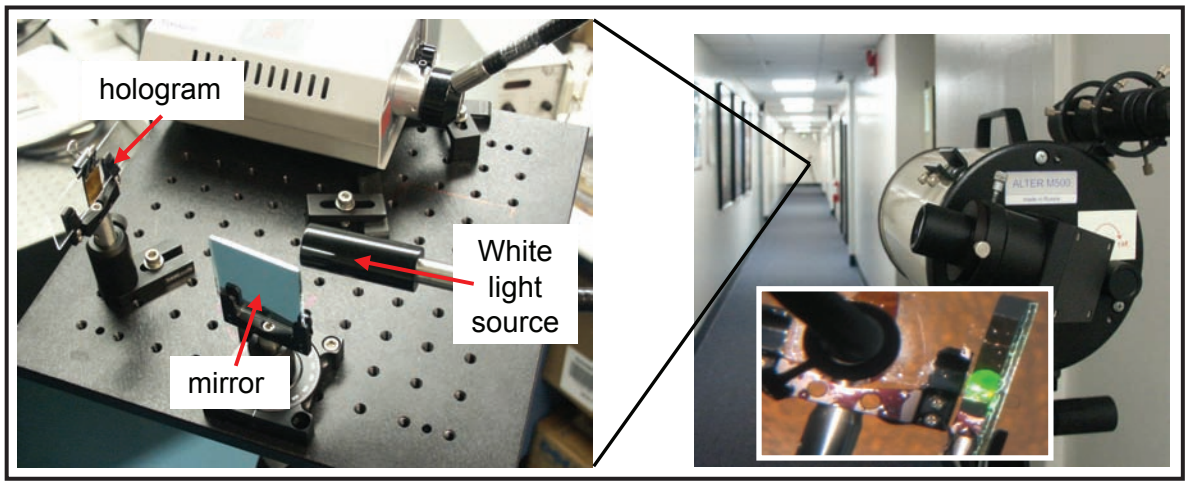

Figure 6. Demonstration of remote sensing application: the platform at the left shows the light source, hologram, and mirror used to send the holographic image to the telescope, placed 26 m away

Conclusion

This project used two enzymes to colorimetrically display the detection of toxic OPs using reactive holograms. We observed 1-μM sensitivity with the BuChE enzyme system and demonstrated a procedure that caused the color change to occur in the presence (rather than absence) of POx. In addition, we demonstrated the utility of a reflective hologram for generating a color change resulting from hydrogel protonation by POx hydrolysis products in the presence of OPH. As expected, detection limits were considerably higher because the amount of POx present directly determined the amount of acid produced. However, since the method does not rely on enzyme inhibition, the OPH system could be used repeatedly. Immobilization of OPH to the hydrogel and repeated use of the sensor was successfully shown. In all cases, detection limits could be improved if hydrogel/hologram thickness and surface area were diminished, to effectively increase the concentration of protonated amines. Furthermore, using smaller solution volumes would generate greater color shifts and more rapid response. Reactive holograms could be utilized for monitoring airborne agents or for continuous monitoring of liquid contamination (e.g., water supply).

While we believe this technology could be further developed to create OP sensors suitable for remote sensing, a significant bottleneck was the lengthy hologram fabrication process (Kimblin, 2006). The ability to print reactive holograms would accelerate the process and permit production of uniform materials. The holograms tested in FY 2006, while brighter, were generally not as responsive as those used in FY 2005. This could be attributed to thicker hydrogel films (more basic groups per surface area) and a higher density of silver in the gratings (more force required to cause a hydrogel volume change). Time did not permit determination of optimal hydrogel thickness and silver densities. Other improvements in the area of remote sensing might include increasing the range of angles over which diffraction occurs, and fabrication of holograms that respond in the infrared or ultraviolet. While this year's work focused on optical changes to indicate the presence of toxic OPs, other applications of swelling hydrogels are foreseen.

Acknowledgments

The authors would like to thank Kory Plakos and Joshua Kimball, of the University of California, Santa Barbara, for help with setting up optical measurements, optimizing assay conditions, and performing tests with BuChE and OPH.

References

Kimblin, C., R. Tiangco, "Reactive Optical Diffracting Materials for Sensing Organophosphates," *Nevada Test Site–Directed Research, Development, and Demonstration*, FY 2005, Bechtel Nevada/National Security Technologies, LLC, 2006, 131–137.

Marshall, A. J., J. Blyth, C. A. B. Davidson, C. R. Lowe, "pH-Sensitive Holographic Sensors," *Anal. Chem.* **75** (2003) 4423–4431.

Mayes, A. G., J. Blyth, R. B. Millington, C. R. Lowe, "Metal ion sensitive holographic sensors," *Anal. Chem.* **74** (2002) 3649–3657.

Millard, C. B., G. Kryger, A. Ordentlich, H. M. Greenblatt, M. Harel, M. L. Raves, Y. Segall, D. Barak, A. Shafferman, I. Silman, J. L. Sussman, "Crystal structures of aged phosphonylated acetylcholinesterase: nerve agent reaction products at the atomic level," *Biochem.* **38** (1999) 7032–7039.

Mulchandani, A., W. Chen, P. Mulchandani, K. J. Wang, K. Rogers, "Biosensors for Direct Determination of Organophosphate Pesticides," *Biosensors and Bioelectronics* **16** (2001) 225.

Rand Corporation (W. Augerson), "A Review of the Scientific Literature as it Pertains to Gulf War Illnesses; Chapter 5: Nerve Agents," http://www.rand.org/pubs/monograph_reports/MR1018.5/, accessed December 15, 2004.

this page intentionally left blank

Coded Aperture Imaging for Location of Nuclear Materials

Brian Cox, Daniel Marks[1]
Los Alamos Operations

The goal of this project was to develop a coded aperture capable of operating at variable fields of view (FOV) for the purpose of identifying a single source. While typical coded apertures can change the field of view simply by moving the mask plane, this method would require large distances between the camera and the mask, and a change of angular resolution. We designed a three-layer coded aperture that is capable of restricting the FOV through the positioning of the mask planes (Figure 1). The mask layers are identical copies of the same uniformly redundant array (URA), having an 82 × 82 block pattern consisting of a 41 × 41 base pattern. A general search procedure was studied for identifying point sources in diffuse backgrounds. The masks, placed in close contact for a maximum FOV, are then separated to narrow the field and "focus" on a point. Simulations have shown that the three-layer design is superior to a single-layer mask for source identification when the dominant background is due to diffuse sources in the FOV.

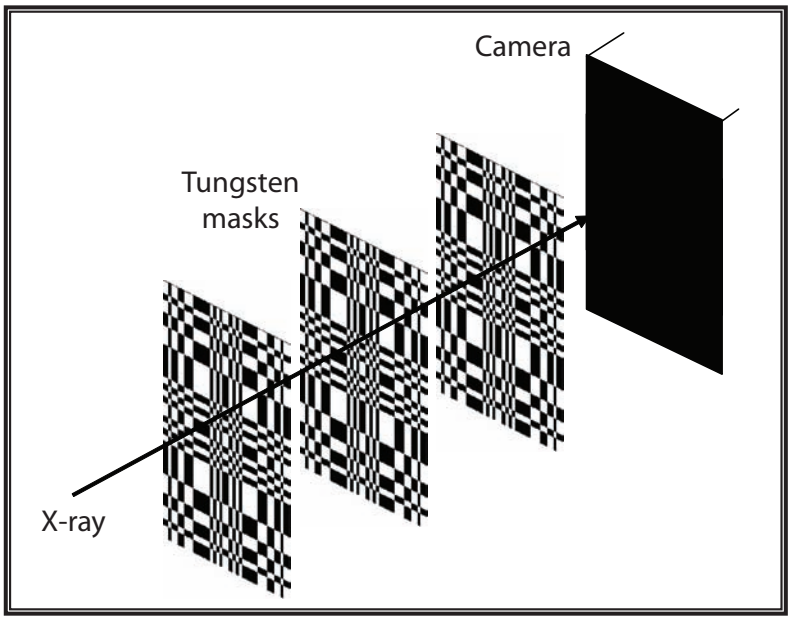

Figure 1. Layout of the three-layer coded aperture camera

[1] marksdg@nv.doe.gov, 505-663-2093

Background

Coded apertures are a well-developed technology in the field of x-ray imaging. Attempts to improve the collecting power of pinhole cameras led to the development of multiple pinhole, zone plate, and, finally, coded aperture cameras based on URAs (Figure 2). In effect, the principle is similar to that of the multiple pinhole camera: the mask pattern is an array of differently sized pinholes; the greater the number of pinholes, the greater the photon collecting efficiency. In a standard URA design, 50% of the photons hitting the mask are collected. Any pinhole pattern can be used to form an image, with the reconstruction performed by deconvolving the pinhole pattern from the image. URAs have blocks arranged in a flat frequency spectrum pattern, so that reconstruction of the source distribution can be performed by convolving the image with the mask pattern.

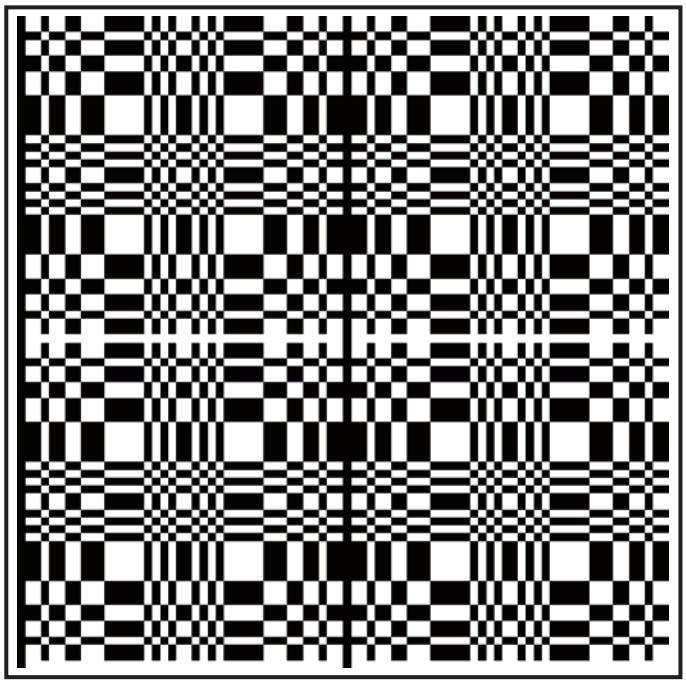

Figure 2. 82 × 82 block pattern used in our design (four groups of repeating 41 × 41 base patterns)

Project

This project benefited from the insight that when searching for a source in a diffuse background, it is the background radiation that forms the dominant noise in the system, and that it is this noise that

lengthens the time it takes to detect the source. In other words, if we were able to reduce the noise, we could locate sources more quickly. This is true for x-ray astronomy and medical imaging, as well as nuclear material detection.

At this point we should clarify our terms. Commonly, background refers to radiation that is detected by a camera from *outside* the FOV and that contains no image information; but for this project, background refers only to a constant or slowly varying source distribution *in* the FOV.

Even though the coded aperture was not designed for a specific application, the design was optimized for imaging 250-keV x-rays. The detector would have a 60° FOV capable of narrowing to 2°. A 3-mm tungsten mask, divided into three 1-mm-thick layers, would provide sufficient stopping power (5% transmission) at 250 keV. To achieve the required angular resolution, 3-mm-wide minimum block units were used with a 6-cm distance between the first mask layer and the camera. The minimum spacing shown in Figure 3 is the contracted position in which the camera starts, giving a 60° FOV. The maximum spacing in the figure shows the camera's extended position, which restricts the FOV to 2°.

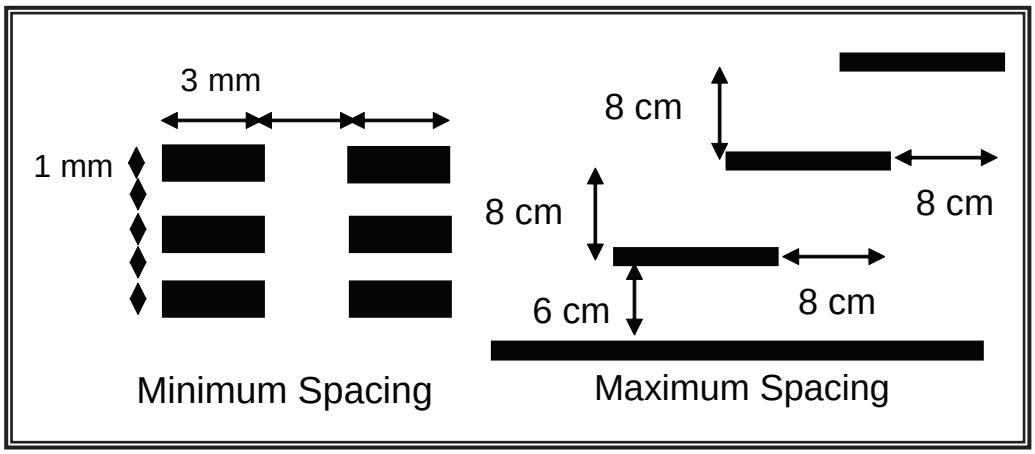

Figure 3. Minimum and maximum spacing between the mask layers in the contracted and extended positions

The test plan for the coded aperture included use of phosphor screens with a pulsed x-ray source. In the field, testing would be done with portable radiation sources and a photon-counting imaging spectrometer (an x-ray camera with energy detection).

The tungsten blocks were to be inserted into steel frames with flexible edges (Figure 4). The spaces between the tungsten blocks would be filled with aluminum blocks, so that the blocks could be stacked by hand and fill the mask plane without the need to measure to position the blocks. The size tolerance of the blocks would be 0.01 mm, meaning that a maximum cumulative uncertainty in the

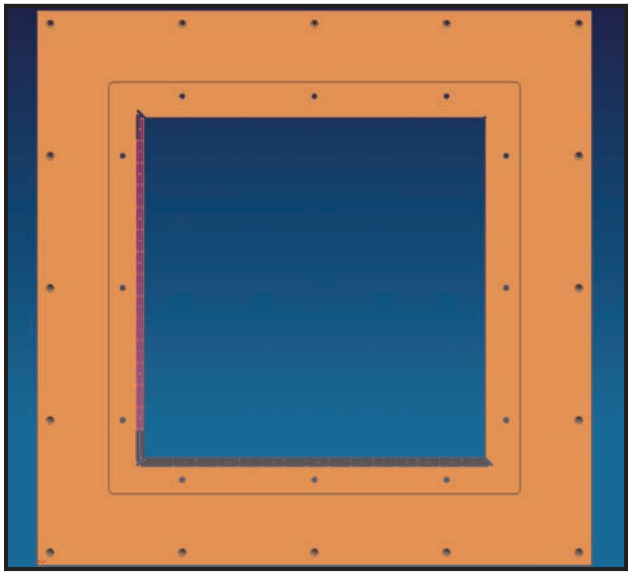

Figure 4. Steel flexure frame for holding the tungsten blocks for a single mask layer

relative position of any block would be 0.3 mm. The holes in the left and bottom edges would allow the frame to flex, to help the inserted blocks have a snug fit. The frame would be filled from the upper right corner and would proceed until the last blocks were inserted along the two flexible edges.

Once the aluminum and tungsten blocks were inserted into the frame, the positions would be tested using the x-ray source and camera, and the accuracy of the mask pattern verified by computer analysis. Then the frames would be shipped to a vendor for an application of a carbon fiber and epoxy coating that would lock the blocks in place and provide structural stability.

Completed mask layers would be mounted on a frame with precision rails for movement in two dimensions, as shown in Figure 5. The mask closest to the camera would be at a fixed position. The second mask could travel up to 8 cm along the z-axes (perpendicular to the mask plane), and ±8 cm on the x and y axes. The third mask plane could travel up to 16 cm along the z axes and ±16 cm on the x and y axes. The rails could be adjusted to fix the positions of all of the layers to within 100 microns. This system would rely on manual control to adjust the positions of the masks to demonstrate feasibility. In a usable system, computer control of the mask positions and automated feedback for locating sources would be required.

Although the system was not built, the machining and delivery of the tungsten and aluminum blocks were completed; mechanical drawings were drafted for all of the parts.

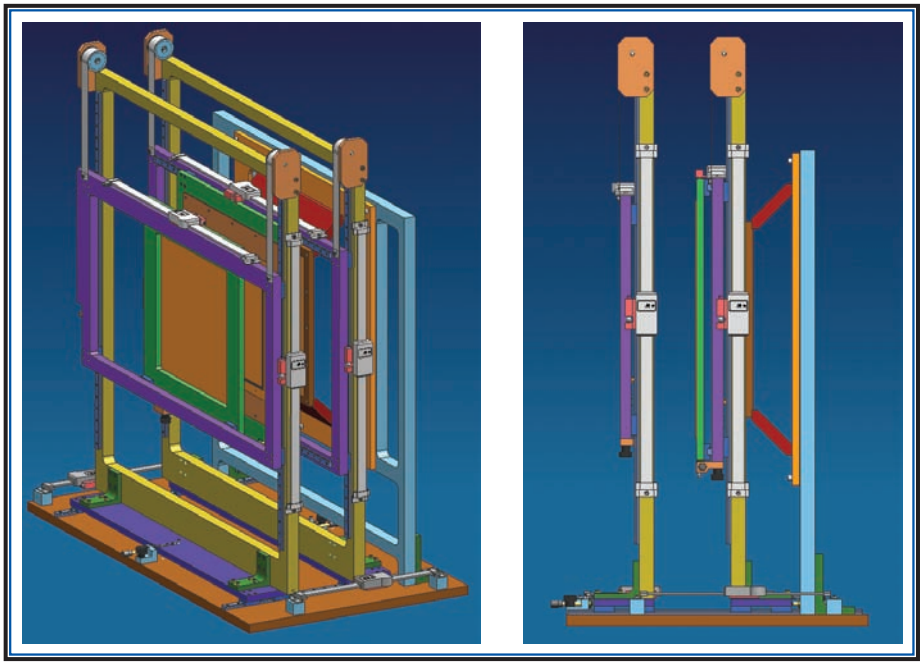

Figure 5. Assembly to hold and position the three mask layers

In lieu of testing, simulations were run using a simple convolution of the data with the mask patterns. The FOV of the system is not a sharp cutoff, since the holes in the mask are of varying size. This produces a rolloff in the system sensitivity to sources in the FOV. The reconstructions were divided by the system response to yield normalized source distributions in order to identify sources. Unfortunately this method produces images with high noise amplification that makes visual interpretation of them difficult; therefore, the divisions by system response data have been omitted from the images used in this report.

We can see the effects of narrowing the FOV in Figure 6. The image on the left is the reconstruction that is formed when the mask layers are 1 mm apart, at their minimum distance from each other. The successive images show narrowing of the FOV as the masks are moved apart to 4 cm, then 8 cm. As the FOV narrows, the point source becomes much more distinct. The apparent increase of brightness of the point source is due to the decreasing noise in the image, caused by the scaling of the image display. As the FOV is restricted, fewer x-rays from the diffuse background reach the detector, leading to a reduction of noise in the image. The increased detectability of the source when the FOV is narrowed around the source is clearly indicated in these images and other simulations.

Next, we designed a series of simulations to compare single- and three-layer masks. We hoped to demonstrate that the multilayer masks located unknown sources more quickly than the single-layer mask. The simulations used a test problem of a 0.1-m-diameter Pu source (in this case our source is

not unknown) embedded in a constant background of 0.1 μCi/m^2 and calculated how long it would take to locate the source with 95% accuracy. For the single-layer mask, the simulations collected a single image for the full search time until the signal level was sufficiently above the noise to positively identify a source. A series of trial-and-error simulations were run with the three-layer mask to determine an optimum search algorithm, which turned out to be only a single movement of the masks. First, the masks start together for the maximum FOV. When a source is identified with 64% certainty, the masks are moved to their full extended position to see if a source is at the suspected location. If no source appears, the masks are moved back to their original position and more data is collected (added to the original data) until a new suspected source is identified. This procedure continues until a source is positively identified.

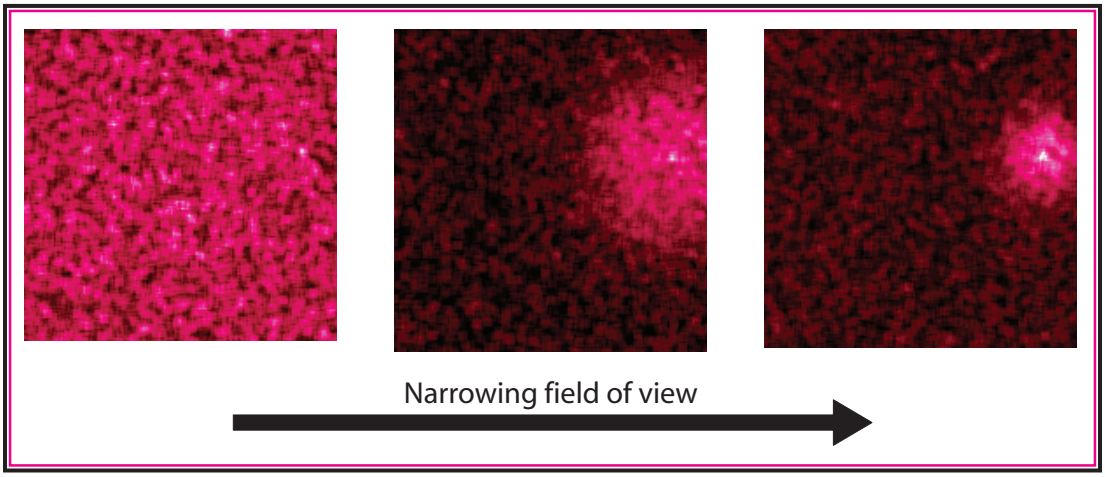

Figure 6. Reconstructions of the same source with narrowing FOV

Plots of the average time for source identification with 95% accuracy versus source strength are shown in Figure 7. Simulation results for a five-layer mask are also included. It is clear that with multiple masks the time to identify a source decreases. The problem with increasing the number of masks is that each mask must be made thinner in order for the maximum FOV to remain at 60°. Thinner masks are more difficult to construct, and having five layers makes for a much more complicated system (we never did mechanical drawings for a five-layer system).

The search procedures for the three- and five-layer masks were optimized for this specific problem of finding a point source embedded in a diffuse background. It is not clear what general choice for moving the mask layers would be best if the nature of the source is unknown (it might be compact or extended, for example).

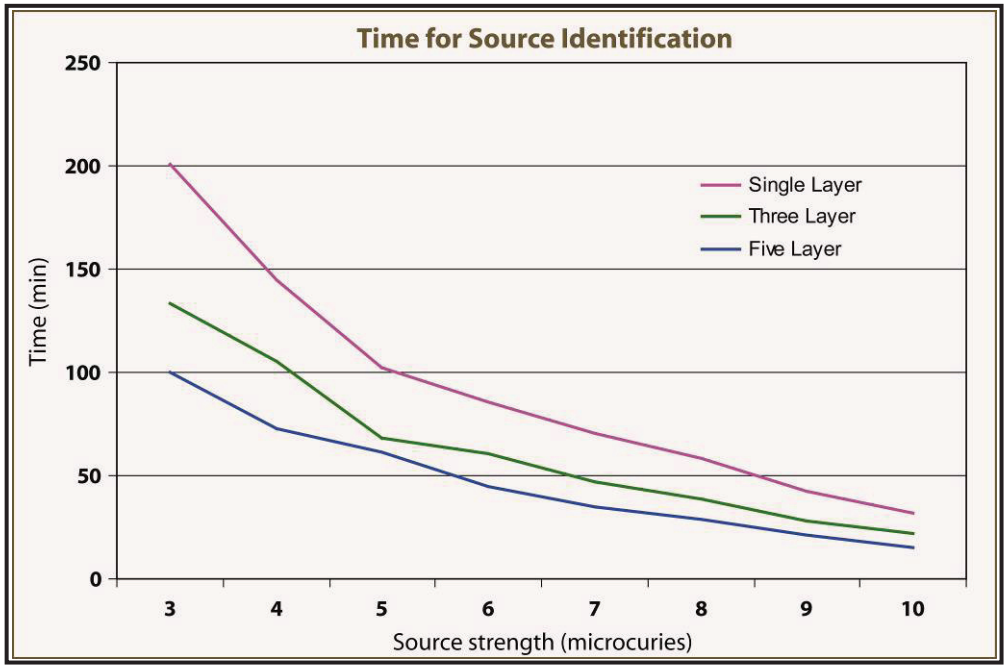

Figure 7. Average times for source identification with 95% accuracy for single-, three-, and five-layer coded apertures

Conclusion

The advantages of using multilayer masks for coded aperture cameras were clearly seen in situations where a single point source needs to be found in a diffuse radiation background. For a five-layer mask design, search times can be cut approximately in half. We demonstrated through mechanical design that a practical three-layer mask could be constructed. The disadvantages of the multilayer design are its increased cost and complexity, its narrower FOV, and the difficulty one would have in trading mask patterns (such as switching an anti-mask pattern) for compensating for source-independent background.

Acknowledgments

We acknowledge the contributions of Kevin McGillivray of North Las Vegas Operations and Morris Kaufman, Dane Morgan, Ron Sturges, Dave Schwellenbach of Los Alamos Operations.

this page intentionally left blank

Aerial Neutron Detection

Rick Maurer,[1] *Ethan Smith*
Remote Sensing Laboratory – Andrews

Tom Stampahar
Remote Sensing Laboratory – Nellis

This comprehensive study of aerial neutron detection involved both static baseline measurements to characterize the detection system and dynamic measurements to demonstrate the effectiveness of aerial neutron detection in real-world applications. Long-range neutron detection has been of interest in the nuclear emergency response community for many years. Recent attention has focused on extending the detection range and intrinsic efficiency for Homeland Security applications. The primary neutron detectors used in our study were two 6-ft neutron modules, each containing eight 6' long × 2" diameter tubes filled with helium-3 (^{3}He). One module was moderated with a ¼-in. polyethylene honeycomb matrix, and one was unmoderated. The neutron sources used were high-intensity californium-252 (^{252}Cf) and americium-241/beryllium (AmBe) radiation sources, providing average neutron energies of 2–3 and 4–5 MeV, respectively. This report summarizes the efforts and measurements completed, and provides future recommendations.

Background

Aerial neutron detection has been developed and deployed by the DOE and other government agencies over the last 20 years. Early DOE sensors consisted of large pod systems for use on helicopter aircraft. Such sensor systems could either be mounted internally, on the aircraft floor, or externally, in a pod beneath or attached to the sides of the aircraft. The detector systems consisted of arrays of ^{3}He-filled tubes enclosed in moderating materials and were typically quite heavy. Interest has recently turned toward an aerial neutron capability that could be used for such activities as locating lost industrial neutron sources. Since no comprehensive study for aerial neutron detection has been conducted, we proposed to pursue this topic by both performing baseline measurements and demonstrating detection capability under a variety of case studies.

The baseline study required a series of ground-based, source-to-detector distance measurements for comparison to Monte Carlo N-Particle (MCNP) model predictions. Such measurements are best performed in an open field environment free from scattering media. These measurements could be

[1] maurerrj@nv.doe.gov, 301-817-3367

augmented by aerial neutron measurements over a point source, a nuclear power plant, and a neutron source in a large ship. We would then conduct additional baseline measurements to characterize the neutron background as a function of altitude.

Project

First we acquired the high-intensity neutron sources necessary for aerial measurements. Long-distance measurements, such as those performed with aircraft, require neutron sources with intensities of $\geq 10^5$ n/s. As such, the goal was to obtain neutron sources with fluence rates of $\geq 10^6$ n/s. An initial search of the NSTec radiation source database for ^{252}Cf fission sources revealed several neutron sources with sufficient activity. However, these sources either could not be loaned out or were not portable, as approved transport containers did not exist. Thus, we decided to procure a 1×10^7 n/s ^{252}Cf source. A search for a high-intensity AmBe composite source revealed one in use at Yucca Mountain, north of Las Vegas, Nevada. Negotiations with the Yucca Mountain Project led to a temporary loan of this AmBe source, which has an activity of 1 Ci ^{241}Am, yielding an intensity of 2.2×10^6 n/s. An approved transport container was procured, loan documentation was completed, and RSL-A received shipment in September.

Using a rented 85-ft boom-type crane, we performed baseline measurements from September 19 to 21, at a DOE facility near Andrews Air Force Base (Figure 1).

Figure 1. A boom-type crane was used to conduct source-to-detector measurements from 10 to 80 ft

The measurements were taken in an open field free of any obstructions. The neutron detectors were placed in the boom basket and raised vertically over the neutron source on the ground. Calculations were made at source-to-detector distances from 10 to 80 ft, in 10-ft increments. All measurements were conducted for 10 minutes. The wire line hanging from the boom basket was marked in 10-ft increments.

Several types of neutron detectors were used in the measurements, but this report focuses on the two large detector arrays that will be further tested in aerial flyovers. These two detector modules each contained eight 6' × 2" stainless steel tubes filled with ^{3}He gas. The modules consisted of two rows of four tubes stacked. One module contained the detectors encased in a ¼-in. polyethylene honeycomb-type moderator; the other held the detectors without shielding or moderation. The two modules were positioned lengthwise across the boom basket, along with the other neutron detectors (Figure 2).

Figure 2. Two 6-ft ^{3}He module detectors extending lengthwise across the basket of the boom crane in the measurement geometry. The 6-ft module at left is unmoderated (bare); the module at right is moderated (tubes encased in polyethylene).

Each individual detector was attached to its own electronics package, which provided batteries, high voltage, an amplifier, and associated electronics. The packages were connected to computers in the data-logging station (Figure 3), using either 150-ft RS-232 or Ethernet cables.

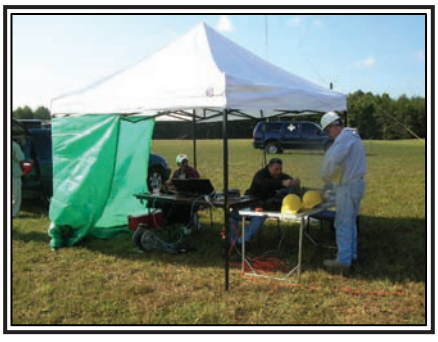

Figure 3. Data-logging station with computer for recording data for each detection system

The first set of computations for each source consisted of distance measurements from 10 to 80 ft in 10-ft increments, with the source in both bare and shielded (i.e., secured in its respective container) configurations. The ^{252}Cf container was a 4.5" diameter × 6.25" long Delrin cylinder (1⅝ in. thick), with the source located in the center. The AmBe container comprised a large cylindrical steel drum holding 12" diameter × 18" long polyethylene inserts.

The preliminary measured data for the bare and shielded ^{252}Cf source, with both moderated and unmoderated neutron modules, for source-to-detector distances from 10 to 80 ft, appears in Figure 4. The data show that the highest sensitivity is for the configuration in which the source is shielded and the detector moderated. The lowest sensitivity is that in which the source is unshielded (bare) and the detector unmoderated.

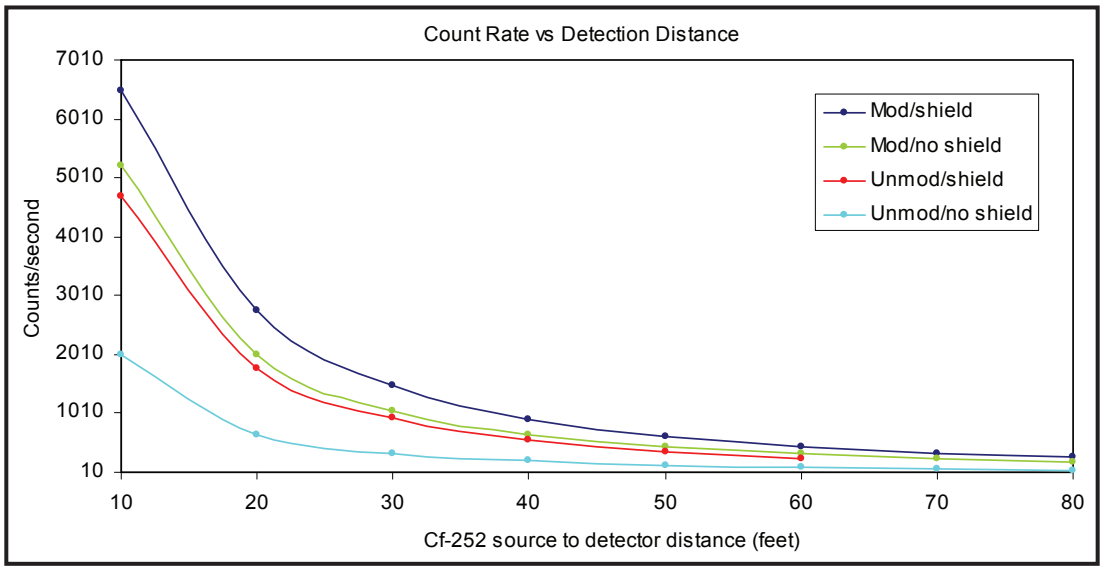

Figure 4. Preliminary data for measurements of the bare and shielded ^{252}Cf neutron source, using both the bare and moderated 6-ft ^{3}He neutron arrays

The second measurement set consisted of positioning the ^{252}Cf source at a fixed distance 10 ft below the boom basket and raising the boom. The neutron source initially started on the ground surface and was then raised in 10-ft increments to a basket height of 50 ft. The goal of this series was to measure the fraction of neutrons scattered from the ground surface into the detector (scattering fraction), in order to determine the magnitude of this contribution to the total measured flux. The experimental geometry, with the neutron source suspended 10 ft below the detectors, appears in Figure 5.

The measured data for the AmBe source and the scattering experiments are being analyzed and will appear in the FY 2007 final report.

Figure 5. The ^{252}Cf source suspended at a fixed distance of 10 ft below the boom basket in a measurement to determine the scattering fraction from the ground surface

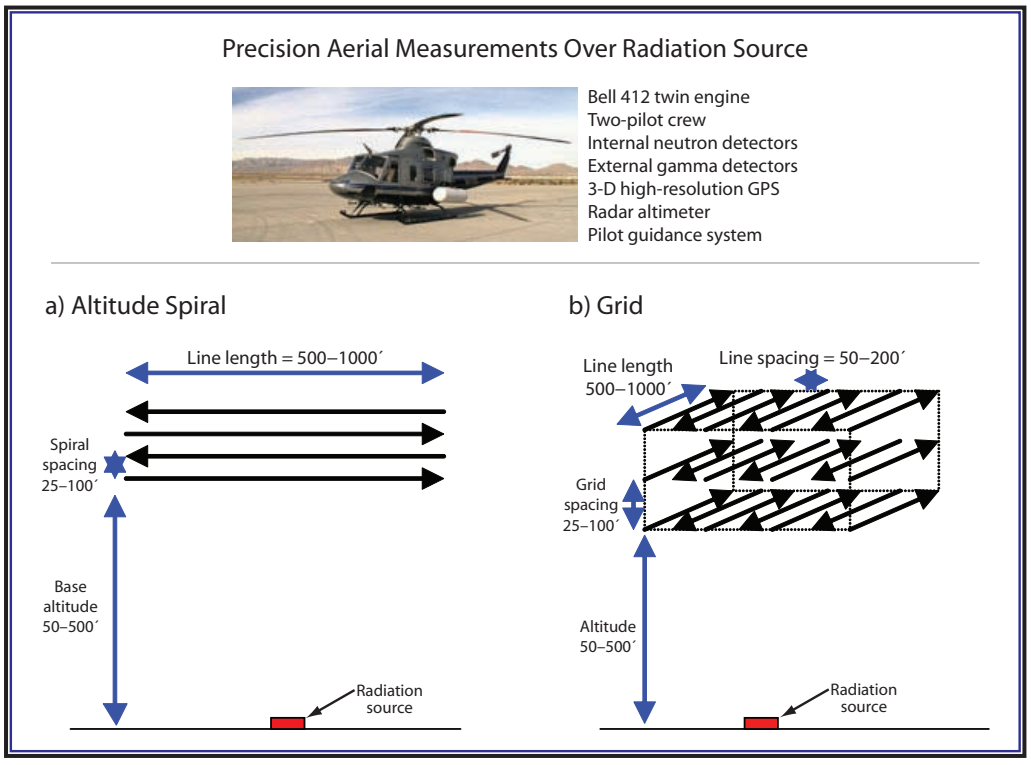

Figure 6. Graphics showing the planned aerial measurements for (a) altitude spirals and (b) altitude profile grid patterns over the neutron point source using the Bell 412 helicopter and internally mounted ^{3}He arrays

Aerial Neutron Detection

With the radiation sources in hand, baseline measurements completed, and neutron detectors operational, the next step is to conduct the aerial measurements. The first planned measurement for FY 2007 is a series of flyovers of the ^{252}Cf source. The flyovers will consist of altitude spirals over the neutron sources at altitudes from 50 to 300 ft, and grid pattern flying with line spacing from 50 to 100 ft. The data from the measurements will determine detection sensitivity and demonstrate the applicability of contouring aerial neutron data. For completeness, all aerial data will be simultaneously collected with the aerial measuring system gamma-ray system. The aerial measurement geometries appear in Figure 6.

Conclusion

A series of baseline measurements was completed in FY 2006 for the aerial neutron-detection study. We acquired two neutron sources, ^{252}Cf and AmBe, with sufficient intensity to conduct long-distance aerial measurements. The data will be compared to MCNP calculations in FY 2007, and the project team will begin the aerial measurements with a point source, nuclear power plant, and a neutron source in a large ship.

Acknowledgments

Special thanks to Steve Kegeler, Jerry Stackhouse, and Cres Watson, for providing the radiation work permit, radiation transport, and Radiation Control Technician field support, and obtaining the neutron sources. Special thanks to John Morse and Al Gogue, for operating the boom crane, and to Troy Waterman, for assisting with data collection.

Multilayer Solid-state Silicon Neutron Detector

Harry McHugh (retired employee),[1] *Ken Moy*
Special Technologies Laboratory

Our team fabricated a multilayer, solid-state neutron detector utilizing amorphous silicon PiN diodes, similar to those used in solar arrays, applied to a boron-10 (^{10}B)-coated substrate. These diodes, mounted on 10 individual microscope glass slides, each having 20 detectors, were very sensitive to alphas. Supporting electronics were also fabricated. Results have verified the basic theory of this approach, though unresolved ^{10}B sputtering problems remain. After successful demonstration in the laboratory prototype, the detector is ready for large-scale commercial development effort.

Background

Helium-3 (^{3}He) tubes have served as the predominant neutron detectors for many years. While quite reliable and accurate, they are very expensive and relatively large, limiting their deployment capabilities. Due to the expense of rare ^{3}He gas and the necessity of manual fabrication, tube cost is unlikely to drop. A ^{3}He detector costs approximately $40/sq. in. New solar cells, which are themselves multilayer semiconductors, can be purchased at retail prices of less than $0.40/sq. in. Adapting this solar cell technology, based on amorphous silicon PiN diode technology, to neutron detection should yield detectors that can be fabricated using large-scale manufacturing processes at correspondingly affordable prices.

Low-cost neutron detectors could be deployed in many Homeland Security installations, including shipyards, border crossings, airports, and highways. The (almost) two-dimensional nature of these detectors makes them easily installable in any of these applications. For example, low-cost detectors could be widely deployed to interdict plutonium-based weapons at seaports. In addition, such a thin detector would facilitate covert installation by other government agencies. Portable neutron detectors could also be readily fabricated using this detector.

The first half of this effort was completed in FY 2005. Working with the National Renewable Energy Laboratory (NREL), very-low-leakage PiN diodes were developed and tested. The leakage currents were so low that they exceeded design goals. Solid-state amorphous silicon PiN diodes were designed and optimized for this work and were successfully tested as alpha detectors. However, serious problems were encountered when attempts were made to sputter ^{10}B onto the substrates. The second year's effort has been devoted to solving the boron-sputtering problem and constructing a multilayer prototype that would increase sensitivity.

[1] mchughhr@nv.doe.gov, 805-686-2454

Boron Sputtering Development

Sputtering boron has proven to be difficult. The substrate of the amorphous silicon diodes must be coated with a thin film of ^{10}B, or a ^{10}B compound, to absorb the neutrons. The percentage of ^{10}B must be maximized for optimal performance. After elemental ^{10}B was sputtered onto a chromium-coated glass slide, the slide was exposed to the atmosphere. The boron immediately started to pit and form craters. It was determined that the boron was reacting to the air, forming oxides and hydroxides. These compounds began to lift from the chromium plating, creating a very rough surface. The amorphous silicon could not be successfully deposited on such a rough surface.

Project

In FY 2006, boron carbide (B_4C) was chosen as the boron compound to be sputtered. In addition to being very inert, B_4C is stable in air, making it a good candidate for this type of application. In addition, B_4C has a higher ratio of boron atoms than most other boron compounds.

MV Systems, Inc., of Denver, Colorado, was selected to perform the B_4C sputtering. They attempted to optimize conditions to produce the maximum sputtering rate (~0.5 μm/h), and they specified the sputtering technique that gave the best results. The most obvious deposition problems encountered with B_4C films were poor adhesion and pinholes. Most of the pinholes originated from the B_4C target flakes falling on the substrate. We conjectured that the flaking originated from a low carbon-sputtering rate. Since the sputtered material flow in steady state should be the same composition as the target bulk, low carbon-sputtering rates pointed to accumulation of excess carbon near the target surface. This excess carbon might form loose flakes. The problem was overcome by interrupting the deposition after one hour, mechanically cleaning the target surface, then continuing the deposition for another hour. This resulted in relatively pinhole-free, 1-μm-thick B_4C film, as confirmed by an X-ray Photoelectron Spectroscopy (XPS) study.

Aside from pinholes, B_4C also exhibited problems adhering to our substrates. At first, glass substrate cleaning procedures were modified. Three procedures were used: detergent + ultrasonic cleaning; detergent + organic solvent + ultrasonic cleaning; and detergent + organic solvent + ultrasonic cleaning with a final rinse in a special high-pressure deionized water apparatus. The last cleaning procedure yielded the best results for as-deposited B_4C films. Yet the films still showed peeling over longer time periods (i.e., a few days). Bare glass and Cr-coated glass substrates were both evaluated. While Cr coating seemed to improve B_4C adhesion, both substrates peeled in the long term. It was later determined that peeling was greatly reduced if the B_4C films were kept under vacuum or in a desiccator. From this, we concluded that the B_4C films might be boron-rich and thus, chemically reactive with atmospheric H_2O and O_2. Our best sample capable of detecting neutrons was grown on a B_4C-coated glass substrate that was further coated with 60 nm of Cr within 24 hours after B_4C deposition; the diode structure was then deposited with little delay.

Future Recommendations for B_4C deposition

From our previous work, we concluded that rigorous control of B_4C deposition is necessary to grow successful neutron detector devices. The B_4C film must have a very high surface quality and must be sealed by a Cr layer immediately after deposition to avoid atmospheric reactions. Ideally, B_4C deposition and diode deposition would be performed in one cluster tool without breaking the vacuum.

The B_4C deposition process has not yet been optimized. First, Ne gas should be used instead of Ar to effectively sputter the light elements B and C off of the target (sputtering is most efficient when the inert gas molecular mass is close to the mass of the sputtered element). Second, film stress management must be performed by carefully selecting the deposition pressure (and thus, the impinging atom energy) to balance the compressive and tensile stresses in the film. Film temperature might be varied as well to facilitate stress management. Third, a reactive sputtering gas such as methane could be added to the sputtering chamber to ensure complete reaction of the elemental boron. Fourth, treating the substrate surface with ion bombardment or plasma cleaning prior to sputtering might lead to better film adhesion.

The maximum thickness of B_4C achieved was approximately 1 μm, less than the optimal thickness of ~2 μm. This reduction in boron will reduce the sensitivity of a single layer by approximately 20%. Additional efforts to optimize the boron sputtering would be required before large scale manufacturing could begin.

Near the end of FY 2006, information became available on B_4C sputtering work being performed by Caterpillar Corporation. Caterpillar has developed sputtering processes to apply thin films of B_4C to silicon and Kapton substrates. Surface roughness measurements indicate that an rms surface variation of ~1 nm has been achieved, with maximum surface roughness peaks of ~12 nm. Their process is compatible with commercial machinery that can perform continuous coating of large rolls of materials such as Kapton. This information can be factored into future proposal work. Caterpillar has spent many man-years developing this process.

Amorphous Silicon Diode Development

PiN diode deposition was modified slightly this year. The deposition temperature was reduced to 200°C, in order to achieve an i-layer with a wider band gap. This change reduced the already low reverse dark current densities. Also, the thickness of the n-layer was increased from 30 to 50 nm, to buffer any possible defects in the underlying B_4C layer (e.g., pinholes and cracks). In many cases, however, the B_4C film defects were too great to be overcome by this method.

The diode chemical vapor deposition process itself was automated using an NREL program written in LabVIEW. The most critical issue was starting the plasma process smoothly, without depositing a thin, poor-quality layer at the interface that was caused by the startup transient condition. Achieving

smooth startup is difficult because the plasma process requires an initial energy of ~5 W, whereas the deposition power is only ~0.7 W. Therefore, after starting the process at 5 W, the power must beimmediately reduced to 0.5 W. We accomplished this goal by controlling the RF supply and using the light emitted from the deposition plasma as feedback. A video camera recorded plasma intensity in real time, and the blue component of the image was integrated over all image pixels. At first, the microwave power was set to 5 W. Plasma startup occurred at any time within ~1 minute after that. Within ~75 ms of detection of the plasma initiation, the RF power was reduced to 0.7 W, thus avoiding "plasma shock" of the interface.

A new electrode mask was developed. Initially, we determined that square contacts as large as 60 mm^2 in area produced sufficiently large signals. Based on this observation, the new electrode mask was designed with long, closely spaced electrode stripes extending to the edge of the sample. This "comb" structure covers most of the sample area, yet allows for easy connection to individual stripes ("pixels") at the sample edge. Each pixel is ~1 cm long and 3 mm wide. Each sample slide of 1" × 1.5" has two pixel rows originating from opposite edges, totaling 22 pixels. One pixel pair was used to contact the bottom electrode of the device. This slide is illustrated in Figure 1.

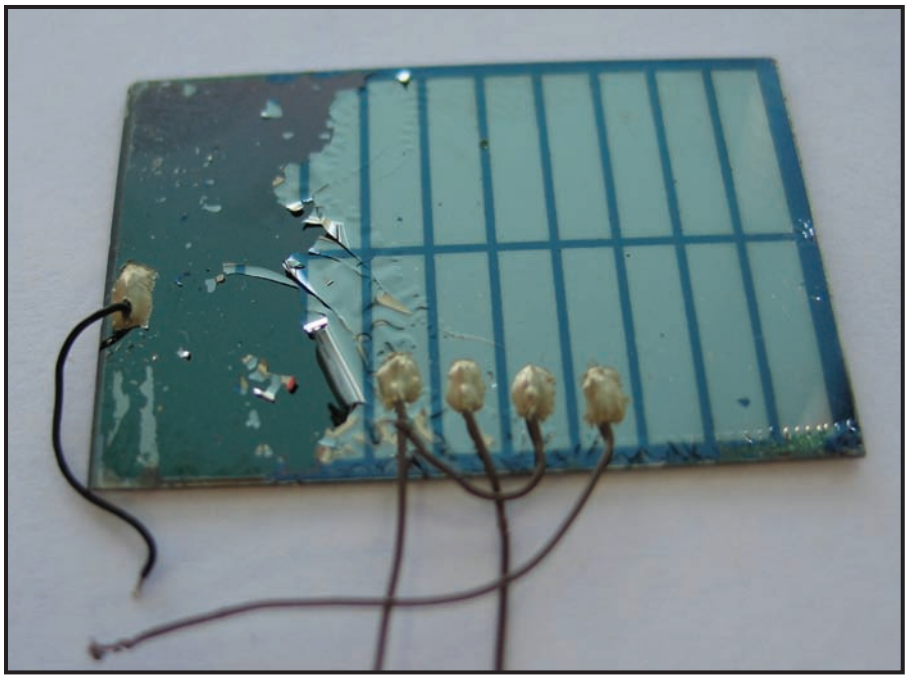

Figure 1. Neutron detector, slide L1696

Single-layer Neutron Test Results

Initial Detector Testing

The 20-segment detector slides were individually tested as received from NREL. Slide No. L1696 (Figure 1) was tested first. Pixels were tested in the portion of the slide not affected by peeling. Despite the peeling, the pixels exhibited both an alpha and a neutron response.

Slides L1711, L1718, L1719, and L1720 were subsequently tested. These slides had much less peeling than slide L1696. However, none exhibited an alpha or neutron response. There were differences in the coating processes used for L1696 and the subsequent slides. For slide L1696, the B_4C was applied directly onto the glass; the B_4C was then immediately covered with 600 Å of Cr. The amorphous silicon was applied later the same day. The other glass slides were first coated with Cr, followed by sputtering of B_4C. The B_4C was not coated with chromium until some days later. The amorphous silicon was applied at an even later date. The improvement in B_4C adhesion of the latter slides is attributed to the application of Cr on the glass. The alpha and neutron sensitivity loss was probably caused by the delay in processing completion, which allowed time for adverse reactions to occur. However, the exact cause of the failure is not known.

Neutron Sensitivity Measurements

Sensitivity of a single-layer detector is determined by the probability of capturing a thermal neutron in a 1–2-µm-thick layer of ^{10}B. (The probability of capturing the emitted alpha in the silicon diode is almost 100%.) There is a ~3% probability of capturing a neutron in a 1–2-µm-thick layer of ^{10}B. Measuring neutron absorption of such a small detector is difficult. The method employed involved comparing the per-unit area count rate of the solid-state detector with that of a known ^3He tube in the same neutron flux. The ^3He detector had an active area that was ~7000 times as large as a single detector element.

We used a ^{252}Ca source encased in ~1 in. of high-density polyethylene as a neutron source. The source strength was 50 µCi. Using this technique, the absolute efficiency was found to be ~2.5%. Thus, 20 layers could yield a detector with a sensitivity of ~50%, nearly that of a typical ^3He tube.

Gamma Response Test

A useful neutron detector must have either an intrinsically negligible gamma response or one that can be electronically excluded from the neutron response. ^3He tubes respond to neutrons, but the energy of the gamma response is much lower than that of the neutron response. Therefore, separation is easy. We measured the gamma response of the solid-state neutron detector using a 50-µCi Co_{57} gamma source. No activity was discernable. Long-term (20-hour) background tests on individual detectors showed results consistent with natural background neutron fluence rates. These results were expected, since the very thin detector should not respond to gammas.

Electronics Development

Because the area of an individual detector is limited by its inherent capacitance, numerous detector cells are needed to achieve significant detector area. Also, multiple layers are required to increase the sensitivity to levels approaching that of ^{3}He tubes. The maximum area for one single-layer detector pixel has been empirically determined to be ~60 mm^2. This means that a preamp is required for every 60 mm^2 of detector area. To provide design margin, the detectors fabricated in this project were 30 mm^2 in area. For a fieldable design, large-scale integrated circuitry could be used with even smaller pixels. For the prototype demonstrated in this project, each detector assembly consisted of a glass slide containing 20 each of 30-mm^2 detectors mounted on a printed circuit board (PCB) with 20 preamps and voltage comparators. The outputs from all the comparators are combined (i.e., there is one logic output from each bank of 20 channels). A total of five 20-detector assemblies were built to approximate a multilayer device.

After the first prototype electronics PCB (Figure 2) was fabricated, the circuit performed properly during testing. It was then connected to a 20-channel detector slide, No. L1696. We obtained a good neutron response, which resulted in a 50-mV peak signal, comparable to that achieved with a large, high-quality commercial neutron detector. However, no neutron or alpha response was obtained from the other detectors. Consequently, the remaining circuit boards were not completed.

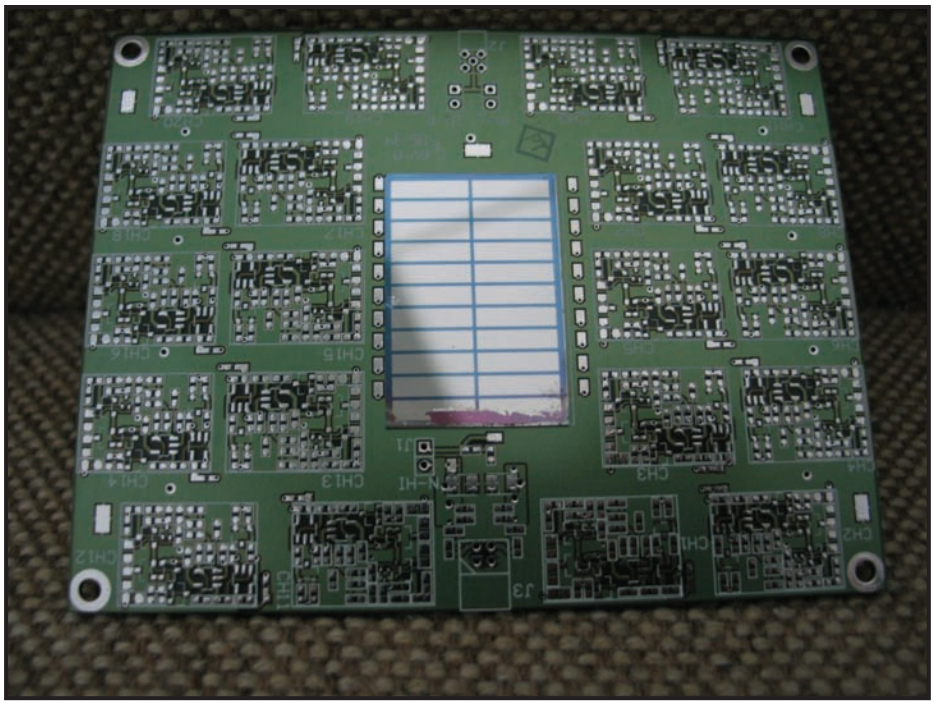

Figure 2. Prototype preamplifier board with neutron detector

Cost Estimate for Large-scale Manufacturing

A detailed cost estimate for mass-producing solid-state neutron detectors in sheet form was prepared with the assistance of a firm currently using similar technology in large-volume commercial applications. The cost breakdown appears in Table 1:

Table 1. Manufacturing Cost Estimate for solid-state neutron detectors

Component	Cost/layer/m^2
Capital equipment amortization	$85
Substrate material	$5
Amorphous silicon material	$10
Metal contact material	$10
^{10}B carbide	$20
Labor, energy, facility	$50
Support electronics for 1 layer	$50
Total cost per layer/m^2	**$230 per single layer of 1 m^2**
Cost per 15-layer device (45% efficient)	**$3450 per complete 1 m^2 detector**

Conclusion

This year's efforts have proven that the solid-state neutron detector based on a ^{10}B carbide/amorphous silicon design will detect neutrons with an efficiency similar to theoretical calculations. However, continuing problems with the sputtering of ^{10}B prevented the completion of a multilayer prototype. There is little doubt that a multilayer device can be successfully developed, pending resolution of the boron-sputtering problem.

Caterpillar Corporation's recent work in the deposition of high-quality B_4C films holds promise for the future. If high-quality B_4C films can be obtained, the present design can be used in small, single-layer detectors. Large, multilayer detectors would still require substantial developmental efforts.

A refined cost estimate for the fabrication of large-area detectors has verified that the solid-state detector can be produced at approximately 10% of the cost of ^{3}He tubes (Table 1).

Acknowledgments

Paul Stradins and Howard Branz of NREL are responsible for the amorphous silicon design and boron sputtering efforts.

this page intentionally left blank

Microreticulated Plates for Neutron Source Imaging

Rick Maurer, Namdoo Moon,[1] Yuping You
Remote Sensing Laboratory – Andrews

This project investigated the feasibility of neutron source imaging to characterize solid-state neutron detector systems using microchannel plate (MCP) technology. This technology, which uses new ceramic materials, was characterized for detecting thermal neutrons with higher efficiency and a lower gamma rejection ratio than previous MCPs because of low lead content. We reviewed six detector systems made by NOVA Scientific, Inc. (three MCPs, one microsphere plate [MSP], and two microfiber plates [MFP]) (Figure 1). In our measurement, the MSP and two MFPs showed low gain. However, new ceramic material with a low-lead MCP detector yielded promising results with a lower gamma rejection ratio at high gain.

Project

MCP Testing

Pioneered by NOVA Scientific several years ago, the MCP neutron detector has been widely reported in numerous peer-reviewed journal articles (Tremsin, 2006, 2005, 2004). It has been primarily tested for use in such high-thermal neutron flux applications as neutron radiography and imaging. Although highly attractive as a compact, solid-state neutron detector, the MCP can be quite expensive to fabricate and currently can only be manufactured in limited format sizes with a maximum dimension of ~50 mm round or square. It operates by converting uncharged neutrons to charged and highly ionizing reaction products (^{4}He and ^{7}Li) from the neutron-^{10}B reaction. The range for an alpha particle is ~3 to 5 μm, which is somewhat greater than the average MCP channel wall thickness. NOVA's study has shown that when a ^{10}B atom absorbs a neutron, there is an ~80% probability that a charged particle produced in the reaction will escape into a channel to initiate an electron cascade.

Three MCPs composed of three different glass systems appear in Figure 1. The HB4 MCP is doped with 10 mol% of enriched ^{10}B isotope, thereby converting a thermal neutron into alpha and ^{7}Li particles. Testing of the HB4 MCP was undertaken at the McClellan Nuclear Radiation Center (MNRC) at the University of California, Davis (UC Davis); test results are reported below.

Alternatively, the B14 MCP glass uses Gd (3 mol%) to perform the neutron conversion, yielding conversion electrons primarily within the 20–90-keV energy range. These electrons then penetrate

[1] moonn@nv.doe.gov, 301-817-3353

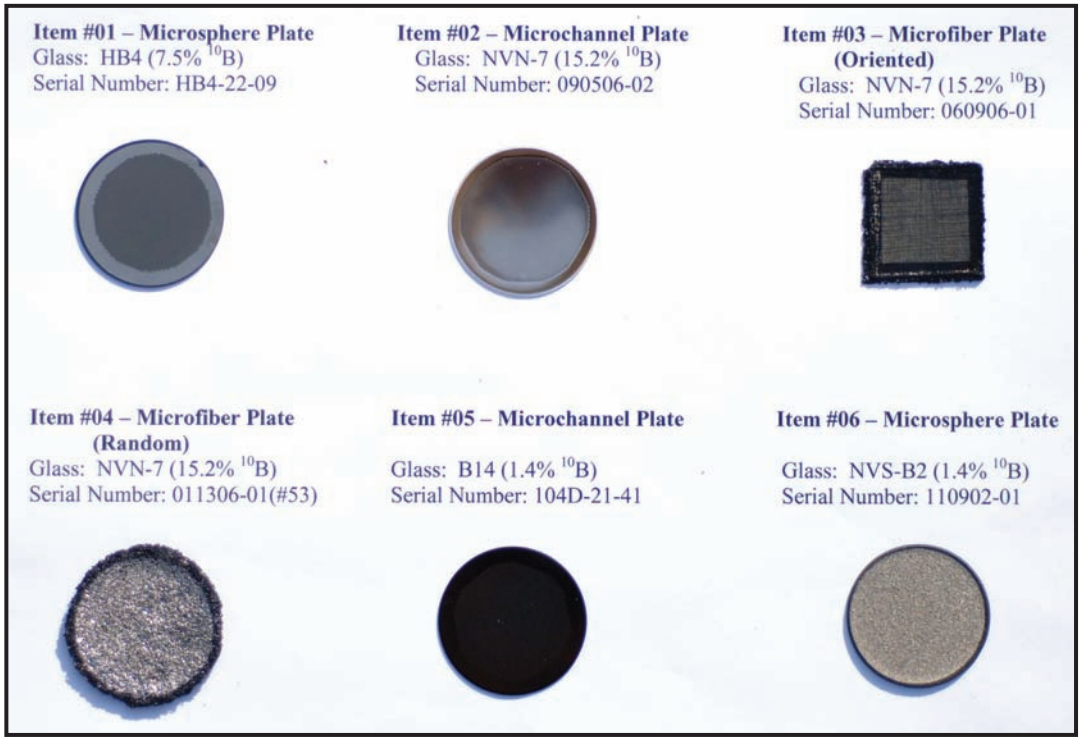

Figure 1. All six detectors

one to several channel walls, initiating electron avalanches through secondary electron emission. B14 MCPs have been quite successful in both high- and low-neutron flux testing. The low background noise level of these plates is exceptional, among the lowest yet recorded with MCPs.

A third glass system, newly developed for use with MCPs, is called the "superclad" MCP. It reduces gamma-ray absorption and hence, interference, by using a lead-free matrix glass highly doped (~13 mol%) with ^{10}B, with no high-Z elements in the MCP matrix glass. A very thin, 1-μm channel wall lining of conventional lead-based electron multiplier glass is also used, although it now constitutes only a small fraction of the total detector volume (it previously comprised 100% of the volume).

At the time of this writing, the NVN-7 MCPs were in the final stages of development processing with an experimental matrix. However, the gain levels already demonstrated using electron inputs are comparable to normal commercial MCPs, which is encouraging. This suggests eventual success in reducing the MCP resistance to usable levels. Process optimization will result in a viable MCP resistance range of several tens to hundreds of MΩ, appropriate for neutron testing in the near future. Currently, the resistance is one to two orders too high for testing in a neutron beam, where dynamic range limitations would strongly impact both measured neutron efficiency and gain levels.

MSP Testing

NOVA's NVS-B2 MSP (Figure 1), composed of ^{10}B-doped glass, is essentially a fused disc of glass microspheres 50–60 μm in diameter. The MSP is thermochemically treated (i.e., high-temperature hydrogen reduction) to provide intrinsic electron multiplication properties. Neutrons reacting with the ^{10}B atoms yield alpha and ^{7}Li reaction particles, which then create detectable electron avalanches.

The MSP sample was successfully tested at NOVA with electron and ion inputs, as well as at the National Institute of Standards and Technology (NIST) with cold neutrons. The overall plate resistance was 2.2 GΩ, with a corresponding bias current level of 1.3 μA at 3 kV. Figure 2 shows a pulse-counting image of the MSP using an MCP backing plate and a crossed delay line imager provided by Sensor Sciences, LLC, in Pleasant Hill, California. A phantom Cd strip attached to the front of the MSP, drilled with several submillimeter holes, is visible across the image, showing the moderate neutron spatial resolution (a possible 100–200 μm with MSPs). The data measured at NIST was obtained from an MSP constructed with 63–90-μm microspheres. However, using larger microspheres decreases thermal neutron detection efficiency because they significantly reduce the alpha particle escape probability and, hence, detector efficiency. This test showed good neutron response, although detection efficiency was estimated at <5% due to the relatively large microsphere diameter, leading to self-absorption of the neutrons and corresponding reaction products.

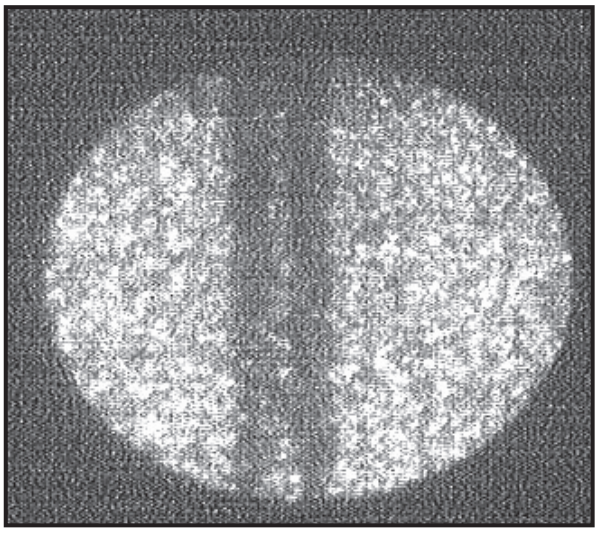

Figure 2. Pulse-counting readout image of an MSP neutron detector from imaging tests at NIST

Preventing any absorption of alpha particles from the neutron-boron reaction would require microsphere sizes to be at the ~7-μm level (i.e., one-half the alpha particle range)—roughly five times smaller than what has yet been achieved. This issue led us to consider using MFPs, as we felt the reaction product escape could be improved using lengthy fibers of small diameter. Also, a reduced number of particles would result in much lower noise levels due to fewer sharp field-emission points. A much smaller number of fibers would be needed in a flat-fused plate, as compared to one constructed of microspheres, which would create far fewer potential point sources of field emission. This much-reduced noise has been observed in practice.

MFP Testing

We tested two MFP samples: one with randomly packed or oriented fibers and one with oriented fibers in an orthogonal x-y or "stacked log" arrangement, resulting in improved uniformity (Figure 4). MFPs were fabricated and tested at NIST for use with high-flux neutron beams (Figure 3). These detectors demonstrated good neutron response when tested in analog (i.e., non-pulse-counting) mode, with a phosphor screen and CCD camera readout, integrating a high-flux cold neutron beam of ~10^8 n/cm^2/s. Obviously, low-level pulse counting, required for sensitive special nuclear material (SNM) detection of only a few nanoseconds, is a very different mode of neutron detector operation than high-flux imaging.

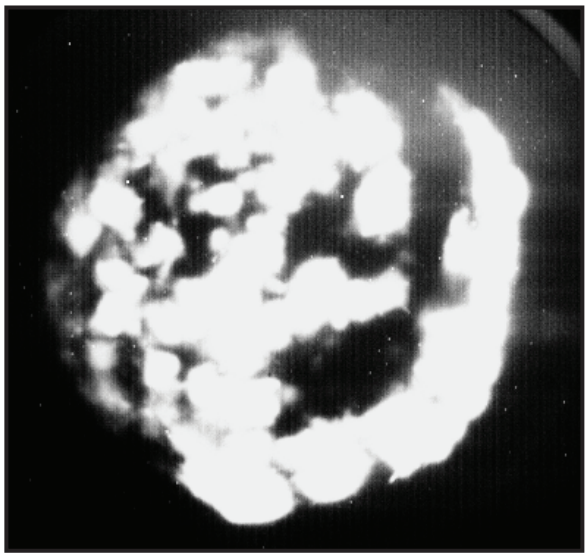

Figure 3. NIST test of randomly oriented MFP using a high-flux cold neutron beam (8-sec integration in neutron beam [3000 V across plate with no backing plate])

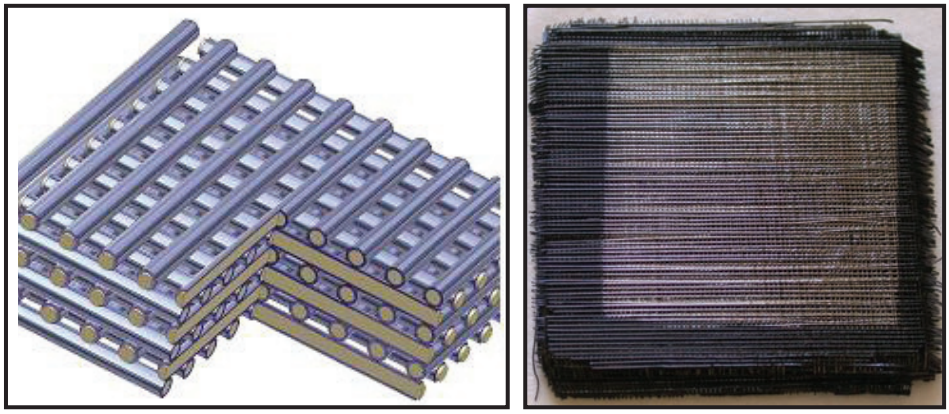

Figure 4. (left) Schematic of orthogonally oriented fiber structure for MFP prototype; (right) photo of orthogonally oriented fiber MFP prototype after fusion and hydrogen reduction

Due to baseline noise levels, gains of $>10^4$ are required for any effective MCP/MFP pulse-counting electronics chain, regardless of whether a simple metal anode or any of the position-sensitive readout alternatives are employed. None of the MFPs currently available have been able to exceed gains of 10^2 with biases of up to 3 kV, even with front surface–detected input electrons (the most favorable scenario). Therefore, we considered it pointless to attempt pulse-counting measurements with thermal neutrons at this time.

The MFP with the orthogonally oriented fibers appeared to operate quite effectively at a modest gain level (tens to hundreds), yielding improved uniformity as compared with the randomly packed fibers (Figure 4). Moreover, this uniformity might be further improved as highly regular machine weaving is incorporated into the MFP fabrication process.

Test and Results

Neutron–Gamma Ray Discrimination

MCP, MSP, and MFP detectors have an inherent gamma-ray detection efficiency of 1–3%, depending on plate thickness and specific gamma-ray energy level. Assuming a rough thermal neutron efficiency of 30–60% would imply a gamma-detection ratio of only 10^{-1}, as compared with neutrons. The standard, widely used ^{3}He neutron detectors are essentially gamma-insensitive and operate at a gamma-neutron ratio at the 10^6 level and greater. Therefore, for the solid-state MCP/MSP/MFP technology to be considered an attractive alternative, the gamma discrimination of these promising new solid-state neutron detectors must be dramatically enhanced, by orders of magnitude.

Several different approaches to this problem are being studied. The most promising, viable approach for attaining high neutron–gamma ray discrimination is to exploit the emission of a 478-keV gamma

ray from the neutron-^{10}B reaction, which occurs in 93% of reactions. A highly efficient and fast gamma-ray detector would capture the 478-keV gamma ray and, using coincidence timing methods, would accept or reject neutron events based on the presence of this specific gamma ray line.

Testing of the HB4 MCP was performed at MNRC using a neutron radiography beamline with a relatively high gamma-ray component and, importantly, the ability to reduce or "tune" the thermal neutron flux down to much lower levels than 10^5–10^8 n/s cm^2. Arguably, this mixed neutron-gamma source approaches an analog of what might be detected from an SNM source, such as ^{252}Cf or Pu. This approach is due to the MNRC reactor's ability to be reduced in power to the level of only a few kilowatts, with a resulting neutron flux of only ~10^2–10^3 n/cm^2/s, yet still with a rather high gamma flux, measured to be at least an order of magnitude higher.

To assess the proposed gamma-ray coincidence method with an HB4 MCP, we utilized a detector configuration in which an MCP acted as a neutron detector, with a scintillator crystal coupled to a photomultiplier tube (PMT) for gamma-ray detection (Figure 5). This setup provided neutron imaging detection and simple gamma-ray detection, with an MCP electronic readout in a 29-mm cross delay line detector, along with a 1-mm-thick Cd mask to remove the neutron component while still transmitting gamma rays. The detector uses a single neutron-sensitive HB4 MCP, in front of an MCP amplifier section consisting of two standard product (non-neutron-sensitive) Photonis Group MCPs.

Figure 5. (left) $LaBr_3$:Ce fast scintillator crystal attached to a Burle Industries 1-in. fast PMT; (right) coupled crystal and PMT, tape-wrapped to prevent stray light input

The $LaBr_3$:Ce gamma scintillator is 1 in. in diameter and 1-in. thick to ensure absorption of the 478-keV gamma ray emitted by the neutron-boron reaction. The crystal is coupled to a 1-in. fast PMT, which in turn is attached to an 8-in. detector vacuum flange.

Testing at MNRC

On September 20–21, 2006, testing with thermal neutrons was performed at the MNRC operated by UC Davis, with assistance from Sensor Sciences. Figures 6–9 show various setup configurations in Bay 4 at the MNRC reactor site.

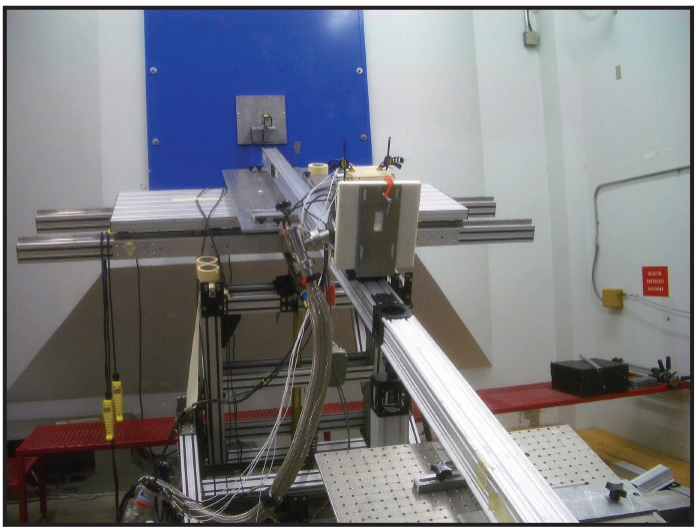

Figure 6. Detector on rail behind Li-blocking sheet, with neutron beamstop at rear

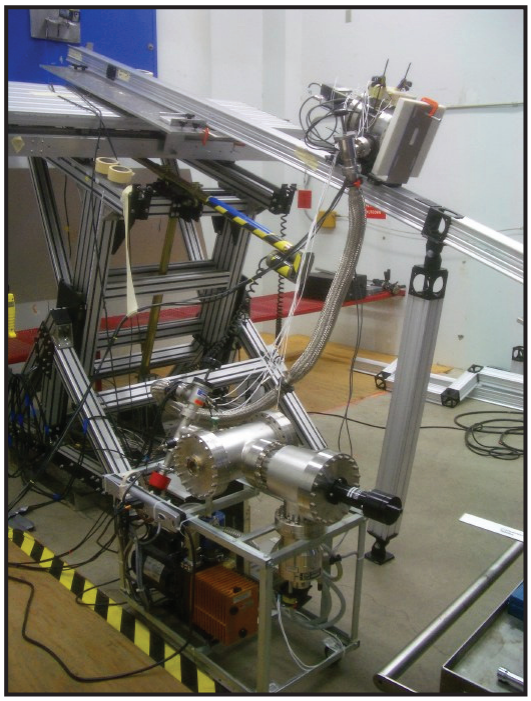

Figure 7. Turbo-pumped, ultra-high vacuum system connected to detector flange, with neutron beam entering from right

Figure 10 shows the measured PMT energy spectrum with a time-gated coincidence window of ~25-ns width. The resultant 478-keV gamma peak resulting from the neutron event is readily apparent.

The measured coincident and noncoincident neutron-gamma events (in MCP and scintillator/PMT detectors) appear in Figures 11 and 12. Evident residual events are due to random coincidences at the PMT/MCP count rates for the 100-ns and 25-ns windows.

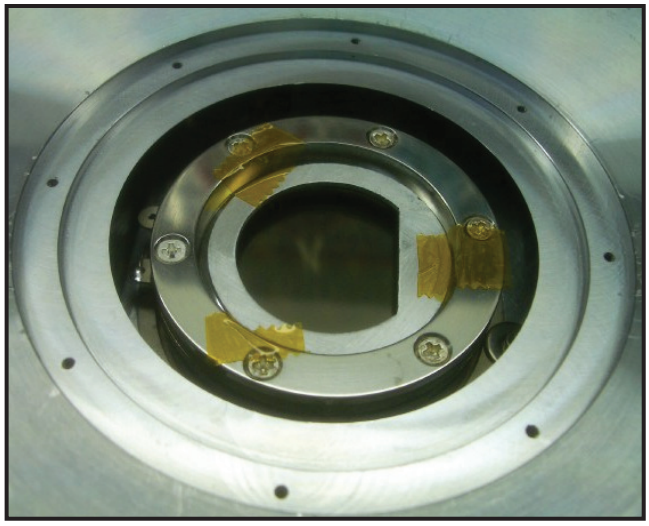

Figure 8. Open-area, 1-in. Cd mask, with chord for gamma background subtraction

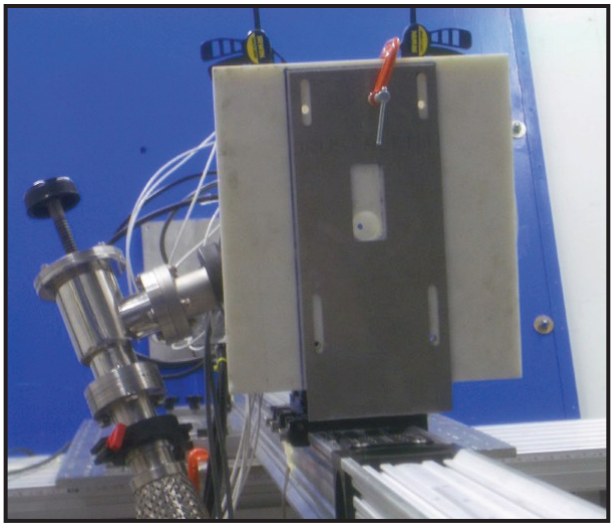

Figure 9. Li-blocking sheet with 1-in. aperture

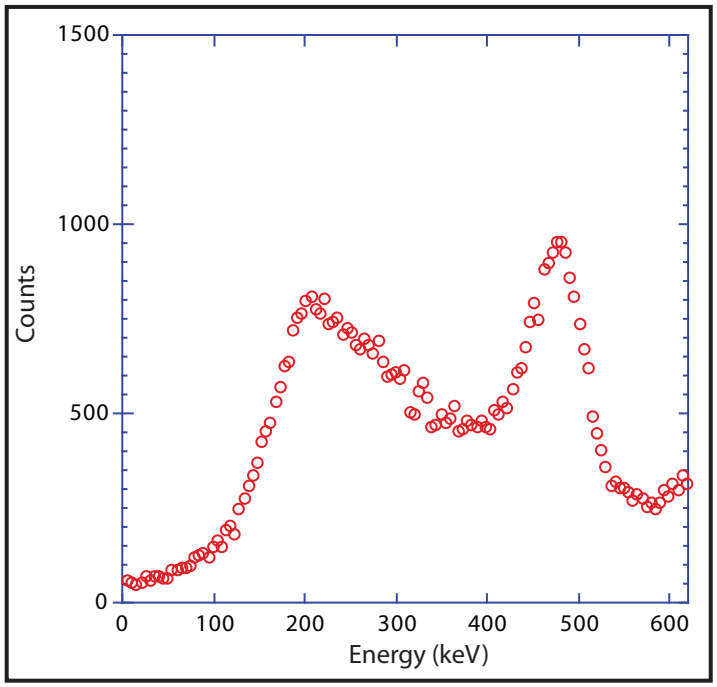

Figure 10. 478-keV gamma peak evident in PMT energy spectrum of time-gated (25-ns) coincidences

The shorter window (Figure 12) removed a majority of events, as compared with the 100-ns window (Figure 11). Random gamma events apparent in the 25-ns window represent 0.2% of those occurring in the 100-ns window, implying a ~500X rejection ratio. Indeed, neutron-gamma discrimination in the 25-ns window is clearly better than in the 100-ns window.

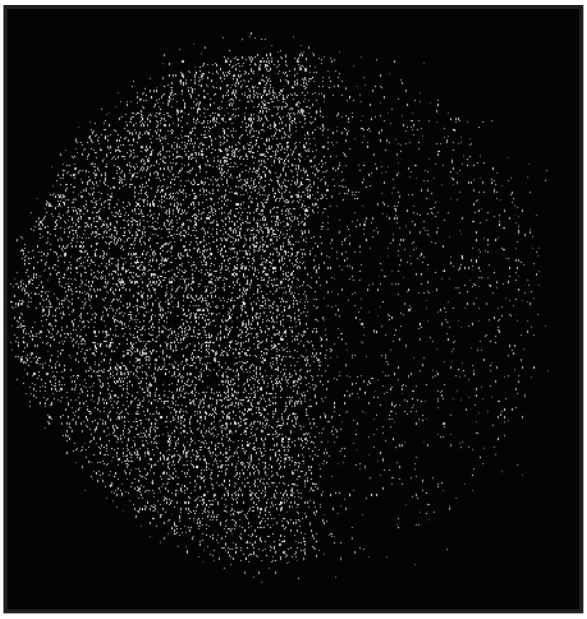

Figure 11. Time-gated coincidences with a 100-ns window; left side is coincident, right side is noncoincident

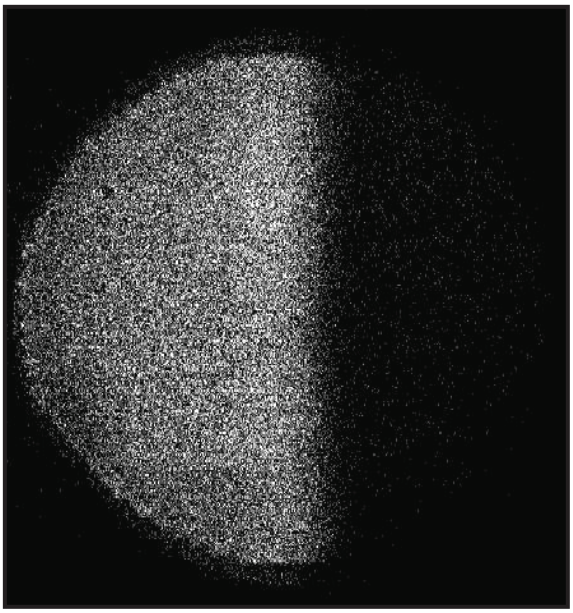

Figure 12 . Time-gated coincidences with a 25-ns window; left side is coincident, right side is noncoincident.

Conclusion

The neutron-sensitive HB4 MCP demonstrated strong neutron sensitivity to a relatively low-flux thermal neutron beam at the MNRC. Rejection of the gamma signal and preservation of the neutron signal was apparent when an MCP detector operated in coincidence with the scintillator/PMT detector. Initial timing-gate windows of 100-ns and 25-ns duration were used.

Demonstration of MCP neutron sensitivity, together with a technique that strongly rejects gamma rays, is deemed essential to successful employment of the MCP/MSP/MFP detector technology for low-level SNM detection from realistic sources (which emit strong gamma rays). Without active discrimination, the MCP/MSP/MFP gamma-neutron detection ratio could never be better than ~10^{-1}, thus creating reduced interest in this technology for SNM detection when compared to the standard performance of ^{3}He gas tube detectors.

The event rate in the MCP detector was 10 kHz (5 kHz of detected neutrons and 5 kHz of detected gammas), with the MNRC reactor operating at 50 kW (normal operation: 1.6 MW). The event rate of gammas in the gamma scintillator detector was 100 kHz. The 478-keV gamma-ray peak resulting from a neutron event is clearly identifiable in the energy spectrum, and the MCP detector accepted the expected number of neutron events. Since the inherent gamma-neutron rejection ratio is determined in time by the number of random coincidences, our preliminary data imply a ~50:1 gamma-neutron rejection ratio using the 100-ns coincidence time-gating window, and a ~500:1 ratio for the 25-ns window. Additional analysis of the data list files should be carried out to more fully calibrate this ratio.

We are highly confident we can achieve an improvement in gamma rejection of at least another order of magnitude or more, resulting in discrimination ratios even better than the 10^5 benchmark. This would involve further refinement of the coincidence time-gating techniques and further testing runs. Completion of MFP/MCP detector development, along with addition of a thin Ta/W composite gamma shield, will prove the viability of the neutron-sensitive electron multiplier approach.

References

Tremsin, A. S., W. B. Feller, "The theory of compact and efficient circular-pore MCP neutron collimators," *Nucl. Instrum. Methods* **556**, 2 (2006) 556–564.

Tremsin, A. S., W. B. Feller, R. G. Downing, "Efficiency optimization of microchannel plate (MCP) neutron imaging detectors. I. Square channels with ^{10}B doping," *Nucl. Instrum. Methods* **539**, 1–2 (2005) 278–311.

Tremsin, A. S., W. B. Feller, R. G. Downing, D. F. R. Mildner, "The Efficiency of Thermal Neutron Detection and Collimation with Microchannel Plates of Square and Circular Geometry," IEEE Nuclear Science Symposium, Rome, Italy, (October 2004) 1020.

High-resolution Gamma Spectroscopy with Cerium Bromide

Sanjoy Mukhopadhyay[1]
Remote Sensing Laboratory – Andrews

Vince Wolfe
Remote Sensing Laboratory – Nellis

Recently, the Department of Homeland Security (DHS) has integrated all nuclear detection research, development, testing, evaluation, acquisition, and operational support into a single office: the Domestic Nuclear Detection Office (DNDO). The DNDO has specific requirements set for all commercial and government off-the-shelf radiation detection equipment and data acquisition systems (DAQ). This project investigated several recent developments in field-deployable gamma radiation detectors that are attempting to meet the DNDO specifications. Commercially available, transportable, handheld radioisotope identification devices (RIID) are inadequate for DHS's requirements, in terms of sensitivity, resolution, response time and reach-back capability. The goal of this project was to build a prototype handheld gamma spectrometer, equipped with a digital camera and an embedded cell phone, to be used as an RIID with high sensitivity (comparable to that of a 7.62 × 7.62 cm sodium-iodide crystal at low gamma energy ranging from 30–3000 keV), better resolution (<3% at 662 keV), and fast response time (able to detect the presence of gamma-emitting radioisotopes within five seconds of approach), all of which will make it useful as a field-deployable tool. The handheld equipment continuously monitors the ambient gamma radiation and, if it comes across any radiation anomalies with higher than normal gamma gross counts, it sets an alarm condition. When a substantial alarm level is reached, the system auto-triggers saving of relevant spectral data and software-triggers the digital camera to take a snapshot. The spectral data including *in situ* analysis and the imagery data will be packaged in a suitable format and sent to a command post using an embedded cell phone.

[1] mukhops@nv.doe.gov, 808-474-2654

Background

Current Trends in Mobile Detection

A number of gamma and neutron detectors of various sizes, sensitivities, and resolutions have been designed, prototyped, and field-tested in recent years at NSTec. These sensors were built with a comprehensive approach towards search localization and screening of radioisotopes of interest. Larger sodium iodide crystals (4" × 4" × 16") for gamma detection and larger arrays of pressurized helium tubes (3' × 2", up to 48 tubes) are deployed for aerial missions, while smaller detector sets with 4" × 2" × 6" sodium iodide crystal and eight 6" × 1" helium tubes are used for handheld systems. These sensors continuously monitor the ambient radiation counts (gamma and neutron) and generate alarm conditions if a higher than normal radiation field is encountered. The software platform Multiple Application Computer Systems (MACS) is the basis of the DAQ, which provides the algorithms for alarm conditions for the detection systems. Recently, a very successful remote sensing radiation detector system, Multiple Platform Systems (MPS), has been developed and deployed for large-area search and radio isotope screening. The Acquisition and Telemetry unit for these detectors uses a PC-104 board stack for gamma and neutron counting and synchronizing radiation data with Geographical Positioning Satellite (GPS) information. The MPS units' data display plots the path of a vehicle-mounted system in real time and accepts and displays spectral data (energy information) from gamma-emitting sources. Newer gamma detectors can quickly determine the relative direction of a point source, which enhances search capability in any mission where directional information would be useful (portable, mobile, aerial). The new feature of this detector is the use of two detector pairs to uniquely define angles and desensitize the system to background radiation.

In FY 2004, our team studied the properties of cerium-doped lanthanum halide ($LaBr_3$:Ce and $LaCl_3$:Ce) crystals (Mukhopadhyay, 2005). Although their energy resolution was excellent (~2.7% FWHM at 662 keV), the first few batches of crystals suffered from inherent alpha and gamma contaminations. The alpha contamination was due to the presence of actinides during mining. The intrinsic gamma radiation was due to the presence of the isotope 138La (0.090%) in 139La, which is impossible to remove without isotopic separation. Since then, the alpha contamination has been eliminated, reducing the intrinsic background of α-particles ranging in energy between 1.5–2.5 MeV from 1–10 to <0.05 Bq/cc and enabling Saint-Gobain Crystals and Detectors, Inc., to commercially manufacture cylindrical crystals sized up to 10 × 10 cm. In the current project, the intrinsic gamma signals were used to control the gains on the amplifier; by subtracting background spectrum, the gamma lines from the contaminant were removed.

Project

A small, handheld search and identification sensor was developed using 5.08 × 5.08 cm lanthanum halide ($LaBr_3$:Ce-5%) crystal and existing MPS electronics. Alarm conditions were generated in Search mode using the traditional MACS algorithm. Four separate buffers of 1024-channel analog-to-digital (ADC) data were continuously saved (each consisting of 3 seconds worth of multichannel analyzer [MCA] data) and at high levels of gamma alarm condition, 12 seconds (6 seconds before and 6 seconds after the alarm has taken place) worth of spectral data would be automatically analyzed by a standard isotope screening routine. A digital camera, software-triggered by the alarm condition, would take a snapshot of the item of interest. The onboard software would produce an extensible mark-up language (XML) report sheet on a high gamma alarm that consisted of the 12 seconds of spectral data, a digital picture of the suspect object, and the GPS location of the incident. A brief report describing the suspected radioisotopes along with the confidence level would be reported. The XML data file would then be sent out to a known location. The crystal with its photomultiplier tube (PMT), associated high-voltage, pulse-shaping, digital signal processing electronics, and an embedded GPS and cell phone card in PC-104 bus (similar to that used in MPS) would be packaged together to build a compact handheld room-temperature gamma spectrometer. Other features of MPS (*viz.* waterfall data, geographical information system–enabled path plot, and instantaneous spectral data) would be available on an attached small notebook. The user would need to have little to no knowledge of gamma spectroscopy).

Monte-Carlo N-Particle (MCNP) Simulation Studies

MCNP (Breimeister, 2000) has been used to study the sensitivity and energy resolution of sodium iodide (NaI:Tl), lanthanum chloride (LaCl3:Ce), and lanthanum bromide ($LaBr_3$:Ce) crystals of cylindrical shape (7.62 × 7.62 cm). The MCNP studies of lanthanum halides show that these crystals are capable of separating the two closely spaced gamma lines emanating from ^{239}Pu at 375 and 414 keV, respectively, while the NaI:Tl crystal cannot (Figure 1). The recently developed MCNP Visual Editor Graphical User Interface (MCNPVISED 4C2) (Schwarz, 1994) was used to characterize the basic scintillation properties and detection parameters of the lanthanum halides. MCNPVISED 4C2 enables a visual creation of an MCNP input file that can be read by the LANL MCNP4C2 (CCC-701) Monte Carlo transport code.

Classical F8 tallies for MCNP (pulse height statistics) were maintained for each of the simulations with specific gamma-emitting sources such as ^{239}Pu. A comparison of simulated pulse height spectra from different 7.62 × 7.62 cm crystals using a ^{239}Pu gamma source shows the higher resolution of the $LaBr_3$:Ce crystal (Figure 1). By computing F4 tallies for the same number of incident photons ranging in energy between 30 and 3000 keV, we calculated relative sensitivities of different scintillation materials, as shown in Figure 2.

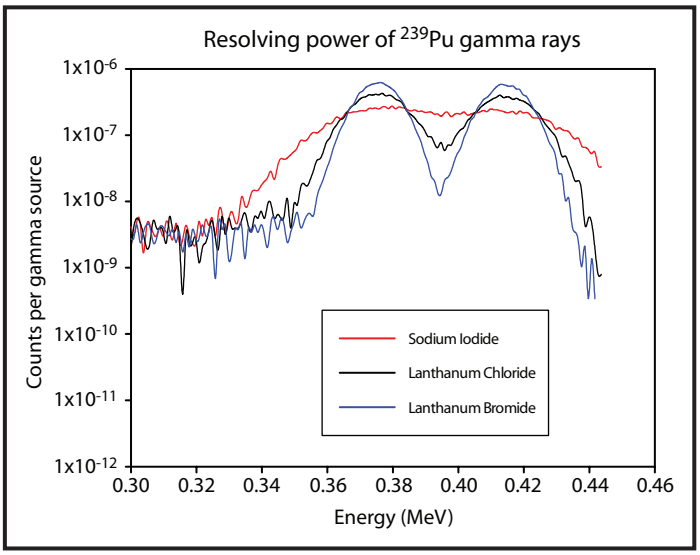

Figure 1. Simulated pulse height spectra from 7.62 × 7.62 cm crystals of NaI:Tl (red), $LaCl_3$:Ce (black), and $LaBr_3$:Ce (blue) scintillator with a 1 Ci ^{239}Pu gamma source. Gamma counts per second per unit energy are shown as a function of gamma ray energy.

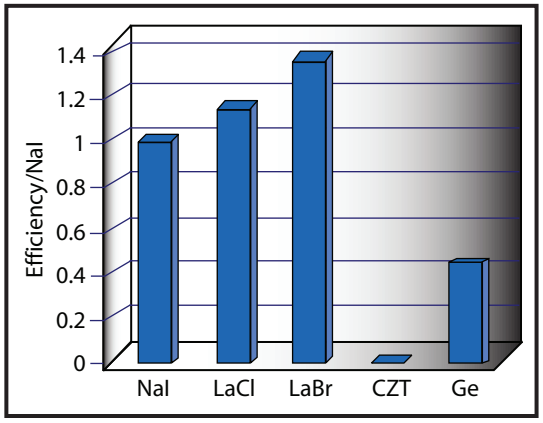

Figure 2. Simulated relative sensitivity of common scintillation materials (30–3000 keV). Expected sensitivity of $LaBr_3$:Ce is ~35% greater than that of NaI:Tl crystals of the same size.

Hardware Specification

$LaBr_3$:Ce Crystal Spectrometer

The spectrometer (hardware components are shown in Figure 3) was made out of a 5.08 × 5.08 cm $LaBr_3$:Ce crystal attached to a PMT and a charge-integrating preamplifier that generated voltage pulses proportional to the photon energy (~50 mV), which were then amplified by a shaping amplifier to 5–10 V and fed to a comparator/discriminator, and finally to an MCA. The spectrometer elements are detailed below.

BrilLance 380 $LaBr_3$:Ce crystal with its online PMT. The crystal is a 5.08 cm × 5.08 cm cylinder requiring 496 VDC to operate.

Phoenix USB 2.0 digital camera from MuTech Corporation. This camera was used to obtain digital pictures of the suspect objects when a radiological alarm would generate a software trigger for the camera. The camera resolution is low (a memory of 1.3 Megapixels) but it is appropriate for traffic monitoring. It was used to take the picture of the LPADC, below.

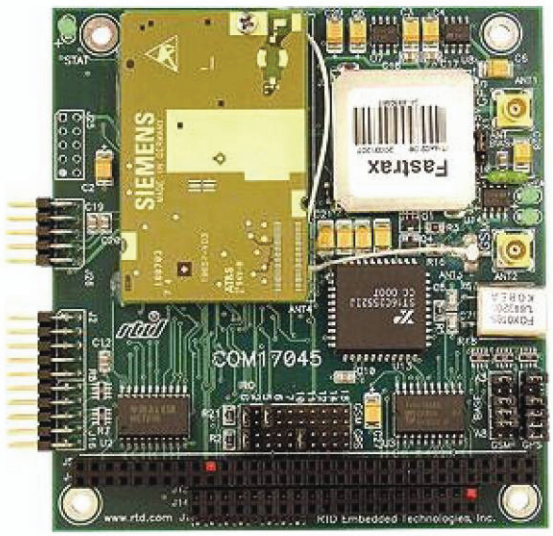

COM17045ER PC-104 cellular modem peripheral module.

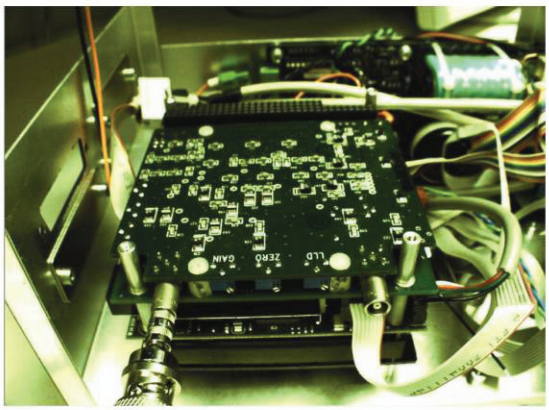

The LPADC board, showing LLD, zero adjustment, and the gain pod. The ADC consumes very little power (~500 mW) and can run for long periods of time on lithium-ion batteries.

Figure 3. Spectrometer elements

GSM Cellular Modem

The Real Time Device COM17045 wireless GPRS GSM modem unit provides a direct and reliable GPRS connection to GPRS GSM 900/1800/1900 MHz mobile fields around the world. GPRS GSM connectivity is achieved using the Siemens MC45. This unit works in the 900/1800/1900-MHz band, supporting GSM 02.22 network service provider personalization. It allows users to connect any standard dual-band GSM antenna directly to the OSX connector of the COM17045. The antenna should be connected to the MC45 using a flexible 50-Ω cable.

GPS Receiver

Integrated on the COM17045 is a fast-fix, 12-channel, low-power iTrax02 GPS receiver from Fastrax. This new receiver works reliably in a variety of installations. The receiver works with either 33- or 50-V active or passive antennas. The power consumption of the GPS receiver is 125 mW fully operational. A fast 1–4 Hz updating rate is achieved using the binary iTalk protocol. Two output formats are available: the NMEA-0183 ASCII protocol or the iTalk proprietary binary protocol. Switching between these protocols is controlled with one bit in the internal board registers.

Digital Camera

The Phoenix USB 2.0 is a 1280 × 1024 (1.3) pixel-density camera with ½-in. optical format. It can scan progressively at a rate of 15 frames per second. It uses USB interface cable and has a data transfer rate of 480. It is also capable of collecting 10-bit raw digital video data. The camera has a built-in frame buffer that avoids data loss due to USB congestion. The most interesting feature of this camera is that it accepts both hardware and software external triggers. It is a plug-and-play system and can adapt to multiple cameras.

MCA

The low-power, analog-to-digital converter (LPADC) is a low-current MCA board in a PC-104 form factor. The board contains a dual-port static configured as a ping-pong histogram memory. Thus, there is no loss of converted data while reading the data from the unit. The LPADC also contains live-time and dead-time counters. Its specifications are: ~500 mW power at background (500 cps); 256–4096 selectable channels; lower level discriminator (LLD); controls 0–5 V semi-Gaussian–shaped input pulse; and successive-approximation ADC with a conversion speed of 10 μsec.

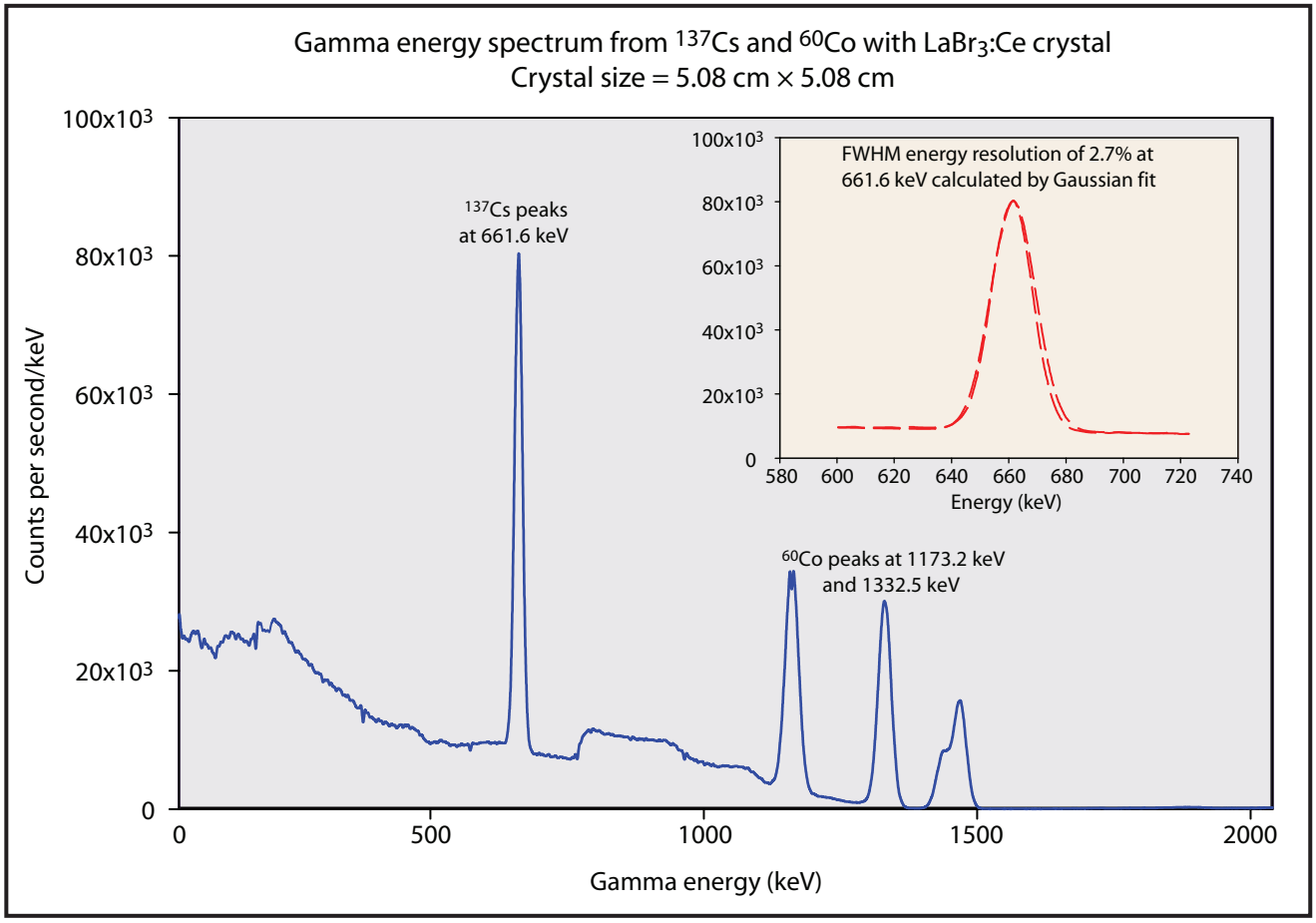

Figure 4. Gamma energy spectrum from ^{137}Cs and ^{60}Co sources taken with 5.08 × 5.08 cm lanthanum bromide cylinder. A simple Gaussian fit of the peak at 661.62 keV shows a FWHM resolution of 2.7%.

Experimental Results

A laboratory setup was built with the 5.08 × 5.08 cm lanthanum bromide cylinder with online PMT and the high-voltage power supply and PC electronic boards packed in a PC-104 card cage that included the LPADC. One crucial aspect of the experiment was to establish a good baseline for gamma energy resolution of the spectrometer (Figure 4). A resolution of 2.7% FWHM was obtained with a 5.08 × 5.08 cm cylinder. Figure 5 shows the waterfall gamma energy spectral data (the vertical axis is the time axis); the horizontal plot is color-coded with intensity varying with counts per energy bin. The software allows the user to look at the spectral data collected over a time period or over a number of events.

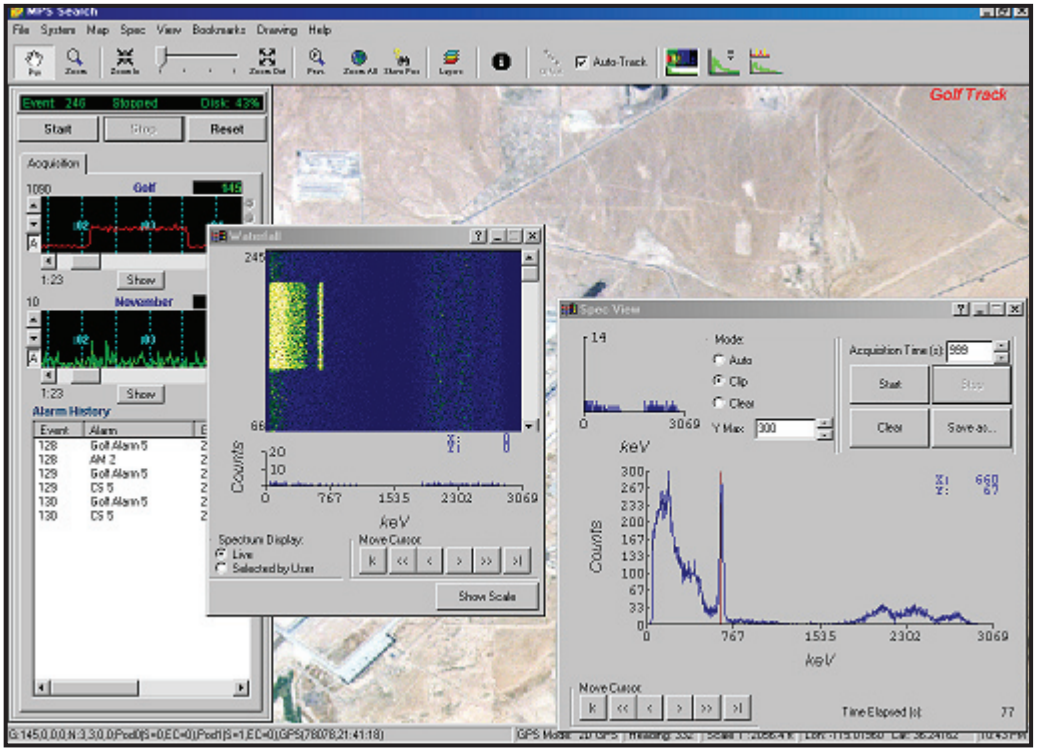

Figure 5. Waterfall and user-selected spectral data are shown on top of the geo-referenced map. Data collected live and the corresponding spectral data for a very short interval are shown at the bottom; due to high resolution, even with low counts, the cesium peak stands out at 661.62 keV and will be identified as such.

Conclusion

A high-resolution gamma spectrometer has been built and tested. It represents an improvement in resolution and portability over NaI-based spectrometers. The following improvements are proposed for the handheld system that will qualitatively change the way data is processed and how the light signals from the scintillators are handled by the digital signal processing electronics.

Quadratic Compression Conversion (QCC) is based on an algorithm related to the square root of the isotope's energy line(s). This optimizes the spectrum so that peaks are well separated at all energies. QCC is of particular importance in applications where a wide energy range must be monitored for unknown sources of radiation. The QCC process makes detection of peaks at all energies equally straightforward. Peaks at low energies are well resolved, while at high energies, peaks are compressed so that the peak-to-background ratio is dramatically improved for a given number of counts. This

directly translates into shorter counting times with better identification and analysis. QCC provides improvements in compensating for the drift of amplification gain due to temperature variation in radiation detectors. Since the compression is a function of energy, the drift will be nearly compensated over a range of temperatures.

Miniature packaging can be obtained by the use of silicon drift detectors (SDD). These ultraviolet-enhanced diodes provide excellent wavelength matching to the 380-nm emission of $LaBr_3$. A recent paper (Fiorini, 2005) presented at the 2005 IEEE Nuclear Science Symposium shows that the SDD has higher quantum efficiency over the PMT. Moreover, the SDD is not as sensitive to drifts due to temperature and bias voltage changes.

References

Breimeister, J. F., ed., "MCNP–A General Monte Carlo N-Particle Transport Code," LA-13709-M, Los Alamos National Laboratory, Los Alamos, New Mexico, 2000.

Fiorini, C., A. Gola, M. Zanchi, A. Longoni, P. Lechner, H. Soltau, L. Struder, "Gamma-ray spectroscopy with $LaBr_3$:Ce scintillator readout by a silicon drift detector," Dipt. di Elettronica e Inf., Politecnico di Milano, Italy; Nuclear Science Symposium Conference Record, 2005 IEEE, Vol. 1, October 2005, 230–234.

Mukhopadhyay, S., "High-resolution room temperature spectroscopy with lanthanum halides," *Nucl. Sci. & Eng.* **151**, 3 (2005) 348–354.

Schwarz, R. A., L. L. Carter, Shrivastava, "Creation of MCNP Input Files with a Visual Editor," *Proceedings of the 8th International Conference on Radiation Shielding*, Arlington, Texas, April 24–27, 1994, American Nuclear Society, La Grange Park, Illinois, 1994, 454–459.

this page intentionally left blank

Disposable X-ray Diode for Fusion Shots

Don Pellinen,[1] *John Yuhas*
Livermore Operations

A compact, disposable, reproducible x-ray diode (XRD) was developed for use in high-radiation environments such as the National Ignition Facility (NIF). The new XRD is disposable, inexpensive to produce, and can be calibrated with minimal effort. This project developed the conceptual design and determined appropriate manufacturing techniques for the XRD. The design concept was expanded to suggest improved design of the spectrometer's monochromator. In addition, the design addressed limitations in frequency response in the diodes now used.

Background

The original idea to build an inexpensive, disposable diode came from the question of how we would handle devices that were likely to become contaminated from fusion experiments at the NIF DANTE spectrometer. It was obvious that the manufacturing technique would be of primary importance, since the XRD should be disposable and reproducible. Furthermore, we were aware of frequency response issues that sometimes plague the current XRD-31: double pulses caused by photoelectrons leaking back into the grid and two-step responses. The design effort was expanded to include these issues. The monochromator, which is easily damaged and contributes to the frequency response problems, was also considered in our XRD redesign.

Project

It was determined that building the XRD using semiconductor hermetic package assembly techniques would be beneficial. Generally, a case made of aluminum oxide is used to enclose the chip. A metal leadframe provides the electrical feedthroughs and connection to the bonding pads on the chip. The leadframe is stamped, or for higher resolution, etched. A "solder" glass frit is applied to the alumina, usually by silk-screening. Typically the case is purchased from the vendor with the glass applied and prefired. The alumina case with the solder glass is loaded onto a process carrier and the leadframe positioned above it. The leadframe is precision-aligned to the alumina case by pins in the process carrier that protrude through precision holes and slots in the leadframe. After the entire process carrier is loaded with parts, it is fed into a precision belt furnace. The first parts of the furnace's temperature zones are set to heat the carrier to ~350°C; this lightly oxidizes unprotected areas on

[1] pellindg@nv.doe.gov, 925-960-2572

the leadframe. As the process carrier passes through a hotter furnace zone, the glass melts and fuses to the alumina and the iron oxide on the leadframe. The furnace's temperature is controlled so that the glass rises about halfway up the side of the leadframe. The process carrier enters cooler furnace zones, where it uniformly cools to room temperature.

At the "pick and place" machine, the process carrier receives a drop of solder glass on the pocket in the case, on top of which a chip is placed. The process carrier is fed into the belt furnace again, and the chip becomes fused to the case. The carrier is next loaded into a wire bonder, where the leads, usually 0.6-mil Al, are automatically welded to the bond pad on the chip and connected to the tip of the leadframe. Caps are inserted in the pockets of another process carrier and the assembly with the wire-bonded chip, and leadframe is placed upside down on the cap. The loaded carrier makes a final run through the furnace and emerges assembled. Normally, glasses with lower melting temperatures are used on succeeding steps. The throughput can be large. A 20-ft-long belt furnace may have 40 carriers inside. For a cycle time of 45 min, more than 500 parts per hour can be made with a 10-position process carrier.

First, a suitable carrier was located. Auer Precision supplied free samples of a carrier for a dual in-line package with a cavity for the ceramic part that was 0.745" × 0.053". Unfortunately the drawing supplied by Auer was for a slightly different part, and our parts didn't fit the actual carriers. Since the carriers were supplied as no-charge samples, there was little recourse. A search to locate a ceramic with the solder glass applied was fruitless. A ceramic body was designed, fortunately to the actual dimension of the cavity rather than to the drawing. Research to procure the solder glass eventually led us to a glass that we hoped would be appropriate for this application. The Kemco International SCC-2 solder glass has a firing temperature of 450°C for 30 minutes and can be reheated to 525°C to allow for successive firing cycles. The carrier and parts are shown in Figure 1. Based on the carrier, ceramic case, and solder glass characteristics, a process was developed, and we began to focus on the design of the XRD.

As stated earlier, three major design objectives piloted our effort. One was to design a part that could be mass-produced economically so they could be discarded if they became activated or radioactively contaminated. Using hermetic packaging manufacturing methods would largely address this. The second objective was to eliminate design flaws in the existing XRD-31. A third was to make the XRD compatible with lower-priced, throw-away components of a spectrometer.

The existing XRD-31's frequency response can be problematic. First, the distance between the high-voltage vacuum feedthroughs is large enough so that a reflection from an impedance mismatch is displayed ~350 ps after the first peak. This reflection produces a two-step (ringing or echoing), rather than the desired single-step response. Another problem occurs on high fluence shots: photoelectrons pass through the grid and are reflected back by the space-charge effect, inducing a second pulse on the photocathode.

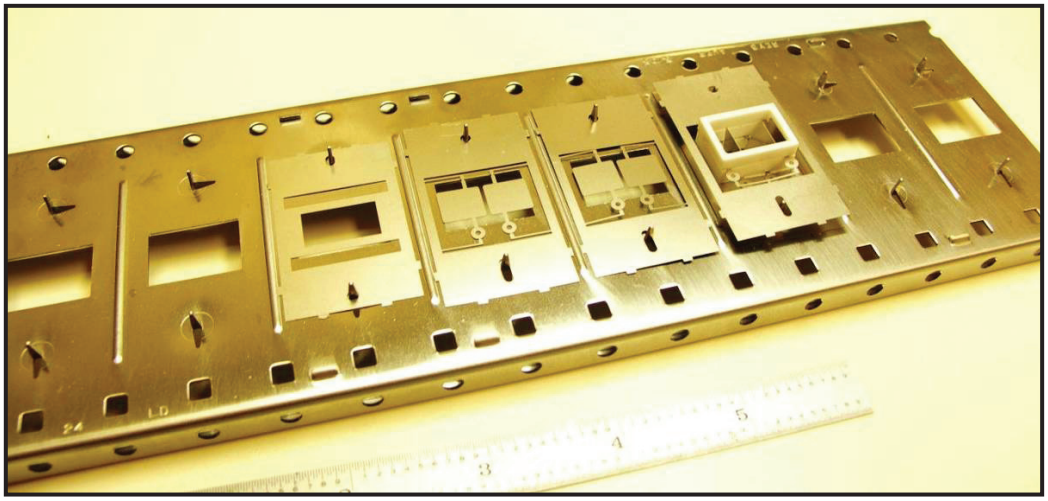

Figure 1. Standard carrier with parts for dual XRD assembly

The monochromator and collimators are parts of the DANTE spectrometer. The monochromator is composed of filters and a grazing incidence mirror for the low-energy channels. The mirror housings are large, and the mirrors are expensive and subject to calibration drift. The filters are expensive and fragile. For example, the lower energy channels can be destroyed in a single experiment. Therefore, our design aimed to allow incorporation of smaller, lower priced, robust monochromators.

The solution to the problem of ringing was to make the device tiny enough so that the time for the first echo would be ~65 ps, thus making the resonance shorter in time than the transit time of the electrons across the space. To fix the space-charge reflection, the simplest solution would be to use a solid anode rather than a grid anode. This also solved several other problems associated with the space charge–induced reflection and use of the large, expensive monochromator.

The only way to accommodate the solid anode was to incline the cathode and anode to the beam at a virtually grazing incidence. This configuration yielded an active cathode area of ~10 mm × 2 mm. Having a 2-mm anode allowed us to reduce the size of the large mirror from 35 cm to 9 cm and likewise reduce the size of the housing. It also enabled the use of a segmented filter holder; unexposed areas of the filter could be used in successive experiments as previously exposed areas were damaged or destroyed.

Another advantage of the inclined photocathode is increased sensitivity. When a low-energy x-ray photon is incident on a material, the photon interaction is primarily by the photoelectric effect. The electromagnetic field of the photon interacts with an electron and gives its energy to the electron. If the energy is greater than the binding energy, an electron will be ejected from the atom. The electron interacts with atoms in the material and scatters in random directions. If the electron has

sufficient energy and wanders to the surface, it can escape the material and become a photoelectron. By inclining the surface, the length to interact is made large and the distance to escape smaller, which should result in increased sensitivity.

We realized that two XRDs could be placed in the same housing. Figure 2 shows a cross-sectional view through the dual XRD, and Figure 3, an exploded view.

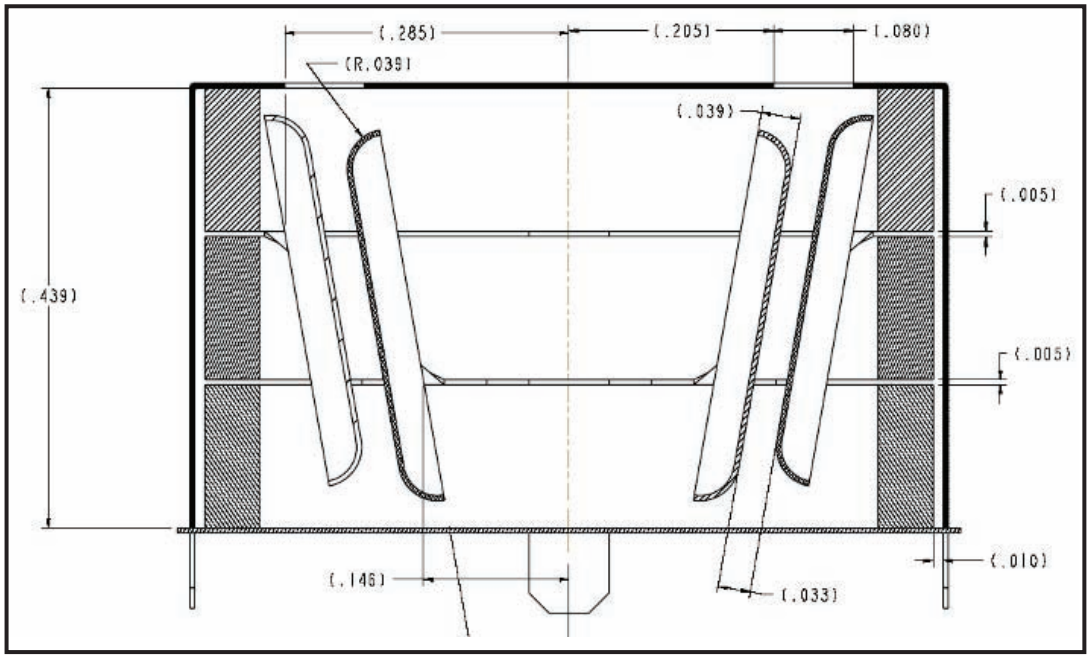

Figure 2. A cross-sectional view through the dual XRD with x-rays incident from above. From left to right are the ceramic wall of the container (cross-sectioned area), photocathode 1 (the nearly vertical electrode), followed by anode 1 and anode 2, and photocathode 2; and finally a cross section through the walls of the container.

As the parts were processed for the dual XRD, a few errors occurred. The drawing for the carrier from the vendor incorrectly identified the diameter of the alignment pins so a fixture had to be built to enlarge the pins. A slight error on the dimension across the diode made assembly difficult. Tooling to correct this error was designed but was not built because it would have taken considerable project time. Because it was important that we assemble a test structure that would rapidly test the basic manufacturing technology, a diode that was the functional equivalent of the XRD-31 was designed and the parts ordered. Several prototypes were built. Based on the experiences from the dual diode, several changes were made. A drawing of the basic frame for the metal parts was the starting point for the design; any metal and the parts were designed to fit within this standard outline. The XRD,

as well as a prototype streaking tube, were built on the standard frame. Realizing that the standard carrier would not serve to assemble all the parts in one furnace pass, we designed a single prototype carrier; several were built.

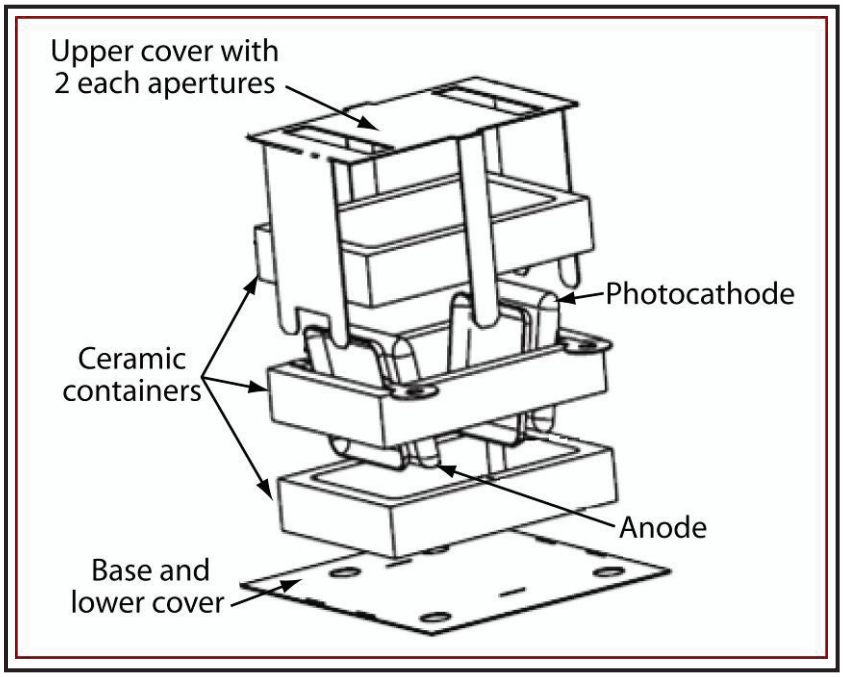

Figure 3. Exploded view of dual XRD

The XRD-31 used on the DANTE spectrometer is shown in Figure 4A, with parts developed by this SDRD project for the new XRD. The new, smaller XRD weighs 3.1 grams vs. 960 grams for an XRD-31. Figure 4B shows an assembled XRD on the left and an XRD in the fixture for firing. Figure 5 is an exploded view of the XRD-31.

The new anode (Figure 4a) replaces the five parts in the upper center of Figure 5, plus three parts on each side that function as support and feedthroughs at the bottom left and right. The new anode costs $2.74, plus a one-time tooling charge of $0.88 each in quantities of 100, and replaces 11-each expensive parts. The new photocathode, which costs the same as the anode, replaces the two conical parts, the screw, and the metal feedthrough part shown in Figure 5, as well as four other external parts not shown in the figure. The 0.75-in.-square base (Figure 4a), 0.005 in. thick, replaces the 3-in. diameter housing shown in grey in Figure 5. In terms of cost, the bodies with the three feedthroughs on the XRD-31 cost $1499.20 each in quantities of 25 in 2006. This did not include the parts broken away. The three metal parts on the developed diode were $3.62 each with the tooling charge or $10.86 for the three-each.

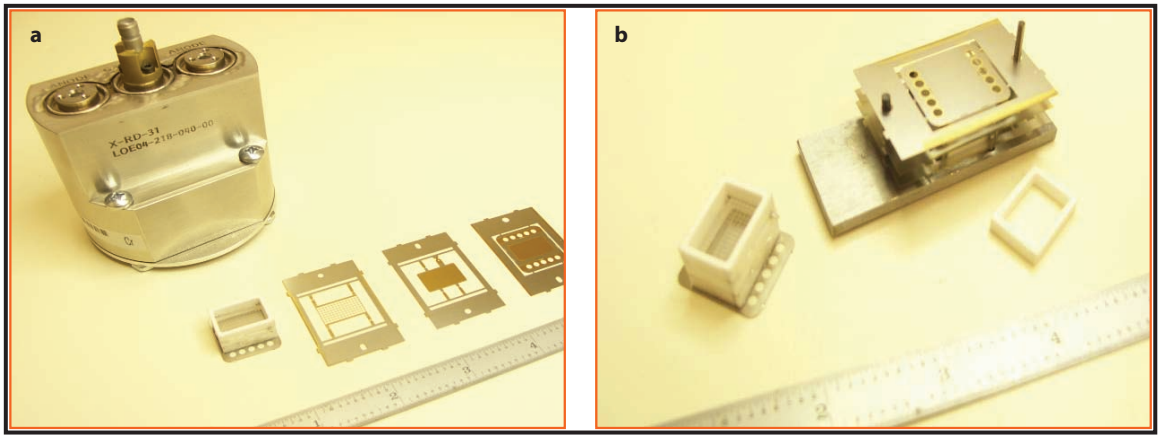

Figure 4. (a) Existing XRD-31 with new assembly and metal parts; from left to right are the assembly, anode, photocathode, and base. Circular and oval holes align parts in the carrier. After the unit is bonded, excess metal parts are removed. (b) Assembled XRD and fixture ready for firing; a ceramic insulator sits in front of the fixture. The ruler shows dimensions in inches for both figures.

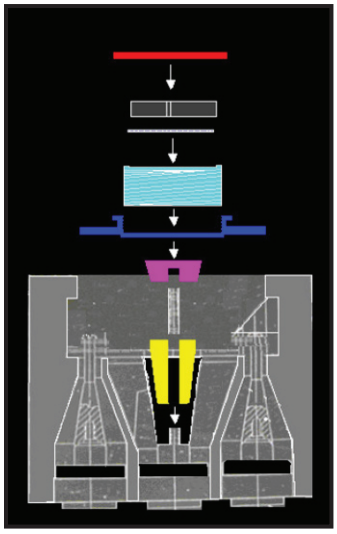

Figure 5. XRD-31, exploded view

Conclusion

A small, disposable XRD unit was designed and prototypes were made. A major reduction in parts and costs was realized. Problems with the performance of the existing XRD-31 were addressed in our design, but improvements remain to be verified in tests. The pulse response of the detector may be tested in the Short-Pulse Laser Laboratory at LO. It is expected the risetime will be almost identical to the current XRD-31 without the ringing present on the XRD-31. A test to check and compare the absolute calibration of the diode with existing diodes may be conducted at the Brookhaven National Laboratory's National Synchrotron Light Source. For these tests to occur, the new XRD would have to be adapted to a blank flange having the same dimensions as the XRD-31 for interchangeability. A technology abstract was produced for this research.

Acknowledgments

A number of people assisted in the project. Encouragement was given by Dean Lee, Jochen Schneider, Kelley Campbell (now with Aspire Technologies), and Franz Weber of LLNL. Mary Kucher procured the items from a variety of vendors. Rob Buckles kindly provided the photos, and Mike Cardenas supplied the instructions for assembling XRD-31s, from which Figure 5 is taken. Terry Richardson guided the researchers through various computer problems.

this page intentionally left blank

Inexpensive Passive Neutron Detection

William Quam, Stephan Weeks[1]
Special Technologies Laboratory

A passive neutron detector with the highest neutron-to-gamma ratio would be of direct benefit in many applications. We examined ^{157}Gd, with its high thermal neutron cross section, as a candidate passive neutron detector that will have essentially no response to gamma rays. Neutron capture in this isotope leads to a stable isotope; the amount of this new isotope created is proportional to the neutron fluence. Monte Carlo N-Particle (MCNP) modeling calculations were used to determine the feasibility of using these neutron-induced isotope changes to detect a neutron source at a distance. Suitable isotope ratio measurement techniques were investigated. Since mass spectrometry (MS) is the obvious initial choice for the measurement of isotope ratios, we also performed a survey of commercial mass spectrometers.

Background

Neutron capture leading to changes in isotopic ratios of *stable* isotopes is an attractive method of monitoring neutron fluence. Some isotopes, ^{157}Gd for example, have very large thermal neutron cross sections and a nonradioactive neutron capture product (i.e., it will not decay away). This could permit evaluation of the neutron fluence using, for example, a mass spectrometer (MS) to detect changes in the isotope ratios as a measure of the neutron capture reactions. Detection that requires only a small physical sample would be advantageous in most instances. The use of stable isotopes would enable long-term (weeks to months) monitoring of neutron fluence.

In this project, we examined the expected isotope changes via MCNP calculation and surveyed existing isotope ratio detection technologies for portability and adequate precision. We explored the feasibility of a very inexpensive field deployment method, together with a simple sampling technique.

The isotope we initially selected was ^{157}Gd, due to its very high thermal neutron capture cross section of 254000 barns. Other isotopes were also considered; ^{113}Cd (originally used at Argonne National Laboratory to demonstrate isotope burnout during the Manhattan Project in the 1940s [Dempster, 1947]), and ^{151}Sm. The isotopes shown in Table 1 yield a stable addition product that will not require extended counting time for evaluation. In addition, the production of a stable isotope addition product is not possible with gamma rays. This ensures that only neutrons are detected by the measured changes in isotope ratio.

[1] weekssj@nv.doe.gov, 805-681-2262

Table 1. Isotopes suitable for neutron detection

Isotope	Abundance	Thermal cross section, barns	Stable result of capture
^{113}Cd	12.26%	20000	Yes
^{149}Sm	13.84%	40800	Yes
^{155}Gd	14.73%	56200	Yes
^{157}Gd	15.68%	242000	Yes

Project

Passive Neutron Detection Method

The passive neutron detection method is based on evaluation of new atoms created during neutron capture. The measured signal should be directly proportional to the neutron fluence, neutron capture cross section, and number of target atoms present. The target isotope should have a large neutron capture cross section and large abundance. The product isotope should be stable and, ideally, of low natural abundance. Practically, the method should be low cost and easy to implement. The beauty of the proposed passive neutron detection method is that it only requires a material (i.e., no electronics, no power supply). The material, however, does need to be monitored (e.g., at portals).

^{157}Gd has the highest known thermal neutron capture cross section. Other Gd isotopes have significantly smaller cross sections. In order to detect neutrons, we investigated quantification of the isotope change from ^{157}Gd to ^{158}Gd upon thermal neutron capture. Both ^{157}Gd and ^{158}Gd are stable isotopes. If the Gd material was contained, for example, in a label on the surface of an object, innovative surface sampling and ionization techniques (e.g., laser ablation [LA]), together with portable laboratory analysis methods, could then determine the ^{157}Gd to ^{158}Gd ratio. Candidate technologies were MS or other suitable selective ionization techniques, including resonance ionization spectroscopies, optogalvanic spectrometry, or other high-resolution optical spectrometries such as diode laser absorption spectroscopy.

The sensitivity, and therefore the feasibility, of this idea was examined using MCNP calculations. In our very conservative scenario, the Gd material was in the form of ink on a label or bar code fastened to an object. The sampling and measurement methodology we initially considered for determining the isotope ratio was some form of portable MS following LA to remove only a small portion (e.g.,10–20 μg) of the Gd-containing ink.

Commercial-grade Gd powder was sent for thermal neutron exposure in a reactor to obtain samples to verify the methodology. This involved small 10 mg amounts of gadolinium oxide (Gd_2O_3) and a

100 to 1000-second irradiation time in a thermal column. Expectations are to demonstrate the isotope capture sensitivity, the possible complication of the neutron capture of the 156 and 158 isotopes, and to later demonstrate the actual MS precision to be found for this adjacent isotope measurement, as well as to compare results to the following MCNP calculation results.

MCNP Study

The MCNP study estimated the neutron capture rates from a small source of about 5×10^5 n/s at a nominal distance of 20 ft. A spontaneous fission source was used in the model. A variety of moderators was also examined to determine the detection efficiencies anticipated in various common exposure venues.

Detector Details

The detector was modeled as a thin label of Gd-containing ink 100 cm^2 in size, containing 10% by weight of Gd. The label was 0.0127-cm thick (5 mils) and had a nominal density of 1.1 g/cm^3. Thus, the Gd density was 0.1 g/cm^3 distributed over the whole label area, which would amount to 0.14 g of Gd in the whole label.

MCNP Details

The fraction of neutrons emitted from the source that would appear at the label location is 1.28×10^{-5} ±0.012. Using the emission rate noted above, we find about 6 n/s incident over the whole label area of 100 cm^2 (the fluence rate using only geometry with no absorption added is about 10.3 n/s incident on the whole label). The MCNP–calculated transmission of neutrons through the label (at thermal neutron energies of 0.025 eV) was about 0.8, suggesting that the Gd capture rate, due almost entirely to the 157 isotope, is about 1 to 2 captures per second over the 100 cm^2 label area. (Note that these are net captures in excess of background.)

Gadolinium Isotope Changes

Using an integration time of three weeks (deemed appropriate for long-term monitoring applications), we find 2.5×10^7 total captures in the label area (again, nearly all due to ^{157}Gd). If the sampled area were 1 mm^2 (an area ratio of 10^{-4} compared to the original 100 cm^2), then the Gd content in this small area would be 14×10^{-6} grams. This represents about 5.4×10^{16} atoms of Gd. Of this amount, there are 8.4×10^{15} atoms of ^{157}Gd and 1.3×10^{16} atoms of ^{158}Gd. The 2500 captures in ^{157}Gd sampled are thus a fractional decrease of 3×10^{-13} in the ^{157}Gd population and a fractional increase of 1.9×10^{-13} of the ^{158}Gd population. Thus, quantitation of the presence of the 5×10^5 n/s neutron source for three weeks at 20 ft will involve estimation of the isotopic changes to a precision of a few parts in 10^{13}.

Null Measurement Target Isotope Possibilities

MCNP work has shown that the neutron fluence rate at the label site due to a spontaneous fission source at 20 ft is low, perhaps 1 to 2 captures per second for ^{157}Gd. The transformation to the next higher isotope will thus be a (very) small fraction of the total number of atoms present.

Since null measurements would yield an easier and more accurate means of detecting species, it was logical to see if there was an isotope with a high neutron cross section that results in a transformation to a *different element during neutron capture*, thus making it easier to separate the addition product from the target atoms.

The target atoms must have a large neutron cross section to enable any effect to be measurable. A list of prospective isotopes appears in Table 2.

Table 2. Isotopes suitable for neutron detection leading to a new element

Isotope	Abundance	Thermal cross section, barns	Result of capture
^{168}Yb	0.14%	11000	No stable isotope, 32-d half-life
^{174}Hf	0.18%	1500	No stable isotope, 70-d half-life

The ^{169}Yb isotope from neutron capture decays via electron capture to ^{169}Tm, but the abundance is low, and the half-life is a little long for the expected three-week exposure time. The ^{175}Hf isotope resulting from neutron capture decays via electron capture to ^{175}Lu, but the abundance, the cross section, and the half-life seem unsuited for the expected three-week exposure. The reactions listed in Table 2, although feasible, do not have a cross section as large as that of ^{157}Gd. This will result in even more difficult detection conditions than the proposed capture reaction of ^{157}Gd to ^{158}Gd.

Neutron Background

There is a neutron background due to cosmic ray interactions. This is enhanced somewhat due to the possibility of cosmic ray–produced showers in adjacent materials, but is estimated to be about 1 n/s cm^2. The cosmic peak is around 0.1 eV, compared to the thermal peak at 0.025 eV. The cross section ratio will be in favor of the thermal capture by a factor of about 5 to 25. The expected cosmic ray–induced reaction rate will thus be ~20 captures per second per 100 cm^2 of the label. As described above, the presence of an isotopic neutron source will increase this to 21 to 22 captures per second, or a crude foreground-to-background ratio of 1.05 at worst.

Secondary Reaction

There is a second reaction that can occur: neutron capture in ^{155}Gd with a thermal cross section of about 60000 barns. This could be used to supplement the ^{157}Gd capture reaction used for the estimation above. The product is a stable isotope of Gd as well, and the mass ratio change resulting from the capture will be small.

Other capture reactions will involve ^{156}Gd to ^{157}Gd, increasing the initial ^{157}Gd amount, and ^{158}Gd to ^{159}Gd, reducing the expected production of ^{158}Gd by the ^{157}Gd capture. To first order, we expect these would cancel out and not affect the isotope ratio determination used to quantify the neutron fluence.

Test and Evaluation Plan

The MCNP calculations noted above suggested that there will be a small, but measurable, change in Gd isotope ratios that could be used to detect neutrons. The isotope ratio changes expected are very small, so to detect the neutrons from any neutron source at the earliest time, a statistically significant change in the isotope ratio must be determined. This means the analytical method used to measure the ^{157}Gd to ^{158}Gd ratio must have very high precision and excellent reproducibility. For this reason, we chose MS.

Although there was not time during the course of this project to actually test analytical methods on Gd samples that had been modified by neutron irradiation, we did develop a test plan to create a larger isotope ratio change. Gd_2O_3 samples were sent to be irradiated in a large thermal neutron fluence using a reactor. This would be best accomplished using a thermal neutron column, typically a graphite array that has a large Cd ratio. This will tend to emphasize the ^{157}Gd to ^{158}Gd transition. This enhanced isotope ratio could later be used to compare the expected mass precisions with actual changes in the isotope ratios, and, hence, predict the overall detection efficiency.

Several reactors have graphite thermal columns suitable for this irradiation. One such reactor is the TRIGA reactor at the Armed Forces Radiobiology Research Institute (AFRRI). This reactor has a graphite thermal column with a Cd ratio of 93 at an accessible irradiation position. This large Cd ratio will minimize unwanted activity (from epithermal neutrons) while giving a significant isotope ratio change from ^{157}Gd to ^{158}Gd. If three exposure times are used, then, for any given isotope ratio precision, extrapolations to lower fluence rates can be performed to quantify neutron detection sensitivity for environmental samples.

Radioactive Contamination from Induced Activity from ^{153}Gd due to Capture in ^{152}Gd

In order to test the feasibility of monitoring the ^{157}Gd-to-^{158}Gd ratio, high neutron fluences are desirable to induce larger changes. However, neutron capture in ^{152}Gd results in the creation of radioactive ^{153}Gd. The parent isotope, ^{152}Gd, has a thermal neutron cross section of 735 barns (Mughabghab, 2006), or 1056 barns, according to newer data from JENDL 3.3 (Japan Atomic

Energy Agency, 2005). We used the value of 1056 barns in the estimate detailed below. Due to safety and shipping concerns, the curie content of the sample must be minimized while at the same time—for the success of the study—the change in the ^{157}Gd-to-^{158}Gd ratio should be maximized. We therefore fashioned a compromise for acceptable neutron fluence rates and sample size.

Using an AFRRI reactor thermal neutron fluence rate of 2.9×10^{11} at a Cd ratio of 93, an estimate of 1.0×10^{-7} Ci for a 1-min irradiation at 1 MW and 1.7×10^{-9} Ci for a 1-sec irradiation at 1 MW for a 1-g sample of Gd metal (assuming no self-absorption or flux depression) was determined. A 1-kW power level should be easily obtained and will imply three decades less activity. Exposure times of 1000, 500, and 100 sec for the samples should be satisfactory from a timing standpoint since the thermal column at AFRRI has no automated sample transfer system (rabbit).

Gd_2O_3 has a 0.87 weight fraction of Gd. For 10-mg samples, the activity numbers above will be $0.87 \times 0.01 = 0.0087$ lower per sample than expected for a 1-g sample. The 1000-sec irradiation time will yield 15 nCi of ^{153}Gd, and the others proportionately less for shorter irradiation times, so the total curie content should be about 24 nCi for the three samples. This is an acceptable curie content both for shipping and for handling in the laboratory.

^{157}Gd Transformation as the Basic Neutron Monitor

The ^{157}Gd should be transformed into ^{158}Gd 241 times faster than ^{153}Gd is created from the ^{152}Gd activation (based on the ratio of thermal neutron cross sections [254000:1056]). A 10-mg Gd_2O_3 sample has 5.1×10^{18} atoms of ^{157}Gd; a 1000-sec irradiation should yield about 2.2×10^{14} atoms of ^{158}Gd. This assumes that the packing fraction of the Gd_2O_3 powder is about 0.5 and neglects flux depression and self-absorption.

The 2.2×10^{14} atoms of ^{157}Gd would be changed into ^{158}Gd atoms via thermal neutron irradiation. Initially there would be 5.1×10^{18} ^{157}Gd atoms. The final amount expected would be reduced by 2.2×10^{14} atoms of ^{157}Gd. The original ^{158}Gd population of 8.2×10^{18} would increase by 2.2×10^{14}. Therefore, an isotope ratio change of about 4.4×10^{-5}, or 44 ppm, using the reactor irradiation is expected. The 500- and 100-sec exposures would be proportionately less. A 44-ppm ratio should be easily quantified by routine MS work.

Sampling Techniques

A primary technical challenge is selection of a sample introduction method at the front end of the MS. The efficiency of the LA method is not well documented and varies with sample and conditions. It has been used for similar purposes in environmental survey work with external ionization. Other viable methods include desorption electrospray ionization, which has the nice feature of providing ions that can be directly taken up by the MS; focused ultrasonic-generated cavitation; and miniature plasma generation techniques, typically using He, N_2, or Ar. Many of these technologies

are commercially available for laboratory instruments. However, significant development would be required to design a field-portable unit that could be readily interfaced with appropriate detection technologies.

Isotope Ratio Detection Technologies

MS and resonance ionization or other optical spectroscopies are technologies that are applicable to isotope ratio detection. For direct isotope analysis of solid samples, laser ablation–inductively coupled plasma MS (LA-ICPMS), and glow discharge MS (GDMS) have replaced spark source MS (SSMS) and laser ionization MS (LIMS). Novel plasma discharges have perhaps the best potential for miniaturization for field applications. Resonance ionization MS (RIMS) (currently) and accelerator MS (AMS) involve complicated and expensive experimental equipment; analysis, including sample preparation, is time-consuming. Thermal ionization MS (TIMS) is a laboratory technique, requiring sample introduction under vacuum conditions. It is, however, a reliable and selective isotope analysis technique used for precise isotope ratio measurements, especially for elements with ionization potentials <7 eV, such as alkali, alkaline earth, and rare-earth elements. Electron impact (EI) MS, which is similar to TIMS, produces near monoenergetic ions and also provides high-precision isotope analysis, but is applied mainly for elements that readily form gases. Laser ablation multicollector ICPMS (LA-MC-ICPMS) is perhaps the most advanced laboratory technique, in which measurements have been reported with precisions of one part in 10^6, under controlled laboratory conditions. Penning ionization MS (PIMS) may also be of interest.

Conclusion

As a passive neutron detection material, ^{157}Gd is suitable. Creation of the Gd paint or ink appears to be simply a technical problem. The ability to conveniently monitor ^{158}Gd in the field presents a challenge. The calculated precision requirement for the isotope ratio measurement scenario is on the order of 10^{13}; this is well beyond current analytical capability, which is estimated to be on the order of 10^6–10^8. In addition, the need for portable sampling technologies and miniature analytical instruments such as mass spectrometers presents further hurdles to field implementation of this method. The detection gap may be narrowed in the future by several factors: the use of a larger sampling area; aggressive commercial R&D on new mass spectrometry tools, leading to rapid development cycles; and the need to develop a mass spectrometer to resolve only ^{157}Gd and ^{158}Gd, which may make the overall instrumentation and method much easier. The ideal instrument would likely be small and battery-powered.

Acknowledgments

This isotopic monitoring approach was originally suggested by Dr. E. Blase, a former employee of EG&G, and we are indebted to discussions with Dr. Blase. Additionally, we acknowledge the cooperation from personnel at AFRRI regarding use of their reactor for neutron irradiation experiments.

References

Dempster, A. J., "Isotopic Changes in Cadmium by Neutron Absorption," *Phys. Rev.* **71**, 11 (1947) 829.

Japan Atomic Energy Agency, Nuclear Data Center, *JENDL-3.3*, http://wwwndc.tokai-sc.jaea.go.jp/jendl/j33/j33.html, accessed November 10, 2005.

Mughabghab, S. F., *Atlas of Neutron Resonances: Resonance Parameters and Thermal Cross Sections, Z=1-100*, Elsevier, Oxford, England, 2006.

Additional details are available from the authors in an Official Use Only report.

Electronics

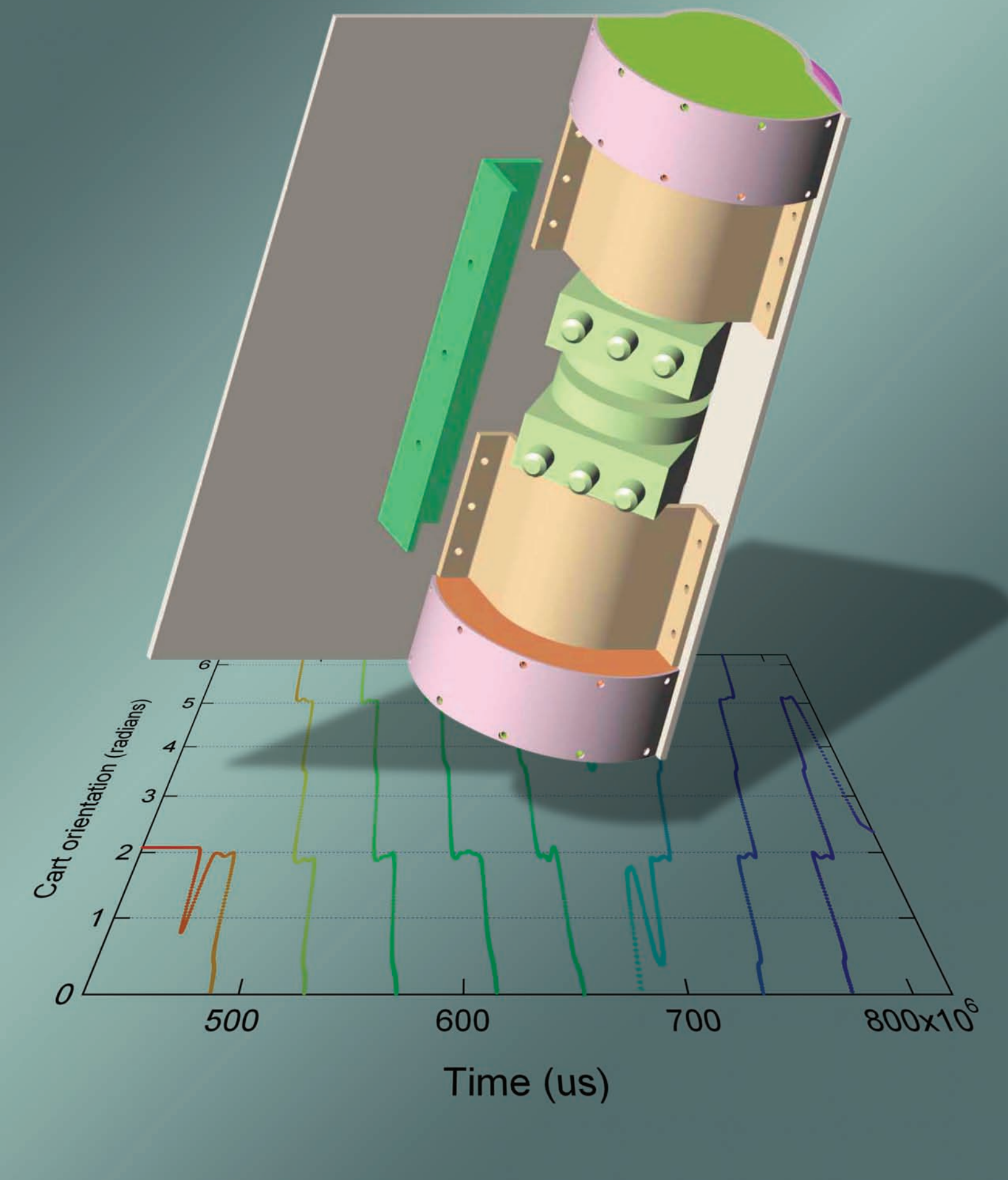

Wide-range Streak Sweep Circuits

D. Taner Bilir[1]
Livermore Operations

Amy Lewis
Los Alamos Operations

Based on previous experience in the design of streak camera deflection circuits, this research aimed to produce a wide-range deflection circuit. Using the combined expertise of two NSTec electro-optics groups from LO and LAO, a prototype design for a sweep circuit with ±1200-V ramps from 2 ns to 500 μs was produced. Prototype circuit board layouts were completed, and initial testing demonstrated ±1200-V ramps from 800 ps to 300 μs.

Background

Sweep circuits, also called ramp generators or streak deflection circuits, produce the carefully tuned voltage ramps necessary to drive a streak tube in any streak camera arrangement. Sweep circuits are generally described in terms of the time it takes for a linear voltage ramp to deflect an electron beam across a streak tube phosphor screen. But this criterion is not necessarily a good performance indicator because each tube has numerous parameters (temporal and spatial resolution, record length, photocathode size and sensitivity, dynamic range, and sweep linearity) that contribute significantly to a streak camera's overall performance. For example, an LO BN50 streak tube has a 50-mm-long photocathode active length, more than nine times the 5.4-mm photocathode area of the Hamamatsu C5680 streak camera (Hamamatsu, 2006). Similarly, the record length of the BN50 tube is 50 mm, compared to 18 mm on the C5680. For the same sweep velocity, this is nearly three times more temporal data. The combined effect of the larger photocathode and phosphor screen means it would take more than twenty-five C5680 cameras to capture the same amount of single-shot data as one NSTec streak camera outfitted with a BN50 tube. The BN50 tube also incorporates spherical geometry to maintain linearity over the entire photocathode and record length, whereas many commercial tube manufacturers utilize planar geometry and sacrifice linearity.

Complexities arise in configuring a streak camera with such high performance characteristics: the sweep circuits must drive higher voltage ramps with higher current to achieve the increased performance; sweep circuit boards must be replaced; bias settings must be altered to match extended sweep speed ranges; and calibrations may require unique speed sweep boards. Not only do these tasks impact schedule and labor costs, they may also invite errors during board switch-outs and setup.

[1] bilirdt@nv.doe.gov, 925-960-2626

Manufacturing costs and component count for the circuit boards also increase when maintaining numerous board designs. These concerns were among the important reasons that led to a novel collaboration between LO and LAO to develop a wide-range, computer-controlled circuit that could work with the LO LOE07 and LAO Gen IV streak cameras.

LO optical streak camera configurations include fixed ramps of 5, 10, and 15 ns, and two variable-speed ramps with ranges 30–480 ns and 3–30 μs. LAO offers configurations in four variable ranges: 20–500 ns, 200 ns–5 μs, 2–50 μs, and 20–500 μs. Therefore, the operating range for this project was specified as 2 ns to 500 μs, with enough linear ramp voltage to drive the deflection electrodes of Photek, Photonis, and the LO BN50 streak tubes. This requirement translates to a 1200-V linear ramp into a 15-pF deflection plate capacitance.

Project

For this project LO used its fast-sweep expertise to design the fast- and medium-speed sweep circuit sections, while LAO slow-sweep experts designed the slow-sweep circuit section. The resulting design is a hybrid circuit that uses avalanche transistor stacks to perform the high-speed ramps, and metal-oxide semiconductor field-effect transistor (MOSFET) stacks to accomplish the moderate and slow sweeps, and also act as a hold-off circuit for the faster ramps. The project was separated into six sections:

- Power supply/control circuit design
- Fast (2–30 ns) and medium (30–300 ns) circuit design
- Slow (300 ns–500 μs) circuit design
- Printed circuit board (PCB) layout design
- Fabrication and testing
- Circuit integration

Power Supply and Control Circuit Design

For any sweep circuit, the design of the high-voltage power supply and control is paramount. The power supply chosen for this design needed to provide enough power for the slower speed ramps, while also being able to decrease the overall power to a level below that of the Electrical Safety Standard (<5 mA if over 50 V). A similar approach was applied to the common-mode power supply, which provides a voltage bias to the streak tube deflection plates, acting as an electrostatic focusing lens for the electron beam, effectively increasing spatial and temporal resolution.

Fast- and Medium-speed Sweep Circuit and PCB Designs

Circuit Design

The fast- and medium-speed circuit designs were based on earlier sweep design work of King, Baker, and Guyton (Baker, 1992; King, 1992). Guyton and Buckles recommended use of Zetex FMMT 417 transistors (Zetex, 2006), and we also noted their high-speed, high-current capabilities as appropriate for our purpose. The FMMT 417 avalanche transistors were arranged in a stack to achieve the specified ramp circuit of 3 kV. Because the avalanche mode of a transistor determines the speed of the ramp, relay-selectable passive filters were added to provide a wide range of fast sweep speeds. Stacked MOSFETs provided voltage hold-off, a feature that prevents the electron beam in a streak tube from overwriting the data. MOSFETs also provided the medium-speed ramps.

PCB Design

The PCB layout design considered the high voltage in the circuits. To prevent arcing, high-voltage points were isolated from low-voltage regions. Grounding and signal paths on the fast/medium circuit required special attention due to the frequencies present in the fast ramps. Engineers and technicians fabricated prototype PCBs using PCB milling methods developed as a result of FY 2004 and FY 2005 SDRD research (Diamond, 2005; Bilir, 2006). The fast circuit showed a maximum linear ramp of ~800 ps for 1200 V, though the first prototype did not incorporate a hold-off circuit (Figures 1 and 2).

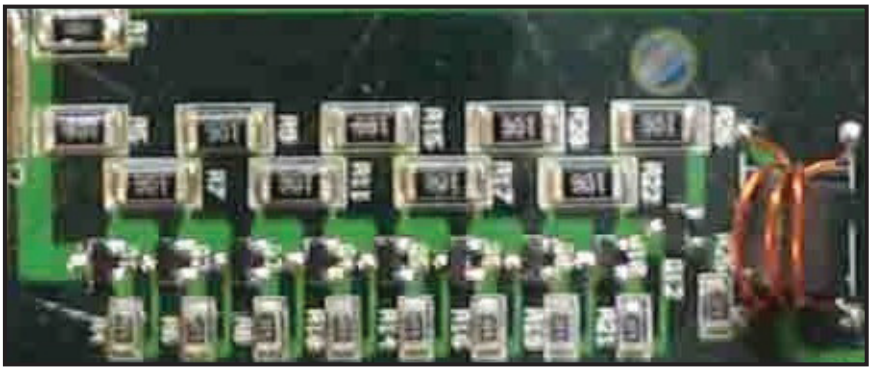

Figure 1. High-voltage avalanche transistor stack built with FMMT 417 avalanche transistors

Slow-speed Sweep Circuit and PCB Designs

The slow-sweep circuit, designed by LAO, relied heavily on the work of Lewis, Rohrer, and Baker (Lewis, 2005). The ramps were created by a double-ended stack of high-voltage MOSFETs. High-voltage reed relays were used to locally modulate the capacitance seen by a MOSFET stack.

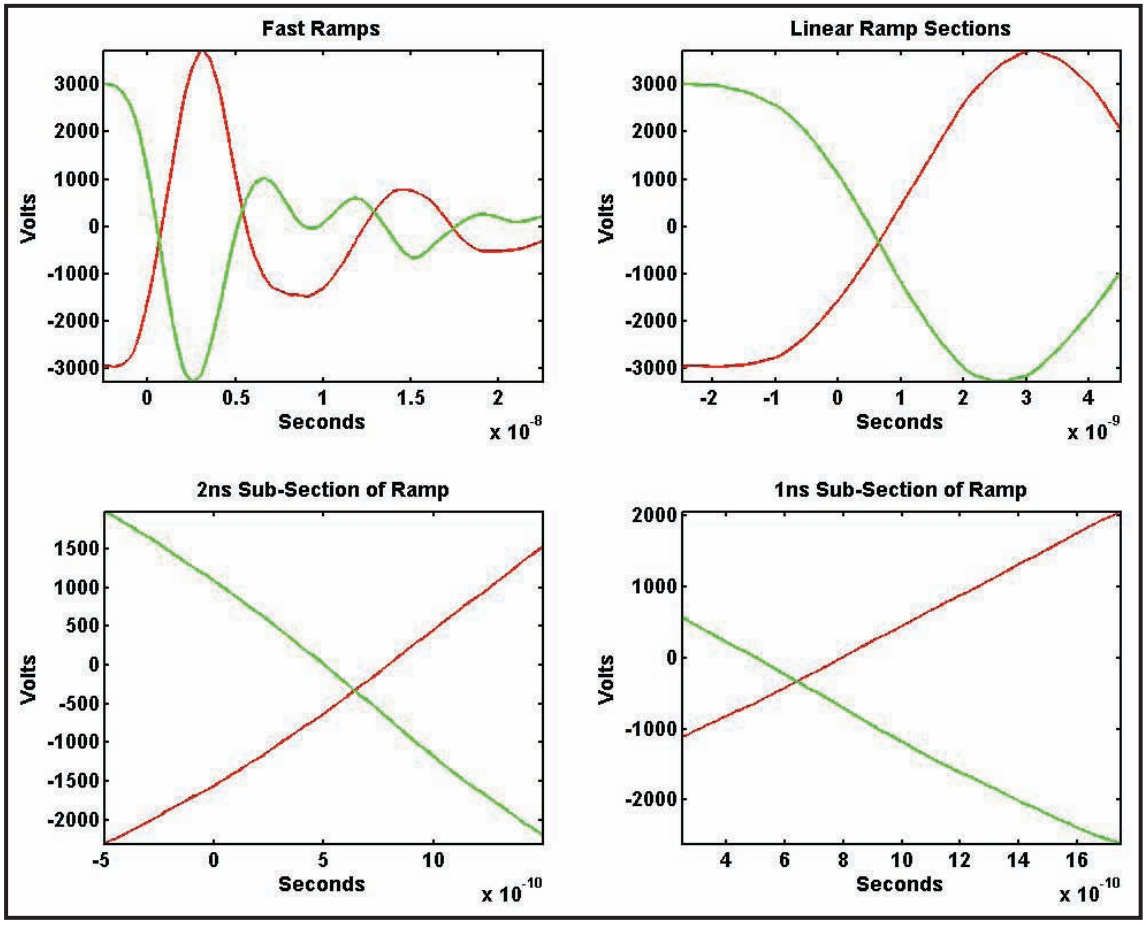

Figure 2. Fast ramp waveforms acquired with a Tektronix TDS684 oscilloscope with P5100 high-voltage probes

This had the effect of changing the sweep speed range for the slow circuit section. Parasitic capacitance in the relays changed the performance of this section to speeds slower than the design theory suggested, but that was actually desirable (Figures 3 and 4). Due to the lower frequencies involved, PCB layout was not as critical for the slow-speed circuit. The circuit was tested by triggering ~100000 times over several days—the number of triggers the circuit was estimated to perform in its life span.

The slower circuits were also tested in a camera configuration, and the images showed good linearity and resolution (Figures 5 and 6).

Figure 3. Waveforms of slow ramps operating at 2 µs (left) and 300 µs (right)

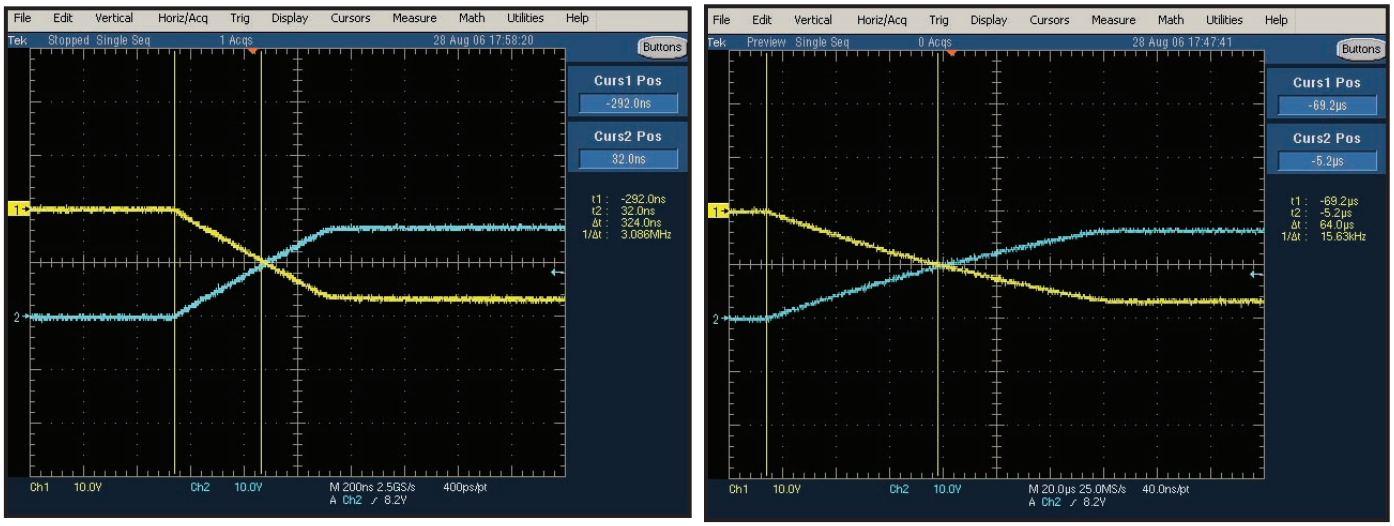

Figure 4. Waveforms at 320 ns (left) and 64 µs (right)

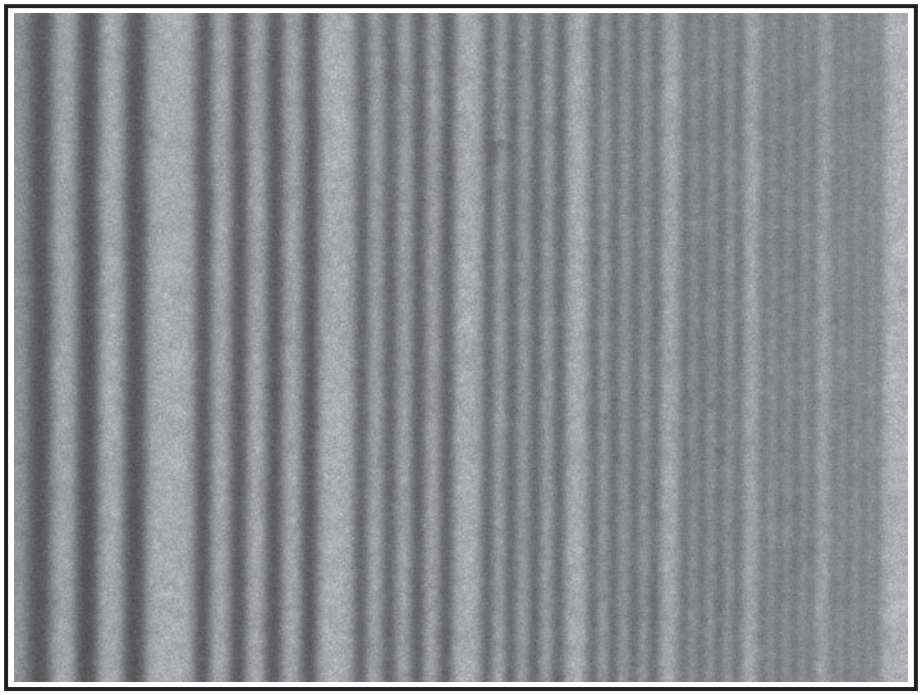

Figure 5. Swept PR-10 resolution target on slow circuit running a 500-ns sweep

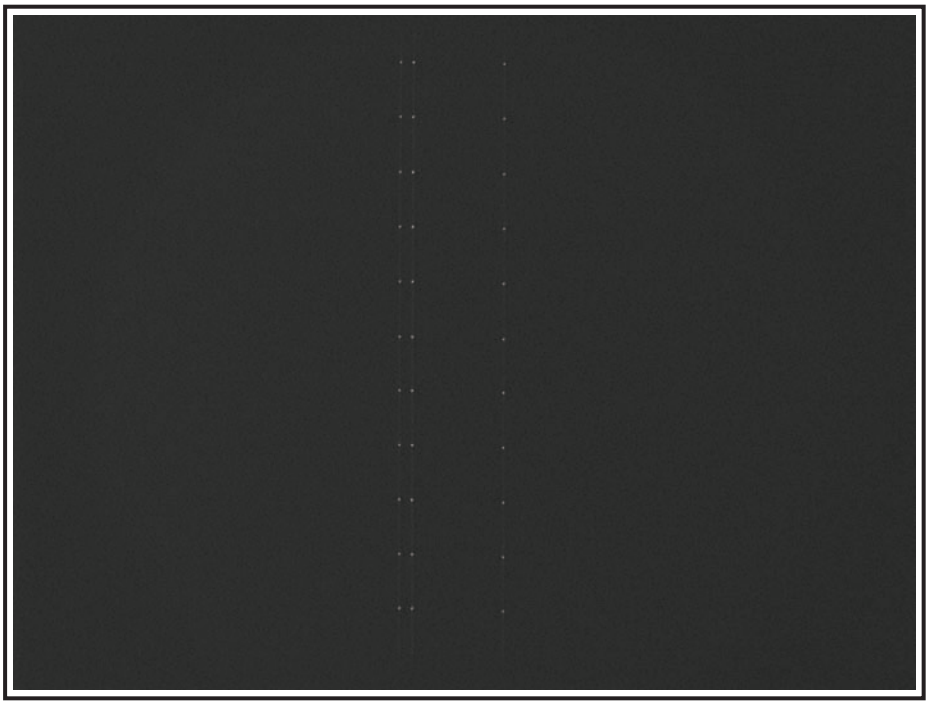

Figure 6. Split comb generator image on slow circuit running a 500-ns sweep

Conclusion

We have demonstrated wide-range sweep circuit operation in a bench-top environment at 800 ps–300 μs. The wide-range goal of 2 ns–500 μs was not achieved, but pushing the range to cover 500 μs is possible by changing a few capacitors. Although slower sweeps were demonstrated in a streak camera, this circuit cannot be described as viable until the faster sweeps are shown. There is still significant work to be done regarding circuit integration, as well as integration with a wide-range gate generator and the above-mentioned power supply and control boards. It would also be desirable to include computer control, a user-friendly interface, and embedded calibration elements, such as a marker or comb generator. Many of these issues have been addressed in a proposal to continue the work in FY 2007.

Acknowledgments

The following team members were essential to the success of this research project: Jonathan O'Connor and Charles Diamond, for circuit design and testing expertise; Claudio Lopez and William Warthan, for fabrication and testing; and Jim Mirador, for circuit-board design and prototype fabrication.

References

Baker, R. J., B. P. Johnson, "Stacking Power MOSFETs for Use in High-Speed Instrumentation," *Rev. Sci. Instr.* **63**, 12 (December 1992) 5799–5801.

Bilir, D. T., "High-Power Pulser," *Nevada Test Site–Directed Research, Development, and Demonstration,* FY 2005, Bechtel Nevada/National Security Technologies, LLC, Las Vegas, Nevada, 2006, 191–196.

Cunin, B., J. A. Miehe, B. Sipp, "Sweep devices for picosecond image-converter streak cameras," *Rev. Sci. Instr.* **51**, 1 (January 1980) 103–110.

Diamond, C. E., "High-Power Pulser," *Nevada Test Site–Directed Research, Development, and Demonstration,* FY 2004, Bechtel Nevada, Las Vegas, Nevada, 2005, 191–196.

Zetex Semiconductors, FMMT415/417 datasheet, http://www.zetex.com/3.0/pdf/fmmt415.pdf, accessed September 28, 2006.

King, N. "Operating Instructions Manual For L-CA-24 Streak Camera," EG&G 10617-4131, April 1992.

Lewis, A., J. Rohrer, "Gen IV Streak Camera Manual," Bechtel Nevada, TM-AA34-003-0, July 2005.

Hamamatsu Photonics, Universal Streak Camera C5680 Series, http://sales.hamamatsu.com/assets/pdf/hpspdf/C5680.pdf, accessed September 28, 2006.

this page intentionally left blank

Simple, Wheeled, Dead-reckoning System

Thomas M. Haard, Michael J. Hornish[1]
Remote Sensing Laboratory – Andrews

The development of a reliable, low-cost, dead-reckoning unit suitable for indoor radiation surveys would be very beneficial to many NSTec missions and serve to complement and enhance existing capabilities, such as the "Pedestrian Mapper" (Mattson, 2005). One potential solution, previously unexplored, involves utilizing high-resolution rotary encoder technology to track the distance traveled by wheels rolling on a smooth surface. The wheels' heading or orientation can be determined either by using a magnetic compass or by measuring the difference in distance traveled by two independent wheels. Distance and directional information can be combined to provide accurate, two-dimensional position maps. The present project successfully explored the feasibility of the rotary encoder technology for indoor mapping purposes and incorporated it into a discrete prototype: a wheeled, carry-on suitcase that can also contain an infield unit capable of measuring localized radiation. Results of the preliminary analysis and testing of this potentially useful tool proved quite promising for future development of an alternative system requiring minimal user input.

Background

A system capable of accurately determining position during indoor radiation surveys, where Global Positioning System (GPS) coverage is drastically limited or otherwise unavailable, would greatly benefit several attributes within Crisis Response and Consequence Management, including radiological mapping, surveying, and source recovery. Although many high-tech solutions exist, they are often cost-prohibitive, inaccurate, or overly intrusive, thereby rendering them ineffective for these purposes. A detailed exploration of some of these solutions, including their characteristics and effectiveness, has already been conducted for pedestrian indoor mapping purposes (Mattson, 2005; McHugh, 2005).

Dead-reckoning pedestrian navigation typically involves estimating position by measuring the heading with a magnetic compass or gyroscope and the velocity with an accelerometer or pedometer. However, these methods often prove too inaccurate for indoor mapping. An alternative solution pursued in this project was to investigate the possibility of incorporating commercial, off-the-shelf (COTS) rotary encoder systems. This technology, which is attractive because of its high rotational resolution, is readily available, relatively inexpensive, and frequently implemented in industrial settings to monitor motion or position.

[1] hornismj@nv.doe.gov, 301-817-3347

When a rotary encoder is coupled to a wheel of known diameter, a measurement of lateral distance traveled by the wheel and encoder unit is determined by simply measuring the number of wheel rotations and the rotational position. The encoder units operate by means of an infrared light–emitting diode shining light through a coded disk, where light transmitted through the disk is detected by an optoelectrical array. Absolute encoders utilize coded disks that provide a distinct "number" associated with discrete rotational positions. Exploiting this technology in conjunction with radiation detectors would enable the development of a wheeled radiological mapper system capable of mapping indoor areas that have smooth terrain, which is precisely the kind of circumstance encountered in survey areas such as airports, metro stations, sports arenas, and ship decks.

Project

The COTS rotary encoder systems chosen for this application were manufactured by FRABA Posital. The rotary encoder units are characterized by a single-turn resolution of 13 bits (8192 steps), which corresponds to 0.044° per step. In addition, these systems are multiturn, absolute encoders that have an extra 12 bits (4096 steps) available to measure the total number of complete rotations. The units contain built-in controllers and Ethernet TCP/IP interfaces, allowing them to be easily incorporated into existing data-acquisition and processing systems. We attached identical wheels to two such encoder units, which in turn were mounted on a common axis to fabricate an initial simple prototype (Figure 1, left).

Run on a small Windows XP computer (OQO Model 1), the data-acquisition system executes a custom Java application that periodically extracts data from the rotary encoders and writes it to a MySQL database. The data include wheel position and a time stamp for each data point. To analyze the data, a scientific analysis package (IGOR Pro) is employed in a postprocess fashion. The difference in wheel position from timeframe to timeframe is used to calculate individual wheel velocities.

The data analysis presently uses the equivalent of Simpson's rule for integration, in order to convert from the angular wheel positions to the center-of-mass coordinates and orientation of the wheeled system. The following expressions for the orientation, $\theta(t)$, and center-of-mass coordinates, $x(t)$ and $y(t)$, are used:

$$\theta(t+\Delta t) = \frac{1}{L}(v_R - v_L)\Delta t + \theta(t), \quad (1)$$

$$x(t+\Delta t) = \frac{1}{2}(v_R + v_L)\cos(\theta(t))\Delta t + x(t), \quad (2)$$

$$y(t+\Delta t) = \frac{1}{2}(v_R + v_L)\sin(\theta(t))\Delta t + y(t), \quad (3)$$

where L is the effective wheel separation, v_R and v_L are the right and left wheel velocities, respectively, and Δt is the time-step interval. The figures show a sample data set for a path traveled around a test area in a carpeted office space (Figure 1, right) and for a path traveled around a square area (Figure 2). To avoid the introduction of orientation error propagation resulting from slight misalignments of the left and right encoders, it became necessary to calculate "effective" wheel diameters and wheel separations. The data set shown in Figure 1, right, constitutes a total distance traveled of 265 m, with an offset of 3 m, corresponding to an error accumulation rate of ~1%.

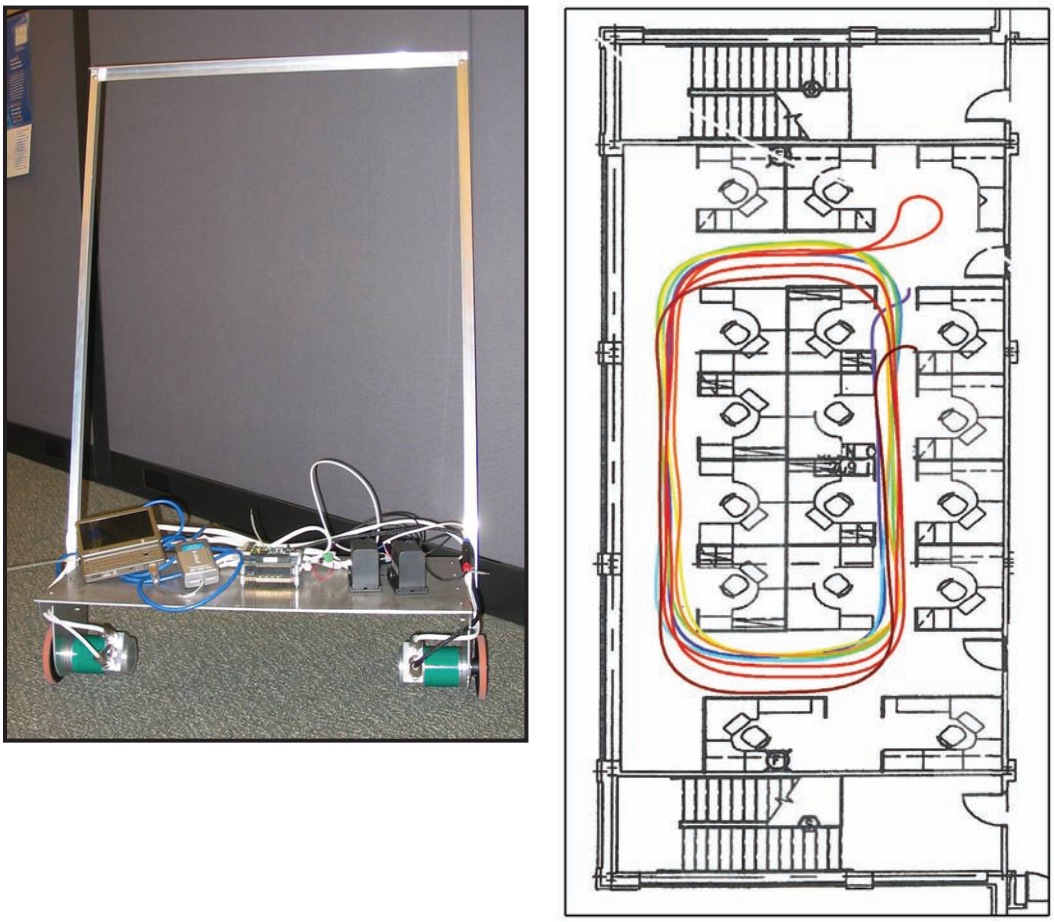

Figure 1. (left) Initial prototype constructed to test the feasibility of the wheeled mapper concept; (right) Sample data set showing the path of the wheeled mapper around a test area. The line color evolves from violet to black as a function of time.

Following the successful tests of the initial proof-of-principle prototype, a second prototype was designed to incorporate the concept into a simple, wheeled suitcase. As such, the ultimate goal would be to develop a discrete system that could be employed clandestinely in high-traffic areas without drawing attention to the measurements being performed. Thus, a compact mounting unit was designed to house the rotary encoders and wheels inside the suitcase base. The mounting unit (Figure 3) was fabricated from black, anodized aluminum, then integrated into a wheeled suitcase that was modified accordingly (Figure 4).

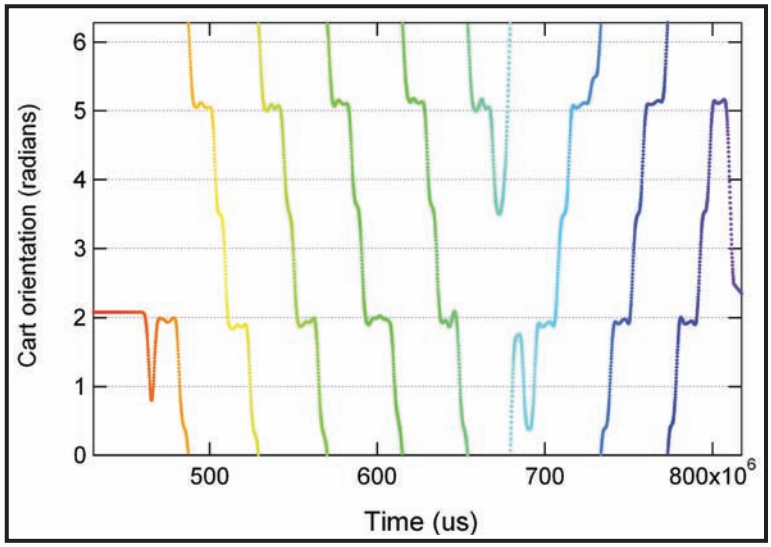

Figure 2. Cart orientation for repeated trips around a rectangular path. Here, the sides of the rectangle appear as short, flat segments in the plot, and the color change (red to blue) simply corresponds to increasing time.

After suitcase prototype assembly, preliminary testing revealed a slight improvement of the drift in the orientation over time, as calculated from the encoder data. This improvement occurred in spite of the fact that the wheel separation in the suitcase prototype was considerably less than that in the first prototype (by more than a factor of two). Thus, there is a smaller difference in the number of turns of the individual wheels for any given turn; hence, one might expect larger errors following repeated turns. However, partially compensating for this effect was the fact that the mounting unit housing the encoders inside the suitcase was designed to reduce encoder misalignments. Furthermore, the unit is considerably more rigid than the initial prototype, thereby minimizing any misalignments arising from torque effects that may have been introduced while turning the prototype.

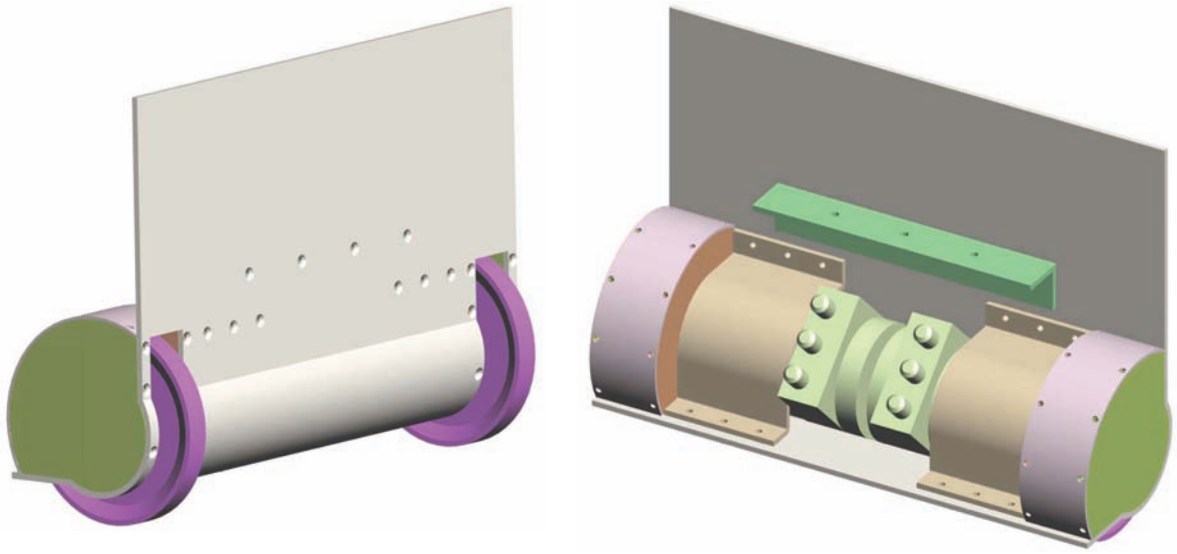

Figure 3. Assembly drawings of the rotary encoder mounting unit for the suitcase prototype wheeled mapping unit

Figure 4. Suitcase prototype, including rotary encoder mounting unit and attached wheels. The photo at right illustrates how well the suitcase mapper system accommodates an existing infield unit.

Independent orientation data can be acquired from magnetic compasses, which can serve to supplement, correct, or altogether replace orientation information calculated from the rotary encoders. In principle, implementing magnetic compass information is straightforward, whereas in practice, this technology has its own limitations and drawbacks that adversely affect performance and accuracy. For example, magnetic compasses tend to have significant error associated with individual, instantaneous readings, as the compass direction will often swing through a wide range of orientations. Even so, on average, the compass reading will tend to be reasonably accurate if integrated over a long enough timeframe. Another obvious difficulty is that simple magnetic compasses are subject to interference from magnetic anomalies, such as those posed by certain system components. For instance, if the compass happens to be placed too closely to power supplies or partially magnetized components containing nonnegligible amounts of iron or steel, the compass will no longer read the true orientation relative to the Earth's magnetic field.

Nevertheless, to improve the overall reliability and performance of the mapper system, we have obtained from Honeywell a gyro-stabilized, digital magnetic compass. This compass contains several built-in compensation algorithms and correction factors based on gyroscope readings and magnetic declination that should help minimize the effect of magnetic anomalies. It is presently installed on the top of the suitcase, far from the electronics and batteries, which reside in a side pocket. Compass data results thus far have been inconclusive, although if this system can be explored further, it may prove to be a valuable extension of the existing encoder mapping system.

Finally, an infield unit was integrated into the system for initial testing. Experimental data (both gamma and neutron counts) are extracted from the infield unit again by means of a custom Java-executable. As with the encoder and compass data, infield data are logged in a MySQL database and then written to file for postprocessing analysis. Preliminary tests have revealed several bugs in the infield-logging software that have not yet been resolved. However, data have been successfully extracted simultaneously from all three system components (rotary encoders, gyro-stabilized magnetic compass, and infield unit). Further overall system refinement and optimization is needed in order to improve the quality of the data and the postprocess data analysis.

Conclusion

A new mapping system using rotary encoder technology for tracking orientation and distance traveled has been designed and tested for indoor surveying. We constructed a functional prototype from a wheeled suitcase and two absolute rotary encoder units. Preliminary tests have revealed an error accumulation rate on the order of 1%. Moreover, the flexibility of the present system allows it to be expanded to incorporate a digital compass and infield unit. With some additional future development, this combined system could become a valuable, reliable tool for indoor radiological surveying, mapping, and source-recovery missions.

Acknowledgments

This project would not have succeeded without significant contributions from numerous individuals: Bob Richmond, for the construction of the initial prototype; Ron Wolff, for designing the suitcase mounting unit; Tim Ashenfelter, for algorithm development and system testing; Scott Battocchi, for significant hardware and software development; Katalin Hopkins, for writing the encoder data acquisition software; Troy Waterman, for assembling the suitcase prototype; and Sarah Clemente, for conducting several test measurements of the encoder and compass performance.

References

Mattson, J. E., "Automatic Logging of Position," *Nevada Test Site–Directed Research, Development, and Demonstration,* FY 2004, Bechtel Nevada, Las Vegas, Nevada, 2005, 177–182.

McHugh, H., D. Piasecki, "Automatic Logging of Position," *Nevada Test Site–Directed Research, Development, and Demonstration,* FY 2004, Bechtel Nevada, Las Vegas, Nevada, 2005, 183–186.

this page intentionally left blank

Construction of a Prototype Traveling Wave Streaking Tube

Don Pellinen,[1] *John Yuhas*
Livermore Operations

We designed a miniature traveling wave streaking tube and the tooling to form it. The tube could be used as a conventional streaking tube or without optics as a very-high-speed photodiode. This research took advantage of another FY 2006 SDRD project that employed techniques similar to those used to produce hermetically sealed integrated circuits to optical diagnostics used in advanced fusion research (Pellinen, 2007). Although the traveling wave streak tube was not built or tested in a camera system, its compact, light-weight design would be favorably received in space-limited and highly radioactive testing environments.

Project

The features designed into the streak tube, listed below, are described in this report.

- Windowless front surface photocathode
- Three electron acceleration stages
- Gating electrode positioned before deflection electrode
- Impedance-matched traveling wave deflection stage
- Mass producible; damaged or radioactively contaminated units may be disposed of safely

The windowless grazing angle photocathode provides high sensitivity and will operate at low energies without correction for windows. The device was intended to be an x-ray camera, but it should be capable of working in the ultraviolet and visible regions. Subpicosecond response may be possible from the tube because of the traveling wave structure on the deflection system.

A cross-sectional view of the tube is shown in Figure 1. Photons, entering from the top at a grazing incidence of ~10°, strike the photocathode, which is biased at a negative voltage. Some of the electrons accelerating toward the anode pass through the slit, where they are accelerated to and through the next slit, and accelerated to and through the gating plates to the offset plates. The offset plates are designed as a constant-impedance, parallel-plate transmission line. The offset ramp waveform is injected from a coaxial transmission line on one side and carried off on the other side by another

[1] pellindg@nv.doe.gov, (925) 960-2572

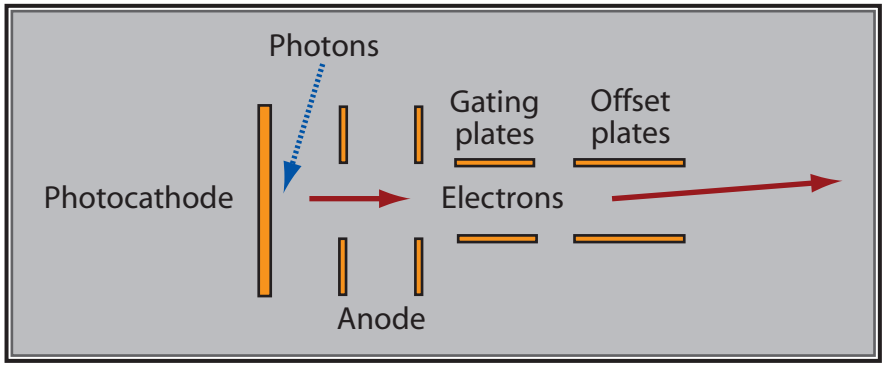

Figure 1. Path of photons and electrons in a cross section of the tube

cable to terminate the signal. Using the constant impedance line, it is possible to avoid the resonances and oscillations common on existing NSTec tubes. In this design, the slit was 0.1 mm wide, and the centerline spacing for leads was 3.1 mm.

The camera may be operated in two modes: with an imaging element, such as a pinhole, the camera would function as a normal streak tube, and without the imaging, it would function as a detector-cable-transient recorder system. This recorder configuration would be free of the frequency response limitations of existing systems that now have risetimes of ~200 ps. The risetime limitation is a combination of factors, including photoelectron transit time across the anode-cathode gap, cable response, and readout response. Since the traveling wave streak system scans the electrons across a screen, rise time will be determined by the width of the streaked electrons and the waveform of the deflection signal. This could be quite fast, possibly in the femptosecond region.

Interior parts for the traveling wave streak tube were designed to be made using ceramic insulators. The outside metal forms are identical to the parts developed for the disposable x-ray diode developed in another FY 2006 SDRD project (Pellinen, 2007). Figure 2 shows the part with the photocathode, the second accelerator stage on the top of the gating plate, and one conductor of the offset transmission line. Figure 3 shows another view of the plates.

The parts in Figures 2 and 3 are etched out of a flat sheet of 0.005-in. alloy 42 or Kovar. The photocathode and the extractor and accelerator plates must be bent so they are perpendicular to the sheet. Normally, tools mounted on a die set are made to do this. We designed tooling to accomplish the 90° bend in two strokes. First, a vertical stroke would bend the parts to ~45°, and second, a horizontal stroke would form another 45° bend. The vertical and horizontal stroke tools are shown in Figures 4 and 5, respectively.

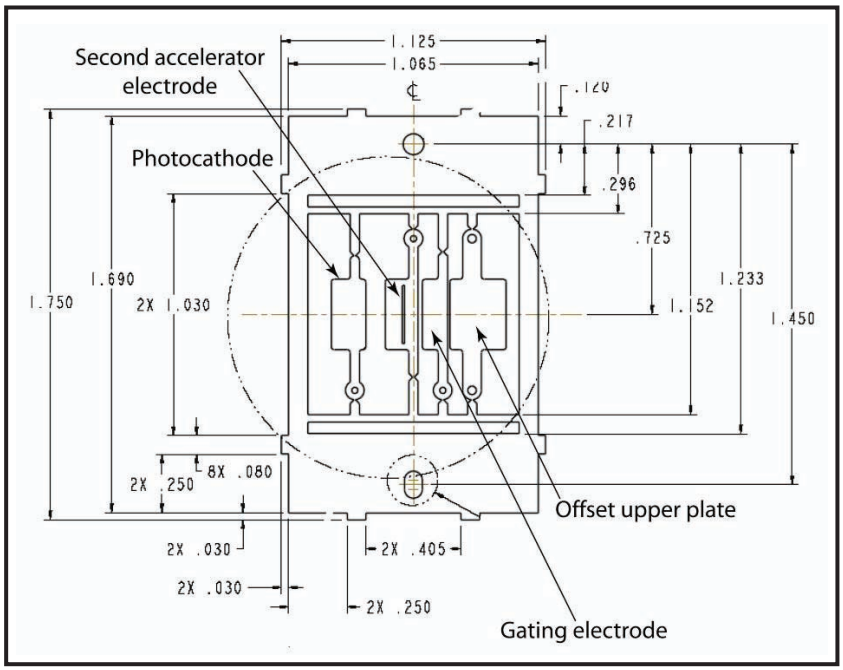

Figure 2. Photocathode, second accelerator and gating electrode, and offset upper plate

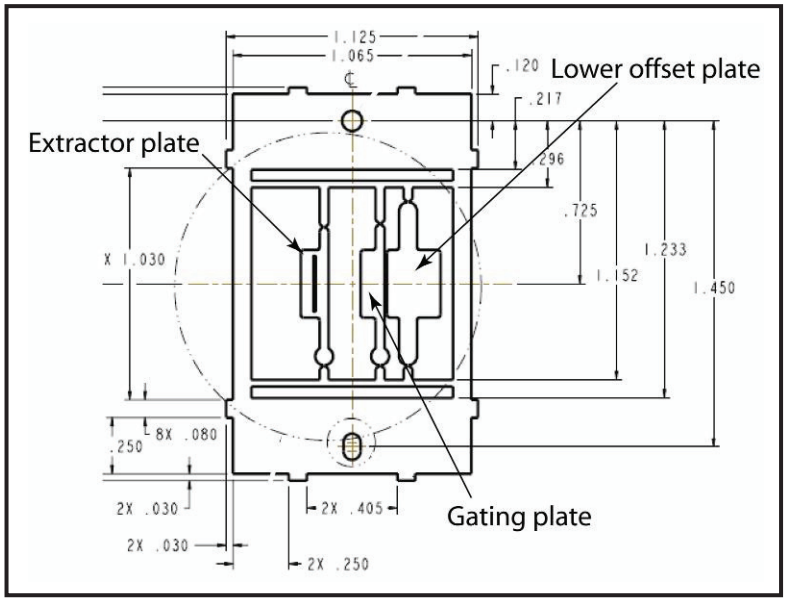

Figure 3. Extractor plate and gating and offset lower plate

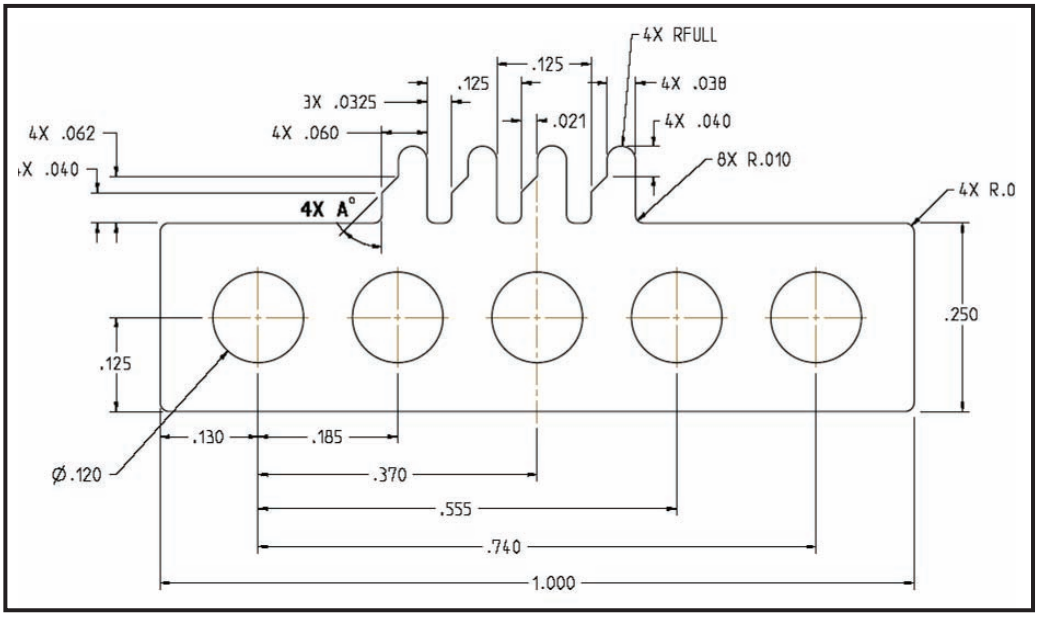

Figure 4. Vertical stroke forming die bends electrodes to ~45°

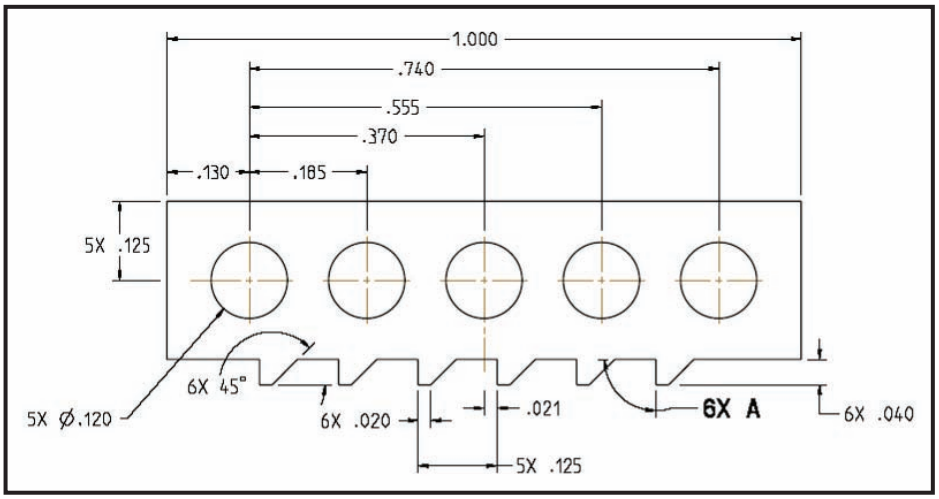

Figure 5. Horizontal stroke forming die bends electrodes another ~45°

Chemical etching a sheet of tool steel would form the vertical die. One piece of alloy or Kovar each would be used to make the top and bottom sections as well as to fashion the parts bent between the angled parts. "Fingers" that we did not intend to bend would be ground off.

The second die would also be formed by chemically etching a sheet of tool steel. All dies would be etched on the same sheet. Since it is difficult to predict springback, a number of different angles would be made and tried until the final 90° angle was reached. The horizontal stroke for this tool would result from the press ram driving an angled part down and the eccentric pushing it and running in a horizontal track.

On the prototype, no shaping of electrodes other than bending them in position was planned, but on an actual device field trajectories would be calculated, and the photocathode, extractor, accelerator, and gating electrodes would be shaped by punches to focus the electrons and minimize electric fields on negative surfaces.

Only a single traveling wave deflection system was included in this design because of special limitations on the existing ceramic and tooling materials. With a longer ceramic and different tooling, the offset waveform could be delayed and fed through multiple offset electrodes. We did not specify a readout device, but envision use of a flash memory chip, yet to be designed.

Conclusion

A traveling wave streak tube design was produced and quotes for fabrication were obtained. The tube design seems feasible. Built and deployed, these cameras could add a time-resolved imaging feature to the National Ignition Facility (NIF) DANTE spectrometer, or supplement the voltage vs. time feature of the camera system used on the NIF OMEGA laser. Were projects such as NIF or the Sandia Z machine to begin developing projected fusion yields, these tubes would greatly enhance radiation safety, as they could be cheaper to produce, and therefore may be disposed of, rather than recovered and decontaminated. The small camera size would allow multiple cameras to be deployed where one camera is deployed now. Their compact size and weight (the camera photocathode, accelerator electrodes, gating electrodes, and offset transmission line weigh ~3.1 grams vs. ~600 grams for a conventional tube) would simplify installation and deployment in locations where space is limited.

Acknowledgments

A number of people assisted in the project: Dean Lee, Jochen Schneider, Kelley Campbell, and Franz Weber of LLNL gave encouragement; Mary Kucher procured quotes from a variety of vendors; and Terry Richardson guided the authors through various problems with the computer.

Reference

Pellinen, D., J. Yuhas, "Disposable X-ray Diode for Fusion Shots," *Nevada Test Site–Directed Research and Development,* FY 2006, National Security Technologies, LLC, Las Vegas, Nevada, 2007, 233–239.

this page intentionally left blank

Superheader

Larry Robbins,[1] *B. T. Meehan, E. Chris Hagen*
North Las Vegas Operations

The objective of this project was to improve the mechanical and electrical performance of the header plate on the dense plasma focus (DPF) primary barrier. This improved header, called a "superheader," will eliminate failure points in the header where the insulation system is highly stressed. The current design of the header plate is not expected to withstand the electrical stresses that would be present if the driving voltage in the capacitor bank were doubled (Hagen, 2005).

Within 5 μs, the energy stored in the capacitor bank is transferred to the DPF device. As this energy is transferred, there is increased mechanical and electrical stress on the header plate and the possibility of electrical failure points between the two potentials. The new header design will reduce the electrical and mechanical stress by eliminating a shorting path that limits our ability to use the tube at higher voltages and higher energy levels, thus restricting neutron yields. This improvement will raise operational efficiency by promoting better reliability and less chance of breakdown on the DPF machine.

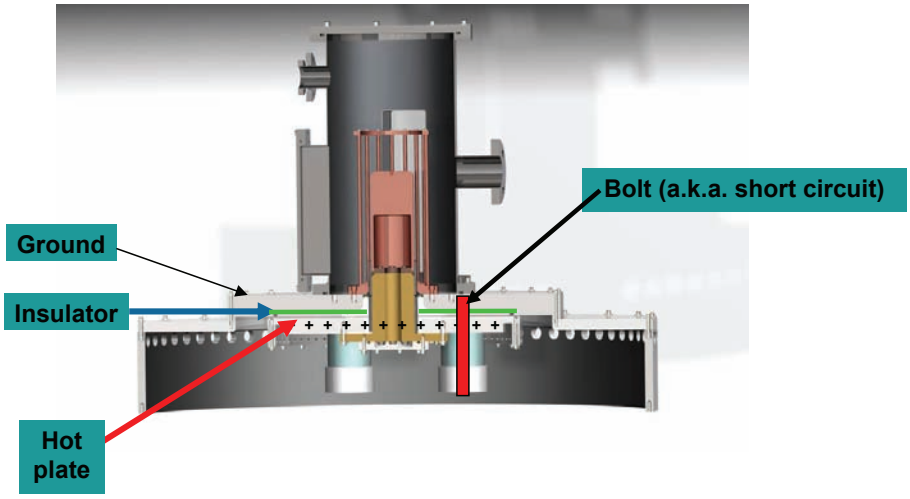

Figure 1. High voltage and ground potentials on the DPF machine, with 1-in. steel bolt penetrating the Mylar insulator

[1] robbinll@nv.doe.gov, 702-295-1058

Background

The basic header assembly appears in Figure 1. The primary reason for pursuing fabrication of the superheader is to prevent catastrophic electrical failure of the insulator (Figure 2). The insulator comprises 24 sheets of 0.0055-in.-thick Mylar. The bolts penetrate the insulator and provide a short circuit for electrical fields applied to the header (Figures 2 and 3). The bolts are used to press the air out of the insulating Mylar layers, holding the ground plate and hot plate very close together. Bolt penetrations through the hot plate cause higher electric field stresses in the dielectric. As one is at ground and the other is at high voltage, a complex, reliable, header assembly is required that maintains mechanical integrity without providing any electrical shorting path.

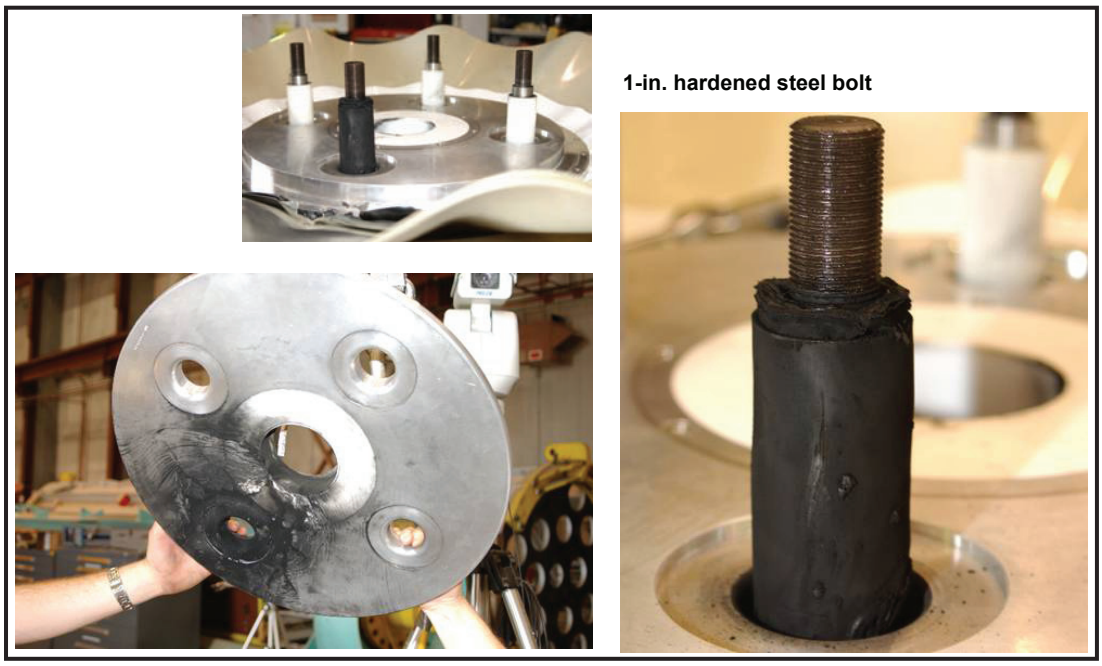

Figure 2. Catastrophic electrical failure of the insulator where (conductive steel) bolts penetrate the Mylar insulating layer. The two photos on the left show the damage from the arc and illustrate the placement of the bolts for mechanical compression. The photo at right details the damage caused by the heat and pressure from the flashover.

Before we could competently design an improvement to the header assembly, our team researched the mechanical and electrical stresses and forces using the Biot-Savart law (Equations 1–5) to calculate the electro-motive forces supplied to the structure by the electrical current pulse. Current enters on the top sheet and leaves on the bottom sheet. The x- and y-force components cancel out due to symmetry, leaving only the z-force component (Figure 4).

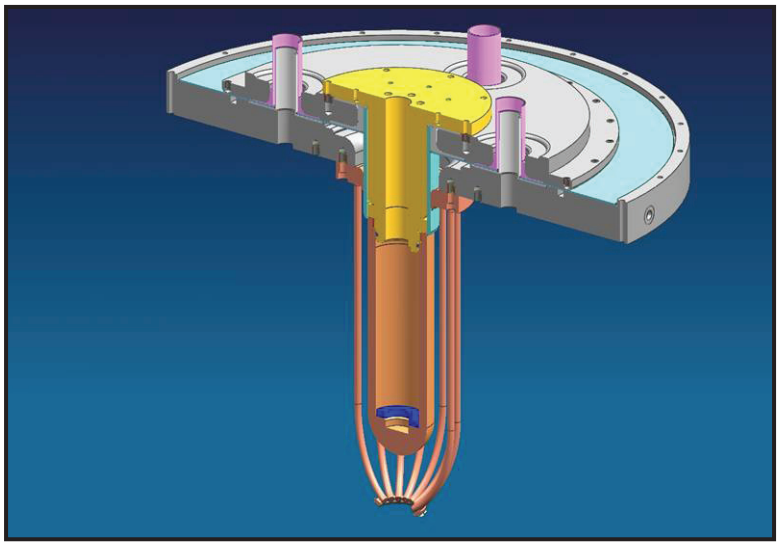

Figure 3. Alternate view of insulator failure points

$$d\vec{F} = \frac{\mu_0}{4\pi}\frac{I_1 d\vec{\ell}_1 \times (I_2 d\vec{\ell}_2 \times \hat{r})}{r^2} \tag{1}$$

$$I_1 d\vec{\ell}_1 = \begin{pmatrix} I_1 \cos\phi \\ I_1 \sin\phi \\ 0 \end{pmatrix} \tag{2}$$

$$I_2 d\vec{\ell}_2 = \begin{pmatrix} I_2 \cos\phi \\ I_2 \sin\phi \\ 0 \end{pmatrix} \tag{3}$$

$$\hat{r} = \begin{pmatrix} \dfrac{\ell_1 \cos\phi - \ell_2 \cos\theta}{\|\vec{r}\|} \\ \dfrac{\ell_1 \sin\phi - \ell_2 \sin\theta}{\|\vec{r}\|} \\ 0 \end{pmatrix} \tag{4}$$

$$\vec{F}_z = \frac{I_1 I_2 \mu_0}{4\pi}\int_0^{2\pi}\int_0^{2\pi}\frac{-d\cos(\theta-\phi)}{(d^2 + r_1^2 + r_2^2 - 2r_1 r_2\cos(\theta-\phi))^{\frac{3}{2}}}d\theta d\phi \tag{5}$$

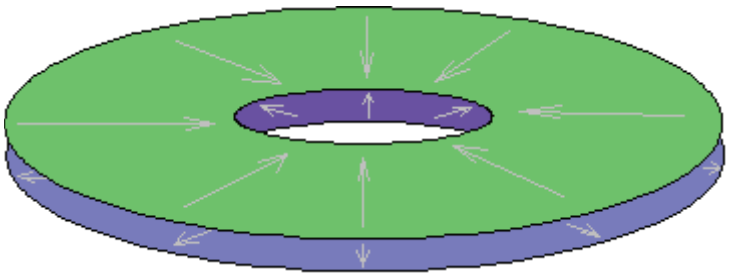

Figure 4. Cancellation of the x- and y-force components due to symmetry

The resulting force in the z direction cannot be integrated directly but grows more powerful with the inverse of the separation between plates (Figure 5). According to the Biot-Savart law (Equations 6–9), the force between the two header plates is proportional to the square of the magnitude of the current. We estimated the peak force separating the plates to be 10^5 N; however, the momentum that the impulse-driving force delivered to the plates was insufficient to cause them to fly apart more than ~1 mm during the shot. Therefore, the primary function of the four bolts is to press the air out of the layered insulating sheets and keep it out.

$$\vec{p} = \int \vec{F}\, dt \tag{6}$$

$$\vec{p} = F_{peak}^{\rightarrow} \int (e^{-at} \sin(bt))^2\, dt \tag{7}$$

$$\vec{p} = \frac{b^2}{4a^3 + 4ab^2} F_{peak}^{\rightarrow} \tag{8}$$

$$\vec{p} = 5.996 \times 10^{-6} F_{peak}^{\rightarrow} \tag{9}$$

Project

The Superheader Solution

For this project, we decided on a C-clamp design, with no hot plate penetrations, which could provide the same pressure on the insulator stack as had been supplied by the failure-inducing bolts without shifting or lifting during a current pulse. This design is far more robust than that required

for the present DPF (130 kJ) and allows for future growth of the capacitor banks (1000 kJ). Such a robust design would be advantageous because each doubling of the current increases the load on the clamps fourfold.

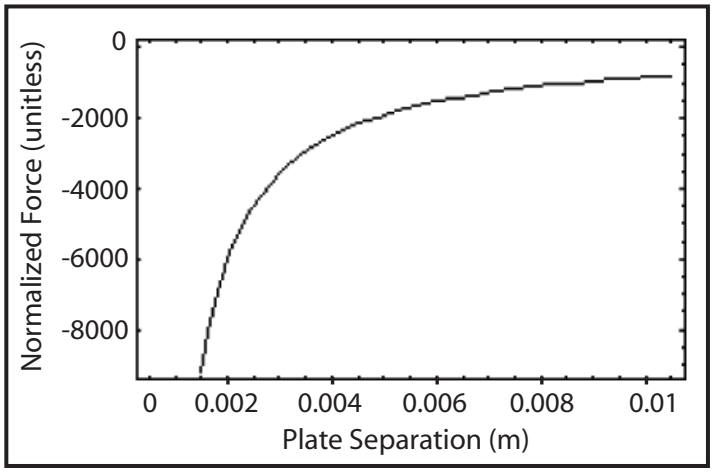

Figure 5. The z force grows more powerful with separation between the plates

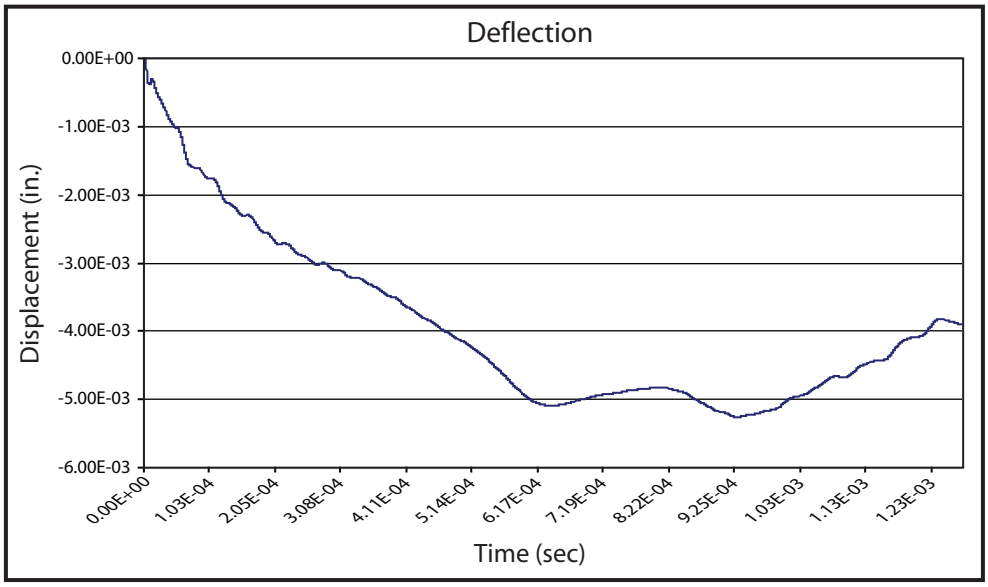

Figure 6. Modeled deflection of a C clamp during current pulse on the DPF

To determine the required size and magnitude of the C-clamp design, calculation and modeling were performed at the University of Nevada, Las Vegas, Department of Mechanical Engineering. After we completed the design, the C-clamp was modeled using a current pulse on the DPF machine. The modeled deflection appears in Figure 6.

The photograph (Figure 7) and renderings (Figure 8) show the results of this project. Figure 7 shows the clamps being tested for fit using existing header parts. The clamps reach from ground, below, around to a disk that they press against four insulating columns. Those pressure-transferring columns must withstand both a transient voltage of 70 kV and a higher voltage spike that occurs at the instant of the Z-pinch.

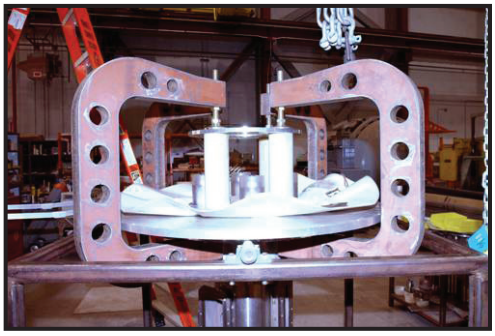

Figure 7. Clamps being tested for fit using existing header parts

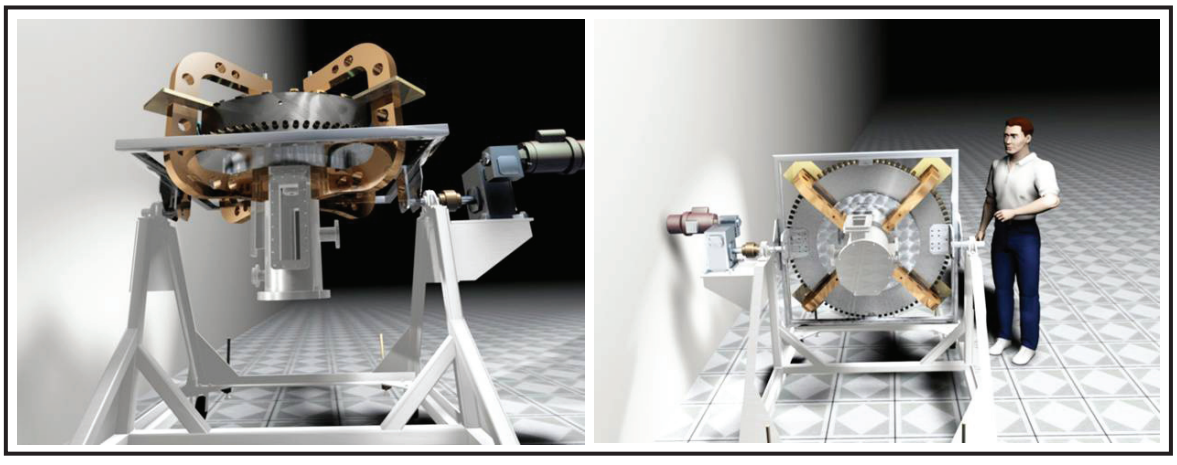

Figure 8. Renderings of the superheader showing scale and robustness of clamps

Conclusion

Due to the success of the design, this header assembly has been constructed and will be first used at half-voltage with the existing OneSys 35kV capacitor bank. The superheader will then be transferred to the TallBoy 75-kV, ½-MJ bank late in 2007, when that bank is installed and energized. At that time it will be exposed to 70-kV pulses from a ½-MJ bank. This 70-kV source will allow NSTec to approach or surpass the current record yields observed from DPF Fusion neutron sources.

Reference

Hagen, E. C., S. Molnar, "Two-Bank DPFA," *Nevada Test Site–Directed Research, Development, and Demonstration*, FY 2004, Bechtel Nevada, Las Vegas, Nevada, 2005, 43–48.

this page intentionally left blank

Urban Localized Position System

Eric C. Wagner[1]
Remote Sensing Laboratory – Andrews

This project evaluated using the wireless communications infrastructure consisting of IEEE 802.11 access points, Global System for Mobile Communication (GSM) cellular phone base stations, and possibly Bluetooth radio beacons as a component of an urban positional localization system. This system is similar to the Enhanced 911 (E911) capabilities that utilize the known locations of many receiving cellular phone base stations to reconstruct where the transmitter (i.e., the cell phone calling 911) is located. Here, we inverted the problem in order for a mobile receiver to determine its location via various stationary radio beacons.

Background

Current georeferencing equipment uses the U.S. Department of Defense's (DoD) Global Positioning System (GPS) due to its high accuracy, near-worldwide coverage, and relatively inexpensive hardware costs. Unfortunately some drawbacks exist, most notably the weakening of the signal that occurs when penetrating obstructions between the receiver and at least three satellites in disparate locations. This is a common scenario in urban environments in which urban canyons, underground facilities, and shielded buildings are common. The technologies discussed below address alternative methods of localizing equipment optimized for an urban environment.

Project

We considered two distinct RF-based georeferencing approaches. The first was a refinement of existing GPS receivers to overcome current deficiencies. The second used ubiquitous, fixed, ground-based radio beacons.

The u-blox company (u-blox, 2006) has developed a new reflection and high-noise-tolerant analysis chip for GPS. This chip yields a significant gain in capability as a simple component replacement for currently deployed receiver technology. The previous generation of analysis chips displayed a significantly worse recorded path of a vehicle traveling along a road (Figure 1).

The new u-blox chip also quite capably worked indoors, in environments in which older GPS receivers failed to function. While this chip represents a significant improvement over existing technology, in some situations, the GPS signal still does not penetrate (e.g., underground subway stations).

[1] wagnerec@nv.doe.gov, 808-474-2654

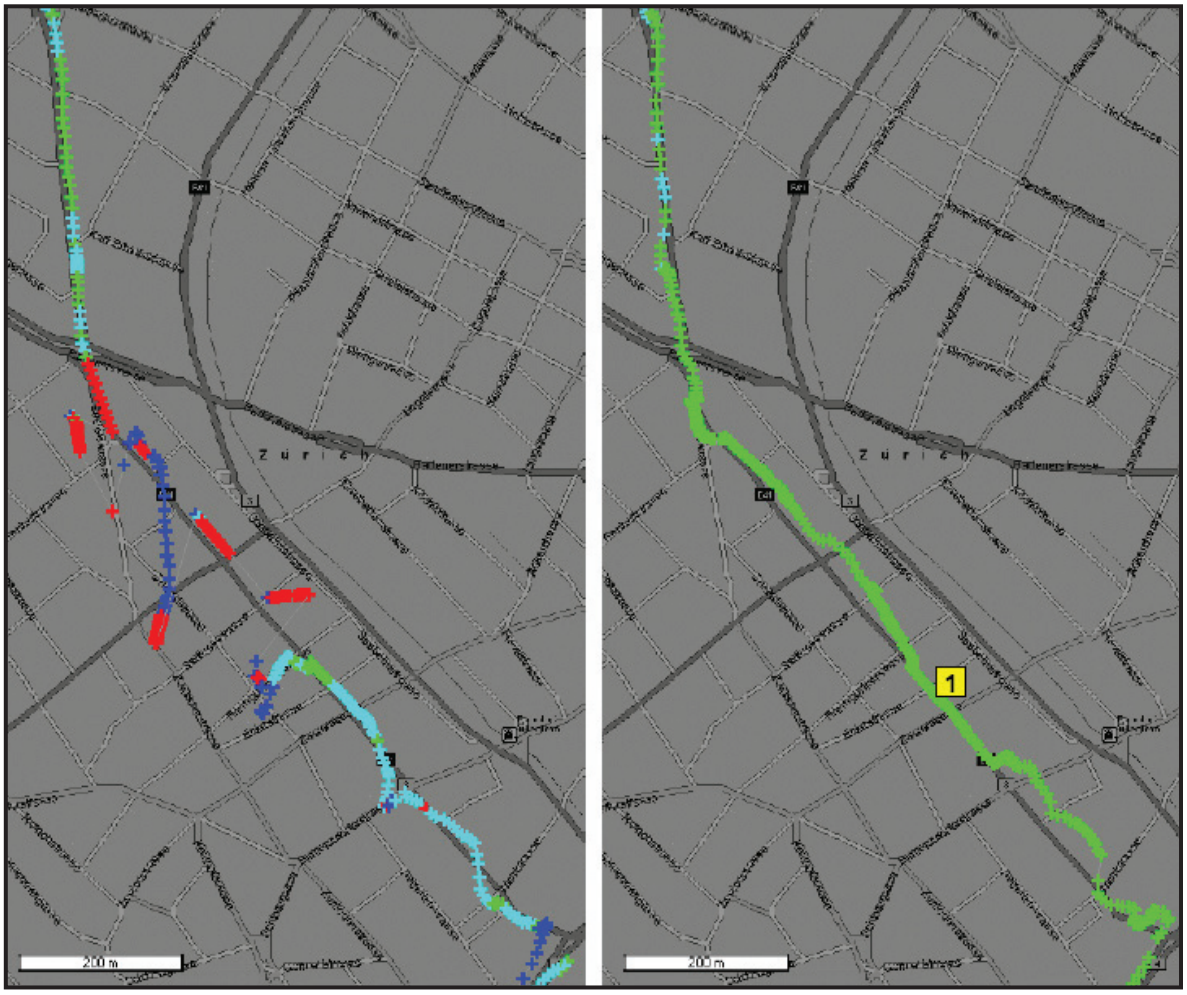

Figure 1. Vehicle track, as recorded from an antenna placed beneath vehicle's front seat. U-blox chip (right) performance significantly surpassed that of the prior generation analysis chip (left), as seen by the signal loss (red crosses).

For situations in which even an improved GPS receiver was not viable, we turned to utilizing radio beacons scattered throughout urban environments that transmit at much higher power levels than GPS. In areas with a low urban density and, hence, a lower concentration of radio beacons, the GPS is the optimal solution. As the urban density increases, the non-GPS radio beacon density also increases, as do obstructions to the GPS signal. This inverse relationship of functional environments is ideal for backup systems.

During the time period in which this work was conducted, considerable work was performed in the academic community on the use of Wi-Fi base stations to provide Internet access at coffee shops, libraries, offices, etc. Intel Research Seattle (2006) consolidated this work into the Place Lab software package, a generic package that can accept inputs from various radio frequency devices, of which Wi-Fi was the most heavily explored.

Most commercial chip sets on current Wi-Fi receivers (Figure 2) provide four key pieces of information: Wi-Fi transmitter identification, signal strength, encryption status, and transmission mode. The first two points are of significant interest as inputs to the Place Lab software package for the purposes of georeferencing.

Figure 2. An example of a Wi-Fi receiver in the PCMCIA form factor

In urban environments, it is very common to have all 11 allocated channels for Wi-Fi in use. With an approximate range of 100 m, depending on antenna type, it is possible to get 15–20 m positional accuracy from "stumbling" (LaMarca, 2005). Stumbling is the process of utilizing radio beacons with known locations to determine an approximate location of an unknown radio beacon. The approximated location is then stored and the new radio beacon is treated as a beacon with a known location. This process allows a radio receiver with knowledge of its starting point to proceed through an environment of unknown radio beacons and maintain an approximate location. Measurement errors do contribute to an increasing uncertainty in absolute location, but this can be mitigated by periodically determining an absolute location, intermittently encountering known radio beacons, recording all measurements, and performing postprocessing on the recorded measurements. Hopefully the same

can be done for the shorter-range RF technology known as Bluetooth. Bluetooth has three power types, with ranges from 10 cm to 100 m. If the density of Bluetooth transmitters increases to saturate the allocated channels, as Wi-Fi already has in urban areas, positional accuracy should increase correspondingly.

The same approach was examined for utilizing cellular telephone base transmitters, particularly the GSM protocol. While Wi-Fi saturation is actually an unwanted symptom of the urban environment and limited unlicensed bandwidth, there is a strong commercial and public safety interest in providing cellular towers with coverage of all areas. In addition, cellular frequencies are licensed and closely regulated to reduce interference. Unfortunately, there is no easy way to extract from a cell phone the identification of cellular towers in range and their received power levels. This is most likely a side effect of single-chip designs of current cellular phones' RF component. The best we found was a line of phones that will report the identification and power levels of all cell towers in range for a single service provider.

In order to verify the possibility of utilizing transmissions from a GSM base transmitter, and to compensate for the inability of commercial-grade cell phones to provide the necessary information, we obtained a Universal Software Radio Peripheral (USRP) (Figure 3).

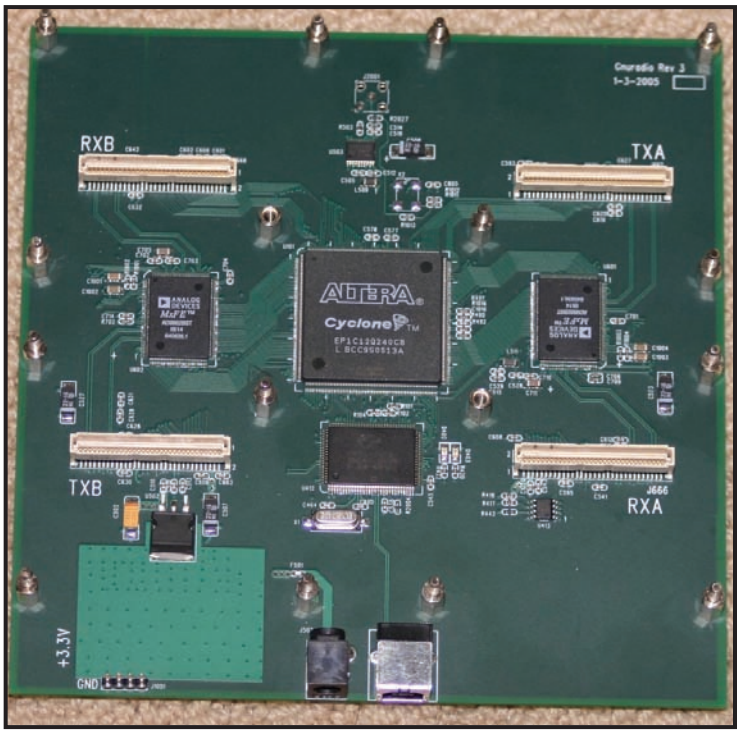

Figure 3. Universal Software Radio Peripheral (USRP)

The USRP is a simple motherboard with high-speed, analog-to-digital converters and associated daughterboards for tuning a 6-MHz-wide band from a particular radio frequency to the base band. The data stream is then fed into a fast computer via the USB 2.0 interface. The GNU Radio (2006) software package can then process this data stream, demodulate it, decrypt it, and output the transmitted data for nearly any frequency.

The GSM standard consists of many radio channels 200 kHz wide. Two scans of the power levels for frequencies transmitted by U.S. GSM base stations appear in Figure 4.

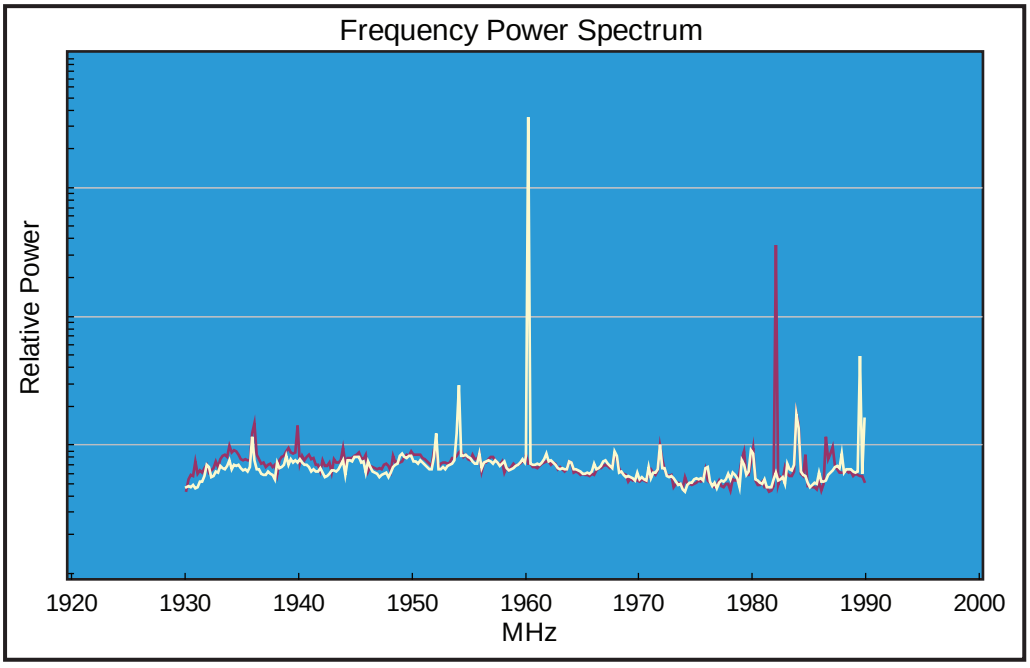

Figure 4. GSM base station transmission power levels

The GSM standard generally calls for the transmitted data frequency to hop as the call progresses. The one exception to this rule is the beacon channels, which stay fixed unless there is a significant network disruption. Therefore, we made several scans to find the consistent presence of beacon channels. The scans needed to be only milliseconds apart, given the GSM standard's rapid-frequency hopping. Once the beacon channels were located, the USRP could focus on a particular channel at a higher resolution (Figure 5).

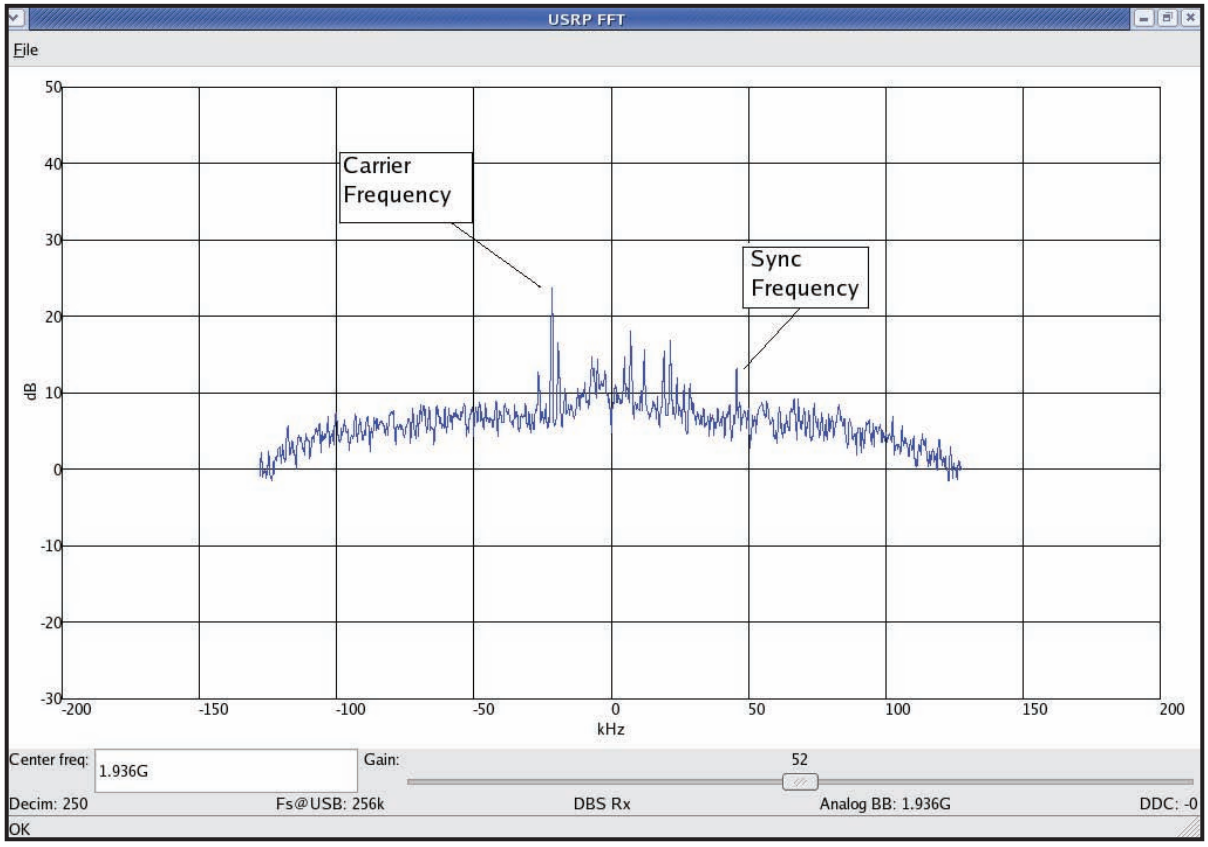

Figure 5. High-resolution power spectrum of the GSM channel centered on 1.936 GHz

A beacon channel can readily be identified by the presence of a synchronization pulse generating a power spike 68 kHz off from the carrier frequency. Demodulating the transmitted data reveals the identification of the transmitting tower, and the decibels measured indicate received power levels. This data can then be fed into the Place Lab software package.

Conclusion

Although geographical locations will still primarily be determined by GPS for the foreseeable future, we have identified at least two feasible implementations of current RF infrastructure to act as novel backup systems. Utilizing Bluetooth beacons is not feasible at this time, given the lack of infrastructure even within the urban environment. In contrast, significant work has been accomplished in the last year on geographical location via "stumbling" over Wi-Fi access points in urban areas. As a result, several online databases are now established with known locations and identifications of Wi-Fi access points. For the most complete non-GPS radio coverage, GSM beacons utilized by the cellular

phone system are available. Within the U.S., the Federal Communications Commission can provide locations for licensed transmitters, and commercial Geographical Information System vendors can provide transmitter locations worldwide. The field measurements we collected, combined with the infrastructure information available, indicate that georeferencing a receiver based on GSM beacons is feasible. Finally, the software radio field bears close observation due to its extraordinary capabilities and the potential for a renaissance in RF communication.

References

GNU Radio, http://www.gnu.org/software/gnuradio/, accessed September 30, 2006.

Intel Research Seattle, http://placelab.org/, accessed September 30, 2006.

LaMarca, A., J. Hightower, I. Smith, S. Consolvo, "Self-Mapping in 802.11 Location Systems," *Proceedings of the 7th International Ubicomp 2005: Ubiquitous Computing Conference*, Tokyo, Japan, September 11–14, 2005, 87–104, Springer, Berlin/Heidelberg, Germany (2005).

U-blox, http://www.u-blox.com/index.html, accessed September 30, 2006.

this page intentionally left blank

Photonics

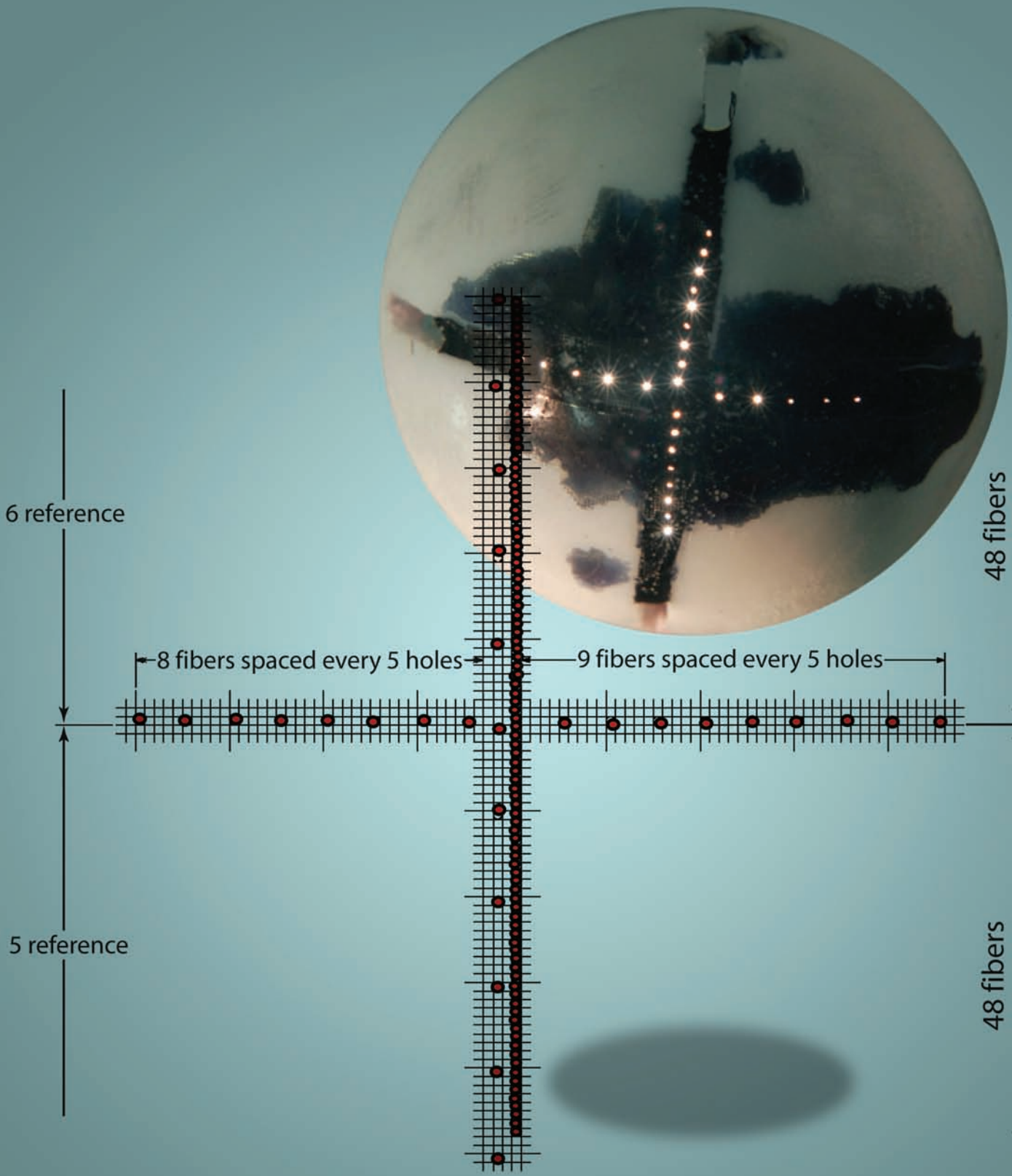
6 reference
48 fibers
8 fibers spaced every 5 holes
9 fibers spaced every 5 holes
5 reference
48 fibers

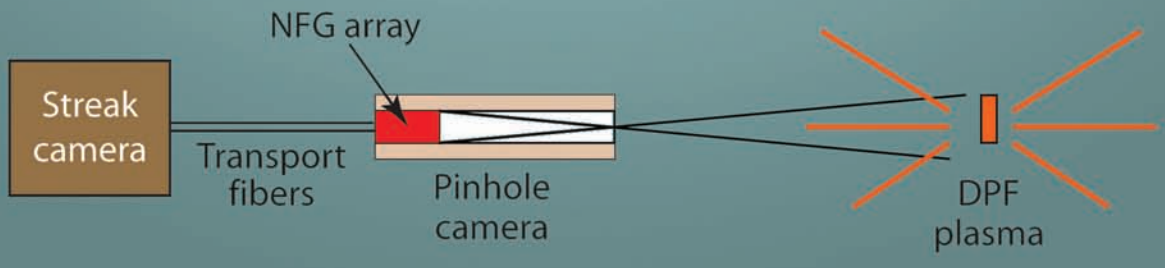
NFG array
Streak camera
Transport fibers
Pinhole camera
DPF plasma

Stereoscopic Borescope

Stuart A. Baker[1]
Los Alamos Operations

Sherman Wu
Remote Sensing Laboratory – Nellis

This project sought to develop a calibrated method of recording a moving or dynamic three-dimensional (3-D) surface undergoing high explosive shock in experiments incompatible with direct line-of-sight (LOS) optical viewing (Figure 1). This optical system could be used on containment vessels requiring vacuum and pressure seals. A framing camera equipped with stereo-imaging optics would record two separate-perspective views of a surface to achieve depth perception. The stereo images would then be processed and cross-correlated to generate both a 3-D digital elevation model (DEM) and an orthoscopic image of the surface. The DEM would provide a grey-scaled topographical map. During this project, our team configured this optical imaging system and recorded stereoscopic images of static 3-D objects and explosively shocked surface experiments. Photogrammetric processing cross-correlated the stereo images of static objects and dynamic shocked surfaces to generate DEMs and orthoscopic images. We also designed image relay optics.

Background

Stereo-imaging technology has been used extensively in artistic photography and in some forms of dynamic shock experiments. We intended to improve on the artistic impression of depth perception in viewing 3-D images with filtered glasses by providing scaled information about the dimensions of features on a surface.

The challenge of this optical image system is to relay the image through a containment vessel port to the recording camera in conditions under which conventional lens elements are impractical, such as with imploding sphere geometry. We used recent improvements in coherent fiber-optic image bundles to develop small-diameter flexible probes suitable for use in explosive containment vessel penetrations to relay the image directly to a recording system. In past years, single-LOS imaging systems have recorded two-dimensional (2-D) images of dynamic explosive surfaces. This type of imaging can detect surface movement and waves but does not provide any depth-perception detail of surface features. Stereoview recording coupled with photogrammetric processing can provide surface depth information.

[1] bakersa@nv.doe.gov, 505-663-2039

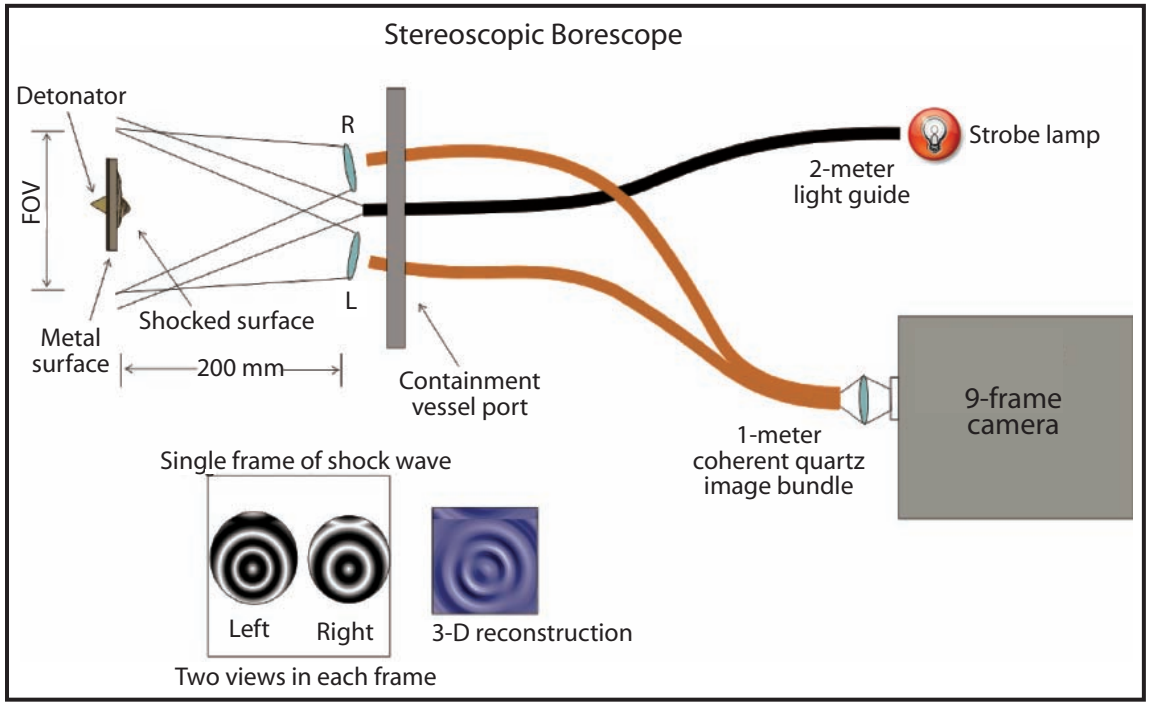

Figure 1. Stereoscopic system overview

Photogrammetric processing has been accomplished at NSTec RSL in an aerial photography configuration on aerial images of terrain and urban scenes. We adapted these techniques and algorithms to create a scaled-down version to process millimeter-scale 3-D surface images. Lighting and image quality suffer in the containment vessel geometry, which affects image correlation factors.

Project

Early in our project, we began discussions with Myriad Fiber Imaging and arranged purchase of the stereo-imaging bundle assembly (Figure 2). Myriad offers a range of imaging fiber bundles from Fujikura of Japan. Our bundle used type FIGH-50 fibers, to take advantage of existing optical designs from Myriad. This allowed the assembly of a flexible stereo-imaging system at a relatively low cost, requiring minimal design time. We arranged focusable lens elements on both ends of the image bundle and had the camera mounting flange built with a standard C-mount lens thread for easy coupling to our framing camera and other cameras. The mounting flange is machined out of delrin plastic to insulate the framing tube high voltage. The FIGH-50 fiber is a 50000 bundle of 4.5-µm fibers with a bundle diameter of 1.025 mm. The FIGH-50 resolution, measured with a

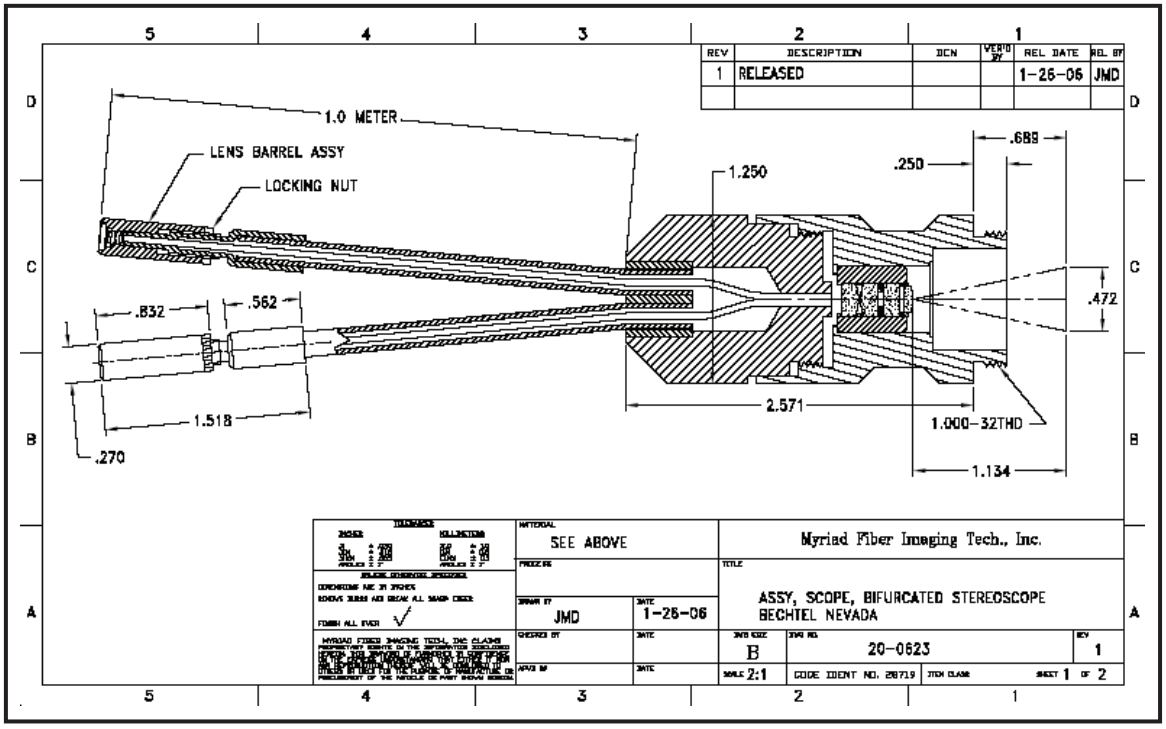

Figure 2. Stereo-imaging bundle assembly

microscope, was 128 line pairs per mm (lp/mm) with white light. This limiting resolution varied with wavelength as follows: 128, 90, and 70 lp/mm for red, green, and blue filtered light, respectively. A sample image bundle resolution measurement appears in Figure 3.

Table 1 shows the differences in two image bundles. The FIGH-50 on our stereoscope is compared to a sample of FIG-100. The FIG-100 is a 100000-fiber bundle of 9-µm fibers. The bundle diameter is 3 mm. The camera readout for this test was a CCD with 6.9-µm pixels. The bundles were imaged onto the CCD with the C-mount proximal lens. A resolution target was measured in contact with the bundle end to measure the bundle's limiting resolution with this readout. Resolution and field of view (FOV) were then measured for an experimental geometry of a 200-mm viewing distance.

For the photogrammetric processing, optical recording parameters and coordinates must be defined to enable cross-correlation of the stereo images. The key parameters in computing image correlation are pixel size, lens focal length, distance between lenses, distance from surface to the lens, and camera tilt angles. Figure 4 shows left and right stereo images of static objects. Such images were used to test the optical system and photogrammetric processing algorithms applied in correlating the stereo images. Figure 5 is a rectified orthophoto generated from a DEM of the correlated stereo images. Some distortion is evident in part of the wave pattern object, possibly due to the repeating

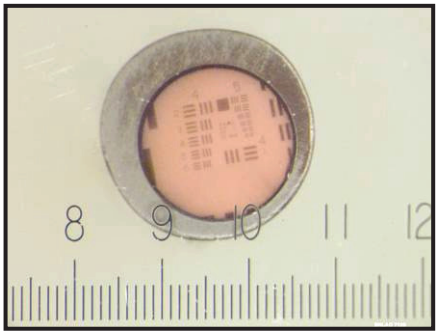

Figure 3. Image bundle resolution measurement (scale units in mm)

Table 1. Image bundle comparison

Fiber Type	Bundle Resolution (lp/mm)	Resolution at 200 mm (lp/mm)	FOV at 200 mm (mm)
FIGH-50	110	2	63 dia.
FIG-100	64	1.5	128 dia.
Bundle resolution with camera readout			

pattern in the object where many pixels' sections look similar. Stereo images have been processed using SoftPlotter software at RSL. This program has many capabilities but requires much manual interaction to generate accurate image correlations. SoftPlotter was used to tailor photogrammetric processing algorithms, to develop a script that can be exported to a portable code version that can be used to provide rapid feedback on experimental results *in situ*. The portable program planned adapts the One-Path Photogrammetric Program, a code developed at RSL for aerial applications to micro-video imaging scales.

A dynamic shot series was recorded at the STL Boom Box. This facility proved to be a great asset in providing explosive shot and recording capabilities on a quick turnaround shot cycle, as a variety of parameters were evaluated in a few days of experiments. In late July, we recorded dynamic shots of five different targets at the Boom Box.

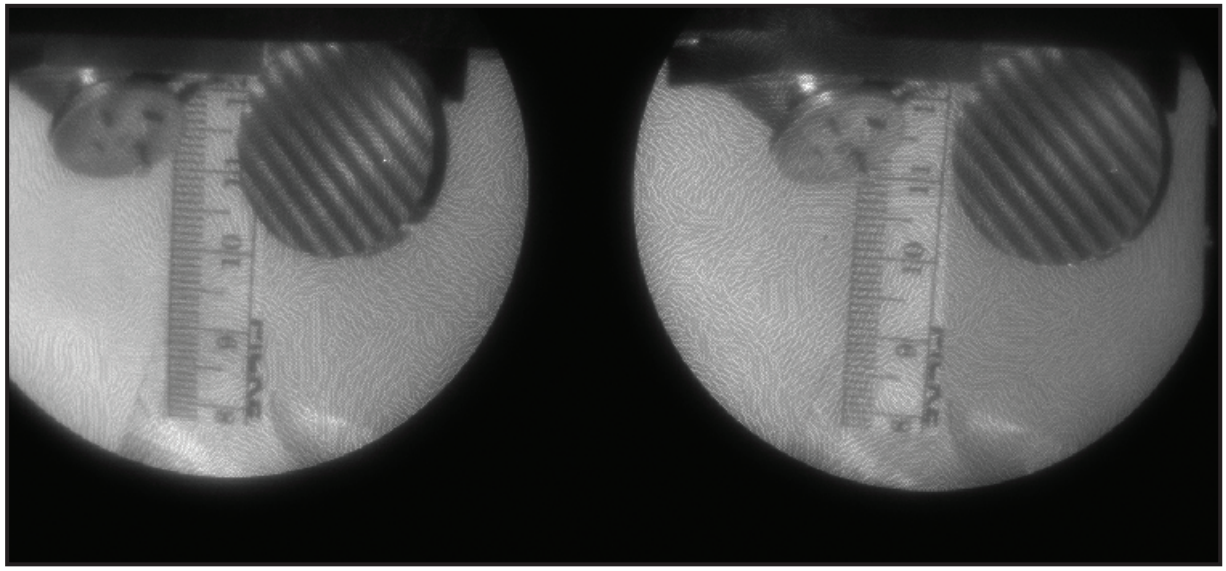

Figure 4. Stereo images of shapes and waves

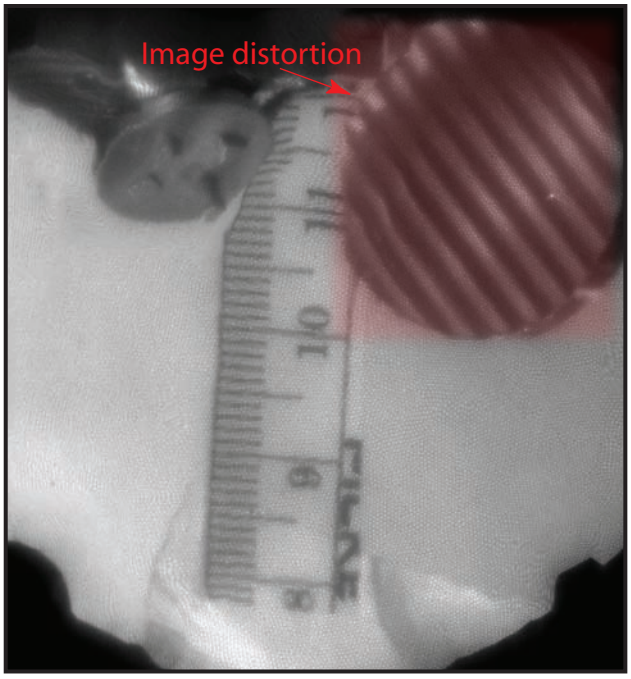

Figure 5. Rectified orthophoto from DEM

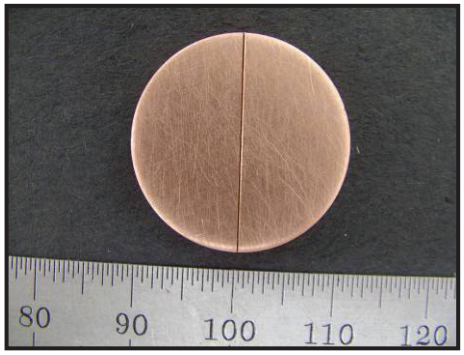

Figure 6. Copper target with groove (scale units in mm)

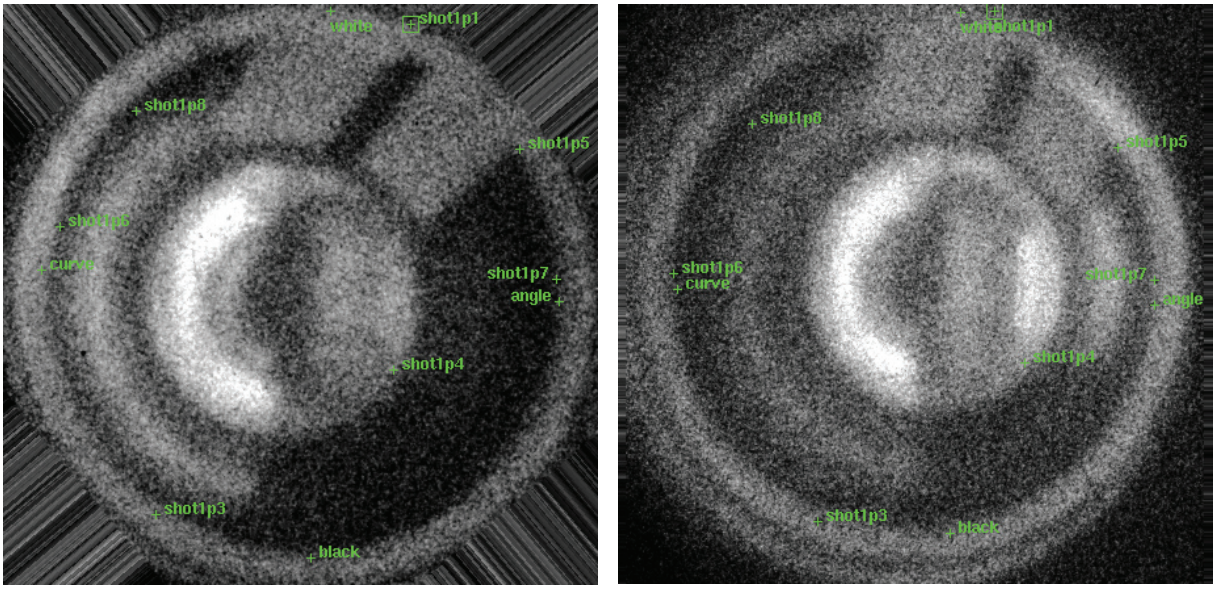

Figure 7. Dynamic shot, left and right views of a single frame

Figure 6 shows a copper target recorded in Shot 1 on July 27, 2006. A groove 100 μm wide and 500 μm deep was machined in this target to create a jet of material during shock. This target proved most interesting in the dynamic shot series due to the obvious 3-D features as well as timing and lighting conditions. In viewing static surfaces and objects, specular reflections from shiny surfaces created difficulties in stereo image correlation. This affected changes during the shot, as the surface

began to break up and become less reflective. Nine frames of each shot were recorded with 500-ns exposure times and 1 μs between frames. The full nine-frame image contains both views per frame and all nine frames. Two strobe lamps illuminated the surface. Strobe light timing was staggered slightly to have less light on the early frames, when the surface is highly reflective, and more light at the end of the sequence. The late frames became very dim, as the surface became very broken.

Two of the nine frames (4 and 6) were processed. The left and right views were cropped and rotated to the same orientation, then sent to RSL for processing. For Frame 6, the DEM was processed with different sample sizes to compute the correlation. Both 50-μm and 100-μm sampling produced good results in the rectified orthophoto. Frame 6 appears in Figure 7. The feature in Frame 6 that looks like a cloud of material indicates a relief elevation of 13 mm. The green markers indicate ground control points used by SoftPlotter to correlate the left and right image.

After the data run at STL, our team became concerned about improving image quality and, ultimately, stereo image correlation. New optics were designed that are superior to those offered by Myriad (Figure 8). We are seeking a better FOV match to our target size, as well as improved resolution and light collection with the new lens design. The proximal image bundle to readout camera optics assembly is built. We may increase distal target optics' diameter to enhance light collection.

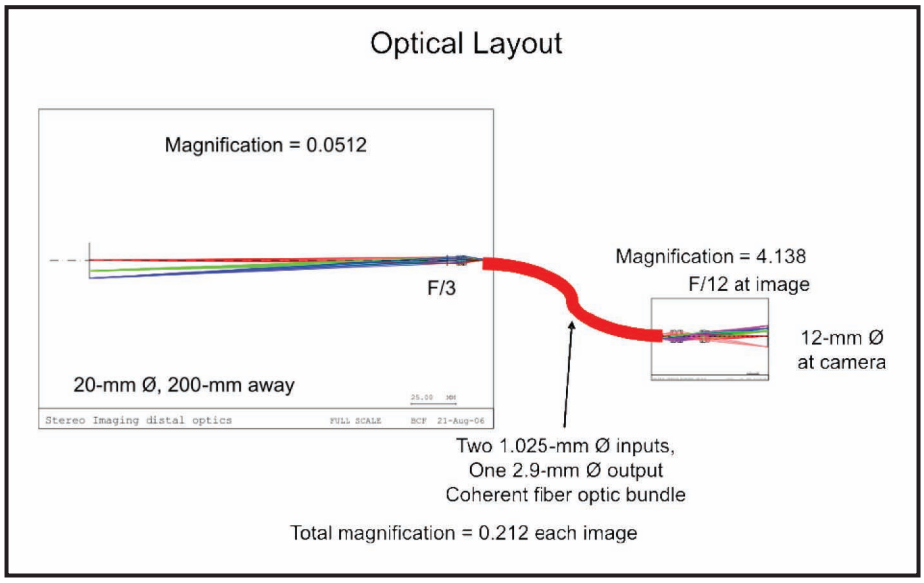

Figure 8. Improved optical layout

Conclusion

We have assembled a stereo-imaging system with probes suitable for use in experimental containment vessel penetrations and acquired stereo-imaging data of static 3-D objects and explosive shots. We have processed stereo-imaging data and generated digital elevation maps of 3-D surfaces, as well as designed and built optics to strengthen image quality. Additional work is needed to streamline the data-processing cycle and develop an automated portable version of the code. Data acquisition and image quality could also be improved with modifications to the fiber-optic assembly and implementation of upgraded optical system design. Hopefully, through development next year, we will transition select programmatic experiments from single-LOS, 2-D imaging to stereo 3-D imaging with the capability of placing dimensional scales on 3-D features recorded in explosive experiments.

Acknowledgments

We would like to acknowledge the following individuals: Doug DeVore, Paul Flores, Brent Frogget, Daniel Marks, Joshua Tybo (LAO); Heather Gledhill (RSL); Mike Grover, Gerald Stevens, Dale Turley (STL); and Dan Sorenson and Mark Wilke (LANL).

Novel Fiber Array Diagnostic Geometry

Michael Berninger,[1] *Bart Briggs, Brian Cata, Dale Crain, Morris Kaufman*
Los Alamos Operations

E. Chris Hagen, Scott Jenkins, B. T. Meehan, Steve Molnar, Scott Myers, Martin Palagi, Larry Robbins, Ron Swegle
North Las Vegas

This project researched a high-transparency (84%), microfabricated mesh to be used in the construction of fiber-optical arrays with small fibers (<400 μm), where the mesh held the fibers precisely within complicated configurations to produce arrays that would be impossible to build with conventional methods. After being used to build a simple linear array, the novel fiber geometry (NFG) was used to construct a trilinear array designed to simultaneously collect two-dimensional (2-D) spatial data in a pinhole camera setup installed on the Dense Plasma Focus (DPF) in North Las Vegas. The spatial and temporal data obtained validated the array design and mesh construction. More complex arrays, a hex-linear array and curved surface arrays, were constructed to exercise the full potential of the mesh-building technique.

Background

NSTec scientists recently desired to build a correlated fiber array with a complex configuration out of small fibers, such as Polymicro FVP 100/110/125 (outer diameter of 125 μm), but they could not identify a mode of construction.

Although useful for building a single, closely-packed linear array, the so-called "slide" technique is geometrically limited. In the slide-build method, individual fibers are positioned side-by-side between two glass microscope slides. This geometry is implicitly linear because of the monolithic rigidity of the glass slides. A multilinear array can be constructed by stacking individual arrays, but the distance between the arrays will be constrained by the thickness of the glass slides and fibers. In addition, the fibers within the multilayer slide-built arrays are not rigorously correlated.

Correlated arrays made by commercial vendors with quartz fibers 6–11 μm in diameter are ubiquitous but constructed with an industrial process that could not be modified to accommodate the special FVP fibers and complicated fiber arrangements. Thus, commercial vendors were unable to build the desired arrays.

[1] berninmj@nv.doe.gov, 505-663-2032

The NSTec scientists imagined a new way to build arrays with a high-transparency, custom, microfabricated mesh that would provide mechanical support and the means to precisely place fibers in complicated configurations. However, it was not clear that a mesh with micron-sized wires would be durable enough to build an array with large numbers of fibers.

Project

This project developed a methodology for using custom meshes to build complex fiber optical arrays. After designing and fabricating the mesh, two fiber arrays were built. The first array, a simple linear design, exercised both the array construction and created an end-to-end system. With this array, we successfully established an array fabrication process. Another array, more complex and difficult to construct by alternate methods, was installed on the DPF and used to validate the mesh-built methodology. Finally, three additional arrays, each with increasing geometric complexity that also included convergent and divergent curved surfaces, proved the efficacy of the NFG.

Mesh Design

The team first developed a set of requirements for a mesh to hold fiber-optical arrays of Polymicro FVP 100/110/125 fibers. The mesh was a grid with 135-μm square holes and 13 ±3 μm nickel wires; these dimensions correspond to 172 lines per inch and 84% transparency, a 16% reduction in the packing density over the close packing of the fibers in the slide-built technique.

The high-quality mesh was fabricated by InterNet, Inc., with an electroplating process. In this process, the array design was made into an image mask then transposed onto a metal plate coated with resin. The image in the resin was removed to reveal the metal substrate where the mesh wires would be formed. The plate was then submerged in a plating solution mixed with electrically charged nickel. By putting the opposite charge on the metal plate, the nickel was attracted into the grooves in the resin, thus forming the mesh wires. A 5" × 5" swatch of the mesh, 13-μm thick, was fabricated in about 36 hours. At the end of the process, the mesh was easily peeled off the metal plate.

Array Designs

The single-row linear array shown in Figure 1 helped the team develop a build process. (The image quality is poor because the fiber polishing was incomplete and fibers are unevenly backlit.) The array contained one hundred FVP 100/110/125 fibers. The insert in the figure's foreground is a close-up that shows the fibers were aligned with high precision. Two layers of the mesh are visible in the image. It took about two hours to construct this array.

The second array designed for the NFG was a trilinear array constructed to simultaneously collect 2-D spatial data in a pinhole camera configuration (Figure 2). A coarse array with 17 fibers was

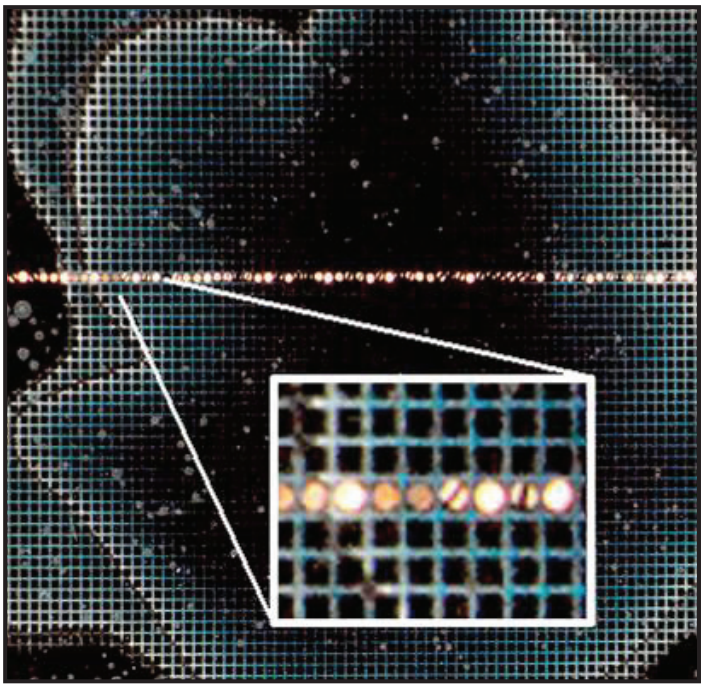

Figure 1. A prototype linear array with a rough polish. The layers of mesh are clearly visible in the image, and each fiber fills a hole.

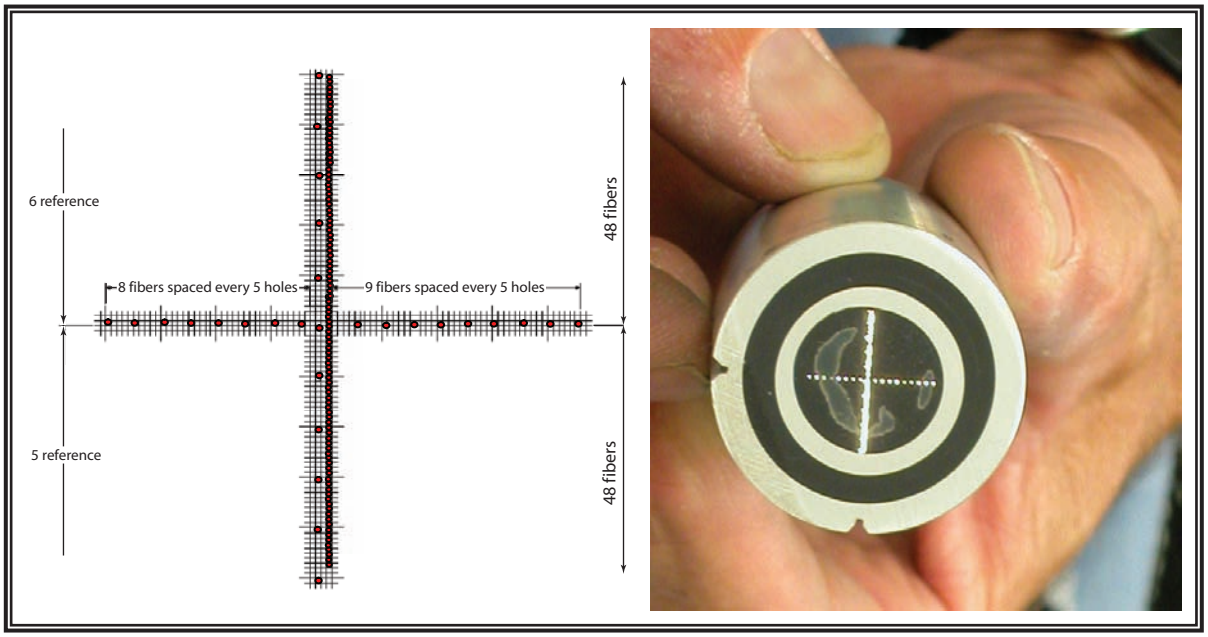

Figure 2. The second linear array design was a trilinear array in a cross pattern having dense and coarse arrays and precision spacing

aligned horizontally at 0°, and two vertical 90° arrays are at right angles to the 0° array. One of the 90° arrays, densely packed with 96 fibers, bisects the 0° array. The second 90° array is a coarse reference array with 11 fibers; it is parallel to the first and set apart by 296 μm.

The trilinear array design demonstrated that the mesh-build methodology has significant advantages over the slide-built technique. The total array was easily and quickly constructed with fiber spacing that varied from coarsely packed to densely packed while being precisely correlated within the array design. The packing fraction was limited only by the wire thickness, 13 μm, in two directions. The right-angle orientation of the trilinear array design would have been impossible to construct with a slide-build technique.

The value of the mesh-build technique was demonstrated when the trilinear array was used to collect dynamic x-ray data with the DPF. In this diagnostic, the trilinear array transported scintillation light created with x-rays to a streak camera (Figure 3). Some of the data is shown in Figure 4, where the horizontal axis of the streaked image is the time axis. Time increases from left to right, with the total period being ~1.4 μs. The vertical axis of the streaked image is the 2-D spatial information from both the horizontal and vertical components of the trilinear array. The top 80% of the streaked image corresponds to the densely packed 90° array that recorded x-ray data on the vertical DPF axis. In this top region, the DPF anode is at the top of the image. The bottom 20% of the streaked image contains the data from the coarse 0° array, with x-ray data collected normal to the vertical DPF axis.

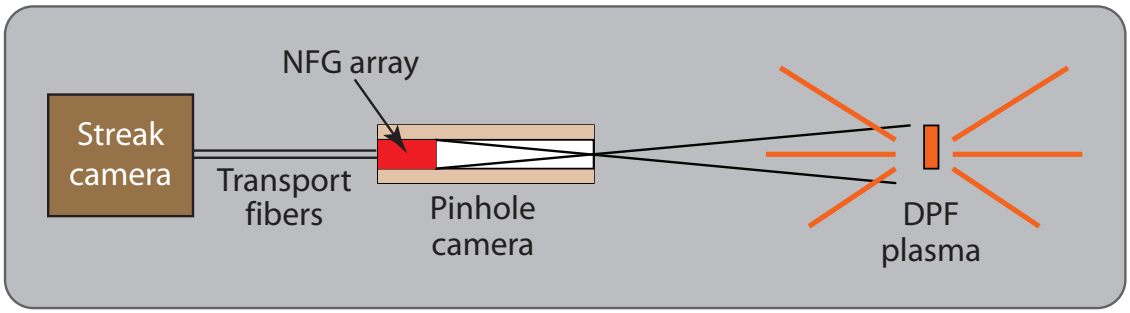

Figure 3. Schematic of dynamic pinhole experiment with the trilinear array

In this application, the coarse 0° array was successfully utilized for precision of alignment of the array onto the central axis of the DPF. The high-resolution 90° array collected data on the spatial distribution of the x-rays over time, while the 90° coarse array correlated spatial power reference (and spectrum information when measuring visible light). Because the mesh oriented the fibers within a precise grid, we were able to correlate the power reference channels to the data channels with high accuracy and do precision alignments *in situ*.

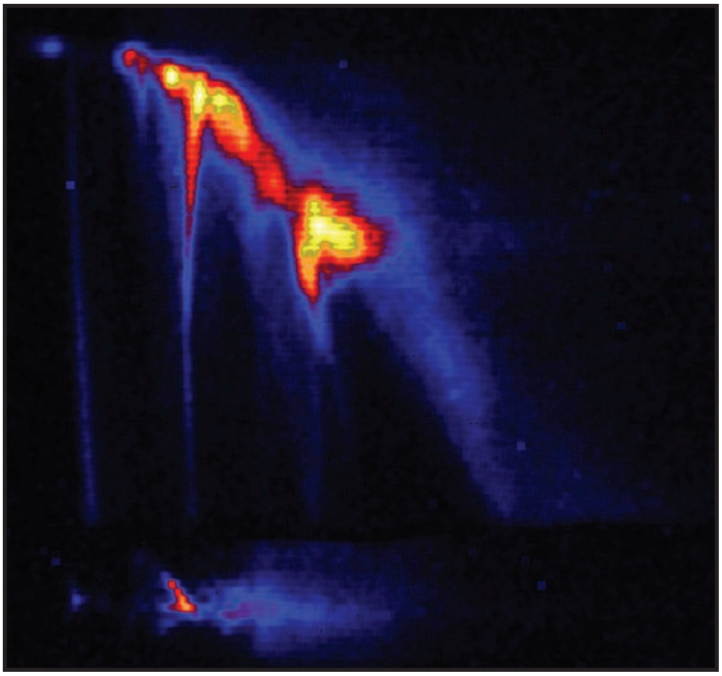

Figure 4. Data from the trilinear NFG array. Data collected with the dense vertical array is above the data from the horizontal alignment array.

Taking advantage of the mesh flexibility and convenience, we built two curved surface arrays with convergent and divergent geometries, as shown in Figures 5 and 6. These curved surface arrays demonstrate that mesh can be shaped to accurately place fibers on a curved surface; however, an additional device such as an angle jig or goniometer is necessary to ensure that the angle orientations of the fibers are precisely measured. A process for measuring the magnitude of the spatial error in the mesh-build technique has yet to be determined.

The NFG was also used to construct a coarse hex-linear fiber array (Figure 7), which may be used as a filtered spectrometer with five or six channels to obtain spatial, temporal, and energy-resolved data. This array will be used to define a process to measure the magnitude of alignment error with a comparitor. The comparitor uses a microscope and grid pattern to measure the spatial precisions and alignments of small parts.

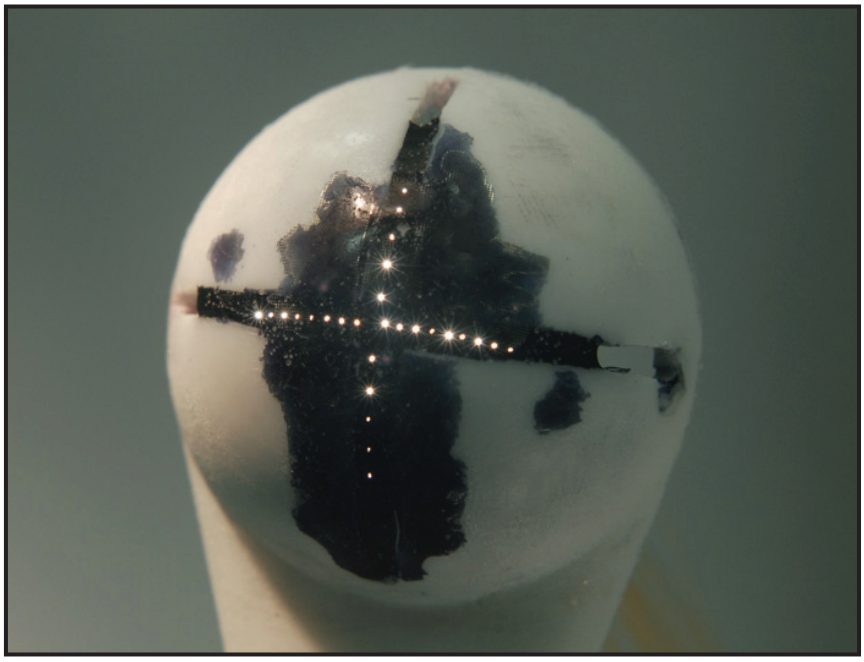

Figure 5. A divergent curved surface array built with the flexible mesh

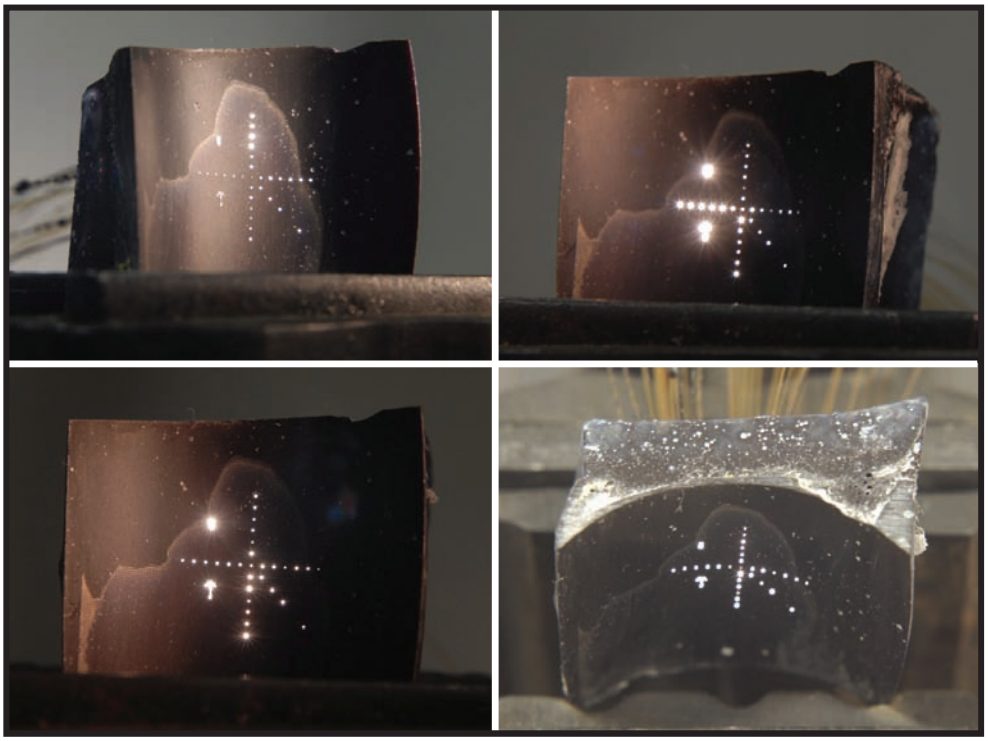

Figure 6. Views of a curved surface array built with the flexible mesh demonstrates the ease with which a convergent geometry array can be constructed

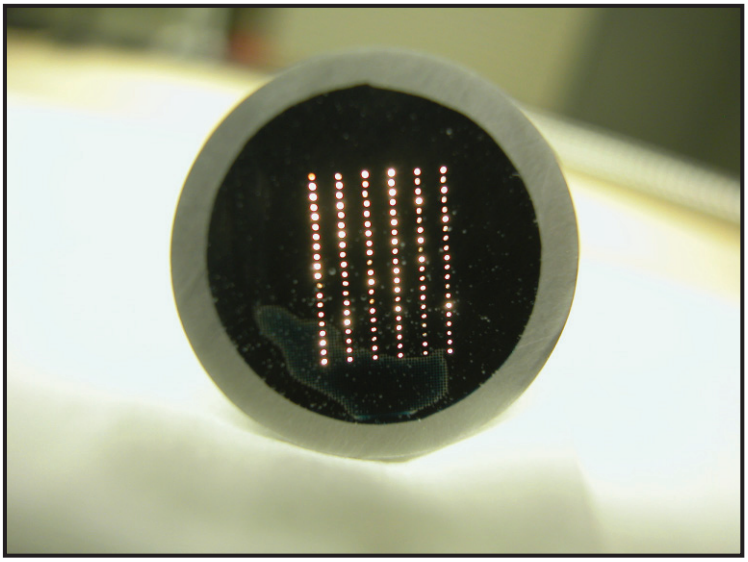

Figure 7. A hex-linear array. The array appears slightly uneven and misaligned, but this is an optical illusion caused by the fact that the opposite end of the array is still rough cut and the backlighting is uneven. The alignment and linearity of this array were verified under the microscope and grid pattern of a comparitor.

Conclusion

The NFG SDRD project successfully developed an array building technique using meshes, and fabricated five arrays with increasing complexity. The NFG method of constructing arrays is intuitively easy to grasp, fast to execute, and affordable. The advantages of the mesh-build technique were proven when a trilinear array collected time-resolved 2-D spatial data on the DPF. These arrays fully exercised the potential of the mesh for building coarse and dense arrays in any planar configuration with highly correlated precision. Two curved surface arrays were also constructed. The NFG effort demonstrated that the mesh-build technique has significant advantages over the slide-build technique.

this page intentionally left blank

Spatial Light Modulators for Dynamic Spatial Laser Profiling

D. Taner Bilir,[1] *Dean E. Simmons*
Livermore Operations

The goal of this project was to develop a feedback system for the spatial flattening of a high-energy calibration laser beam profile. A reflective, liquid-crystal (LC) spatial light modulator (SLM) and a detection camera with a software-controlled feedback system were used to achieve local modulation in the beam intensity. Development of a LabVIEW-integrated software interface began.

Background

Many streak camera systems are calibrated with laser-based measurements; one such is the flat-field measurement conducted by the NSTec LO Long-Pulse Laser (LPL) Laboratory. The streak cameras are illuminated with a high-intensity, spatially uniform field of light, and the image on the back of the streak camera is captured by a CCD camera. If the laser source contains nonuniformities in its beam profile, these intensity variations will be transferred through the streak camera to the calibration images, and can increase the uncertainty in the resulting camera characterization. The typical nonuniformities of interest range from noise and dead zones to spherically or cylindrically symmetrical wave fronts and hot spots. LO currently relies on a technique employing image-processing algorithms to remove the nonuniformities in the images. While this technique results in a flat-field correction for the laser output, it limits the dynamic range of the streak camera system.

We proposed developing a dynamic software-based feedback system to adjust the degree of uniformity in the laser's spatial profile in real time using a polarization-modulating effect. A CCD camera would capture a snapshot of the laser intensity profile/image from a holographic beam sampler, and then analyze the sampled beam to determine the degree and spatial characteristics of its nonuniformities. This nonuniformity information could then address an LC SLM. The SLM would apply a pixel-wise polarization of the sampled spatial beam to locally modulate beam intensity, creating an optimal and spatially flat beam intensity profile. With beam uniformity controlled, calibrations would be more precise, leading to higher quality experimental data.

[1] bilirdt@nv.doe.gov, 925-960-2626

Project

Our tasks assumed four phases:

- Surveying the existing technologies and options available for SLM systems
- Designing the optical system to accommodate and control the laser input
- Determining a software package to be used and integrating it into the feedback and analysis system for profiling the laser input, and
- Testing our concept to demonstrate its usefulness for SLM-based laser intensity control.

SLM Survey

Nonuniformities in beam profiles are traditionally corrected with specialized optics, but the problems inherent in this method of optical control have led a push to explore SLM methods. Traditional optical controls are typically limited to correcting only a few specific optical aberrations (Olivier, 2006). Furthermore, these controls are time-consuming and difficult to align, and the fabrication expenses can be quite substantial because of the accuracy or criteria specified in the manufacture of the system. SLM technology promised a simpler, less expensive, and possibly more effective solution (Olivier, 2006; Topic 12, 2005). Therefore, we identified and evaluated several specific SLM devices for possible use (Figure 1).

Figure 1. Some SLM technologies

The laser system of interest was the LO LPL. The LPL is a frequency-doubled Nd:YAG laser at 532 nm with a 9-mm diameter; the 350-mJ pulse has a 100-ns pulse duration and a 1-second repetition rate. Due to the size of the laser beam, one of the criteria for the SLM was that it have a large area (>1 cm^2). Another major criterion was the maximization of the number of spatial elements. Large

array size allows for better localization of the beam modulation. As large-area, large-array SLMs are relatively new, there were a few types that were most often cited and documented as representative of the better SLMs (Monteverde, 2006; Olivier, 2006; Topic 12, 2005). These were:

Digital Mirror Device (DMD)

This microelectromechanical system (MEMS) employs a tiny two-dimensional array of micron-scaled moveable mirrors that are electrostatically tilted to reflect light into or out of an optical imaging plane (Dudley, 2006; Hornbeck, 2006). The typical response time from an electrostatic impulse is on the order of tens of microseconds, and alternating the tilt of the mirrors brings a selectable grayscale to the images transferred. This technology is used widely in projection displays (Monteverde, 2006).

Grating Light Valve (GLV)

This MEMS uses a one-dimensional array of metallic mirrored ribbons about 20–30 μm long and 2–3 μm wide. In the GLV, an electrostatic force pulls the ribbons closer to the base to create a square-well diffraction system (Monteverde, 2006). Here, the desired reflected orders are sent to the image plane while the diffracted orders are sent out of the system. The response time is in nanoseconds. We found that the one-dimensionality of this technology was not ideal for our application.

Electrically Addressed LC (Reflective or Transmissive)

The LC is a polarization-adjustment technique, in which the LC structure becomes transparent or opaque to incoming light based on an applied voltage or electrical field (Olivier, 2006). The field is applied through thin-film transistors and a transparent indium-tin-oxide electrode in transmissive devices and through mirrors on a silicon backplane in reflective devices (Prototyping Projects, 2005; Topic 12, 2005). The maximum effect of this variety of SLM requires linearly polarized laser input, since the polarization axis rotation in the LC molecules provides the intensity change in transmitted or reflected light.

The electrically addressed LC-based SLM (EASLM) typically has the slowest response time, ~3 ms, but it excels in producing grayscale and high-resolution (1280 × 768) images (Dudley, 2006; Topic 12, 2005). Another bonus is its small, durable packaging (Olivier, 2006). An added benefit to selecting the EASLM with the reflective LC on silicon (LCoS) was that the vendor would include an additional liquid crystal display for damage testing in return for our data on how the device performed during high-energy laser exposure (Prototyping Projects, 2005; Topic 12, 2005). The vendor's damage threshold data for the product were previously recorded with a much less energetic but higher peak-power laser (doubled Nd:YAG laser at 532 nm, 1.7-mm diameter; 5-mJ pulse, 10-ns duration, 20-Hz repetition rate).

System Fabrication

The experimental design called for use of the LPL, which would allow examination of the reflective sensitivity across the face of the SLM as well as the linearity and damage threshold as the laser output energy approached its upper limit. Due to programmatic obligations for the LPL system, the test configuration substituted a small helium-neon (HeNe) laser (although the beam size of this laser is similar to the LPL, it is a continuous wave, red laser with much lower energy), two polarizers, a negative lens, an iris, and a PixeLINK 3.5-μm pixel, 2208 × 3000 CCD camera. The negative lens was used to expand the HeNe beam across the largest cross section of the SLM display, while the polarizer combination controlled the laser input to the reflective LCoS EASLM.

Software Development and SLM System Performance

Having set up the HeNe laser system and before applying the SLM's amplitude control to the HeNe laser output, we began investigating the SLM itself to become more familiar with its user interface and main application software. Our ultimate plan was to use LabVIEW and IDL software packages to integrate the control and analysis aspects of the system software. First, however, using the SLM's software, we applied some fundamental optical functions to the SLM and examined the degree and uniformity of modulation across the CCD image from our PixeLINK camera. Each elementary optical function was varied in grayscale or modulation percentage and captured for intensity data.

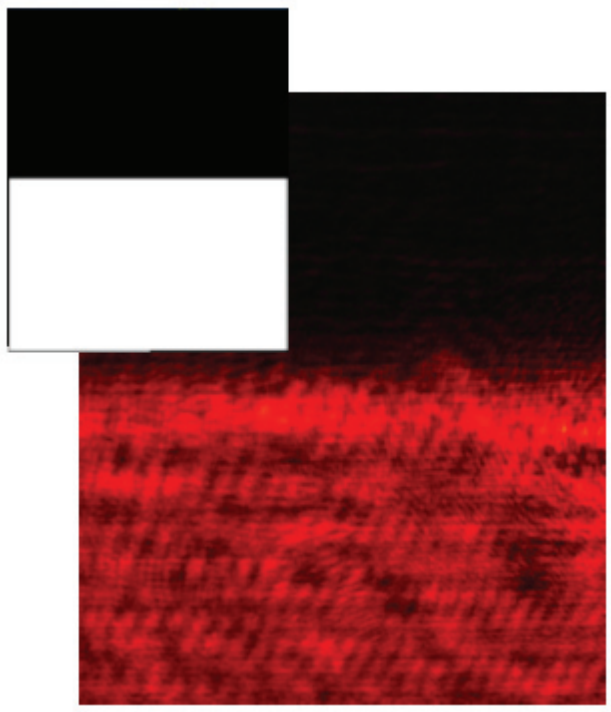

Figure 2. Knife-edge diffraction pattern with modulated SLM image

Since resolution capability and contrast control were the principal features that drove us to propose an SLM-based system, demonstrating the performance of those features defined our testing phase. The SLM's software package included a library of predesigned functions that allowed the SLM to simulate the effects of diffraction gratings, axicons, and zone plates. Most of our tests used a knife-edge function, in which a horizontally or vertically divided binary test function (a half-white and half-black rectangular image) was imposed on the SLM. These patterns gave us the means to observe the single-edge (one black/white cycle) and multiple-edge (higher spatial frequencies) resolution quality with the SLM, as well as any diffractive effects caused by the optical system. These optical functions also allowed us to examine the area-effects of the SLM, such as pixel-to-pixel variation and fixed-pattern phenomena (Topic 12, 2005). The knife-edge function in Figure 2 gave a consistently even pixel-to-pixel response on the dark side of the single-cycle step, and as the spatial frequency increased, diffractive maxima could be seen within the darker bands. The defining edges did not change in sharpness for either the horizontal or vertical step function variations. Of interest was the presence of some unexpected spatial structure within these images. This spatial structure is seen in the form of a slight sinusoidal diagonal pattern across the lighter side of the knife-edge cycle. This structure persisted through images captured using other optical functions.

We suspect that this was caused by surface variations the polarizing elements in our optical system, but could also be the result of the orientation of the SLM in the laser axis or CCD camera irregularity.

Summarizing the SLM relative intensity plot over the entire 8-bit (256-level) opacity range, the images produced by each function seemed to show some nonlinearity across the opacity ranges from 0 to 150 and above 200, but were linear between 150 and 190 (see Figure 3). This gave us a smaller range of linearity than expected, but allowed us to establish a definitive relationship between opacity and relative intensity within that range, as shown by the linear region in our intensity response curve (see Figure 3).

Although our research did not address the following factors, we think it possible they could have some effect on the measured brightness levels and additional artifacts in the white portion of the optical knife-edge function:

- Automated gain and exposure settings in the CCD camera. Although an effort was made to account for many of the camera's automated or default controls, there may be some influence not yet found that may account for the jumps in brightness and darkness so consistently across the range of images from captured functions.
- Inconsistencies from polarizer combinations. An additional examination of these sheets could reveal some insight into the nature of some of the patterning in the knife-edge images and in the nonblack portions of the captured images.

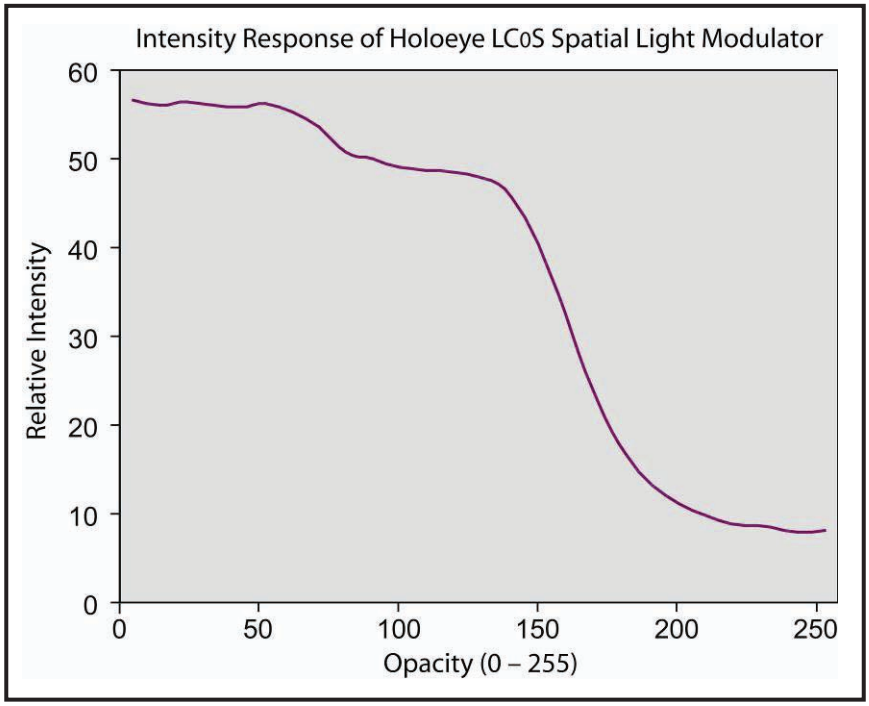

Figure 3. Relative image measurements obtained with the LCoS EASLM

- Optical components. The negative lens and iris combinations were assembled to more fully cover the SLM's available area so that the image would be expanded as much as possible before it was captured by the CCD camera. Experimenting with a different negative lens and/or C-mount lens for the CCD could improve the contrast and focus for future data runs.

Conclusion

We surveyed and analyzed the current SLM technologies and principles; designed, procured, and fabricated the mechanical and optical parts for the optical system setup; developed and documented several process steps, optical arrangements, and unifying software components that can be used to further any continued SLM-based wave front intensity adjusting or phase recording experimental development; and utilized an LC-based amplitude-modulating SLM system with sufficient success to suggest that continuing research might result in an attractive alternative to traditional optical control methods. In addition, the steps necessary to finalize the integrated software feedback system and/or extending the project toward wave front phase controlling elements also present in the SLM system was outlined. A proposal for continuing work to develop the software controls and to add a wave front phase control and recording aspect to the SLM system was prepared.

It is especially important to all future calibration testing and laser-based imaging processes that we can develop an accurate method of keeping the laser source illumination as consistent in spatial amplitude as possible across the profile of the pulsed beam. With this capability in place, characteristics such as dynamic range, flat field, and the resolving capabilities of the cameras being tested can be accurately determined. It is no less important as a tool for diagnosing possible problems with optical components or the laser system itself. As laboratory processes become more efficient and less operator-intensive, methods that allow for self-correction or automated feedback will aid researchers in their work and lessen the time they devote to overcoming the limitations of laboratory tools.

References

Dudley, D., W. Duncan, J. Slaughter, "Emerging Digital Micromirror Device (DMD) Applications," *SPIE Proceedings* **4985** (2003), dlp.com/dlp_technology/images/.../152_NewApps_paper_copyright.pdf, accessed August 27, 2006.

Hornbeck, L., "Digital Light Processing for High-Brightness, High-Resolution Applications," *21st, A Publication for the Unique Consumer*, http://www.vxm.com/TIDLP.html, accessed August 27, 2006.

Monteverde, R., "Spatial light modulators illuminate a wide variety of application spaces," *Laser Focus World* **40**, 11 (January 2004) 93–96, http://www.laserfocusworld.com/issue/toc.html?volumeNumber=40&issueNumber=1&publicationId=12, accessed August 27, 2006.

Olivier, S. S., "Wavefront Correction Technologies," NSF Center for Adaptive Optics, presentation, August 7, 2003, cfao.ucolick.org/pubs/presentations/aosummer03/Olivier.pdf, accessed August 27, 2006.

"Prototyping Projects–Liquid Crystal on Silicon (LCoS) Spatial Light Modulators (SLMs)," University of Colorado (Boulder), http://me-www.colorado.edu/centers/yclee-group/proj/lcos.html, accessed November 16, 2005.

"Topic 12: Spatial Light Modulators and Modern Optical Systems," *Modern Optics*, University of Edinburgh, Department of Physics, Applied Optics Group, www.ph.ed.ac.uk/~wjh/teaching/mo/slides/slms/slm.pdf, accessed August 7, 2005.

this page intentionally left blank

High-Radiometric Output, Flat-field, Pulsed Light Source

D. Taner Bilir, Jerold Cradick, Charles Diamond,[1] Jim Mirador
Livermore Operations

The researchers studied the use of the latest light-emitting and laser diode technologies applied as a high-radiometric output, flat-field, pulsed light source capable of producing an intense, narrow-band, uniform, fast, flat-top, variable-width pulse for characterizing and calibrating electro-optical elements in diagnostics systems. We chose to develop a source based around ultrabright, light-emitting diodes (LEDs) due to their fast-response, narrow-band, high-intensity optical characteristics. The uniformity was derived from a light source driving an integrating sphere, while the fast pulse was adapted from a pulser designed in a previous SDRD project (Bilir, 2006). The flexibility of the new system will aid characterizing and calibrating electro-optical elements of CCD cameras, gated CCD cameras, microchannel plate intensifiers (MCPIs), proximity-focused diodes (PFDs), and streak tubes and cameras.

Background

Electro-optical elements such as CCD cameras, gated CCD cameras, MCPIs, PFDs, and streak tubes and cameras are currently characterized and calibrated using a xenon flash lamp, an optical projection system, and a band-pass filter. The xenon flash lamp produces a nonvariable, semi-Gaussian-shaped, 10-µs, full-width at half-maximum (FWHM) polychromatic light pulse. Because the flash lamp is polychromatic, it requires a band-pass filter to convert the light source to a quasi-monochromatic light source. The quasi-monochromatic light is focused by a TV Optoliner projection system onto the electro-optical element being characterized. The nonrepeatable xenon flash lamp requires a complicated calibration and monitoring system to accurately calibrate electro-optical elements. Recent advancements in ultrabright fast LEDs, integrating spheres, and solid-state switching devices can be combined to produce a light source with an intense, narrow-band, uniform, fast, flat-top, variable-width pulse.

Project

This project began with a survey of the latest ultrabright, fast LEDs and laser diodes, to select the best devices to test. LEDs from Cree, Lumileds, Opto Technology, Super Bright LEDs, and American Opto Plus LED Corporation were purchased and tested with a variety of pulsers we designed specifically for this work.

[1] diamonce@nv.doe.gov, 925-960-2540

The first tests, using an NSTec-designed avalanche pulser, recorded the rise and fall times of the LEDs' optical pulse. While the pulser drove the sample LEDs, a PIN 10D diode was used to determine the LEDs' optical response time. The test setups and results for two LED types are shown in Figure 1.

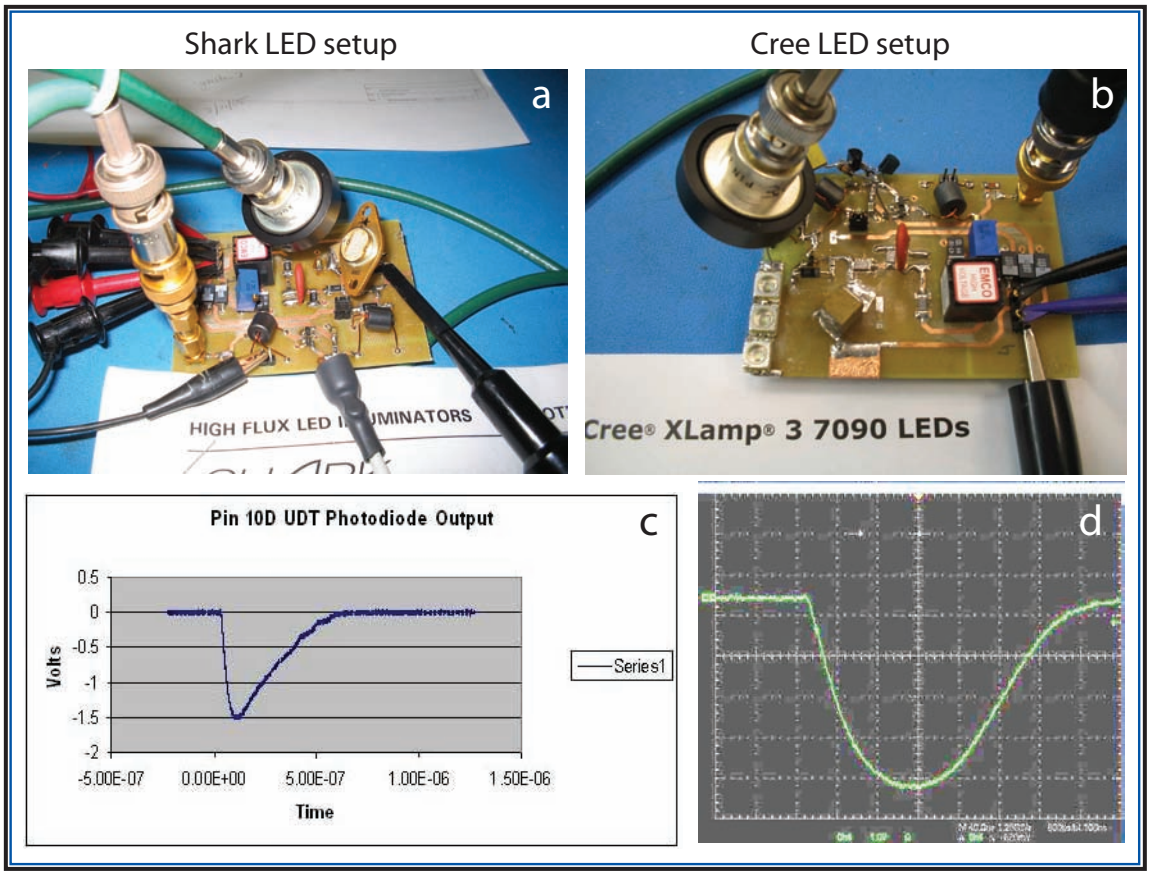

Figure 1. Optical response time of LEDs: a) setup for Opto Technology Shark Series LED array, b) Setup for Cree LEDs, c) optical response of the Opto Technology Shark Series LED array, d) optical response of the Cree LEDs

In order for the optical pulse to be uniform in the temporal domain, we needed a flat-top pulse to drive the LEDs. It was also suspected that the PIN 10D photodiode's response was bandwidth-limited and that it did not represent the true rise and fall times of the LED's optical pulse. Therefore, we designed a flat-top pulser and purchased a diode with higher bandwidth than the PIN 10D

for use in further testing. This setup was used to test the rise and fall times of the Opto Technology Shark Series LED array's optical pulse. The electro-optical test results shown in Figure 2 compare the responses of both diodes.

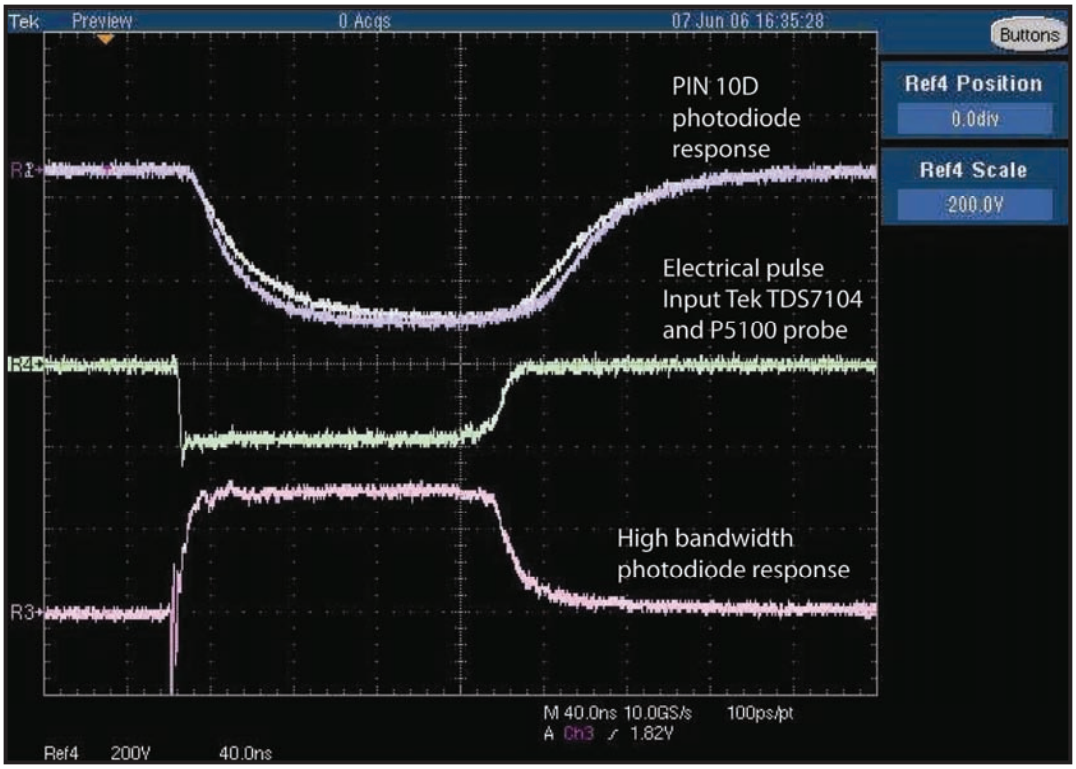

Figure 2. Electro-optical test results utilizing the Opto Technology Shark Series LED array

The Opto Technology Shark Series LED array holds 50 (10 parallel sets of 5 in series) LEDs in a single TO-66 power package. The Shark series comes in a variety of colors. In Figure 2, the Shark array tested was green with a dominant wavelength of 530 nm. During these flat-top pulser tests, we noticed that both the Cree and Shark "green" LEDs changed color; the green appeared differently when the LEDs were pulsed compared to when powered with a DC supply. The red LEDs (dominant wavelength of 625 nm) did not exhibit this behavior. A test was run on a spectra radiometer with the Shark LED arrays to determine the exact wavelength shift of the green LED arrays, and to ensure that the red LED arrays did not shift wavelengths. Figure 3 shows the results of these tests.

The wavelength shift differences between the green and the red LEDs can be explained by materials used to manufacture the LEDs. The green LEDs utilize InGaN and the red utilize AlInGaP. The InGaN in green LEDs causes their wavelength to decrease with increasing forward current (Ott,

2003). Other than InGaN, no LED material has this dependency; conversely, no other material emits green light as brightly. The green LEDs also developed another problem: when pulsed, they had a high failure rate. The cause of the high failure rate was not investigated, and the remainder of this discussion reports on only the red Shark arrays.

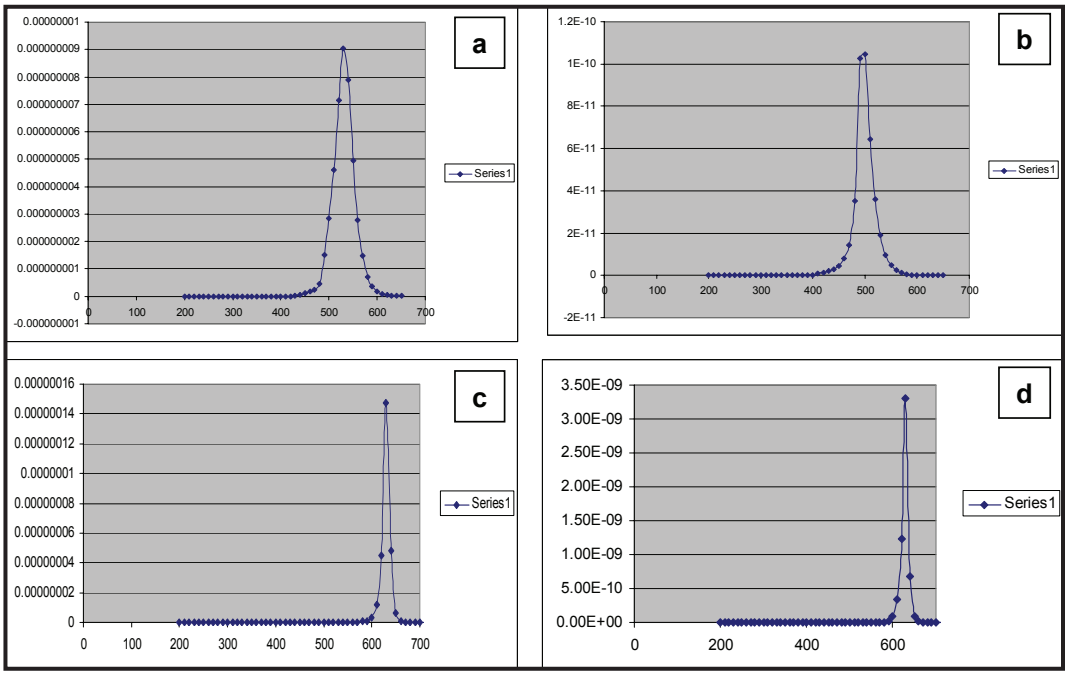

Figure 3. Spectraradiometer data from Shark LED arrays: (a) green, DC, 530-nm, peak 40-nm FWHM, (b) green, pulsed 500-nm, peak 30-nm FWHM, (c) red, DC, 630-nm, peak 20-nm FWHM, (d) red, pulsed, 630-nm, peak 20-nm FWHM

Based on the knowledge gained through avalanche and flat-top pulse testing, we proceeded with scaled-up testing, increasing the optical power to drive an integrating sphere. The first scaled test placed three Shark LED arrays in series. The LEDs were driven by a scaled-up pulser designed for this test and similar to the flat-top pulser used previously. The pulser schematic and final devices for the scaled tests are shown in Figure 4.

The scaled-up, flat-top pulser drove the 3-series LED circuit, whose light was homogenized by an integrating sphere before it was recorded on an NSTec50 tube-based streak camera. The data were captured on a 4K × 4K unbinned CCD camera without the aid of an MCPI. Although the CCD counts were low, the technique showed promise. The entire test setup was scaled up in power

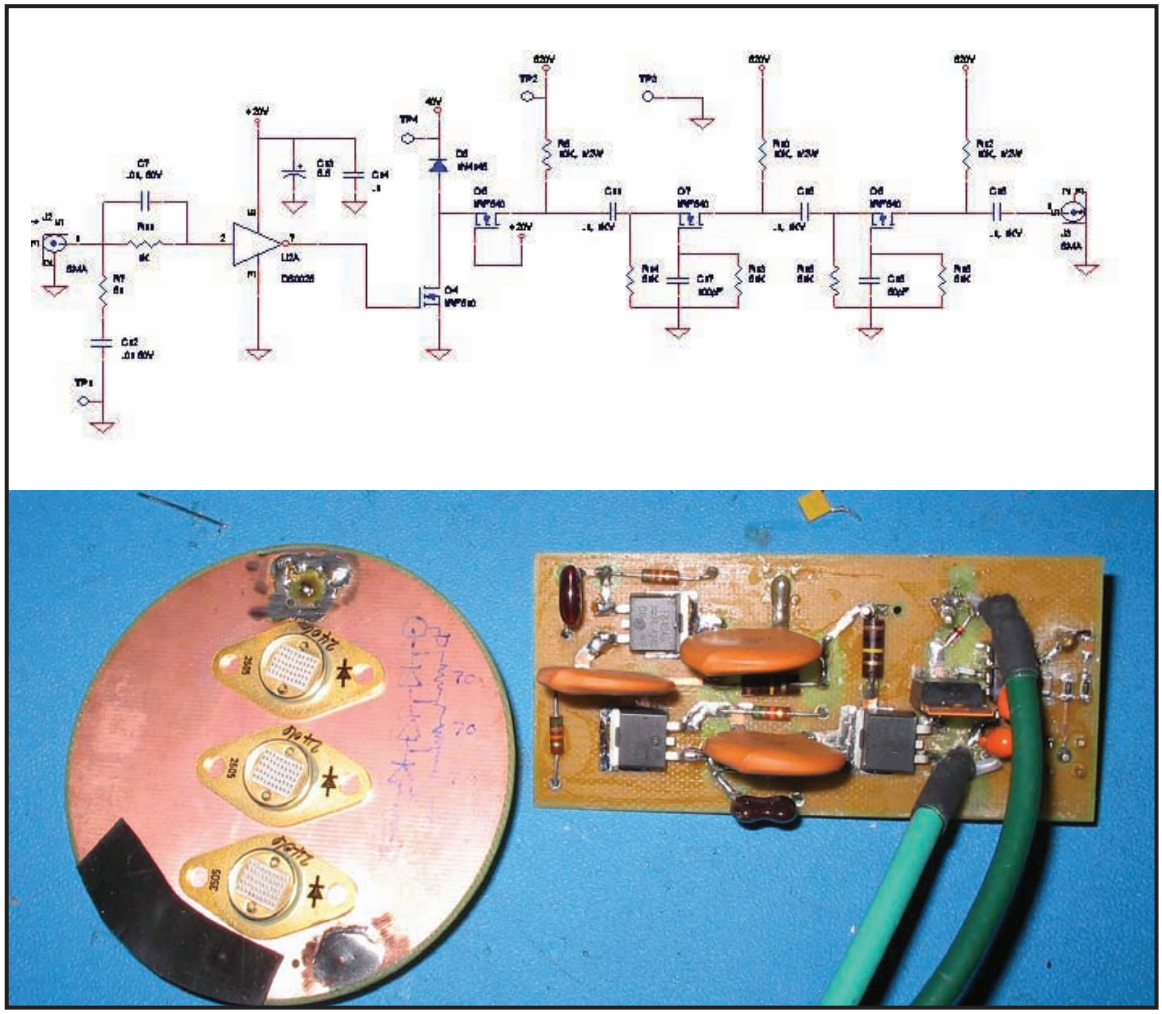

Figure 4. Scaled flat-top pulser schematic (top) and 3 series LED array board and pulser assembly (bottom)

once more: a 3 parallel × 3 series LED array board (built in-house) capable of producing a higher-intensity LED pulse was used with a pulser modified from a previous SDRD project (Diamond, 2005; Bilir, 2006) to drive the 3 × 3 LED array (Figure 5).

Using the 3 × 3 LED array assembly, pulser, and integrating sphere, a flat-field file was developed that could then be used to correct subsequent files by removing the fixed pattern noise and nonuniformities associated with the streak camera cathode, phosphor, fiber-optic input/output windows, and CCD camera fiber optics. As can be seen in Figure 6, the signal-to-noise ratio was improved by a factor of nearly four, and the image on the right is flat compared to the uncorrected image on the

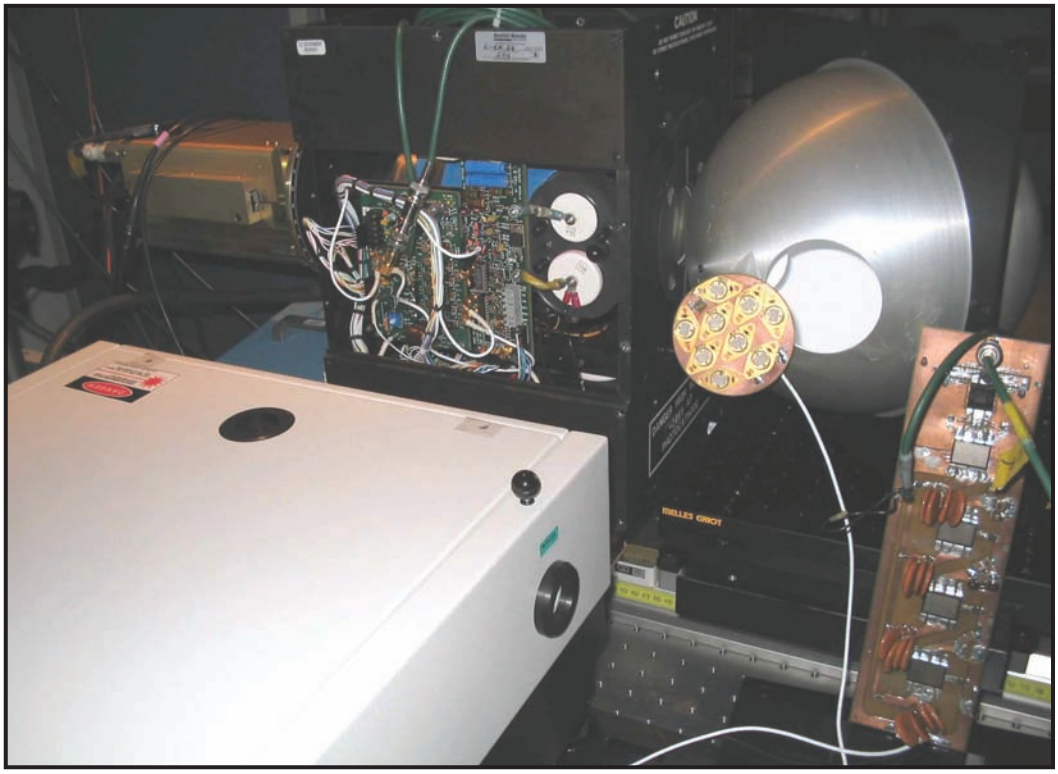

Figure 5. 3 × 3 LED array, pulser, integrating sphere, and streak camera system with CCD readout

left. The flatness improves from a full-scale of ~2000 counts to a full-scale of ~250 counts. The sweep direction is up. Nonuniformities in the horizontal direction are due to the size of the integrating sphere. The slight nonlinearity of the streak camera ramp circuits requires that the flat-fielding process be done at each sweep rate. As the sweep rates increase, so must the intensity of the LEDs so that the CCD camera is operating in the linear region to develop the flat-field files. The 3 × 3 LED array is capable of performing the flat-field process at 480- and 240-ns/40-mm sweep rates.

Finally, an 8 parallel × 3 series LED array board was designed and built. In order to maintain the same overall dimension of the array board, the LED arrays were laser-cut to reduce the package size. The 8 × 3 LED array board also required a new pulser board driver to increase the overall intensity. The testing phase of the 8 × 3 LED array was not completed; however, the LED array was assembled (Figure 7). The 3 × 3 LED array is also shown in Figure 7 to illustrate the modification to the LED arrays and to emphasize the light intensity required for the faster sweep rates.

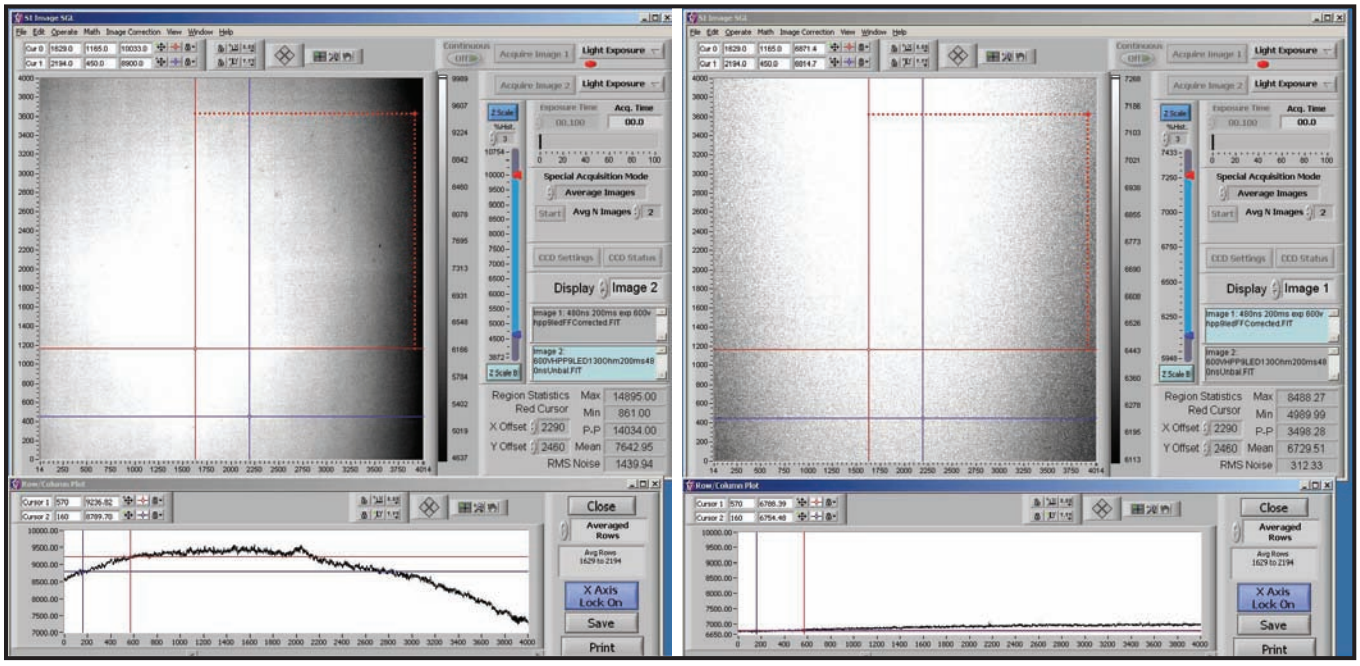

Figure 6. Results of the 3 × 3 LED array tests (of different intensities), showing the 480-ns/40-mm sweep rate uncorrected image with vertical lineout (left) and the corrected image with vertical lineout (right)

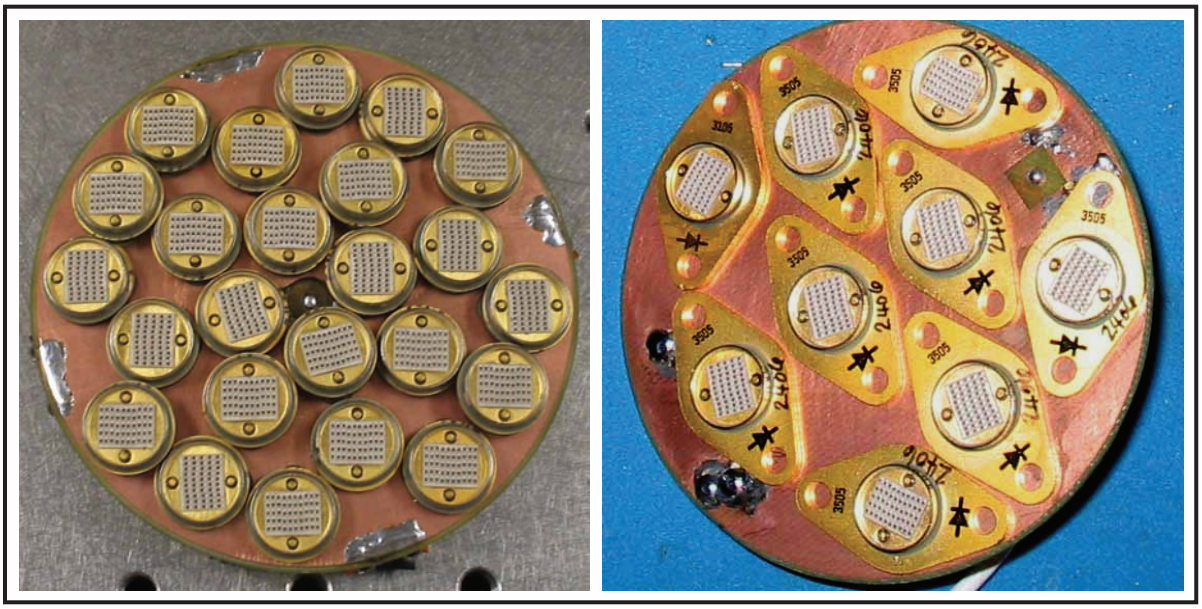

Figure 7. LED array matrixes. The 8 × 3 LED array board with modified LED arrays (left) is shown with the 3 × 3 LED array board with standard LED arrays.

Conclusion

The increased intensity and decreased response time of today's LEDs and LED arrays can be used in a number of applications for diagnostic characterization and calibration, replacing hazardous, expensive Class IV laser systems, to remove nonuniformities and the fixed pattern noise in diagnostics. As demonstrated with the LEDs, pulser, and integrating sphere, this process has been simplified to the point of automation. This project produced a light source capable of generating a fast, flat-field, pulsed light for streak cameras, MCPIs, and gated CCD cameras.

As noted above, the light source is not capable of generating flat fields for fast-sweep-rate (200-ns or greater) streak cameras; however, we expect that with the 8 × 3 LED array, this is possible. The final intent of this project was to build four 8 × 3 LED array boards and drive the large integrating sphere that has four input ports and a larger/flatter output port.

Acknowledgments

In addition to the excellent work provided by the team, the author would like to acknowledge the following individuals: J. Anderson, Mary Kucher, and Elizabeth Silbernagel, for support in purchasing numerous LEDs and associated electronic parts for the pulser; Rob Buckles, for his assistance in determining the maximum current the Shark LED arrays could handle; and last, but certainly not least, Tim Sammons, for his advice and support.

References

Bilir, D. T., "High-power Pulser," *Nevada Test Site–Directed Research, Development, and Demonstration*, FY 2005, Bechtel Nevada/National Security Technologies, LLC, Las Vegas, Nevada, 2006, 223–230.

Diamond, C. E., D. T. Bilir, "High-power Pulser," *Nevada Test Site–Directed Research, Development, and Demonstration*, FY 2004, Bechtel Nevada, Las Vegas, Nevada, 2005, 191–196.

Ott, H., L. Plotz, M. Byrne, "Dimming InGaN LEDs," Opto Semiconductors Application Note, January 8, 2003.

Line VISAR for Curved Surfaces

Dan Frayer, Brent Frogget[1]
Los Alamos Operations

This research studied techniques to improve signal collection across a specular curved surface for line velocity interferometer system for any reflector (VISAR) systems. Techniques we explored included telecentric optics, field flattening, and varying the depth of field. Code V optical models were created to discover the behavior of light on curved surfaces. We found that field-flattening methods improved signal collection for limited applications.

Background

To understand material properties, measurements of their dynamic response to shock impulses are made. VISAR measurements are routinely performed on flat surfaces (Barker, 1972). Signal collection from reflected and scattered light off planar surfaces is well understood; however, under dynamic conditions, the surface under study does not always remain flat or perpendicular to a probe. In addition, frequently the dynamic properties of cylindrical and spherical objects need to be measured to understand these dynamics. Nonplanar objects are studied on Atlas at NTS, on many subcritical experiments at NTS, on Z at Sandia, National Ignition Facility (NIF) at LLNL, and in other locations.

When a surface moves, tilts, or changes shape, the light reflected or scattered back to the signal collection system varies. Figure 1 shows light loss at the sides of a sample immediately after shock breakout and decreasing light afterward. Recently, a Code V modeling study of the illumination return across a flat, shocked surface under various conditions through a line VISAR optical relay was performed by Malone (2003). The results were surprising. The shape of the illumination across a surface is different when the impulse results in surface tilts, curvature, or even as the surface moves toward the probe. Velocity information retrieval may also be affected.

This SDRD study was proposed to explore, develop, and apply optical techniques in optical modeling programs to line VISARs that study material velocity from curved surfaces under dynamic conditions. This would help determine the optimal illumination and light collection requirements for a curved reflective surface. We investigated the use of telecentric lenses, approaches for field flattening of the target image, and increasing or decreasing the depth of field with the aim of applying promising techniques in future physical experiments.

[1] froggebc@nv.doe.gov, 505-663-2015

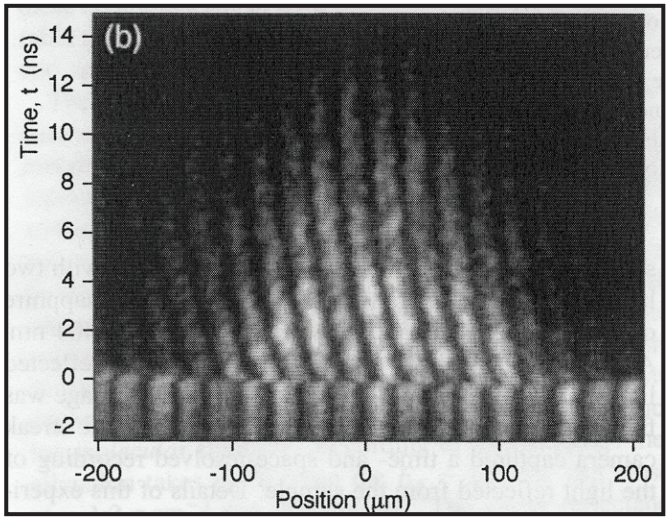

Figure 1. Sample line VISAR streak image (Celliers, 2000)

Project

Code V Model

For this SDRD project, an optical Code V model was created of a simple line VISAR illumination and collection system with a midrange f number, representing typical VISAR systems with which we have worked. Past systems include the Orvis system at the Z-machine at SNL, the Atlas line VISAR at NTS, and the NIF VISAR system. The NIF VISAR is the fastest at F/3; the others have larger f numbers. The model used a laser source exiting a 1-mm-diameter core illumination fiber at NA 0.2 (F/2.5). Simple lenses collimated the light and focused it at 2X, giving F/5 illumination onto a 2-mm-wide target. The light reflected off the target was collected and split off from the illumination beam, after which it was imaged at a camera with a magnification from the target of 3X. The result of this magnification was a 6-mm-wide image at F/15 at the camera (Figure 2).

Discussion

The initial plan was to expand Malone's preliminary study (2003) to analyze the light collection in Code V using vignetting factors. But these factors only worked until target movement, curvature, or tilt caused the vignetting to become as large as the chief ray; then ray trace errors occurred. That meant that light collection could only be calculated down to 50% transmission. To remedy that, chief ray aiming was used to steer the chief ray through the system.

As various chief ray aiming points were used, it was discovered that the illumination results would vary. By examining Code V footprint plots of the vignetting, it was discovered that the x-direction

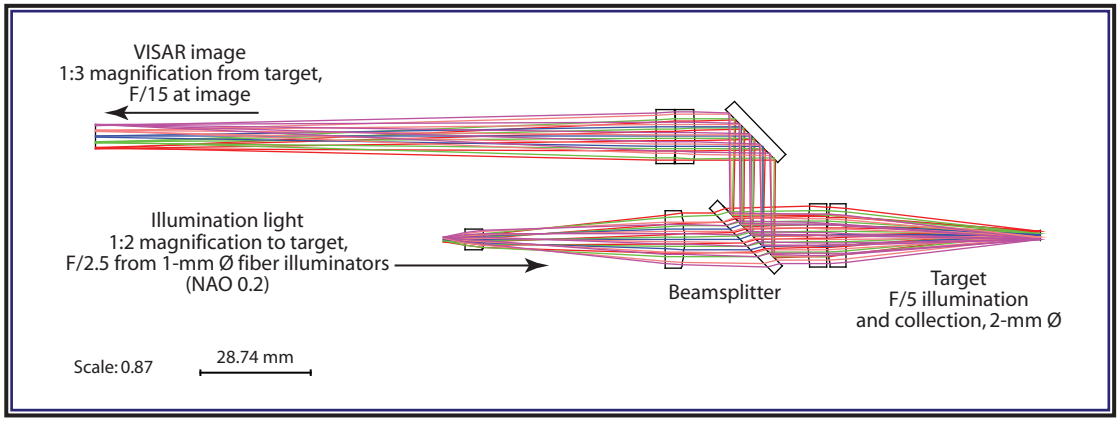

Figure 2. Code V line VISAR model ray trace

vignetting factors were not giving the complete story of light through the lenses. The shapes of the footprint plots were not simple ellipses centered on the chief ray. Therefore, a more accurate way to compute the illumination through the system was to use the footprint data listing of throughput area for each field point at the pupil or an appropriate surface.

Analysis

The footprint area at the first lens surface for light coming from the target was used to compute throughput. The data for each case was normalized using the data for that field point with a flat specular target at the nominal target position, normal to the axis of the optical system.

Cases were produced for intensity versus target position, intensity versus target curvature, and intensity versus target tilt. These cases were also run on a model with the first collection lens aperture stopped down so that light from the surface was collected at F/7. Movement of the target was tracked as follows: toward the lenses was negative, away from the lenses was positive. For target radius of curvature, negative numbers refer to when the center of curvature was toward the lenses, and positive numbers refer to when the center of curvature is away from the lenses.

Figure 3 shows the results of target position models. In this case, apertures in the optics begin to vignette the light at the edges of the target for both positions closer to and farther from the lens. As the target is moved further from zero, light is also reduced at the center.

Figure 4 shows intensity versus target curvature. Again, we see vignetting starting at the edges of the target as the curvature increases. Intensity remains at 100% at the center for every curvature as a "glint" off a specular surface. Negative numbers refer to a concave target; positive numbers refer to a convex target.

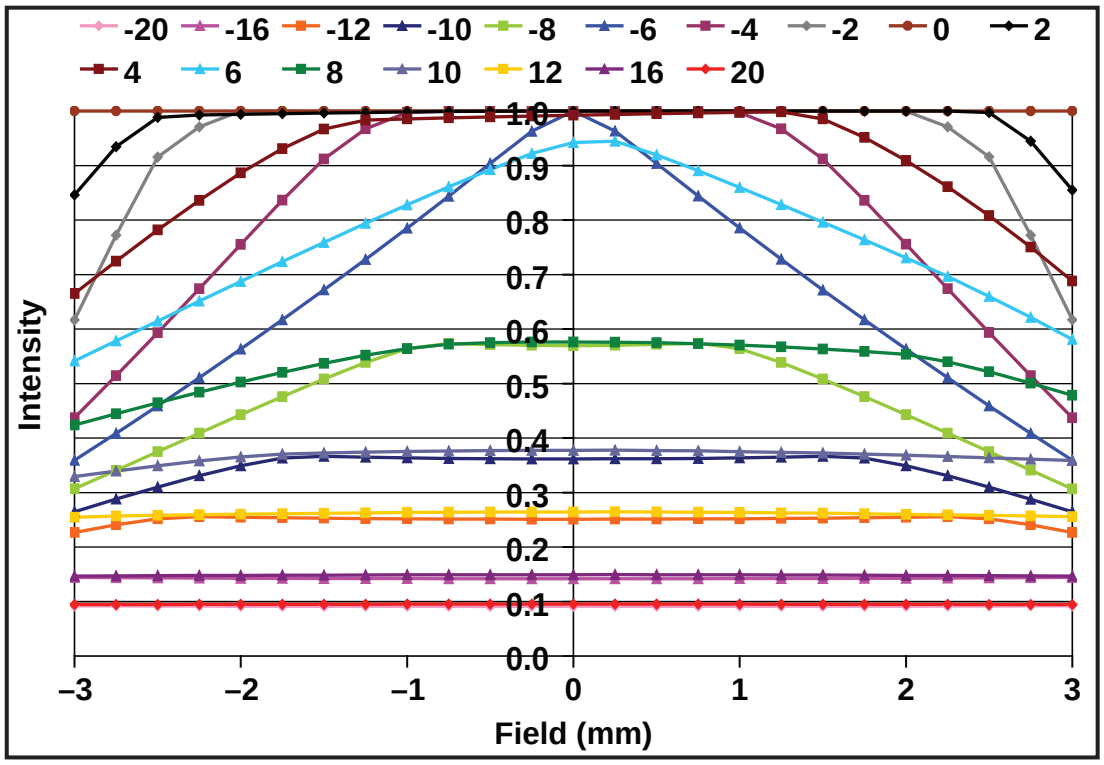

Figure 3. Signal intensity vs. target position (target movement away from the lens is represented by positive numbers; movement toward the lens is denoted by negative numbers)

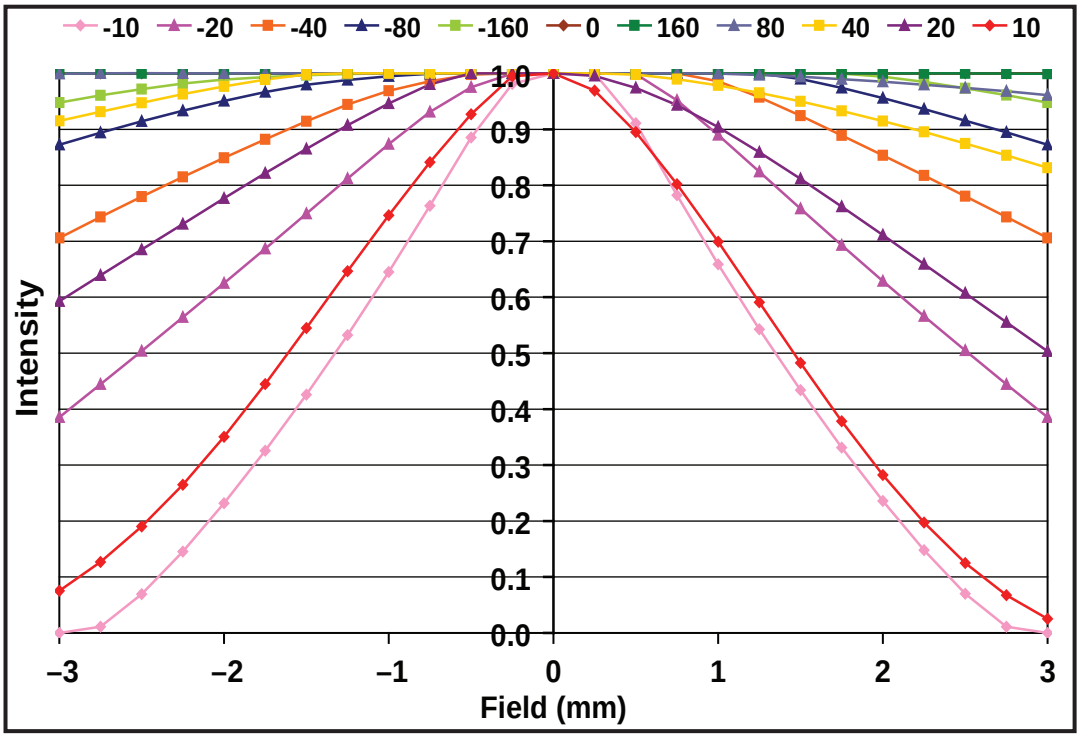

Figure 4. Signal intensity vs. target curvature (spherical curvature: convex targets are represented by positive numbers and concave targets by negative numbers)

We also modeled target tilt. The intensity versus target tilt data were plotted (not shown) as straight lines with the light reducing increasingly across the field depending on the direction and amount of tilt.

The model used in this study was nearly telecentric at the target. Since most of the systems we have used for experiments have been nearly telecentric, changing to telecentric systems when modeling curved surfaces would not significantly change the illumination. Therefore, we evaluated the effects of stopping down the system.

Figure 5 shows a ray trace of the stopped-down F/7 model. The limiting aperture was placed on the lens surface closest to the target with other apertures left at original sizes.

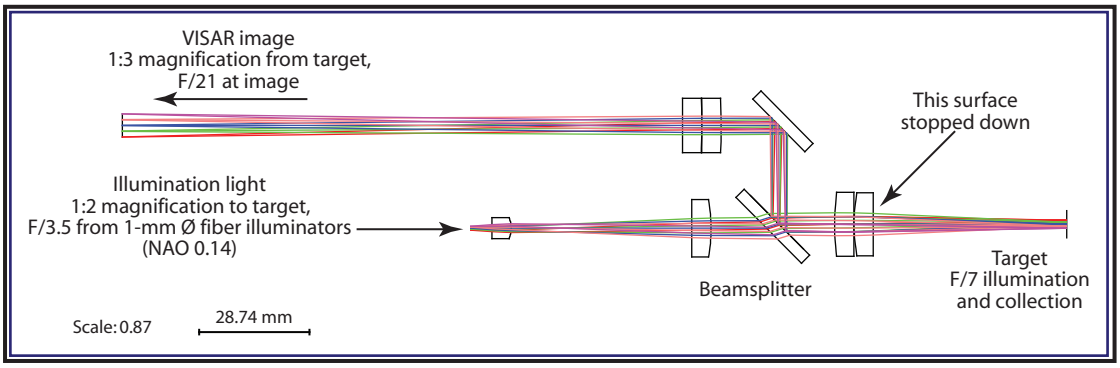

Figure 5. Ray trace of stopped-down F/7 model

Figure 6 shows the results of target position for the stopped-down F/7 model. In this case, the intensity at small distances closer than best focus is greater than 100% for off-axis field points because more light gets past the first aperture (the one that is stopped down) and enters the optical system without getting reduced by subsequent apertures at their original size. At greater distances, intensity is lost, but it falls off more slowly than with the wide-open aperture (F/5).

Figure 7 shows the results of target curvature for the stopped-down F/7 model. For small concave curvatures, the target acts as a field lens, increasing the light collection at the edges of the field. This did not show up with the F/5 system because other apertures in the system vignetted additional light. As curvature increases, light intensity is lost. Light intensity is also lost for convex curvatures. Intensity remains at 100% at the center of the field for every curvature as a "glint" off a specular surface.

The intensity-versus-target tilt plot for the stopped-down F/7 model (not shown) is similar to that of the wide-open model. Each tilt curve was composed of nearly straight lines. However, tilts of a couple degrees or less increased the light transmitted through the system on one side of the field, while the signal decreased in the center and on the other side of the field.

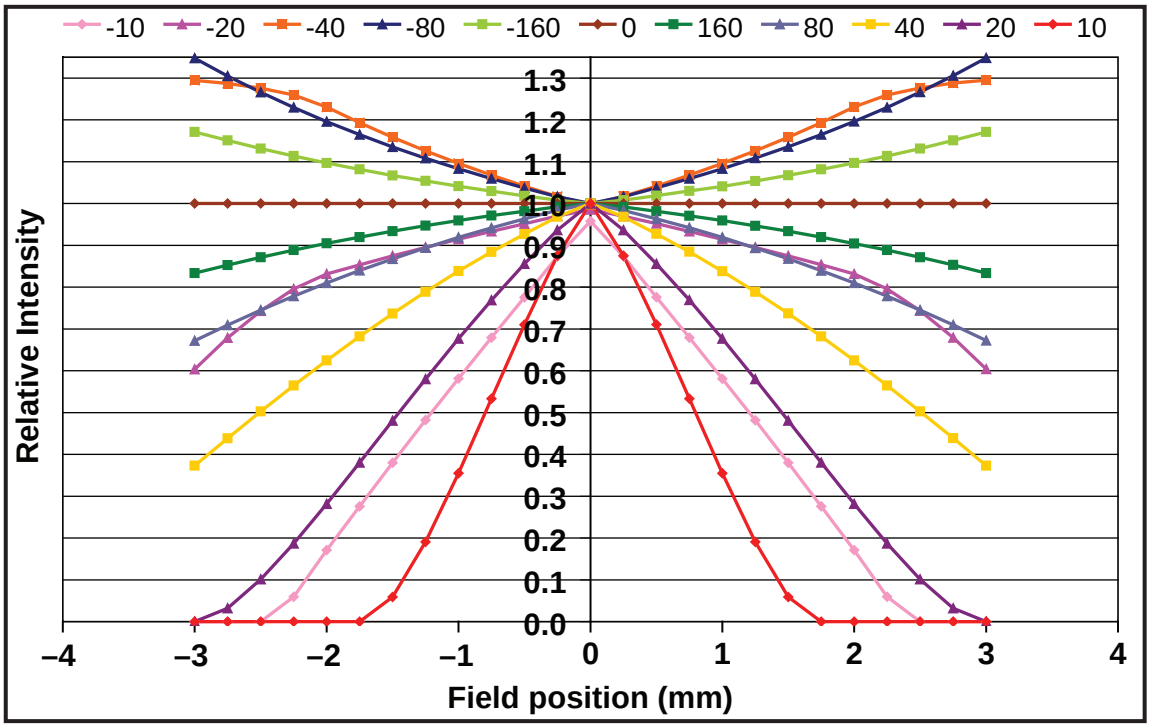

Figure 6. Signal intensity vs. target position of stopped-down F/7 model (target movement away from the lens is represented by positive numbers; movement toward the lens is represented by negative numbers)

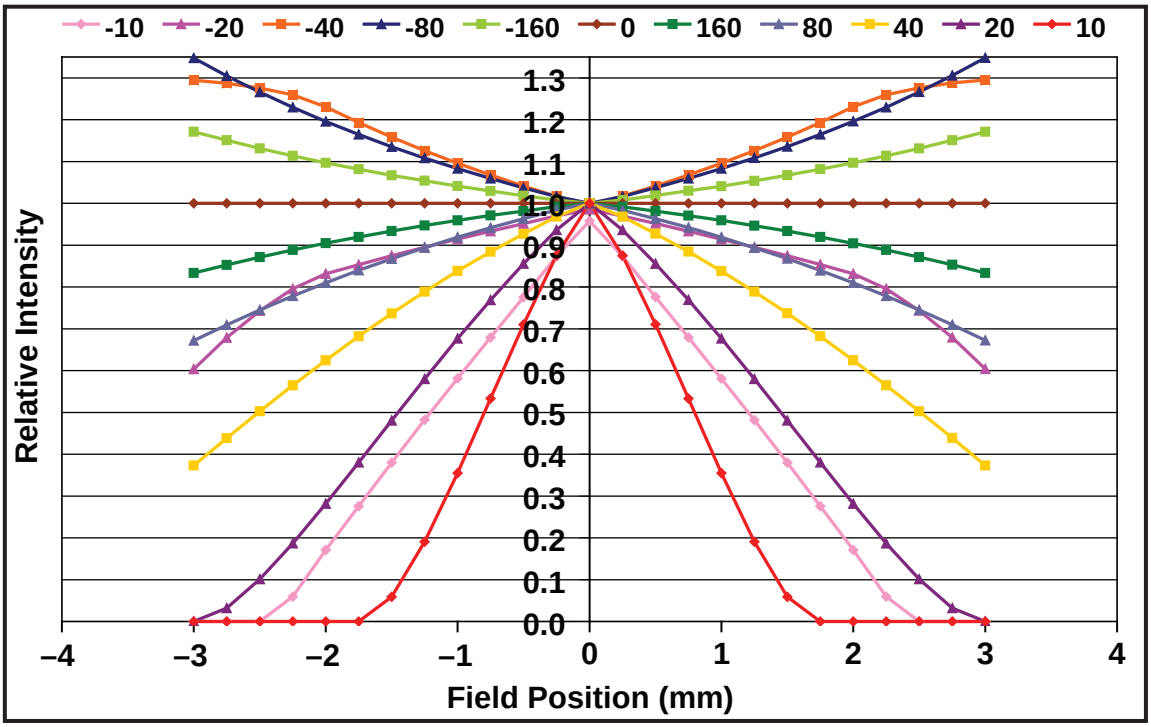

Figure 7. Signal intensity vs. target curvature of stopped-down F/7 model (spherical curvature: convex targets are represented by positive numbers and concave targets by negative numbers)

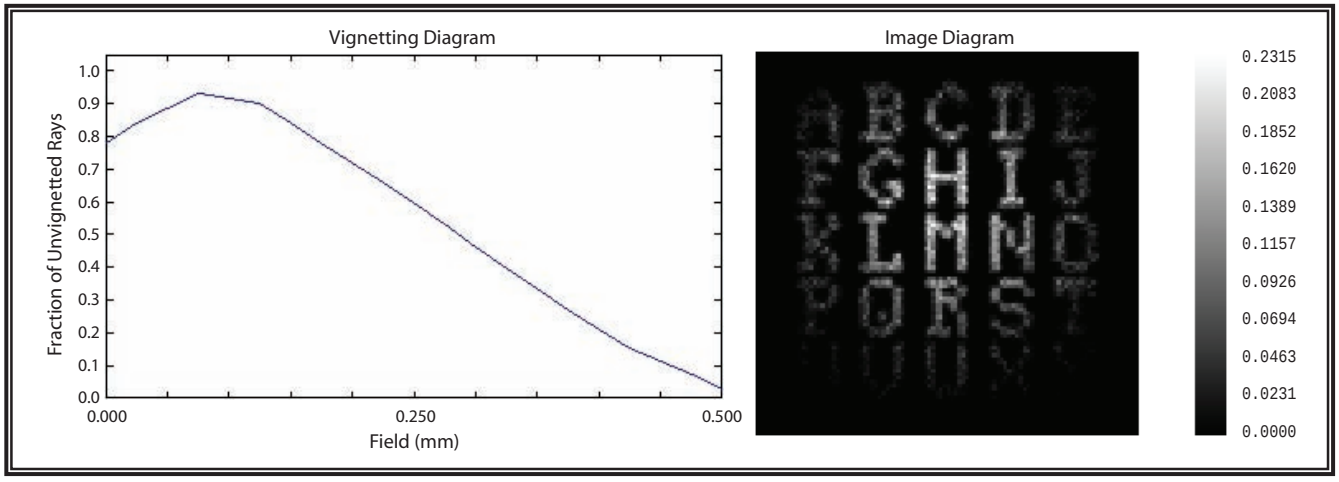

Figure 8. Signal intensity vs. target field position vignette plot and image diagram without field lens

Cylindrical surfaces were also checked with the "line" of the line VISAR along the axis of the cylinder, but these did not give different results than a flat surface.

As a means to correct light reduction over the field from a curved surface, field lenses were modeled. Figure 8 shows the light versus field position without a field lens. The light intensity dropped off toward the edges of the field. Figure 9 shows light versus field position with a field lens. These figures show an improvement in illumination flatness using a field lens for a curved surface static case. If the target starts out flat and a field lens is added to the system, performance of the system at the edges of the field degrades. As the target curved dynamically, performance would improve until the curvature became too great to allow for field lens correction. Therefore, adding a field lens to a line VISAR optical relay would be useful if dynamic target shape could be predicted. If the dynamic target shape could not be predicted, adding a field lens to a line VISAR may degrade the overall signal intensity.

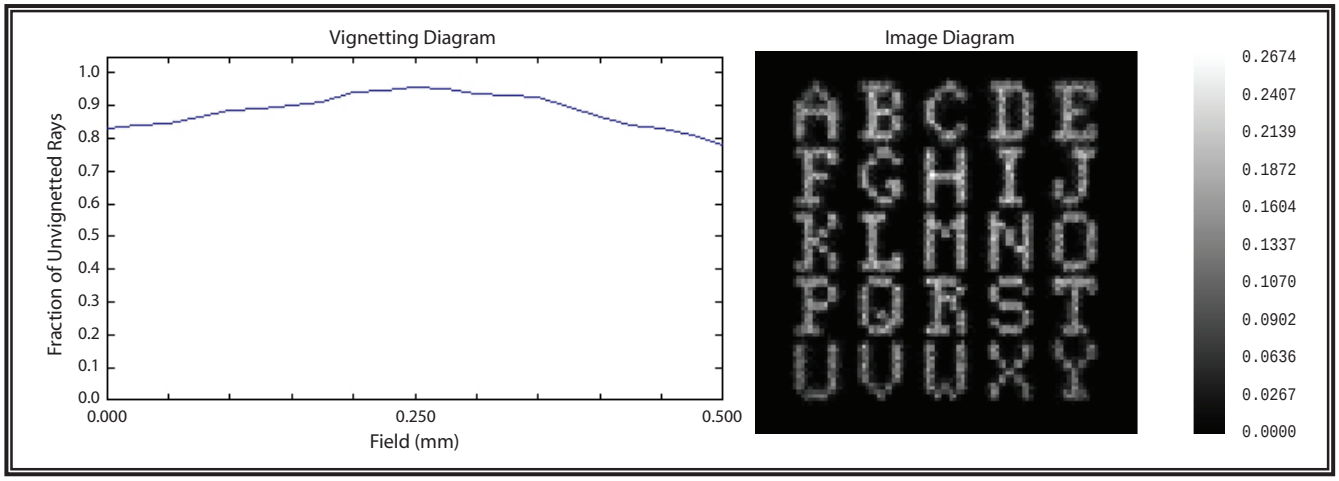

Figure 9. Signal intensity vs. target field position vignette plot and image diagram with field lens

Conclusion

The project improved understanding of line VISAR signal performance across a target. The collection angle and relay apertures do affect signal collection uniformity as a target moves, curves, or tilts. In general, the use of telecentric optics would not improve our line VISAR systems. Specific line VISAR configurations with predicted dynamic target shapes can use field lens techniques to improve signal intensity across the field if an element may be placed near the target.

References

Barker, L. M., R. E. Hollenbach, "Laser interferometer for measuring high velocities of any reflecting surface," *J. Appl. Phys.* **43** (1972) 4669.

Celliers, P. M., G. W. Collins, L. B. DaSilva, D. M. Gold, R. C. Cauble, R. J. Wallace, M. E. Foord, B. A. Hammel, "Shock-Induced Transformation of Liquid Deuterium into a Metallic Fluid," *Phys. Rev. Lett.* **84** (2000) 5564–5567.

Malone, R. M., B. C. Frogget, M. I. Kaufman, P. W. Watts, P. M. Bell, J. R. Celeste, T. L. Lee, "Design of an imaging VISAR diagnostic for the National Ignition Facility (NIF)," *Proceedings of the Society of Photo-Optical Instrumentation Engineers (SPIE)* **5173** (2003) 26–37.

Mach-Zehnder Velocimeter

Cenobio H. Gallegos[1]
Los Alamos Operations

Velocity interferometer system for any reflector (VISAR) velocimeters are large (ranging from a 4' × 8' table to an 8" × 12" case) Michelson interferometer optical systems that are expensive to assemble, difficult to align, and require a controlled environment to minimize expansion and contraction of the table and optical holders that destabilize the interferometer. This project applied a Mach-Zehnder (M-Z) interferometer (a commercially available, single-mode, fiber-based miniature interferometer that was hermetically sealed) to velocimetry. Initially, it enabled higher velocity recording capabilities when applied to a photon Doppler velocimeter (PDV). The second set of experiments utilized the M-Z interferometer characteristics to measure direct velocity. The use of M-Z as a velocimeter can essentially eliminate optical alignment and reduce fielding time from as much as three weeks and three people to a half-day and one person.

Background

The standard for pulsed velocity measurements is the VISAR, consisting of a Michelson interferometer that requires large optical breadboards and intensive effort to align, field, and maintain. A velocimeter that would demand virtually no optical alignment, fit into a cigarette pack–sized box, and be made of commercially available components would save thousands of man-hours and eliminate the cost of manufacturing custom interferometers. A commercially available modulator, also known as an M-Z interferometer, is housed in a small, hermetically sealed package (65 × 12 × 5 mm). It can be used strictly as an interferometer or RF–modulated.

This simple device might be employed in a PDV to optically down-convert the data to a harmonic frequency that can be recorded when the data is beyond the recording system's bandwidth. The optical down-conversion could also be used with a lower bandwidth recording system not requiring costly, cumbersome, high-bandwidth digitizers. In addition, the M-Z could be utilized as an interferometer measuring the phase change caused by the Doppler shift of the accelerated light.

Project

M-Z interferometers are single-mode channels laid out on a lithium-niobate substrate, with polarization maintaining single-mode fiber pigtails terminated with FC/APC connectors. The system operates with a 1550-nm infrared laser. An RF electrical signal is placed on the electrode, where

[1] gallegch@nv.doe.gov, 505-663-2056

a voltage change causes the refractive index of one leg of the M-Z to change, producing a changing interference pattern at the output. This change in refractive index is directly proportional to the electrical signal. The DC voltage can be used to tune the M-Z to the desired initial throughput. The Vπ (voltage required to induce π phase shift) of the RF port is ~2 V (Figure 1), and for the DC bias port, ~15 V.

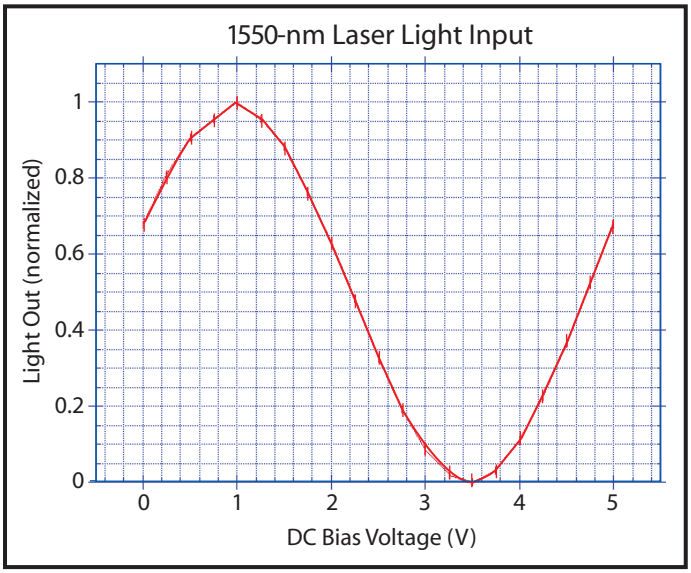

Figure 1. M-Z output vs. DC bias voltage at RF input port

Mach-Zehnder/PDV Test

The initial tests were performed using channel 1 of a four-channel PDV and an M-Z/PDV using the same probe. This setup was a two-PDV system, with the M-Z modulated with an RF signal of 2 GHz and applied to the external PDV as the unshifted light source (Figure 2).

The first target was a 5-μm copper foil accelerated by a 100-mJ, 140-ps laser at 532 nm (Meidinger, 2007). The target was placed ~1 cm in front of the focal point of the focusing lens. A microscope slide was inserted at an angle between the target and the probe, eliminating unwanted reflections and probe damage. This required the probe to be a few centimeters from the target. The M-Z was DC-biased to maximum throughput (~1 V).

At 200 m/s, the initial data was identical for the PDV and the M-Z/PDV. However, the signal contrast was not optimal, as insufficient unshifted light was present in the signal.

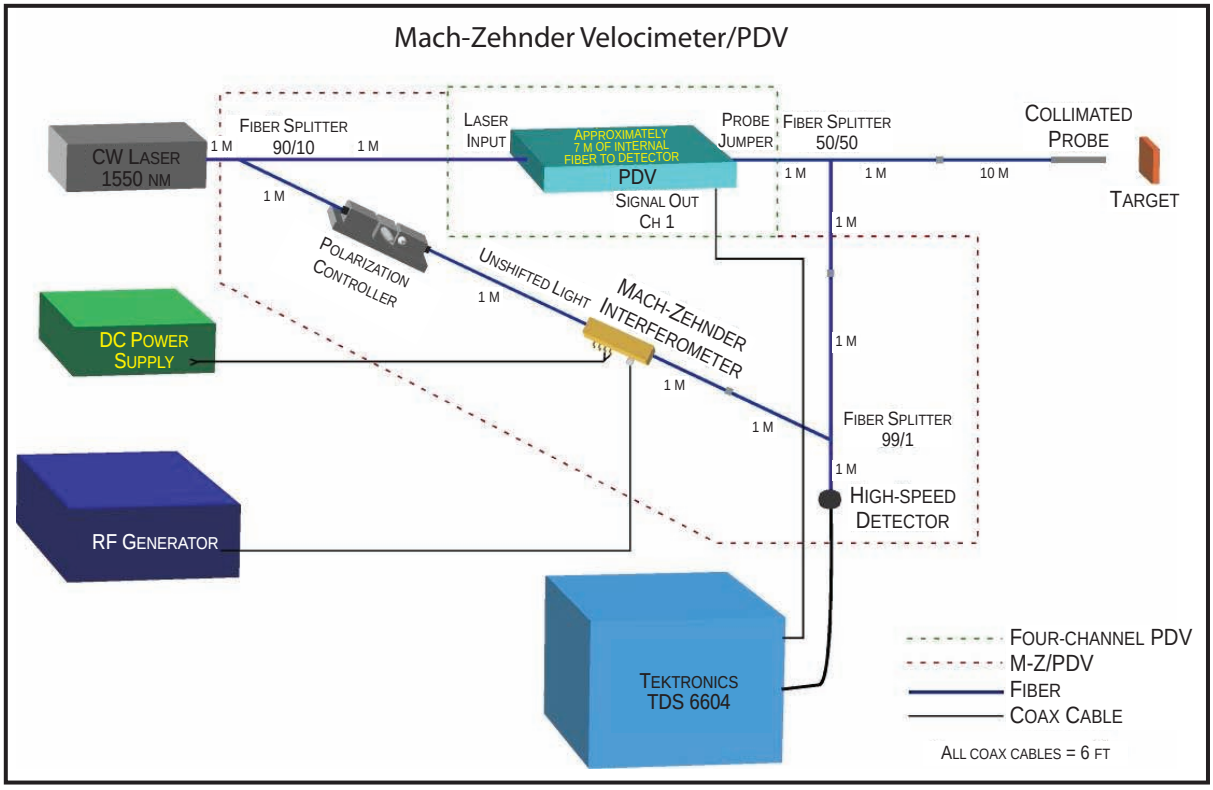

Figure 2. Test setup with M-Z modulated at 2 GHz and applied as unshifted light

In the second data set, the laser mirrors were modified such that the 532-nm light and the fundamental 1064-nm light were at the target. The target was changed to a 10-µm copper foil. The M-Z unshifted light was increased to improve data contrast (Figure 3). The shift from 1- to 2-GHz modulation did not affect the contrast.

Mach-Zehnder Interferometer Test

The second series of experiments tested the M-Z and the PDV (Figure 4) operated as separate velocimeters and compared their performance. The M-Z is DC-biased to 45° (~0.5 V). The first run was with the collimated probe and all the laser power of both wavelengths (532 and 1064 nm). The probe was damaged after the first shot and replaced with a bare fiber probe. The numerical aperture required the probe to be about 1 mm from the target surface. The data comparison of the PDV and M-Z is quite interesting (Figure 5).

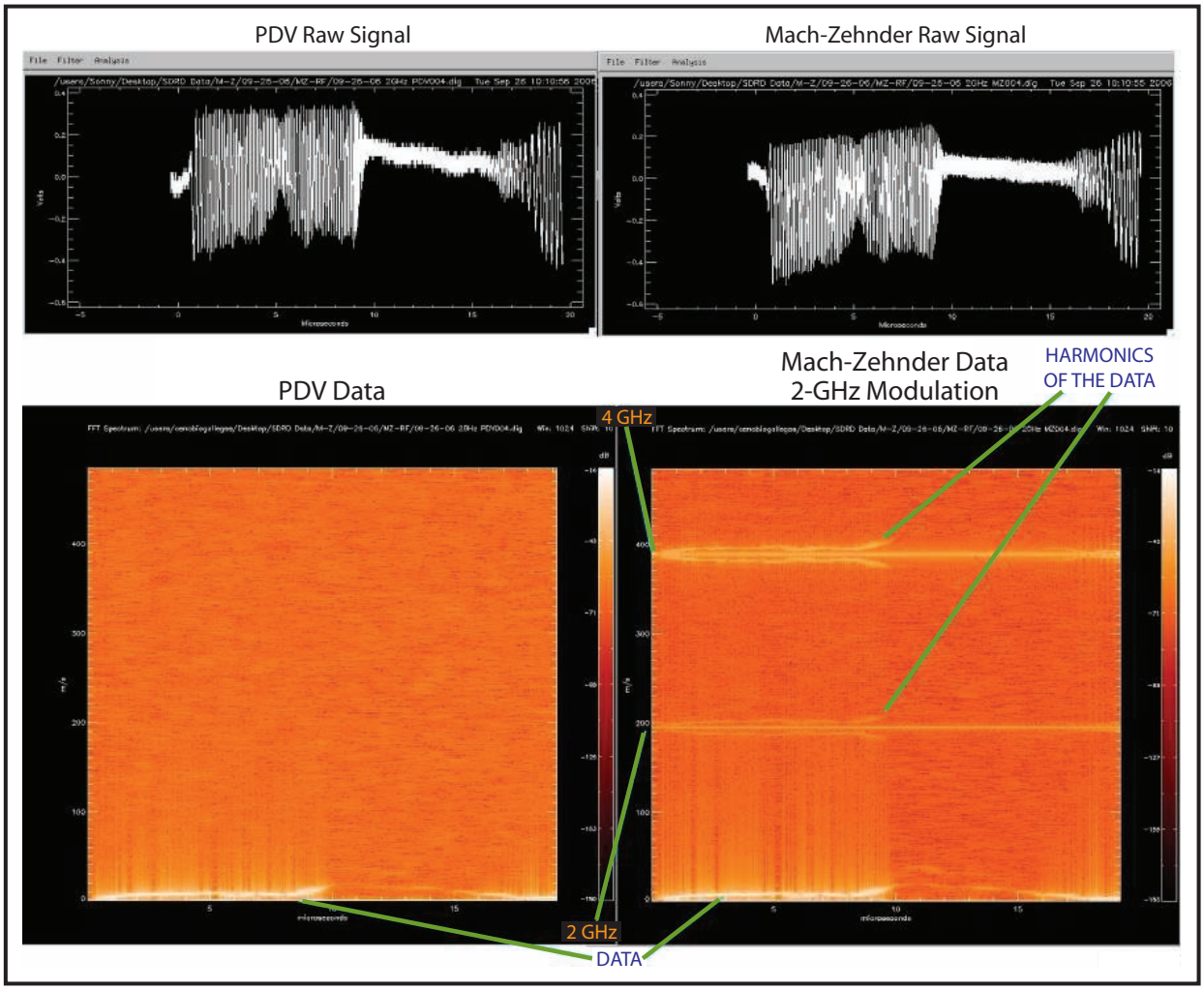

Figure 3. PDV and M-Z improved contrast of data and harmonics

Initial breakout velocities were relatively low (20–300 m/s). A new target of 10-μm copper foil layered on a 1-mm glass plate was placed at the laser's focal point. The fundamental 1064-nm light was diverted so that only the 532-nm light hit the target. Both velocimeters produced identical analyzed data depicting velocities of about 0.85 km/s (Figure 5). Figure 6 shows expanded views of the raw and analyzed data for both velocimeters. Velocities of up to 1.5 km/s were recorded with this setup. The M-Z proved less sensitive than the PDV, especially at lower velocities.

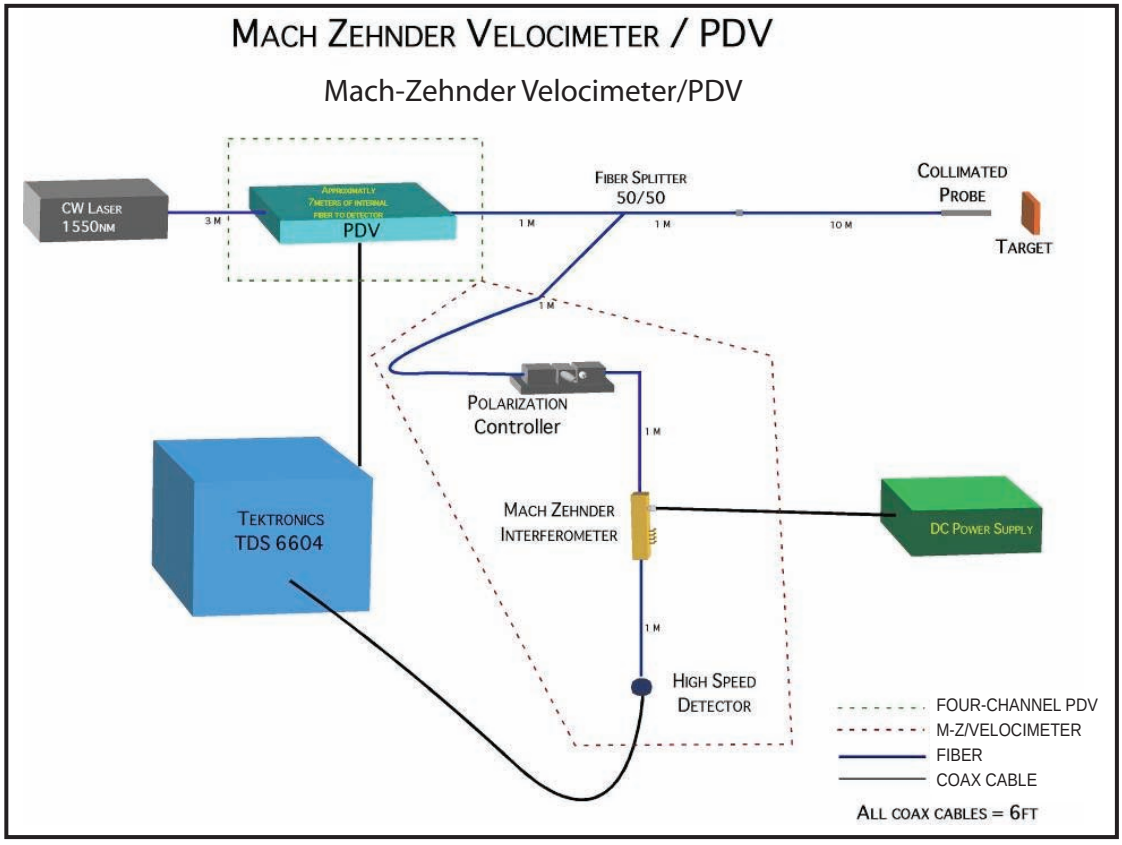

Figure 4. Test setup of the PDV and the M-Z as a separate interferometer

Conclusion

The use of a modulated (1- or 2-GHz) M-Z in the PDV unshifted light leg produced well-defined harmonics of the actual data. The ability to optically down-convert the frequency can potentially 1) record data beyond the capabilities of the best available recording systems, and 2) use lower bandwidth recording systems (reducing bandwidth lowers recording costs).

The M-Z interferometer produced data beyond any expectations. The differences in the data are interesting, yet enough similarity exists to believe what we see is real. However, does one system record phenomenon that the other velocimeter cannot? Is some undesired unshifted light inadvertently injected into the M-Z system, producing the similarities in the data? More comprehensive tests must be conducted in order to answer these and other questions, and also to determine M-Z data accuracy.

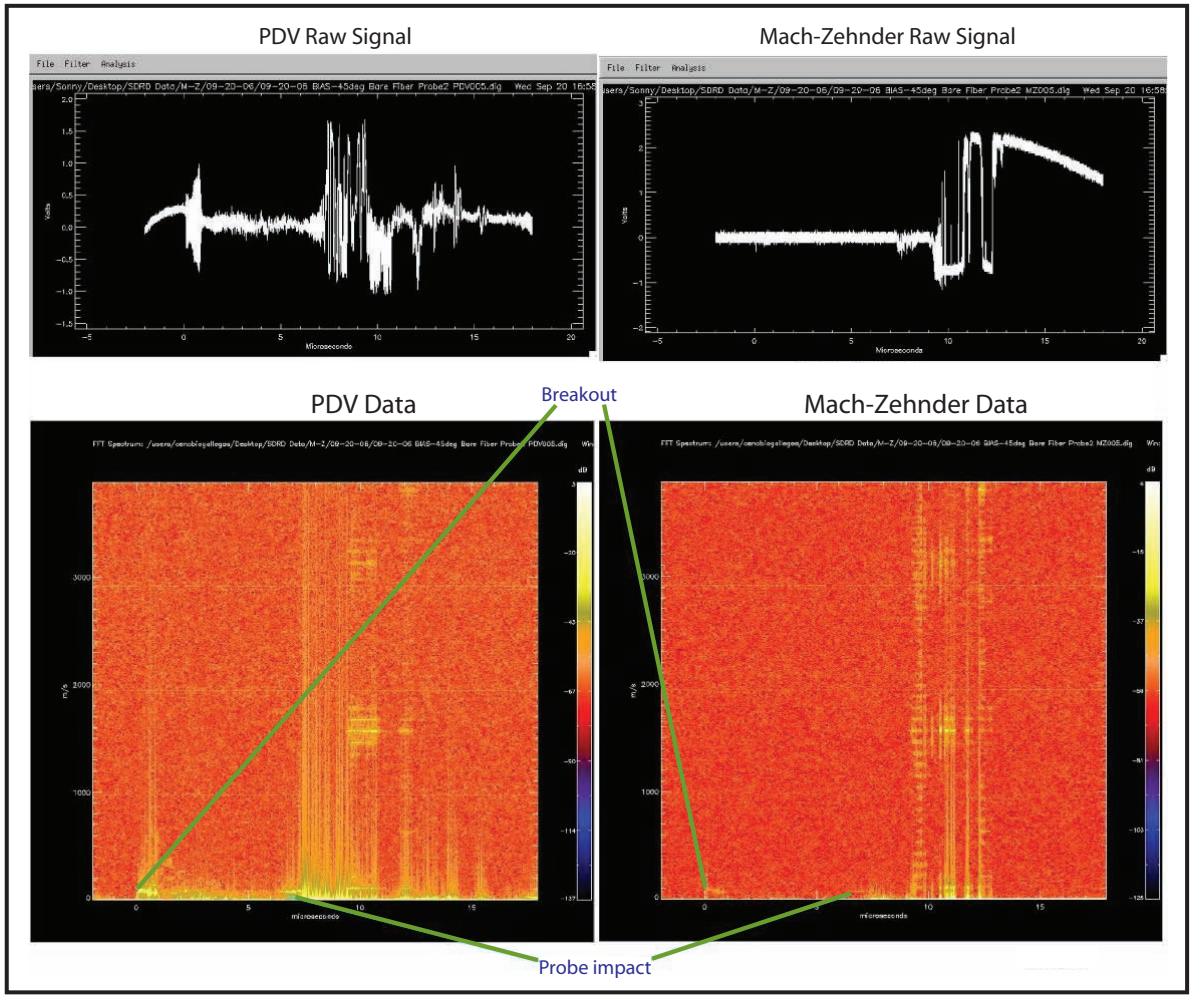

Figure 5. Data comparison, PDV and M-Z

Acknowledgments

The author wishes to thank Bruce Marshall (STL), for his encouragement and expert advice; Al Meidinger (LAO), for use of the diagnostic shock source that enabled the data collection; Adam Iverson (LAO), for his help and expertise in the PDV and equipment use; the late Mike Rutkowski (LAO), for use of his invaluable tunable laser; Dave Holtkamp (LANL), for use of his high-bandwidth digitizer; and lead technician Matthew Teel (LAO), whose work was critical to this project.

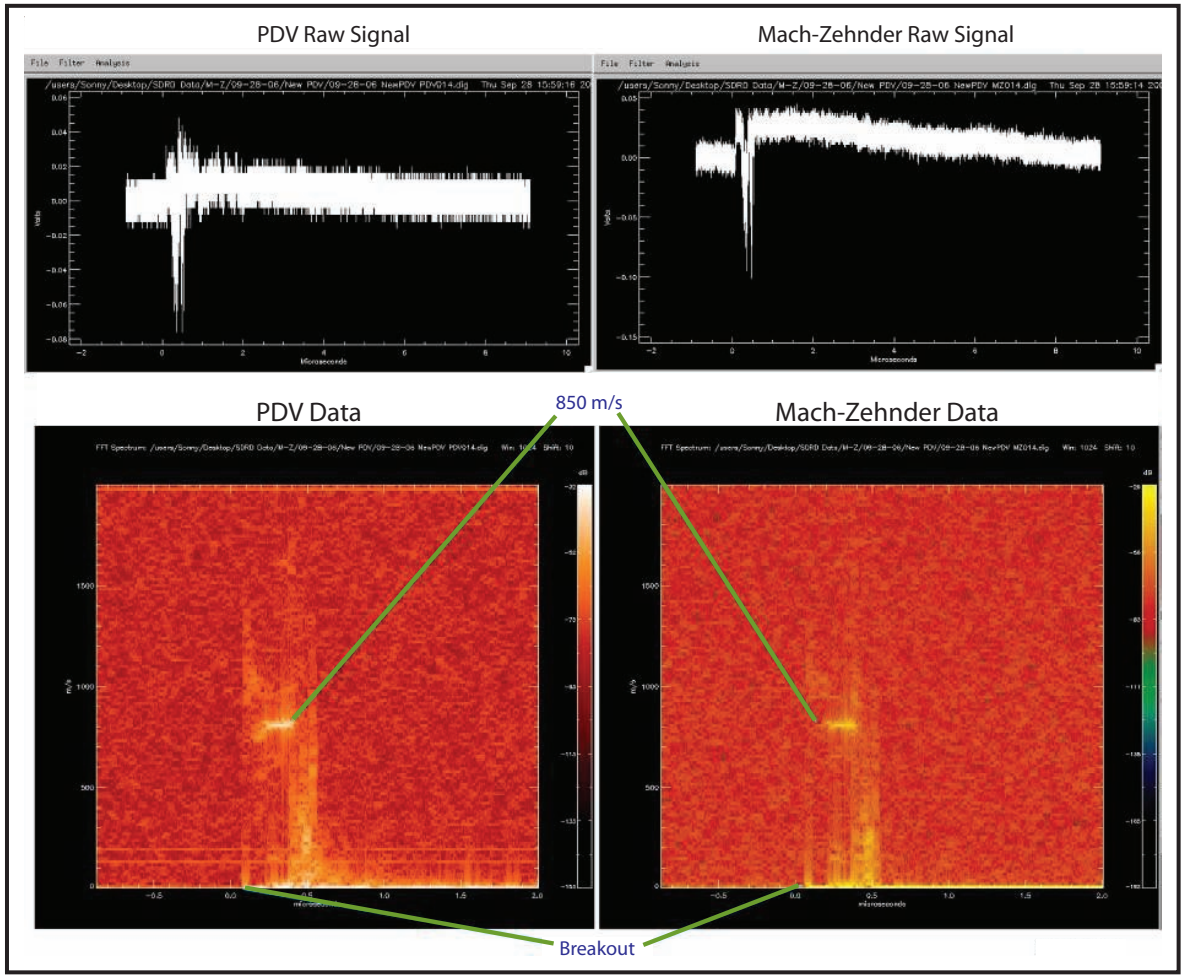

Figure 6. PDV and M-Z analyzed data

Reference

Meidinger, A., "Diagnostic Shock Source," *Nevada Test Site–Directed Research and Development,* FY 2006, National Security Technologies, LLC, Las Vegas, Nevada, 2007, 355–361.

this page intentionally left blank

Slapper Simulator

Cenobio H. Gallegos[1]
Los Alamos Operations

Velocity interferometer systems for any reflector (VISARs) are calibrated with slapper units that operate under high voltages and large electrical currents, producing a Doppler shift of incident laser light. This experiment simulated a Doppler shift of a VISAR from a slapper by using the different frequencies of two lasers at low power (5 mW or less).

Background

Many velocity measurement systems (VISAR, Fabry-Perot, photonic Doppler velocimeter) use controlled, high-voltage velocity inducers, or "slappers," to calibrate a system. These slappers produce relatively consistent velocities; however, they are cumbersome, require special equipment, and pose safety hazards of high voltage with large capacitance capable of high currents, in addition to the hazards associated with high-power lasers.

In this experiment, a system would insert a low-power (5-mW or less), single-frequency laser into the velocimeter receive fiber and then switch in a second low-power laser that would be a few megahertz to several gigahertz away from the frequency of the first laser. This fast change, which would appear to be the Doppler-shifted light of a slapper, could be accomplished with a Pockels cell or acoustooptic modulator.

For proof of principle, we used two Continuum Verdi lasers. The amount of power needed varied from 10 μW to 1 mW, depending on the velocimeter under test.

Project

The experiment was conducted with 5-W and 6-W Verdi lasers. An acoustooptical modulator operating at 250 MHz was placed in front of the 5-W laser. The second acoustooptical modulator, operating at 440 MHz, was positioned in front of the 6-W laser. For stability, each laser's output power was set to 500 mW (the lasers will not lock in at lower power levels). Neutral-density filters were placed in front of each laser. Power output was 1.1 mW for the 5-W laser and 1.2 mW for the 6-W laser. One output of the 50/50 splitter is connected to a photomultiplier tube (PMT) for dynamic alignment, timing check, and troubleshooting. The second output of the 50/50 splitter is

[1] gallegch@nv.doe.gov, 505-663-2056

connected to the VISAR; the power was 20.8 μW for the 5-W laser and 20.5 μW for the 6-W laser, with measurements performed in continuous wave mode. Figure 1 shows the initial setup diagram (the blue area was inserted to conduct tests with an unstable laser).

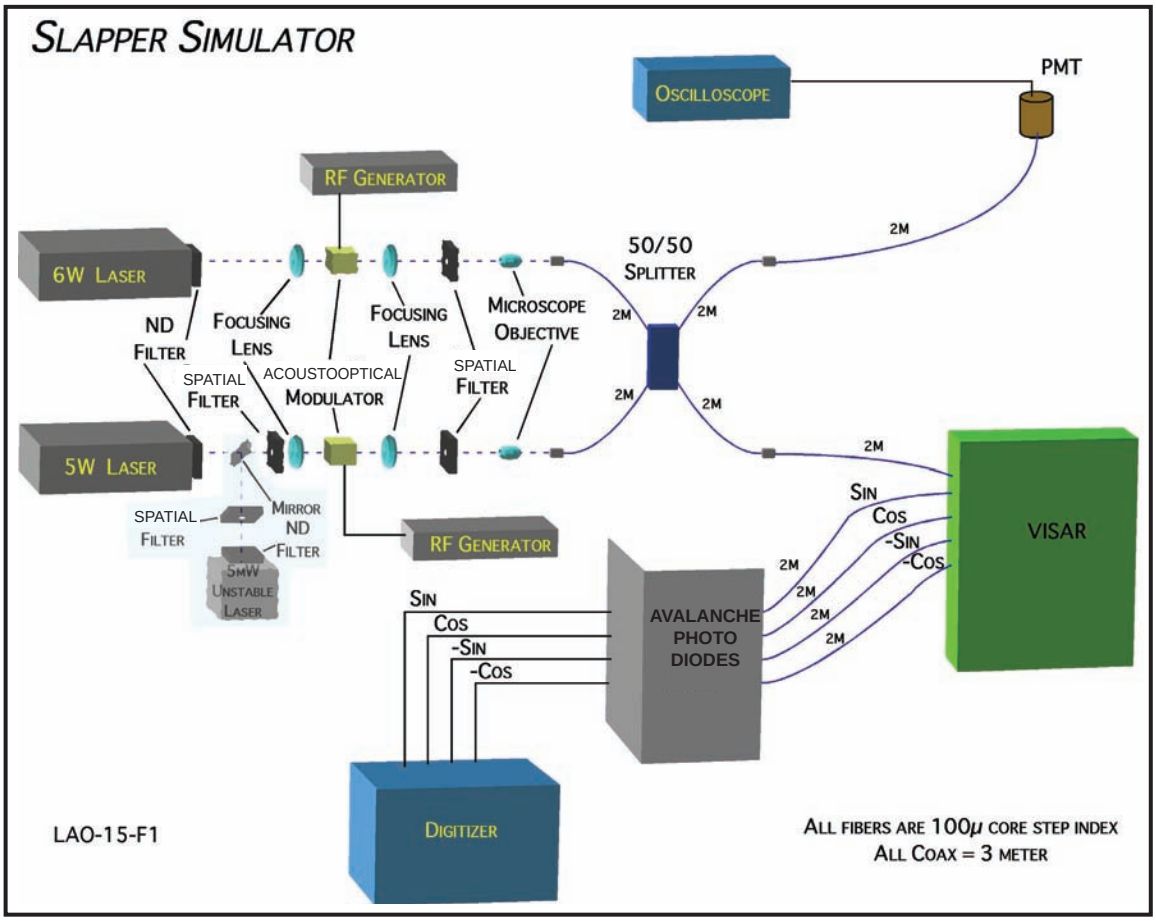

Figure 1. Initial setup of slapper simulator

Applying the acoustooptical modulator drivers with a 100-μs pulse, the rise time of the 440-MHz system is 16 ns, and the fall time is 16 ns. For the 250-MHz system, the rise time is 162 ns, and the fall time is 68 ns. The 440-MHz system was used for the baseline or reference and calibration (mirror and etalon data records) of the VISAR. The 250-MHz system was used to simulate the Doppler shift of a dynamic target by timing the turn-on to ~80 μs after the reference laser was initialized. Figure 2 data show a velocity of ~21 m/s, a frequency difference of ~79 MHz

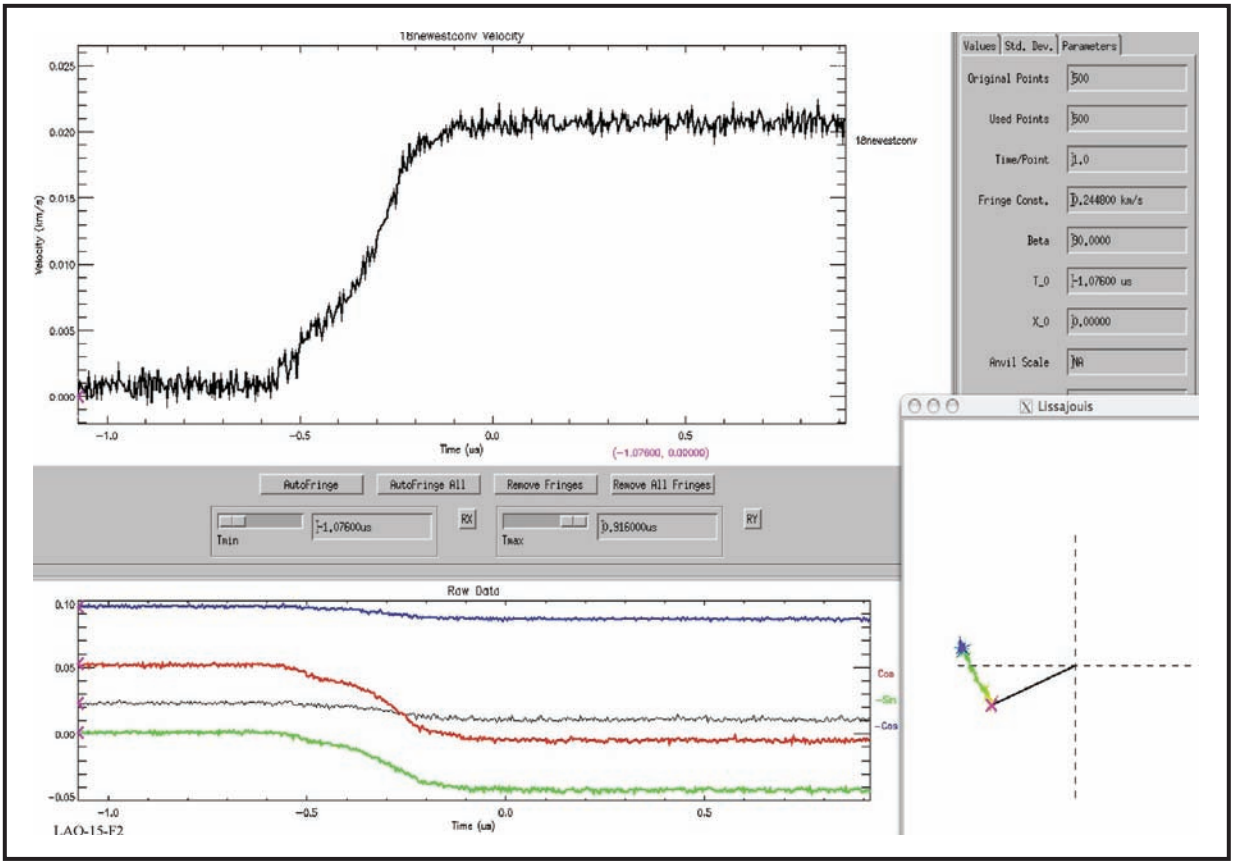

Figure 2. Simulated velocity measurement of ~21 m/s

(532 nm = 563519.661 GHz). The Lissajous depicts a phase shift. Figure 3 shows a velocity measurement of about 20 m/s or a frequency difference of 75.187 MHz. In Figure 4 are data with the 5-W laser not locked in (unstable mode), recording a simulated velocity of ~51 m/s, or a frequency difference of 191.73 GHz.

The first special filter used on the 5-W laser was moved in front of an Intel 5-mW unstable laser, as shown in the light blue area of Figure 1. Figure 5 depicts the analyzed data recorded on most of the shots taken. However, one event recorded an interesting phenomenon (Figure 6), which was not repeated.

The unstable lasers' instabilities are in the amplitude and frequency domains, and are not useful as a source for normal operation of a VISAR. However, if the instabilities are in a consistent pattern, they produce what may be an ideal source for the simulation of a dynamic velocity change, as indicated in Figures 5 and 6.

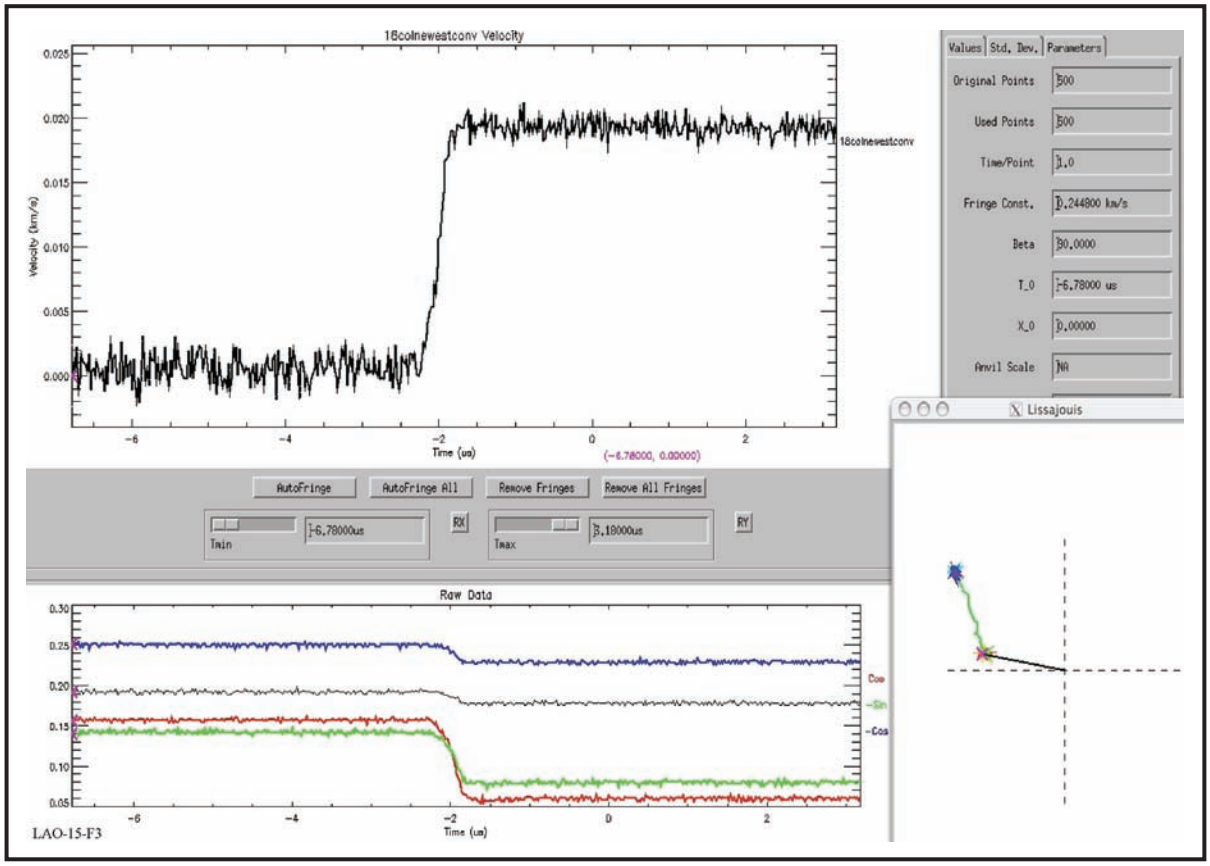

Figure 3. Simulated velocity measurement of ~20 m/s

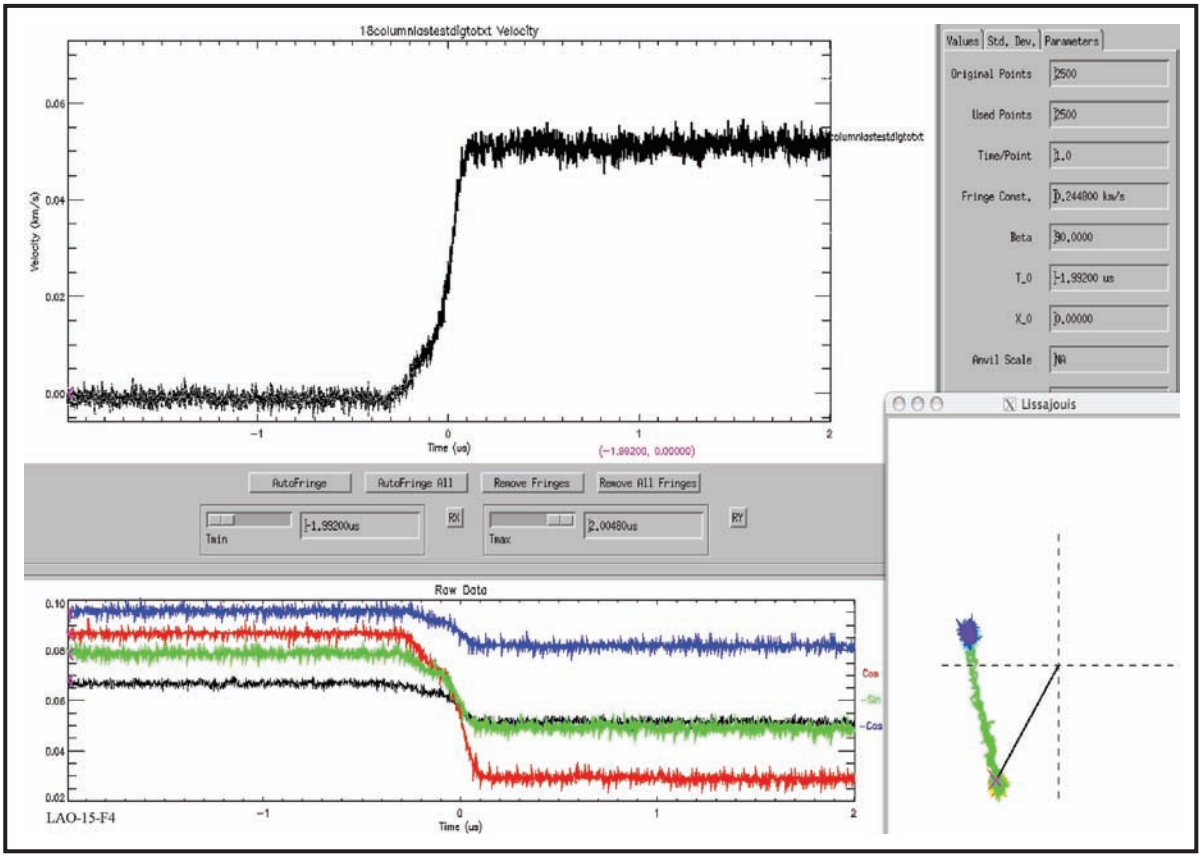

Figure 4. Simulated velocity measurement of ~51 m/s with the 5-W laser in the unstable mode

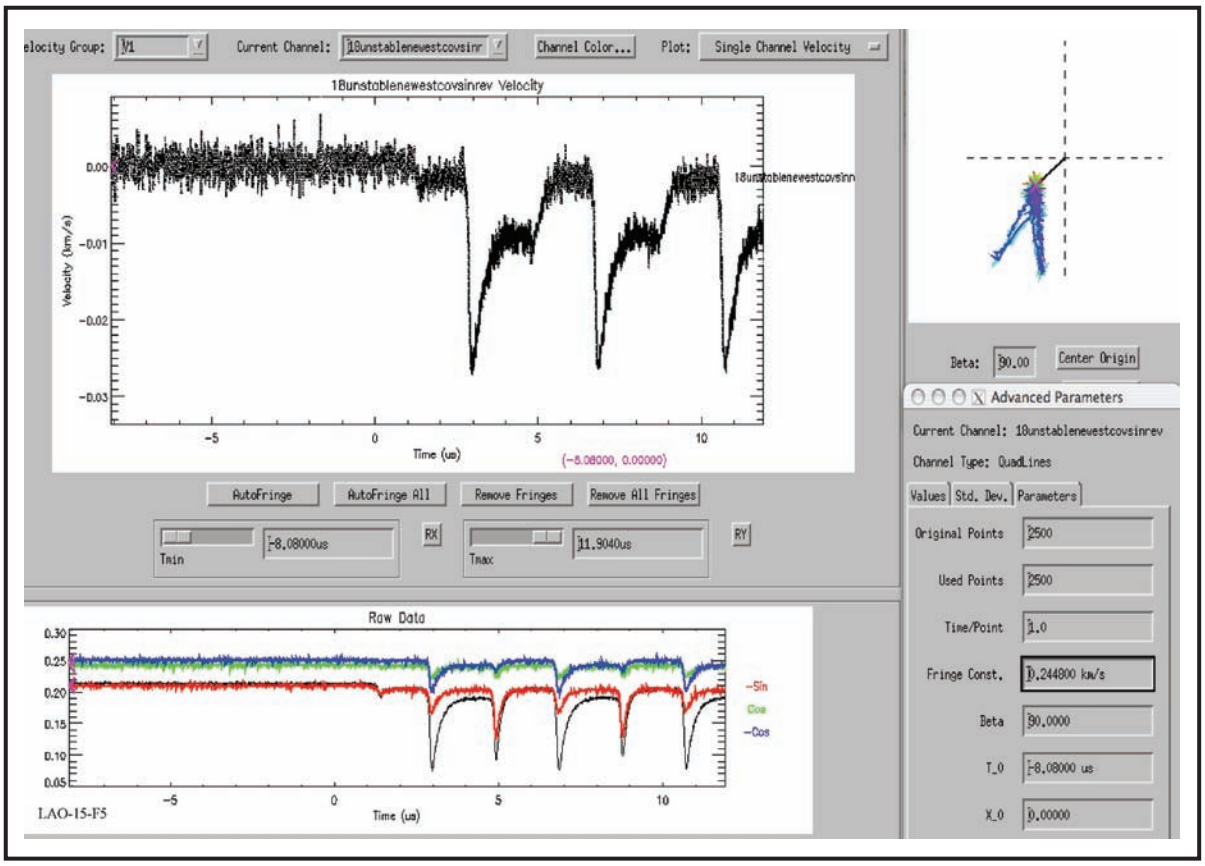

Figure 5. Data with 6-W Verdi as reference and a 5-mW Intellite unstable laser

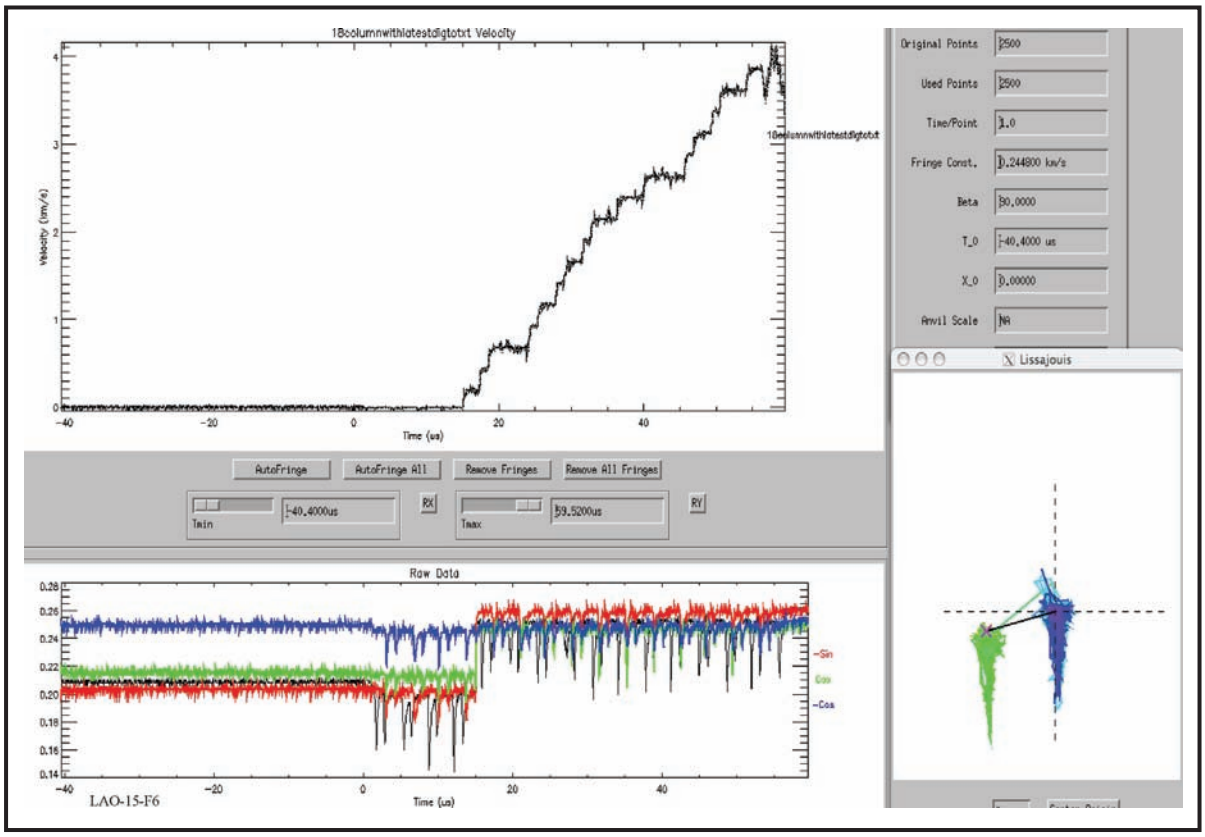

Figure 6. Data from the 6-W Verdi as reference and a 5-mW Intellite unstable laser

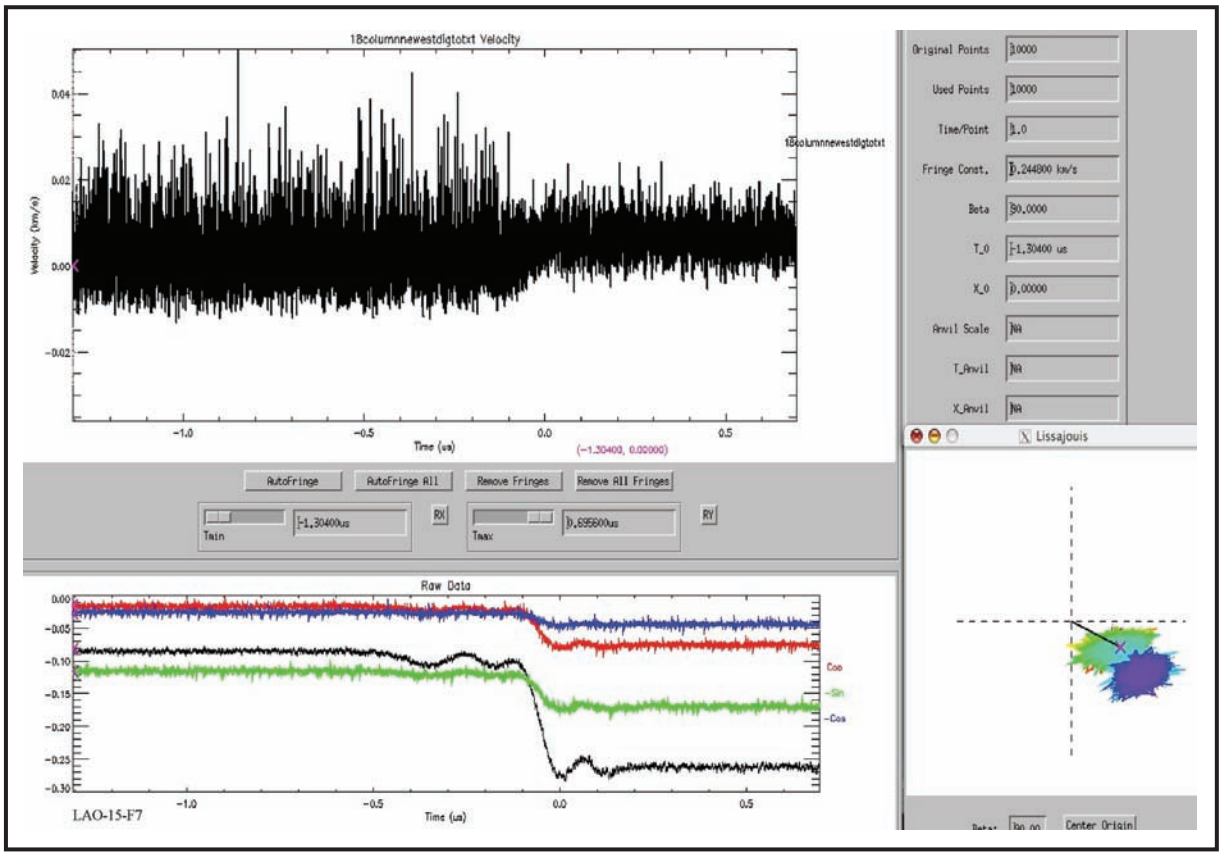

Figure 7. Data from the two new 5-mW Intellite lasers

Conclusion

With the Verdi lasers warmed up and locked in, the data appear to be relatively consistent (Figures 2 and 3). The Lissajous also show a repeatable phase shift. The frequency difference between the Verdi lasers was enough that special techniques are not needed to enhance the difference to record usable data. The concept appears to work well. Comparisons with a slapper and this setup must be made to verify that a true phase shift has occurred, and if so, that it is enough of a phase shift for an accurate calibration.

The insertion of an unstable laser showed some interesting phenomena (Figure 5) and one set of intriguing data (Figure 6). It is not certain that a phase shift was observed in the VISAR or if what was observed was only an amplitude change. More tests need to be conducted with this setup.

Replacing the Class IV Verdi lasers with low-power Class IIIa Intellite lasers does work; however, the light frequencies are so close that data contrast is poor (Figure 7), and the simulated Doppler shift is low. We must test new techniques that will change and stabilize the center frequency of one laser to a desired frequency difference. This will enable a simulation of different velocities for the various VISAR fringe constants.

Acknowledgments

The author wishes to thank Vincent Romero, for the use of his acoustooptical modulators and his useful suggestions during setup; Adam Iverson, for his help with the Bruce Marshall miniature VISAR; Greg Lare, for his help with the Verdi lasers; and lead technician Sheri Dance, whose work and dedication made this project possible.

this page intentionally left blank

Displacement Interferometry

Bruce Marshall[1]
Special Technologies Laboratory

This project explored technologies for enhancing the performance of displacement interferometry, also known as photonic Doppler velocimetry (PDV) measurements. The areas of interest included quadrature systems, optical heterodyne or downconversion techniques, signal improvement and noise reduction, probe design, optical sources, and integration with velocity interferometer system for any reflector (VISAR). A number of the ideas proved successful, some functioned adequately but were not useful enough to implement, and a few simply failed.

A total of six invention disclosures resulted, including novel designs for a coherent single-mode velocimeter, a coherent ellipsometer, and a polarization controller.

Background

Over the last few years, PDV has been recognized as a valuable tool for shock measurements, primarily due to the efforts of Ted Strand, LLNL (2006). A basic PDV system is shown in Figure 1. The critical technical basis of PDV lies in the heterodyne gain obtained when the shifted light is mixed with the higher powered local oscillator, and in the use of frequency domain analysis to pull data out of noise. The technique has become feasible due to both the availability of equipment developed for telecommunications applications, and to deep-memory, high-speed digitizers that can record the high fringe rates and long record lengths produced.

The main advantages of PDV are its robustness and its ability to measure rough or free surfaces on which probe efficiency is low and multiple velocities would destroy the fringe contrast in a VISAR signal. Its low cost and equipment size are also significant factors.

PDV still faces some challenges: improving time resolution, overcoming the Brillouin scattering power limit in long fibers, and reducing signal dropouts due to speckle. This project investigated several ideas to improve PDV performance.

[1] marshabr@nv.doe.gov, 805-681-2266

Project

PDV Configurations

PDV configurations can be grouped according to the local oscillator source. In the simplest type (Figure 1), the reference beam is generated in the probe. This arrangement is very attractive because it avoids polarization and coherence issues. A variation, in which the reference beam is generated using a 1 × 2 tap-off, allowing amplitude control and phase modulation of the reference, appears in Figure 2. A more flexible configuration, in which the reference beam or local oscillator is directed to a coupler, where it interferes with the shifted light from the probe, appears in Figure 3. This arrangement can be used for optical heterodyne downconversion, quadrature detection, and other variations, at the cost of increased complexity.

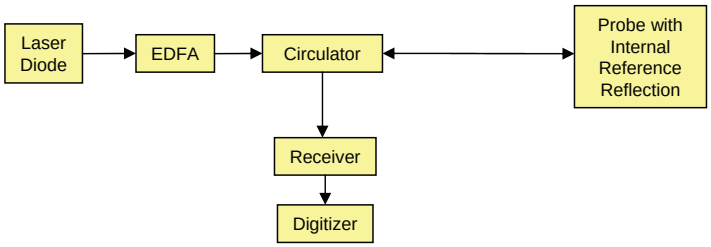

Figure 1. Basic PDV system

Quadrature PDV Systems

Quadrature signals might be helpful in the direct unfold of the phase, which in turn might improve PDV time resolution. A 3 × 3 star coupler provides outputs at 120° phase, from which sine and cosine outputs and optical path difference (OPD) can be calculated:

$$I_s = A_0\left(1+V\cos\left(\frac{2\pi}{\lambda}\times OPD\right)\right) \quad (1)$$

$$I_+ = A_0\left(1+V\cos\left(\frac{2\pi}{\lambda}\times OPD+\frac{2\pi}{3}\right)\right) \quad (2)$$

$$I_- = A_0\left(1+V\cos\left(\frac{2\pi}{\lambda}\times OPD-\frac{2\pi}{3}\right)\right) \quad (3)$$

$$OPD = \frac{\lambda}{2\pi}\arctan\left(\sqrt{3}\,\frac{I_+ - I_-}{2I_s - I_+ - I_-}\right) \quad (4)$$

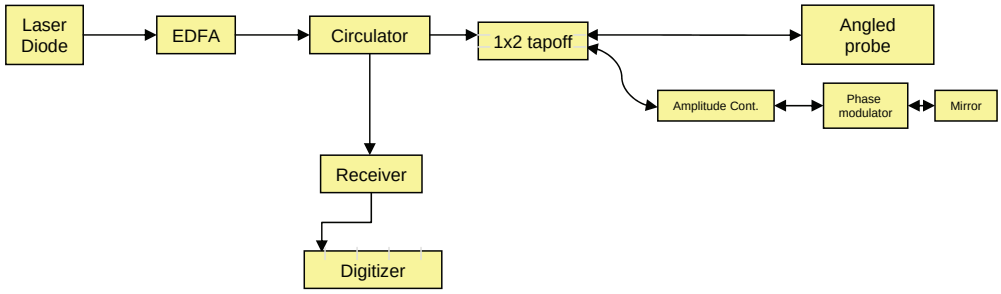

Figure 2. Basic PDV system with external reference

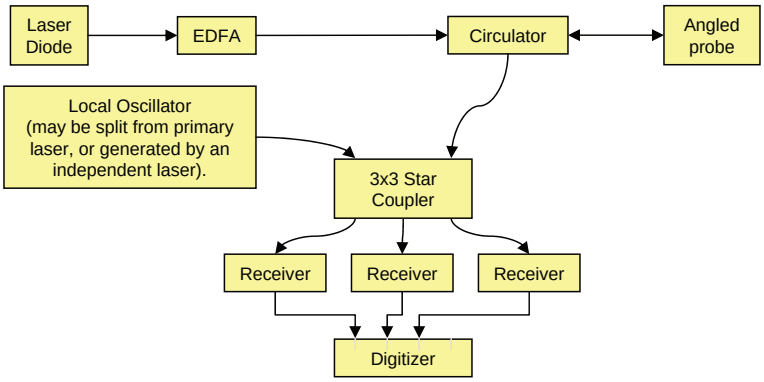

Figure 3. 3 × 3 PDV with local oscillator and 120° outputs

Figure 4 depicts velocity measurements of a moving mirror using both conventional and quadrature PDV signals obtained from the system appearing in Figure 3. The quadrature data correctly identify the change in direction, while the fast Fourier transform (FFT) does not. The arctangent data were smoothed with the same number of points used in the sliding FFT.

VISAR Integration

A coherently detected, single-mode velocimeter that integrates PDV with a single-mode velocimeter appears in Figure 5. A local oscillator is mixed with the outputs of a delay Mach-Zehnder interferometer, greatly enhancing the signal levels. The single-mode interferometer incorporates Faraday mirrors to avoid polarization control in the cavity. Device outputs consist of PDV fringes with an envelope modulated by the single-mode velocimeter signals (Figure 6). We used this system to measure the velocity of a Mylar film driven by an air gun. The phase relation of the single-mode velocimeter outputs is readily visible in the expanded graph at the bottom of Figure 6. Figure 7 shows the velocity profile obtained from the FFT of the PDV data, overlaid by the velocimeter data in blue. The velocimeter analysis, which is not very sophisticated, is still under development.

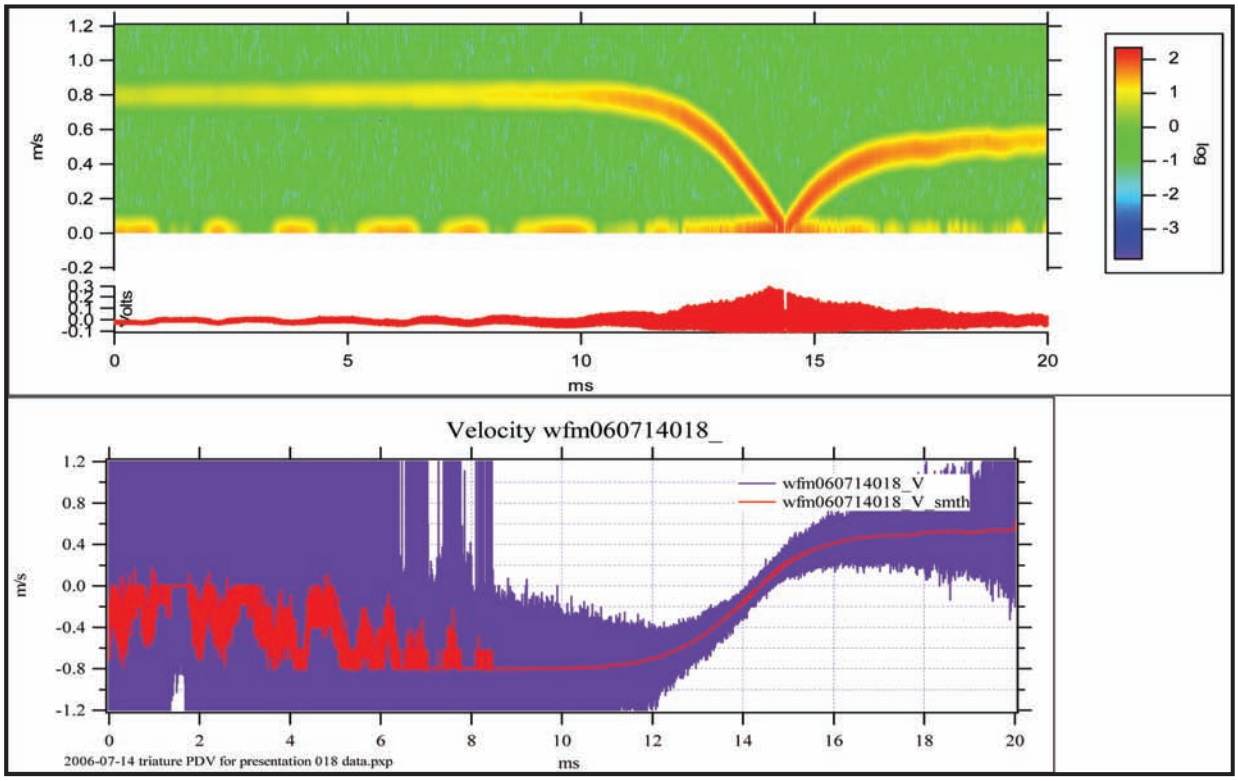

Figure 4. Quadrature PDV from sliding mirror: (top) conventional sliding FFT analysis; (bottom) arctangent unfold

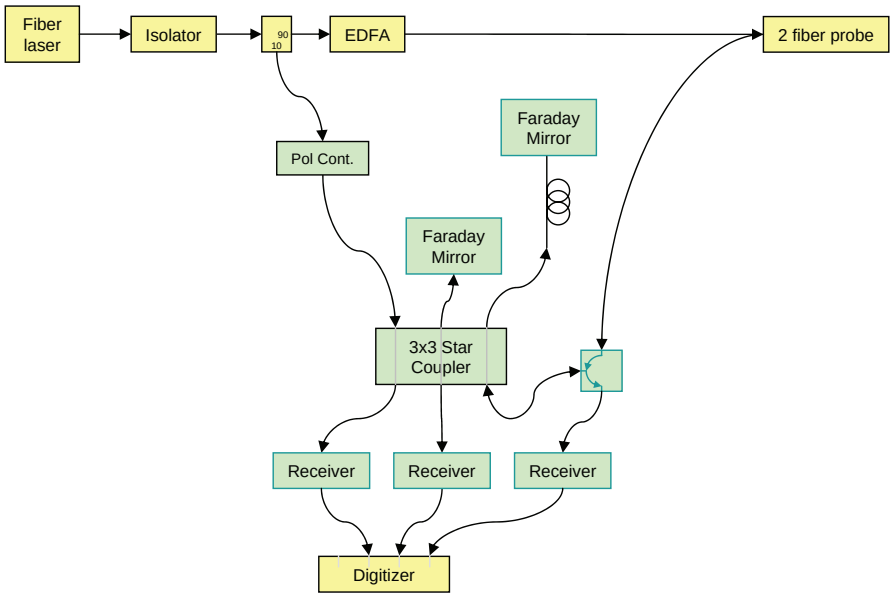

Figure 5. PDV/single-mode velocimeter system layout

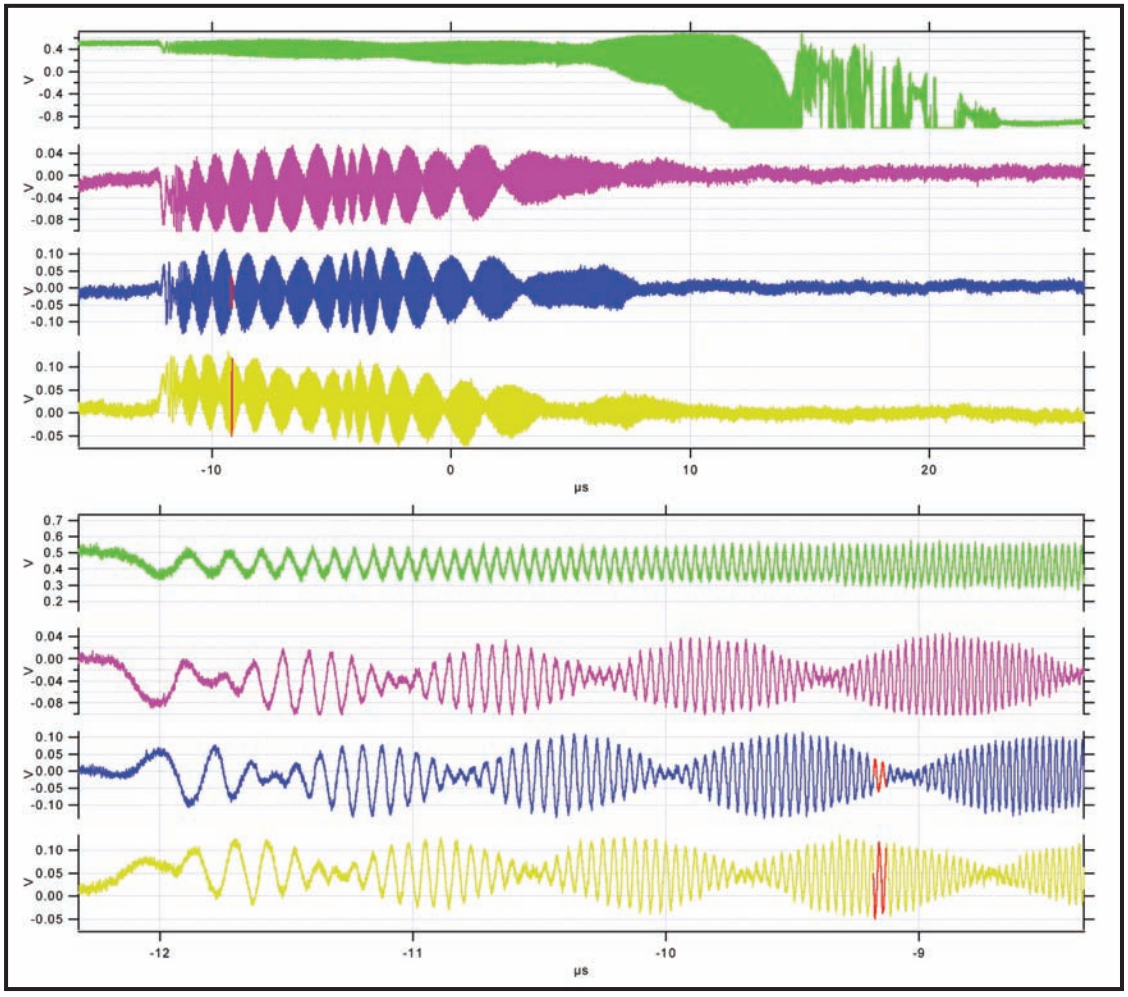

Figure 6. Signals from coherent single-mode velocimeter

Downconversion

Frequency downconversion would allow us to measure higher velocities with a given recording system bandwidth. Optical downconversion techniques essentially consist of using a frequency-shifted local oscillator as a reference beam. Two downconversion systems were tested. We demonstrated that simple Mach-Zehnder heterodyne PDV (Figures 8–9) could multiply velocity coverage for a given recording bandwidth by 3x or 5x. The more complex, single-sideband (SSB) modulator system (Figure 10) generated a less complex signal and was more difficult to adjust. Sideband suppression was about –20 dB.

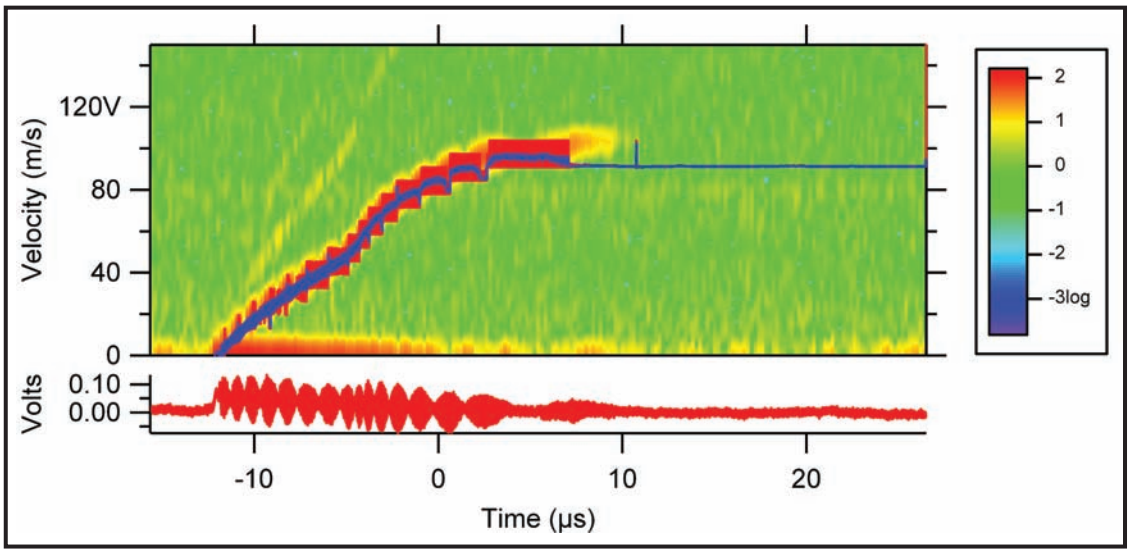

Figure 7. Velocity vs. time for air gun measurement

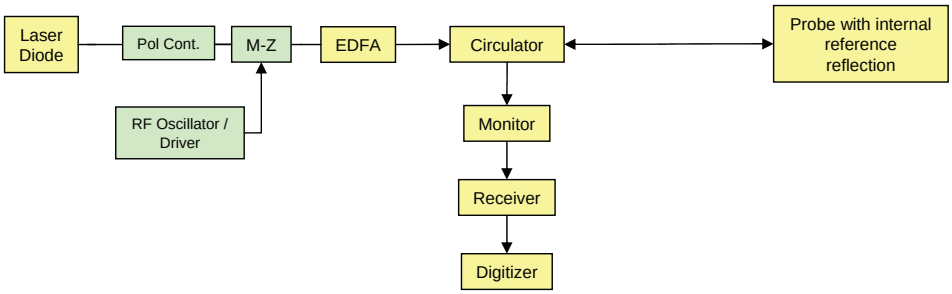

Figure 8. Mach-Zehnder heterodyne PDV with probe reference

Erbium-Doped Fiber Amplifier (EDFA) to Boost Output Signal

Brillouin scattering limits the optical power delivered to the target in PDV systems with long fibers. We overcame this problem by reducing the input power and optically amplifying the return signal (Figure 11). Because of the low input signal levels, a narrowband filter is necessary to block the spontaneous emission. EDFA bandwidth, linearity, and noise figure make this the preferred method of signal-boosting. For the low power level that would be delivered to a detector, linewidth is essentially unchanged. Figure 12 presents PDV data from a rough target using a bare fiber probe with 2-mW laser power. Clearly the EDFA-amplified signal has a considerably better signal-to-noise ratio. Amplifying the returned, shifted light also raised the power level to a point at which automatic gain control might be practical.

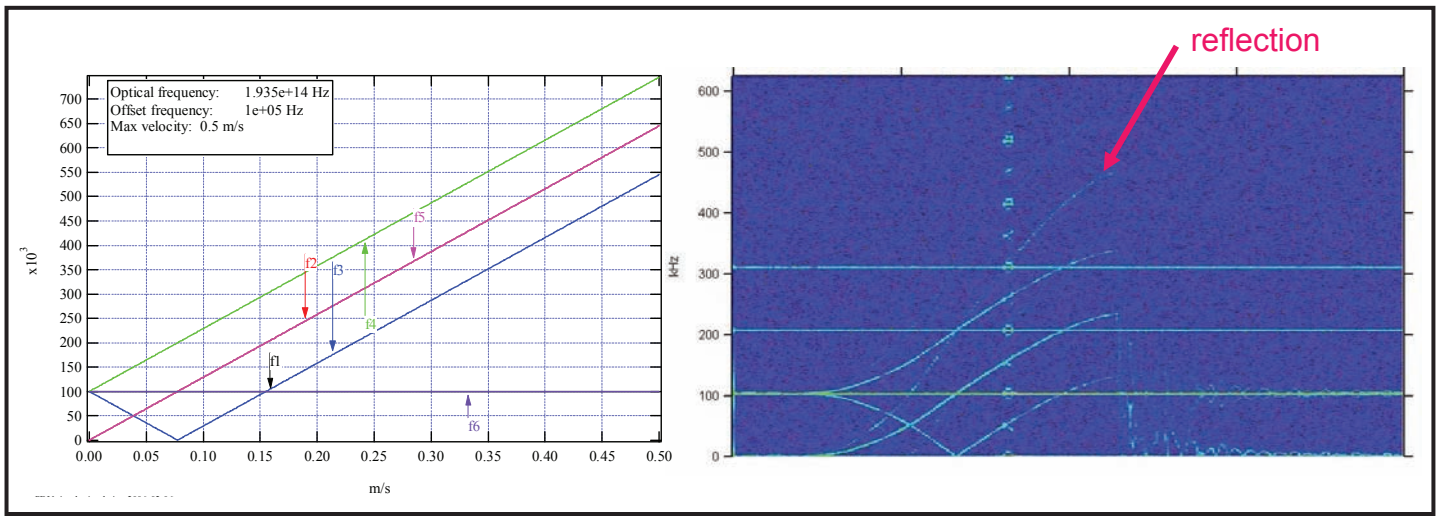

Figure 9. Mach-Zehnder heterodyne system data

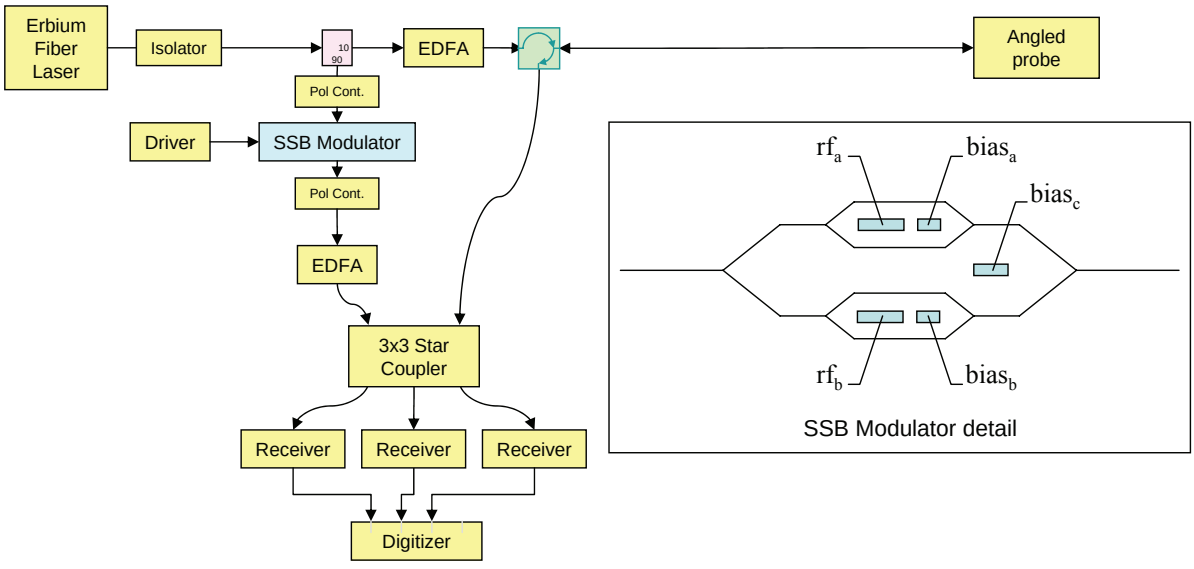

Figure 10. Quadrature PDV system with SSB modulator

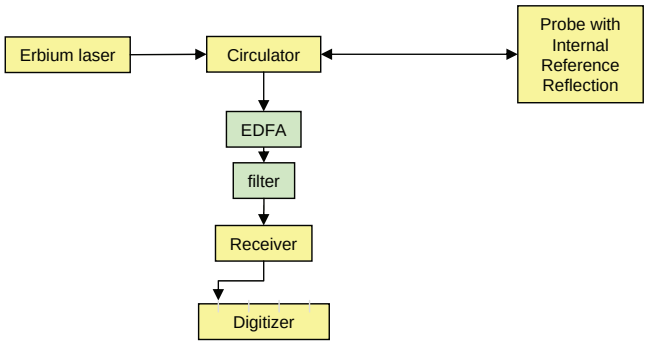

Figure 11. Erbium-doped fiber amplifier in a basic PDV system

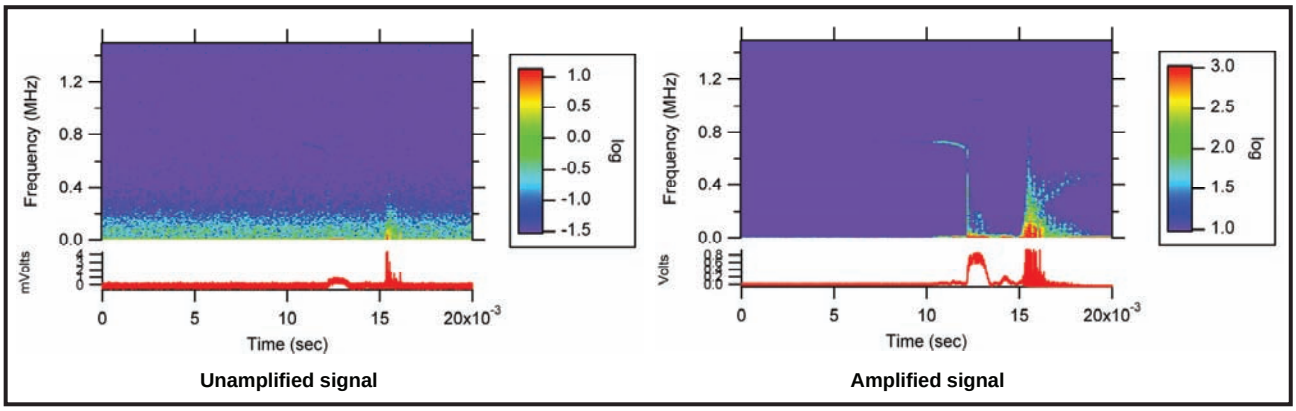

Figure 12. PDV fringes amplified by EDFA (2-mW input laser power, bead-blasted target surface, bare fiber probe): (bottom left) unamplified signal; (bottom right) amplified signal

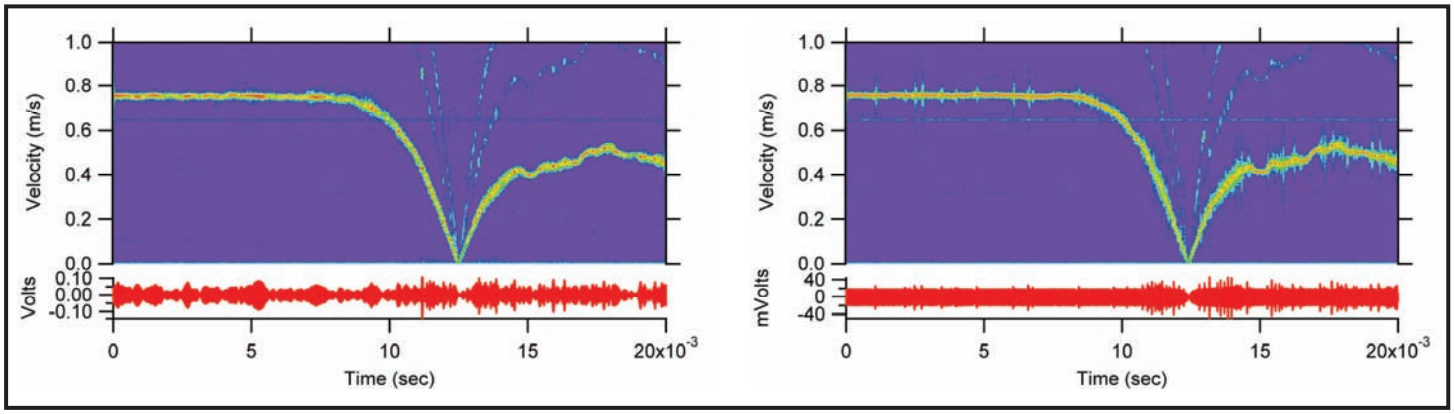

Figure 13. Optical power regulator: (left) unregulated; (right) regulated

Other Technologies

Optical Power Regulation

We tested an optical power regulator from Boston Applied Technologies. The regulated and unregulated signals from a low-velocity PDV measurement appear in Figure 13. The spectrogram of the regulated data shows better amplitude uniformity than for unregulated data. However, when regulation failed, it produced wide noise spikes in the frequency domain. Optical power regulation appears feasible but would require an engineering effort to produce a fast, stable feedback circuit suited to a high-velocity measurement.

Multimode PDV

Use of multimode fibers for PDV would raise the Brillouin limit on optical power in long fibers and should improve the probe's collection efficiency. In practice, there does not seem to be a clear advantage for multimode. However, the problem is best viewed from the standpoint of spatial coherence of the reference wavefront with the shifted wavefront returned from the target. Overall, we reached no definite conclusion, but multimode PDV did not appear to have any outstanding advantage.

Pulsed Laser

A pulsed laser could be smaller and much less expensive, deliver higher optical power, and consume less energy than the continuous wave lasers typically used in PDV. We unsuccessfully attempted to tailor the drive pulse for a distributed feedback to produce a rectangular, 100-μs-wide pulse from an EDFA. Due to the dynamics of the erbium-excited state, this proved impossible.

Panel-mounted Polarization Controller

In the course of this project, we developed a compact, panel-mounted, fiber-pigtailed polarization controller that occupies only 1 in. of front panel width.

Conclusion

Several improvements to PDV were developed and shared with the community. Some of these have been or are being incorporated in field instruments. A total of six invention disclosures resulted from this work: "Single-mode velocimeter with coherent detection," "Ellipsometer/velocimeter with coherent detection," "Panel-mounted manual fiber-optic polarization controller," "Velocity interferometer in single-mode fiber with quadrature outputs," "VISAR probe using concentric dual core fiber," and "Phase-modulated VISAR."

Reference

Strand, O. T., D. R. Goosman, C. Martinez, T. L. Whitworth, W. W. Kuhlow, "Compact system for high-speed velocimetry using heterodyne techniques," *Rev. Sci. Instrum.* **77** (2006) 083108.

this page intentionally left blank

Diagnostic Shock Source

Michael Berninger, Alfred Meidinger,[1] Richard Yeh (former employee)
Los Alamos Operations

A 140-ps pulse length, 100-mJ, frequency-doubled neodymium:yttrium-aluminum-garnet (Nd:YAG) laser was used to generate shock in copper foils in a laboratory setting. Results indicate that breakout velocities >1000 m/s can be achieved with this source. It will be used to develop optical velocimetry diagnostic systems.

Background

Material properties of solids are routinely investigated by observing the materials under shock conditions. Numerous methods exist for creating the required shock, including flash heating by pulsed high-power lasers. Although laser-induced shock is limited by available shock (laser) energy and power densities, the use of lasers to produce shock in material is attractive in laboratory experiments. Systems are reliable, sizes are reasonably small, no chemical explosives or pulsed-power discharges are required, and consequently, stray energy and momentum releases are minimized. Furthermore, the power density and energy density of the source are easily varied by changing the beam spot size and laser energy, respectively.

Laser shock can be generated by several different techniques. The material can be directly illuminated, thus creating shock through the ablation process. A variation of this method uses a transparent substrate as a backplane for the shock material. Another method uses the laser to drive a slapper into the sample. In this case, the slapper is accelerated by laser ablation of an adjacent layer of absorbing material, such as carbon or graphite. A third method employs laser-driven hohlraums to generate x-ray drive. Since the shock load is generated by a number of photon-material interactions, such methods suffer one drawback: difficulty in analytically determining shock load as a function of laser parameters. Nonetheless, because of the aforementioned benefits, along with quick turnaround time, laser shock-loading is very useful as a shock source for diagnostic system development.

Project

For this development effort, we used the direct-drive ablation method. During the start of the laser-sample interaction, laser energy is deposited in the sample surface to the material's skin depth. As energy is absorbed, the surface ablates to form plasma, which absorbs laser energy in conjunction

[1] meidina@nv.doe.gov, 505-663-2018

with the sample surface. As the surface ablates and the plasma heats, the material reaction and plasma expansion create a pressure load on the foil surface, which subsequently propagates through the foil as a pressure wave.

Experiments were performed using a Positive Light frequency-doubled Nd:YAG regenerative laser. This laser produces 140-ps pulses with ~100 mJ of energy per pulse (715 MW) at a 532-nm wavelength (although some experiments were conducted by superimposing the fundamental wavelength on the frequency-doubled component, energy and power values are not known, since energy measurements were not conducted in this configuration). Note that the pulse-width information is anecdotal; high-speed diagnostic equipment for measuring actual pulse width was unavailable. A 150-mm focal length lens was used to focus the laser onto the copper targets, which consisted of 5- and 10-μm foils and 10-μm copper deposited on a 1-mm glass substrate. Experiments were conducted in air, which limited spot size and power density due to air ionization.

Breakout material velocities were measured optically, using photon Doppler velocimetry (PDV) and Mach-Zehnder velocimetry. (This report presents only selected PDV results.) Figure 1 provides a schematic representation of the laser-sample interaction. While some experimental configurations used collimated optical probes with a protective glass slide between the foil and sample (to minimize copper deposition on the probe surface), a configuration without the protective slide using bare fiber probes yielded the best data. The bare probes were placed approximately 1 mm from the sample surface. This close proximity, combined with larger numerical aperture, resulted in improved signal strength compared to the collimated probe configuration.

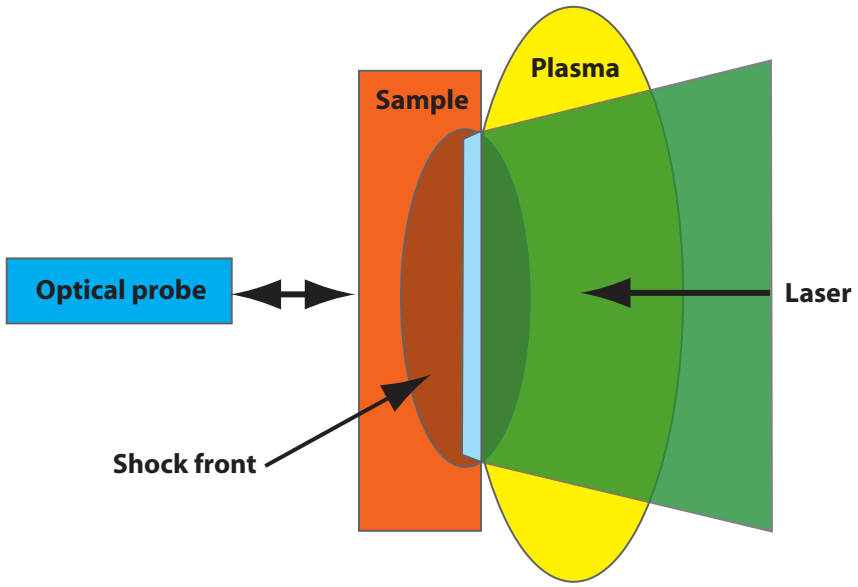

Figure 1. Laser-material interaction

Initial tests were conducted using ring-mounted, unsupported, 5-μm-thick copper foils. The foils were positioned ~5 mm in front of the beam focal point, as determined by the air ionization point. Figure 2 illustrates the typical foil "blowout," which indicates the predominant release of layers in a chad-like form. It is not clear that the diameter of the hole, ~500-μm, matches the laser spot diameter. Based on this diameter, the lower bounding limit on the surface irradiance was 364 GW/cm^2.

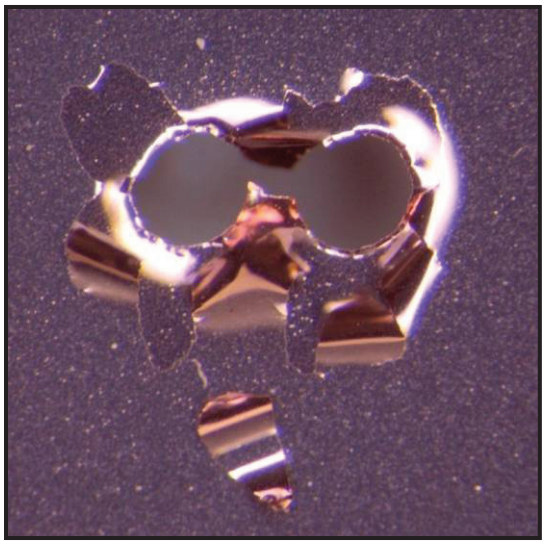

Figure 2. Probe side of typical blowouts using a 5-μm copper foil

Figure 3 shows a typical PDV signal captured while ablating a 5-μm foil, where the feature immediately following time zero indicates shock breakout. Data analysis shows that the material traveled at ~160 m/s (Figure 4). The raw data were filtered to remove frequencies below 30 MHz, then transformed using a fast Fourier transform spanning 1064 data-point increments with a data interval of 50 ps. Of particular interest in this velocity data is the apparent pullback and subsequent release of a spall layer, as seen in the first 100 ns of the trace. The remainder of the trace points to a ringing in the released layer.

Release velocities of 1300 m/s are reached when using copper on glass substrate, as indicated by the data in Figure 5. In this case it is unclear that actual spalling occurs, since there is no apparent pullback prior to release (the initial data spike is assumed to be an artifact caused by the velocity extraction routine). An interesting feature is the velocity after 290 ns, the result of material recoil from the probe tip.

Although the data in Figure 5 were filtered to remove frequencies below 200 MHz, some noise remained, as indicated by the spikes (and negative-valued components) in the 400-ns vicinity, along

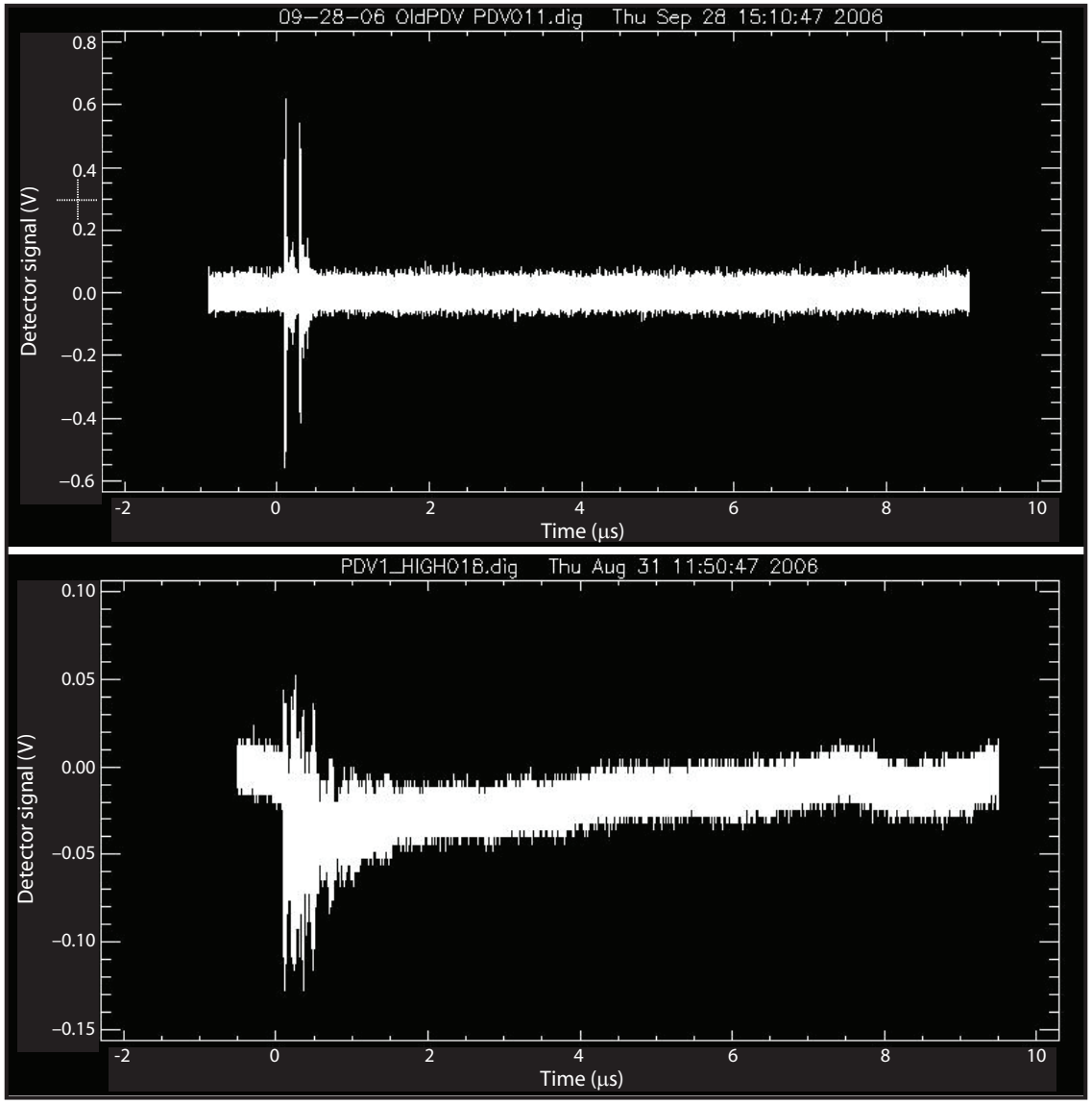

Figure 3. Typical PDV shock data using 5-µm unsupported copper foil

with the noise preceding the release at 100 ns. Figure 6 illustrates the filtered data before application of the fast Fourier transform (spanning 256 data-point intervals) used to generate the velocity profile in Figure 5. The two prominent spikes in Figure 6 correspond to surface breakout and material recoil from the probe tip.

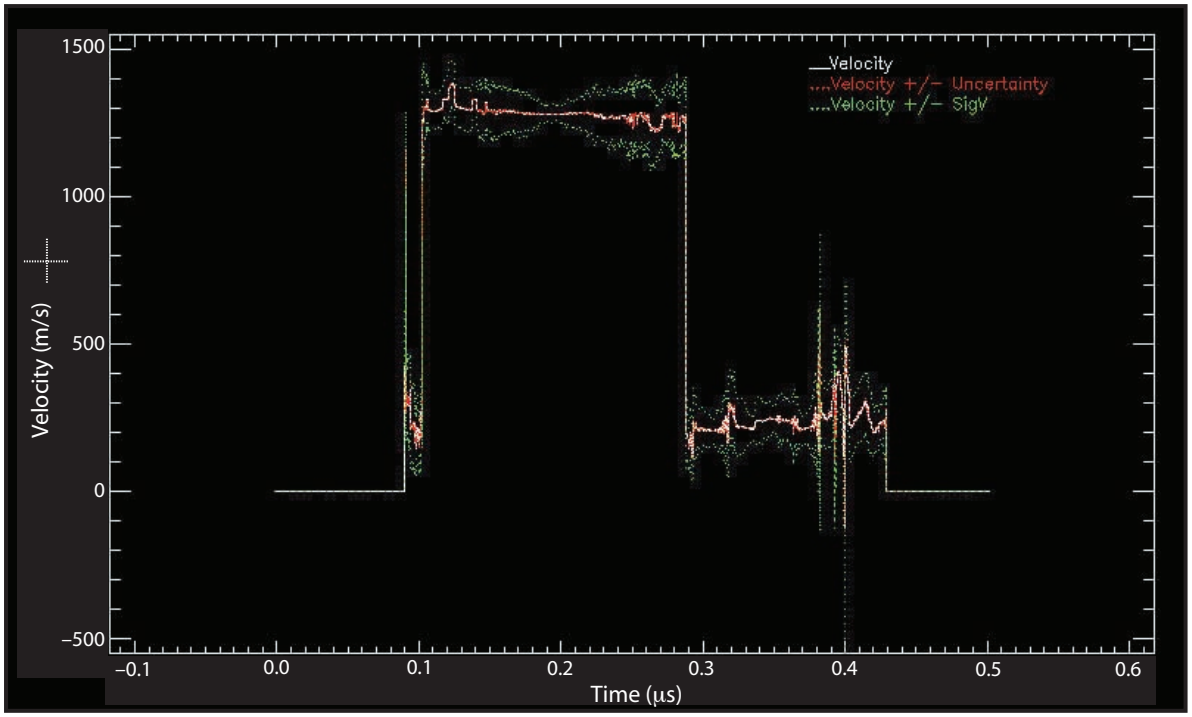

Figure 4. Calculated surface velocity for data used in Figure 3. Both the pullback and release, as seen in the first 100 ns of the trace, and the apparent ringing in the remaining trace, indicate spall layer detachment. The spike at the end of this data set is assumed to be an artifact from the velocity extraction routine.

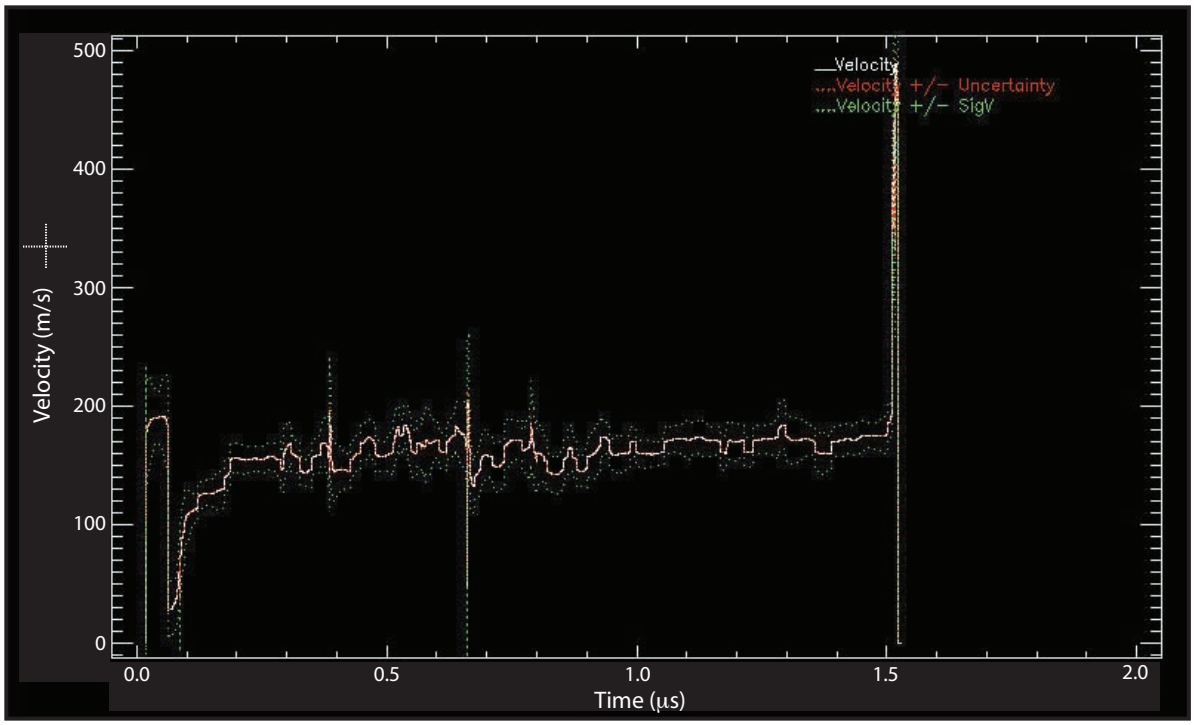

Figure 5. Copper on glass substrate data showing a release velocity of 300 m/s. The data after 290 ns indicate material recoil from the probe tip.

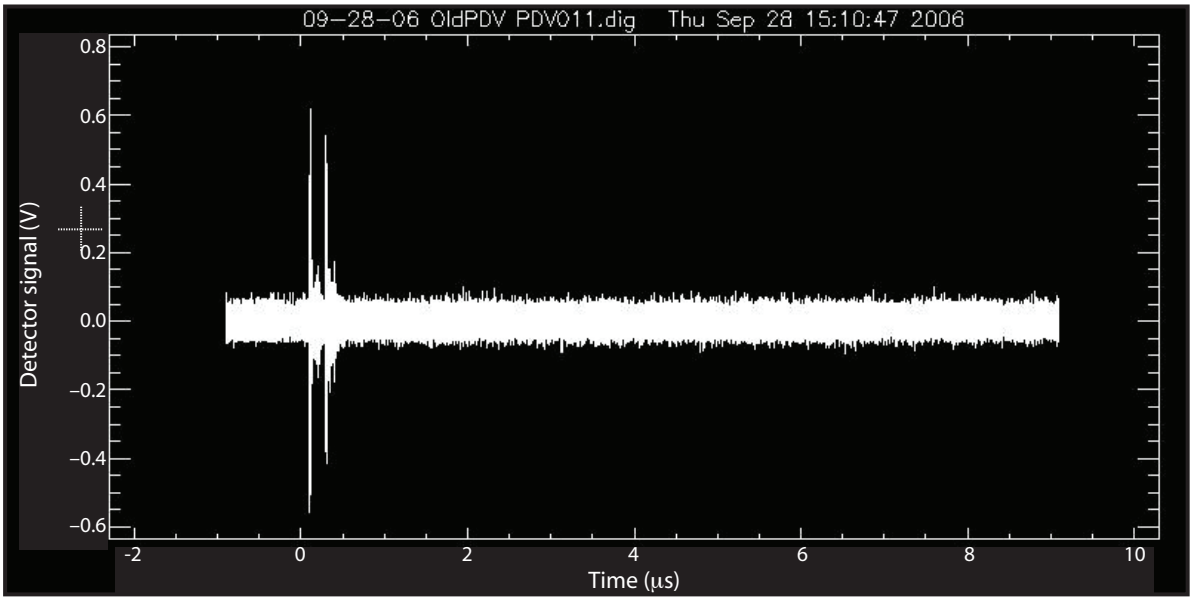

Figure 6. PDV data after applying a high-pass filter at 200 MHz. The first event corresponds with release; the second corresponds with material recoil from the probe tip.

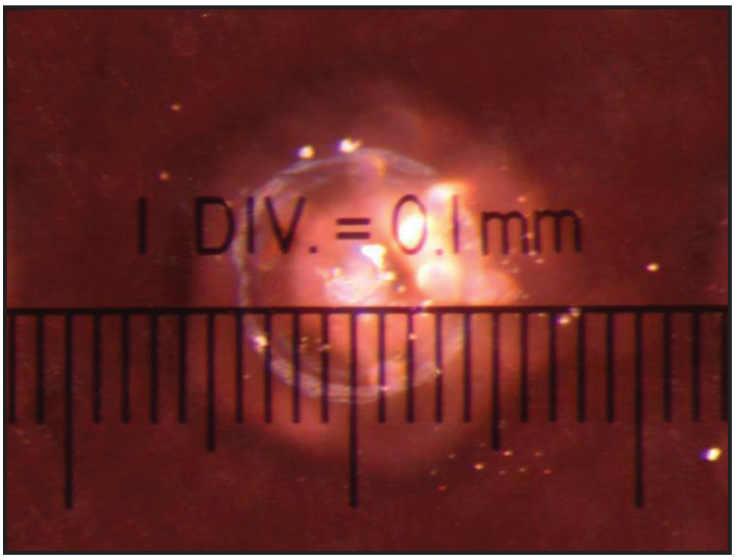

Figure 7. Laser damage in glass substrate

The glass substrate–backed material exhibited an order of magnitude increase in velocity compared to that of foil without backing. This increase is more than would be expected from reflected pressure alone. It is unclear what caused it, but we speculate that the laser focused to a smaller spot in the glass substrate than in air, and heating and dielectric breakdown in the substrate added to the ablation-plasma pressure of the copper. Figure 7 shows a close-up image of the glass substrate damage. For this experiment, the sample was positioned such that the air ionization point was located inside the substrate, directly in front of the copper layer. The damaged portion (the small circle in the center of the image) is ~200 μm in diameter. This spot can safely be assumed to match the beam diameter, since the beam is nearly flat-topped. At this focus, the irradiance of the glass-copper interface is >2 TW/cm^2. Substrate damage is likely caused by a combination of effects, including plasma heating at the interface and dielectric breakdown in the substrate.

Conclusion

We developed a laboratory-scale shock source using an available high-power laser. Tests show that, when a copper-on-glass substrate is used, breakout velocities exceeding 1000 m/s can be achieved. This corresponds well with the velocities seen in material studies of subcritical experiments. Therefore, this source will provide a valuable tool to assist in developing diagnostic systems for material studies.

System development will continue with breakout velocity characterization using different materials at varying thicknesses and possibly in a vacuum configuration (to increase power density by eliminating air ionization). In addition, breakout velocities will be correlated to laser spot size and laser lamp energies.

Acknowledgments

The authors would like to thank Gene Capelle (STL), Bob Malone, Sheri Dance, Vince Romero, and Greg Lare for their assistance in setting up and operating the laser shock source. Additional thanks to Adam Iverson, Jason Young, Sonny Gallegos, and Matthew Teel, for operation of the PDV and Mach-Zehnder data acquisition systems.

this page intentionally left blank

Electro-optic Differentiator

E. Kirk Miller[1]
Special Technologies Laboratory

This project sought to develop a fiber-optic transmission line that delivers the time derivative of the electrical input signal. The derivative often contains valuable information about the experiment, yet it is typically recovered by directly recording the signal, smoothing, then differentiating, which compromises bandwidth. We have demonstrated the technique in two ways: by integrating the differentiated signal to recover the input and by calculating the log-derivative of a signal without requiring smoothing.

Background

Using time-delay interferometers to measure the time derivative of an event is the core of the velocity interferometer system for any reflector (VISAR) diagnostic. The electro-optic (EO) differentiator technique has many similarities to VISAR. In both cases, light is phase-shifted close to the experiment and demodulated at the recording station, typically 100 m away; in VISAR the phase shift occurs as the reflecting surface accelerates toward the probe. In the EO differentiator, it happens as the electrical input to the phase modulator from a radiation detector (such as a vacuum compton diode) increases in voltage. At the recording station, the signal is demodulated by interfering two copies of the light with a well-known time delay, thus creating an interference pattern based on the phase change during the time delay.

Project

We used a 10-Gb/s lithium niobate ($LiNbO_3$) phase modulator from Avanex (model IM10-P). Phase modulators are simpler than Mach-Zehnders (M-Zs), in that they do not require actively controlled DC-bias. Thus, they are particularly attractive for remote experimentation where bias control at the recording station may be simpler than it would be close to the experiment.

In the EO differentiator system, demodulation of the phase of the light can be performed in several ways. A fiber-delay interferometer can be assembled, a bulk-optic interferometer (essentially a single-mode VISAR) can be made, or an etalon can be used. For this work, we employed off-the-shelf demodulators designed for 10-Gb/s and 42-Gb/s digital communications, which use bulk optics in a miniature, ruggedized case. These Optoplex demodulators had interferometer delays of 100 ps and

[1] millerek@nv.doe.gov, 805-681-2237

20 ps, respectively. The demodulator board appears in Figure 1. Both demodulators were available with a controllable bias, which employs a heater to warm one leg of the interferometer through a 100-Ω resistor.

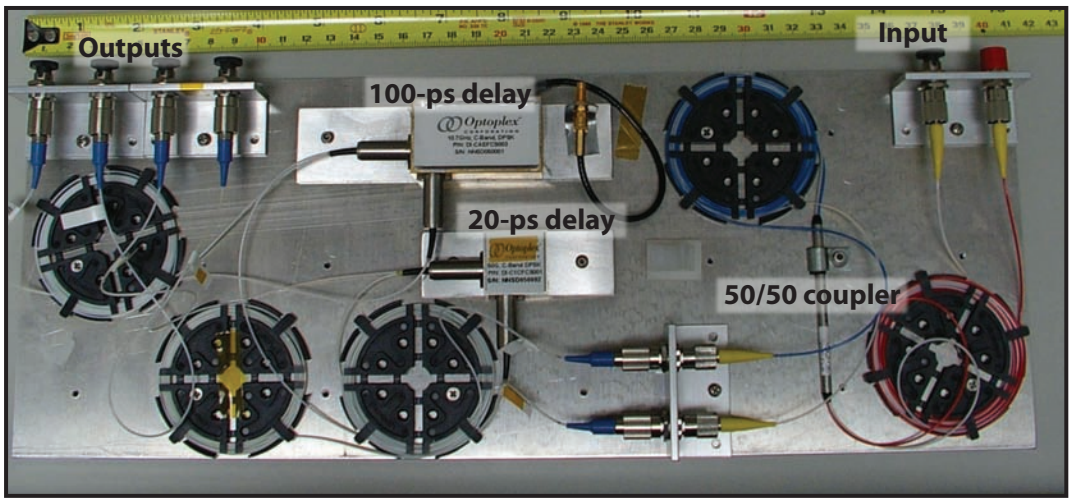

Figure 1. Differentiator demodulator board

The relationship between the input electrical signal and the output light intensity from the fiber is:

$$P_{OUT} = P_{MAX} * \frac{1}{2}\cos\left(\pi \frac{\Delta V_{IN} / \Delta t}{V_{\pi}} + \theta\right), \quad \textbf{(1)}$$

where:

$(\Delta V/\Delta t)$ = differential of the input voltage in the delay time, Δt, of the demodulator,

P_{MAX} = maximum output power,

V_{π} = half-wave voltage of the modulator (typically <6 V), and

θ = phase of the interferometer at t = 0.

During this work, we realized that the recorded output signal magnitude depended on the slew rate of the input voltage. However, few detectors have both high bandwidth and high output. Thus, expected signal amplitude and rise time had to be carefully considered during system design. Another consequence was that, for modest bandwidth signals, amplitude of the signal from the 20-ps delay interferometer was only 20% of that from the 100-ps delay interferometer.

The first test of a new transmission and recording scheme is to record step functions and compare results with well-known, trusted recording systems. Figure 2 shows the result of recording a 40-V step with a 250-ps rise time (~1.4-GHz effective bandwidth), using the 100-ps delay interferometer. The red trace shows the signal recorded directly on a high-bandwidth oscilloscope. The black trace is the one-shot differentiated record integrated to return the input function. (The step-top overshoot, possibly due to the 100-ps differentiation latency, is manageable.) Of particular interest is the high-frequency noise suppression at the pulse foot (Figure 2, inset). This suppression derives from the fact that the Fourier transform of the integral of a function is the Fourier transform of the function itself divided by the frequency. In practice, this means that high-frequency detail is suppressed, and very-low-frequency noise is introduced. This behavior can quickly be verified by synthesizing Gaussian white noise and integrating it.

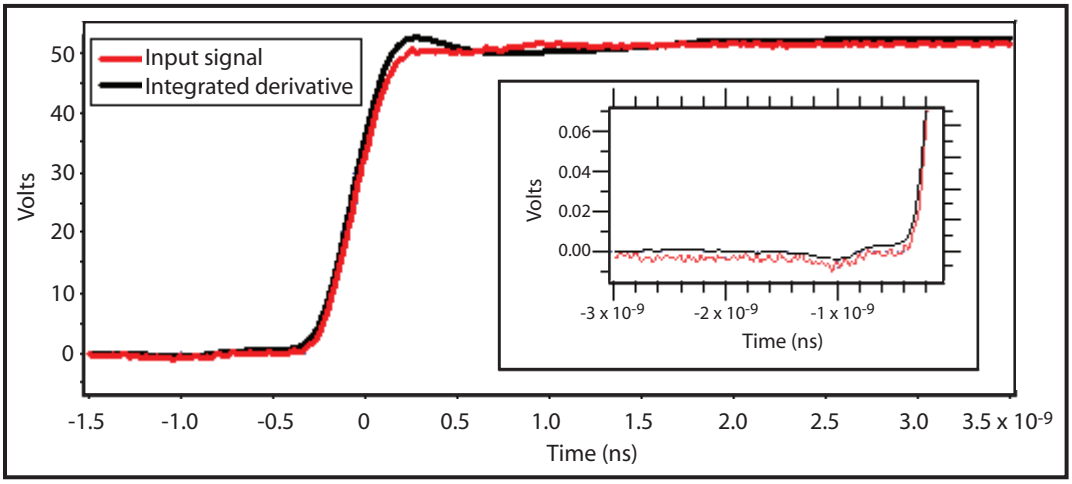

Figure 2. 250-ps step with integrated derivative signal

Just as the optically differentiated signal integral has lower high-frequency noise than the directly recorded step, so the optically differentiated signal itself has lower noise than the derivative of the directly recorded step (Figure 3).

One application for high-bandwidth electro-optic links is in underground tests in which the signal is locally represented by a rising exponential:

$$V = V_0 \exp(\alpha t), \quad (2)$$

where, in general, $\alpha = \alpha(t)$. Test pulses with reasonably constant α can be created from a fast step by running the step through series of resistors and delay lines. An example of such a pulse appears in Figure 4.

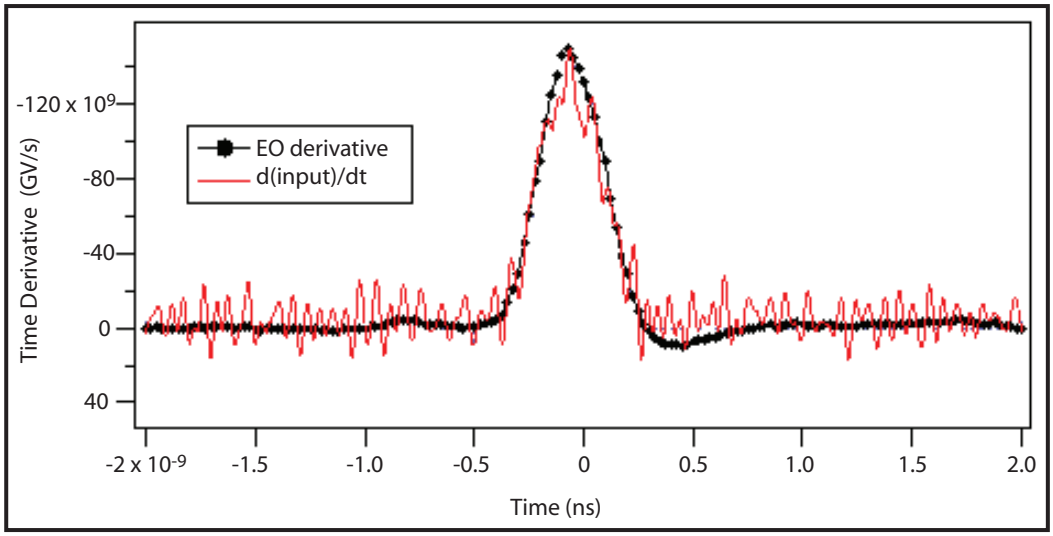

Figure 3. Derivative of step function

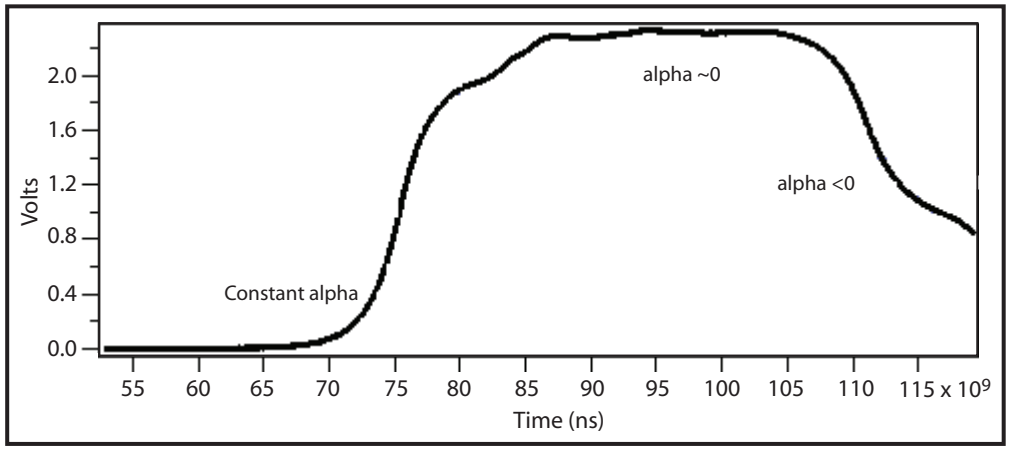

Figure 4. Test pulse with constant α on rising edge

The accuracy with which the resistors are matched and the delay lines properly sized determines the uniformity in time of the α value on the rising edge of the pulse. Mismatched resistors or delay lines can lead to a steplike structure on the pulse and an oscillating α value. While no pulse shaper is perfect, some have more pronounced oscillations than others and/or oscillate at different frequencies.

We recorded pulses of up to ~50 V with α values of 100/μs, 200/μs, 500/μs, 800/μs, and 2000/μs, representing the range of available pulse shapers. The 500/μs pulse shaper was found to have a particularly interesting structure, so it will be presented as a case study. Figure 5 shows the one-shot recorded derivative (red trace) and the derivative taken by differentiating a direct recording of the input pulse (black trace) (averaged 10000 times to reduce noise). Clearly, the imperfections in the pulse shaper can be seen as ~2-GHz oscillations near the top of the trace. The red trace faithfully reproduces the derivative from the black trace.

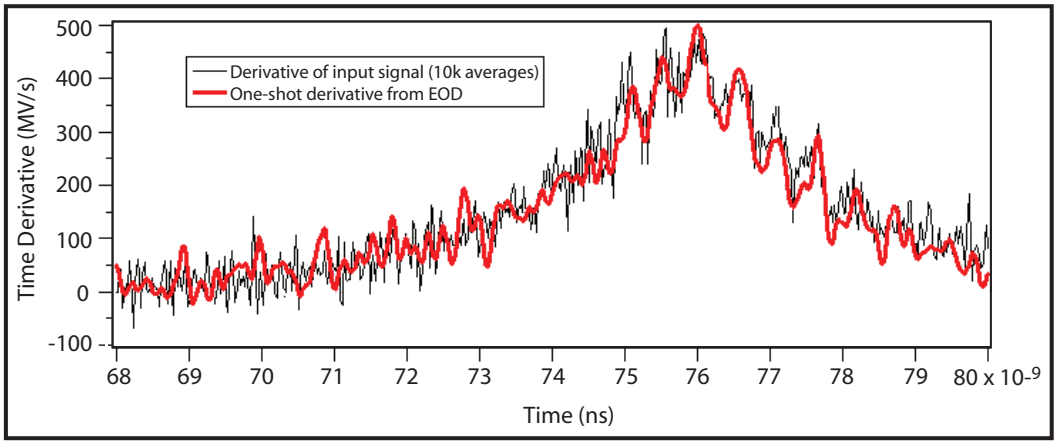

Figure 5. Derivatives of 500/μs α pulse

The log derivative, α, is defined as:

$$\alpha(t) = \frac{d}{dt}\ell n(V) = \frac{dV/dt}{V}. \quad \textbf{(3)}$$

Therefore, we can compute instantaneous values of α by using the value of *V* recorded on an M-Z link (to extend the scope's dynamic range) and the value of *dV/dt* recorded with the EO differentiator. Results appear in Figure 6. The pink trace is the natural log of the input voltage, as recorded by the M-Z; the "turnarounds," where the M-Z has low sensitivity and, hence, high noise, are seen as ripples at ~71 ns and ~73 ns. The green trace is *dV/dt* recorded with the EO differentiator and is identical to the red trace in Figure 5. The red, blue, and black traces in Figure 6 (bottom) are three calculations of α*(t)*. Using a 2-ns sliding window (red trace) smoothes over the structure in the derivative. The black trace uses both records, *dV/dt* and *V(t)*, to compute α*(t)* using Equation 3. The blue trace is the derivative of the pink trace after it has been smoothed to 100 ps to match the time delay in the EO differentiator.

Clearly, once the signal emerges from the noise at ~74 ns, the black and blue traces track each other well. Based on the derivative data in Figure 5, however, we expect that the intrinsic noise in the EO-differentiated link would be lower than the noise in the log derivative of the directly recorded signal.

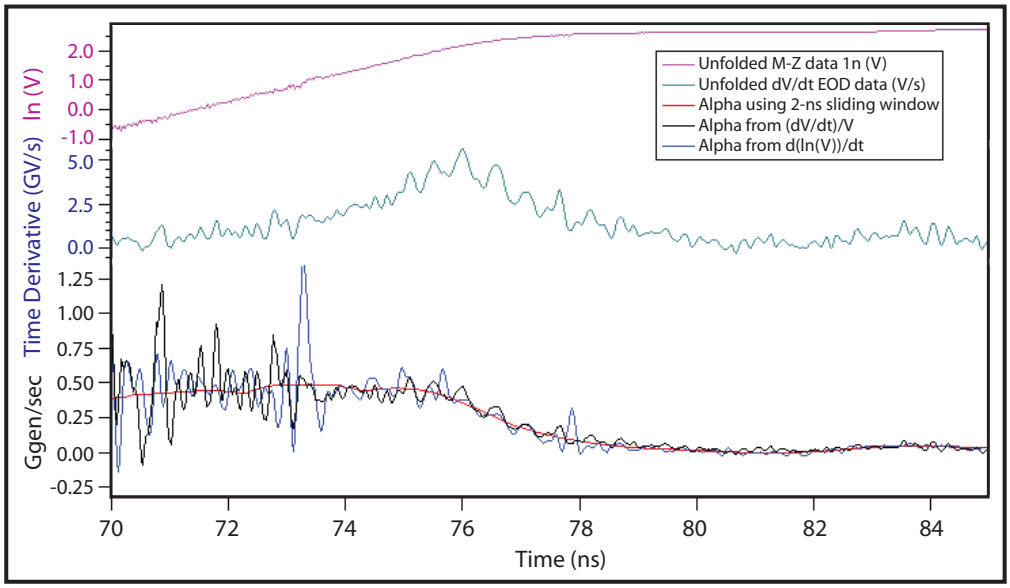

Figure 6. Alpha (α) curves recorded with M-Z and EO differentiator links

Conclusion

We have realized the recording of optically differentiated signals in a simple, high-bandwidth analog data link. The performance of the scheme compares well with the established techniques of using M-Z interferometers as intensity modulators. This method can be tuned to a variety of signal rise times and amplitudes by choosing an appropriate delay for the demodulation interferometer. Clearly, it is best suited to applications in which signal duration is many times longer than the delay duration, so short-pulse experiments, such as laser-driven fusion, would require very short delays.

Quadrature Optical Modulator

E. Kirk Miller[1]
Special Technologies Laboratory

This project sought to develop a dual-output, single-fiber-optic modulator with intensities 90° out of phase, or "in quadrature," for use with high-bandwidth analog data links. Two approaches were investigated. The first utilized a gallium-arsenide polarization modulator, with the quadratures encoded in the light polarization. The second approach, using a phase modulator with two demodulation channels 90° out of phase, proved valuable for high-bandwidth recording applications. Due to its compatibility with current experimental configurations, the latter approach was recommended for implementation.

Background

Mach-Zehnder (M-Z) modulators with sinusoidal transfer functions are valuable data links for underground test diagnostics, such as vacuum Compton diodes, as well as for inertial-confinement fusion (ICF) diagnostics, such as gas Cerenkov detectors. However, conventional M-Zs have either single or complementary outputs. Adding quadrature outputs would enhance data robustness in two ways. First, it would eliminate ambiguity when the recorded intensity turns around. This can happen when the input electrical signal passes through a local minimum or maximum, or when signal amplitude passes through a multiple of the modulator's half-wave voltage, Vπ. Second, it would improve the signal-to-noise ratio (SNR) in the vicinities of turnarounds, where M-Z sensitivity falls to 0, since one channel would be at its most sensitive while the other would be at an extremum. Currently, quadrature signals to measure overlapping time regions are routinely used in velocity interferometer systems for any reflector (VISARs) but not in M-Z systems.

Project

The first approach we investigated was a gallium-arsenide polarization modulator, which takes an input electrical signal and alters light polarization around the Poincaré sphere, from horizontal (H), to right-circular polarization (RCP), to vertical (V), to left-circular polarization (LCP) (Figure 1).

[1] millerek@nv.doe.gov, 805-681-2237

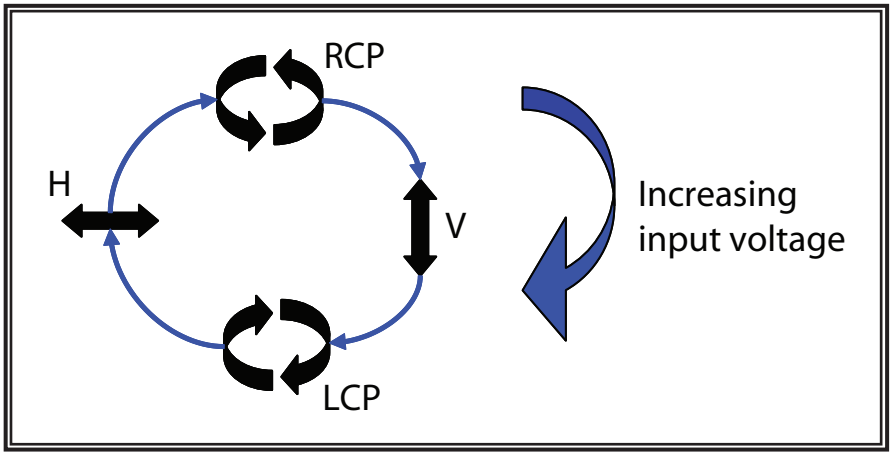

Figure 1. Polarization modulation transfer function

The modulator we used was JGKB Photonics' (a.k.a. Versawave) Model EOM-PL-40G-5-1550-V-0-FCP-FCU. It has a specified bandwidth of >30 GHz and polarization-maintaining fiber input, with an integrated polarizer and single-mode fiber output. The modulator's half-wave voltage is 5.5 V, which is comparable to that of modern lithium-niobate ($LiNbO_3$) modulators. Modulator cost is $8500, comparable to other same-generation modulators but well above the $3000 price tag for a 12–15 GHz device. We selected the gallium-arsenide polarization modulator over a $LiNbO_3$ modulator because of the diagonal tensor for the second-order nonlinearity. In other words, modulation around the Poincaré sphere should not result in scrambled polarization states, as one would expect with a $LiNbO_3$ modulator. This JGKB modulator can be implemented as a transmitter identically to modern M-Z modulators, by using a DC bias, an RF input to modulate polarization, and light from a conventional telecommunications diode laser. For more exotic photonic applications, such as quantum cryptography, a laser source with superior coherence, such as an erbium fiber laser, would typically be used.

Quadrature demodulation was accomplished by using a polarization controller (PC1), a 50/50 splitter, then a polarization controller (PC2a and PC2b) and a polarizer (P2a and P2b) on each channel. We used three polarization controllers to set PC2a and PC2b to have the desired relative phase after the light passed through the analyzing polarizers (P2a and P2b). At the same time, we allowed an "upstream" polarization control (PC1) to compensate for transmission fiber changes, which could range from 10 m in a small ICF experiment to ≥1 km in an underground test. A schematic of the demodulator appears in Figure 2.

The polarization control (PC1) essentially mapped the Poincaré sphere at the recording station to the Poincaré sphere of the modulator near the experiment. Since the polarization received at PC1 after traversing the transmission fiber was very sensitive to the fiber's temperature and mechanical

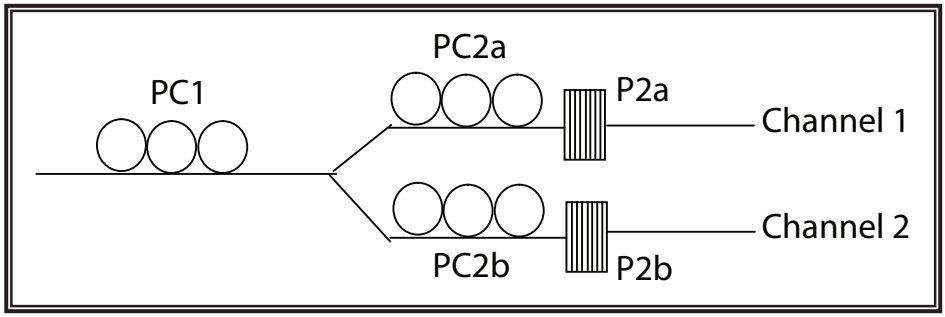

Figure 2. Polarization demodulator

conformation, PC1 would require automated, two-dimensional optimization to compensate for the slowly varying polarization changes due to the transmission fiber. The complexity of tracking this polarization, though not insurmountable, would create a significant cost increase per transmission channel and introduce several delicate instruments. The advantage of using the polarization scheme would be the ability to use a conventional diode laser as the light source, as detailed below.

Data from the polarization demodulator show the elegance of quadrature data unfolds, in which the arctangent of the input signal can be calculated. The input pulse we used was a slow (~500 ns) ramp of 12-V amplitude, so each channel passed through two extrema. The ramp with the unfolded data, showing both conventional arcsine unfolds of the individual channels and an arctangent unfold using both channels together, appears in Figure 3. Figure 4 shows the residuals when an arbitrary linear fit is subtracted from the data so that fine detail can be seen; the lower plot shows the normalized raw data from the two channels, demonstrating the locations of the modulation extrema.

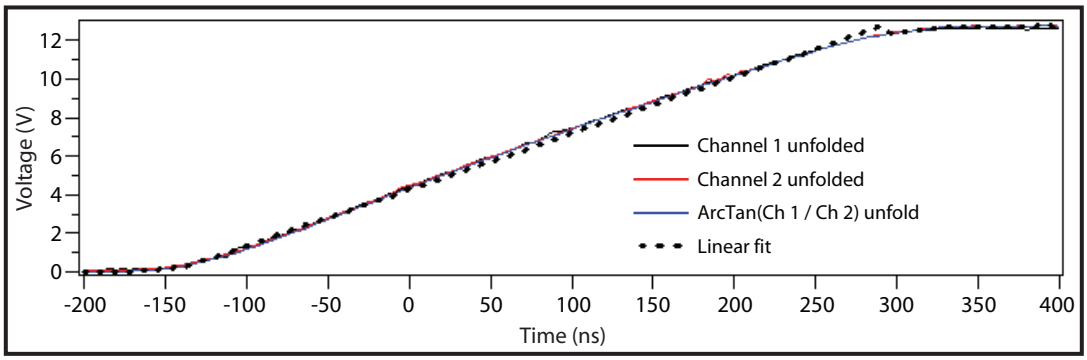

Figure 3. Ramp input unfolded from quadrature modulator data

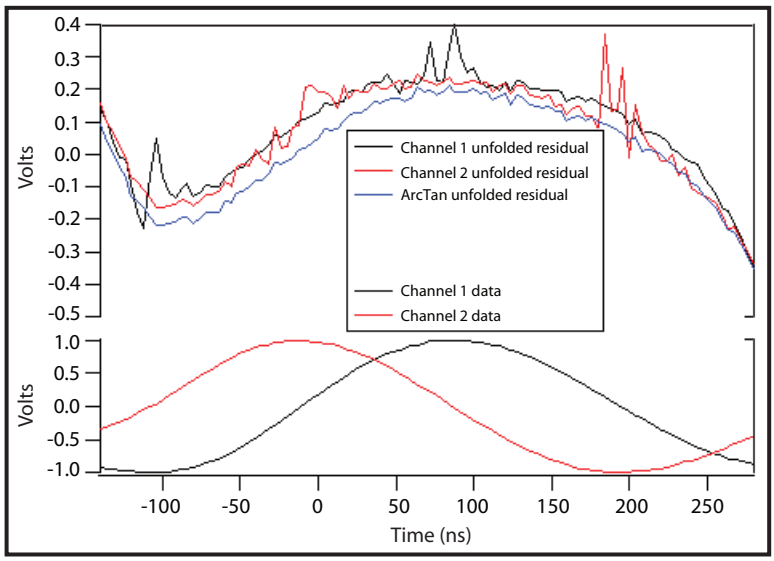

Figure 4. Residuals after line fit is subtracted

The second approach to quadrature demodulation employed a $LiNbO_3$ phase modulator and two "twinned" demodulation interferometers (Figure 5). The 2×2s are 50% fiber-optic couplers, and the Faraday rotator mirrors eliminate the need for polarization control or a polarization-maintaining fiber. The two delay loops would typically be longer than our experimental window of interest (e.g., ~100 ns), and would provide a "storage" of unshifted light to interfere with phase-shifted light from the experiment. Bias control, presumably using fiber-stretching devices, such as those available from Optiphase Inc., could be implemented as part of the delay loop.

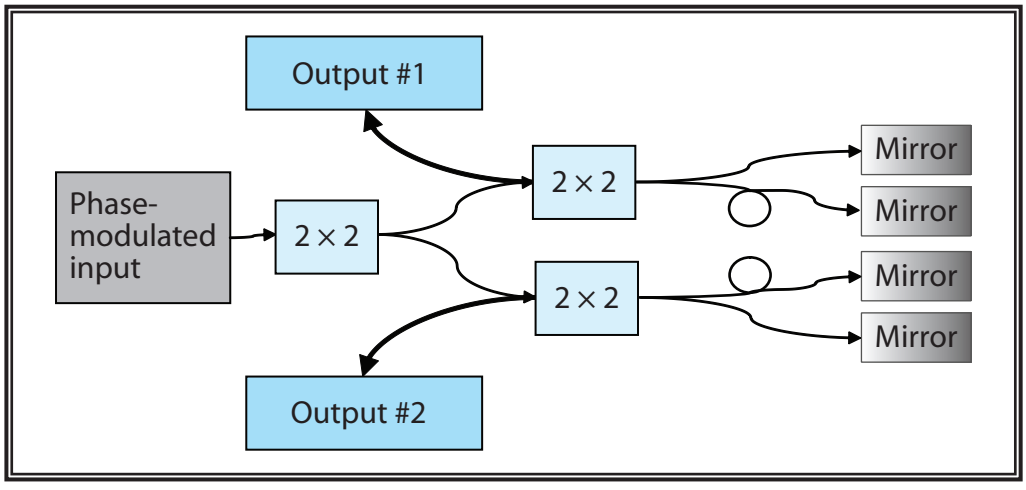

Figure 5. Twinned interferometer method for achieving quadrature demodulation

During testing, we discovered that the conventional laser diodes used in the telecommunication industry did not have low enough phase noise to serve in this system as a light source (though they had a measured linewidth of <100 kHz). Their phase coherence was only useful over delay lengths of <3 ns. Instead, we implemented a fiber-laser from NP Photonics, which had a very narrow linewidth of <5 kHz. The phase of the interferometer was found to drift appreciably with time, ~180 degrees every 2 sec. The phase drift changed direction approximately every 10 sec. Sources of this drift could have been the laser itself or thermal equilibration of the fibers. Extinction was nearly 100%, indicating that the issue was one of interferometer phase, not polarization or other anomalies. Given this drift rate, it is quite conceivable that we could lock this interferometer using automatic bias controllers driving fiber stretchers in the delay lines.

During the engineering of the delay lines, we made an additional, unrelated discovery: we found we could introduce a series of delays to optically replicate an incoming signal, and either interleave the pulses with the digitizer samples or average signal copies to improve the SNR. (An invention disclosure was submitted for this concept in FY 2006.) Figure 6 shows a schematic of the system used to duplicate pulses.

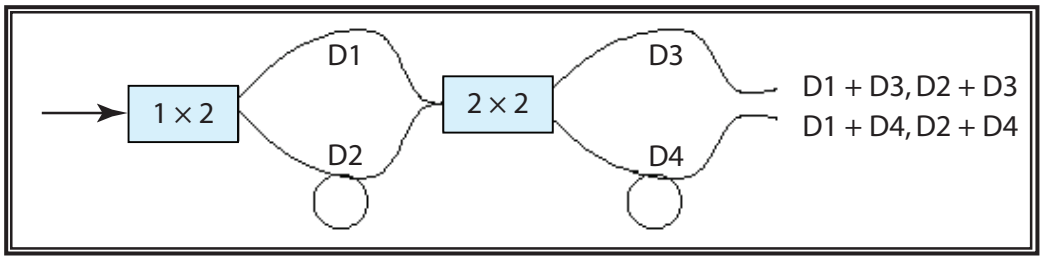

Figure 6. Delay line scheme for recording pulse copies, including four delay times (right)

By tuning D2 and D4, we were able to adjust the spacing between pulse arrivals such that when the records were time-shifted to compensate for delays, the effective sample rate was four times the actual digitizer sample rate on modern digitizers (160 GS/s rather than 40 GS/s). Conversely, if D2 and D4 were not carefully controlled, one could simply average the four copies to reduce the SNR. The records in Figure 7 show a 70-ps-wide pulse recorded in this manner on two scope channels. Prior to the one-shot recording, delays were tuned and amplitudes measured for data postprocessing, so there was no reliance on recorded data for the shifting and scaling parameters.

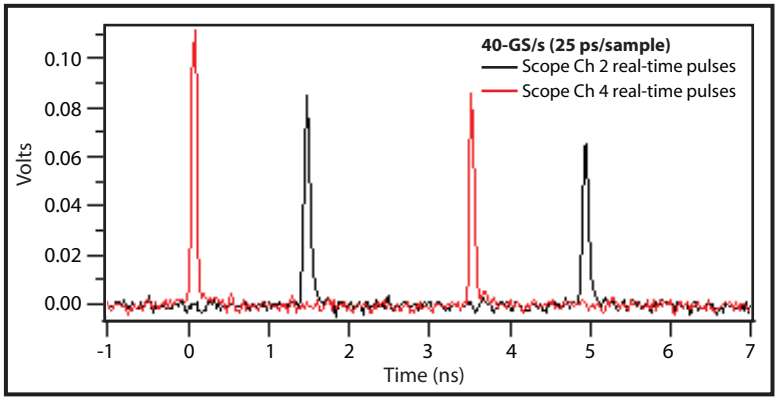

Figure 7. Four copies of input pulse recorded in real-time

When the data were interleaved, they overlaid very well with an equivalent-time (ET) record of the same pulse (Figure 8). The ET record had 2 TS/s, with no averaging, so the noise evident in the red line was caused by: (a) digitizer noise, (b) pulse-to-pulse amplitude variation, and (c) timing jitter. Figure 8 shows points from the four copies, with different markers for clarity.

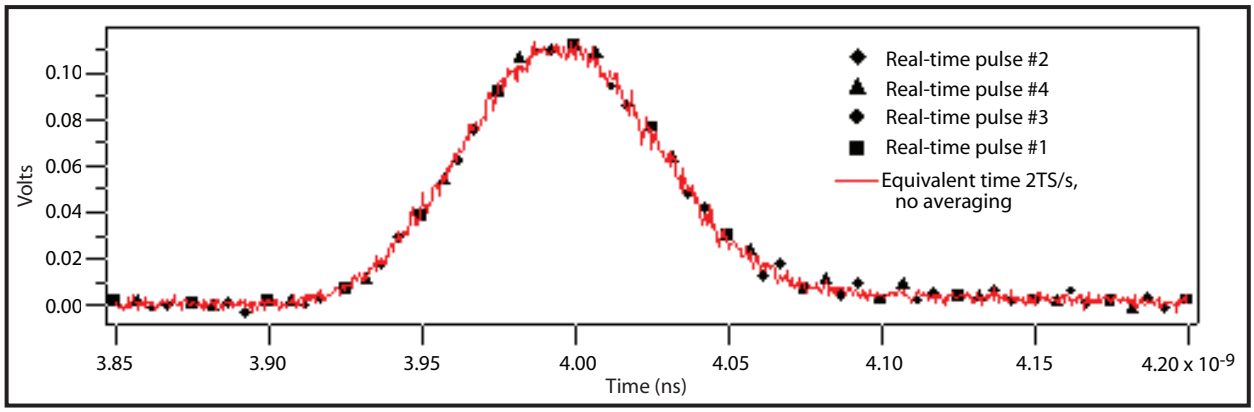

Figure 8. Interleaved real-time records (black marks) overlaid with ET record

Conclusion

We have successfully demonstrated high-bandwidth recording of quadrature optical signals via two methods: polarization modulation and phase modulation. The improvement in unfolded data was especially significant, since arctangent unfold can be used to recover data and eliminate regions of zero sensitivity. Because the polarization control required on the polarization scheme is cumbersome and expensive, we recommend a system based on phase modulators for systems to be fielded on large experiments. Automatic bias control of the phase demodulator should be achievable with off-the-shelf components, and we feel that this method is a superior way to transmit and record signals of varying bandwidth and high amplitude.

this page intentionally left blank

Applications of Si Nanowire and Carbon Nanotubes to Phototubes

Donald Ng[1]
Livermore Operations

Zinc oxide (ZnO) nanowires were grown on a quartz faceplate coated with indium-tin-oxide (ITO). Illumination of the nanowires with 254-nm UV light with applied voltages from 4 kV to 12 kV showed no photoenhanced field emission. Efforts to grow nickel oxide (NiO) nanowires on sapphire substrates were delayed, as was fabrication of Si nanowires that depended on ZnO work being completed and equipment becoming available. Several milligrams of multiwall carbon nanotubes (CNT) were dispersed in water with a commercial surfactant and spread onto glass faceplates as a conductive transparent coating. The uniformity of the coating was poor, and work has been suspended until new methods can be developed.

Background

Multialkali photocathodes used in phototubes made at LO degrade when exposed to air or contaminants. Previous work by Kendrick Liu (2001) involving Si field emitter arrays fabricated on a silicon substrate demonstrated the concept of photoenhanced field emission as a substitute for traditional multialkali photocathodes. Unfortunately, obstacles to utilizing these microscopic devices as photon detectors or photocathodes exist: it is difficult to fabricate the emitter arrays, and the sharp element tips eventually erode. In an effort to avoid both of these obstacles, the use of semiconducting nanowires as field emitters was investigated. Semiconducting nanowires can be fabricated by bottom-up approaches, where the nanowires are grown from the substrate, or by a top-down approach, such as that used in conventional semiconductor device manufacturing. The band gaps of some candidate semiconductor materials promise photosensitivities in the visible and near-UV.

A second part of this project was to investigate the use of CNT as a possible replacement of the Ni underlay on S-20 photocathodes processed at LO. The current 50-Å Ni layer increases electrical conductivity of the photocathode but reduces the light reaching the photocathode surface by one-half. We proposed that a thin layer of CNT might provide similar electrical conductivity but with less light absorption than Ni, thereby increasing the effective quantum efficiency of the photocathode.

[1] ngdp@nv.doe.gov, 925-960-2506

Project

Nanowire Growth

Three materials were chosen for this project, each offering a balance between ease of fabrication and potential band-gap energy. The easiest of the three to produce, ZnO, grows in an aqueous solution at 95°C and doesn't require any high-temperature processing or hazardous chemicals (Greene, 2003; Law, 2005; Greene, 2005). However, ZnO has a band gap of 3.4 eV, placing its absorption edge in the UV region and requiring a quartz substrate. The second material is NiO, which is grown in an aqueous solution at 300°C and 1500 psi pressure (Mintz, 2005). The band gap of NiO nanowires has been measured at 2.65 eV, placing its absorption edge in the visible blue region. However, the NiO nanowire growth conditions require the use of sapphire substrates, as quartz erodes under the required growth conditions. Si was the third material used in this study. With a band gap of 1.1 eV (Sze, 1983), Si allows good absorption of visible light, but the fabrication method does not work well on glass substrates. Without an epitaxial substrate to grow on, oriented Si nanowires could not be grown with bottom-up approaches such as the vapor-liquid-solid method that uses gas phase constituents. For Si, a top-down approach, deep reactive ion etching, in conjunction with nanoscale patterning using electron beam lithography, was considered.

Fabrication of ZnO nanowires was conducted under the auspices of the Molecular Foundry at LBNL. Using a process developed by Lori Greene and coworkers at the University of California, Berkeley, two quartz, 40-mm image-intensifier faceplates with 0.150-μm ITO thin film were coated with ZnO nanowires. ZnO seeds were formed by spinning on a zinc acetate solution, followed by pyrolysis at 300°C in an air oven. The ZnO seeds self-align their (0001) direction perpendicular to the substrate surface during the bake; this creates vertically oriented nanowires. ZnO nanowires roughly 1 μm long and 50–100 nm in diameter were grown by immersion in zinc nitrate solution (Figure 1).

A ZnO nanowire–coated faceplate was sealed to a 40-mm diode body under vacuum (Figure 2) and tested with high voltage (Figure 3). The gap between the nanowire–coated faceplate and a metal mesh used for electron extraction was set at 1.5 mm. However, application of voltages up to 12 kV did not produce any detectable field emission current. Illumination of the nanowires with a 254-nm UV light with 12 kV applied showed a current of 50 nA flowing across a 5-GΩ series resistor, but the measurement was not repeatable. The field gradient in the diode was 8 kV/mm on nanowire tips ~50 nm wide. In comparison, previous work with fabricated Si field emitter arrays having 100 V applied across a 0.4-μm gap gave a field gradient of 250 kV/mm (Liu, 2001). It is clear that a smaller gap between the nanowires and the extraction mesh must be maintained or much higher voltages are needed to achieve higher field strengths. Because of the very sharp tips of the nanowires, it was expected that lower voltages would be required to initiate field emission of electrons, but a better understanding

of the field gradient concentration at the nanowire tips from numerical modeling is necessary. Also, the electron mobility in ZnO nanowires had been determined to be 1–5 cm^2/Vs (Law, 2005), which compares with a value of 1500 cm^2/Vs for silicon (Sze, 1983).

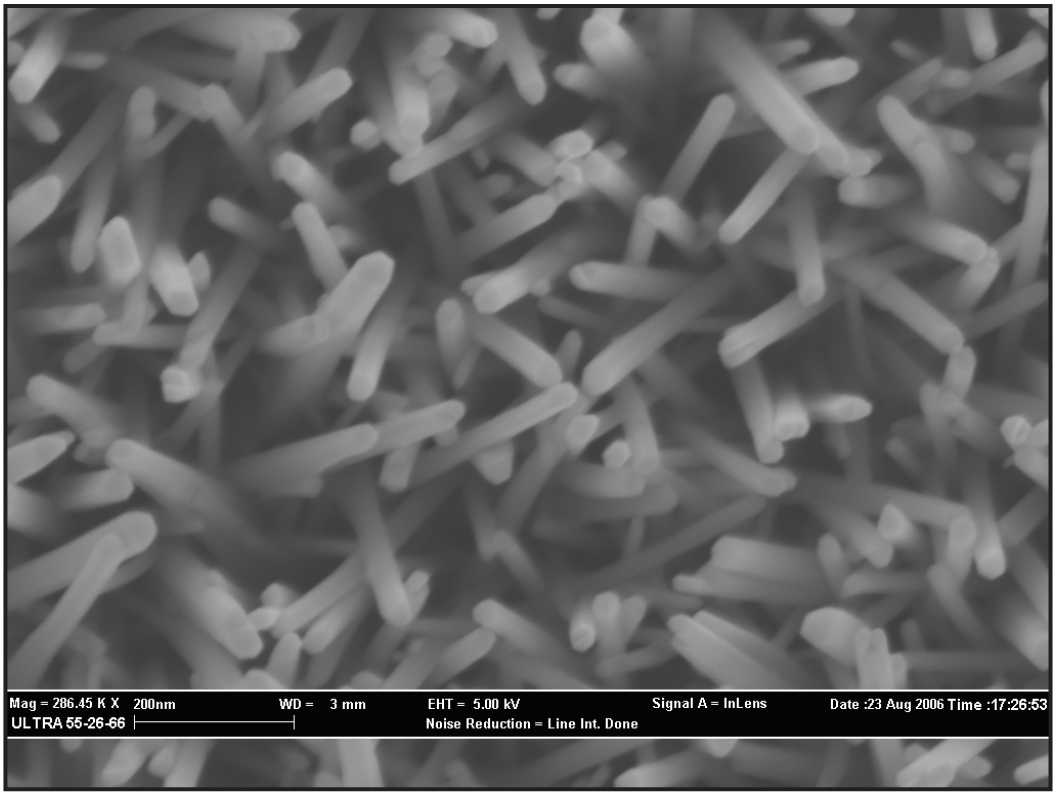

Figure 1. Scanning electron micrograph of 1-µm ZnO nanowires grown on an ITO–coated, quartz, 40-mm faceplate

Once it was discovered the NiO nanowires had a band gap of 2.65 eV and behaved as a semiconductor, despite the bulk material being an electrical insulator, an effort to utilize NiO nanowires as field emitters began midyear. A contract was signed with the Materials Science and Engineering department at UC Berkeley to grow NiO nanowires ~25 nm wide and 0.5–1 µm long. Using a method devised for growing NiO (Mintz, 2005) nanowires on Alloy 600, a Ni base alloy with 15% Cr and 8% Fe, NiO nanowires would be grown on $Ni._{80}Cr._{20}$ thin film deposited on 40-mm image-intensifier sapphire faceplates. The process involves reacting the substrate in lithium and boron hydroxide solution at 300°C at a pressure of 1500 psi to form NiO. Then, by applying a controlled potential to the substrate, growth of NiO nanowires can be initiated and controlled. The length of the nanowires is determined by the time of reaction.

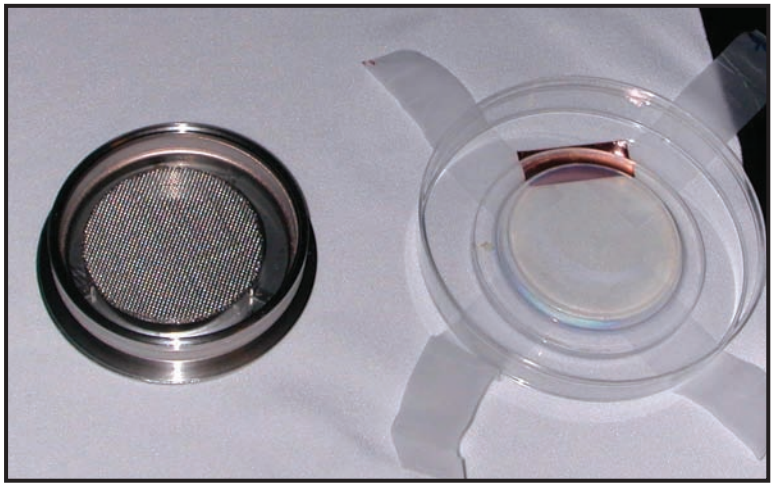

Figure 2. 40-mm diode body with extraction mesh and ZnO nanowire–coated quartz substrate

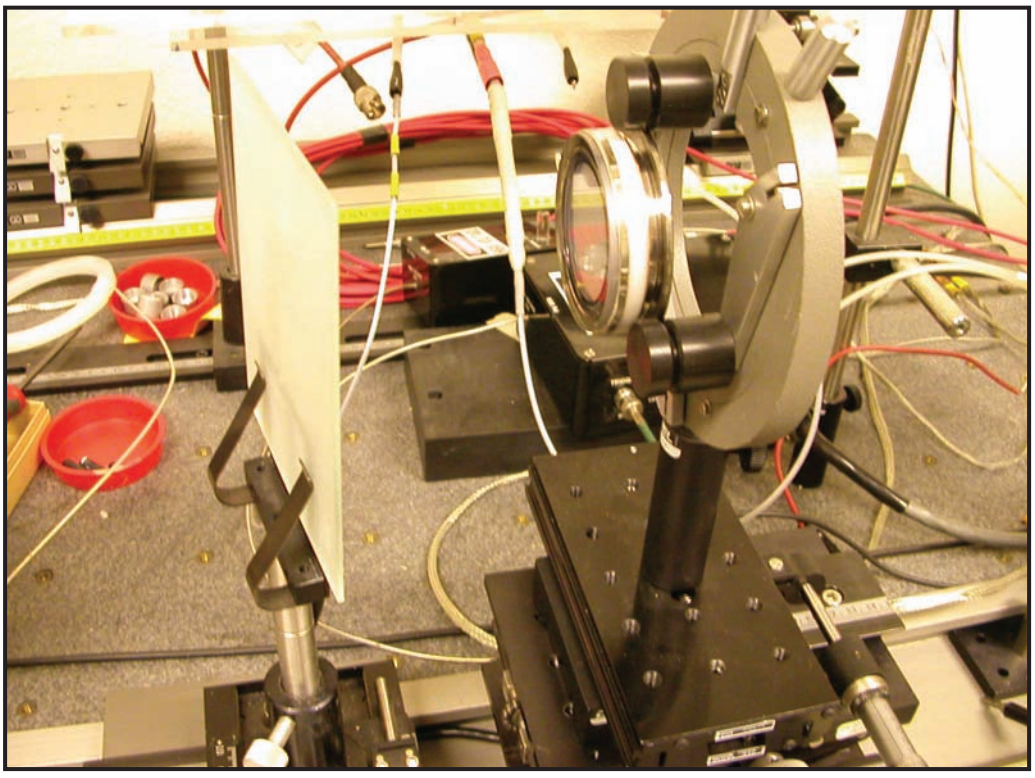

Figure 3. ZnO nanowire–coated diode body under test without UV illumination

A pressure vessel large enough to accommodate a 40-mm image-intensifier input window was procured and a titanium autoclave was designed (Figure 4). A schematic depicting the growth process is shown in Figure 5.

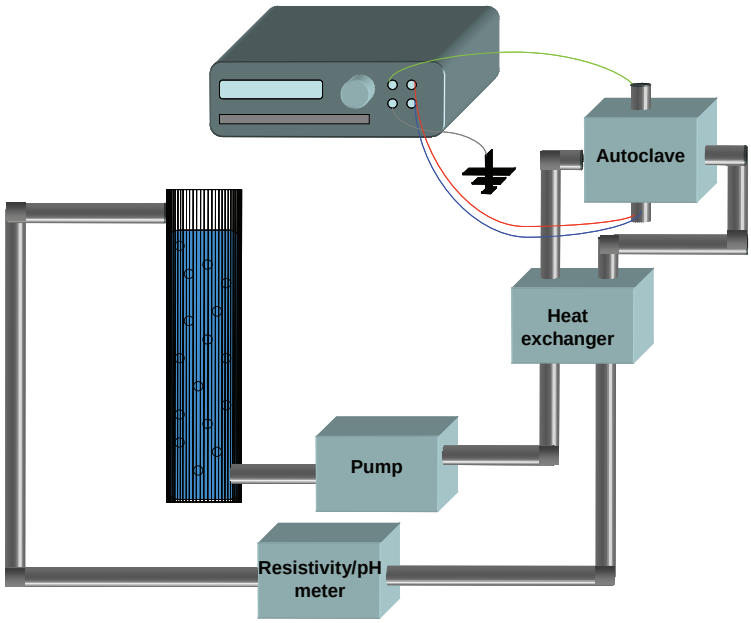

Figure 4. Layout of autoclave system for NiO nanowire growth

The effort to grow Si nanowires using a top-down approach took the form of a research proposal to the Molecular Foundry at LBNL. Because the work to grow ZnO nanowires had been approved prior to the proposal to fabricate Si nanowires, this work could not progress until the ZnO nanowire work was finished. When the Si nanowire project was approved, the e-beam lithography system required for this work was unavailable. As a result, the patterning and fabrication of Si nanowires did not occur.

CNT

A second part of this project was to investigate the use of CNT as a potential replacement of Ni as an underlay for S-20 photocathodes. Multiwall CNT was purchased from NanoLab, Inc., of Newton, Massachusetts, along with a dispersant, Nanosperse AQ. An aqueous solution was prepared with the CNT and dispersant and spun onto a 40-mm image-intensifier faceplate. The resulting films of CNT were nonuniform after drying, and various spinning speeds and solution-dispensing volumes did not solve the problem. Further effort was suspended to concentrate on nanowire fabrication.

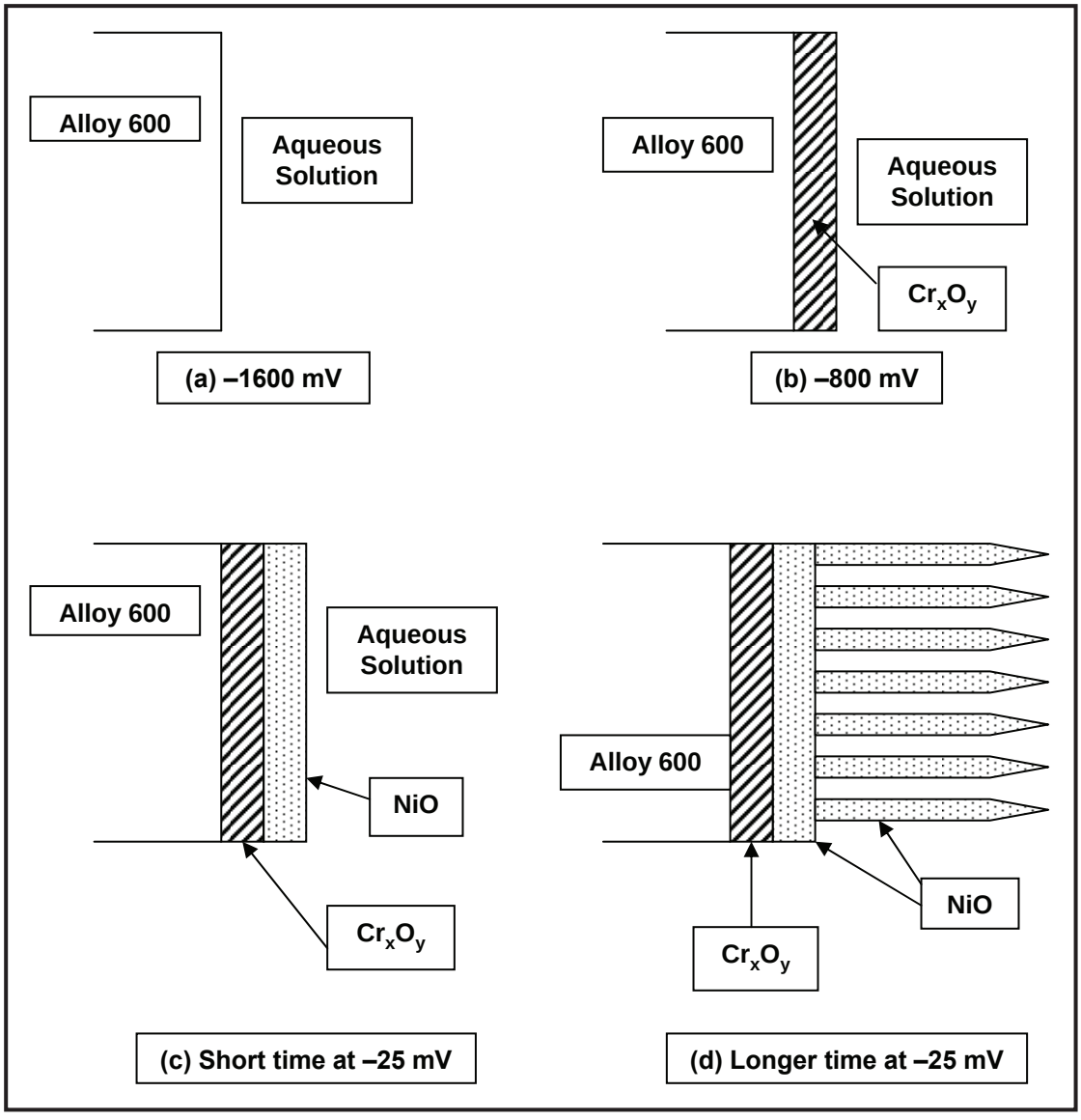

Figure 5. Schematic cross section of growth interface of NiO nanowires on Alloy 600 in 2 ppm Li+ and 1200 ppb B in water at 288°C

Conclusion

The growth of ZnO nanowires on an ITO-coated glass substrate was successful. Testing revealed the need to understand the field gradient at the nanowire tips to successfully set the extraction mesh distance and voltage. Fabrication of Si nanowires on a glass substrate presented unique problems, but the unavailability of a required e-beam lithography machine and the late approval of a research project proposal at the Molecular Foundry at LBNL prevented the fabrication of Si nanowires. The effort to grow NiO nanowires at UC Berkeley has so far resulted in the procurement and fabrication of an autoclave system to carry out the growth process. New techniques should be explored for depositing more uniform coatings of CNT on 40-mm image-intensifier input windows.

It is hoped that the fabrication of NiO and Si nanowires, which have absorption in the visible light region, and in the case of Si, higher electron mobility, will lead to reproducible field emission and the observation of light enhancement. For the use of CNT as a transparent conductive layer as an underlay for S-20 photocathodes to be viable, the CNT coating properties must be uniform and reproducible before it can be evaluated against Ni.

References

Greene, L. E., M. Law, J. Goldberger, F. Kim, J. C. Johnson, Y. Zhang, R. J. Saykally, P. Yang, "Low-Temperature Wafer-Scale Production of ZnO Nanowire Arrays," *Angewandte Chemie Int Ed.* **42** (2003) 3031–3034.

Greene, L. E., M. Law, J. Goldberger, D. H. Tan, M. Montano, G. Somorjai, P. Yang, "General Route to Vertical ZnO Nanowire Arrays Using Textured ZnO Seeds," *Nano Letters* **5**, 7 (2005) 1231–1236.

Law, M., L. E. Greene, J. C. Johnson, R. J. Saykally, P. Yang, "Nanowire Dye-Sensitized Solar Cells," *Nature Materials* **4** (June 2005) 455–459.

Liu, K.-X., "Broad Spectral Response Photocathode Using Gated Silicon Field Emitter Array," Bechtel Nevada, Livermore Operations, Livermore, CA, 2001.

Mintz, T. S., Y. V. Bhargava, S. A. Thorne, R. Chopdekar, V. Radmilovic, Y. Suzuki, T. M. Devine, "Electrochemical synthesis of functionalized nickel oxide nanowires," *Electrochemical and Solid State Letters* **8,** 9 (2005) D26–D30.

Sze, S. M., ed., *VLSI Technology*, McGraw-Hill Book Company, New York, 1983, 640.

Portions of this work were performed at the Molecular Foundry, Lawrence Berkeley National Laboratory, which is supported by the Office of Science, Office of Basic Energy Sciences, of the U.S. Department of Energy, under Contract No. DE-AC02--05CH11231.

this page intentionally left blank

Framing Tube Performance Upgrades

J. M. Richter[1]
Livermore Operations

The framing tube developed in previous SDRD research has become the basis for subsequent SDRD projects, and users have requested such performance upgrades as higher image resolution with less distortion and a larger active area. Electron trajectory modeling with Charged Particle Optics' three-dimensional boundary element code (CPO-3D) was used to determine the performance limits of the tube and to explore possible improvements. Due to difficulties with analyzing the modeling output, the initial goal of generating design drawings of proposed changes was not met. In the course of this work, several pre- and postprocessing routines were developed that will facilitate future modeling efforts.

Background

The framing tube developed under SDRD funding (Baker, 2004; Ng, 2004) has been the basis for several other SDRD projects, including the long data-length transient recorder (Sun, 2005, 2006) and the x-ray framing tube (Sun, 2006). To explore possible improvements in the tube, electron trajectory models were generated with the CPO-3D boundary element code (CPO, 2006), which had been evaluated in an earlier SDRD project (Richter, 2006).

The framing tube is an electrostatic inverting image tube with two orthogonal pairs of deflection plates that allow the input image to be sequentially displayed at several discrete locations on the output screen. Two mesh electrodes near the photocathode extract the photoelectrons into the tube and also allow the electron flow to be gated off while the output image is being repositioned on the screen. The four-frame and nine-frame display modes are illustrated in Figure 1.

In the four-frame mode, the image at the screen is symmetrically deflected by equal amounts along both transverse axes so each image tends to exhibit the same distortions. For the nine-frame mode, the central image is undeflected, and all the surrounding images (X, Y, and XY) are obtained by applying X-only, Y-only, or X-and-Y deflection potentials. Table 1 gives the nominal dimensions of the cathode and screen, the individual input and output image sizes for both display modes, the composite multiframe display size, and the required orthogonal image deflection from screen center for the multiframe mode.

[1] richtejm@nv.doe.gov, 925-960-2511

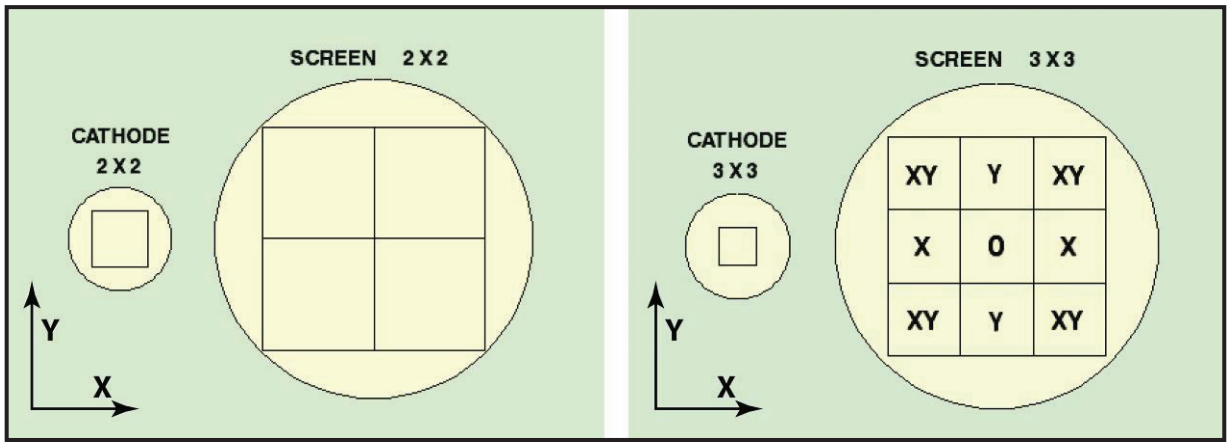

Figure 1. Nominal framing tube image layouts for four-frame and nine-frame display modes. Note that the tube provides an image magnification of two. The input at the cathode must be masked to prevent image overlap at the screen.

Table 1. Nominal dimensions for the framing tube display modes depicted in Figure 1

Framing Tube Display Modes					
			Image size or Deflection (mm)		
Framing Tube Component	Active Diameter (mm)	Inscribed Square (mm)	4-frame 2 x 2	9-frame 3 x 3	Image Description or Function
Cathode	26	18	14	9	Input
Screen	80	56	28	18	Output
Screen Display			56	54	Multiframe
Frame Deflection			14	18	X or Y Deflect

Project

Several framing tube users were consulted to obtain recommendations for performance upgrades and tube modifications. The consensus was improved image quality with higher resolution and lower distortion over the entire active screen area. One user requested a larger active area and a lower image magnification (currently 2X) to facilitate lens input coupling and to increase image brightness at the screen.

The existing framing tube design was based on electron trajectory modeling with SIMION 3D (SIMION, 2006). This finite-difference code uses rectangular mesh cells, which can never accurately model sloped or curved electrodes. The CPO-3D trajectory code used for this project employs conformal boundary elements to accurately model the electrode profiles. Electron trajectories are then calculated from the charge distribution on the electrodes.

The CPO-3D code was updated by the vendor to provide all of the trajectory intercept data needed to fully automate the analysis of focal quality. The updated code identifies the intercept data for each ray at each test plane and electrode in a concise format that is convenient for input to a postprocessor. Near the end of the project, upgraded versions of the Field Precision 2D and 3D finite element trajectory codes (Field Precision, 2006) were purchased and installed to provide validation of the CPO-3D results.

To begin, a quarter model of the optical framing tube with transverse X and Y symmetry was generated for CPO-3D. This model supports electron trajectories with common-mode potentials on the two sets of deflection plates. Later, a full CPO-3D model was generated to support deflection studies. A filename structure was devised to systematically track and catalog the large number of trajectory files that were created.

Interactive data language (IDL) (IDL, 2006) pre- and postprocessor routines were developed to generate ray launch parameters for CPO-3D and to read, analyze, and plot the trajectory output data. The IDL program FRAY generates launch parameters for a flat cathode with any number of rays launched from multiple positions with specified emission angles and energies along the transverse X and Y axes.

The IDL program ReadCPO extracts trajectory data from a CPO output file with any number of rays, launch points, and test planes. The program calculates the mean position, energy, travel time, magnification, focal spot size, eccentricity, and focus condition for each ray launch group at each test plane or electrode intercept. Ideally, all of the rays from a given launch point should come to a point focus at the screen. By examining the velocity components of the outermost rays of each launch group at each test plane, it can be determined whether the test plane is before or after best focus, i.e., whether the rays are converging or diverging. These calculated results, together with the ray launch positions and the operating potentials, are saved in an IDL data file and a print file. The ReadCPO program can be readily modified to handle the output generated by the Field Precision modeling codes.

The IDL data file from ReadCPO can be used to generate multiframe focal spot plots or to perform additional analyses. IDL iTool object graphics were used to generate a gridded array of plots depicting the spot profile of the ray intercepts for each selected launch point. A reference circle can be provided for scale reference. The object graphics can be easily manipulated via a point-and-click interface. New plots can be generated via IDL batch files. These files can be edited as needed to select the desired data and plot format.

After determining the X and Y deflection sensitivities via several CPO-3D test models, the focal properties for the nine-frame display mode were examined via four launch points at the corners of one quadrant of the input image. Figure 2 shows the electron trajectories in a CPO-3D model with dual deflection, and Figure 3 shows these trajectories projected onto the X–Z plane. Note that the Z axis coincides with the tube axis and that the X deflection plates precede the Y deflection plates.

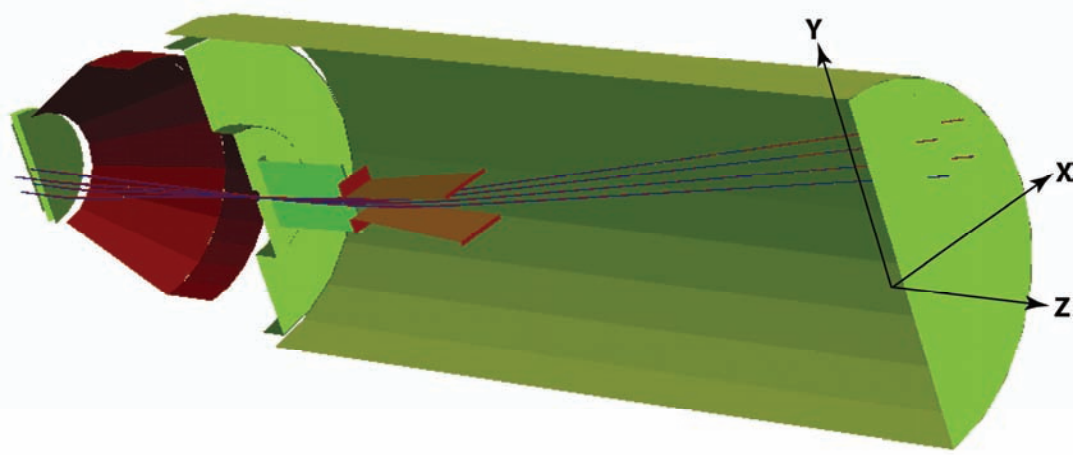

Figure 2. CPO-3D framing tube model showing four groups of five rays emitted from the corners of one 5-mm quadrant at the cathode. The rays have been deflected up (+Y) and to the right (+X) by 18 mm, thus representing the outer quadrant of a corner image in the nine-frame display mode (see Figure 1).

Four separate runs were made with the same four launch points but with different deflection potentials to obtain 16 focal spots at the screen. The nominal positions of the launch points at the cathode and the ray intercepts at the screen are shown in Figure 4. As noted in Table 1, nominal deflections of 18 mm up, right, and diagonally are required to simulate the nine-frame display mode. The operating potentials for these models were 0, 180, 220, 260, and 15000 V for the cathode, mesh-1, mesh-2, focus, and anode electrodes, with X and Y deflection potentials of 482 and 574 V, respectively, and no common-mode deflection bias.

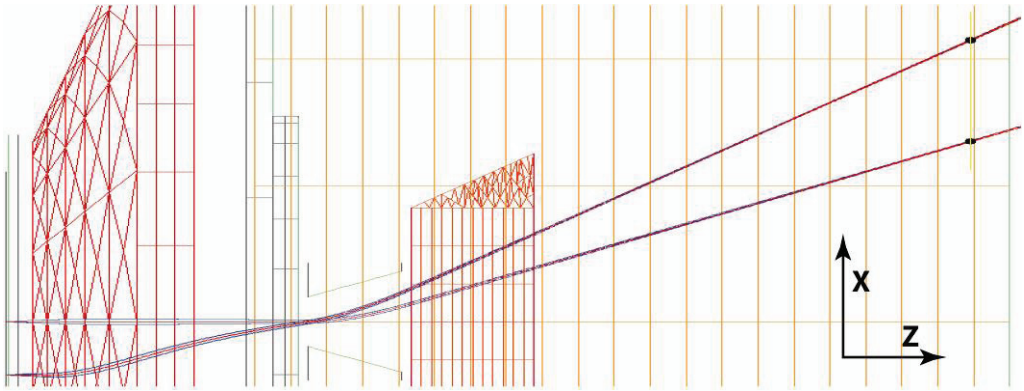

Figure 3. View of the trajectories in Figure 2 projected onto the X–Z plane, showing 18-mm deflection along the X axis with the X deflection plates shown in profile. The boundary cells for each electrode are shown with the same colors as Figure 2.

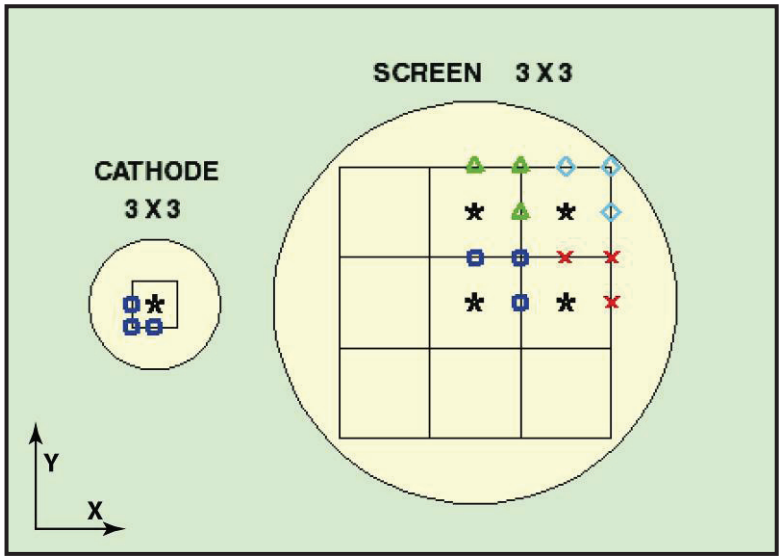

Figure 4. Location of the electron launches from one quadrant of the source image at the cathode and the locations of the ray intercepts at the screen for the undeflected image (blue square), X deflection (red cross), Y deflection (green triangle), and XY deflection (cyan diamond). The asterisks mark the center of each image. The focal spots at each of the indicated screen positions are shown in Figure 5.

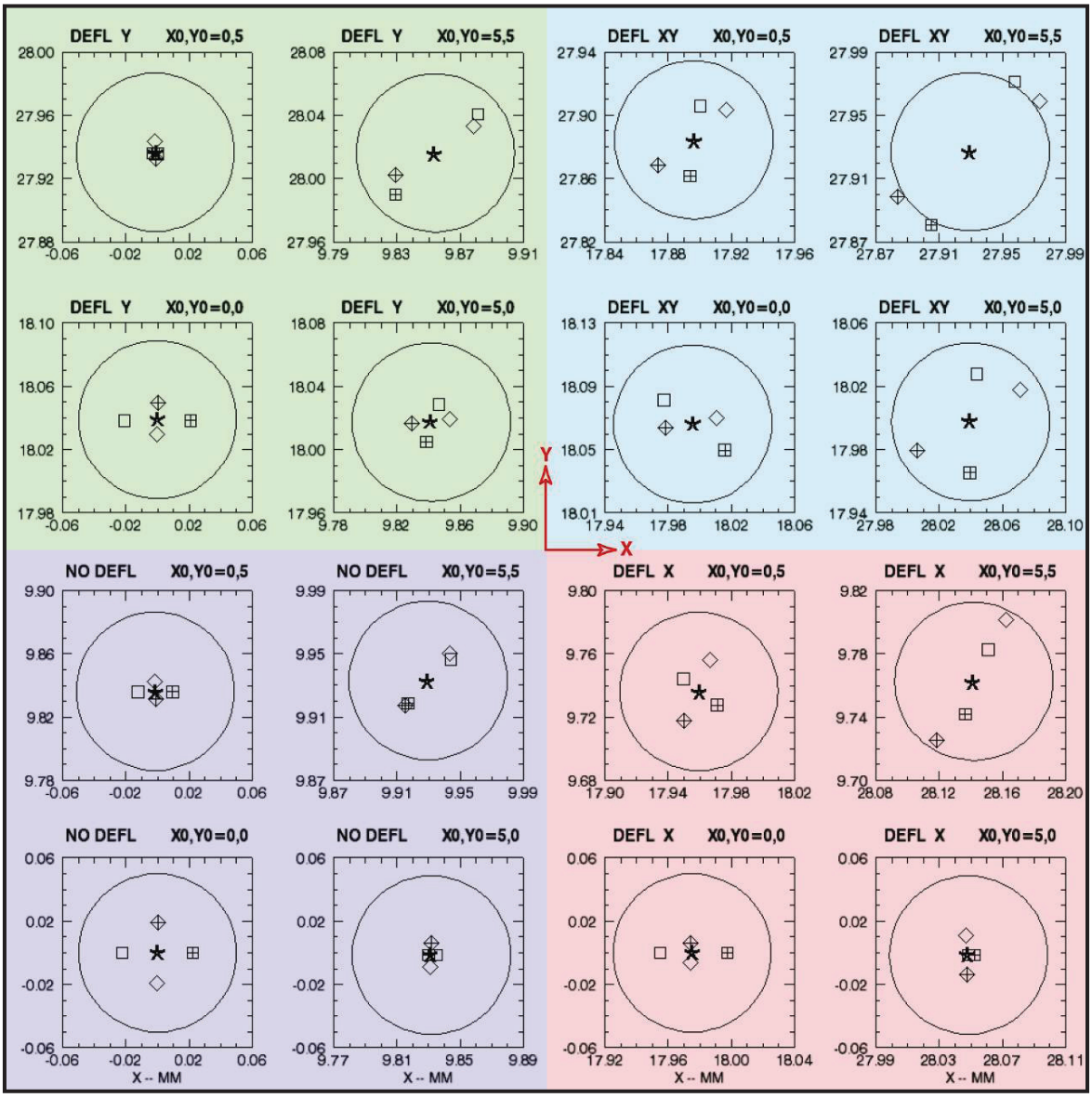

Figure 5. Spot diagrams representing the screen intercepts for four groups of five rays from one 5-mm quadrant on the cathode. The focal spots are arranged and color-coded to match Figure 4. The ray starting position and deflection direction are noted. The 100-µm reference circle is centered on the mean position of each group. Asterisks indicate rays emitted parallel to the tube axis. Rays emitted at ±10° in the X and Y directions are marked with squares and diamonds, respectively, and with a + sign for positive emission angles.

To provide some measure of focal quality, five 1-eV electrons were emitted at each launch point with emission angles of 0 ±10° in the X–Z and Y–Z planes. The screen intercepts for the 16 focal spots are shown in Figure 5. The background colors for each quad of focal spots match those in Figure 4. Only one set of focal spots (top right) failed to fit inside a 100-μm circle. Resolutions ranged from 9 to 90 line pairs per millimeter.

The relative position of the rays in the focal spots provides some information about the focal condition. If the rays are converging when they reach the screen, the rays with positive emission angles will be above (Y axis) or to the right (X axis) of the rays with negative emission angles. The spot pattern at the lower left in Figure 5 indicates that the rays are still converging and that the screen is positioned before the best focus. Because both the cathode and screen are flat, rays emitted away from the tube axis will have a longer travel path and a tendency to reach best focus prior to reaching the screen. Deflected rays will have an even longer path length, exacerbating this situation. Beam deflection also tends to shorten the focal length.

Note that the rays emitted from the outside corner of the source image are all diverging at the screen. They also exhibit an apparent rotation whereby all the rays are aligned with the diagonal from the tube axis. Some of this rotation could be caused by field interactions between the two sets of deflection plates, but the rotation with no deflection was not expected. There could be some distortion introduced by the interaction of the spherical field at the aperture with the planar field at the first deflection plate. This model was completed near the end of the project; therefore, diagnostic runs were not made to analyze this situation.

Operating experience with the LO streak tube has shown that a common-mode deflection bias shortens the focal length along the deflection axis without affecting the transverse focal length. Since each frame on the framing tube screen is generated by a different set of four potentials on the two pairs of deflection plates, it should be possible to optimize the focus of each individual frame by adjusting the common-mode bias on one or both sets of deflection plates.

Conclusion

The IDL pre- and postprocessors developed for this project provide a convenient means to generate and analyze electron trajectories via CPO-3D. The IDL codes can be readily adapted for use with the Field Precision trajectory codes. IDL's multiplot format, combined with the imaging calculations from ReadCPO, assist the evaluation of image quality, resolution, and distortion as a function of electrode configuration and operating potentials. The plot layout can be readily changed to any desired one- or two-dimensional grid.

These IDL processing tools used in conjunction with the CPO and Field Precision trajectory codes provide a powerful mechanism for analyzing the performance of both new and existing tube designs. Slight differences in the front-end geometry of the optical and x-ray framing tubes need to be

evaluated. The possibility of improving the uniformity of focus across the entire output screen by adjusting the common-mode bias on one or both sets of deflection plates on a frame-by-frame basis should be explored.

Laboratory validation of modeling results is critical before committing to new designs. Eight new high-voltage power supplies are now being configured for the ganged voltage control needed to fully test and characterize a framing tube.

References

Baker, S. A., "Framing Tube Design and Fabrication," *Nevada Test Site–Directed Research, Development, and Demonstration*, FY 2003, Bechtel Nevada, Las Vegas, Nevada, 2004, 123–126.

CPO, Charged Particle Optics, boundary element code, CPO Ltd., http://www.electronoptics.com/, accessed September 28, 2006.

CPO, Charged Particle Optics, boundary element code, http://www.simion.com/cpo/, accessed September 28, 2006.

Field Precision, finite element code, Field Precision LLC, http://www.fieldp.com/index.html, accessed September 28, 2006.

IDL, Interactive Data Language, ITT Visual Information Solutions, http://www.ittvis.com/idl/, accessed September 28, 2006.

Ng, D., "Framing Tube Fabrication," *Nevada Test Site–Directed Research, Development, and Demonstration*, FY 2003, Bechtel Nevada, Las Vegas, Nevada, 2004, 135–136.

Richter, J. M., "Electron Trajectory Codes for Image Tube Design," *Nevada Test Site–Directed Research, Development, and Demonstration*, FY 2005, Bechtel Nevada/National Security Technologies, LLC, Las Vegas, Nevada, 2006, 99–105.

SIMION, finite difference code, http://www.simion.com/, accessed September 28, 2006.

SIMION, finite difference code, Scientific Instrument Services, http://www.sisweb.com/simion.htm, accessed September 28, 2006.

Sun, K.-X., "Ultra-High-Speed, Long-Data-Length Transient Recorder," *Nevada Test Site–Directed Research, Development, and Demonstration*, FY 2004, Bechtel Nevada, Las Vegas, Nevada, 2005, 305–309.

Sun, K.-X., "Two-Dimensional, Long-Data-Length Transient Recorder (Phase II)," *Nevada Test Site–Directed Research, Development, and Demonstration*, FY 2005, Bechtel Nevada/National Security Technologies, LLC, Las Vegas, Nevada, 2006, 349–357.

Sun, K.-X., "Versatile, Higher Dimension X-ray Imager," *Nevada Test Site–Directed Research, Development, and Demonstration*, FY 2005, Bechtel Nevada/National Security Technologies, LLC, Las Vegas, Nevada, 2006, 359–370.

this page intentionally left blank

Versatile, Higher Dimension X-ray Imager

Travis Pond, Ke-Xun "Kevin" Sun,[1] John Yuhas
Livermore Operations

During this SDRD research, we made significant progress in developing the versatile, higher dimension x-ray imager. Multifunction scanning electronics for the image tube, mounts for the image tube, a microchannel plate intensifier (MCPI) and CCD camera, and the associated test system were designed and built. The project team has developed a functioning x-ray imager that may benefit from further research and development.

Background

The versatile, higher dimension x-ray imager may be used in applications such as advanced laser fusion ignition experiments and high-energy density physics studies. The imager takes advantage of the NSTec-designed optical framing tube, which is equipped with a pair of deflection plates in each of two orthogonal axes. The versatility of the camera is evident in its several operational modes: streaking in orthogonal directions, raster scan, or multiframe image capture. Previous research focused on design and fabrication of the optical framing tube, the x-ray framing tube, and the high-voltage RF electronics, plus the demonstration of the raster scan operation of the framing camera. The work done this year also included the design and construction of the versatile x-ray imager and the associated testing system, plus the repair of the optical framing tube.

Project

Multifunction Scanning Electronics

The scanning electronics enable two key functions: raster scanning of the electron beam, and streaking in both directions.

Initial versions of the electronics were designed and tested in previous SDRD projects (Sun, "Versatile," 2006; Sun, "Two-Dimensional," 2006). In the current effort, the goal was to improve the circuitry and then integrate it into a multifunction unit. Two such units are needed for each versatile camera. Figure 1a shows the block diagram and two views (b, c) of the prototype construction in the framing camera enclosure. The raster scan function is realized with a 600-V RF generator at 14 MHz. The ramp board generates a 3-kV ramp for sweeps. At a full sweep of 600 V, the effective sweep time

[1] sunke@nv.doe.gov, 925-960-2514

is ~1 ns. Other electronics circuits are mounted on a separate card because of the size of the prototype. Specifically, an additional synchronously triggered oscillator-amplifier chain generates an adjustable step voltage from 100 kHz to 1 MHz.

Optical Versatile Imager

Because the raster optical framing tube had been successfully used to demonstrate the raster scan concept in our SDRD project last year, we attempted to test the dual streaking concept with the same tube. However, the tube needed repair for a vacuum leak, so the tests could not be completed.

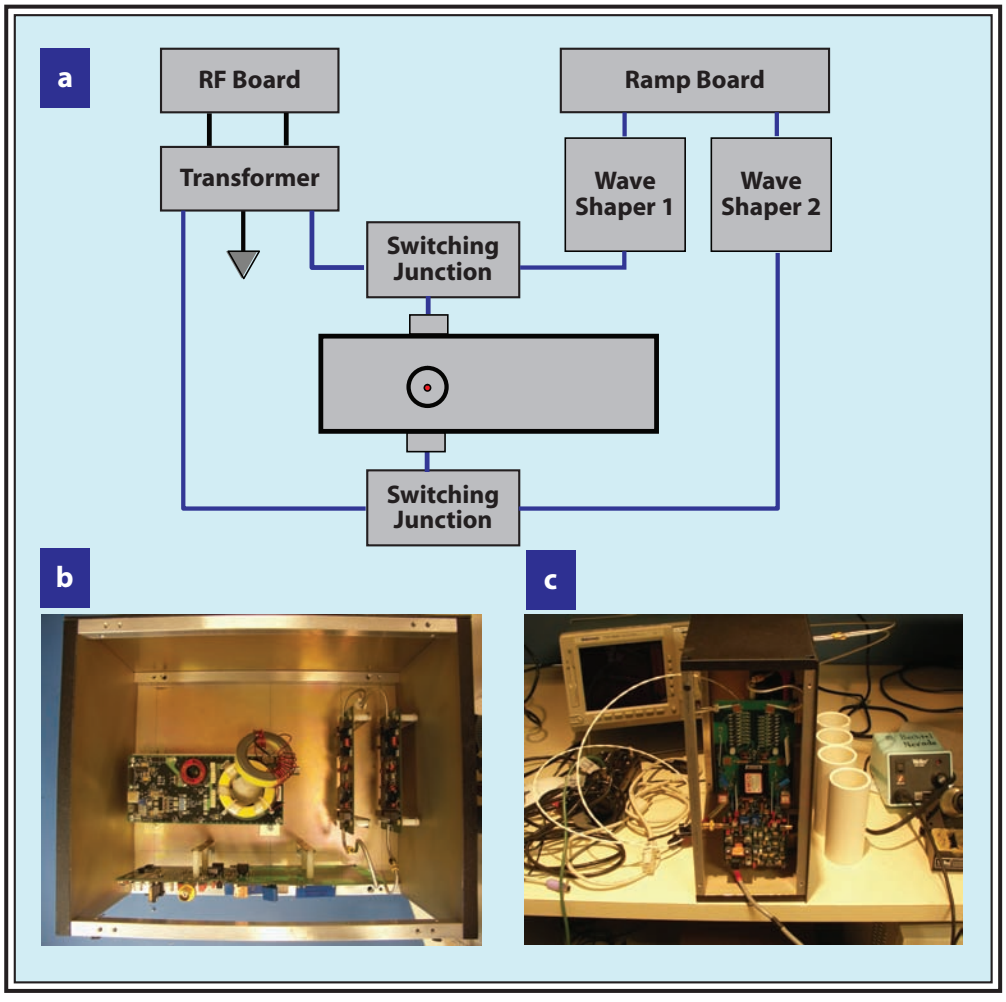

Figure 1. (a) Electronics block diagram for the multifunction scanning unit, (b) electronics box prototype construction top view, (c) electronics side view; the circuit is under test

Versatile X-ray Imager Design

The x-ray framing tube, designed and fabricated under another SDRD project (Sun, "Two-Dimensional," 2006) held a good vacuum seal and was therefore used in the design and fabrication of the x-ray imager. The x-ray framing tube must be operated under a high vacuum. Consequently, the design process became more complicated. In addition, based on previous tube testing results and experiences, we wished to have a complete design at the first attempt, to avoid expensive future modifications. The design goals were based on realistic fusion diagnostic requirements. Specifically, the design requirements incorporated the following important features:

1) The vacuum interface at the front end of the x-ray framing tube must accommodate an imaging snout to support realistic imaging experiments. The imaging snout will entirely reside inside the vacuum; therefore, a second vacuum interface, in addition to the x-ray framing tube flange, will be implemented.

2) The associated test vacuum system should allow various imaging snouts to be used. The distances between the target chamber center and the pinhole plane, and the tilt angles of the snout-camera assembly, should also be adjustable.

3) The mechanical design must allow the x-ray framing tube to safely operate at 15 kV without using potting.

4) The CCD camera mechanical design must allow flexible imaging sensitivity by accommodating a swappable MCPI, and image size settings by allow both contact and telescope imaging relay from with MCPI or streak tube output screen.

The final design met all these self-imposed requirements. Figure 2a shows a model of the design, while Figure 2b shows an assembly drawing of the large parts: the x-ray framing tube, front vacuum panel, adjustable connection bellow, CCD sliding mounts, and modularized chassis.

Versatile X-ray Imager Construction Details

Following the design was the construction of the versatile x-ray imager and test vacuum system. Extensive testing led to further design improvements that were incorporated into the final construction. Figure 3a is a front side view of the camera, emphasizing the x-ray framing tube, and Figure 3b is a rear side view of the camera, emphasizing the CCD mounting mechanism.

The CCD mount and its base box can house a CCD camera and an MCPI, allowing direct coupling of the x-ray framing tube to the intensified CCD. We estimate that the x-ray sensitivity of the camera will be enhanced by ~100X compared with the previous test configuration, in which the coupling between the CCD and framing tube output screen was through free-space imaging optics, and there was no MCPI between the CCD and the framing tube.

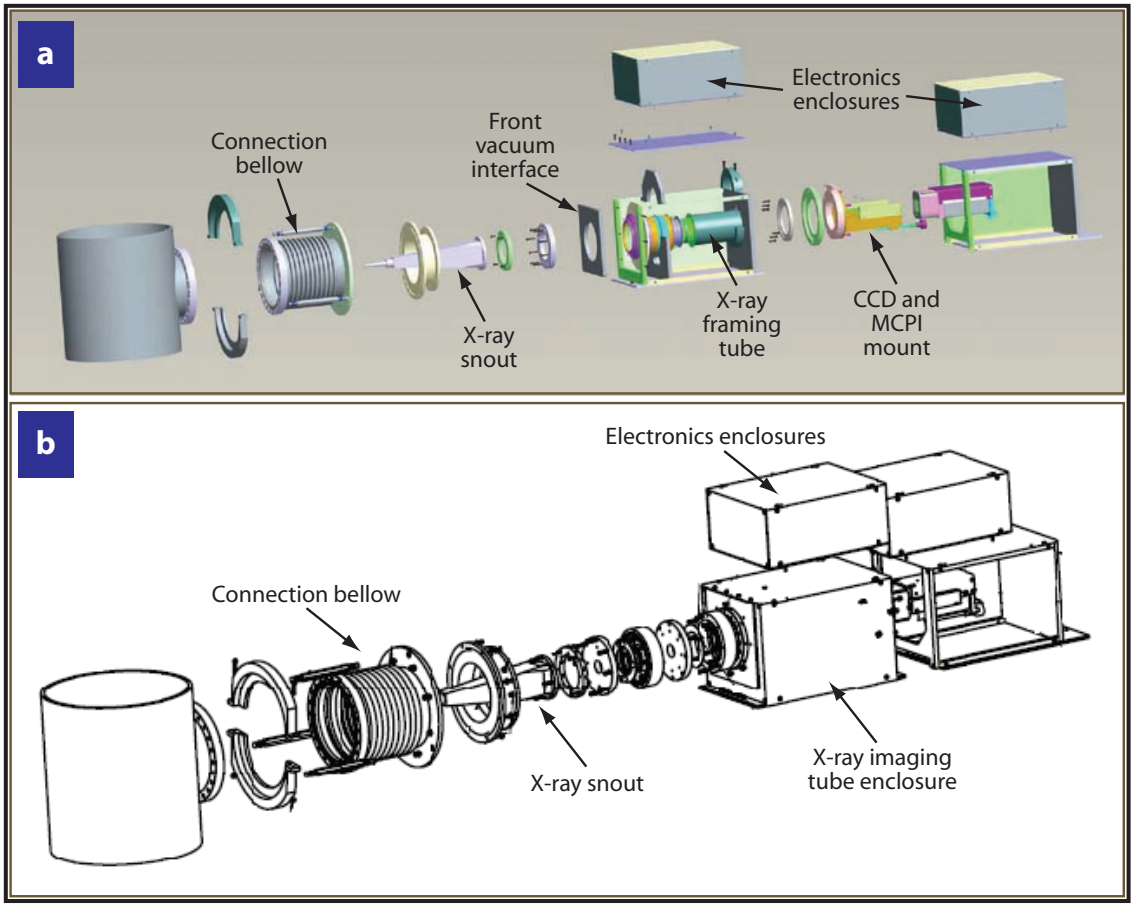

Figure 2. (a) Model for the versatile x-ray imager, (b) partial assembly drawing showing the front-end vacuum interface

The vacuum interface front panel, shown in Figure 3c, is adjustable in three dimensions: along the optical axis and the two orthogonal axes. This feature ensures alignment while minimizing potential stresses to the tube's sensitive structure. The adjustability provides other benefits: quick exchange of framing tubes with slight dimensional differences and more precise alignment for imaging or spectroscopic experiments.

The hole patterns on the vacuum panel are compatible with the NSTec x-ray streak camera. The entire family of imaging snouts designed for the x-ray streak camera can be mounted on the versatile x-ray imager.

Much effort has been devoted to interface design. The vacuum seal design is illustrated in the model in Figure 3d.

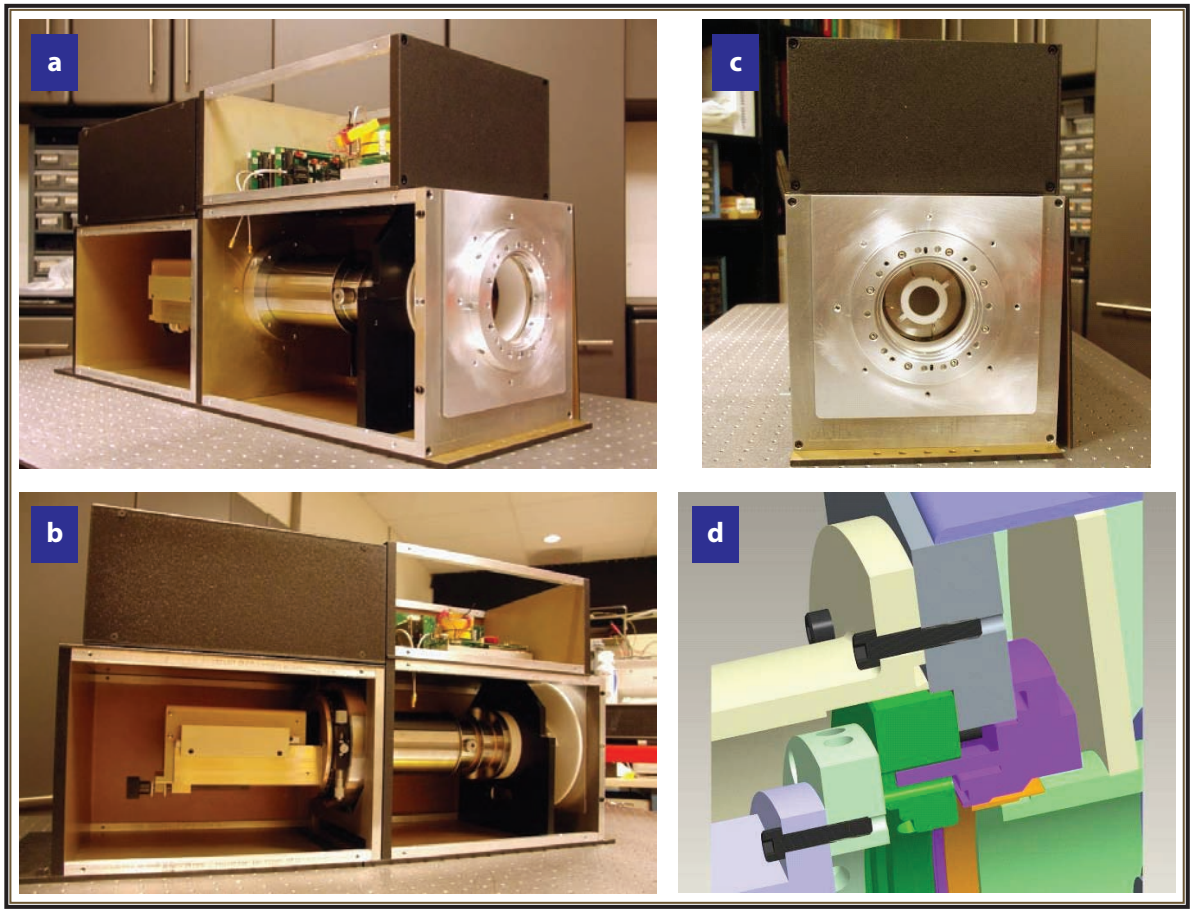

Figure 3. (a) The versatile x-ray imager: front side view. (b) The versatile x-ray imager: rear side view. (c) Front view showing the photocathode aperture, the flange, and the vacuum front panel. (d) Vacuum seal detail.

The modular design of the camera chassis provides flexibility for further development of the electronics system. Because the camera operates at high voltages, an insulative plate between the front flange and the electrode lead section was added. This structure has been tested using 15 kV of high voltage.

Conclusion

In the past two years, a small SDRD team has undertaken the challenge of developing a new class of novel x-ray imagers that could be used to support advanced fusion diagnostics. We designed, fabricated, and improved the optical framing tube; x-ray framing tube; RF, high-voltage raster-scan electronics; dual streaking electronics; versatile x-ray imager; and the vacuum test system and novel

vacuum interface between the vacuum chamber and the camera, which allows realistic imaging and spectroscopic experiments. The optical versatile imager was designed, constructed, and demonstrated. Software was developed for multi-imaging x-ray streak (MIXS) camera image processing and for use on the long-data-length recorder.

Figure 4 shows the new, advanced R&D platform that was built. Such a platform will provide a solid foundation for future research.

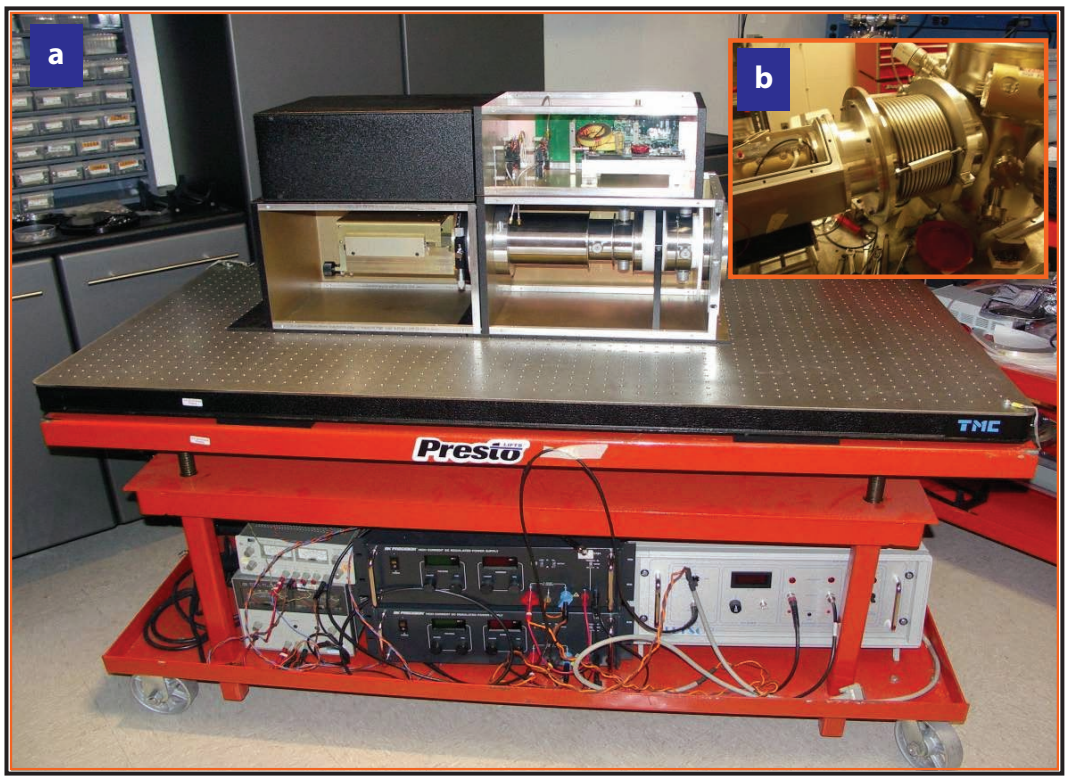

Figure 4. (a) The versatile x-ray imager on the optics table with power supplies below. (b) Illustration of the vacuum test system.

References

Sun, K.-X., R. Guzman, M. A. Karrick, M. LaFrancesca, L. MacNeil, D. Max, D. Ng, B. Nishimura, J. Richter, J. Yuhas, "Versatile, Higher Dimension X-ray Imager," *Nevada Test Site–Directed Research, Development, and Demonstration*, FY 2005, Bechtel Nevada/National Security Technologies, LLC, Las Vegas, Nevada, 2006, 359–370.

Sun, K.-X., M. LaFrancesca, R. Shellman, J. Yuhas, "Two-Dimensional, Long-Data-Length Transient Recorder (Phase II)," *Nevada Test Site–Directed Research, Development, and Demonstration*, FY 2005, Bechtel Nevada/National Security Technologies, LLC, Las Vegas, Nevada, 2006, 349–357.

NNSA/NA-116

Karen Callahan	(1)	Lucille Gentry	(1)	Jamileh Soudah	(1)

NNSA Service Center

Russel Edge	(1)	Julianne Levings	(1)

NNSA/NSO

Carol Shelton	(2)	Laura Tomlinson	(1)

NSTec

Dennis Barker	(1)	Howard Bender	(2)	Rob Buckles	(2)
John Ciucci	(1)	Nelson Cochrane	(1)	Ken Cooke	(1)
Jim Gatling	(1)	Steve Goldstein	(1)	Chris Hagen	(2)
A. C. Hollins	(1)	Jim Holt	(1)	Steve Iversen	(2)
Warnick Kernan	(2)	Bill Kost	(1)	Ping Lee	(1)
Wil Lewis	(1)	John Manning	(1)	Michael Martinez	(1)
Masafusa Nishimura	(1)	Brent Park	(1)	PIs	(1 ea)
Dave Post	(1)	Carson Riland	(1)	Bob Summers	(1)
Oliver Sweningsen	(1)	Tom Waltman	(1)	B.J. Willeford	(1)
Steve Younger	(1)				

LANL

Frank Cverna	(1)
LDRD Office	(1)
(ATTN: William Priedhorsky)	

LLNL

Larry Wiley	(1)
LDRD Office	(1)
(ATTN: William [Bill] Craig)	

SNL

Raymond Leeper	(1)
John Porter	(1)
LDRD Office	(1)
(ATTN: Hank Westrich)	

OSTI

Electronic copy	(1)

Resource Centers

RSL-Nellis	(1)	Technical Library	(1)

Nevada Test Site–Directed Research and Development
FY 2006 Report
DOE/NV/25946--247
Report Date: August 2007